PROCEEDINGS

ECCOMAS MSF 2021

5th International Conference on Multi-scale Computational Methods for Solids and Fluids

June 30 - July 2, 2021
Split, Croatia

Editors:
A. Ibrahimbegovic, M. Nikolić

ECCOMAS 2021 5th International Conference on Multi-Scale Computational Methods for Solids and Fluids

Adnan Ibrahimbegovic and Mijo Nikolić

CIP - Katalogizacija u publikaciji
Nacionalna i univerzitetska biblioteka
Bosne i Hercegovine, Sarajevo

531/532:004(063)(082)

INTERNATIONAL Conference on Multi-Scale Computational Methods for Solids and Fluids (5 ; 2021 ; Split)

ECCOMAS 2021 [Elektronski izvor] / 5th International Conference on Multi-Scale Computational Methods for Solids and Fluids, June 30 - July 2, 2021 Split, Croatia ; [editors] Adnan Ibrahimbegovic and Mijo Nikolić. - El. zbornik. - Sarajevo : Faculty of Civil Engineering = Građevinski fakultet Univerziteta, 2021

Način pristupa (URL): http://gf.unsa.ba/eccomas-msf-2021/. - Nasl. sa nasl. ekrana. - Opis izvora dana 9. 6. 2021.

ISBN 978-9958-638-66-4

COBISS.BH-ID 44416262

Organized by:
Faculty of Civil Engineering, University of Sarajevo, Bosnia-Herzegovina
Faculty of Civil Engineering, Architecture and Geodesy, University of Split, Croatia
University of Technology of Compiègne, Alliance Sorbonne University, Paris, France

ECCOMAS MSF 2021 Conference held:
June 30 - July 2, 2021, Split, Croatia

Editors:
Adnan Ibrahimbegovic, Mijo Nikolić

Publisher: Faculty of Civil Engineering, University of Sarajevo,
Patriotske lige 30, 71000 Sarajevo, Bosnia and Herzegovina

Electronic version link: http://gf.unsa.ba/eccomas-msf-2021/

Number of printed copies: 0

Date: June 2021

ECCOMAS MSF 2021

5th International Conference on Multi-scale Computational Methods for Solids and Fluids

June 20 – July 2, 2021, Split, Croatia

EDITORIAL

Adnan Ibrahimbegović[1,3,4], **Mijo Nikolić**[2]

[1]*Université de Technology Compiegne – Alliance Sorbonne Université, 60200 Compiegne, France, e-mail: adnan.ibrahimbegovic@utc.fr*
[2]*Faculty of Civil Engineering, Architecture and Geodesy, University of Split, 21000 Split, Croatia, e-mail: mijo.nikolic@gradst.hr*
[3]*Institut Universitaire de France, Paris, France*
[4]*Academy of Sciences and Arts of Bosnia and Herzegovina, 71000 Sarajevo, Bosnia and Herzegovina*

Abstract: ECCOMAS MSF 2021 is the fifth in the series of International Conferences focusing upon Computational Methods in Solids and Fluids, held every two years in different countries in Europe. Previous meeting have all been organized under umbrella of ECCOMAS, 'The European Community on Computational Methods in Applied Sciences', as the sponsor of ECCOMAS conference series. For this particular Conference, we have an additional sponsor from the host country: University of Split, from host country, Croatia. The institutions organizing ECCOMAS MSF 2021 are Faculties of Civil Engineering, Architecture and Geodesy in Split, Croatia and of Civil Engineering and of Mechanical Engineering of University of Sarajevo, B-H, in collaboration with University of Technology Compiegne, a member Alliance of Sorbonne University. The ECCOMAS MSF 2021 is held from June 30 to July 2, 2021 in Split, after the short course offered to young participants held from June 27 to 29, 2019. The Conference seeks to provide a platform for learning from some of the worlds' leading specialists in numerical methods, coming from different engineering disciplines and applied mathematics.

OBJECTIVES OF ECCOMAS MSF 2021 CONFERENCE

The main idea of this ECCOMAS MSF 2021 Conference is to examine recent advances in numerical methods in currently most active research domains, with applications to interface and/or interaction of Civil and Mechanical engineering and other pertinent disciplines. The multi-physics models and methods of this kind are often bridging the phenomena taking place at multiple scales in space and time, which ought to be placed in interaction or accounted for simultaneously in order to provide the most reliable results explanations. This class of problems calls for the development and combination of different modeling tools and computational methods in order to advance the field towards currently relevant industrial applications. A number of different schools have developed in various domains, both in engineering sciences and mathematics, with sometimes very little or no interaction between them. It is an explicit goal of this ECCOMAS MSF 2021 Conference to bring all the different communities together, in the truly open scientific spirit, and thus provide a sound basis for a fruitful exchange and cross-fertilization of ideas among them.

INTERNATIONAL SCIENTIFIC COMMITTEE

Nikolic Z., Croatia
Kojic M., Serbia
Kozulic V., Croatia,
Marovic P., Croatia,
Gotovac H., Croatia,
Trogrlic B., Croatia
Jajac N., Croatia
Ho Ba Tho M-C., France
Salsac A-V., France
Murín J., Slovakia
Filipovic N., Srbia
Dinkler D., Germany
De Vuyst F., France
Ouashine A., France
Perez Aparicio J.L., Spain
Demirdzic I., Bosnia and Herzegovina
Smoljanović H., Croatia

LOCAL ORGANIZING COMMITTEE

Conference Chairman: Prof. Adnan Ibrahimbegovic, UTC-Alliance Sorbonne University,
Conference Chairman: Prof. Mijo Nikolić, University of Split,
Honorary Co-Chairmen: Prof. Pavao Marović, Prof. Željana Nikolić, University of Split
University of Sarajevo & UTC Organizing Committee: Ms. Emina Hadzalić, Ms. Emina Hajdo, Mr. Ismar Imamović, Mr. Emir Karavelić

ECCOMAS MSF 2021 TOPICS AND DISTINGUISHED LECTURES

The ECCOMAS MSF 2021 Conference topics to be addressed concern not only 'classical' domains of Solid, Structural and Fluid Mechanics, but also a number of currently 'hot' domains, such as: Heterogeneous materials, Complex structures and systems, Material and structure failures, Smart structures and multi-physics coupling, Mechanics of porous media, Biological fluid-structure interaction, Turbulence, Model reduction, Stochastic processes, Uncertainty propagation, Industrial applications ...

The conference will regroup invited speakers: Jose L. Perez Aparicio (Polytechnic Valencia, Spain), Bostjan Brank (University of Ljubljana, Slovenia), Alvaro Luiz Gayoso de Azeredo Coutinho (University of Rio de Janeiro, Brazil), Dieter Dinkler (TU Braunschweig, Germany), Christian Hellmich (TU Vienna), Adnan Ibrahimbegović (UT Compiegne, France & ANU, BH), Ivica Kožar (University of Rijeka, Croatia), Pierre Ladeveze (ENS-Paris-Saclay, France), Nikolaos Limnios (UT Compiegne, France), Hermann Matthies (TU Braunschweig, Germany), Roger Ohayon (CNAM, France), Abdellatif Ouashine (UT Compiegne, France), Paulo M. Pimenta (University of Sao Paulo, Brazil), Patrizia Trovalusci (University Sapienza Rome, Italy), Florian De Vuyst (UT Compiegne, France). Each one will deliver a distinguished lecture giving overview of both current research in his fields and still open questions and explorations to come. The keynote and standard lectures of each of the conference days will address a number of issues concerning computational methods in wide variety of topics.

ECCOMAS MSF 2021 LIST OF MINI-SYMPOSIA

The following organized Mini-Symposia (containing 6 or more papers) are scheduled at the conference:

MS - Risk assessment and resilience estimation of civil engineering structures and systems (Organizers: Ž. Nikolić, Univ. Split, Croatia, E. Benvenuti, Univ. Ferrara, Italy, K. Beyer, EPFL, Switzerland, N. Ademović, Univ. Sarajevo, BH)

MS - Modeling of concrete and reinforced concrete structures. (Organizers: Ž. Nikolić, P. Marović, Univ. Split, Croatia)

MS - Experimental mechanics (Organizers: L. Krstulović-Opara, Univ. Split, Croatia, Z. Tomicević, Univ. Zagreb, Croatia, E. Karavelić, Univ. Sarajevo, BH)

MS - Modeling of fracture and failure of materials and structures (Organizers: M. Nikolić, Univ. Split, Croatia, L. Skec, Univ. Rijeka, Croatia)

MS - Multiscale Modelling with Spline Functions: Numerical Algorithms and Applications in Computational Mechanics (Organizers: H. Gotovac, Univ. Split, Croatia, V. Kozulić, Univ. Split, Croatia)

MS - Advances and Applications in Combined Finite-Discrete Element Method (Organizers: H. Smoljanović, Univ. Split, Croatia, Ante Munjiza, Univ. Split, Croatia)

MS - Transient Problems and Fluid-structure Interaction (Organizers: M. Torlak, Univ. Sarajevo, BH, E. Džaferović, Univ. Sarajevo, BH)

MS - Modelling of Masonry Structures (Organizers: M. Hrasnica, Univ. Sarajevo, BH, S. Medić, Univ. Sarajevo, BH)

MS - Structures and Soil (Organizers: S. Dolarević, Univ. Sarajevo, BH, A. Skejić, Univ. Sarajevo, BH)

MS - Wrinkling, stability, dynamics and calibration of structural systems (Organizers: B. Brank, Univ. Ljubljana, Slovenia, M. Brojan, Univ. Ljubljana, Slovenia)

MS - Internal and External Flows (Organizers: A. Hasečić, Univ. Sarajevo, BH, E. Hadžalić, Univ. Sarajevo, BH)

MS - Advanced Analysis of Steel and Steel-Concrete Composite Structures (Organizers: I. Imamović, Univ. Sarajevo, BH, E. Hajdo, Univ. Sarajevo, BH, E. Mesić, Univ. Sarajevo, BH)

MS - Modeling Applications in Civil and Environmental Engineering (Organizers: Z. Milašinović and A. Serdarević, BH)

ECCOMAS MSF 2021 - PROGRAM AT GLANCE

ECCOMAS MSF Short Course: 9 a.m. – 6 p.m. from Sunday 27 to Tuesday 29 June 2021

Conference Registration:	4 p.m. – 7 p.m., on Tuesday June 29, 2021
	(FGAG = Civil Eng. Bldg., address: Ul. Matice hrvatske 15)
Distinguished Lectures MS:	9 a.m. – 6 p.m., Wednesday 30 June 2021
Keynote & Standard Lectures	9 a.m. – 6 p.m. Thursday 1 July 2021
Keynote & Standard Lectures	9 a.m. – 6 p.m. Friday 2 July 2021
	(FGAG = Civil Eng. Bldg., address: Ul. Matice hrvatske 15)
Conference Banquet:	7 p.m. Thursday Thursday 1 July 2021
	(FGAG = Civil Eng. Bldg., address: Ul. Matice hrvatske 15)

ECCOMAS MSF 2021 VENUES

FIG. 1 – **Faculty of Civil Engineering, Architecture and Geodesy = CIVIL ENG. BLDG. (Address : Ul. Matice hrvatske 15)**

Contents

1. DISTINGUISHED LECTURES

NUMERICAL PREDICTION OF THE HYDRODYNAMICS AND BEHAVIOUR OF A SHIP IN RESTRICTED WATER

Zhaoyuan HUANG, Abdellatif OUAHSINE , Dong DING

Sorbonne universités, Université de technologie de Compiègne, Laboratoire Roberval, Centre de Recherche Royallieu CS 60319 - 60205 Compiègne , France
zhaoyuan.huang@utc.fr, ouahsine@utc.fr, dong.ding@utc.fr

1. Introduction

In the more severely restricted river channels, due to the increased resistance, the speed of ships can even be reduced by up to 60%[1,2]. At the same time, the ships will be subjected to fluid pressure force in shallow water, resulting in trim and sinkage phenomena, referred to as the ship's squat, which greatly affects the maneuverability of ships in shallow water area[3,4]. There are many factors affecting ship motion in restricted waters: water depth, ship speed, river bank slope, etc., which require continuous and in-depth research[5].

Numerical methods, especially the Computational Fluid Dynamics (CFD) approach has become increasingly important and is now an indispensable part for ship dynamics research. The wave elevations of ship in restricted waterway was simulated to obtain the change law of ship waves. This study also aims to investigate the forward resistance and squat of ship and realize the prediction of ship's general behavior in restricted waterway through numerical simulation method.

2. Numerical models

2.1 Hydrodynamic model equations

The governing equations for mass and momentum conservation are given by

$$\frac{\partial \rho}{\partial t} + \nabla \cdot (\rho \boldsymbol{U}) = 0 \tag{1}$$

$$\frac{\partial \rho \boldsymbol{U}}{\partial t} + \nabla \cdot \left[\rho\left(U - U_g\right)\boldsymbol{U}\right] = -\nabla p_{rgh} - \boldsymbol{g} \cdot \boldsymbol{x}\nabla\rho + \nabla \cdot \left(\mu_{eff}\nabla \boldsymbol{U}\right) + (\nabla \boldsymbol{U}) \cdot \nabla \mu_{eff} + \boldsymbol{f}_\sigma \tag{2}$$

where $\boldsymbol{U}$ is the fluid velocity, ρ is the fluid density. $\boldsymbol{U_g}$ is the grid velocity taking into account the mesh motion. $p_{rgh} = p - p\boldsymbol{g} \cdot \boldsymbol{x}$ is a modified pressure, where $\boldsymbol{x}$ is the position vector, $\boldsymbol{g}$ is the gravity acceleration. $\mu_{eff} = \rho(\nu + \nu_t)$ denotes the effective dynamic viscosity, where ν and ν_t are the kinematic and eddy viscosities respectively. ν_t is obtained from a specific turbulence model.

$\boldsymbol{f}_\sigma$ is the surface tension term defined by:

$$\boldsymbol{f}_\sigma = \sigma\kappa\nabla\alpha_p \tag{3}$$

where α is the surface tension coefficient ($0.07 kg/s^2$ in water), κ is the curvature of the free surface interface, given by $\kappa = -\nabla \cdot (\nabla\alpha_p/|\nabla\alpha_p|)$.

In this study, the SST (Shear Stress Transport) $k-\omega$ model is adopted. It is a two-equation eddy-viscosity model which combines the advantages of the $k-\varepsilon$ and $k-\omega$ models. The $k-\omega$ model is used in the boundary layer and the $k-\varepsilon$ model in the free stream flow. Thereby it is less sensitive to free stream conditions and has better performance predicting the flow separation and reattachment.

2.2 Multiphase model equations

The VOF (Volume-of-fluid) approach is used for multiphase flow simulations, together with an artificial compression technique. The transport equation reads:

$$\frac{\partial \alpha_p}{\partial t} + \nabla \cdot \left[\alpha_p (\boldsymbol{U} - \boldsymbol{U}_g)\right] + \nabla \cdot \left[\alpha_p (1 - \alpha_p)\boldsymbol{U}_r\right] = 0 \quad (4)$$

where $0 \leq \alpha_p \leq 1$ is the phase fraction. $\alpha_p = 0$ and $\alpha_p = 1$ correspond to gas and liquid respectively. $\boldsymbol{U}_g$ is the grid velocity taking into account the mesh. $\boldsymbol{U} = \alpha_p \boldsymbol{U}_\omega + (1 - \alpha_p)\boldsymbol{U}_\alpha$ is the effective velocity, and $\boldsymbol{U}_r = \boldsymbol{U}_\omega - \boldsymbol{U}_a$ is the relative velocity between the two phases, where the subscripts 'ω' and 'a' denote water and air respectively. The density and dynamic viscosity are calculated according to the following equations

$$\rho = \alpha_p \rho_\omega + (1 - \alpha_p)\rho_a \quad (5)$$

$$\mu = \alpha_p \mu_\omega + (1 - \alpha_p)\mu_a \quad (6)$$

2.3 Channel geometry

This study uses a trapezoidal channel. By controlling different channel widths and depths, different restriction of channel can be realized. The cross-sectional view of the channel and ship is shown in Figure 1, three probes can capture three transects of waves. And the parameters of different channels are shown in Table 1 and Table 2.

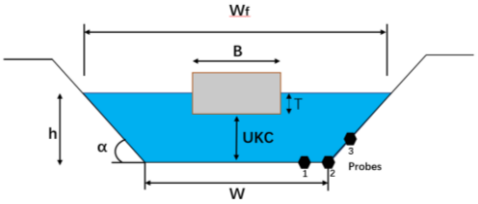

Figure 1. Channel section model and probes locations

Table1. Channel cross-sections for varying width and bank slope, with fixed T=3m, h=4.5m and W=36m

Studied cases	Width W_f	Slope tanα
Case 1	36m	∞
Case 2	54m	1/2
Case 3	63m	1/3
Case4	72m	1/4
Case 5	81m	1/5

Table2. Channel cross-sections for varying depth, with fixed W_f=54m, W=36m and T=3m

Studied cases	Depth h
Case 1	4.5m
Case 2	6m
Case 3	8m
Case 4	11m

3 Numerical results

3.1 Wave elevation analysis

The wave elevation coutours for various channels are shown in figure 2. Extracted wave elevations in different width channels at three different distances (y is the distance from the sailing line, y=1m,1.5m and 2m) from the hull are shown in the figure3-a. It can be seen that wave height at the ship's location has dropped. In restricted channels, as the distance from the ship increases, the wave's fluctuations gradually become smoother. Also, with the increase of tanα, the width of the waterway decreases, which has the consequences of increasing the degree of restriction, that will lead to increased fluctuations in wave elevation.

Wave elevations at three different distances from the hull for different channel widths are shown in figure3-b. It can be seen that, whatever the distance from the ship's hull, the depth of the channel clearly influences the variation in the wave elevation amplitude.

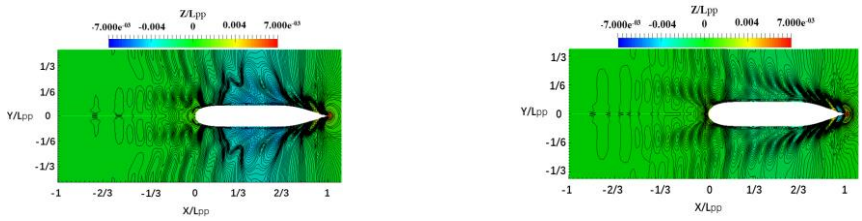

(a) (b)

Figure 2. Wave elevation contours for various channels. (a) tanα=1/3, h/T=1.5; (b) tanα=1/2, h/T=2.

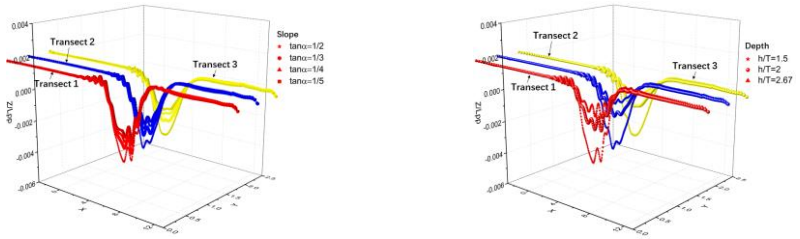

(a) (b)

Figure 3. Wave elevations along three transects for various (a) width and (b) depth of the channel.

3.2 Advancing resistance, sinkage and trim

Due to the blockage effects in the flow, hydrodynamic performances of a ship in confined waterways are significantly different from those in deep waters.

Firstly, a set of data is selected for comparison with experimental data in the same environment (the experimental data comes from the CNR [6]). The comparison results are shown in Figure 4, and the simulation results are in good agreement with the experimental results.

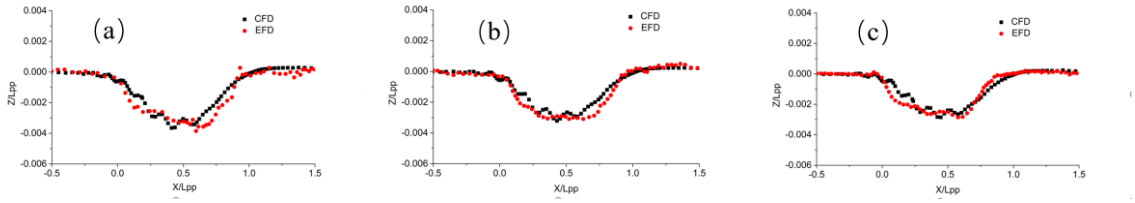

Figure 4. Comparison between numerical and experimental results for various slope of the channel. (a) tanα=1/3;(b) tanα=1/4 and (c) tanα=1/5.

In restricted waters, due to the hydrodynamic effects of river banks and limited water depth, it will affect ship resistance. The cases of ships in different restricted waters are calculated to characterize their properties. It can be seen that the effect of the width of channel on the ship's C_T in Figure 5-a and the effect of the depth of channel on the ship's C_T in Figure 5-b. Where $C_T = \frac{R_T}{\frac{1}{2}\rho U^2 s_{w0}}$ is the total resistance coefficient and s_{w0} is the wetted area of ship. The ship's C_T increases with increasing channel width and decreases with increasing water depth. It's more regularity.

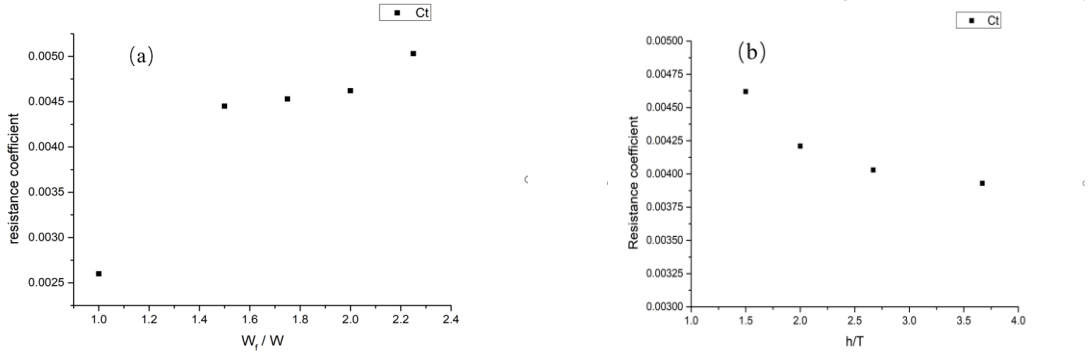

Figure 5. Total resistance coefficients against (a) W_f/W and (b) h/T.

The squat effect, a combination of trim and sinkage, is the hydrodynamic phenomenon when a vessel is navigated in waters with limited width and depth and the flow around the vessel is altered, causing a return current and depression of water level. This phenomenon is caused when water that

should normally flow under the hull encounters resistance due to the close proximity of the hull to the seabed. In this study, the effect of the dynamic squat on ship hydrodynamics is investigated by coupling an Unsteady Reynolds-Averaged Navier-Stokes (URANS) based CFD solver with dynamic mesh method.

Figures 7 and 8 respectively show the influence of different river channels on ship sinkage and trim. It can be clearly found that as the depth of the river increases, the squat phenomenon of the ship is suppressed, and the sinkage and trim of the ship are slightly reduced. Similarly, increasing the width of the river channel will also reduce the ship's squat phenomenon.

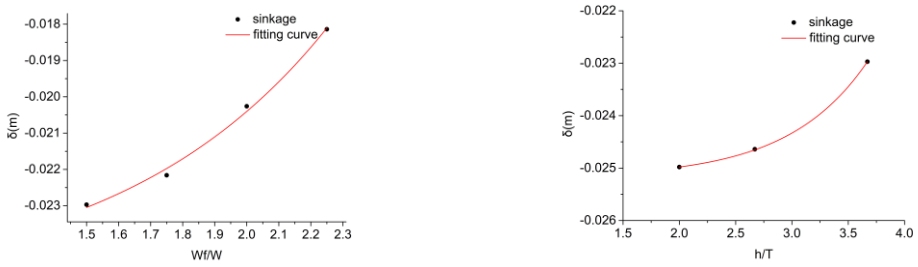

Figure 6. Sinkage(δ) against W_f/W and h/T.

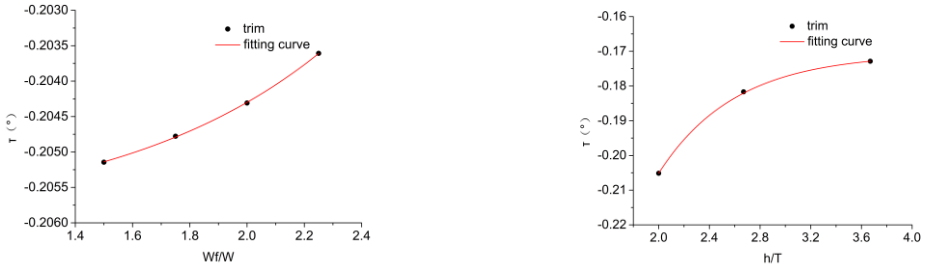

Figure 7. Trim(τ) against W_f/W and h/T.

4 Conclusion

A 3-D numerical model based on the Navier-Stokes equations and the SST $k-\omega$ turbulence model has been used to simulate the ship hydrodynamics in restricted waterway. The comparison between numerical and experimental results shows that this model predicts accurately the general hydrodynamics behavior of the ship. The results show that the ship resistance increases with increasing channel width and decreasing channel depth. By analyzing the sinkage and trim of ship in various restricted waters , the results also show that as the width and depth of the channel increases, the squat effect of the ship can effectively be reduced.

References

[1] Du, P., Ouahsine, A., Sergent, P., & Hu, H. (2020). Resistance and wave characterizations of inland vessels in the fully-confined waterway. *Ocean Engineering*, *210*, 107580.

[2] Tezdogan, T., Incecik, A., & Turan, O. (2016). A numerical investigation of the squat and resistance of ships advancing through a canal using CFD. *Journal of marine science and technology*, *21*(1), 86-101.

[3] Linde, F., Ouahsine, A., Huybrechts, N., & Sergent, P. (2017). Three-dimensional numerical simulation of ship resistance in restricted waterways: effect of ship sinkage and channel restriction. *Journal of Waterway, Port, Coastal, and Ocean Engineering*, *143*(1), 06016003.

[4] Ji, S.C., Ouahsine, A., Smaoui, H., & Sergent, P. (2014). 3D Modeling of sediment movement by ships-generated wakes in confined shipping channel. *International Journal of Sediment Research*, *29*(1), 49-58.

[5] International Towing Tank Conference Maneuvering Committee. (2014). *27th International Towing Tank Conference(ITTC)*, Copenhagen, Denmark.

[6] CNR (Compagnie nationale du Rhône). (2014). Étude des ondes de batillage sur modèle physique au 1/30. Phase 2 : Influence de l'inclinaison du talus sur les ondes de batillage (2/1,3/1,4/1,5/1)[R]. *Laboratoire d'Hydraulique et d'Essais de Matériaux, C753-DLLAB* 077997-853, France .

SCALE COARSENING STOCHASTIC MODEL REDUCTION FOR FAILURE MECHANICS

Adnan Ibrahimbegovic[1,2,3]

[1] UTC – Alliance Sorbonne Universite, France, adnan.ibrahimbegovic@utc.fr
[2] IUF – Institut Universitaire de France
[3] ANUBiH – Akademija Nauka i Umjetnosti BiH / UNSA, BiH

In this paper we deal with constructing best possible scale bridging when passing the detailed information on failure mechanics provided by the meso-scale plasticity model towards the corresponding reduced model at macro-scale. This is accomplished by using Bayesian inference resulting with the probability distribution of reduced model parameters represented as random fields. Such a technique, normally used to find an optimal scheme for data compression in a dynamic analysis of sequence of data, is here recast as the optimal scheme for scale bridging in order to provide reduced model that is capable of providing the best representation for the quantity of interest. The procedure is first developed for concrete meso-scale model (see [1]), for the case when response is not only governed by elasticity, but also by plasticity with hardening typical of fracture process zone and by plasticity with softening typical of localized failure mode. We show that the optimal macro-scale model is not necessarily the same for each phase of inelastic response. Yet, we also show how to combine them all together at the level of a particular finite element with enhanced predictive properties.

We discuss in detail the model reduction for a macro-scale concrete model that will have the local (point-wise) plasticity criterion for fracture process zone with parameters defined as random variables, along with the embedded-discontinuity finite element localized failure criterion with parameters also defined as random variables. The reinforced bars or short fibers can also be included within an enriched version of the proposed framework for localized failure (see [2]).

We consider two sources of uncertainty in development of this scale bridging: i) uncertainties in the choice of reduced model macro-scale parameters and ii) uncertainties in the microstructure of meso-scale model. For former source of uncertainty, the proposed approach applied to fixed microstructure but with different loading programs. In elastic regime, this merely confirms the standard homogenization-type results for material properties governing elastic response. The real value of the proposed approach is revealed in handling plastic hardening and localized softening response phase, given the most adequate choices for the distance function measuring the scale separation. For latter source of uncertainty with different realization of microstructure, the proposed approach indicates that, as far as elastic response is concerned, the concrete is statistically very close to isotropic material. A more exciting result is again revealed by the proposed approach in plastic hardening and localized failure regimes indicating the sensitivity of computed probability distribution for random variables corresponding to inelastic response macro-scale model parameters.

Three different methods for Bayesian inference have been tested and compared in the proposed approach, with each unknown parameter of reduced model represented as a random field, which can further be reduced to random variables by functional approximation (see [3]). Such a description has two constituents, the measurable function and the measure. One method (MCMC) is identified as updating the measure, whereas the other two methods (EnKF and PceKF) change the measurable

function. We formulate both groups of methods as functional approximation of stochastic problems, and introduce especially in combination with the second group of methods a new procedure that does not need any sampling, hence works completely deterministically. It also seems to be the fastest and more reliable when compared with other methods [4]. These findings thus extend what we have already shown in somewhat simpler setting (see [5, 6]) that it also works for highly nonlinear non-smooth problems with non-Gaussian measures.

Acknowledgements: This work is funded by ANR and DFG (project SELF-TUM) and by IUF Institut Universitaire de France (Senior Member appointment). I also acknowledge numerous fruitful discussions on the subject with H.G. Matthies, E. Karavelic, M. Nikolic, M.S. Sarfaraz, B. Rosic.

References

[1] E. Karavelic, M. Nikolic, A. Ibrahimbegovic, A. Kurtovic, '*Concrete meso-scale model with full set of 3D failure modes with random distribution of aggregate and cement phase. Part I: Formulation and numerical implementation*', Comp. Methods Appl. Mech. Eng., 344, 1050-1072, (2019)
[2] T. Rukavina, A. Ibrahimbegovic, I. Kozar, '*Fiber reinforced brittle material fracture models capable of capturing complete set of failure modes including complete fiber pull-out*', Comp. Methods Appl. Mech. Eng., 355, 157-192, (2019), (2019)
[3] H. Matthies, E. Zander, B. Rosic, A. Litvinenko, O. Pajonk, '*Inverse problems in Bayesian setting*', in (ed. A. Ibrahimbegovic) '*Computational Methods for Solids and Fluids: Multiscale Analysis, Probability Aspects and Model Reduction*', Springer, 245-286, (2016)
[4] A. Ibrahimbegovic, H.G. Matthies, E. Karavelic '*Reduced model of macro-scale stochastic plasticity identification by Bayesian inference in application to quasi-brittle failure of concrete*', Comp. Methods Appl. Mech. Eng., in press, (2020)
[5] S.M. Sarfaraz, B. Rosic, H. Matthies, A. Ibrahimbegovic, '*Stochastic Upscaling via Linear Bayesian Updating*', Coupled Systems Mechanics, 7, 211-231, (2018)
[6] Sarfaraz M.S., B. Rosic, H.G. Matthies, A. Ibrahimbegovic, '*Bayesian stochastic multi-scale analysis via energy consideration*', Advanced Model. Simulation Eng. Science, 7, 50-85, (2020)

ON (BAYESIAN) FINITE ELEMENT MODEL UPDATING OF CIVIL ENGINEERING STRUCTURES BY USING MODAL FEATURES

Blaž Kurent[1], Noémi Friedman[2], Boštjan Brank[3]

[1] University of Ljubljana, Faculty of Civil and Geodetic Engineering, Slovenia, bkurent@fgg.uni-lj.si
[2] Institute for Computer Science and Control, Budapest, Hungary, n.friedman@ilab.sztaki.hu
[3] University of Ljubljana, Faculty of Civil and Geodetic Engineering, Slovenia, bbrank@fgg.uni-lj.si

The assessment of the dynamic characteristics – such as natural frequencies, mode shapes, and modal damping ratios – of existing civil engineering structures by performing in-situ measurements has become an appealing research worldwide, see e.g. [1,2,4] and references therein. With the help of the in situ measurements, which may be based either on ambient or forced vibrations, a corresponding high-fidelity finite element model can be developed. In the herein presented framework, the vibration measurements are not only used for an estimation of the dynamic characteristics of an existing civil engineering structure but also for an update of the corresponding finite element model. The new, updated (i.e. calibrated) finite element model can be useful for checking the assumptions of the structural design, for examination of the assumptions adopted when creating the initial (i.e. the best-engineering-judgement) finite element model, and for enabling more accurate predictions of the response of the considered structure under various loading conditions. The calibrated model can also be used for assessing the suitability of different numerical models that may be considered for the given structure, or can serve as a representative model for the structural condition at the time of measurements, which can be further applied for structural health monitoring purposes, see e.g. [2].

As for the in-situ measurements, for civil engineering structures usually output-only ambient vibration tests (AVT) are performed. Such tests measure structural response due to unmeasured ambient excitations, which vary with time, and consequently the related estimates of the dynamic characteristics may vary from one data block of measurements to another. On the other hand, in an input-output modal testing, both the excitation force (that is applied by shakers) and the corresponding dynamic response are measured, which allows to estimate frequency response functions (FRFs) and use them to get more reliable estimation of the as-built structural modal properties in comparison with AVT, see e.g. [3]. In particular, using the FRF-based methodology, the properties of the higher modes of vibration are much easier to measure and investigate. However, the FRF based methods have been seldom applied for civil engineering structures. One reason are the practical difficulties that are related to performing forced excitation of a structure without damaging it, and an other reason is the complication in measuring responses simultaneously across usually large and/or tall civil engineering structures. The later difficulty can be solved by using synchronised wireless accelerometers, see e.g. [3].

Before the finite element model updating is performed, the experimental and the numerical vibration modes need to be correlated, where usually a larger (i.e. numerical) model is reduced to match a smaller model of the experimental data, see e.g. [4]. An important part of the model updating is a judicious choice of the parameters of the model that is to be calibrated. In this step sensitivity analysis can play a crucial role. A deterministic model updating is done by calibrating the chosen parameters such way that the finite element analysis gives a best fit to the measured dynamic characteristics in the sense of some metric, defined by a suitable cost function. This classical optimization procedure, is often easier to perform and demands much less computation time than the Bayesian updating.

The probabilistic framework of Bayesian updating [5,6,7] though can take into account the uncertainties of both the measurements and the model inputs by modeling these uncertainties in the form of probability distributions. With such procedure, instead of finding one deterministic value − a local minimum of some predefined cost function − we compute the conditional probability distribution of our model inputs given the measured value of the modal properties. The resulted updated stochastic finite element model is much more informative than the model that we get from a local minimum point.

For determining the Bayesian posterior distribution of the input parameters, we sample from it using the Markov Chain Monte Carlo (MCMC) method. The procedure requires a large number of deterministic solver calls of the finite element model, which may lead to prohibitively large computational times when one forward analysis of a large and/or tall civil engineering structure takes several minutes. The computational effort can be reduced by constructing a surrogate model (e.g. by general Polynomial Chaos Expansion [8]) for frequencies and mode shapes. However, creating a surrogate model for mode shapes may turn to be a challenging task, because the (higher-order) mode shapes typically rearrange for each new set of the values of updating parameters, and correlation of the mode shapes becomes difficult. Keeping track of eigenfrequency switching may be further complicated when the experimental data have spatial aliasing because the sensors did not capture enough motion of the structure.

In the talk, we will report about our experience with the application of deterministic and Bayesian finite element model updating for civil engineering structures. We have been involved during the past years into a European campaign related to the identification of the dynamic properties of existing tall timber buildings [9]. Therefore, we will present, as a study case, the deterministic and the Bayesian finite element model updating, based on modal features, of the seven-storey building from Glasgow, called Yoker, which is completely made of cross-laminated timber panels. The forced vibration testing of the Yoker building in operation, which was performed by the group of prof. A. Pavic from the University of Exeter, resulted in high-quality experimental data for eight vibration modes, among which the first six and the first five were used for the deterministic (see [10]) and Bayesian finite element model updating, respectively. The results of the deterministic and Bayesian finite element model updating will be presented and the strategies for Bayesian updating incorporating the measured modal properties will be discussed.

Acknowledgements
The support of ERA-NET Cofund Forest Value (DynaTTB project) and the corresponding funding body (Ministry of Education, Science and Sport of the Republic of Slovenia) is gratefully acknowledged. We also acknowledge the financial support of the Slovenian Research Agency (J2-2490) and the Hungarian National Research, Development and Innovation Office (SNN 134368).

References
[1] C. Argyris, C. Papadimitriou, P. Panetsos, P. Tsopelas. *Bayesian Model-Updating Using Features of Modal Data: Application to the Metsovo Bridge*, Sensor and Actuator Networks, 9,27, 2020.
[2] Y. Huang, C. Shao, B. Wu, J. L. Beck, H. Li. *State-of-the-art review on Bayesian inference in structural system identification and damage assessment*, Advances in Structural Engineering, 22(6) 1329–1351, 2019.
[3] W.K. Ao, A. Pavic. *FRF-based modal testing of sway modes using OCXO synchronised accelerometers for simultaneous force and response measurements*, Eurodyn 2020 Conference (online).
[4] N.M.M. Maia, J.M.M. Silva e Silva (eds.), *Theoretical and experimental modal analysis*, Wiley, 1997.
[5] C. Pepi, M. Gioffré, M.D. Grigoriu, H.G. Matthies. *Bayesian updating of cable stayed footbridge model parameters using dynamic measurements*, Eccomas Proceedia UNCECOMP, 330-342, 2019.
[6] H.G. Matthies, E. Zander, B.V Rosić. et al. *Parameter estimation via conditional expectation: a Bayesian inversion*. Adv. Model. and Simul. in Eng. Sci. 3, 24. https://doi.org/10.1186/s40323-016-0075-7, 2016.

[7] N. Friedman, C. Zoccarato, E. Zander, and H. G. Matthies. *A Worked-out Example of Surrogate Based Bayesian Parameter and Field Identification Methods*. Under print, accepted for the chapter in CRC Press Taylor & Francis Group, ed. Juan Chiachio Ruano, Shankar Sankararaman, Manuel Chiachio Ruano, Bayesian inverse problems: Fundamentals and Engineering Applications., 2021
[8] D. Xiu, G. E. Karniadakis *The Wiener–Askey polynomial chaos for stochastic differential equations*. In: SIAM journal on scientific computing 24.2, pp. 619–644., 2002.
[9] R. Abrahamsen, et al. *Dynamic response of tall timber buildings under service load - the DynaTTB research program*. Eurodyn 2020 Conference (online).
[10] B. Kurent, B. Brank, W.K. Ao. *Model updating of seven-storey cross laminated timber building designed on frequency-response-functions-based modal testing*, Structure and Infrastructure Engineering, 2021.

MODELING AND NUMERICAL INVESTIGATION OF THE MICROSCOPIC BEHAVIOUR OF CONCRETE

Dieter Dinkler [1], Christian Flack [2], Felix Ockelmann [3]

[1 2 3] Institute of Structural Analysis @ Technische Universität Braunschweig

1. Motivation

Concrete and its reinforcement are the most important materials for civil engineering constructions. The design of reinforced concrete is well established, since it deals with stiffnesses and failure loads on the macroscopic scale of cross sections of beams, slabs and shells. Nonetheless, the mathematical modeling und the description of the processes on the scales beneath are of general interest, because they give hints for a better understanding and an optimization of the overall structural behavior. The modeling of the processes on the different scales has to take into account different constraints as the geometry of the components and the interaction of processes as deformation, cracking, diffusion of substances and chemical reactions. Furthermore, due to the geometrical complexity of the structure, different discretization methods can be applied to describe the processes of interest. Fig 1 shows on the right the macroscopic scale with a certain distribution of cracks. Here, the continuum mechanics approach with smeared properties of the material is in general a sufficient modeling for the design of structures, since processes on the scales below could be described by means of internal variables. In the middle of fig. 1 the micro-scale gives insight in the arrangement of aggregates, cement-stone and pores which is hardly a continuum, and needs another modeling approach. On the left, the nano scale needs a complete different description, because of of the cristal-needles as a product of chemical reactions during the hardening of concrete.

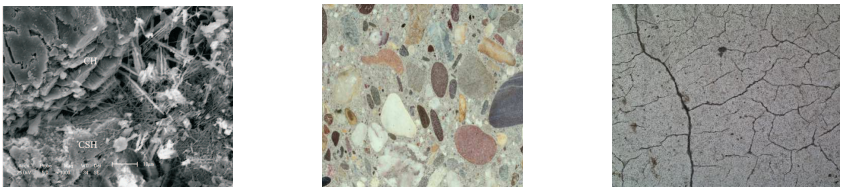

Figure 1: Concrete structure on the nano-, micro- and macro-scale

The aim of the paper is to establish a model, which is able to describe physical and chemical processes and its interaction beneath the macroscopic level in order to get a better understanding of the properties of concrete on the macroscopic level. Thus, the modeling of the concrete behavior on the meso- and micro-scale has to integrate thermo-mechanical and transport processes and chemical reactions, if the hardening of early concrete and the damage of aged concrete under loading conditions are of intererest.

Usually, the governing equations on the macroscopic scale are applied to describe the processes on the micro-scale, which are discretized by means of the finite element method. This may lead to problems, since the solution of the governing equations of the continuum mechanics approach show singularities, if corners or cracks are taken into account, where an extension of the equations and very fine meshes are needed. To overcome these problems localisation of strains are described with gradient methods or with phase-field mothods. Nonetheless, the question arise, whether the equations of continuum mechanics

and the discretization with the finite element method is a proper approach to describe the processes on the microscopic scale, if the pore structure and other discontinuities are essential. Here, the discrete element method offers advantages, since it can describe the grading curve of the material by means of particles, which are connected by springs and dampers.

2. Discrete element modeling of deformation-processes in concrete

In contrast to the continuum approach, the discrete element method is a framework to describe different components by means of different particles. The method is originally developed for granular media by *Cundall and Strack* [1] but can be applied to the discretization of other processes as well. Here, the motion of the particles is described by displacements and rotations with respect to the space dimensions, and the deformation behavior and the contact conditions between particles may be described by springs and viscous dampers, which properties could be distributed randomly over the structure.

In a first step, particles may have a regular pattern, the same size and normal and tangential springs between the particles, which properties are adapted to the macroscopical properties of concrete. Cracking of concrete is described by means of a failure criterion with respect to the elongation of the springs. As an example a slab is loaded under compression in one dimension, see figure 2, what leads to a failure due to shear. The experiment is documented by *Kupfer et. al.* [3] and the numerical investigation by *Ockelmann* [5], [6]. The failure pattern of the numerical simulation and the strain behavior are in good agreement with the experiment.

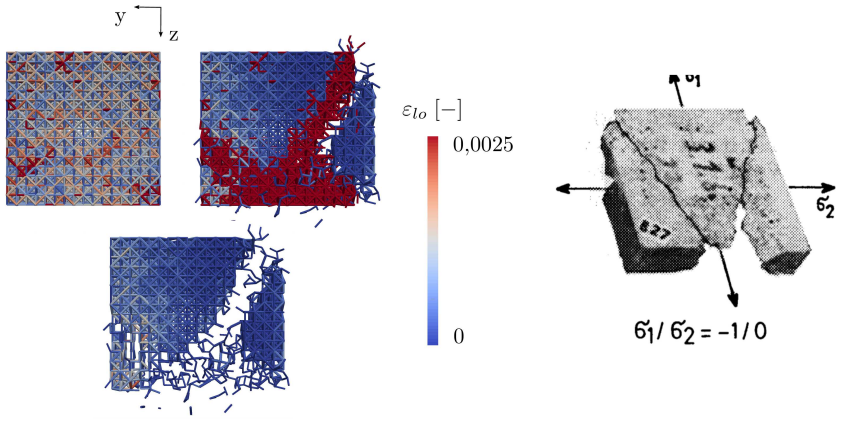

Figure 2: Discrete element simulation of a concrete slab under compression

In a further step the behavior of micro-fibres is taken into account. Micro-fibres are able to bridge a crack and stabilize the post-cracking behavior of concrete. As part of the model, randomly distributed micro-fibres are embedded and modeled by means of rheological models as well, whereat the softening due to the debonding of fibres is related to the crack-opening. Fig. 3 shows the deformation behavior of

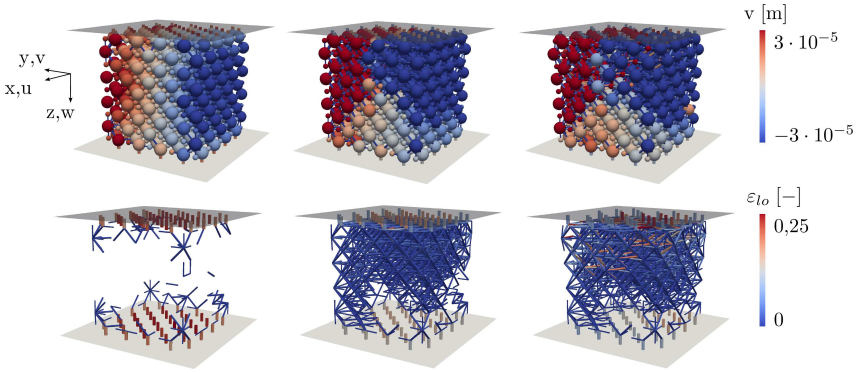

Figure 3: Discrete element simulation of a fibre reinforced UHPC-cube under compression

a concrete cube under compression. The horizontal displacements of the particles are shown in the upper

row, whereat the compression is increaesed from the left to the right. The lower row shows the activation of the fibres due the development of cracks. On the left only the fibres at the boundary constraints are activated. Increasing the compression leads to an overall crack pattern and thus to an activation of fibres all over the cube.

3. Multi-phase processes in concrete

A realistic description of the geometric structure of concrete is possible, if the grading curve is basis for the distribution and size of the particles. Fig. 4-left represents the irregular distribution of particles within a cube of 100 mm edge length, if about 10^4 particles of different size are filled into the cube by gravity. The volume between the particles is basis for the representation of the pore volume and is space for the hydration of cement and other chemical reactions. Since transport processes as heat conduction and diffusion of chemical substances have to be taken into account, the volume between the particles is represented by a pore-network, which was originally proposed by *Fatt* [2]. Figure 4 shows on the right hand side the corresponding pore-network.

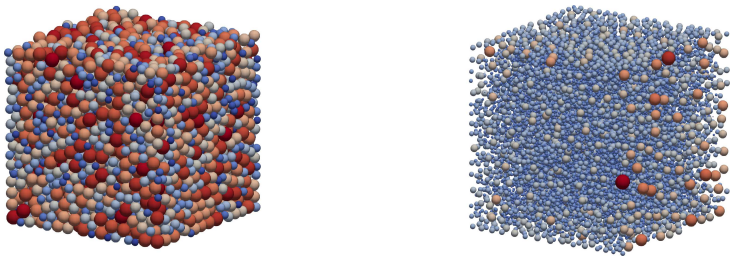

Figure 4: Irregular particle distribution due a real sieve curve and pore network of a concrete cube

Now different processes may be described within the particles, between particles and within the pore space. Figure 5 indicates which processes are taken into account.

- inelastic deformation between particles
- volume changing due to heat storage within the particles
- heat conduction between particles
- diffusion of substances between pores
- chemical reactions onto the surface of particles

All processes are coupled to each other in order to describe hydration and dehydration of cement, transport and reaction of chemical substances and of degradation of stiffness due to reactions.

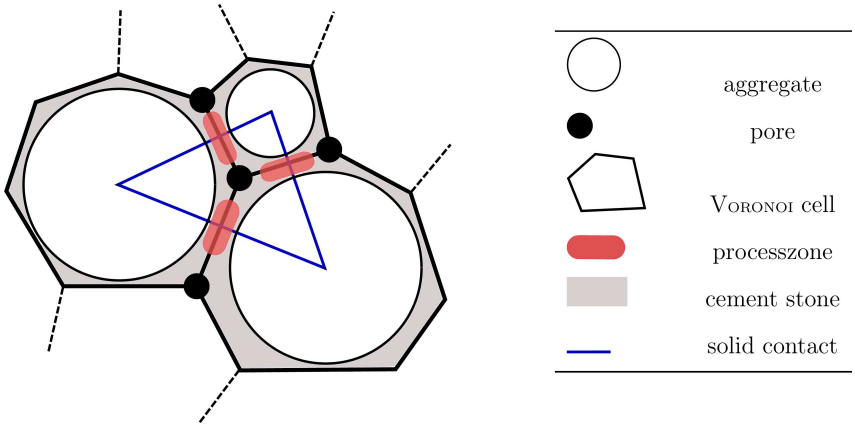

Figure 5: Process zones within the geometrical alignment of particles

4. Simulation of sulfate attack

In the following the sulfate attack of a concrete cube of 50mm edge length is simulated. The cube is placed into a solution of 0.5% sodium sulfate. The development of the concentration with respect to 730 days is shown in figure 6. The left hand side presents a characteristic sodium sulfate concentration within the pore-network of the cube and on the right hand side its temporal development. The mechanical properties of the concrete changes due to the chemical reactions onto the particles, which lead to a degradation of the stiffness and strength of the contact conditions.

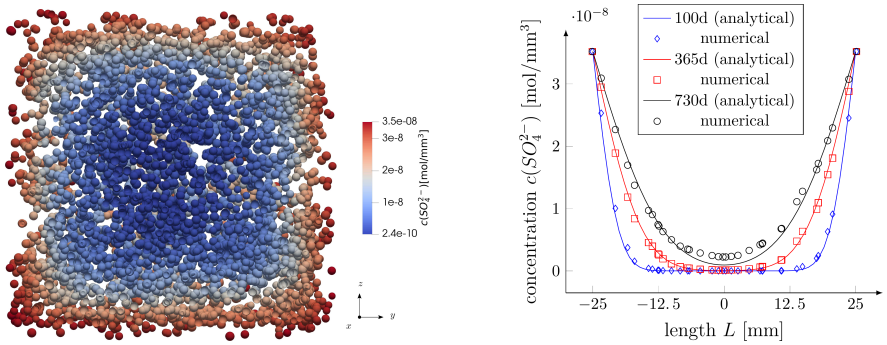

Figure 6: Sulfate concentration within the pores due to diffusion

Figure 7 shows the remaining and broken contact of the particles within the cube under compression after 100 and 365 days of rest within the solution. Although the failure pattern is similar to a cube without sulfate attack, the strength of the material is degradated by about 23% near the surface of the cube, what leads to substantial reduction of the overall limit load of the cube.

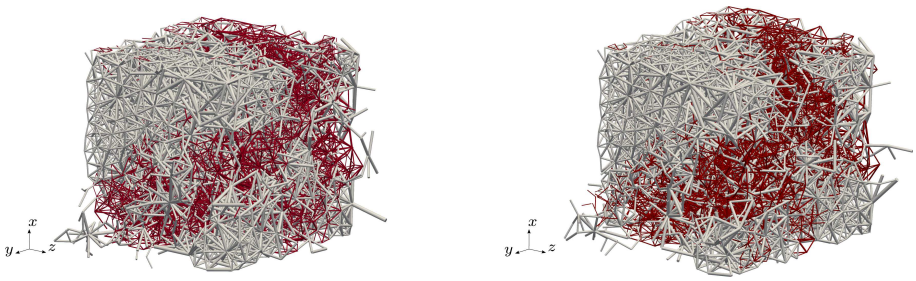

Figure 7: Fracture of concrete cube under compression after sulfate attack

Acknowledgement: The authors like to express their gratitude to the "Deutsche Forschungsgemeinschaft" and the substantial support of the work within the "Graduiertenkolleg 2075".

References

[1] P. A. Cundall, O. D. Strack: A discrete numerical model for granular assemblies. Geotechnique 29, pp. 47-65, 1979.

[2] I. Fatt: The Network Model of Porous Media. Transactions of the AIME 207, pp. 144-181, 1956.

[3] H. Kupfer, C. Zelger: The behavior of concrete under multi-axial short time loading with special emphasis to the two-axial loading. Construction and proving of a testing site for two-axial loading. in german, Ernst, 1973

[4] C. Flack: Multi-field modeling of concrete with the discrete element method. in german, PhD-Dissertation, Technische Universität Braunschweig, 2019.

[5] F. Ockelmann: Modeling and numerical analysis of concrete and fibre reinforced UHPC with the discrete element method. in german, PhD-Dissertation, Technische Universität Braunschweig, 2018.

[6] F. Ockelmann, D. Dinkler: A discrete element model for the investigation of the geometrically nonlinear behaviour of solids. Computational Particle Mechanics 5, pp. 335-344, 2018.

PHYSICS-INFORMED NONINTRUSIVE MODEL-ORDER REDUCTION OF PURE ADVECTION PROBLEMS

Florian De Vuyst [1], Pierre Villon [2]

[1] Université de Technologie de Compiègne, Alliance Sorbonne Université,
Laboratoire Mathématiques Appliquées de Compiègne, fdevuyst@utc.fr
[2] Université de Technologie de Compiègne, Alliance Sorbonne Université,
Laboratioire Roberval, pierre.villon@utc.fr

Many Engineering applications involve transport or convection processes. For convection-dominated problems, the physical transport equations have to be treated in a particular way in order to ensure both stability and accuracy of numerical solvers, using e.g. characteristics methods or upwinding differencing strategies.

For model-order reduction of such convection-dominated problems, standard ROM methods fail because of two reasons: i) the Kolmogorov N-width is generally high and ii) static reduced bases (like POD modes [1]) are not able to capture a moving front in a stable way.

In recent years, one can find contributions in the reduced-order modeling community in order to deal with advection problems, see for example [2, 3, 4, 5]. In this communication, we present a new computational nonintrusive ROM approach able to return very accurate and stable solutions of pure linear multidimensional advection problems involving discontinuous initial conditions [6]. We believe that the approach shows several advantages with possible extensions to convection-reaction-diffusion problems.

The so-called ROW (reduced-order warping) method include additional equations of 'space warping' due to the convection phenomenon. Then a reduced basis of warping modes is determined using a DMD-related method [7]. The resulting approach can be interpreted as a 'Physics-informed' artificial neural network (see [8] for example about this topic). Future works will address the case of multiscale problems involving a constitutive law at the small scale and dominated convection at the large scale.

References

[1] G. Berkooz, Ph. Holmes andd J. Lumley, The Proper Orthogonal Decomposition in the analysis of turbulent flows, Ann. Rev. Fluid Mech., vol. 25, pp. 539–575 (1993).

[2] M. Ohlberger, S. Rave, The method of freezing as a new tool for nonlinear reduced basis approximation of parameterized evolution equations, C.R. Mathematique, 351, 23-24 (2013), 901–906.

[3] A. Iollo and D. Lombardi, Advection modes by optimal mass transfer, Physc. Rev. E, 89(2), 022923 (2014).

[4] N. Cagniart, Y. Maday and B. Stamm, Model order reduction for problems with large convection effects. In *Contributions to Partial Differential Equations and Applications*, pages 131–150, Springer (2019).

[5] T. Taddei, A registration method for model order reduction: data compression and geometry reduction, SIAM J. Sci. Comput. 42(2), A597–A1027 (2020).

[6] F. De Vuyst, P. Villon, *A space warping method for model order reduction of linear hyperbolic advection problems*, Computers & Fluids, in revision, 2021.

[7] J.H. Tu, C.W. Rowley and D.M. Luchtenburg, On dynamic mode decomposition: theory and applications, J. Comp. Dynamics, AIMS, Vol. 1(2), pp. 391–421 (2014).

[8] L. Lu, X. Meng, Z. Mao and G.E. Karniadakis, DEEPXDE: a deep learning library for solving differential equations, ArXiv preprint, 2019.

ADVANCES IN THE SIMULATION OF GRAVITY CURRENTS

Gabriel Guerra[1], Malu Grave[2], Gabriel F. Barros[2], Romulo M. Silva[2], Tulio L. Santos[2], Linda Gesenhues[2], Jose J. Camata[3], Adriano M. A. Cortes[2], Renato N. Elias[2], Fernando A. Rochinha[2], Alvaro L.G.A. Coutinho[2]

[1] Fluminense Federal University, Brazil, gguerra@id.uff.br
[2] Federal University of Rio de Janeiro, Brazil, malugrave@nacad.ufrj.br, gabriel.barros@coc.ufrj.br, romulo.silva@coc.ufrj.br, tulioligneul@coc.ufrj.br, linda@nacad.ufrj.br, adrimacortes@gmail.com, rnelias@nacad.ufrj.br, faro@mecanica.ufrj.br, alvaro@nacad.ufrj.br
[3] Federal University of Juiz de Fora, Brazil, camata@ice.ufjf.br

Gravity currents consist of flows generated from small differences in the local fluid density, often known alternatively as density currents. The difference in density promotes a pressure gradient that drives the flow, resulting from local changes in salinity or temperature. Moreover, it can also be due to the presence of sediment particles in suspension. The particles can be carried for long distances, and eventually, they will settle, being responsible for sediment deposits generating geological formations of considerable interest for the oil and gas industry. Sedimentation and erosion promoted by particle-laden flows can mold the seabed, producing different geological structures such as canyons, dunes, and ripples. Indeed, gravity currents are present in many different contexts and occur naturally, and can be caused by human actions [1]. The first case that can be cited as examples are avalanches, deep water turbidity currents, and volcanic eruptions. On the other hand, industrial accidents can cause the dispersion of heavy gasses in the atmosphere that propagate through a forehead. Of particular interest here are turbidity currents, which carry sediments across the ocean floor and one of the principal mechanisms that lead to the formation of basins hosting oil reservoirs. Detailed modeling of this phenomenon may offer new insights to help geologists understand the deposition mechanisms and the final stratigraphic form of the reservoir. As turbidity currents propagate over the seafloor, they trigger the evolution of a host of topographical features through the processes of deposition and erosion, such as channels and sediment waves. The simulation of gravity and turbidity currents poses many challenges, and it is fundamentally a coupled multi-scale problem involving turbulence, fluid-structure interaction, non-Newtonian flows, to cite a few. Several models are possible. We will focus on shallow-water event-driven approaches to simulate turbidity currents at stratigraphic scale [2] and fully resolved three-dimensional simulations [3]. More advanced topics related to complex rheologies [4], morphological changes [5], data analysis and advanced visualization [6], and emerging scientific machine learning tools [7,8] will also be discussed.

References

[1] E. Meiburg, B. Kneller, Turbidity currents and their deposits. Annual Review of Fluid Mechanics 2010; 42:135–156.
[2] Túlio L. Santos, Alexandre A. O. Lopes, Alvaro L. G. A. Coutinho, A shallow water event-driven approach to simulate turbidity currents at stratigraphic scale, Int J Numer Meth Fluids. 2020;1–32.

[3] G. M. Guerra, S. Zio, JJ Camata, et al. Numerical simulation of particle-laden flows by the residual-based variational multiscale method. Int J Numer Methods Fluids. 2013;73(8):729-749.
[4] L. Gesenhues, JJ Camata, A. M. Côrtes, F. A. Rochinha, A. L. G. A. Coutinho, Finite element simulation of complex dense granular flows using a well-posed regularization of the μ (I)-rheology. Computers & Fluids, 188, 102-113, 2019.
[5] M. Grave, J. J. Camata, A. L. G. A. Coutinho, Residual-based variational multiscale 2D simulation of sediment transport with morphological changes. Computers & Fluids, 196, 104312, 2020.
[6] J. J. Camata, V. Silva, P. Valduriez, M. Mattoso, A. L. G. A. Coutinho, In situ visualization and data analysis for turbidity currents simulation. Computers & Geosciences, 110, 23-31, 2018.
[7] G. F. Barros, M. Grave, M., A. Viguerie, A. Reali, A., A. L. G. A. Coutinho. Dynamic Mode Decomposition in Adaptive Mesh Refinement and Coarsening Simulations. arXiv preprint arXiv:2104.14034, 2021.
[8] M. Raissi, A. Yazdani, G. E. Karniadakis, Hidden fluid mechanics: Learning velocity and pressure fields from flow visualizations, Science, 367(6481): 1026-1030, 2020.

EXPRESSING BEHAVIOURAL NON-UNIQUENESS BY STOCHASTIC SOLUTIONS

Hermann G. Matthies [1], Tymofiy Gerasimov [2], Ulrich Römer [2],
Andjelka Stanić [3], Jaroslav Vondřejc [2], Laura De Lorenzis [4]

[1] TU Braunschweig, Germany, h.matthies@tu-bs.de
[2] TU Braunschweig, Germany
[3] University of Twente, Netherlands
[4] ETH Zürich, Switzerland

There are settings where the seemingly same real situation leads to different behaviour, apparently caused by imperceptible random fluctuations of loads or actions, boundary or initial conditions, or material properties, etc. One such example is the propagation of cracks, which we will focus upon here. But similar phenomena occur widely also in other areas, where the mathematical description typically allows for multiple solutions, such as turbulence, buckling, etc., where it may be hard to see what controls the exact outcome.

Now what is desired is a way to capture the multitude of possible behaviours. For this we propose the concept of *stochastic solution*. This approach abandons the idea of a unique deterministic solution, the exact nature of which is controlled by unknown or imperceptible influences. The idea is to capture all possible outcomes together with their *probability of occurrence.*

This contribution will be largely based on situations investigated in references [1] and [2]. The subject is the propagation of cracks in a quasi-brittle solid. As cracking is a kind of softening phenomenon, in an energy formulation (e.g. [1]), this is mathematically connected with the minimisation of non-convex functionals, so that non-uniqueness is possible and not surprising. Some examples are shown in Fig. 1. These are computational results, but it is well known that similar phenomena may be observed in real-life situations or experiments. The computational results shown in Fig. 1 are modelled with a phase-field formulation [1], and the top and bottom row show different solutions for some crack-propagation problems.

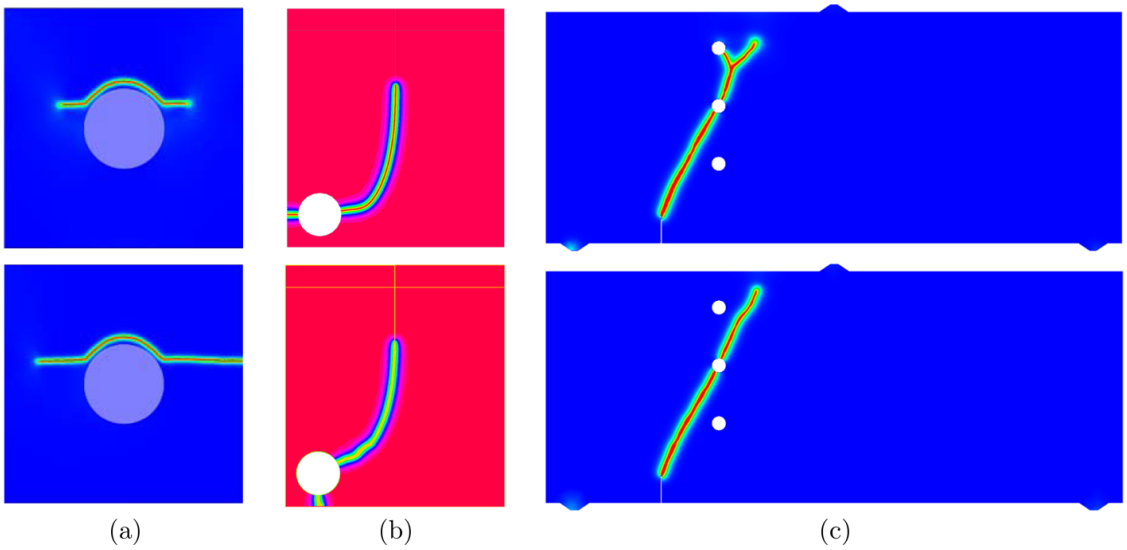

Figure 1: Non-uniqueness in crack propagation; from [1], where additional references may be found.

The difference between the two rows is either the computational mesh or the load step. The delamination of a fibre — in cross-section in a plane strain situation — from the surrounding matrix under vertical tension is shown in column a), where for the same load two different solutions have been computed. In column b) a square with a circular hole in the lower left corner and a pre-existing crack or notch from the middle of the top boundary in anti-plane shear is depicted, with the left and right parts of the top boundary pushed in opposite directions. This example will be used more extensively here. The crack, after starting from the tip of the notch, may travel to the hole, and then continue from the whole either at the side or at the bottom. In the third row c) one may see a three-point bending test of a specimen with three holes and a pre-existing crack or notch at the lower left edge, where the crack starts propagating. Again one may observe two different solutions, which either branch into the top hole or not.

Even in case the first crack appears at a completely random location, it may be still the case that, conditioned on that first crack, the further development is much more regular. One such example is shown in Fig. 2, it is the well known thermal shock experiment, here computationally modelled with embedded discontinuity elements [2]. A thin plate is brought into contact with a cold medium at the bottom edge. As the side and top edges are fixed, the strains from the thermal contraction result in tensile horizontal stresses. If the temperature difference is larger than ΔT_c, the cracks will develop. The

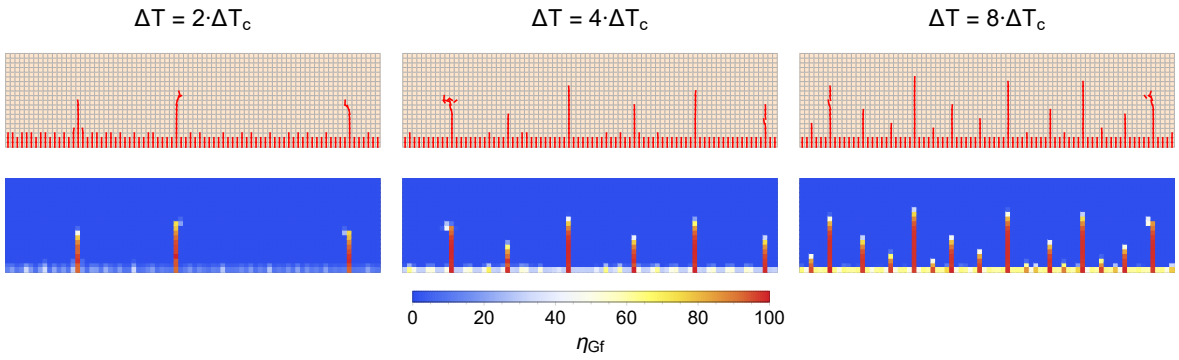

Figure 2: Cracks from thermal shock; from [2], where additional references may be found.

random appearance of the first crack is triggered by having a slight randomness in the critical stress at the lower boundary. The three columns show for three different temperature differences the mesh with the damaged elements in the top row and the percentage of the total fracture energy dissipated in the bottom row. One may glean from Fig. 2, particularly from the higher loading intensity, that a regular pattern of cracks of different depth develops, conditioned on the random appearance of the first crack.

What is desired, is a mathematical description which can capture such phenomena, and also the spatial dependencies and correlations, as well as the probabilities of the different solutions paths. We will show that random fields satisfy these demands. Of course, one has first to physically identify which or what kind of uncertain or unknown imperceptible influences control the occurrence of the different solutions. If such non-unique behaviour is also observed in real situations or experiments, we prefer to identify a physical quantity or quantities which are assumed to have slight but unknown variations, rather than numerical or computational parameters like mesh-width or load step size.

The so identified quantity is then modelled as a random variable or field of a certain strength $\eta > 0$. This will make the the solution a random field as well. We then look at the behaviour of these random field solutions in the limiting case $\eta \to 0$.

To show this on one example we go back to the square in anti-plane shear in column b) of Fig. 1. This model will be further investigated: in the first three columns in Fig. 3 different sample computations are shown, where the only difference are slight perturbations of the shape of the hole in the lower left corner. What is colour coded is the value of the phase-field [1], where for vanishing phase-field (blue) the material is completely intact, whereas for the phase field reaching unity (red), the material is completely damaged and a crack appears.

As one may glean from the nine samples in the first three columns of Fig. 3, there are essentially three very different crack paths. One situation is where the crack goes more or less straight down to

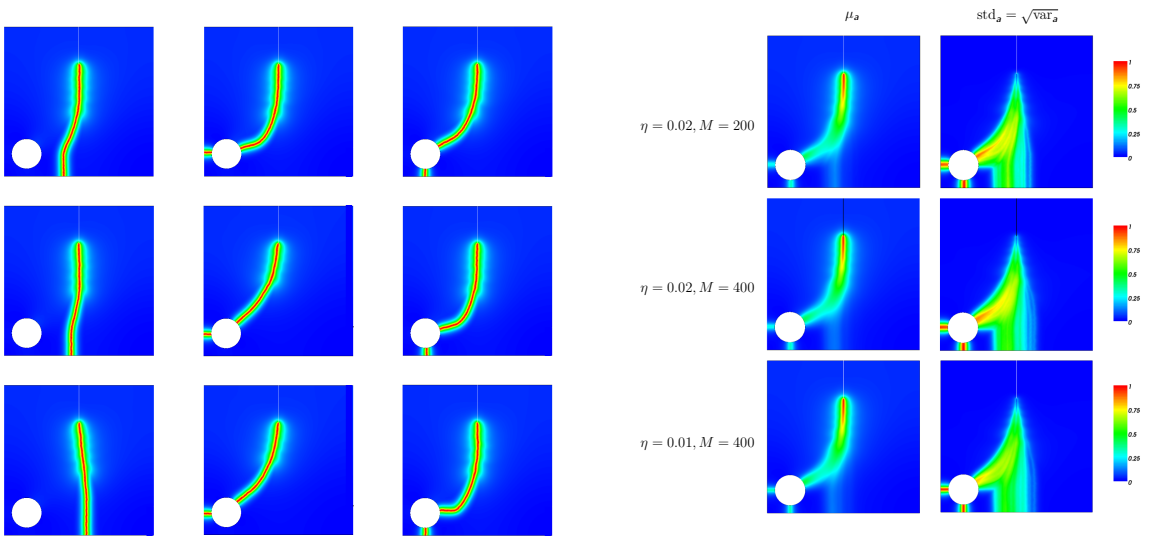

Figure 3: Non-unique cracks in the anti-plane shear example; from [1]. Samples with randomly perturbed hole in the first three columns. In the right two columns the mean and standard deviation of the random phase-field variable computed from M Monte Carlo samples for different perturbation strengths η.

the lower boundary, shown in the three samples in the first column. Another situation is when the crack propagates to the hole, and then continues on the opposite side of the hole towards the left boundary, depicted in the three samples in the second column. And the third situation is when the crack propagates to the hole and the goes from the hole downward towards the lower boundary, as may be seen in the three samples in the third column. From the right two columns of Fig. 3, which show the mean and standard deviation of the random phase-field, one may see that the computation stabilises for $\eta \to 0$ to a random field, from which then other quantities like probabilities and correlations of the different crack paths may be computed.

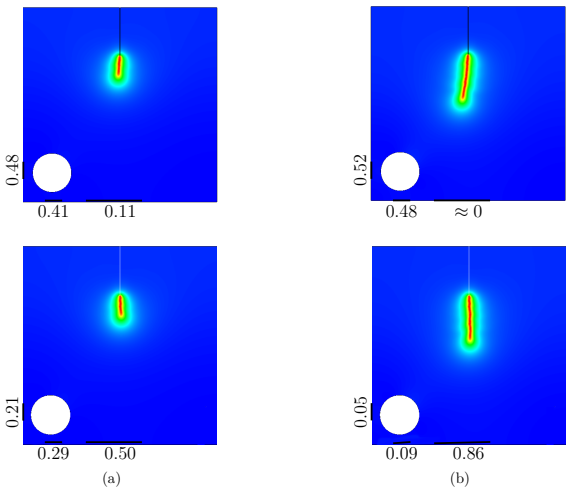

Figure 4: Crack exit conditional probabilities.

To demonstrate on this example what kind of results one may obtain from such a description, we show in Fig. 4 four examples where the crack path has advanced up to a certain point. From the previously mentioned random phase-field solution it is now possible to obtain the probability will reach a certain boundary, resp. that ultimately one of the previously mentioned three situations will be the final outcome. The resulting conditional probabilities have been marked on the boundaries of the four examples. Let us point out here one interesting observation, namely, as may be observed in the two columns of Fig. 4, slight variations of the pre-existing crack may lead to quite different outcomes for the conditional exit probabilities at a certain boundary.

References

[1] T Gerasimov, U Römer, J Vondřejc, HG Matthies, L De Lorenzis. *Stochastic phase-field modeling of brittle fracture: Computing multiple crack patterns and their probabilities*, Computer Methods in Applied Mechanics and Engineering, **372** (2020) 113353, doi: 10.1016/j.cma.2020.113353.

[2] A Stanić, B Brank, A Ibrahimbegović, HG Matthies. *Crack propagation simulation without crack tracking algorithm: embedded discontinuity formulation with incompatible modes*, arXiv:2012.09581 [math.NA], 2020.

INVERSE STOCHASTIC MODELS FOR FIBER REINFORCED CONCRETE

Ivica Kožar[1], Natalija Bede[1], Anton Bogdanić[1], Silvija Mrakovčić[1]

[1] Faculty of Civil Engineering University of Rijeka, ivica.kozar@gradri.uniri.hr
[1] Faculty of Civil Engineering University of Rijeka, natalija.bede@uniri.hr
[1] Faculty of Civil Engineering University of Rijeka, anton.bogdanic@gradri.uniri.hr
[1] Faculty of Civil Engineering University of Rijeka, silvija.mrakovcic@uniri.hr

Fiber-reinforced concrete (FRC) is a composite material where small fibers made from steel or polypropylene or similar material are embedded into concrete matrix. In a material model each constituent should be adequately described, especially the interface between the matrix and fibers that is determined with the 'bond-slip' law. 'Bond-slip' law describes relation between the force in a fiber and its displacement. A rather detailed investigation of bond-slip relation in steel FRC can be found in [1]. However, bond-slip model in [1] is deterministic and cannot explain variations in experimental results. In order to accommodate experimental results we have adopted stochastic model that is based on the 'fiber bundle representation'.

In the fiber bundle model (FBM) fibers are connected in parallel and have elastic and optionally, plastic properties. After reaching the peak load fiber either breaks down or degrades gradually, depending on the adopted model. Each fiber has slightly different material or geometric properties according to some probabilistic distribution, e.g., normal, uniform, cosine, etc. More details about FBM could be found in [2]. In our FBM the fiber peak tension load and the fiber area are described with the Gauss (normal) probability distribution. Each fiber has simple multi-linear load-displacement relation but observed as a bundle, they present a non-linear stochastic function. Behavior of each fiber is essential for material properties or bond-slip relation, as could be seen from [3].

The above description represents the so-called 'forward model' as it takes initial assumption about the material local properties (fibers) and produces the global material behavior, one that could be observed in a laboratory, e.g., load-displacement or bond-slip law. Often, we need the opposite: global material behavior has been known from the experiments and we would like to determine the local material properties, individual fiber properties in the case of FBM. This inverse relation is described as an 'inverse model', or 'inverse stochastic model' in the case of stochastic material properties. In the later case, we speak about estimation of the local material properties, like mean value and variance of parameters. Inverse models for various FBMs are described in [3], [4], [5] and [6]. The main ingredient of an inverse stochastic model is transformation of implicit equations into a product of simpler relations. The simplest fiber bundle model consists of only elastic fibers with stochastic cross-section area that break at tension force 'F_t'. The fiber bundle model relating the total force 'F' and displacement 'δ' reads

$$F_{total} = \sum_{i_f=1}^{n_f} F_{i_f}\left(\delta, F_t, p(\mu A, \sigma A)\right)$$

Here, '$p(\mu A,\sigma A)$' is (normal) probability distribution function with mean 'μA ' and variance 'σA '. We could assume e.g., that variance 'σA ' is constant in the model so that 'μA', 'δ ' and 'F_t' remain the only

parameters. The problem is that the parameters we would like to estimate are within a function 'p' that is within a function 'F_{if}'. Solution of such a problem could be very difficult or even impossible, depending on the actual formulation of functions. However, data driven approach could alleviate the solution process. We introduce data approximation '$H(\mu A)$' of the probability function ' $p(\mu A)$' where '$H(\mu A)$' is histogram function from known data. In that case, new force - displacement relation for a fiber bundle model reads

$$F_{total} = \sum_{i_f=1}^{n_f} H(\mu A) \cdot F_{i_f}(\delta, F_t)$$

This problem is much easier to solve, especially since '$H(\mu A)$' could be pre-computed for assumed parameter value 'μA'. This model could be made more elaborate by adding additional parameters, like plastic and unloading behavior of each fiber. The more elaborate model with 6 stochastic parameters proved to be successful in estimation of stochastic parameters from tension experiments where we were pulling-out fibers from a concrete block, see [2],[3] and [4].

A more complex problem emerged during experimentation with three-point bending of beams. Namely, we wanted to pullout fibers in bending, not only in tension, since bending is the most common loading for fiber reinforced beams.

Numerical model for bending of beams assumed layered approach: beam is through height divided into layers where some layers could represent fibers. Each layer has a predefined force - displacement behavior based on the fiber bundle model, similar to the model above. The beam model is described with a system of two nonlinear equations

$$F(\varepsilon, \kappa) = \Delta h \sum_{i}^{layers} F_c[(h_i - \varepsilon\, h) \cdot tan\, \kappa] = F_{load}$$

$$M(\varepsilon, \kappa) = \Delta h \sum_{i}^{layers} (h_i - \varepsilon\, h) \cdot F_c[(h_i - \varepsilon\, h) \cdot tan\, \kappa] = M_{load}$$

Here, 'Δh' is layer height (equal for all layers), 'h_i' is the position of layer 'i', 'h' is the total beam height, '(ε,κ)' are neutral axis position and the curvature, respectively, and 'F_c' is concrete force - displacement behavior in tension. 'F_{load}' and 'M_{load}' represent external beam loading. Observe the additional function '$(h_i$-$\varepsilon\, h)$' describing the layer position in the moment balance equation. Multiplication with this additional function prevents us from using the same approach as above.

Data approach could be used if the solution pairs are tabulated for gradually increasing levels of loading. This system of equations has two pairs of solution '(ε,κ)' for certain intensities of loading, one in the pre-peak and the other in the post-peak region, i.e., the resulting moment - curvature function decreases after the peak load. The solution algorithm tracks the solutions in time thus choosing the right solution. At the same time, function '$(h_i$-$\varepsilon\, h)$' is tabulated for the corresponding solution. Shape of the concrete force - displacement function is assumed

$$F_c(x) = \mathrm{A} \cdot \mathrm{C}(x)^2 \cdot x \cdot Exp(-B \cdot C(x) \cdot x)$$

where 'A' and 'B' are unknown parameters and '$C(x)$' is some known function that could be tabulated. Notice that the displacement 'x' in our model equals '$x=(h_i$-$\varepsilon\, h)$'. When summation is performed, function '$C(x)$' is different for each layer and becomes '$C_i(x)$' but parameters 'A' and 'B' remain equal for each layer. Equation for parameter identification now becomes (note that only one equation is sufficient for the identification procedure)

$$Y_m(x) = \sum_{i}^{layers} \mathrm{A} \cdot C_i(x_i)^2 \cdot x_i \cdot Exp(-B \cdot C_i(x_i) \cdot x_i)$$

where '$Ym(x)$' is measured moment - curvature diagram and '$x_i=(h_i$-$\varepsilon\, h)$'. The solution procedure is based on differentiation and application of the differentiation matrix on measured data. Numerical

experiments have demonstrated successful estimation of unknown parameters '*A*' and '*B*' for the case of two layers. It is expected that numerical experiments are also going to be successful for larger number of layers.

Acknowledgment: This work has been supported through project HRZZ 7926 ”Separation of parameter influence in engineering modeling and parameter identification” and project KK.01.1.1.04.0056 ”Structure integrity in energy and transportation”, which is gratefully acknowledged.

References

[1] T. Rukavina, A. Ibrahimbegovic, I. Kožar. *Fiber-reinforced brittle material fracture models capable of capturing a complete set of failure modes including fiber pull- out*, Comput Methods Appl Mech Eng 355, 157-192, 2019.
[2] I. Kožar, N. Torić Malić, T. Rukavina, *Inverse model for pullout determination of steel fib*ers, Coupled Syst. Mech. 7, 197–209, 2018.
[3] I. Kožar, N. Torić Malić, Ž. Smolčić, D. Simonetti. *Bond-slip parameter estimation in fibre reinforced concrete at failure using inverse stochastic model*, Eng Fail Anal (104), 84-95, 2019.
[4] I. Kožar, N. Torić Malić, D. Simonetti, Ž. Božić. *Stochastic properties of bond-slip parameters at fibre pull-out*, Eng Fail Anal (111), 104478, 2020.
[5] I. Kožar, N. Torić Malić, S. Mrakovčić, D. Simonetti. *Combining deterministic and stochastic parameter estimation for fiber reinforced concrete modeling*, ECCOMAS MSF 2019 (ed.: A. Ibrahimbegovic, S. Dolarević, E. Džaferović, M. Hrasnica, I. Bjelonja, M. Zlatar, K. Hanjalić), Sarajevo, 2019.
[6] I. Kožar, N. Torić Malić, S. Mrakovčić, D. Simonetti. *Parameter estimation in fiber reinforced concrete*, Proceedings of the International Conference on Sustainable Materials, Systems and Structures (SMSS2019) (ed.: I. Gabrijel, C. Grosse, M. Slkazčoć) - RILEM Publications S.A.R.L., 75-81, 2019.

HYSTERETIC SIMULATION OF MAGNETOSCTRICTIVE MATERIALS WITH NL FE FORMULATION

José L. Pérez-Aparicio [1], Roberto Palma [2], Robert L. Taylor [3]

[1] Universitat Politècnica de València, jopeap@mes.upv.es
[2] Universidad de Granada, rpalgue@ugr.es
[3] University of California at Berkeley, taylor@ce.berkeley.edu

As in many scientific and technological fields, piezoelectric studies started from the necessity of develop practical devices: the initial emphasis in the decade of 1960 was in applicability, and while the electrical and mechanical basics were rapidly understood, more advanced issues were dealt with in the 1990s. From a mechanical point of view piezoelectric devices have been extensively studied for both small and large strains. In contrast, some electrical behavior has not yet been completely simulated; one of these is the Debye effect, also called Debye memory.

The current work is based on an already presented article [1] on Debye memory of piezoelectric materials, but while Debye defined his theory for electricity, to the best of our knowledge nothing has been formulated for the magnetism until a recent work [4] was published. Here, we extend Debye memory to magnetoestrictive materials, including their Finite Element (FE) implementation. Differently from piezoelectrics, actuators based in magnetoestrictives are suitable for applications requiring large mechanical displacements even under low magnetic fields; for instance Terfenol-D made out of rare earth-iron components can produce important strains. The problem is that these actuators exhibit hysteretic non-linear (NL) behavior, making it very difficult to experimentally characterize them: therefore, sophisticated numerical algorithms to develop computational tools are necessary.

Theoretically and within the framework of non-equilibrium thermodynamics, the hysteresis is introduced by the Debye–memory relaxation. Consider the generic solid of Fig. 1; the magnetic nature of the medium is represented by a number i of magnetic dipoles with north and south poles, and the magnetic moment of each dipole is denoted by m_i. The randomness of the dipoles is controlled by the material coefficient μ, see Eq. (3).

Since Ω is filled with magnetostrictive material, the momentum balances must include mechanic and electromagnetic contributions. The latter are obtained from the magnetic Maxwell's laws in the absence of free current:

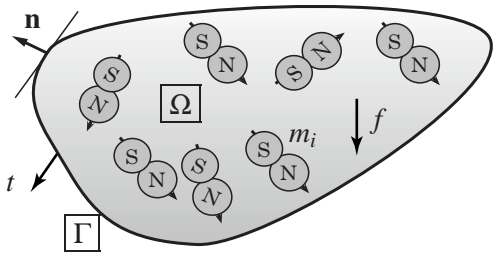

Figure 1: A magnetostrictive domain Ω of paramagnetic material, its boundary Γ with outward normal **n**; randomly oriented magnetic dipoles m_i, body forces f and boundary tractions t.

$$\begin{aligned} &\rho_m\,\ddot{u} = \nabla\cdot\sigma_T^{\top} + f\,; && \sigma_{Mx}^{sy} = \frac{\mu_0 B\otimes H + \mu_0 H\otimes B - B\cdot B\, I}{2\mu_0} \\ &\nabla\cdot B = 0\,; && \nabla\times H - \frac{\partial D}{\partial t} = \boldsymbol{0} \end{aligned} \tag{1}$$

where D, B and H denote electric displacement, magnetic induction and magnetic field, respectively, μ_0 the permeability of vacuum and u the elastic displacement. The total stress tensor of the first Ec. (1) is given by $\sigma_T = \sigma_C + \sigma_{Mx}^{sy}$ where the first term is the Cauchy tensor and the second one the symmetric part of the Maxwell tensor (σ_{Mx}^{sy}, MST, see Eq. (1)). The compatibility equations are:

$$\nabla^{sy}\,u := S\,; \qquad\qquad H = -\nabla\varphi. \tag{2}$$

where S is the strain tensor and φ the scalar magnetic potential. The second equation implies $\nabla\times H = \boldsymbol{0}$, then the fourth (1) or Ampère's law is automatically satisfied for low and medium frequencies $\dot{D}\approx\boldsymbol{0}$.

In Fig. 1, the dipoles tend to align parallel upon application of H and then the material becomes more ferromagnetic. In practice, magnetic materials are neither perfectly paramagnetic nor perfectly ferromagnetic. Therefore, a momentary delay appears when the magnetic dipoles return to their original orientations upon removal of H. This delay is measured by the magnetic relaxation time τ_M and its consideration will require the addition of an irreversible term in the total internal energy of the system.

Finally, several equilibrium and non-equilibrium thermodynamics are developed in [4], giving the time-dependent constitutive equations:

$$\begin{aligned} \sigma_T &= \mathbf{C} : S - (e^{\varphi})^{\top}\cdot H + \sigma_{Mx}^{sy} + \sigma_R \\ \tau_M\dot{B} + B &= e^{\varphi} : S + \mu\cdot H. \end{aligned} \tag{3}$$

where $\mathbf{C}$, μ and e^{φ} denote the fourth-order elastic, second-order permeability and third-order piezomagnetic tensors, respectively and σ_R the residual stress tensor.

Numerically, the main novelty is the time integration, coupling Newmark-β (for mechanical) and convolution integrals (for magnetic constitutive equations) similar to those of viscoelasticity; the non–linearity is solved by a standard Newton–Raphson algorithm and constitutive non-linearities are incorporated with the Maxwell stress tensor, quadratically dependent on H.

The numerical code is validated using analytical and experimental solutions for rods of Terfenol–D with properties given in [5]. For the first, a 1D fixed-free rod of length 6×10^{-3} [m] is studied. Magnetically, $\bar{\varphi}_b = 0$ is prescribed at the fixed end and its value at the other end is given by $\bar{\varphi}_t = -N_a I_a$; N_a, I_a denote the number of turns in the coil and prescribed electric current, respectively. The rod is free-to-expand, then σ_T is zero; from (1) and (3) a 1D closed solution for the strain S_{33} (along the magnetization direction) versus the applied magnetic field H_3 is:

$$S_{33} = \underbrace{\frac{e_{33}^{\varphi}}{C_{33}^{H}}H_3}_{\text{linear}} + \underbrace{\frac{(\mu_{33}^{T})^2 - 2\mu_0\mu_{33}^{T}}{2\mu_0 C_{33}^{H}}\,H_3^2}_{\text{MST}} - \underbrace{\frac{\sigma_{R33}}{C_{33}^{H}}}_{\text{Preload}} \tag{4}$$

where $\mu_{33}^{T} = \mu_{33}^{S} + (e_{33}^{\varphi})^2/C_{33}^{H}$ (permeabilities at constant stress and at constant strain, stiffness at constant field) and σ_{R33} is a stress along the length from a compressive preload, applied before the magnetic field. In Fig. 2 the numerical and analytical solutions are plotted, which for this simple case agree perfectly.

For the second validation, a commercial MMA experimentally measured in [6] is modeled. The mini actuator is composed of two cylindrical Terfenol-D rods, two flat end plates made out of Ni-Fe, two coils to generate the magnetic field and a bolt to preload the rods, besides auxiliary parts. According to [5], the magnetic permeability of the plates is three orders of magnitude greater than that of Terfenol-D,

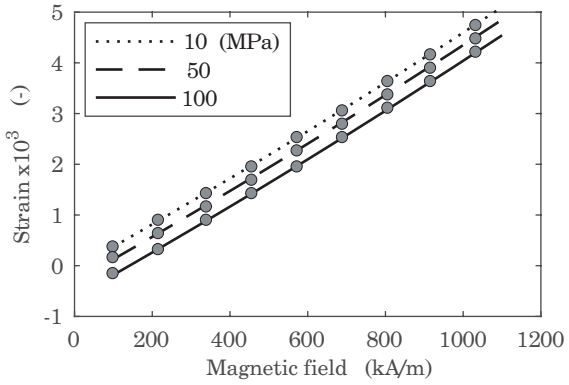

Figure 2: Strain vs. applied magnetic for several pre–compression stresses using FE including Maxwell tensor. Analytical (lines) and numerical (circles).

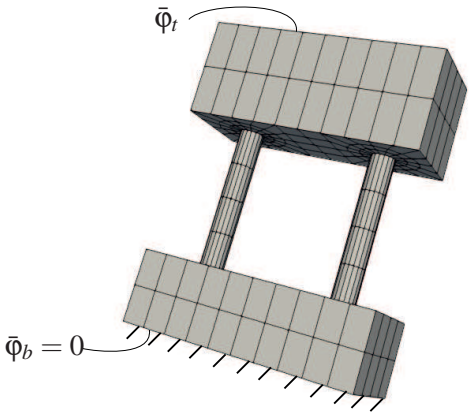

Figure 3: Finite element mesh to simulate the MMA of Fig. 2: pre-compressed Terfenol-D rods and end iron plates.

allowing for an easy closing of the magnetic lines. In Fig. 3, the 3D FE mesh is shown; notice that thanks to the current formulation no coils, bolts or other parts need to be simulated. The MA is mechanically clamped at the bottom plate, and as in the experiment of reference, the top end plate is free to move vertically. Magnetically, $\bar{\varphi}_b$ is set to zero at the bottom and the prescribed value at the top is again $\bar{\varphi}_t = -N_a I_a$.

Figure 4 compares the experimental response (which tries to exclude the effect of temperature) against the numerical results obtained by the present FE formulation, including MST and under σ_{R33} = 9.6 [MPa]. If the MST term is not considered, the prediction is linear and only valid for small values of I_a, but completely failing for medium or high values. With MST, three different zones in the non-linear distribution may be observed:

- $I_a \leq 100$ [mA]: the response is practically linear and both experimental and FE results fit very well.
- $100 \leq I_a \leq 320$ [mA]: the experimental response exhibits a strong concave shape that cannot exactly be captured by the FE results.
- $I_a \geq 320$ [mA]: numerical and experimental results agree very well again.

The good agreement in the first and third zones could be due to the positions of the magnetic dipoles of Fig. 1: in the first and for a ferromagnetic magnetostrictive they are much aligned with H and in the second almost perpendicular to H (close to saturation); in these two zones, classical continuum mechanics (CCM) is a good theory to model the response of the MA. The disagreement of the second zone could be due to two reasons or to the combination of both:

(a) Experimentally it is, at least, difficult to measure the response due to the overheating of the coils, as argued in [6]: the influence of thermal strains has influence on the curve.

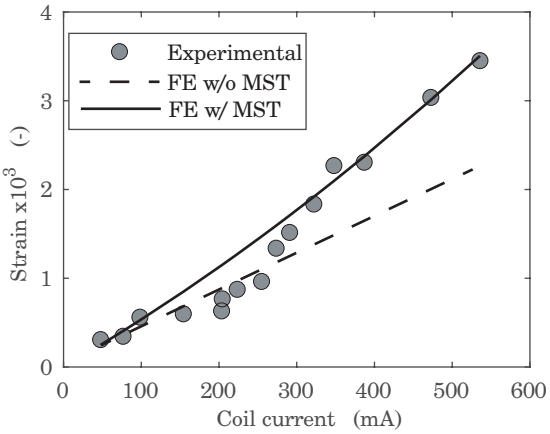

Figure 4: Generated strain in the mini actuator vs. electric current applied to the coils; experimental (circles) from [6] and numerical (lines) results.

(b) Numerically, the present FE formulation has three main simplifications:

- The strong Joule's heating of the Terfenol-D and of the coil is not incorporated in the model.
- The scalar potential FE formulation is a good approximation but assumes uniform H in the rods: in reality this field is not uniform due border effects.
- According to CCM, each material point only transmits linear momentum.

In reality the strain is not only due to stretch but also to the rotation of magnetic moments m_i, which should be considered in this type of situations. Ongoing work is directed to include in the formulation Cosserat mechanics including microrotations, and its coupling with the magnetic field.

Acknowledgments

This work was supported by the project of Generalitat Valenciana PROMETEO/2020/016: Applications of topological isolators in spintronics and thermoelectricity (TOP-TERM). This support is gratefully acknowledged.

References

[1] R. Palma, J.L. Pérez-Aparicio, R.L. Taylor, *Dissipative finite element formulation applied to piezoelectric materials with Debye memory*, IEEE/ASME Transactions on Mechatronics, 23(2), 856-863, 2017.

[2] R. Palma, J.L. Pérez-Aparicio, R.L. Taylor, *Non-linear and hysteretical finite element formulation applied to magnetosctrictive materials*, Computational Mechanics, 65, 1433-1445, 2020.

[3] R.L. Taylor, *A Finite Element Analysis Program: User Manual*, University of California, Berkeley, 2010.

[4] R. Palma, J.L. Pérez-Aparicio, R.L. Taylor, *Non-linear and hysteretic finite element formulation applied to magnetostrictive materials*, Computational Mechanics, 65,1433-1445, 2020.

[5] K.S. Kannan, A. Dasgupta, *A non-linear Galerkin finite-element theory for modeling magnetostrictive smart structures*, Smart Materials and Structures, 6, 341–350, 1997.

[6] M. Anjanappa, J. Bi, *Magnetostrictive mini actuators for smart structure applications*, Smart Materials & Structures, 3, 383–390, 1994.

DYNAMICAL SYSTEMS RELIABILITY IN MARKOVIAN ENVIRONMENT

Nikolaos Limnios[1]

[1] Universite de Technologie Compiegne, nikolaos.limnios@utc.fr

This presentation concerns non-ergodic dynamical systems in random environment, encountered in engineering modelling. The goal of the proposed analysis is to obtain a reduced model by a functional asymptotic approach within weak topology. The system considered here are with general state space and continuous-time. While the initial system is very complex, the reduced one is much simpler to handle by analytical and numerical methods.

THE STRUCTURAL MECHANICS OF THE VIENNA TRAMWAY RAILS: ADVANCED BEAM THEORY-ASSISTED 1D/2D FE MODELLING

Patricia Kuttke (née Hasslinger)[1], Stefan Scheiner[2], Valentin Jagsch[3], Christian Hellmich[4]

[1] TU Wien, Vienna, Austria, patricia.kuttke@tuwien.ac.at
[2] TU Wien, Vienna, Austria, stefan.scheiner@tuwien.ac.at
[3] TU Wien, Vienna, Austria, valentin.jagsch@tuwien.ac.at
[4] TU Wien, Vienna, Austria, christian.hellmich@tuwien.ac.at

Vienna disposes over the sixth largest tramway system in the world, having continuously grown until its inception as a horse-drawn system in 1865 and its full electrification completed in 1902. Given the considerable age of the system, rail durability issues and fractures increase, motivating deeper scientific scrutiny of chemo-mechanical characteristics of the respective grooved rails, a type of rails much less investigated and understood than the Vignole rails used for inter-city rail connections. We here report three recently studied aspects of the mechanics of grooved rails: (i) the 3D stress distribution throughout grooved rail can be efficiently computed through a novel 1D/2D Finite Element approach derived from the Principle of Virtual Power applied to beams with strongly warping cross sections [1,2], (ii) the macroscopic elastic properties are fairly homogeneously distributed across the rail cross sections, their magnitude being driven by metal matrix embedding microcracks [3], and (iii) discontinuities in the elastic support increase the rail stresses [4]. Given the almost perfect match of stress peaks predicted by the novel 1D/2D approach with actual failure patterns impressively highlights (e.g. decay- or maintenance-induced) discontinuities in the elastic support of the rails as an important factor increasing the fracture risk of ageing rails, on top of the temperature and production-induced residual stresses which have been comparatively well studied in the past.

References

[1] P. Hasslinger, A. Kurfürst, T. Hammer, E. Fischmeister, Ch. Hellmich, S. Scheiner, S. *Shear stress concentrations in tramway rails: Results from beam theory-based cross-sectional 2D Finite Element analyses*, Engineering Structures 195, 579-590, 2019.
[2] P. Kuttke, P., A. Kurfürst, S. Scheiner, Ch. Hellmich. *Sequential 1D/2D Finite Element analyses of tramway rails under bending and restrained torsion, based on the principle of virtual power,* Mechanics of Advanced Materials and Structures, 28, 1147-1169, 2021.
[3] V. Jagsch, P. Kuttke, O. Lahayne, L. Zelaya-Lainez, S. Scheiner, Ch. Hellmich, *Multiscale and multitechnique investigation of the elasticity of grooved rail steel,* Construction and Building Materials 238, 117768, 2020.
[4] P. Kuttke, P., Ch. Hellmich, S. Scheiner, S. (2020). *A principle of virtual power-based beam model reveals discontinuities in elastic support as potential sources of stress peaks in tramway rails,* Acta Mech 231, 4641–4663, 2020.

5th International Conference on Multiscale Computational Methods for Solids and Fluids
ECCOMAS Thematic Conference, June 30-July 2, 2021, Split, Croatia

Discrete to scale dependent (non-classical/non-local) continuous approaches for materials with microstructure: theoretical and computational issues

Patrizia Trovalusci

Department of Structural and Geotechnical Engineering, Sapienza University of Rome,
patrizia.trovalusci@uniroma1.it (https://orcid.org/0000-0001-7946-3590)

Introduction

The mechanical behavior of materials endowed with specific microstructure, characterized by complex non-linear behavior and complex internal sub-structure (micro), strongly depends on their microstructural features. In particular, in the modelling of these materials, such as particle composites, that are polycrystals with interfaces or with thin or thick interfaces, as well as rock or masonry-like materials, the discrete and heterogeneous nature of the matter must be taken into account, because interfaces and/or material internal phases dominate the gross behaviour. And this is definitely ascertained. What is not completely recognized instead, is the possibility of preserving memory of the microstructure, and of the presence of material length scales, without resorting to the discrete modelling that can often be cumbersome, in terms of non-local continuum descriptions.

In particular, for materials made of particles of prominent size and/or strong anisotropic media, by lacking in material internal scale parameters and in the possibility of accounting non-symmetries in strains and stresses, the classical Cauchy continuum (Grade1) does not always seem appropriate for describing the macroscopic behaviour taking into account the size, the orientation and the disposition of the micro-heterogeneities. This calls for the need of non-classical continuum descriptions [1-3], that can be obtained through multiscale approaches, aimed at deducing properties and relations by bridging information at proper underlying sub-levels via energy equivalence criteria. In the framework of such a multiscale modelling, the non-local character of the description is then crucial for avoiding physical inadequacies and theoretical computational problems. In particular, in problems in which a characteristic internal (material) length is comparable to the macroscopic (structural) length [4]. Among non-local theories, it is useful to distinguish between 'explicit' or 'strong' and 'implicit' or 'weak' non-locality [5]; where implicit non-locality concerns generalised continua with extra degrees of freedom, such as micromorphic continua [2] or continua with configurational forces [3].

This talk wants firstly to focus on the origins of multiscale modelling, related to the corpuscular(molecular)-continuous models developed in the 19th century to give explanations 'per causas' of elasticity (Cauchy, Voigt, Poincare), in order to find conceptual guidelines for deriving discrete-to scale-dependent continua, that are essentially non-local models with internal length and dispersive properties [5, 8]. Then, a discrete-to-scale dependent continuous formulation, developed for particle composite materials basing on a generalized version of Voigt's molecular/continuum approach, is proposed [6, 7]. Finally, with the aid of some numerical simulations - concerning ceramic matrix composites (CMC), microcracked media and masonry assemblies – focus will be on the advantages of the micropolar modelling with respect to other generalised continuum formulations [9-14].

Keywords: Multiscale approaches, generalized continua, anisotropic media with internal lengths

1. Coarse-graining approaches for complex materials and non local continuum formulations

A material can be defined 'complex' due to the presence of an internal structure and to its complex constitutive behaviour. For these materials, since many years, the multiscale modelling, perceived as the

dialogue among different material scales, has been widely exploited [15-16]. In many cases in mechanics of materials, only two scales of description are needed to be linked: a conventional (*fine*) microscopic scale, detectable at very different length levels, and the continuum (*coarse*) macroscopic scale, so dealing with homogenization or coarse-graining procedures.

As well known in the description of complex materials, such as composites but also geomaterials, as granular media/rocks, masonry-like materials, etc., the discrete and heterogeneous nature of matter must be taken into account, because interfaces and material internal phases dominate the gross behavior; and this is definitively ascertained. In particular, it is known that the presence of material length scales can be accounted for by direct discrete modelling, with generally high computational cost. What is not completely recognized instead, is the possibility of preserving 'memory' of the microstructure by resorting to continuum scale-dependent non-local theories.

In order to derive continuum theories suitable for representing the material microstructure, avoiding physical inadequacies and theoretical/computational problems, the non-local character of the description is crucial. Non-locality, by definition, implies the presence of internal lengths and spatial dispersion properties in wave propagation [18], which allows us to by pass some well known drawbacks such as ill-conditioning in the field equations and mesh-dependency in numerical solutions, arising in problems in which a characteristic internal length, l (material length), is comparable to the macroscopic lenght, L (structural length). Among non-local theories, it is useful to distinguish, according to some authors, between 'explicit/strong' and 'implicit/weak' non locality. The so-called explicit/strong non-locality is related to the well known theory by Kroner and Eringen, that evaluated the response of a process (for instance stress) over a enough wide (non-local) neighbourhood; while implicit/weak non-locality concerns continua with extra degrees of freedoms, that in the literature are named in different ways: generalised /non classical/non simple/microcontinua or even multifield continua. The extra degrees of freedom represent the physical microstructure (dislocations, disclinations, grain boundaries, etc.), or the geometrical microstructure in reduced dimension models, as in Timoshenko's bar [5, 12, 13].

Non-local (scale dependent) theories have the following main features that allow us to deal with well-posed problems and avoid mesh dependency in numerical solutions: i) presence of internal lengths and ii) spatial dispersion properties; iii) thermodynamic compatibility, in the case of 'implicit' non-local models with additional DOFs, satisfied with no need of additional dissipation inequalities as it occurs in internal variable models for instance.

Multiscale procedures can be also formulated for non-local continua [5-14]. Generally speaking, the mechanical behavior of real-life materials are often related to only two scales. Among the various homogenisation/coarse graining procedures, adopted for deriving both classical and non classical continua, the focus here is on approaches based on lattice mechanics and energy equivalence, governed by 'a priori' kinematical maps between discrete and continuum descriptors, that can be reconducted to the models of the classical molecular theory of elasticity, developed at the beginning of 19th century by Navier, Cauchy and Poisson [5-7]. These models are made of point-like particles ('molecules') interacting in pair through forces depending on the mutual distance and directed along the line connecting their centres, the so-called 'central force' scheme. In order to overcome some experimental difficulties related to this, *local*, scheme, concerning the number of elastic constants and the determination of Poisson's coefficient, Voigt and Poincaré successively introduced some important refinements. Voigt by introducing a molecular model based on the potential of particles/molecules interacting in pair through forces and moments, as pairs of rigid bodies; Poincare' by introducing a multibody potential model with molecules interacting in triplets or more. It can be shown that both obtained non-local description with internal length and dispersion properties.

At present multiscale techniques allowing the derivation of macroscopic models for complex materials by defining direct links with lattice systems are still among promising approaches in material science. Not very

differently than in the past, in current atomistic modelling, as well as in mechanics of composite materials, there are many circumstances in which the inadequacy of Cauchy) hypotheses, of central-forces (a) and homogenous deformations (b), calls for the need of improved models for by passing experimental discrepancies related to phenomena dominated by the microstructure size, as strain localisation phenomena for instance, but also, stress concentration phenomena in the presence of geometrical or load singularities in elasticity (cracks/holes/inclusions, concentrated loads) [7].
The strategies proposed in the literature are essentially based on: (1) the removal of hyp (a) of central-forces, as done by Voigt or Poincaré (obtaining continua with additional DOFs or multibody potential descriptions), or (2) removing the hyp (b), of homogeneous deformations, obtaining higher order models, that is obtaining, in the former case implicitly and in the latter explicitly non local models with the required features of: internal lengths, spatial dispersion and, in the former case, also thermodynamic compatibility.

2. A discrete-to-scale dependent continuous model for materials with microstructure and numerical simulations

A virtual work equivalence criterion is adopted in order to built and calibrate a scale-dependent continuum (the coarse model at the macro-scale) gathering the response of the original materials (the fine model at the micro-scale), using a generalized version of Voigt's molecular/continuum approach [8-11, 14]. A lattice system is employed to describe the material at the microscale, thus the multiscale approach is performed to introduce the multifield, non-local, continuum model at the macroscale. The derived constitutive relations take into account the shape, size, texture and orientation of the inclusions allowing to properly represent the material anisotropy and size effects.
As prototype material, a composite material made of a matrix with a distribution of mutually interacting fibers/particles/crystals and flaws (pores or microcracks) is adopted. This can be a fibre reinforced material, a metal/ceramic matrix composite, or also, by changing the internal length scale, a masonry-like material (brick-block masonry) or a rock system ('jointed system'). The coarse model and the fine one are compared within a linear kinematic framework. In particular, the particles are described as rigid bodies, and the defects as 'slits', conceived as devices for transmitting to the matrix additional forces due to displacement jumps over the actual flaws. As in the molecular models above mentioned, a-priory kinematical maps (not necessarily homogeneous) relating the discrete degrees of freedom (DOFs) to the continuum field descriptors are assumed, and these maps unambiguously determine the kind of macroscopic model to identify, that can be shown to be a continuum with a rigid (micropolar) [1, 2] and a deformable (affine) microstructure or a continuum with configurational forces [1, 3].
Results are presented and discussed through different paradigmatic cases. i) In the first case only the flaws (microcracks/pores) are present, while the particle rotations are absent or frozen (i.e. constrained to have rotation equal to the local rigid rotation) and only the deformable microstructure emerges [8, 11]. The case of a polycrystalline material in tension and of a one-dimensional microcracked bar under free as well as forced oscillations is shown. ii) Secondly, a material characterized by the presence of particles/fibres, without microcracks is proposed. In this case the continuum corresponds to a continuum with only the rigid microstructure: i.e. a micropolar/Cosserat continuum [9, 10, 14]. iii) 3) Finally, the case of a material with no flaws and frozen particles is considered. In that case, under the hypothesis of non-homogeneous deformations (second order), a second gradient (explicitly non-local) equivalent continuum is obtained, while under the hypothesis of homogeneous deformations (first order) the classical equivalent continuum is achieved [9]. The non-local effects are shown highlighting the effectiveness of non-local descriptions in reproducing size dependent behaviours with reference to masonry panels or two-dimensional particle

composites belonging to different material symmetry classes, in the presence of load or geometrical singularities [12, 13].

4. Final remarks

Robustness and efficiency of the proposed multiscale strategy are evaluated comparing the results of the various macro-scale, local and non-local, models in comparisons with those provided by numerical finite elements simulations, built in agreement with discrete micro-scale models as benchmark.

Providing that a constitutive characterization obtainable via multiscale procedures is furnished, non-local models, of both explicit and implicit type, can be effectively used for representing the behaviour of complex materials, in particularly thanks to the crucial features of internal lengths and spatial dispersion in wave propagation. Among non local models the micropolar model (Cosserat) must be preferred mostly due to: high computational efficiency; ease of implementation; non-complexity of boundary conditions; better performance in the case of anisotropic, media due to the skew-symmetries of strain and stress measures.

[1] Capriz G. (1989), Continua with Microstructure, Springer-Verlag, New York

[2] Eringen, A.C. (1999), Microcontinuum Field Theories, Springer-Verlag, New York

[3] Gurtin, M. E. (2000), Configurational Forces as Basis Concept of Continuum Physics, Springer-Verlag, Berlin.

[4] Trovalusci P., Ed. (2016), Materials with Internal Structure. Multiscale and Multifield Modeling and Simulation, P. Trovalusci (Ed.), Springer Tracts in Mechanical Engineering, Vol.18:109-131, Springer.

[5] Trovalusci P. (2014), Molecular approaches for multifield continua: origins and current developments. CISM (Int. Centre for Mechanical Sciences) Series, 556: 211-278, Springer.

[6] Trovalusci P., Capecchi D., Ruta G. (2009), Genesis of the multiscale approach for materials with microstructure, *Archive of Applied Mechanics*, 79(11): 981-997.

[7] Capecchi D., Ruta G., Trovalusci P. (2011), Voigt and Poincaré's mechanistic–energetic approaches to linear elasticity and suggestions for multiscale modelling, *Archive of Applied Mechanics*, 81(11), 1573-1584.

[8] Trovalusci P., Varano V., Rega G. (2010), A generalized continuum formulation for composite materials and wave propagation in a microcracked bar, *Journal of Applied Mechanics*, 77(6):061002/1-11.

[9] Trovalusci P., Pau A. (2014), Derivation of microstructured continua from lattice systems via principle of virtual works. The case of masonry-like materials as micropolar, second gradient and classical continua". *Acta Mechanica*, 225(1):157-177

[10] Fantuzzi N., Trovalusci P., Dharasura S. (2019), Mechanical behaviour of anisotropic composite materials as micropolar continua, Frontiers, 59 (6):1-11 (https://doi.org/10.3389/fmats.2019.00059).

[11] Settimi, V., Trovalusci P., Rega G. (2019), Dynamical properties of a composite microcracked bar based on a generalized continuum formulation, *Continuum Mechanics and Thermodynamics*, 1-18.

[12] Tuna M., Trovalusci P. (2020), Scale dependent continuum approaches for discontinuous assemblies: 'explicit' and 'implicit' non-local models", *Mechanics Research Communications*, 103, 103461, 2020 (https://doi.org/10.1016/j.mechrescom.2019.103461).

[13] Tuna M., Leonetti L., Trovalusci P., Kirka M. (2020) 'Explicit' and 'implicit' non-local scale dependent continuous descriptions for a plate with a circular inclusion in tension, Meccanica, 55(4), 927-944.

[14] Colatosti M., Fantuzzi N., Trovalusci P., Masiani R, (2021), New insights on homogenization for hexagonal-shaped composites as Cosserat continua, *Meccanica*. In print.

[15] Sadowsky, T., Trovalusci P., Eds., (2014), Multiscale Modeling of Complex Materials. Phenomenological, Theoretical and Computational Aspects, Series: 'Courses and Lectures', CISM (International Centre for Mechanical Sciences) 556, Springer, pp. 1-278.

[16] Ibrahimbegovic A., Ed., (2016), Computational Methods for Solids and Fluids: Multiscale Analysis, Probability Aspects and Model Reduction, Springer, pp. 1-493.

[17] Schmauder S., Schafer I. (2016), *Materials Today*, **19**(3), pp. 130-131. Multiscale Materials Modelling: Approaches to full multiscaling, De Gruyter.

[18] Kunin I.A., (1984) On foundations of the theory of elastic media with microstructure. International Journal of Engineering Science, 22, pp. 969–978

A FULLY NONLINEAR KIRCHHOFF-LOVE FINITE ELEMENT WITH THICKNESS CHANGE FOR COMPOSITE SHELLS

Paulo de Mattos Pimenta[1], Matheus Lucci Sanchez[2] and Cátia da Costa e Silva[3]

[1] Polytechnic School at University of São Paulo, Brazil, ppimenta@usp.br
[2] Polytechnic School at University of São Paulo, Brazil, matheusanchez@gmail.com
[3] Polytechnic School at University of São Paulo, Brazil, catiacosta@ifsp.edu.br

Shell simulation in FEM is an important topic in research due to its application in structural engineering (slabs, domes, metal sheet, thin structures, for instance). When simulating very thin structures, one may face numerical difficulties with current commercial finite element software. This problem is generally related to numerical unreal stiffness of the shell (or thin 3D domain) at finite element level, causing a phenomenon named "locking". This is the main motivation of the development of the current model, as well as the pursue for simplicity. This research is the continuation of previous work made by the group (see [1], [2], [3] and [4] for example).

The current research develops a new multi parameter Kirchhoff-Love shell finite element with thickness variation able to reliably simulate thin nonlinear shell for static structural boundary value problems. The element has 6 nodes and uses penalty (or optionally Lagrange method) to deal with the C1 continuity, which is a kinematical requirement of the Kirchhoff-Love shell model. It is also used a nonconform field of an incremental rotation variable φ_Δ (this parameter is firstly introduced in [3]) to assist with the C1 continuity on element edges. For the thickness variation, it is implemented a double linear non conform field similarly to [1] to represent the quadratic displacement at transverse normal to midplane of the shell. The quadratic displacement field of the mid plane is represented as usual by the 6 parameters at the 6 nodes of the element.

As a novelty in this study, the C1 continuity on the edges between elements is not further guaranteed by the maintenance of the kinking angle (as done in [2]) or by the equivalence of φ_Δ calculated through the displacements and the DoF shared by elements (as done in [3] and [4]). Now the C1 continuity is achieved by enforcing the transverse shear strain to zero.

References

[1] PIMENTA, P. M et al. A fully nonlinear multi-parameter shell model with thickness variation and a triangular shell finite element. Computational Mechanics, 2004.
[2] Viebahn N. et al., A simple triangular finite element for nonlinear thin shells: statics, dynamics and anisotropy. Computational Mechanics, 2017.
[3] Costa e Silva, C. (2020) Geometrically exact shear-rigid shell and rod models. Ph.D. Thesis, USP, Brazil
[4] SANCHEZ, M. L. et al. A simple fully nonlinear Kirchhoff-Love shell finite element. LAJSS, 2020.

A physics-compatible approach to data-driven computational solid mechanics

Pierre Ladevèze, Paul-William Gerbaud and David Néron

Université Paris-Saclay, ENS Paris-Saclay, CNRS, LMT
Laboratoire de Mécanique et Technologie
4 avenue des Sciences, 91190 Gif-sur-Yvette, France
e-mail: {ladeveze,gerbaud,neron}@ens-paris-saclay.fr

2

Within the framework of the thermodynamics of irreversible processes, this work introduces a general vision of data-driven computational mechanics, adapted to history-dependent materials and 3D-problems through the concept of Experimental Constitutive Manifold (ECM). The mathematical structure of ECM, that involves internal state variables, constitutes the material model associated with the experimental data for computation. The hidden internal variables are not known a priori but are calculated from the experimental data thanks to the so-called "Central Problem" of ECM.

This talk will present the fundamentals of this data-driven approach and the questions it raises. In particular, we will propose a way to reduce the enormous amount of data needed to build ECM, i.e. to extend the available experimental data. The potential applications will be illustrated.

References

[1] P. Ladevèze, D. Néron and P.-W. Gerbaud. *Data-driven computation for history-dependent materials*. Comptes Rendus Mécanique, 347:831-844 (2019).

[2] P.-W. Gerbaud, D. Néron and P. Ladevèze. *Solving a fundamental problem at the core of a data-driven approach for history-dependent materials* (to appear).

Modal Analysis of Prestressed Liquid-Structure Free-Free Systems

Roger Ohayon[1]

[1] CNAM, roger.ohayon@lecnam.net

We review the basic equations and corresponding variational formulations of the linearized vibrations of a liquid with a free surface contained in an elastic structure (hydroelasticity, sloshing, vibroacoustics).

In hydroelastic standard situations, the liquid is considered as incompressible, gravity –sloshing effects are taken through appropriate fluid-structure interface operator referred as *elastogravity operator* using a scalar field (pressure and/or displacement potential fields for the fluid).

Compressibility effects for the fluid can be introduced, neglecting gravity free surface effects as in *vibroacoustic problems* or taking them into account through some approximations.

Recently, we have analysed on a rigorous manner the basic equations of compressibility/gravity interactions: the fluid irrotationality condition being replaced, in general, by a *plane-irrotationality* equation.

We present here some basic appropriate corresponding variational formulations. Current investigations concern active/passive treatment for the vibration reduction as well as surface tension effects and various damping effects.

References

[1] H. Morand, R. Ohayon, *Fluid-Structure Interaction*, Wiley, 1995

[2] R. Ohayon, J.-S. Schotte, *Modal analysis of liquid–structure interaction*, pp. 423-438, Advances in Computational Fluid-Structure Interaction and Flow Simulation, New Methods and Challenging Computations, Modeling and Simulation in Science, Engineering and Technology, Y. Bazilevs, K. Takizawa, edts., Birkhauser, 2016

[3] R. Ohayon, J.-S. Schotte, *Fluid-structure interaction problems*, Chapter 23, 1001-1012, Encyclopedia of Computational Mechanics Second Edition, Vol. 4, Solids and Structures, E. Stein, R. de Borst, T. Hughes, edts, Wiley 2017

2. KEYNOTE LECTURES

INSTABILITY OF FRAME STRUCTURES UNDER NON-CONSERVATIVE LOADS

Emina Hajdo[1], Rosa Adela Mejia-Nava[2], Ismar Imamovic[3], Adnan Ibrahimbegovic[4]

[1] Faculty of Civil Engineering, University of Sarajevo, emina.hajdo@gmail.com
[2] Université de Technologie Compiégne, Laboratoire Roberval de Mécanique, rosa-adela.mejia-nava@utc.fr
[3] Faculty of Civil Engineering, University of Sarajevo, imamovic.ismar@gmail.com
[4] Université de Technologie Compiégne, Laboratoire Roberval de Mécanique, adnan.ibrahimbegovic@utc.fr

The requirements of modern architecture are tall, elegant buildings, open concepts, which result in structural elements with large spans and slenderness. Designing slender and lightweight structures can result in fatal consequences of loss in structural stability. The instability phenomena imply that for the reduced structural stiffness at so-called critical equilibrium state, a small perturbation can lead to a disproportional increase in response (displacement, strain and stress) and possible failure of structure. The instability analysis of complex structures, and adequate measures to prevent its occurrence, has again become one of the main engineering problems. Besides, different types of structures, next to so-called dead load, or gravitational forces, are also subjected to various loads. In general, all the forces that act upon the structure can be classified in two categories: conservative and non-conservative. The forces attributed to external actions (e.g. wind or fluid flow, or yet a frictional force) are often non-conservative [1]. The work of nonconservative forces cannot be computed from a potential, and it depends on the path taken. It is a essential finding of Bolotin [2] that the structure instability under non-conservative forces may occur dynamically, leading to increasing vibration amplitudes (yet called flutter instability). Therefore, the problem of structural instability under non-conservative forces should be examined within the dynamics framework.

The analytic solutions, for the classical problems of a column buckling under non-conservative load, is already available ([3]-[6]). This kind of non-conservative force is also called a follower force ([7]-[10]). Follower forces depend on the deformation of structures. To be specific, these forces follow the structure motion (e.g. rotation of cross-section), and are thus path-dependent and not possible to derive from a potential [1]. The stability analysis of such a column under follower force cannot be obtained by using the statics approach of studying the critical equilibrium state ([11], [3], [12]), but requires using the dynamics framework.

It was first shown by Bolotin ([2], [4]) that in case when we have the follower force we have to place the instability problem within the dynamics framework. We now consider a deformed configuration of a beam under compressive axial force P, which undergoes vibrations that should be examined within the dynamics framework (Fig. 1).

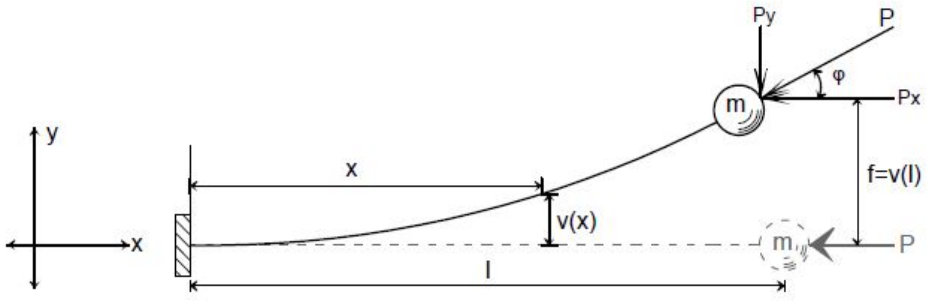

Fig. 1 Euler-Bernoulli cantilever beam under follower load

The analytic solution for cantilever Euler-Bernoulli beam under follower force is:

$$P_{cr} = \frac{2.05\pi^2}{l^2} EI \tag{1}$$

The analytic solution for Timoshenko beam buckling under follower force is obtained as:

$$P_{cr} = \frac{\sqrt{1+4\dfrac{2.05\pi^2 EI}{GA_c}}-1}{\dfrac{2}{GA_c}} \tag{2}$$

To solve the instability problem of a cantilever under the follower force, we construct the corresponding dynamics framework. We show how such dynamics framework can be generalized to more complex problems that can be solved by using the finite element method. In constructing the weak form solution, we use the von Karman type of strain measure. In our previous work ([11], [3]), the von Karman strain was used for formulating instability problems as linear buckling analysis of structures, which reduces to solving the linear eigenvalue problem. Here, we carry on further to introduce the Euler-Bernoulli beam with the von Karman strain measure, as the model capable of accounting for geometric nonlinearities. We also add the finite element that can take into account the follower force as the source of instability. We obtain the tangent stiffness matrix, which consists of material and geometric matrices:

$$\begin{gathered} \mathbf{K}_t = \mathbf{K}_m + \mathbf{K}_g \quad ; \\ \mathbf{K}_m = \int_l \left(\bar{\mathbf{N}}^T EA \bar{\mathbf{N}} + \mathbf{B}^T EI \mathbf{B} \right) dx \quad ; \quad \mathbf{K}_g = \int_l \bar{\mathbf{H}}^T \bar{\mathbf{H}} N dx \end{gathered} \tag{3}$$

Where **N** are derivatives of linear shape functions, $\bar{\mathbf{H}}$ and **B** are first and second derivatives of Hermite's polynomials, respectively. To take into account the shear deformation, we modify the material stiffness matrix, as shown in our previous work [13].

The follower force is tied to a particular cross-section [14]. The contribution of the follower force applied at the node *a* to the virtual work principle is:

$$G_{ext} = \delta \boldsymbol{\varphi}_a \mathbf{f}_a^{ext} = \delta \boldsymbol{\varphi}_a \boldsymbol{\Lambda}_t \mathbf{p}_0 \tag{4}$$

where $\mathbf{p}_0$ is the initial value of the follower force, and $\boldsymbol{\Lambda}_t$ is the rotation matrix. The rotation matrix in our case is defined as:

$$\boldsymbol{\Lambda}_t = \begin{bmatrix} 1 & -\dfrac{dv}{dx} & 0 \\ \dfrac{dv}{dx} & 1 & 0 \\ 0 & 0 & 1 \end{bmatrix} \tag{5}$$

The corresponding contribution to the beam element tangent stiffness matrix can be obtained as:

$$\mathbf{K}_f = \begin{bmatrix} 0 & 0 & -p_2 \\ 0 & 0 & p_1 \\ 0 & 0 & 0 \end{bmatrix} \tag{6}$$

In first numerical example we study a cantilever beam under follower force P. At the top of the cantilever, we also apply a small horizontal perturbation force of $0.01P$. The chosen material and geometrical properties of the cantilever are as follows: E=10^{6}N/cm^2, cross-section area A=1.0cm^2, moment of inertia I=0.001cm^4, and length is l=100.0 cm. By replacing these values into the analytical solution of the problem, we obtain the critical force value P_{cr} = 2.02N. We here perform numerical analysis for different number of elements, from 10 to 100. The obtained results are given in Fig. 2. The analysis performed using our model indeed results with instability phenomena for the analytical value of critical force – 2.02N.

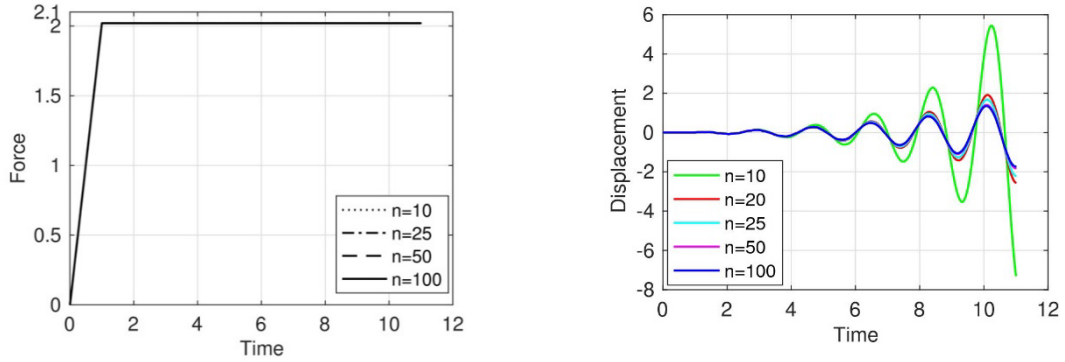

(a) Vertical force – time diagram (b) Time vs transverse displacement

Fig. 2 Cantilever instability under follower force

Next, we will show how shear deformation affects the value of the critical force. We analyze the same kind of cantilever as in the first example, but with possibility to include shear deformation by using the Timoshenko beam model. We take all the same properties, and also the shear modulus equal to G=0.5*E. In Fig. 3, we give the results for four different values of the shear correction coefficient. We also see that the presence of shear deformation reduced the value of critical load.

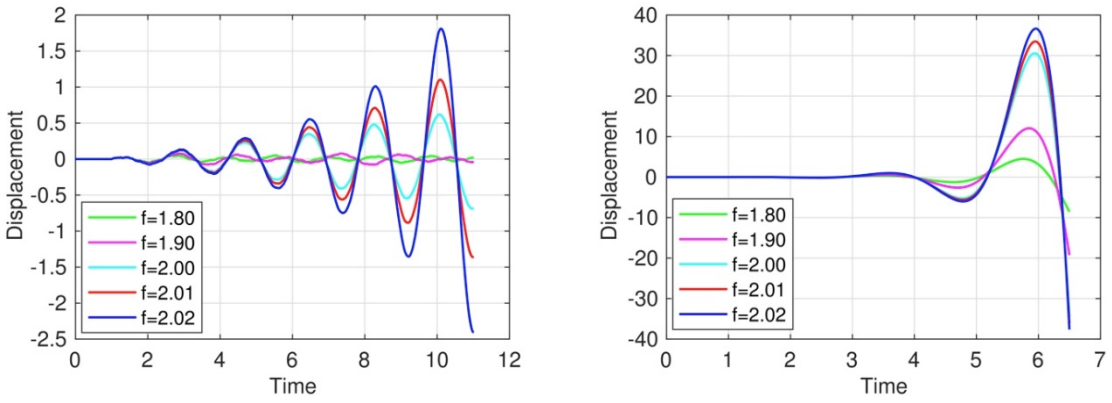

(a) k=0.002 (b) k=0.00002

Fig. 3 Shear deformation impact to the loss of stability

We found out that the solution obtained in the numerical example of cantilever column under follower force shows a very good agreement with the analytic solution for the critical force. After the shear deformation is included, the value of the critical load is reduced, which is also in agreement with the tendencies we should find for this kind of problems.

References

[1] Sugiyama Y., Langthjem, M.A. and Katayama, K. (2019), *Dynamic Stability of Columns under Nonconservative Forces: Theory and Experiment*, Springer

[2] Bolotin V.V. (1964), *The Dynamic Stability of Elastic Systems*, Holden-Day Inc.

[3] Hajdo E., Ibrahimbegovic, A. and Dolarevic, S. (2020), "Buckling analysis of complex structures with refined model built of frame and shell finite elements", *Coupled Systems Mechanics*, **9**, 29-46. http://dx.doi.org/10.12989/csm.2020.9.1.029

[4] Bolotin V.V. (1963), *Nonconservative Problems of Theory of Elastic Stability*, Pergamon Press

[5] Lacarbonara, W. and Yabuno, H. (2006), "Refined models of elastic beams undergoing large in-plane motions: theory and experiment", *Int. J. Solids Struct.*, **43**(17), pp. 5066–5084. https://doi.org/10.1016/j.ijsolstr.2005.07.018

[6] Jeronen J. and Kouhia, R. (2015), "On the effect of damping on stability of nonconservative systems", *Proceedings XII Finish Mechanics Days*, (eds. R. Kouhia et al.), pp. 77-82.

[7] Timoshenko S. and Gere, J.M. (1961), *Theory of Elastic Stability*, McGraw Hill

[8] Langthjem M.A. and Sugiyama, Y. (2000), "Dynamics stability of column subjected to follower load", *Journal of Sound and Vibration*, **238**(5), 809-851. https://doi.org/10.1006/jsvi.2000.3137

[8] Beck, M. (1952), "Die Knicklast des einseitig eingespannten, tangential gedrückten Stabes", *Journal of Applied Mathematics and Physics* (ZAMP), **3**, 225–228. https://doi.org/10.1007/BF02008828

[9] Farhat, C., Kwan-yu Chiu, E., Amsallem, D., Sholte, J. and Ohayon, R. (2013), "Modeling of fuel sloshing and its physical effects on flutter", AIAA Journal, 51(9), 100-114. https://doi.org/10.2514/1.J052299

[10] McHugh, K.A. and Dowell, E.H. (2020), "Nonlinear Response of an Inextensible, Free–Free Beam Subjected to a Nonconservative Follower Force", *J. Comput. Nonlinear Dynam.*, **15**(2): 021003. https://doi.org/10.1115/1.4045532

[11] Ibrahimbegovic A., Hajdo, E. and Dolarevic, S. (2013), "Linear instability or buckling problems for mechanical and coupled thermomechanical extreme conditions", *Coupled Systems Mechanics*, **2**, 349-374. http://dx.doi.org/10.12989/csm.2013.2.4.349

[12] Imamovic I., Ibrahimbegovic, A. and Hajdo, E. (2019), "Geometrically exact initially curved Kirchhoff's planar elasto-plastic beam", *Coupled Systems Mechanics*, **8**, 537-553. https://doi.org/10.12989/csm.2019.8.6.537

[13] Medic, S., Dolarevic, S. and Ibrahimbegovic, A. (2013), "Beam model refinement and reduction", *Eng. Struct.*, **50**, 158-169. https://doi.org/10.1016/j.engstruct.2012.10.004

[14] Ibrahimbegovic A. and Taylor, R.L. (2002), "On the role of frame-invariance of structural mechanics models at finite rotations", *Computer Methods in Applied Mechanics and Engineering*, **191**, 5159-5176. https://doi.org/10.1016/S0045-7825(02)00442-5

FRACTURE PROPAGATION MECHANISMS WITH EMBEDDED STRONG DISCONTINUITIES AND DISCRETE LATTICE ELEMENT APPROACH

Mijo Nikolić[1], Adnan Ibrahimbegovic[2]

[1] University of Split, Faculty of Civil Engineering, Architecture and Geodesy, Matice hrvatske 15, 21000 Split, Croatia, mijo.nikolic@gradst.hr
[2] Université de Technologie de Compiègne/Sorbonne Universités, Laboratoire Roberval de Mécanique, Centre de Recherche Royallieu, 60200 Compiègne, France, adnan.ibrahimbegovic@utc.fr

Fracture propagation mechanisms are complex phenomena with many challenging aspects that needs to be properly captured in computational simulations. Lattice element method [1] (LEM) is developed as a class of discrete element method (DEM), where structure is represented as an assembly of one dimensional elements (Figure 1). Such method can be well used is capturing various peculiarities of fracture development. For instance, initiation and propagation of multiple fractures in all failure modes (Figure 2.), as well as failure and fracturing of the various materials in statics or dynamics, multiphysics with volumetric fluid structure interaction such as porous media, thermodynamics etc.

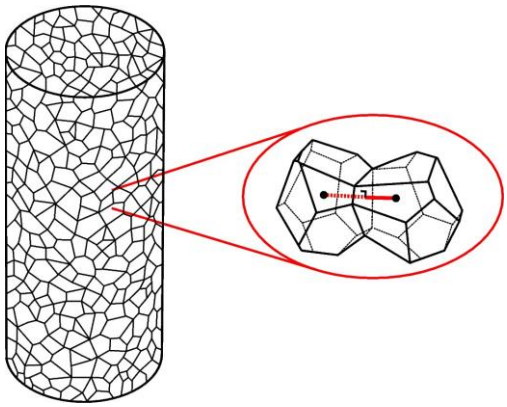

Figure 1: Lattice element representation of the domain: Voronoi cells kept together by cohesive links

The methodology and applications of the method, including the complex failure mechanisms of rocks [3, 4], multiphysics problems of saturated and unsaturated porous media [5] and failure of biocemented sands are presented [6]. The problems of dynamic crack propagation with impact load and crack branching are presented as well [2]. The method can provide the crack path which can be dependent on the material microstructure, as well as the computation of the all energy components in dynamically driven localized failure propagation. In this work, we will show some of the well-known benchmark problems used to validate models for fracture propagation.

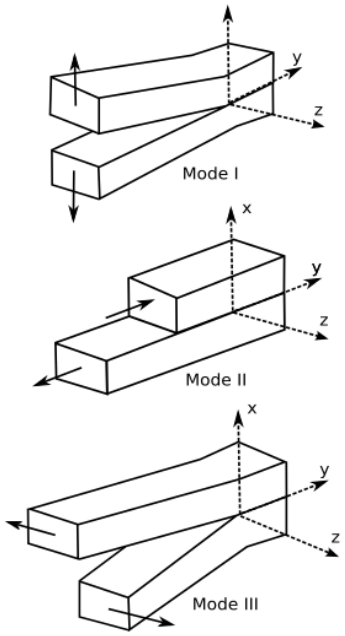

Figure 2: Failure modes, mode I – tensile opening, mode II – shear sliding, mode III - tearing

The framework of the presented method allows development of the computationally very efficient models for capturing fracture propagation mechanisms. In order to correctly describe those mechanisms, embedded strong discontinuities are used for representation of discontinuous displacement field, i.e. displacement jumps (Figure 3). Such implementation ensures that correct energy dissipation is always obtained, even when using different mesh size elements. In this work we also show how to compute the parameters of the discrete lattice mesh in order to obtain the linear elastic response and elastic uniformity when using irregular grids, which is often an issue in discrete modelling techniques.

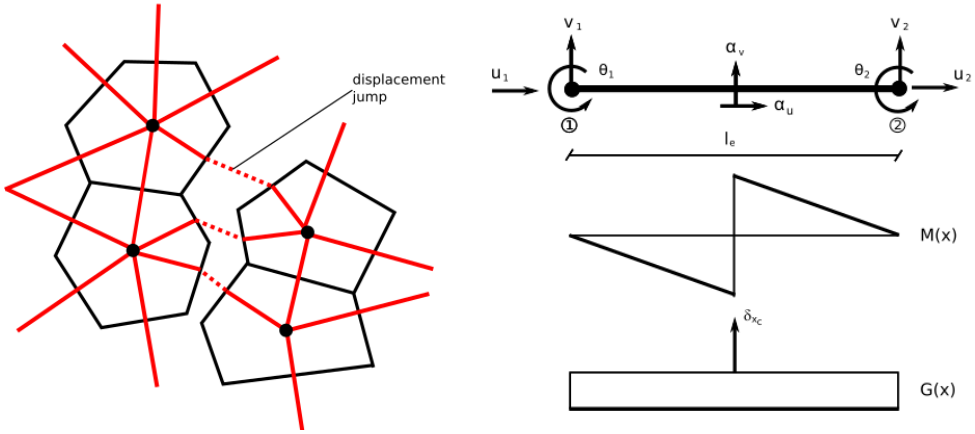

Figure 3: Implementation of displacement jumps in the discrete lattice mesh (left) and embedded strong discontinuities with discontinuous function (right)

Acknowledgements

This work has been supported through the project 'Parameter estimation framework for fracture propagation problems under extreme mechanical loads' (UIP-2020-02-6693), funded by the Croatian Science Foundation, and the project KK.01.1.1.02.0027, co-financed by the Croatian Government and

the European Union through the European Regional Development Fund - the Competitiveness and Cohesion Operational Programme.

References

[1] M. Nikolic, E. Karavelic, A. Ibrahimbegovic, P.Miscevic. Lattice element models and their peculiarities. Arch. Computat. Methods in Engrg., 25 (3): 753-784, 2018
[2] M. Nikolic, X.N. Do, A. Ibrahimbegovic, Z. Nikolic. Crack propagation in dynamics by embedded strong discontinuity approach: Enhanced solid versus discrete lattice model. Comput. Methods Appl. Mech. Engrg., 340: 480-499, 2018
[3] M. Nikolic, A. Ibrahimbegovic, P. Miscevic, Brittle and ductile failure of rocks: Embedded discontinuity approach for representing mode I and mode II failure mechanisms, Internat. J. Numer. Methods Engrg. 102: 1507-1526, 2015
[4] M. Nikolic, A. Ibrahimbegovic, Rock mechanics model capable of representing initial heterogeneities and full set of 3D failure mechanisms, Comput. Methods Appl. Mech. Engrg., 290: 209-227, 2015
[5] M. Nikolic, A. Ibrahimbegovic, P. Miscevic, Discrete element model for the analysis of fluid-saturated fractured poro-plastic medium based on sharp crack representation with embedded strong discontinuities, Comput. Methods Appl. Mech. Engrg. 298: 407-427, 2016
[6] Z.H Rizvi, M. Nikolic, F. Wuttke. Lattice element method for simulations of failure in biocemented sands. Granular Matter 21, 18, 2019

APPLICATION OF THE COMBINED FINITE DISCRETE ELEMENT METHOD IN ANALYSIS OF REINFORCED CONCRETE STRUCTURES

Nikolina Živaljić[1], Hrvoje Smoljanović[1], Željana Nikolić[1], Ante Munjiza[1]

[1] University of Split, Faculty of Civil Engineering, Architecture and Geodesy, Split, Croatia
[nikolina.zivaljic@gradst.hr, hrvoje.smoljanovic@gradst.hr, zeljana.nikolic@gradst.hr, ante.munjiza@gradst.hr]

Modelling and monitoring behavior and collapse of reinforced concrete (RC) structures due to hazardous loading conditions such as intensive seismic excitation, explosions, missile impact etc., represents a great challenge for researchers. Also, behavioral monitoring of the structure after failure, including the transition from continuum to discotinuum, is very important in the modelling of the load capacity and collapse of reinforced structures subjected to extreme loads.

For predicting the collapse of RC structures, the numerical model should be able to include effects of the behavior of RC structures under dynamic loading conditions in the linear-elastic stage, crack initiation and propagation, energy dissipation by nonlinear effects, inertial effects due to motion, contact impact and state of rest, which is a consequence of energy dissipation in the system, which is possible with the Combined Finite-Discrete Element Method (FDEM).

FDEM combines the advantages of both the finite and the discrete elements and enables the simulation of initiation and propagation of cracks, as well as interaction of a large number of discrete elements. Transition from continua to discontinua in FDEM is a result of failure, fracture or fragmentation. Fracture occurs through alteration, damage, yielding or failure of microstructural elements of the material. That process is included in the combined single and a smeared crack model which is based on an approximation of experimental curves for modelling the behavior of cracked concrete.

The aim of this paper is to present the application of the FDEM in analysis of 2D and 3D RC structures [1-3]. In presented numerical model, the reinforcing bar finite elements are implemented within the concrete finite elements and simulate the behavior of the reinforcing bar within the uncracked concrete assuming the linear elastic behavior of the reinforcing bar in the concrete finite element and a perfect bond between the concrete and the reinforcing bar. Fracture and fragmentation as well as material nonlinearity are described with contact elements for concrete and contact element for reinforcing bars which are implemented within the finite element mesh.

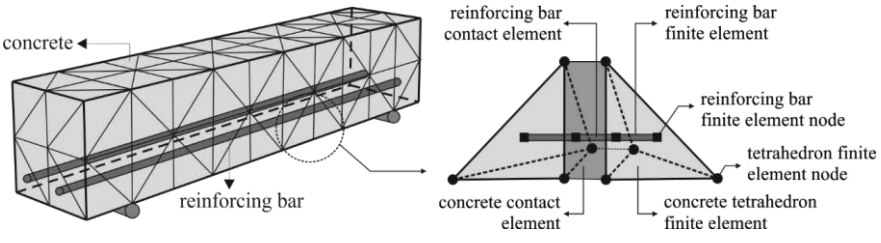

Figure 1. Discretization of 3D reinforced concrete structure

The model, implicates few numerical algorithms which are based on approximation of the experimental curves for material behavior of the concrete and steel which are important for description of main non-linear effects in reinforced concrete structures [1, 3]. In presented model non-linear material model for steel is based on experimental stress-strain curve, while the cyclic behavior of the steel during the cyclic load is modelled with improved Kato's model [1-3].

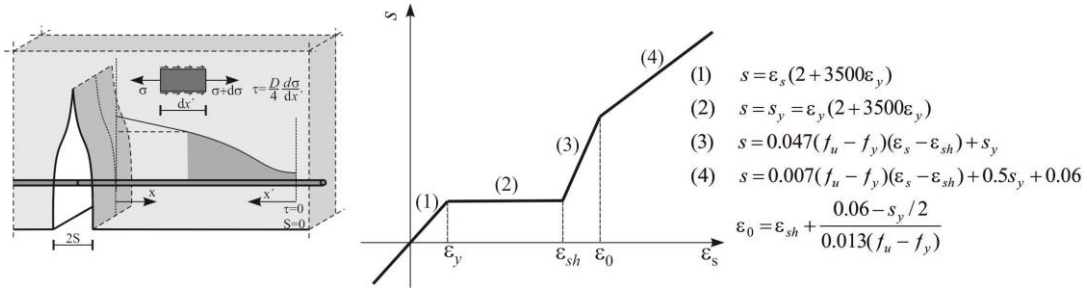

Figure 2. Discrete crack and steel strain-slip relation under monotonic loading

Verification, validation as well as application of the presented model were performed on numerous examples that show the advantages of the FDEM method.

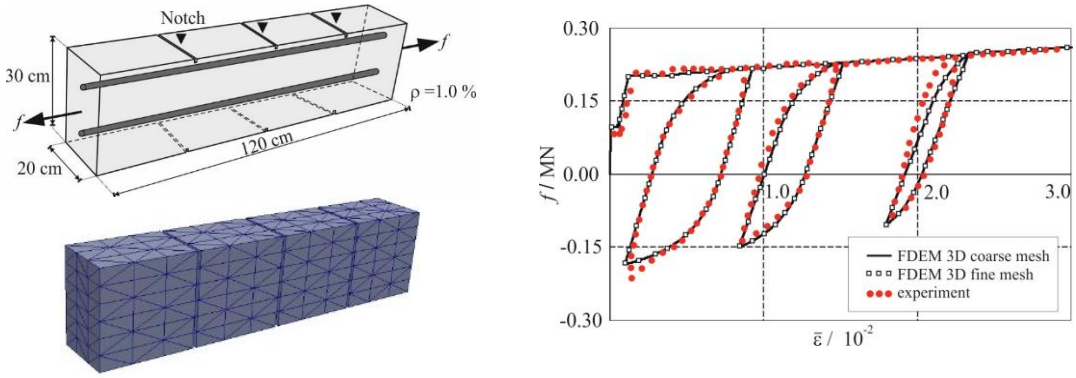

Figure 3. Verification of model on the RC beam under cyclic load

A series of examples will show that the presented model has great potential for estimating the failure mechanism and collapse load of both new and existing reinforced concrete structures exposed to seismic and impact loads.

Acknowledgements

This research is partially supported through project KK.01.1.1.02.0027, a project co-financed by the Croatian Government and the European Union through the European Regional Development Fund - the Competitiveness and Cohesion Operational Programme.

References

[1] N. Živaljić, H. Smoljanović, Ž. Nikolić. *A combined finite-discrete element model for RC structures under dynamic loading*, Engineering computations, page 982-page 1010, 2013.
[2] N. Živaljić, Ž. Nikolić, H. Smoljanović, A. Munjiza. *Numerical simulation of reinforced concrete structures under impact loading*, Materialwissenschaft und Werkstofftechnik, page 599-page 610, 2019.
[3] Ž. Nikolić, N. Živaljić, H. Smoljanović. *Three-Dimensional Finite-Discrete Element Framework for the Fracturing of Reinforced Concrete Structures*, Tehnički vjesnik: znanstveno-stručni časopis tehničkih fakulteta Sveučilišta u Osijeku, page 1314-page 1326, 2019.

CONTROL OF INSTABILITY PROBLEM UNDER NON-CONSERVATIVE LOAD

Rosa Adela Mejia Nava [1], Adnan Ibrahimbegovic [1], Rogelio Lozano Leal [3]

[1] Université de Technologie Compiègne, Laboratoire Roberval de Mécanique, France
rosa.mejia-nava@utc.fr, adnan.ibrahimbegovic@utc.fr.
[2] Université de Technologie Compiègne, Heudiasyc UMR CNRS 7253, France
rogelio.lozano@hds.utc.fr

The structural instability in dynamics (yet called flutter) and corresponding vibrations control are of great interest for many applications in engineering [1] [4]. Namely, the continuous innovation in intelligent materials, with better performance at a more accessible price, allow for constructing slender structures that become more sensitive to instability, under various loads with the most important here as non-conservative loading, some examples are: highrise buildings, bridges, aeroplane wings, wind-turbines flexible blades, or other kind of slender with high sensitivity to instability phenomena (see Fig.1).

Figure 1: Tacoma bridge-flutter instability

One such example that we studied recently [5] but not from the stand point of structural instability, comes from the domain of wind turbine technology used as renewable power generation that can help meet the sustainable development goals through provision of access to clean, secure, reliable and affordable energy. The progressive electrification of the transport and heating sectors is becoming a tangible reality that should be further enabled by efficient green energy assets. The latter may help with capped costs, and at the same time, it should be virtuously balanced by the flexible demand of these sectors. If we try to motivate the used for instability studies, we can say that the wind turbine technology has made significant advances over the past decade. Larger and more reliable turbines, along with higher heights and larger rotor diameters, have combined to increase capacity factors. This also makes them more and more sensitive for instability phenomena. Today, virtually all onshore wind turbines are horizontal axis turbines, predominantly using three blades. In the future design of a wind turbine different factors intervene, variations may include different land-use and transportation requirements.

Wind turbines have been built in optimal locations like the ocean front. If we want to ensure an enlarged number of turbines and put the wind turbine technology in any other location, we have to play with increasing the flexibility of blades, making easy to start moving with slow wind, like leaves in the tree. If a flexible blade is easy to start moving, contrary to the stiff wind turbine, it is easy to have excessively large motion and the instability. The correct design of wind turbines is very important because a bad design might have catastrophic consequences. Structures behaviour under dynamic loads control is very important for preventing their instability phenomena that can lead to the turbine collapse. One kind of structure control under dynamic loads can be achieved by adding damping (see Fig.2) provided by some kind of external damping mechanism to the structure, such as simple dampers or a smart shape

memory alloy. This kind of control is equivalent to the well-known concept of passivity [7] [7] [6] .

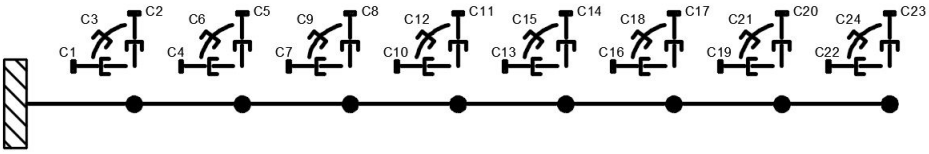

Figure 2: Dampers in each degree of freedom of a beam

Lightweight structures may lead to loss of structural stability. The later can be produced by applying critical forces on structures, which are classified into two categories: conservative forces and non-conservative forces such as follower force (see Fig. 3). Wind forces acting on wind turbines, buildings on bridges, these forces are non-conservative (e.g. fluid flow exerted pressure). The stability of structures under fluid flow should generally be placed in the category of non-conservative stability problems, which are of main interest for our present studies. Structures under non-conservative forces represent a special class of problems that are prone to losing their stability dynamically.

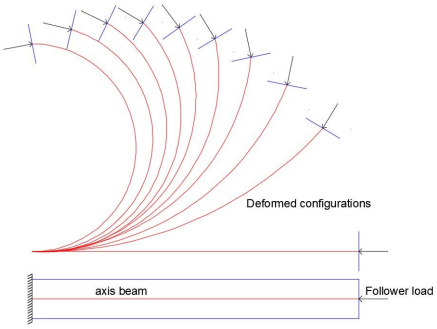

Figure 3: Follower load

We propose numerical solution procedures for solving the instability problems under both conservative and non-conservative loads. The details of theoretical developments are given in terms of the non-linear dynamical equations obtained by using the principle of virtual work [1][2]. All the structural models used for solving more complex problems are built with a numerical approach based upon the finite-element method and the geometrically exact beam models capable of describing finite rotations. It is show as well that the proposed models can successfully handle large overall motion under static and dynamic instability (or flutter) under both conservative and non-conservative loads.

References

[1] A. Ibrahimbegovic, *Nonlinear Solid Mechanics: theoretical formulations and finite element solution methods*, Spriger, (2009).

[2] A. Ibrahimbegovic , Ademovic N., *Nonlinear Dynamics of Structures Under Extreme Transient Loads*, CRC Press, pp. 1-253,(2019).

[3] B. Brogliato, R. Lozano, B. Maschke, O. Egeland, *Dissipative Systems Analysis and Control*, Springer Series in Communications and Control Engineering, (2008).

[4] M. R. Gutierrez, G. Silva *Control de vibraciones en estructuras tipo edificio usando actuadores piezoeléctricos y retroalimentación positiva de la aceleración*, Dyna, 80(179), 116-125, (2013).

[5] A. Boujleben, A. Ibrahimbegovic, E. Lefrancois *An efficient computational model for fluid-structure interaction in application to large overall motion of wind turbine with flexible blades*, Applied Mathematical Modelling, 77,(2020).

[6] M. E. Guerrero-Sanchez, H. Abaunza, P. Castillo, et al,*Passivity-based control for a Micro Air Vehicle Using Unit Quaternions*, Applied Sciences, (2016).

[7] P. Castillo, R. Lozano, A. E. Dzul *Modelling and Control of Mini-Flying Machines*, Springer, (2004).

ECCOMAS MSF 2021 THEMATIC CONFERENCE
30 June – 2 JULY 2021, SPLIT, CROATIA

DYNAMIC RESPONSE OF THE CURVED BEAM BY USING MESH BASED METHOD AND MESHLESS METHOD

Vedrana Kozulić, Blaž Gotovac

University of Split, Faculty of Civil Engineering, Architecture and Geodesy
vedrana.kozulic@gradst.hr ; blaz.gotovac@gradst.hr

Abstract

This paper presents two different numerical approaches for analysis of the curved beam structures with constant curvature in the plane under the dynamic loading. The first numerical model is based on the Finite Element Method (FEM) that applies exact curved beam element with six degrees of freedom. The second numerical model is based on the Fup Collocation Method (FCM) which allows the application of the strong formulation and uses the Fup basis functions. By introducing inertial forces in the system of three differential equilibrium equations of the second order for the static analysis, the differential formulation for obtaining dynamic response of the curved beam is obtained. The results obtained by using these two numerical methods are compared.

Key words: dynamic analysis; exact curved beam element; collocation method; Fup basis functions.

1. Mathematical model for a curved girder

The plane curved beam structure with constant curvature and constant cross-section is considered.

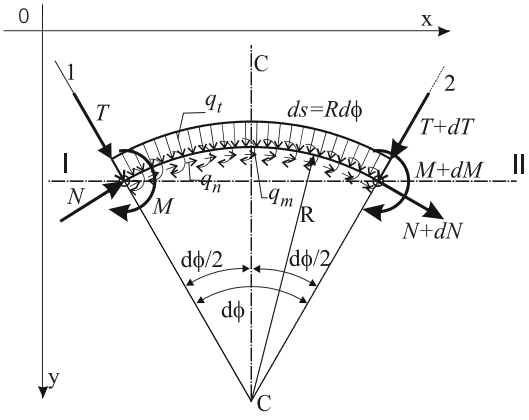

Fig. 1: Differential part of the arch element

If relationships between internal forces M, T and N and tangential displacement u, radial displacement w and cross-section rotation angle φ are introduced into equilibrium equations of the differential part of the arch beam (Fig. 1), the system of three differential equations of the second order

is obtained [3]. This system of equations arises from the complete formulation of equilibrium conditions of the curved beam and therefore it includes the coupled influences of bending, shear and axial forces.

When dynamic loading acts to an elastic structure, displacements are functions not only of the spatial coordinate ϕ but of time t as well:

$$\mathbf{u} = \left[u(\phi,t),\, w(\phi,t),\, \varphi(\phi,t)\right]^T$$

The mathematical formulation of the curved beam subjected to dynamic load is completely described with the system of three differential equations:

$$\begin{aligned}
&m\ddot{u} + c\dot{u} - \frac{EA}{R^2}u'' + \frac{kGA}{R^2}u + \frac{EA+kGA}{R^2}w' - \frac{kGA}{R}\varphi = q_n(t)\\
&m\ddot{w} + c\dot{w} - \frac{EA+kGA}{R^2}u' + \frac{kGA}{R^2}w'' + \frac{EA}{R^2}w + \frac{kGA}{R}\varphi' = q_t(t)\\
&m\ddot{\varphi} + c\dot{\varphi} - \frac{kGA}{R}u - \frac{kGA}{R}w' - \frac{EI}{R^2}\varphi'' + kGA\varphi = q_m(t)
\end{aligned} \qquad (1)$$

with corresponding boundary and initial conditions.

2. Dynamic analysis of the curved beam using FEM

The shear locking and membrane locking in arch structures and removing of their negative effects in numerical results were the subjects for investigations of various authors [5]. Two node finite element, whereby these effects are completely eliminated in static analysis of arch girders, was derived in [1] and [3].

The system of differential equations (1) which describes the mathematical model of dynamics of the arch structures includes the coupled influences of bending, shear and axial forces. As a result of this complete formulation of equilibrium conditions, negative influences of the shear and membrane locking effects are completely eliminated and simply monitoring of these effects on dynamic response of the structure is enabled.

From the system of three differential equations of the second order, algebraic-trigonometric basis functions of arch element are derived [3], [1]. Three basis functions are assigned to each unit displacement. Therefore, 9 basis functions are assigned to each node of the finite element.

By standard procedure for minimization of the functional of potential energy and using the algebraic-trigonometric basis functions, the exact stiffness matrix **K** of the curved beam element with constant curvature was derived [1], [3].

In the case of concentrated static load which acts in nodes, these exact curved finite elements ensure exact solutions with minimal number of finite elements [3]. Therefore, numerical solutions for dynamic problem of the curved beams will approach to exact solutions in the best way using a minimal number of exact finite elements.

The system of dynamic differential equilibrium equations is solved by the adaptive Runge-Kutta Verner method [6].

3. Meshless dynamic analysis of a curved beam

This numerical model is based on the collocation method by using $Fup_2(x)$ basis functions which belong to the class of atomic basis functions [2]. These functions are infinitely differentiable finite functions with compact support that enable their efficiently applications in the strong formulation procedures [4].

Approximate solution base is formed on the unit virtual domain defined by the curvilinear coordinate ξ. An approximate solution in terms of spatial coordinate is sought in the form of linear combinations of displaced basis functions in $N_\xi + 1$ equidistant collocation points, namely using $N_\xi + 3$ basis functions, where N_ξ denotes number of intervals on the given domain. Mapping a real domain in which the problem is defined into a virtual unit domain defined by the curvilinear coordinate ξ is performed by the mapping rule $d\phi / d\xi = \alpha$.

The system of algebraic equations in *n* collocation points can be written in the matrix form:

$$[\mathbf{M}]_{3n\times 3n} \cdot \left[\frac{d^2\mathbf{u}}{dt^2}\right]_{3n} + [\mathbf{C}]_{3n\times 3n} \cdot \left[\frac{d\mathbf{u}}{dt}\right]_{3n} + [\mathbf{S}]_{3(n+2)\times 3(n+2)} \cdot [\mathbf{C}_{ki}]_{3(n+2)} = [\mathbf{P}_{ki}(t)]_{3n} \qquad (2)$$

$$k = u, w, \varphi \ ; \qquad i = 0,..., n+1$$

where **M** is diagonal mass matrix in which masses are concentrated in collocation points, **C** - diagonal matrix of damping, **S** - matrix of static system, $\mathbf{C}_{ki}$ - vector of unknown coefficients of linear combinations, $\mathbf{P}_{ki}(t)$ - vector of dynamic loading. A size of the matrix **S** is $3(n+2)\times 3(n+2)$ because it contains a system of *3n* algebraic equations which satisfy differential equations in collocation points and 6 algebraic equations which satisfy boundary conditions. Matrix **S** should be mapped so that it can be described through the displacement functions in collocation points like matrices **M** and **C**.

Substituting static part of the system (2), $[\mathbf{S}]\cdot[\mathbf{C}_{ki}]$, in terms of flexibility matrix **F** and displacement vector of collocation points $[\mathbf{u}_{ki}]_{3n}$, the system of differential equations of the second order which represents a numerical model of the dynamics of curved beam structures described by meshless method using Fup_2 basic functions is obtained:

$$[\mathbf{M}]_{3n\times 3n} \cdot \left[\frac{d^2\mathbf{u}}{dt^2}\right] + [\mathbf{C}]_{3n\times 3n}\left[\frac{d\mathbf{u}}{dt}\right] + [\mathbf{F}]^{-1}{}_{3n\times 3n} \cdot [\mathbf{u}_{ki}]_{3n} = [\mathbf{P}_{ki}(t)]_{3n}. \qquad (3)$$

The system of differential equation (3) is reduced to solving the process in time by explicit procedure using Runge-Kutta-Verner integration method [6].

4. Example

The dynamic numerical models are illustrated by example of arch structure shown in Fig. 2. The arch girder has hollow rectangular cross section of 20/40 cm in size, $A = 0.0224\,m^2$, $R = 4.0$ m, $\alpha = 120°$, $E = 3\cdot 10^7$ kN/m^2 and $\nu = 0.17$. Arch is subjected to constant dynamic forces $P(t) = 650\,kN$ that act in concentrated masses $m_1 = 8\,t$ and $m_3 = 128\,t$ in thirds of the arch length, and $m_2 = 32\,t$ in the center of the arch.

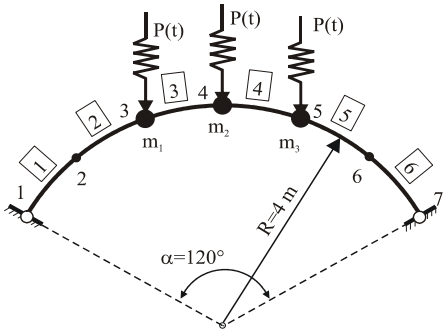

Fig. 2: Example of the arch structure for dynamical analyses

The numerical solution by FEM is obtained with 6 exact curved finite elements, namely 63 algebraic-trigonometric basis functions. The same number of basis functions in the FCM corresponds to solving dynamic problem of arch by 61 equidistant collocation points. Fig. 3 shows a comparison of results for transversal oscillations of the first mass for example shown in Fig. 2.

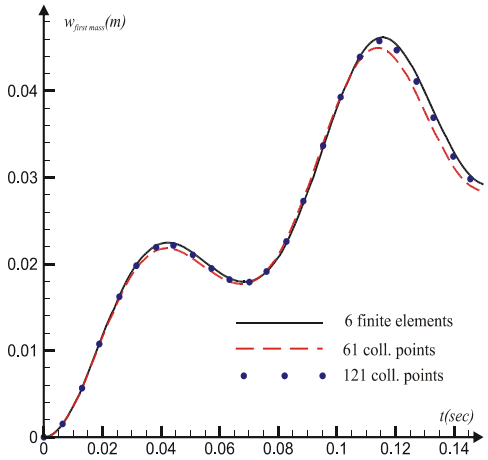

Fig. 3: Comparison of numerical solutions obtained by FEM and FCM

It can be seen from Fig. 3 that numerical solution obtained with a larger number of collocation points converges to numerical solution obtained by exact curved beam elements which can be regarded as exact solution. By direct comparison of results obtained with these two essentially different numerical methods described here, we confirmed their accuracy.

Numerical models created in this work can be applied in engineering practice for simple and precisely analyses of the arch beams subjected to different dynamic loadings and under different boundary conditions.

References

[1] Litewka, P., Rakowski, J., 1998. The exact thick arch finite element, Computers & Structures, 68, 369-379.

[2] Rvachev, V.L., Rvachev, V.A., . *Non-classical Methods for Approximate Solution of Boundary-Value Problems*, Naukova dumka, Kiev, In Russian, 1979.

[3] Gotovac, B., Sesartić, R., Kozulić, V., Exact formulation of a curved girder element, Građevinar, 59(12), 1129-1141, 2009.

[4] Kozulić, V., Gotovac, B. *Computational modeling of structural problems using atomic basis functions*. In: Advanced Structured Materials, Vol. 70, pp. 207-230, Springer, 2015.

[5] Stolarski, H., Belytscho, T., 1983. Shear and membrane locking in curved C^0 elements, In: Computer Methods in Applied Mechanics and Engineering, 41, 279-296.

[6] Verner, J. H., 1994. A classification scheme for studying explicit Runge Kutta pairs, In: Scientific Computing, S. O. Fatunla (editor), Ada and Jane Press, Benin City, Nigeria, 201-225.

SEISMIC ASSESSMENT OF HISTORICAL STONE MASONRY BUILDINGS

Željana Nikolić[1], Luka Runjić[1], Nives Ostojić Škomrlj[1], Vedrana Kozulić[1], Gabrijela Grozdanić[1], Elena Benvenuti[2]

[1] University of Split, Faculty of Civil Engineering, Architecture and Geodesy, zeljana.nikolic@gradst.hr, nives.ostojic@gradst.hr, vedrana.kozulic@gradst.hr, gabrijela.grozdanic@gradst.hr
[2] University of Ferrara, Engineering Department, bnvlne@unife.it

Many countries of moderate to high seismic risk, including Croatia, have old city cores with buildings built of stone or brick long before any regulations on construction in earthquake areas came into force. Some of them are categorized as cultural heritage and should be preserved for future generations. Strong earthquakes cause significant damage and demolition of such buildings and numerous casualties. Rehabilitation requires significant financial resources that cannot be secured at once. Therefore, systematic care and planning is necessary in order to detect the vulnerability of buildings to earthquakes, to determine priorities in rehabilitation and continuously provide funds for the reconstruction of such buildings. Between different approaches for the evaluation of structural vulnerability, static non-linear (pushover) method is recognized as reliable tool for analysis of capacity of structure and failure mechanism.

In this work, seismic vulnerability index method and static non-linear (pushover) analysis are used for seismic vulnerability assessment of stone masonry buildings in the historic city center of Kaštel Kambelovac (Fig.1). The investigation represents one of the activities of the PMO-GATE project, focusing on the preventing, managing and overcoming natural-hazards risks like seismic, floods and extreme sea wave risks.

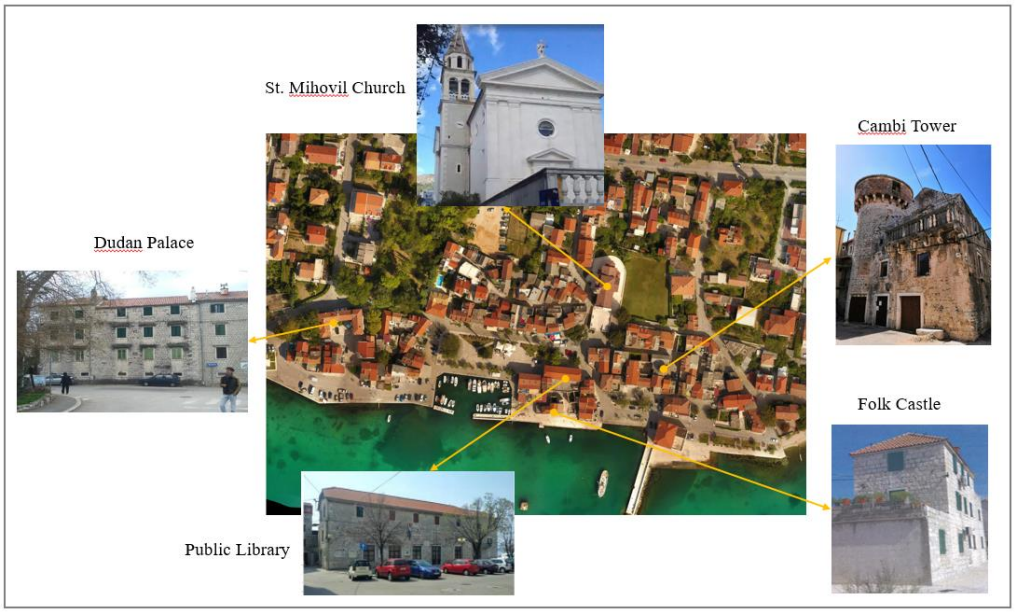

Fig. 1. Historical center of Kaštel Kambelovac with analysed buildings

The evaluation of the global structural capacity is performed according to Eurocode 8 [1] and corresponding Croatian standard [2, 3]. It is shown for 5 masonry buildings, built between the 15th and 19th centuries. The buildings are made of stone blocks with mortar joints with a thickness of the walls between 45 and 75 cm and flexible wooden floors.

The response of the structure is investigated along the two geometrical orthogonal axes, in both the positive and negative directions. Non-regular distribution of the masses inside the structure is considered by the assumption of an eccentricity of the lateral loads equal to ±5% of the maximum floor dimension at each level. Three lateral load distributions (uniform, linear and modal distribution) with the presence of eccentricity in positive and negative direction give in total 24 analyses.

Each pushover analysis results with the MDOF capacity curve. After the transformation of the MDOF curve in the SDOF one, bilinear curve is obtained. Then, capacity of the structure expressed in peak ground acceleration corresponding to the end of bilinear curve is calculated.

Seismic vulnerability assessment is performed by TREMURI software [4]. Complete 3D models of masonry structures can be obtained assembling 2-nodes macro-elements, representing the non-linear behaviour of masonry panels and piers. The macro-element considers both the shear-sliding damage failure mode and its evolution, controlling the strength deterioration and the stiffness degradation, and rocking mechanisms, with toe crushing effect, modelled by means of phenomenological non-linear constitutive law with stiffness deterioration in compression.

The seismic demand is defined by elastic acceleration response spectrum. Type 1 response spectrum [2] and soil class A [5] are used for HR test site Kastel Kambelovac. The design ground acceleration defined by seismic hazard map for the return period of 475 years is equal to a_g=0.22g. The seismic capacity of the buildings will be defined by checking if the seismic demand represents with 475 years is satisfied.

Numerical predictions of the collapse acceleration by non-linear static analyses show that no building meets the seismic requirement equal to a_g=0.22g in either directions. Namely, the peak ground acceleration corresponding to the collapse of the buildings are in the range of 0.07g and 0.10g. The failure occurs due to different collapse modes such as shear, bending, tension and compression failures. The analyses shows that pushover analysis of stone masonry buildings can provide an insight into both global seismic resistance and the mechanisms that lead to the structural failure. The seismic resistance capacity and obtained vulnerability indexes for chosen buildings are discussed.

Acknowledgements

This work has been supported through the project “Preventing, managing and overcoming natural-hazards risks to mitigate economic and social impact” (PMO-GATE), funded by the European Union through the programme Interreg Italy-Croatia, and the project KK.01.1.1.02.0027, co-financed by the Croatian Government and the European Union through the European Regional Development Fund - the Competitiveness and Cohesion Operational Programme.

References

[1] EN 1998-1 Eurocode 8: *Design of structures for earthquake resistance - Part 1: General rules, seismic actions and rules for buildings*. European Committee for standardization CEN, 2004.

[2] HRN EN 1998-1:2011. *Design of structures for earthquake resistance. Part 1: General rules, seismic actions and rules for buildings*. Croatian Standards Institute, 2011.

[3] HRN EN 1998-3 Eurocode 8. *Design of structures for earthquake resistance. Part 3: Assessment and retrofiting of buildings*. Croatian Standards Institute, 2011.

[4] TREMURI software. S.T.A.DATA, Professional version, Torino, 2019.

[5] G. Bohm, F. Da Col, F. Accaino, F. Meneghini, A. Schleifer, Ž. Nikolić. *Characterization of shallow sediments in an urban area (Kaštela, Croatia) by analysis of P, SV and Sh seismic velocities using a tomographic approach*, Near Surface Geoscience Conference & Exhibition 2020, 2020, Belgrade, Serbia.

3. OTHER LECTURES

STABILITY OF CAISSON-TYPE BREAKWATER USING DISCONTINUOUS DEFORMATION ANALYSIS

Dong Ding, Abdellatif Ouahsine, Zhaoyuan Huang

Sorbonne Université, UTC-Compiègne, Lab Roberval, 60203 Compiègne Cedex, France
dong.ding@utc.fr, ouahsine@utc.fr, zhaoyuan.huang@utc.fr.

1. Introduction

Breakwaters are composed of a vertical caisson and armour units. The motion of the caisson may cause the failure of breakwaters [1]. Armour units are generally used to break waves in seaward and improve stability in shoreward. In this article, we numerically examine the stability of coastal structures subjected to strong hydrodynamic impacts. As these protection structures are discontinuous media, because they often consist of shaped blocks or rockfill blocks, we propose in this study a numerical model of Discrete Elements (DEM) based on Discontinuous Deformation Analysis (DDA). The study takes into account the contact between the armour units constituting the shoreward of the breakwater, where the contact stresses are imposed through a penalty method. The performance of the DDA method can be evaluated by considering three breakwaters consisting of cubic, accropode, and tetrapod blocks which are simulated under hydrodynamic forces.

2. Theoretical background and numerical models

2.1. Discontinuous Deformation Analysis

The ballast stones are considered as a stack of rigid blocks moving against each other. At the first-order displacement approximation the vector of variables associated with an individual block is [2, 3]:

$$\mathbf{d}^T = \{u_0 \quad v_0 \quad \gamma_0 \quad \varepsilon_x \quad \varepsilon_y \quad \varepsilon_{xy}\}^T \tag{1}$$

where u_0, v_0 and γ_0 are the translations and the rotation at the centroid of the block. ε_x and ε_y are the normal strains in x and y directions. ε_{xy} is shear strain. In two dimensions, the first order approximation of the displacement (u, v) at any point (x, y) of a block i reads:

$$\begin{pmatrix} u \\ v \end{pmatrix} = [\mathbf{T}] \cdot \{\mathbf{d}\} \tag{2}$$

where **[T]** is the transformation matrix, given by:

$$[\mathbf{T}] = \begin{pmatrix} 1 & 0 & -(y-y_0) & (x-x_0) & 0 & (y-y_0) \\ 0 & 1 & -(x-x_0) & 0 & (y-y_0) & (x-x_0) \end{pmatrix} \tag{3}$$

The equilibrium formulation in the DDA method is provided by the principle of potential energy minimization. For a system of N blocks, the total potential energy, π, maybe expressed as

$$\pi = \sum_{i=1}^{N} \frac{1}{2} \int_A [\varepsilon]^T [\sigma] dxdy - f_e \tag{4}$$

where $[\sigma]$ is the stress vector $[\varepsilon]$ is the strain vector and f_e is the work done by the external forces. The first term in Eq.(4) describes the total deformation energy of N blocks, while the second term is the total work done by the external forces on the blocks including gravity loads, block-to-block contact forces, inertia forces, and boundary loads. The minimisation of the potential energy π for block i with respect to its displacement variables gives:

$$\frac{\partial \pi_i}{\partial \mathbf{d_j}} = \mathbf{k_{ij}}\mathbf{d_j} - \mathbf{f_j} = 0 \qquad j = 1,...6 \tag{5}$$

The complete global equilibrium system for N blocks can be written in matrix form as follows:

$$\begin{pmatrix} \mathbf{k_{11}} & \mathbf{k_{12}} & \mathbf{k_{13}} & \dots & \mathbf{k_{1n}} \\ \mathbf{k_{21}} & \mathbf{k_{22}} & \mathbf{k_{23}} & \dots & \mathbf{k_{2n}} \\ \mathbf{k_{31}} & \mathbf{k_{32}} & \mathbf{k_{33}} & \dots & \mathbf{k_{3n}} \\ \vdots & \vdots & \vdots & \vdots & \vdots \\ \mathbf{k_{n1}} & \mathbf{k_{n2}} & \mathbf{k_{n3}} & \dots & \mathbf{k_{nn}} \end{pmatrix} \begin{pmatrix} \mathbf{d_1} \\ \mathbf{d_2} \\ \mathbf{d_3} \\ \vdots \\ \mathbf{d_n} \end{pmatrix} = \begin{pmatrix} \mathbf{f_1} \\ \mathbf{f_2} \\ \mathbf{f_3} \\ \vdots \\ \mathbf{f_n} \end{pmatrix} \tag{6}$$

where $\boldsymbol{f_i}$ is a 6×1 vector of forces acting on block i. The off-diagonal sub-matrices $\boldsymbol{k}_{ij}$ $(i \neq j)$ contain the stiffness components associated with the contact between block i and j , and $\boldsymbol{k}_{ii}$ refers to the components of the material stiffness of block i. The penalty method is used to enforce contact constraints at block interfaces [2]. Consider two blocks i and j, where point P_1 of block i penetrates a depth, δ, into edge P_2P_3 of block j. Using the penalty method is equivalent to placing a spring between point P_1 and the edge P_2P_3, as shown in Fig.1 The perpendicular distance δ can be calculated as follows:

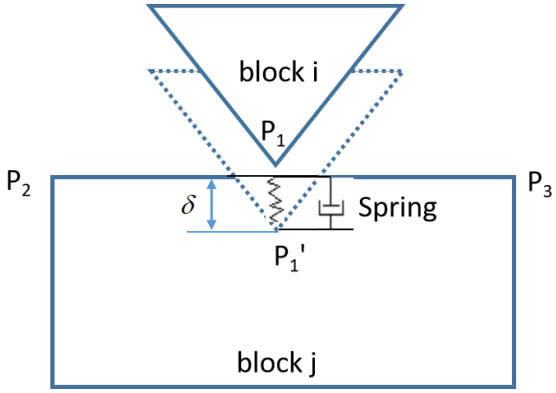

Figure 1: Interaction between two contacting blocks

$$\delta = \frac{\Delta}{l} = \frac{1}{l}\begin{vmatrix} 1 & x_1+u_1 & y_1+v_1 \\ 1 & x_2+u_2 & y_2+v_2 \\ 1 & x_3+u_3 & y_3+v_3 \end{vmatrix} \tag{7}$$

where l is the length of P_2P_3. Denoting the first term by S_0, the Δ can be then approximated as:

$$\Delta = \begin{vmatrix} 1 & x_1 & y_1 \\ 1 & x_2 & y_2 \\ 1 & x_3 & y_3 \end{vmatrix} + \begin{vmatrix} 1 & x_1 & v_1 \\ 1 & x_2 & v_2 \\ 1 & x_3 & v_3 \end{vmatrix} + \begin{vmatrix} 1 & u_1 & y_1 \\ 1 & u_2 & y_2 \\ 1 & u_3 & y_3 \end{vmatrix} + \begin{vmatrix} 1 & u_1 & v_1 \\ 1 & u_2 & v_2 \\ 1 & u_3 & v_3 \end{vmatrix} \tag{8}$$

The last term in Eq.(8) can be neglected since it is an infinitesimal second order function of the displacements. Denoting the first term by S_0 and combining Eq. (2), (7) and (8) gives:

$$d = \frac{S_0}{l} + \boldsymbol{E}\boldsymbol{D_i} + \boldsymbol{G}\boldsymbol{D_j} \tag{9}$$

where: $\boldsymbol{E} = \frac{1}{l}[\boldsymbol{T}_i(x_1,y_1)]^T \begin{pmatrix} y_2-y_3 \\ x_3-x_2 \end{pmatrix}$ and $\boldsymbol{G} = \frac{1}{l}[\boldsymbol{T}_j(x_2,y_2)]^T \begin{pmatrix} y_3-y_1 \\ x_1-x_3 \end{pmatrix} + \frac{1}{l}[\boldsymbol{T}_j(x_3,y_3)]^T \begin{pmatrix} y_1-y_2 \\ x_2-x_1 \end{pmatrix}$

The strain energy of the contact spring between blocks i and j for k-th iteration is given by [3]:

$$\pi_k = \frac{1}{2}pd^2 = \frac{1}{2}p(\frac{S_0}{l} + \boldsymbol{E}\boldsymbol{D_i} + \boldsymbol{G}\boldsymbol{D_j})^2 \tag{10}$$

where p is a large positive penalty number which is also the spring stiffness. The contact strain energy, given by Eq.(10), should be approximately equal to zero when total potential energy is minimized.

2.2. Breakwater model and input force

During the impact process the caisson is assumed to be subjected to the horizontal forces: $F_i(x,t)$ resulting from the impact of the wave on the caisson and $F_f(x,t)$ the friction of the caisson on the ground (see Fig. 2). The time history of the input force is obtained from [4] (see Fig. 2(b)) where the hydrodynamic loading on the caisson under a violent solitary wave impact was calculated. The numerical simulations are done by considering a breakwater with rear-side armour units as shown in Fig. 2 (a), where the time history of the input force (see Fig. 2 (b)) and physical parameters (see.Table. 1) are used.

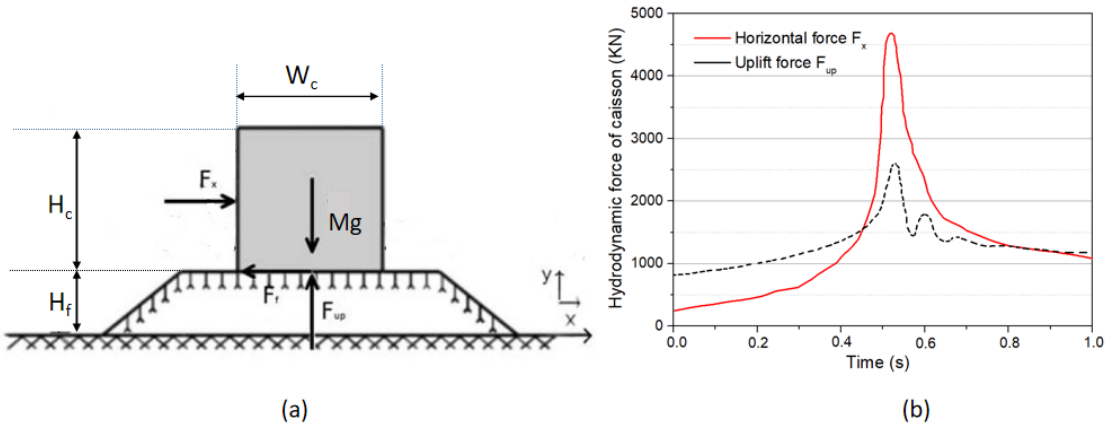

Figure 2: Sketch of the studied model and input force used for the validation: (a) The model of caisson breakwater without armour units: H_c=W_c=13 m; H_f=9 m; (b) Time history of the input force [4].

Table 1: Material parameters used for simulation

Young's modulus E	Poisson's ratio ν	Stiffness spring p	Friction coefficient μ
50 GPa	0.30	2×10^8 N/m	0.5

3. Numerical results

Three typical armour units are modeled and placed on the rear side of the caisson breakwater. The material parameters for the simulation are given in Table. 1 [5]. Six units, numbered from 1 to 6, were marked (see Fig. 3). It should be noted that for each hydrodynamic impact corresponds a displacement of the units, and therefore the greater the number of hydrodynamic impacts, the greater the displacement of the units. Thus, in the present numerical simulations, we assume that the caisson is subjected five times to consecutive hydrodynamic impact. The history of input hydrodynamic force is obtained from Fig. 2 (b). Block units are optimally arranged to make sure the initial position stability, as shown in Fig. 3 (a). The final simulation position of caisson and armour units are shown in Fig. 3 (b).

In general, the displacement of tetrapod-shaped units significantly smaller than the other two shaped units. It is because cubic armour units blocks bring resistance to breakwater by the mass whereas tetrapod and accropode units bring resistance through the mass and block interlock forces. Therefore, the cubic and tetrapod units by sliding and rotation, respectively, to reach a stable state. Besides, the jump in the horizontal displacement for the accropode units can be explained by accropode armour units' rearrangement. The design of the tetrapods is stable even in the most extreme weather and marine conditions, and when arranged together in lines or heaps, they create an interlocking.

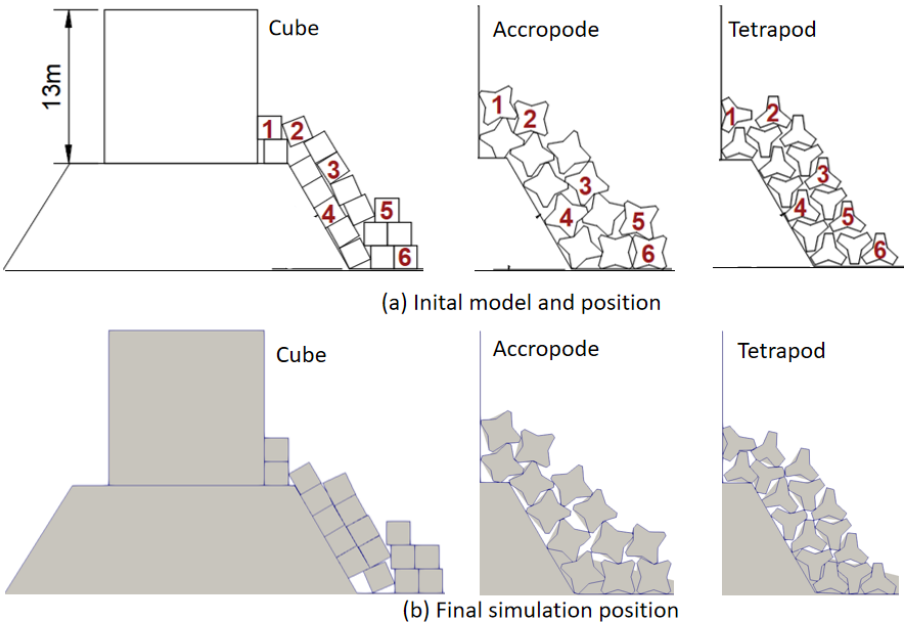

Figure 3: Shapes of breakwater armour units (slope=1:0.5): (a) Initial model and position, (b) Final simulation position

4. Conclusions

A numerical model based on the Discontinuous Deformation Analysis (DDA) method, was proposed to study the rear-side stability of the breakwater under hydrodynamic loading. This study took into account the armour units shapes and contacts between shaped armour units. The results of the simulation showed that the shape of the armour units played an important role in the stability of the breakwater, where the tetrapods and the acropods gave better satisfaction than the cubic shapes, with a clear superiority of the tetrapods.

References

[1] D. Ding, A. Ouahsine, W. Xiao. *CFD/DEM coupled approach for the stability of caisson-type breakwater subjected to violent wave impact*, Ocean Engineering, Vol.223, 108651, 2021.

[2] D. Ding, A. Ouahsine, W. Xiao. *Numerical study of ballast-flight caused by dropping snow/ice blocks in high-speed railways using Discontinuous Deformation Analysis (DDA)*, Transportation Geotechnics, Vo. 22,100314, 2020.

[3] G.-H, Shi. *Discontinuous deformation analysis: a new numerical model for the statics and dynamics of deformable block structures*, Engineering computations.Vol.9, N°2 , 157-168, 1992.

[4] Martin-Medina M, Abadie S, Mokrani C, et al. Numerical simulation of flip-through impacts of variable steepness on a vertical breakwater. Applied Ocean Research, Vol.75, 117-131, 2018.

[5] S. Kaidi, M. Rouainia. and A. Ouahsine. *Stability of breakwaters under hydrodynamic loading using a coupled DDA/FEM approach*, Ocean Engineering. Vol.55, 62-70, 2012.

IMPROVED SSI ANALYSIS BASED ON UHS TIME HISTORY SELECTION

Bogdanovic A.[1], Shalic R.[2], Stojmanovska M.[3] and Edip K.[4]

[1] Institute of Earthquake Engineering and Engineering Seismology, Skopje, N.Macedonia, saska@iziis.ukim.edu.mk
[2] Institute of Earthquake Engineering and Engineering Seismology, Skopje, N.Macedonia, r_salic@iziis.ukim.edu.mk
[3] Institute of Earthquake Engineering and Engineering Seismology, Skopje, N.Macedonia, marta@iziis.ukim.edu.mk
[4] Institute of Earthquake Engineering and Engineering Seismology, Skopje, N.Macedonia, kemal@iziis.ukim.edu.mk

The importance of SSI is observed when a high rise building rests on soft subsoil where there is a need to estimate deformations caused by application of high loads from earthquake time histories. In simulation of SSI problems it is of great importance to select the most reliable time histories which would reliably adhere effects in the simulation problem [1, 2]. Within this paper a ten storey frame structure was analyzed considering soil structure interaction as given in Figure 1.

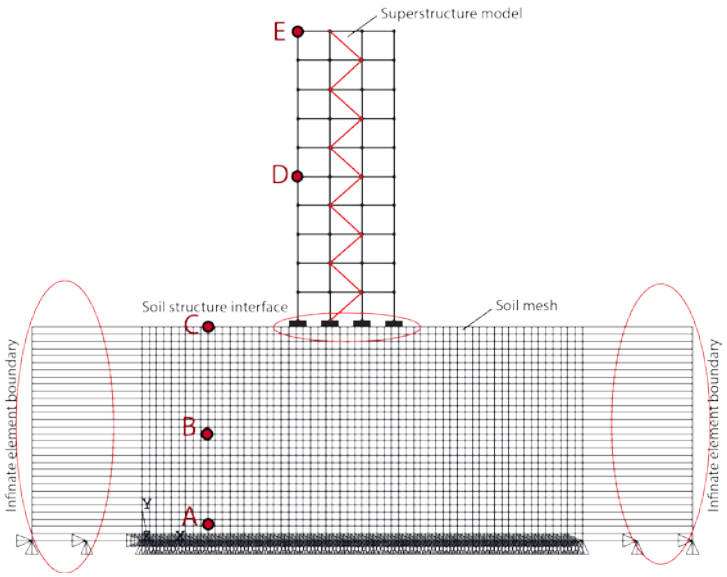

Figure 1. Soil structure interaction model with points of interest (A-E)

The site specific uniform hazard spectrum is used as target spectrum in selecting and scaling of earthquake records as an input in nonlinear dynamic analysis. For analyzing of the selected structure, several earthquake time-histories are used and obtained results were compared and discussed.

Calculation analysis of the frame structure considering spectral analysis and time histories of several different earthquakes reveal several conclusions. Firstly, the spectral analysis considers various frequency content although analysis is limited to linear analysis. On the other hand, the selected earthquakes are in time domain and can be used in non-linear analysis. The results obtained from the analysis show that correctly selection of earthquake time histories has important influence on the results and have to be considered in simulation of soil structure interaction problems obtained results were compared and discussed.

References

1. Bogdanovic, A., K. Edip, and M. Stojmanovska, *Simulation of soil structure interaction problems considering material properties* Journal of Scientific and Engineering Research, 2016. **3**(2): p. 132-139.
2. Bogdanovic, A., K. Edip, and M. Stojmanovska, *Influence of Height in Simulation of Soil Structure Interaction Problems with Dampers.* Selected Scientific Papers: Journal of Civil Engineering, 2016. **11**(2).

AN OPEN SOURCE APPLICATION FOR DETERMINATION OF THE PROOF STRENGTH BASED ON THE PLASTIC EXTENSION METHOD

Alen Grebo[1], Lovre Krstulović-Opara[2]

[1]University of Split, Faculty of Electrical Engineering Mechanical Engineering and Naval Architecture
Alen.Grebo.00@fesb.hr
[2]University of Split, Faculty of Electrical Engineering Mechanical Engineering and Naval Architecture
Lovre.Krstulovic-Opara@fesb.hr

Introduction

In the past we relied on operator precision and moral codex for even the basic of operation. As it stands, machines are more efficient and more productive than average human estimation of obtained data. This paper proposes automatized parameter evaluation, what differs to standard manual approaches defined by international codes.

One of the first though and classical tests in mechanical engineering is a tensile test. It is performed daily on numerous test pieces. That same test struggles with a concept called repetitiveness. Not in a sense the test can be repeated, but in the analysis part. The specimen is tested until failure occurs. Failure in any defined sense, because the definition can be arbitrary and assigned by the operator or by the same person who ordered the test. After the specimen suffers failure, it is analysed manually by the operator after which some key material features (parameters) are obtained. List of relevant features are often Young modulus, Poisson ratio, Maximum strength, Proof stress or strength.

This list of values depends on material being tested, but for the sake of simplicity it is assumed that evaluated specimen is of a metallic material without an emphasized elastic limit. While presented approach works relatively good for metallic material, with emphasized elastic limit, all here presented examples will be based on those without WHAT. Officially this analysis is called Proof Strength determination based on plastic extension method and is described in the EN ISO 6892-1, 2010 [1]. This analysis is mostly done manually by the tensile test operator without a follow up procedure that can be repeated. The here presented approach will replace the analysis part (manual estimation) which currently can be done using these approaches:

• Printing the diagram and drawing a "good fit" line, which is the most common technique, but its objectivity is questionable

• Microsoft Excel chart. While it can provide good results, it still requires a great deal of patience to carefully analyse the data set, find all the irregular values "Not a number (Nan)" or 0, delete unwanted measurement rows, copy and paste the right values, what-finally takes up to 20 minutes for a single diagram.

• MATLAB. Solutions that are based on a graphical user interface (GUI short), where the process is as follows: the user draws a line which starts at (0,0) and evaluates up to which point on the diagram does the linear trend persist. This is practically the same as print and draw technique, but performed automatically on a computer. Also, it requires MATLAB to be installed as it comes in a form of a package that needs to be installed in the program package library [2].

• Other GUI based solutions like those mentioned above.

All these solutions are non-deterministic in nature i.e. there is no underlying algorithm that can be evaluated and potentially corrected.

The application

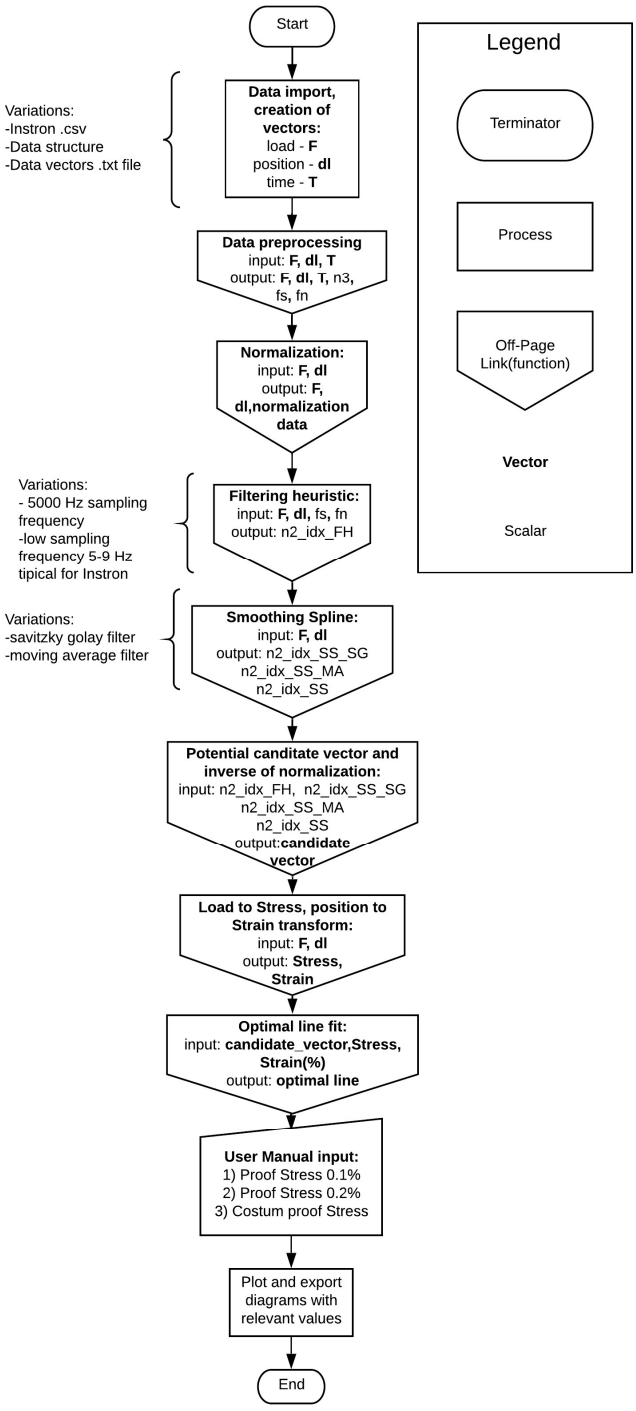

Figure 1. Application flowchart

As the application is quite complex, basic steps will be explained using a flow chart. Data import part imports revenant data vectors from standard .csv table format into data vectors to be processed. Import dataset step also checks if there are any extensometers active. If they are active, position data is rewritten with extensometer, providing higher precision then by standard LVDT position measurement. Pre-processing consists of removing not a number (Nan) values, shifting the diagram towards 0,0 and determining the cut-off point on the diagram, i.e. the point after which data points are irrelevant and the test data evaluation is stopped.

After data pre-processing follows the data normalization part. Assuming x is original data, the normalized values x' are given by: Returned values are then scaled between

$$x' = \frac{x - min(x)}{max(x) - min(x)} \qquad (1)$$

[0,1], this improved the execution time, as well as optimal line fit process whose explanation will come later in the text.

Filter heuristic part of the application solves a specific problem: up to which index point should linear regression be considered. It can be performed for all data points, but that would coincide with evaluating ***n-1*** slopes if there are ***n*** data points, which is not optimal from code runtime perspective. Basic idea of the heuristic is as follows: apply a lowpass filter, calculate the slope between all consecutive points, average those by some small step to filter the data even more, and then look for a point that is as close to the minimum as possible. As this was proven false, the search was performed for the last point before the mean value (see Figure 3). If this is done for only one value of lowpass filter, these is a high probability of missing said value. If filtration is done with more than one filter value and repeating the process above it turns out, find the last good data point we were searching for (see Figure 3) This last good data point is the first that constructs “potential candidate vector”. Next part of the application is smoothing spline.

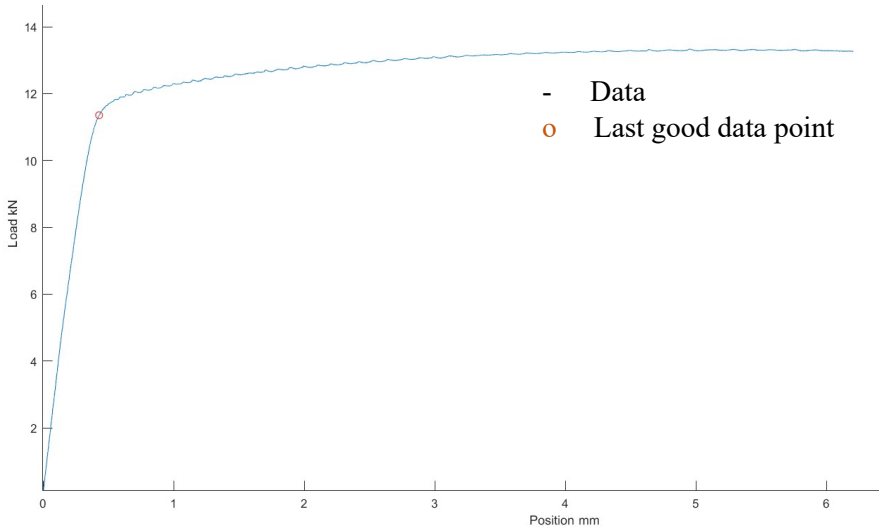

Figure 2. Result of Filter Heuristic

This method has the same ~~core~~ motivation as before, i.e. to find last good data point up to which is considered doing linear regression.
The cubic smoothing spline estimate *f'* of the function *f* is defined to be the minimizer (over the class of twice differentiable functions) of [3]:

$$p\sum_{i}^{n} w_i(y_i - s(x_i))^2 + (1-p)\int\left(\frac{d^2s}{dx^2}\right)dx \qquad (2)$$

Where:
• p - smoothing parameter, p =0 produces a least-squares straight-line fit to the data, p =1 produces a cubic spline interpolant [3], for here presented case smoothing parameter of $p = 0{,}9999999$ was applied
• w_i- specified weights
• $s(x_i)$- spline
• $\frac{d^2s}{dx^2}$ - second derivative of the spline with respect to x_i data points, i.e. the position in this case
• y_i- y component of data points, Load in this case.
After finding a good fit curve, take two derivatives of a function and find the minimum index.

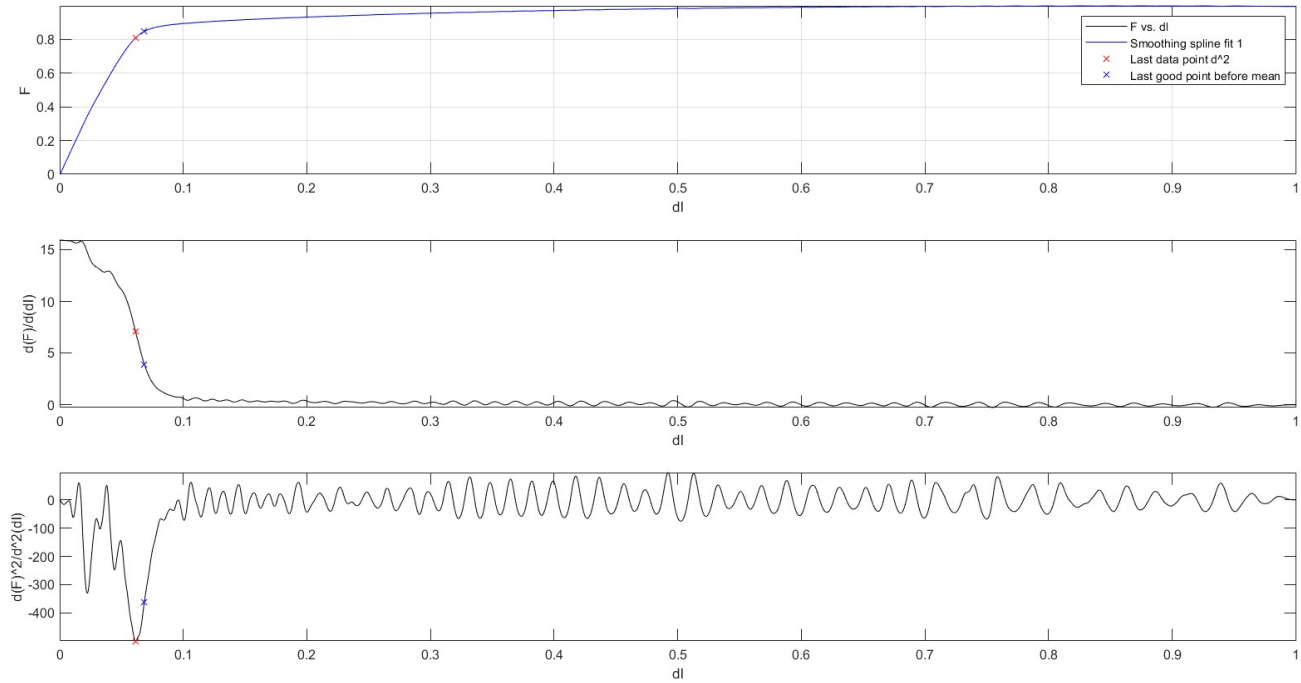

Figure 3. Smoothing spline output

To provide more accuracy, two filters are applied: Savitzky Golay [5] and Moving average [6]. To provide redundancy in each data set find the minimum of the second derivative and the point before the first derivative approaches the mean value of the data for the first derivative. In total that provides four new values for potential candidate vector. Finally, we filter the "bad" values from these two methods, and we fit an optimal line through every surviving potential candidate vector. Optimal line is determined by finding the minimum of the cost function:

$$J(k) = \frac{1}{n}\sqrt{\sum_{n}^{i}(\sigma_i - \varepsilon_i * k)} \tag{3}$$

Where:

k-slope

σ – stress transfored from load

ε – strain transformed from position

Results are shown on Figure 4.

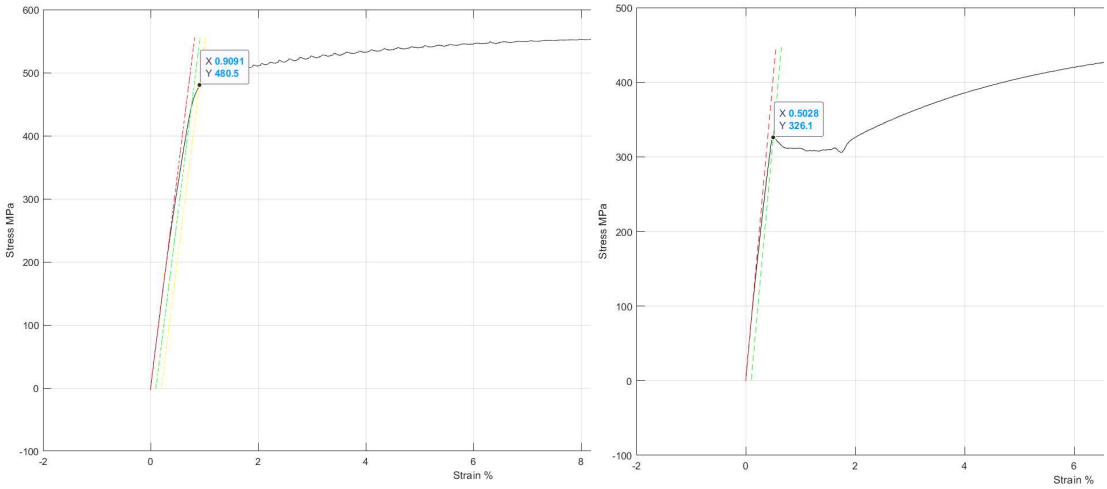

Figure 4. Results for: a) Aluminium specimen b)Steel specimen

Conclusion

With here presented application, the repeatability of the tests was achieved. Regarding the testing phase of the application, it entailed 42 datasets with mean run time of approximately 18.1 seconds with user input and 12.3 seconds without it. Total mean RAM memory requirement of the application per dataset is 2,34 Gb, what is more than acceptable for the todays standard. By strictly following the norm validation procedure, we would summarize that this application is not valid for testing. It can be concluded that current norm needs to be revisited with new validation methods that are less rigorous and that don't assume operator is right, as there is no algorithmic way of confirming this statement.

References

[1] Metallic materials – Tensile testing – Part 1: Method of test at room temperature, HRN EN ISO 6892-1, 2010.

[2] Benoît S.: from https://bit.ly/3oDfJ7p , 01. 02. 2021.

[3] Matlab Cubic smoothing spline, from web, https://de.mathworks.com/help/curvefit/csaps.html, 13.7.2020

[4] Savitzky, A.; Golay, M.J.E.: "Smoothing and Differentiation of Data by Simplified LS…", 1964.

[5] Hydrologic Variability of the Cosumnes River Floodplain Booth et al., San Francisco Estuary,2006

A MACHINE LEARNING APPROACH TO THE SEISMIC FRAGILITY ASSESSMENT OF BUILDINGS

Alessandro Rocchi[1], Andrea Chiozzi[2], Marco Nale[3], Zeljana Nikolic[4], Elena Benvenuti[5]

[1] University of Ferrara, alessandro.rocchi@edu.unife.it
[2] University of Ferrara, andrea.chiozzi@unife.it
[3] University of Ferrara, marco.nale@unife.it
[4] University of Split, zeljana.nikolic@gradst.hr,
[5] University of Ferrara, elena.benvenuti@unife.it

Evaluating the likelihood of damage in buildings undergoing earthquake actions is a difficult and time-consuming task. In the context of Performance-Based Earthquake Engineering (PBEE), an intensity measure (IM) provides a link between the probabilistic seismic hazard analysis and the probabilistic structural response analysis [1-2]. The purpose of this study is to develop a structural damage classifier and improve current prediction on the basis of a given intensity measure and different supervised machine learning algorithms [3]: Support-Vector Machine (SVM), Logistic Regression (LR) and Random Forest (RF).

In particular, the efficiency of four different IMs for estimating the seismic response of three different kind of buildings is evaluated, namely peak ground acceleration (PGA), spectral acceleration evaluated at the principal period T_1 ($S_a(T_1)$), average spectral acceleration $S_{a,avg}$, filtered incremental velocity (FIV3) [4]. The classifier will be able to predict the post-earthquake damage state, given the geometry of the building and the intensity of the ground motion input. In particular, the purpose of this classifier is to accelerate post-earthquake damage evaluation of critical buildings. This will allow faster recovery time and decrease financial losses expected from downtime and repair.

A focus is made on three different buildings typologies that can be used to represent the majority of the building stock in the city of Ferrara (Itay). A schematic representation of the chosen building typologies is depicted in Fig. 1: one and two-story houses, low-rise buildings (3-6 stories), medium-rise buildings (8-15 stories).

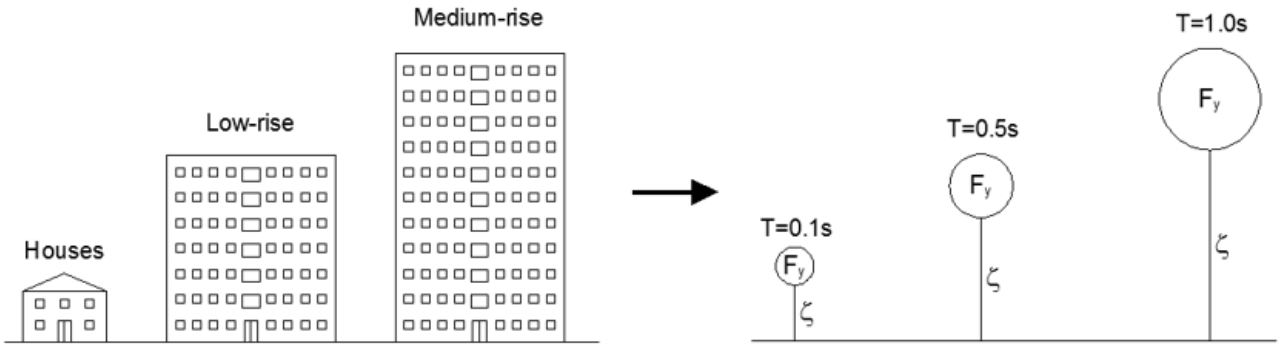

Figure 1. Types of buildings. On the left, real buildings. On the right, reduction into SDOF-systems

The right panel in Fig. 1 shows the way in which these real structures can be simplified into single degree of freedom (SDOF) systems, characterized by their corresponding period of vibration (T), lateral strength (Fy), and damping ratio (ξ). The lateral strength of each system was chosen such that the proportion of collapses of each SDOF is around 5%.

We will focus on these simplified systems with T=0.1s, 0.5s, 1.0s while ξ will be kept equal to 5% as usually done in practice. The force-displacement behavior of the simplified models was based on common structural engineering parameters, having a bilinear form with a post-yield stiffness ratio of -2%.
The dataset is built from the outcomes of nonlinear dynamic analyses on the three oscillators for an unbiased set of 274 different input ground motions.

Using the app *MATLAB* Classification Learner, we create an analytic model to classify the various samples (buildings) in two categories, respectively representatives of a state of collapse or non-collapse.

We evaluate the precision of the model by analyzing the confusion matrix and calculating three different parameters for each of the two classes. Using the collected parameters, we determine the predictive reliability of the selected IMs (Figs. 2-4).

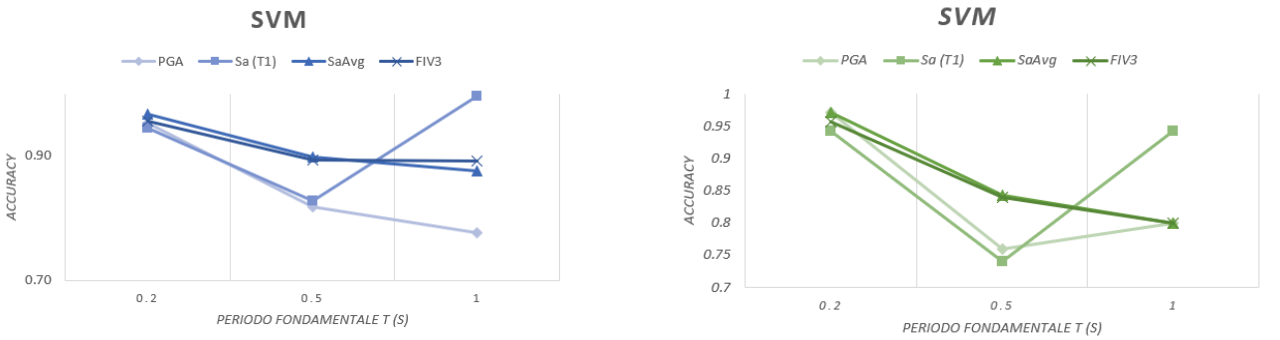

Figure 2. SVM. Accuracy vs Fundamental Period. On the left, elastic oscillator. On the right, elastic-plastic oscillator.

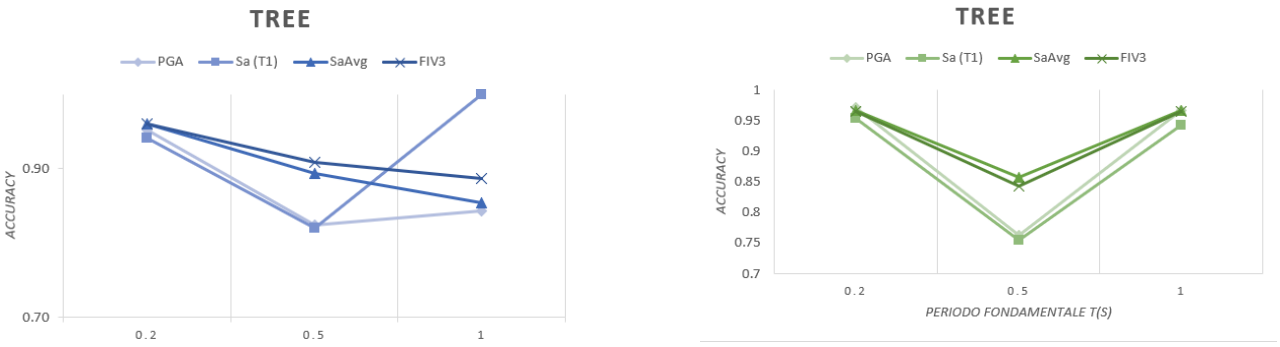

Figure 3. Tree. Accuracy vs Fundamental Period. On the left, elastic oscillator. On the right, elastic-plastic oscillator.

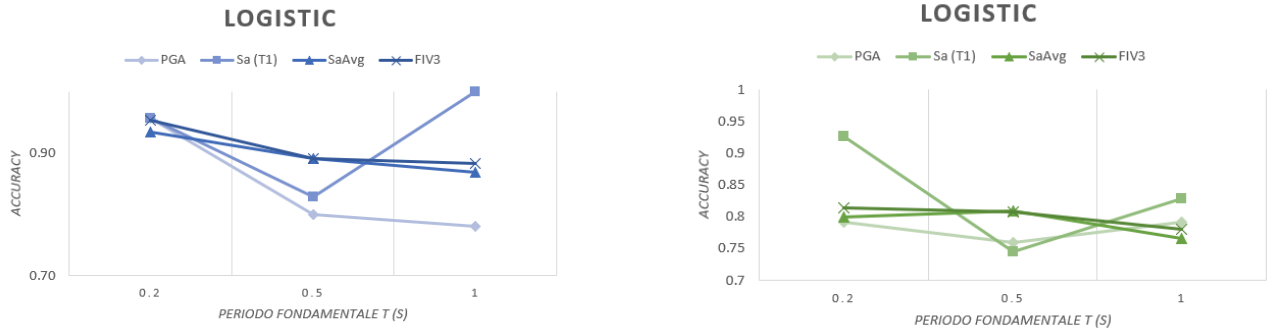

Figure 4. Logistic Regression. Accuracy vs Fundamental Period. On the left, elastic oscillator. On the right, elastic-plastic oscillator.

Acknowledgements

This work has been supported by the project “Preventing, Managing and Overcoming natural-hazards risks to mitiGATE economic and social impact” (PMO-GATE), funded by the European Union in the context of the Interreg Italy-Croatia program.

References

[1] P. Heresi, E. Miranda. *Intensity measures for seismic performance assessment of wood-frame single-family houses*, Proc. of the 17th World Conference on Earthquake Engineering, 2017.
[2] F. Appiotti, V. Assumma, M. Bottero. *Definition of a risk Assessment Model within a European Interoperable Database Platform (EID) for Cultural Heritage*, Journal of Cultural Heritage, 46, pp. 268-277, 2020.
[3] P. Heresi, H. Davalos. *Improving efficient seismic collapse intensity measures using machine learning*, Stanford Internal Report, 2016.
[4] H. Davalos, E. Miranda, *Filtered incremental velocity: A novel approach in intensity measures for seismic collapse estimation*, Earthquake Engineering and Structural Dynamics, 48(12), 1384-1405, 2019.

THE IMPORTANCE OF APPLYING AN APPROPRIATE APPROACH TO MODELLING WASTEWATER TREATMENT PLANTS

Alma Dzubur[1], Amra Serdarevic[2]

[1] Department of Sanitary Engineering and Department of Environmental Engineering, Faculty of Civil Engineering, University of Sarajevo, Sarajevo, Bosnia and Herzegovina, alma.dzubur@gf.unsa.ba
[2] Department of Sanitary Engineering and Department of Environmental Engineering, Faculty of Civil Engineering, University of Sarajevo, Sarajevo, Bosnia and Herzegovina, amra.serdarevic@gf.unsa.ba

Abstract
Wastewater treatment plants (WWTPs) are designed and built to remove contaminants from wastewater. WWTPs are composed of various facilities equipped with hydro-mechanical and electrical equipment. This paper presents a comparison of two different approaches for WWTPs modelling. Static modelling is suitable for determining the dimensions of facilities and equipment capacity. Dynamic modelling is expensive, time consuming and requires great expertise in the use of simulators, models and very good understanding of the treatment processes. Also, dynamic modelling is very important to use for optimization, consideration of future scenarios and also possible scenarios on the plant.
The comparison of two approaches was made on the input data from the most important plant in Bosnia and Herzegovina (B&H) – WWTP Butila (Sarajevo). The main idea is to show the differences between two demanding accesses. The II phase of the plant, which includes the removal of nutrients, is planned in several years and therefore the importance of research has increased.
Keywords: wastewater treatment, input data, modelling, steady state, dynamic

1. Introduction and Motivation

WWTP categorization is contained in wastewater legislation. Usually, plant categorization is expressed in two ways: pollutant equivalent (PE) and daily load of pollutants in kg/day (most often according BOD_5). The European Directive 91/27/271 (Urban Waste Water Directive) and B&H legislation categorize the plants in small and large. However, the developed countries with a population connection rate to the sewage system and wastewater treatment over 90%, have in their legislation more than two categories. One such example is the German regulation „AbwV“ (https://www.gesetze-im-internet.de/abwv/AbwV.pdf), where the plants are divided into 5 groups (GK1-GK5). According the 5 categories, the values of emission limit are prescribed there, with stricter conditions for large vs. small plants of discharging effluent into watercourses.
WWTPs classification into more than two categories enables better systematization of treatment technologies. Generally, unconventional treatment technologies and technologies with activated sludge in fixed growth are recommended for small plants, while conventional technology with activated sludge in suspended growth system, SBR, MBR etc. [1] are recommended for large plants.
Calculation and dimensioning of WWTPs can be static (steady state) and dynamic [2, 3]. Both approaches have their own significant place in use. An example of guidelines for static modelling of WWTPs is the German DWA-A131 (2016) [4] and they are commonly used in practice. Dynamic modelling is more used in North-America than in Europe [5, 6]. This approach is mostly used for process optimization, improvement of treatment effects, fine-tuning in plant operation etc.
Each of the approaches is based on a representation of reality but does not completely correspond to it. The difference (static vs. dynamic) can be shown based on the mass balance. For the mass balance it is

a combination of: degradable matter, transport processes and reaction mechanisms [8]. For the completely mixed reactor, mass balance is [3]:

$$\frac{dM}{dt} = \frac{dc}{dt} \times V = (Q_{in} \times c_{in} - Q_{ou} \times c_{ou}) \times r_c \times V \quad (1)$$

Change in mass = transport + conversion

In steady state calculation the term which describes the change of mass is equal to zero. The balance of mass simplifies the equation and equalizes transport term with conversion term.

$$Q_{in} \times c_{in} - Q_{ou} \times c = -r_c \times V \quad (2)$$

Where: c – concentration (g/m^3), V – volume (m^3), Q – flow (m^3/s), r_c – net rate of biomass production, gVSS/m^3,d, in – inlet to AT, ou – outlet from AT.

2. Materials and methods

For static modelling of WWTPs the necessary input data are the plant capacity (in PE) or flow and parameters of influent composition. For newly planned WWTPs, a minimum number of inputs data is usually available. By adopting assumptions, constrains and safety coefficients, the flow of calculations and dimensioning is monitored.

For dynamic modelling of WWTPs, in addition to the basic input data on the connected inhabitants to the sewerage system, it is necessary to have a number of inlet data for its implementation. Flow and composition of wastewater can be measured or generated by one of the methods. One such method is "HSG-Sim" ("Hochschulgruppe Simulation") [9, 6]. It is used for generation of diurnal variation for influent data and is incorporated in simulator SIMBA#, from "Ifak Institute", Magdeburg, Germany (https://www.ifak.eu/en), which is also used for holistic modelling of wastewater [7].

Depending on the set goal of the dynamic simulation, the modelling conditions differ. A different type of input data is required: influent data, physical data of WWTP, operational settings and effluent conditions [2]. If the goal of simulation is optimization, then the input data must be detailed and with minute time equidistance, as opposed to e.g., testing possible scenarios where input data with 2h-composite samples in 3-7 days campaign are required.

There are several simulators for static and dynamic modelling. One of the simulators for static modelling is Aqua Designer BitControl, Germany (https://www.bitcontrol.info/en/). For dynamic modelling of WWTPs there are a lot of different programs with free downloading like STOAT (https://www.wrcplc.co.uk/ps-stoat) and others that need to be paid. One of the commonly used software is GPS-X from Hydromatis, Canada (www.hydromantis.com).

3. Results and Discussion

The WWTP Butila was built for the first time in 1982. During the war in B&H (1992-1995) it was devastated and in 2016 reconstructed for the I phase (600,000 PE). More details about the plant, input data, measurement techniques and treatment processes can be found in previously published papers [10, 11]. For the WWTP Butila the volume of the aeration tank (AT) is analyzed and calculated. According to the project (I phase) V_{AT} is 21,980 m^3 [12]. The calculation done in Aqua Designer 8.0 resulted in a higher volume value, i.e., 23,204 m^3 (+5.5%). The future expansion of the plant (II phase) is planned for 2030, including the removal of nutrients. The project calculated that the volume of the aeration tanks should be 106,393 m^3 and 108,604 m^3 according the guideline DWA-A 131 (+2.1%). The differences are minor than for I phase, but the ratio of denitrification zone in relation to the total volume (V_D/V_{AT}) differs for 35-40%.

In opposite to static modelling, the results of aeration system optimization with dynamic modelling and possible future scenarios of the plant operation were obtained in regarding changes in the flow of influent and wastewater composition.

Dynamic simulations were performed using the GPS-X simulator (see Fig. 1). Unlike static modelling, the results of requested and obtained goals refer to optimization of the aeration system and the possible future scenarios of the plant regarding the change in quantity and composition of the influent wastewater.

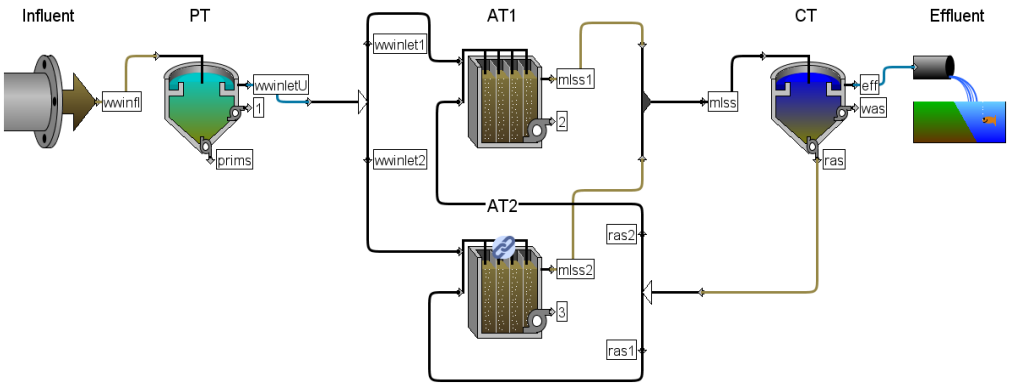

Fig. 1: WWTP Butila - Model in GPS-X

General data requirements for modelling of WWTP Butila are presented in Table 1.

Table 1: Input data requirements for WWTP Sarajevo (Butila) [6]

Input data WWTP	Sarajevo (I phase) Project [12]	Sarajevo (I phase) measuring 2019	General data requirements for modelling	
			steady state	dynamic
PE (Pollutant equivalent)	600,000	-	necessary	necessary/preferably
Q_{ADWF} (m^3/dan)	169,000.00	140,159.45	preferably	necessary
COD (g/m^3)	424.80	569.14	preferably	necessary
TSS (g/m^3)	247.80	338.35	preferably	necessary
TKN (g/m^3)	38.90	29.22	preferably	necessary
TP (g/m^3)	6.40	5.76	preferably	necessary
Oscillations of the influent flow and quality parameters during hours and days	-	-	unnecessarily	necessary*

PE – Pollutant equivalent, Q_{ADWF} – Average dry weather flow, COD – Chemical oxygen demand, TKN – Total Kjeldahl Nitrogen, TP – Total phosphorus, f_{Qinf} - Fraction of infiltration water/total flow (-)
* how detailed and which parameter depending on the goal of modelling

4. Conclusion

Static modelling is an adequate choice for planning new plants and gives reliable results of facility dimensions (including sometimes significant reserves). Static simulators recommend a set of process coefficients, which can be adjusted, thus avoiding oversizing of facilities and equipment, while dynamic modelling is recommended for plants in operation and in the reconstruction/expansion phase. Their application is more adequate to describe the behavior of the treatment processes.

It is very important to analyze which of the approaches we should apply for plant modelling. It depends on a large number of factors. Static modelling has been applied in all previous WWTP projects, while dynamic modelling represents a new approach in B&H. This paper presents two general approaches: static and dynamic and both of them were used for modelling of the existing WWTP Butila, which is in function.

The total number of WWTPs in function over 5,000 PE in B&H is 16 and this indicates that it is time to use a “deeper” modelling approach that will, in addition to the dimensions of facilities and equipment, explore the treatment processes themselves, possible scenarios on WWTP etc. An important project, whose focus of research is modelling WWTPs, is a PhD thesis at the Faculty of Civil Engineering, University in Sarajevo, and its draft version review is ongoing.

Acknowledgements

Input data for modelling, i.e. flow and water quality parameters, are ceded from municipal utilities of Sarajevo (ViK Sarajevo) with the support of the plant employees.

References

[1] Metcalf & Eddy, *Wastewater Engineering, Treatment and Resource Recovery*, Fifth Edition, New York: McGraw-Hill Education, 2014.

[2] Rieger L., Gillot S., Langergraber G., Ohtsuki T., Shaw A., Takács I., Winkler S., *IWA Task Group on Good Modelling Practice - Guidelines for Use of Activated Sludge Models*, IWA Publishing, 2013.

[3] Serdarević A., Džubur A., *Wastewater Process Modelling*, Coupled Systems Mechanics-International Journal of Interactions of Coupled Systems, Vol. 5, 21-39, 2016.

[4] DWA-A 131. Bemessung von einstufigen Belebungsanlagen. Die Deutsche Vereinigung fur Wasserwirtschaft, Abwasser und Abfall e. V. (DWA), Hennef, Germany, 2016.

[5] Hauduc H., Gillot S., Rieger L., Ohtsuki T., Shaw A., Takacs I., Winkler S., *Activated sludge modelling in practice: an international survey*, Water Sci. Technol., 60 (8), 1943–1951, 2009.

[6] Dzubur A., Serdarevic A., *Daily Influent Variation for Dynamic Modelling of Wastewater treatment plants*, Coupled Systems Mechanics, Vol. 9, 111-123, 2020.

[7] Schütze M R., Butler D., Beck M. B., *Modelling, Simulation and Control of Urban Wastewater Systems*, Springer-Verlag, 2002.

[8] Jeppsson, U., *A General Description of the Activated Sludge Model No. 1 (ASM1): Modelling Aspects of Wastewater Treatment Processes*, Lund Institute of Technology, Lund University, Sweden, 1996.

[9] Spering, V., Alex, J., Langergraber, G., Ahnert, M., Halft, N., Hobus, I., Weissenbacher, N., Winkler, S., Yücesoy, E., *Using dynamic simulation for design of activated sludge plants*, Proceedings "International Symposium on Sanitary and Environmental Engineering - SIDISA.08", 24-27 June 2008, Florence, Italy, 2008.

[10] Džubur A., Serdarević A., *Kontrola i održavanje PPOV – Primjer PPOV Butile, Sarajevo, BiH*, 5. Konferencija „Održavanje 2018“, 10-12 may 2018, Zenica, Bosna i Hercegovina, 103–110, 2018.

[11] Serdarević A., Džubur A., *Importance and Practice of Operation and Maintenance of Wastewater Treatment Plants*, Advanced Technologies, Systems, and Applications III, Springer Nature Switzerland AG, 121-137, 2019.

[12] As Built Design – Reconstruction Works at Sarajevo Wastewater Treatment Plant at Butila, "Unioninvest" d.d. Sarajevo and "Passavant, Energy & Environment", 2016.

ECCOMAS MSF 2021 THEMATIC CONFERENCE
30 June – 2 JULY 2021, SPLIT, CROATIA

NUMERICAL INVESTIGATION OF THE PRESSURE DRIVEN PERCOLATION AND DEVELOPED FLUID PATHWAYS: HYDRO-MECHANICAL LATTICE MODEL

Amir Shoarian Sattari[1], Zarghaam Haider Rizvi[2], Frank Wuttke[3]

[1] Geomechanics and Geotechnics Group, CAU Kiel, Germany, amir.shoarian-sattari@ifg.uni-kiel.de
[2] Geomechanics and Geotechnics Group, CAU Kiel, Germany, zarghaam.rizvi@ifg.uni-kiel.de
[3] Geomechanics and Geotechnics Group, CAU Kiel, Germany, frank.wuttke@ifg.uni-kiel.de

Abstract

In this research, the application of the in-house developed coupled hydro-mechanical lattice model on numerical simulation of the hydraulic fracking process and the development of flow channels in geomaterials is investigated. The mechanical model is based on the equation of motion, known as Newton's second law, which is solved using Newmark-β model and Newton-Raphson Jacobian. According to the conservation of fluid mass in the domain and with the generation of artificial cavities on the polygonal vertices, the fluid flow is simulated. The developed hydraulic pressures on the polygonal vertices, after the saturation of the pore volumes, are then transferred into the mechanical model. The Mohr-Coulomb failure criterion with a tension cutoff is implemented here to simulate the fracking process. Eventually, the advantage of lattice models to account for inherent and stochastic irregularities and heterogeneities that exist in geomaterials are depicted.

1 Introduction

During the last decade, the application of hydraulic fracking in extraction of oil and natural gases from shale reservoirs has been extensively studied. Similarly, the artificial salt caverns have been used for storage of various from of energy carriers. Finite Element Methods (FEM) and Phase field methods are widely used to simulate the hydraulic fracking in geomaterials [1, 2]. During the past decade and with the computational power growth, the application of discrete element methods in simulation of hydraulic fracking are also begun to emerge [3]. Recently, the mechanical lattice model's application is extended from the static cases [4] to the dynamic models [5]. The existing hydraulic lattice models are based on the dual lattice model, where boundaries of the polygonal cells are considered as flow channels [6]. In the conducted study, the application of the in-house developed coupled hydro-mechanical lattice model on the simulation of hydraulic fracking is investigated.

2 Domain Discretization

The vectorizable random lattice approach is implemented here to generate the nuclei in the domain. The defined randomness factor (α) in this approach varies from 0 to 1, where 0 results in regular square shaped element patterns. The irregularities that exist in particles scale can be attained with the greater randomness factor values. The Voronoi Tessellation and Delaunay Triangulation theories are considered here to generate the polygonal shape Voronoi cells and lattice elements, respectively (Fig. 1a, Fig. 1b). The pursued mesh refinement technique around the cavities and pre-known fracking paths reduces the computational demand of the algorithm. Additionally, with rearrangement of Voronoi vertices of all cells surrounding the predefined fracks and cavities, smooth crack surfaces for better visualization as well as accurate stress distribution around crack tips are generated (Fig. 1c).

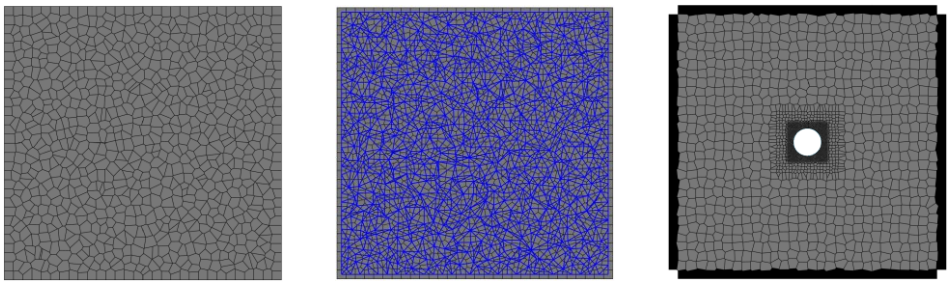

(a) (b) (c)

Figure 1. Domain discretization: (a) generated Voronoi cells ($\alpha \approx 1$), (b) Delaunay Triangulation and generation of lattice elements ($\alpha \approx 1$), and (c) mesh refinement and defined cavity ($\alpha \approx 0.5$)

3 Implementation of Dynamic Lattice Model

Initially, the regularization of the lattice model is carried out and a correlation between the lattice element and the continuum properties is driven. According to the implemented regularization method, the stored strain energy in a unit cell (U_{cell}) is equal to the stored strain energy in the continuum (U_R). Therefore, the mesh independent results are granted.

$$U_{\text{cell}} = U_R, \qquad U_{\text{cell}} = \frac{1}{2}\sum_{b=1}^{b=N_b} l_b^2 \left(R' \;\; n_i\, n_j\, n_k\, n_m\, \varepsilon_{ij}\, \varepsilon_{km}\right)_b \tag{1}$$

A series of spring lattice elements between each pair of Voronoi cells are generated, where the resistance to axial (k_n), transverse (k_s) and rotational (k_ϕ) displacements are defined. The dynamic lattice model formulation is based on the equation of the motion, known as Newton's second law. The acceleration ($\ddot{\boldsymbol{u}}$), velocity ($\dot{\boldsymbol{u}}$) and displacement ($\boldsymbol{u}$) of the defined constant masses on the nuclei are solved using the Newmark-β model. The mass ($\boldsymbol{M}$), damping ($\boldsymbol{C}$) and stiffness matrixes ($\boldsymbol{K_g}$) are assembled in global coordinates.

$$\boldsymbol{M}\ddot{\boldsymbol{u}}(t) + \boldsymbol{C}\dot{\boldsymbol{u}}(t) + \boldsymbol{K_g}\boldsymbol{u}(t) = f_{ext}(t), \quad t_{(i+1)} = t_{(i)} + \Delta t, \tag{2}$$

where f_{ext} is a vector of external dynamic loads and Δt is the timestep. The incremental formulation of motion equation can be solved under the assumption of different γ and β parameters. For an instance, when $\beta = \frac{1}{4}$ and $\gamma = \frac{1}{2}$ the Newmark method is unconditionally stable and implicit.

$$\delta\ddot{\boldsymbol{u}} = \frac{1}{\beta\Delta t^2}\delta\boldsymbol{u} - \frac{1}{\beta\Delta t}\dot{\boldsymbol{u}} - \frac{1}{2\beta}\ddot{\boldsymbol{u}}, \qquad \delta\dot{\boldsymbol{u}} = \frac{\gamma}{\beta\Delta t}\delta\boldsymbol{u} - \frac{\gamma}{\beta}\dot{\boldsymbol{u}} + \Delta t\left(1 - \frac{\gamma}{2\beta}\right)\ddot{\boldsymbol{u}} \tag{3}$$

Eventually, to solve the system of nonlinear equations with multiple variables, the Newton-Raphson Jacobian approach is implemented. In order to simulate the fracking process, the Mohr Coulombs failure criterium with tension cutoff, where the mode I and II failure of elements is permitted, is implemented. The convergence of the dynamic lattice model depends on the wavelength, length of the lattice elements and the magnitude of the timestep.

4 Development of Hydro Lattice Model

The implemented hydraulic lattice model is based on the dual lattice theory, where the boundaries of the Voronoi cells are considered as flow channels. The vertices of the Voronoi cells are then defined as artificial cavities, in which the fluid flows are directed. The conservation of mass theory is implemented here to determine the fluid mass transfer in different timesteps. The assumption of viscous laminar flow is chosen to simulate the flow rate through conduct channels using Darcy's law.

$$q = \frac{dm}{dt} = -\frac{P_{f,j} - P_{f,i} - \rho_f g\left(Z_j - Z_i\right)}{R_h} \tag{4}$$

The mass transfer through each conduct channel is dependent on the length of the channel (l), cross-section length of the channel (hydraulic aperture, a), flow potential (Φ), density (ρ), and the viscosity of the fluid (υ). The cubic flow rule is considered here to determine the flow resistance (R_h).

$$\Delta m_{f,ij} = f(Sr)\frac{P_{f,j} - P_{f,i} - \rho_f g\left(Z_j - Z_i\right)}{R_h}\Delta t, \quad m_f^{t+1} = m_f^t + \Delta m_f, \tag{5}$$

where $f(Sr)$ is a dimensionless saturation degree function defined to reduce the effective permeability of the conduct channels. With the amount of the excessive fluid mass that flows into each cavity the

pore pressures are measured. The fluid pressures in each timestep are dependent on the bulk modulus of the fluid, volume of the cavity, and the excessive fluid mass that has been rushed into the saturated cavity.

$$P_f^t = P_f^{t-1} + K_f \frac{\Delta m_f}{\rho_f V_{\text{cav}}^t} \quad \text{if} \quad \text{Sr}^t = 1, \qquad P_f^t = 0 \quad \text{if} \quad \text{Sr}^t < 1 \tag{6}$$

In the 3D flow model, artificial cavities are generated between each pair of neighboring Voronoi cells. Then, the Delaunay Triangulation approach is implemented to generate the conduct elements. The coupling of the hydro-mechanical model is based on the weak coupling scheme, where the fluid pressures in the cavities are transferred into the mechanical model. Afterward, the emerged hydro-mechanical deformations are transmitted into the hydro model.

5 Numerical Studies

5.1 Crack Initiation and Propagation under Monotonic Loading

The numerical simulation of the frack propagation in a 2D domain under the constant confining stress and zero hydraulic pressure is presented in Fig. 2. The deviatoric stress is gradually increased ($\Delta\sigma_v$) till the frack process initiated. The change of the displacement wave field (along x-axis) before and after the fracking process is shown in Fig. 2b.

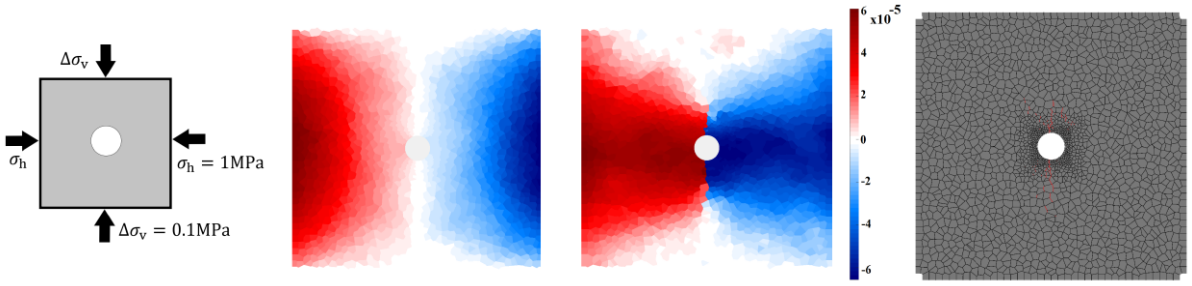

(a) (b) (c)

Figure 2. Crack initiation and propagation under mechanical monotonic loading: (a) boundary condition, (b) displacement wave fields along x-axis (h) before and after fracking, and (c) crack path

5.2 Fluid Flow and Pore Pressure Diffusion

The 2D simulation of a fluid flow in the conduct elements and saturation of the defined artificial cavities are studied and presented in Fig. 3. The flow pathways are arbitrary and dependent on the inherent stochastic irregularity that exists in the lattice models. The saturation of the artificial cavities (Voronoi vertices) and flow channels in three different timesteps are shown in Fig. 3b. The results indicate the time dependent fluid flow pathways and developed fluid pore pressures.

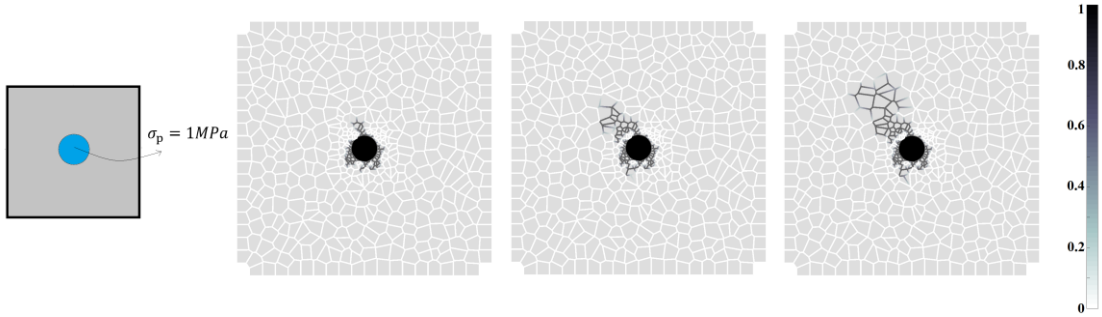

(a) (b)

Figure 3. Fluid flow in geomaterials: (a) boundary condition, and (b) saturation of artificial cavities and flow channels in three timesteps

5.3 Fluid Pressure Driven Percolation in Heterogenous Geomaterials

In the 3D lattice model and with definition of a heterogenous geomaterial with the embedded layering, the generation of the crack surfaces under the coupled hydro-mechanical loading condition is

simulated (Fig. 4). In the first cubic sample, the fluid injection direction is perpendicular to the layering orientation. In the second case, the fluid injection direction is parallel to the layering orientation. The results indicate the dependency of the fracking and flow paths on the defined embedded layering orientation of geomaterials, like what can be found in shale and claystone.

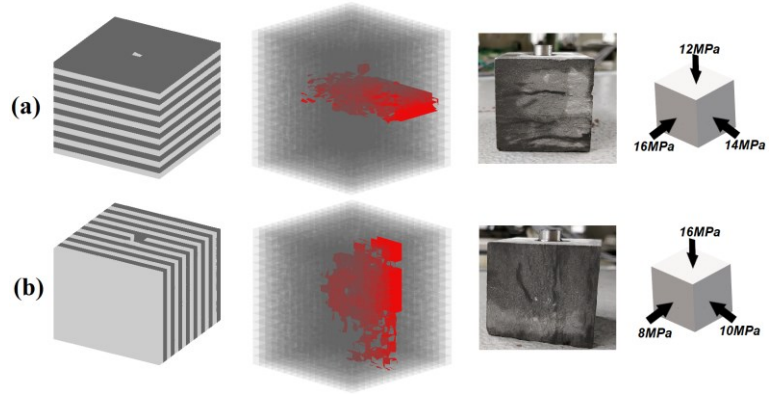

Figure 4. The 3D hydro-mechanical lattice model and simulation of fracking surfaces (shown with red) in a heterogenous geomaterial: fluid injection (a) perpendicular to the layering orientation, and (b) parallel to the layering orientation. (experimental tests of Opalinus claystone [7])

6 Conclusion

The presented lattice model in this study is capable of simulating crack initiation and propagation, pressure driven percolation and pore pressure diffusion in the coupled hydro-mechanical problems. The inherent stochastic irregularity that exist in lattice models is ideal for simulation of the fracking in geomaterial, as it can account for irregularities that are present in particle scale. The 3D simulation results depict the ability of the lattice model to simulate the realistic fracking and flow paths in a heterogenous geomaterial. Beside the qualitative studies that are presented here, a quantitative analysis of the lattice model outcome is under development.

Acknowledgments

This research project is financially supported by research grant ‘’GeomInt2’’ provided by the Federal Ministry of Education and Research (BMBF), Germany with a grant number of 03G0899B.

References

[1] Wangen, Magnus. Finite element modeling of hydraulic fracturing in 3D. Computational Geosciences. Mars. 1-13, 2013.

[2] Yoshioka, Keita & Chukwudozie, Chukwudi & Bourdin, Blaise. A Variational Phase-Field Model for Hydraulic Fracturing in Porous Media. Computer Methods in Applied Mechanics and Engineering. 347. 957-982, 2019.

[3] Marina, S., Derek, I., Mohamed, P. et al. Simulation of the hydraulic fracturing process of fractured rocks by the discrete element method. Environ Earth Sci 73, 8451–8469, 2015.

[4] Rizvi, Z.H., Nikolić, M. & Wuttke, F. Lattice element method for simulations of failure in bio-cemented sands. Granular Matter 21, 18, 2019.

[5] Rizvi Z.H., Mustafa S.H., Sattari A.S., Ahmad S., Furtner P., Wuttke F..Dynamic Lattice Element Modelling of Cemented Geomaterials. In: Prashant A., Sachan A., Desai C. (eds) Advances in Computer Methods and Geomechanics. Lecture Notes in Civil Engineering, vol 55. Springer, Singapore, 2020.

[6] Grassl, Peter. A lattice approach to model flow in cracked concrete. Cement and Concrete Composites, 31, 7, Pages 454-460, 2009.

[7] Kolditz, O. and Görke, U.-J. and Konietzky, H. and Maßmann, J. and Nest, M. and Steeb, H. and Wuttke, F. and Nagel, Th. GeomInt–Mechanical Integrity of Host Rocks, Terrestrial Environmental Sciences, Springer, 2021.

ECCOMAS MSF 2021 THEMATIC CONFERENCE
30 June – 2 JULY 2021, SPLIT, CROATIA

ASSESSMENT OF POTENTIONAL MINIMIZATION OF LEACHATE PRODUCTION WITH WATER-BALANCE MODELING

Amra Serdarevic[1], Zeljko Lozancic[1]

[1] Faculty of Civil Engineering, University of Sarajevo, amra.serdarevic@gf.unsa.ba
[1] Faculty of Civil Engineering, University of Sarajevo, zeljko.lozancic@gf.unsa.ba

Abstract
Regional Waste Management Center (RWMC) Smiljevići is the largest facility of this type in Bosnia and Herzegovina (BiH), with yearly disposal of approximately 200,000 tons of waste. One of the major issues at the Smiljevići RWMC is a large amount of generated leachate (average leachate discharge measured at the site in the period 2017 - 2019 is 3.5 l/s). The reason for leachate generation is the large open operation area of the landfill and also the area covered with a temporary cover of approximately 0.5 m thick soil/inert material layer on which grass and small vegetation is grown. The first step in improvement of leachate management would be to minimize leachate generation. For this, the considered part of the landfill should be closed with a permanent cover. Closure of the landfill implies that an impermeable or semipermeable top cover should be used to seal the body of a landfill, reducing air intrusion and liquid infiltration into the landfill body. In this paper results of the leachate production modeling for several closure scenario for the Smiljevići landfill in Sarajevo Canton are presented.

Key words: Leachate, landfill body, rainfall, infiltration, water balance modeling, top cover

1. Introduction

Landfill leachate can be defined as all water that has been "in contact" with landfill waste. Primarily this refers to the percolation of the precipitation through the body of the landfill. However, the water balance of a landfill also includes waste moisture or, in the case of inadequately bottom liner, the penetration of groundwater into the landfill body. The problem of leachate water is always a complex issue at the sanitary landfill in operation [1].
Capping systems of the landfill are often the only efficient solution by the long–term safety concept for environment and leachate production minimization. The composite liner is the main component of standard landfill capping's for municipal waste landfills. According to the European Council Directive on the landfill of waste the impermeable mineral layer is recommended for the surface sealing of non-hazardous landfills and the composition of artificial sealing liner and impermeable mineral layer for hazardous landfills. The composite liner is a technically highly effective but very expensive system. Various alternative capping and suitable systems for capping has a different impact on the leachate production, what is presented further in this paper.

Several projects in this domain, funded by local ministries and IFIs, have been implemented in last years, with an objective to improve waste management in BiH and Canton Sarajevo. Project for minimization of leachate generation in the Smiljevići landfill, the lifespan analysis and the assessment of progressive

closure for leachate minimization has been conducted in 2018/2019[2]. Alternative capping systems and leachate production minimization were investigated for the Smiljevići landfill in Sarajevo Canton. Leachate production at the Smiljevići landfill, under the different capping systems and conditions on the site, has been modeled by water balance calculation. Results of the leachate production modeling and recommendations are presented and interpreted in this paper, in the light of the experience in this field.

2. Study area

Regional Waste Management Center (RWMC) Smiljevići is the largest facility of this type in Bosnia and Herzegovina (BiH). The waste is disposed at the site since 1962 and until 1997 the site has been used as a dumpsite. Since 1997 operational and technical measures have been introduced, so in the year 2001 the first real controlled landfill cell with a multi-barrier bottom seal and leachate collection system at the site was constructed. Also, the gas collection and utilization systems were developed, as well as the leachate treatment plant. The wide area of uncovered fresh waste at the landfill in combination with flat slope inclination at the fully utilized, but uncapped landfill surface with approximately 10 hectares is a one of the main reasons leading to high leachate generation rate in average ~ 400 m³/d[1]. The Cantonal environmental action plan put this issue as a priority with the goal to instantly minimize leachate generation rate by construction of a final capping system in the areas of the landfill that reached end of operation[2]. Total footprint of the landfill is around 27.4 ha, while total area considered for final capping at the Smiljevići landfill is around 11.7 ha (Cell 3) and it is divided into three areas (Figure 1.).

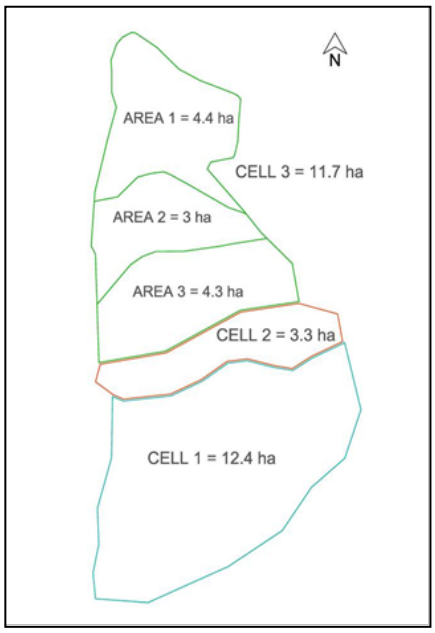

Figure 1. Schematic drawing of the Smiljevići landfill footprint. Cell 1 – old waste covered with temporary cover, Cell 2 – active cell, Cell 3 – considered for final cover

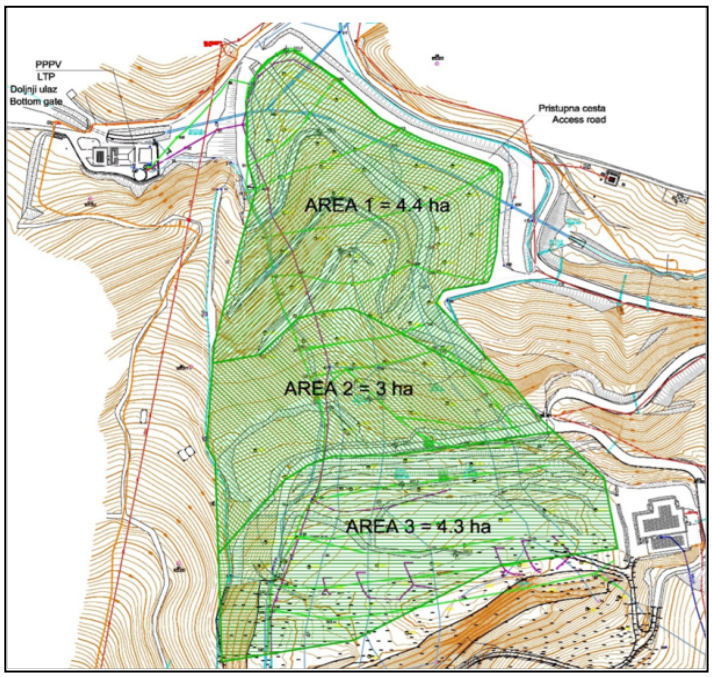

Figure 2. Total area considered for final capping (Cell 3 consisting of Areas 1, 2 and 3)

Bottom impermeable layer of Cells 2 and 3 consists of hardly permeable clay (up to 1 m) and a high-density polyethylene layer (2.5 mm). Multi-barrier bottom layer has been constructed on the consolidated old waste (thickness app. 20m - 40m). Collection of leachate from the landfill is carried out using three drainage systems, two below the multi-barrier bottom layer, and one drainage system constructed on the top of the multi-barrier layer. Drainage system collects the leachate and transports it to leachate treatment plant (LTP) where appropriate MBR technology is used. The estimated total amount of generated leachate ranges from 2.5 to 3.5 l/s[4]. Composition of leachate corresponds to the methane phase of the landfill condition (waste older than 20 years)[4].

3. Water Balance Modeling

There are different models to assess the leachate generation modeling [3,5]. Application of any of the model to the Smiljevići landfill is very difficult due to complexity of the site, generation of leachate and the various drainage systems collecting the leachate. As the site is not entirely sealed with a bottom layer and as such separated from the adjacent area, there is likely an influence of groundwater draining from surrounding area, not only from the landfill/waste footprint [3].
Taking into consideration all of the above-mentioned, a relative simple Excel-based model, already used for leachate modeling on other landfill sites was applied. . This model is capable to estimate the quantity of leachate as well as the flux of contaminants. The model is based on the water balance equation and calculates the quantity of leachate based on the area of the site, waste disposal rate and age of disposed waste, average rainfall, evaporation and run off, top cover etc. [3]. The model can also deal with recirculation and additional water sources. It also can easily be adjusted for site-specific needs. Leachate generation is calculated using water balance equation as follows:

$$L = P + R - aET - Q$$

Where: L = leachate generation (mm), P = total annual precipitation (mm), R = leachate recirculation (mm), aET = actual evapotranspiration, Q = surface runoff.

The climate data used for the model were obtained from the Meteorological Station Bjelave – Sarajevo, for the period from 1981 to 2010 [2,4] For the calculation average monthly values were used. Average annual precipitation for this period is 932 mm, while the average temperature is 10.1°C. The actual evapotranspiration is calculated using Thornthwaite formula, and for this period it was 650,8 mm. The potential infiltration is calculated as the difference between average annual precipitation (P) and surface runoff (Q). The surface runoff is calculated by multiplying total precipitation with estimated runoff coefficient C which is different for model cells in regards to cell cover and inclination as well as the cell activity. Finally, for the calculation of leachate discharge (m^3) on the annual basis, the calculated leachate generation (mm) was multiplied by the total area of the landfill cell.
For the initial leachate model of the existing situation the climate data were used and different runoff coefficients were associated to the three Cells. The leachate values obtained by the model were compared to the measured values and the runoff coefficients were adjusted in order to leachate values from the model meet the measured values.
Two types of the final cover for the Cell 3 have been considered. The impermeable and semipermeable final covers which consist from following layers:

- Topsoil layer – approx. 0.2 m thick topsoil layer to promote vegetation growth;
- Protective Layer – approx. 0.8 m thick layer of low permeability soil to act as a protective layer;
- Drainage Layer – approx. 0.2 m thick coarse sand and gravel layer to promote drainage towards the landfill boundaries – optional for impermeable final cover;
- Barrier Layer – impermeable synthetic geomembrane liner to prevent water infiltration into the landfill - optional for impermeable final cover;
- Leachate and Gas Layer – approx. 0.2 m coarse layer to grade landfill surface, provide stability and ensure leachate and gas drainage.

A total of four closing options for the part of the landfill (Cell 3) were analyzed, on which no further disposal of waste will be carried out:

- Option 1 – Area 1 and 2 impermeable layer (total 7.4 ha), Area 3 (4.3 ha) semipermeable layer;
- Option 2 – Area 1 impermeable layer (total 4.4 ha), Area 2 and 3 (7.3 ha) semipermeable layer;
- Option 3 – Area 1, 2 and 3 impermeable layer (total 11.7 ha);
- Option 4 – Area 1, 2 and 3 semipermeable layer (total 11.7 ha).

4. Discussion

In regards to selection of options for implementation the result of the leachate production modeling is between 12% to 26%. If only Cell 3 is considered, reduction of leachate varies between 47 and 100%. Since it is planned to cover the part of the landfill (Cell 3), from which leachate is collected by shallow drainage, influence of the final cover will only be on reduction of leachate generated from this area. If estimated leachate reduction is viewed in relation to the estimated leachate generation from the landfill area with the bottom multibarrier liner (Cells 2 and 3), reduction of leachate is from 46% to 63% depending on the selected capping option.
In order to minimize overall leachate production at the landfill, the capping system of entire landfill should be constructed, leachate from the active area should be separated from the existing leachate drainage systems and potential unwanted infiltration in the drainage system needs to be considered and investigated, where possible infiltration or inflow points in the existing leachate drainage systems increases the leachate quantity [2,3,4,5].

5. Conclusions

For this study, the model was applied as the one of the most commonly used statistical-empirical approaches to predict the water-balance components of landfill capping systems, and several conclusions could be drawn from modeling results.
The modeling results were realistic reflecting observed outflow and leachate data, even with a limited set of input data. The surface area factor strongly affected the leachate generation as well as situation with infiltration of the potential sources or streams.
Thus, it should be aware that valid input data are absolutely ultimate for the success of a simulation run. It should be taken into account that the modeling simplifications and possible errors may cause modeling uncertainties. Additional sensitivity analysis is also very important to be conducted in order to determine the influence of individual factors on the modeling result.
In summary, the water balance model allowed to predict the leachate production and prove the functionality of a temporary capping system under the given weather and site conditions. In order to finally validate some values (e.g. water fluxes through the compacted waste), a more physically based model could give better insight into the variations in waste - soil - water characteristics. For the Sarajevo sanitary landfill it is necessary to continue with monitoring of the hydro-meteorological data for further steps in modeling. Physical and numerical modeling of leachate production should be a part of further researches, as well as researches on the leachate composition, treatment and its impact on the environment.

References

[1] A.Serdarevic, D. Tuhtar, Z. Milasinovic, F. Babic, *Membrane filtration for the landfill leachate treatment–case study of the pilot plant in Sarajevo*, Proceedings, CISA, Cagliari, Italy; 2007
[2] World Bank and SIDA, *Improvement Of Seven Solid Waste Disposal Sites in BiH*;Task3 – Smilijevici Landfill Sarajevo, april 2019.
[3] K.U. Berger, *On the Current State of the Hydrologic Evaluation of Landfill Performance (HELP) Model*, Waste Management 38: 201-9.
[4] Serdarevic A. (2018) *Landfill Leachate Management—Control and Treatment*. In: Hadžikadić M., Avdaković S. (eds) Advanced Technologies, Systems, and Applications II. IAT 2017. Lecture Notes in Networks and Systems, vol 28. Springer, Cham. https://doi.org/10.1007/978-3-319-71321-2_54
[5] Rainer M. Zeh, Karl J. Witt; *Water Balance Models and Programmes - Comparisons and Calculation Results*; Bauhaus-University Weimar, Thuringia, Germany

DISCRETE FINITE ELEMENT MODEL FOR SAFETY EVALUATION OF ARCH-DAMS

Ana Nanevska[1],Violeta Mircevska[2],Miroslav Nastev[3]

[1] PhD student, Institute of Earthquake Engineering and Engineering Seismology, Univ. Ss. Cyril and Methodius, Skopje, R.N. Macedonia. (corresponding author), e-mail: nanevska@iziis.ukim.edu.mk
[2] Professor, Institute of Earthquake Engineering and Engineering Seismology, Univ. Ss. Cyril and Methodius, Skopje, R.N. Macedonia, e-mail: violeta@iziis.ukim.edu.mk; mircevska.violeta@gmail.com
[3] Research Scientist, Natural Resources Canada, Geological Survey of Canada, Quebec City, Canada G1K 9A9. E-mail: miroslav.nastev@canada.ca

Topic : Advances and Applications in Combined Finite-Discrete Element Method (mini-symposia)

The arch dam design exploits the capacity of concrete to withstand large compressive loads and the convenient shape of the arches that efficiently and effectively carry the static and dynamic compressive loads into the abutments and foundation. It is well-known that the tensile strength of concrete is poor and that large tensile stresses sometimes computed in the massive concrete monoliths are simply a result of the unrealistic assumption of concrete linear behaviour. Tensile stresses can be generated during the construction phase of arch dams due to temperature variations and moisture loss leading to concrete shrinkage. High environmental temperature variations and intense back and forth movements during an earthquake also develop tensile stresses [1][2]. To control the appearance of tensile stresses, arch dams are built with vertical cantilever monoliths separated by contraction joints. It is therefore important that static and dynamic analyses of arch dams consider the work of the vertical contraction joints along the adjacent cantilever monoliths.

Numerical analyses with finite-discrete elements apply 'joint elements' as a convenient way to simulate the repeated opening and closing of the discrete construction joints [3][4][5]. The disadvantage of a discrete element modeling with contact elements is the double-nodding in the finite element mesh connecting two adjacent monoliths. This results in an increased size of the matrices and large number of equations involved in the solution [6][7]. The substructure modeling technique is applied in the process of FE discretization precisely to reduce the number of nodes. Accordingly, the system is discretized into a number of substructures, each composed of a certain number of finite elements. The respective nodes can be classified into: nodes representing the 'external degrees' of freedom that constitute the matrices and contribute to solution of the governing static and dynamic equations, and nodes representing the 'internal degrees' of freedom that define the finite elements within the substructures. Each substructure corresponds to a part of the cantilever monolith defined vertically between two successive elevations of arches and horizontally between two construction joints placed at the contact with the adjacent monolithic blocks. Two different types of nodes are applied to describe the joint elements: basic 'dependent' nodes related to external substructural nodes between two monoliths, and 'independent' nodes interpolated between the basic nodes of the construction joint to define the sub-contact elements [8]. Here, the double nodding is related to the basic nodes only. The essence of the method is in the elimination of the effect from the independent freedom degrees in the substructure. The elimination is done by means of the so-called static condensation process applied prior to both static and dynamic analyses. Joint elements are capable to

simulate the relative displacement among a pair of nodes that belong to the adjacent monolith blocks. Of major concern is the mechanism and extent of opening and closing of the cracks at the joints inevitably followed by sliding, which most probably takes place continuously, i.e., cracks open and close gradually. The structural joints play a significant role in the seismic behavior and consequently in the seismic safety of arch dams. Since they are the weakest part of the dam structure, the nonlinear response and failure of the construction joints occur much earlier than any damage is detected in the monoliths. The partial opening and in-plain sliding of the construction joint actually decrease the tensile stresses that would otherwise appear in the monoliths, thus protecting them from extensive cracking. The tensile and shear failures of joints and the concomitant redistribution of internal forces significantly affect the stress-state in the monoliths. This was confirmed with nonlinear analyses which indicate reduced tensile stress at the expense of joint opening and increased compressive stress in the construction joints during the reversal closing process [9].

The dynamic analyses of arch dams aiming at the accurate evaluation of the seismic safety have to account for the combined action of the construction joints. To this end, an algorithm to simulate the plain type of construction joint with coupled shear - tensile behavior has recently been developed and implemented in ADAD-IZIIS software [10]. This software was specially designed for static and dynamic FEM-BEM-DE analysis of concrete gravity and arch dams. Uniaxial nonlinear constitutive material model is employed to simulate the behavior of the joint elements in the normal direction. The constitutive material model for both tangential directions of the joint interface complies with the Coulomb's friction law. The model controls the nonlinear behavior of the grouting mass and properly simulates the joint opening and closing cycles together with the sliding motion under seismic action. The non-linear analysis applies to the construction joints, whereas the substructures of the massive concrete monoliths are with linear behaviour.

The objective of the present study is to investigate the static and dynamic response of arch dams with vertical construction joints. The example considered herein is a double-curvature dam with a structural height of 130 m. The cantilever monoliths are represented with 10 m high and 15 m wide substructures. Construction joints are placed at the lateral contacts with the adjacent monoliths.

The static loads include self-weight, hydrostatic pressure of the 120 m deep impounded water, and environmental temperature. A temperature gradient is chosen to deform slightly the dam in upstream direction and introduce tensile stresses and lower compressive stresses at the upper part of the dam extrados prior to the introduction of dynamic action. Therefore, initial static stress conditions are developed for joints opening at the dam extrados in case of dynamic loading. The linear temperature gradient within the dam body varies between 18 °C at the dam intrados and 6 °C at the dam extrados. The applied temperature load represents difference between the stress-free temperature, when the joints between cantilever monoliths are grouted, and the assumed environmental temperature.

According to ICOLD recommendations two different types of earthquakes are used for dynamic analyses [11]: Maximum Credible Earthquake (MCE) and Operating Base Earthquake (OBE). In this paper presented are results for the stronger MCE earthquake excitation, where the dam is subjected to the horizontal component of the 1989 M6.9 Loma Prieta earthquake scaled at horizontal peak ground acceleration of PGA(y)=0.78 g and vertical PGA(z)=0.5 g. The applied duration of the record is 10 sec, assumed sufficiently long to generate the appearance of crack opening, closing and shear sliding of vertical joints under seismic loading.

Among the most relevant results is the observed maximal deflection which occurs at the dam crest practically at the same time with the respective maximum response acceleration. Both extremes occur following the onset of the peak ground acceleration of the input motion. Snapshots of the extreme deflection in the vertical construction joints in streamwise direction are also presented. The locations of the manifested joint openings occur mainly in the upper portion of the dam. The distribution of tensile stresses and openings in the vertical construction joints is presented along with the time histories of the developed normal and tangential stresses and strains for joints with extreme tensile and shear failure. For earthquake action in the streamwise direction, tensile failure occurs in the

joints at the top of the central cantilever with extreme normal opening of 1.3mm. The extreme sliding is observed at the upper quarter section of the construction joints, at the same time shear failure is not observed.

In order to better understand the effect of the construction joints with non-linear behavior, the respective results are compared with those of the analysis conducted with joint linear behavior only. For both cases only the stress distribution for the dam central construction joint is presented. Any tensile stresses higher than the allowable as a consequence of opening in case of nonlinear behavior of the joints could not be observed.

References:

[1] G. E. Myers, *Analytical Methods in Conduction Heat Transfer*, McGraw Hill Book Co., New York, 1971.

[2] L. A. Crivelli, S. R. Idelsohn, *A temperature-based finite element solution for phase-change problems*, International Journal for Numerical Methods in Engineering, **24**, pp. 117-128, 1987.

[3] H. Arabshahi, V. Lotfi, *Nonlinear dynamic analysis of arch dams with joint sliding mechanism*, Engineering Computations, **26**, pp. 464-482, 2009.

[4] J. M. Hohberg, *Seismic arch dam analysis with full joint non-linearity*, Proceeding of International Conference on Dam Fracture, Denver, Colorado, pp. 61-75, 1991.

[5] D. T. Lau, B. Noruziaan, *Modelling of contraction joint and shear sliding effects on earthquake response of arch dams*, Earthquake Engineering and Structural Dynamics, **27**, pp. 1013-1029, 1998.

[6] P. A. Cundall, R. D. Hart, *Numerical modeling of discontinua*, Engineering Computations, **9**, pp. 101-113, 1992.

[7] K. J. Bathe, E. L. Wilson, E. L, *Numerical methods in finite element analysis*, Prentice-Hall, Inc., Englewood cliffs, New Jersey, 1976.

[8] V. Mircevska, S. Durgevic, A. Nanevska, I. Gjorgeska, *Dynamic response of arch-dams using ADAD-IZIIS software*, Proceedings of 14th International Scientific Conference INDIS 2018, pp. 21-23, Novi Sad, Serbia, 2018.

[9] X. L. Du, J. Tu, *Nonlinear seismic response analysis of arch dam-foundation systems- part II opening and closing contact joints*, Bulletin of Earthquake Engineering, **5**, pp. 121-133, 2007.

[10] ADAD-IZIIS, Analysis and design of arch dams – User's manual, Institute of Earthquake Engineering and Engineering Seismology – IZIIS, University of Ss. Cyril and Methodius, Skopje, R. N. Macedonia, 2018.

[11] ICOLD, *Selecting seismic parameters for large dams - Guidelines*, Committee on Seismic Aspects of Dam Design., ICOLD Bulletin, pp. 1–78, 2009.

COMPARISON OF DIFFERENT DIGITAL IMAGE REGISTRATION TECHNIQUES FOR DAMAGE ANALYSIS OF FIBER REINFORCED POLYMERS

Ana Vrgoč[1], Zvonimir Tomičević[2], Andrija Zaplatić[3], François Hild[4]

[1] University of Zagreb, Faculty of mechanical engineering and naval architecture, University of Zagreb, Ivana Lučića 5, 10002 Zagreb, Croatia, ana.vrgoc@fsb.hr
[2] University of Zagreb, Faculty of mechanical engineering and naval architecture, University of Zagreb, Ivana Lučića 5, 10002 Zagreb, Croatia, zvonimir.tomicevic@fsb.hr
[3] University of Zagreb, Faculty of mechanical engineering and naval architecture, University of Zagreb, Ivana Lučića 5, 10002 Zagreb, Croatia, andrija.zaplatic@fsb.hr
[4] Université Paris-Saclay, ENS Paris-Saclay, CNRS, LMT - Laboratoire de mécanique et technologie, 91190 Gif-sur-Yvette, France, Francois.Hild@ens-paris-saclay.fr

Due to their enhanced material properties, fiber reinforced polymers (FPR) have emerged as an effective substitute for conventional engineering materials in major structural applications [1]. However, the limited predictability of material failure during the whole service cycle contributes to high safety limits for the allowable construction design. In addition, the heterogeneous and anisotropic nature of FRPs induces the initiation of various damage mechanisms, hence the failure of FRP components is a direct result of the cascade of microscale interactions. In this regard, advanced non-destructive testing (NDT) methods are essential for early detection of damage initiation and monitoring of damage growth. Owing to the recent improvements in image-processing algorithms, Digital Image Correlation has found widespread applications in experimental solid mechanics [2]. This full-field measurement technique is based on registering gray level images of specimen and/or component surfaces, while the acquired images are correlated to measure displacement fields and calculate strain fields [3]. Introducing DIC measurements in the analysis of FRP has proven to be an effective tool in improving the understanding of their complex behavior. However, the proposed technique does not provide insights into the underlying behavior in the material bulk. The more advanced Digital Volume Correlation (DVC) technique enables displacements to be measured in the 3D space, while the correlation analysis is conducted on 3D images (*i.e.* reconstructed from scans) obtained via X-Ray Computed Tomography [4]. Thus, the main advantage of such an approach is reporting the bulk material response as well as comprehensive identification of underlying failure mechanisms [5].

In this work, a comparison study between DIC and DVC employed in the damage initiation and growth analysis of FRP is presented. The experimental work was performed on 5.8 mm thick dogbone samples made of epoxy resin reinforced with glass fiber mat. The uniaxial tensile test was conducted in a displacement-controlled mode with a prescribed stroke rate of 2 mm/min. FE-based DIC was performed to measure displacement fields and calculate strain fields. The global material behavior was estimated during the test with a DIC gauge positioned over the Region of Interest (Figure 1). From the reported stress strain curve, the Young's modulus is equal to 6.8 GPa. In addition, the gray level residual maps, corresponding to the gray level residuals at convergence of the correlation procedure, were investigated to detect discontinuities and monitor damage growth on the specimen surface.

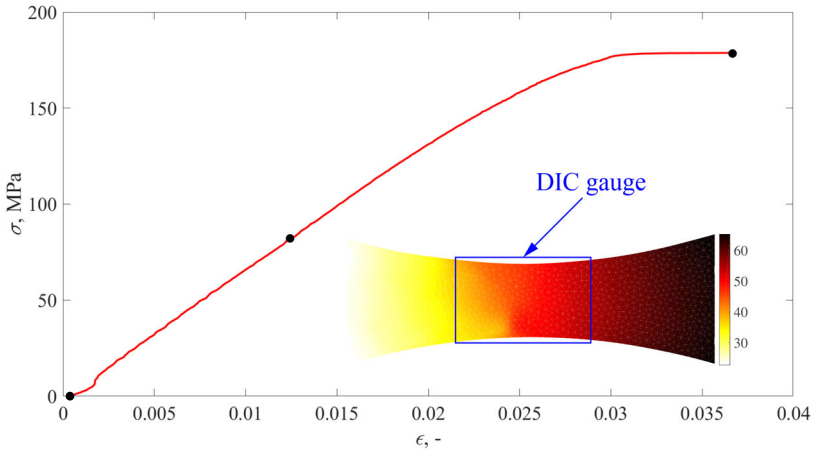

Figure 1: Stress-strain curve obtained from the monotonic uniaxial tension. The solid black circles depict the images for which the correlation residual maps are extracted to monitor damage growth.

The total amount of images analyzed to detect damage on the investigated specimen surface was equal to 313. The first 50 images were acquired in the unloaded configuration to assess measurements uncertainties. Figure 2(a)-(b) shows the initial residual map and maximum eigen strain field corresponding to Image 50. The correlation residuals are homogeneously distributed over the ROI, while the values remain low, thereby indicating the influence of the optical setup. As the load levels become higher, the correlation residuals increase over the entire ROI (Figure 2(c)). The first detected discontinuities correspond to Image 144 captured in the linear elastic regime (Figure 1), *i.e.* four distinct regions of elevated residuals are observed at the sample ligament edges (Figure 2(d)). Such localized phenomena are also visible in the maximum eigen strain field (Figure 2 (c)). Further, as shown in Figure 2 (e)-(f) acquired prior to specimen failure, strain localization phenomena become even clearer, and the dominant macrocrack is observed in the narrowest gauge section.

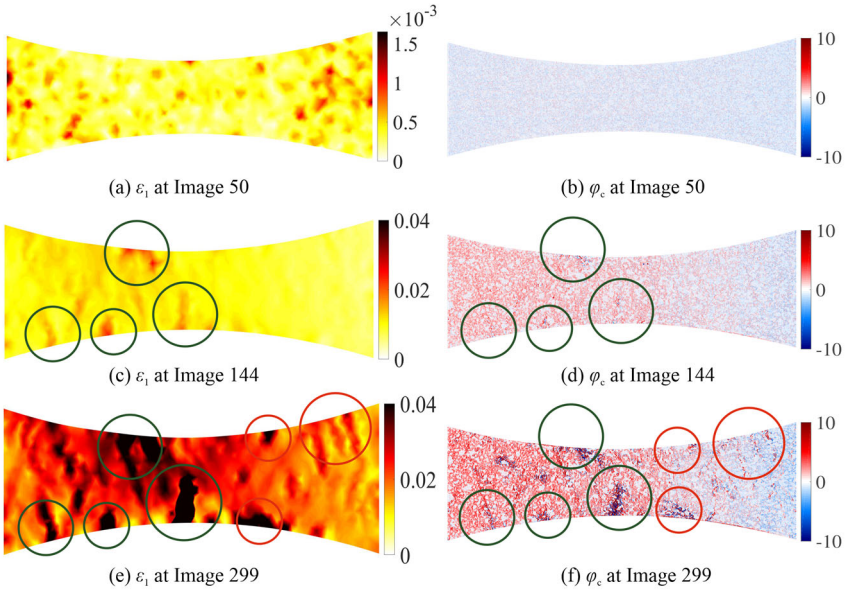

Figure 2: Maximum eigen strain fields (left) and gray level residual maps (right) for different loading levels of the uniaxial tensile test (Figure 1). The green circles depict the first detected discontinuities, while the red circles correspond to additional areas of high correlation residual levels.

Moreover, Figure 3(a) shows the displacement field measured in the longitudinal direction prior to specimen failure. The high gradient in the displacement field corresponds to the previously observed dominant macrocrack revealed through both gray level residuals and maximum eigen strain field. The

observed macrocrack path (marked with the black dashed line) is not straight, thereby indicating the influence of the underlying mesostructure.

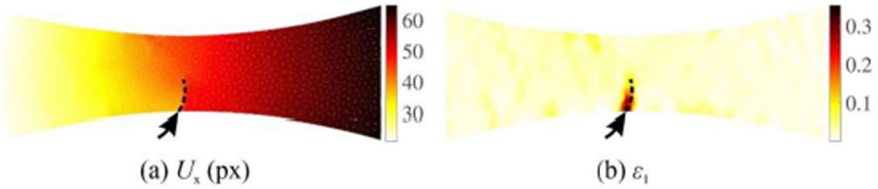

Figure 3: Displacement field in the loading direction (*i.e.* x axis) expressed in pixels (a) and maximum eigen strain field (b) for Image 299. The black dashed line depicts the dominant macrocrack path, while the black arrow shows the damage initiation location.

The reconstructed volumes were analyzed utilizing FE-based digital volume correlation to measure displacements in the material bulk. The reconstructed volume as well as the finite element mesh employed in the correlation analysis are shown in Figure 4.

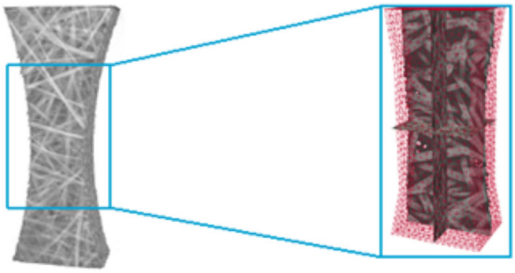

(a) (b)

Figure 4: Reconstructed volume (a) and FE mesh employed in the DVC analysis (b).

The gray level residuals extracted from the correlation analysis were analyzed to observe damaged zones, *i.e.* the gray level residuals were overlaid with the corresponding microstructure to detect crack initiation and monitor damage growth during the applied loading conditions. The proposed approach revealed damage initiation at the microstructural level and its subsequent mesoscale and macroscale propagation, as well as enabling for the precise identification of the damage mechanism.

The work performed herein indicates that regularized FE-DIC with the analysis of gray level residual maps can efficiently detect mesocracks on the surface of FRP. However, the proposed measurement technique does not provide an insight into the material bulk. Therefore, DVC measurements were performed to measure displacement fields and calculate strain fields in the 3D space. Such approach enabled for the identification of underlying damage mechanisms on the surface and in the bulk of the investigated FRP.

Acknowledgements

This work was performed within the FULLINSPECT project supported by the Croatian Science Foundation (UIP-2019-04-5460 Grant).

References

[1] S. Prashanth, KM Subaya, K. Nithin. *Fiber Reinforced Polymer – A Review*, Journal of Materials Sciences and Engineering (6), 1-6, 2017.

[2] M. Grédiac, F. Hild, A. Pineau. *Full-Field Measurements and Identification in Solid Mechanics*, ISTE/Wiley, 2012.

[3] M. Sutton. *Computer Vision-Based, Noncontacting Deformation measurements in Mechanics: A Generational Transformation,* Applied Mechanics Review (65), 050802, 2013

[4] E. Maire, P. Withers. *Quantitative X-ray tomography*, International Materials Reviews (59), 1-43, 2014.
[5] A. Buljac, C. Jailin, A. Mendoza, J. Neggers, T- Taillandier-Thomas, A. Bouterf, B. Smaniotto, F. Hild, S. Roux, *Digital Volume Correlation: Review of Progress and Challenges,* Experimental Mechanics (58), 661-708, 2018.

PARAMETER IDENTIFICATION IN DYNAMIC CRACK PROPAGATION

A. Stanić [1], M. Nikolić [2], N. Friedman [3], H. G. Matthies [4]

[1] University of Twente, Faculty of Engineering Technology, The Netherlands, a.stanic@utwente.nl
[2] University of Split, Faculty of Civil Engineering, Architecture and Geodesy, Croatia, mijo.nikolic@gradst.hr
[3] Institute for Computer Science and Control (SZTAKI), Hungary, friedman.noemi@sztaki.hu
[4] Technische Universität Braunschweig, Institute of Scientific Computing, Germany, wire@tu-bs.de

Introduction

The subject of our research work is the identification of unknown parameters in a numerical model, that enables simulation of crack propagation in a structural element subjected to dynamic loads. In order to describe a crack formation and opening in quasi brittle 2d solid we use the embedded strong discontinuity method ([1]). It provides mesh-independent solution since the fracture dissipation energy is associated with the discontinuity and does not depend on the finite element size. Usually, we do not possess all the necessary data available to carry out the numerical simulation of an experiment. Therefore, the stochastic Bayesian inverse method ([4]) is applied to identify the input parameters, that can not be measured directly – such as the fracture energy which dissipates when cracks propagate through the model domain.

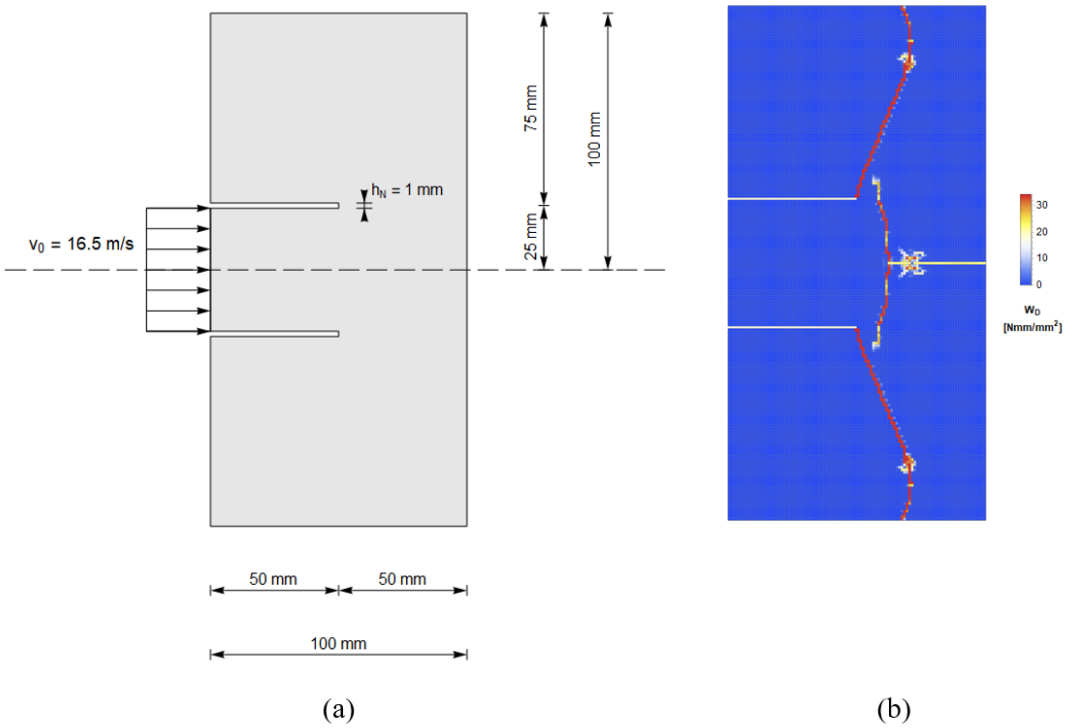

Figure 1: Kalthoff's test: (a) Geometry and boundary conditions. (b) Specific dissipated fracture energy at the end of simulation with the embedded discontinuity quadrilaterals Q6 (see [5]).

Representative example

The Kalthoff's test on a high-strength steel plate with two notches from [2] is chosen as the representative example of fracture dynamics. Fig. 1(a) illustrates geometry and boundary conditions of the specimen. Fig. 1(b) shows the field of dissipated fracture energy at the end of a deterministic simulation, where the crack path is composed of three lines: two lines propagates from each notch and one horizontal line starts at right side of the plate and bifurcates into two branches.

Lattice model calibration

In this work we use two different finite element models for modeling crack propagation with embedded strong discontinuity: the lattice element from [3] and the quadrilateral Q6 element from [5]. The lattice model is a discrete model of continuum, therefore the stiffness matrix of a lattice element has to be calibrated at first, such that the pressure and shear waves in lattice model have the same velocity as in the elastic solid model. For this purpose we introduce correction factors for longitudinal k_L, transversal k_T and rotational stiffness k_R of a lattice element.

The stochastic method Markov Chain Monte Carlo (MCMC) is employed for the identification of three correction factors, that are set to be random variables with the uniform distribution $U(0.1,\ 5)$. In this procedure, the Kalthoff's test is modified such that the imposed constant velocity of $v_0 = 16.5$ m/s is replaced with the distributed horizontal load $q_F = q_F(\lambda) = \lambda q_{F,0}$, where $q_{F,0} = 4.08 \times 10^6$ N/m. The material parameters are: Young's modulus $E = 190$ GPa and Poisson's coefficient $\nu = 0.3$. The measurements are displacements in 22 assimilation points presented in Fig. 2(a). The true measurement is generated from the deterministic simulation with the Q6 finite elements. The response of the lattice model is replaced with the generalized PCE model degree of 12, where the regression is used for computing the corresponding polynomial coefficients.

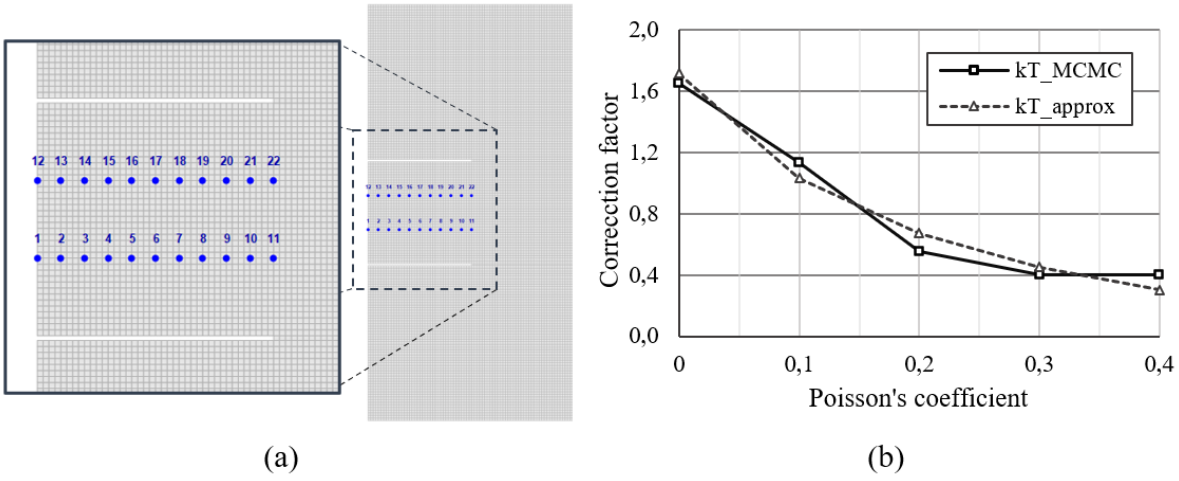

Figure 2: Kalthoff's test: (a) Position of 22 assimilation points. (b) The diagram shows the shear correction factor k_T in a lattice finite element for various Poisson's coefficients ν. The curve $k_{T,MCMC}$ presents the posterior mean values of the factor k_T obtained by the identification procedure with the MCMC method. The line $k_{T,approx}$ illustrates the eq. (1).

The diagram in Fig. 2(b) collects the results for the correction factor $k_{T,MCMC}$ obtained with the stochastic analysis. The MCMC method is applied for different values of Poisson's coefficient ν. One can see that the factor $k_{T,MCMC}$ decreases towards 0.4 for higher Poisson's coefficient ν. In other words, when $\nu > 0.15$, the elastic stiffness of a lattice element in shear direction should be reduced, otherwise it should be increased. Based on the results, an approximation function for the correction factor of transversal elastic stiffness in lattice elements is proposed:

$$k_{T,approx} = \frac{1.2 - 1.5\nu}{0.7 + 3.2\nu} \tag{1}$$

We note, that the proposed approximation in eq. (1) is valid only for the considered numerical model. The generality of the approximation (1) has to be further investigated.

This research work shows that the Bayesian inverse method can be a very effective tool for determination of the unknown parameters (e.g. correction factors) that can not be expressed explicitly from the equilibrium equations due to the complexity of the relation between the finite element model response and the input parameters – as is the case for the lattice model.

Acknowledgements

This work has been supported through the project 'Parameter estimation framework for fracture propagation problems under extreme mechanical loads' (UIP-2020-02-6693).

References

[1] Ibrahimbegovic, A. 2009. *Nonlinear Solid Mechanics. Theoretical Formulations and Finite Element Solution Methods*. Dordrecht, Springer Netherlands: 574 p.

[2] Kalthoff, J. F. 2000. *Modes of dynamic shear failure in solids*. International Journal of Fracture 101: 1–31.

[3] Nikolić, M., Do, X.N., Ibrahimbegovic, A., Nikolić, Ž. 2018. *Crack propagation in dynamics by embedded strong discontinuity approach: Enhanced solid versus discrete lattice model*. Computer methods in Applied Mechanics and Engineering 340: 480–499.

[4] Matthies, H. G., Zander, E., Rosić, B. V., Litvinenko, A., Pajonk, O. 2016. *Inverse Problems in a Bayesian Setting*. In: Ibrahimbegovic A. (eds) Computational Methods for Solids and Fluids. Computational Methods in Applied Sciences, vol 41. Springer: 245-286 p.

[5] Stanic, A., Brank, B., Ibrahimbegovic, A., Matthies, H. G. 2021. *Crack propagation simulation without crack tracking algorithm: embedded discontinuity formulation with incompatible modes.* Submitted for publication. Preprint is published at: https://arxiv.org/abs/2012.09581

IDENTIFIABILITY OF LUDWIK'S LAW PARAMETERS DEPENDING ON THE SAMPLE GEOMETRY VIA INVERSE IDENTIFICATION PROCEDURE

Andrija Zaplatić[1], Zvonimir Tomičević[2], Damjan Čakmak[3], François Hild[4]

[1] University of Zagreb, Faculty of mechanical engineering and naval architecture, University of Zagreb, Ivana Lučića 5, 10002 Zagreb, Croatia, andrija.zaplatic@fsb.hr
[2] University of Zagreb, Faculty of mechanical engineering and naval architecture, University of Zagreb, Ivana Lučića 5, 10002 Zagreb, Croatia, zvonimir.tomicevic@fsb.hr
[3] University of Zagreb, Faculty of mechanical engineering and naval architecture, University of Zagreb, Ivana Lučića 5, 10002 Zagreb, Croatia, damjan.cakmak@fsb.hr
[4] Université Paris-Saclay, ENS Paris-Saclay, CNRS, LMT - Laboratoire de mécanique et technologie, 91190 Gif-sur-Yvette, France, Francois.Hild@ens-paris-saclay.fr

Understanding the engineering component response under prescribed workloads is essential to improve its operating lifetime. Moreover, insight into the material elastoplastic behavior is crucial since it can be described by various material models. Therefore, to determine the elastoplastic material response, mechanical tests with different loading regimes are carried out.

The material response can be monitored by advanced measurement methods such as Digital Image Correlation (DIC), which stands out as one of the most widely used optical method. In this study, an FE-based approach [1] was employed. The resulting measurements (*i.e.* nodal displacements of the FE mesh) form a straightforward connection with numerical simulations. An inverse problem for determining elastoplastic material parameters can be set by coupling FE-based DIC and numerical simulations in a single advanced identification routine. For this study, *Finite Element Model Updating* (FEMU) [2] was employed. FEMU has proven to be a valuable identification tool used for both uniaxial [3] and for biaxial [4] loading histories.

In this work, a study was performed to evaluate the influence of sample geometry on the identified material parameters. Two distinct sample geometries were considered, namely, the central part of the ligament of the first sample was thinned with a radius of 75 mm (*i.e. Dogbone* sample, see Figure 1(a)), whereas the latter is designed with two parallel edges (*DIN* sample, Figure 1(b)). Both tested samples were 2 mm thick and made from high strength HARDOX 450 steel. They were subjected to uniaxial and monotonic loading regimes under displacement control with a prescribed rate of 0.5 mm/min. The material response was monitored by a single CCD Dalsa camera with a definition of 3258 × 1728 pixels and an image acquisition rate of 1 fps. In the FE simulations, the nonlinear material behavior was described with Ludwik's isotropic hardening law

$$\sigma_{\mathrm{eq}} = \sigma_{\mathrm{y}} + K\varepsilon_{\mathrm{pl}}^{n}, \tag{1}$$

where σ_{eq} corresponds to von Mises' equivalent stress, and $\varepsilon_{\mathrm{pl}}$ to the accumulated plastic strain. The sought material parameters identified in the scope of this work were the yield stress σ_{y}, hardening modulus K and hardening exponent n. Furthermore, the Young's modulus E was also calibrated to reliably describe the linear-elastic material behavior. Although Poisson's ratio ν sensitivity was evaluated, it was not considered for identification purposes.

The FE-DIC framework *Correli 3.0.* [5][2] was used to measure displacement fields. Three noded (T3) elements were used for the measurement step, and C3D8R meshes for the identification were extruded from Q4 meshes of each sample (Figure 1). The measured nodal displacements were then prescribed to the C3D8R FE models as Dirichlet boundary conditions on the stressed edges (Figure 1).

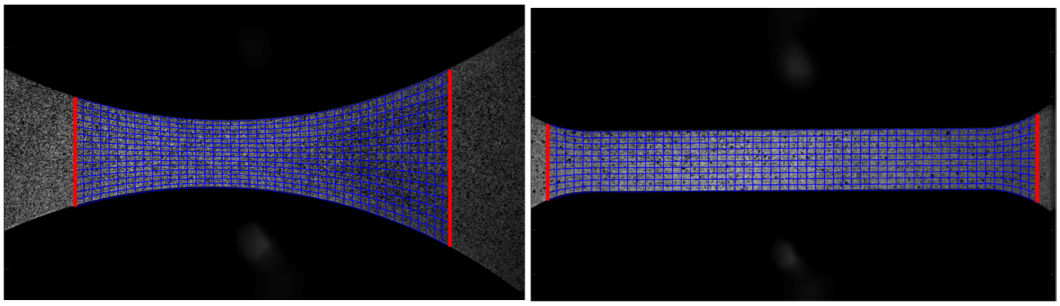

(a) (b)

Figure 1. Four-noded FE meshes. (a) Dogbone sample, (b) DIN sample. The red lines depict Dirichlet edges of the FE model.

The FEMU method was employed to calibrate the aforementioned material parameters. Within that framework, two cost functions related to the measured quantities during the mechanical test are iteratively minimized. The first cost function considers the difference between measured ($\mathbf{u_m}$) and calculated ($\mathbf{u_c}$) nodal displacements

$$\chi_{\mathrm{u}}^2 = \left\| \{\mathbf{u_m}\} - \{\mathbf{u_c}\} \right\|^2 . \tag{2}$$

The second cost function is associated with the difference between the measured load ($\mathbf{F_m}$) and the sum of reaction forces ($\mathbf{F_c}$) extracted from the FE model

$$\chi_{\mathrm{F}}^2 = \left\| \{\mathbf{F_m}\} - \{\mathbf{F_c}\} \right\|^2 . \tag{3}$$

Moreover, Tikhonov regularization was implemented to ensure the convergence of the algorithm.
First, the sensitivity of each parameter can be observed from the Hessian matrices that gather the displacement and force sensitivities to parameter change

$$H_{\mathrm{DB}} = \begin{array}{c} \\ \boldsymbol{E} \\ \boldsymbol{v} \\ \boldsymbol{\sigma_y} \\ \boldsymbol{K} \\ \boldsymbol{n} \end{array} \begin{array}{c} \begin{array}{ccccc} \boldsymbol{E} & \boldsymbol{v} & \boldsymbol{\sigma_y} & \boldsymbol{K} & \boldsymbol{n} \end{array} \\ \begin{bmatrix} 45 & 1 & -2 & -1.5 & 0.5 \\ 1 & 0.2 & -0.14 & -0.05 & 0.03 \\ -2 & -0.14 & 31 & 7.3 & -6.4 \\ -1.5 & -0.05 & 7.3 & 2 & -1.5 \\ 0.5 & 0.03 & -6.4 & -1.5 & 1.4 \end{bmatrix} \end{array} \times 10^3, H_{\mathrm{DIN}} = \begin{array}{c} \begin{array}{ccccc} \boldsymbol{E} & \boldsymbol{v} & \boldsymbol{\sigma_y} & \boldsymbol{K} & \boldsymbol{n} \end{array} \\ \begin{bmatrix} 14.2 & 0.2 & 3 & -2.3 & -0.8 \\ 0.2 & 0.1 & -0.1 & -0.04 & 0.01 \\ 3 & -0.1 & 34 & 4.3 & -7.6 \\ -2.3 & -0.04 & 4.3 & 5.9 & -0.3 \\ -0.8 & 0.01 & -7.6 & -0.3 & 0.2 \end{bmatrix} \end{array} \times 10^3. \tag{4}$$

The off-diagonal terms in the Hessian matrices show the correlative influences of parameters, whereas the diagonal terms describe the sought parameter sensitivities when considered independently.
It is observed from the Dogbone Hessian H_{DB} that for the first parameter E, the sensitivity is greater than for its H_{DIN} counterpart. This is also the case for parameters v and n. However, for σ_y and K the values are slightly larger for the DIN sample. Furthermore, differences are also observed from the identified parameters gathered in Table 1. The identified modulus E, yield stress σ_y and n are greater for the Dogbone sample than for its counterpart, whereas K is larger for the DIN sample. Young's modulus E for the DIN sample displayed decreased sensitivity. For both samples, the identified values provide good agreement between the measured and calculated load curves (Figure 2). Although the values of E differ for both samples, good agreement between the aforementioned curves is reported in elasticity. However, in early plasticity the agreement is slightly better for the Dogbone sample as the curve for the calculated load follows the measured curve more closely.

Table 1. Initial and calibrated material parameters for the Dogbone and DIN samples

Parameter	E (GPa)	σ_y (MPa)	K (MPa)	n
Initial	210	1200	700	0.2
Dogbone	219	1146	922	0.19
DIN	211	1064	981	0.18

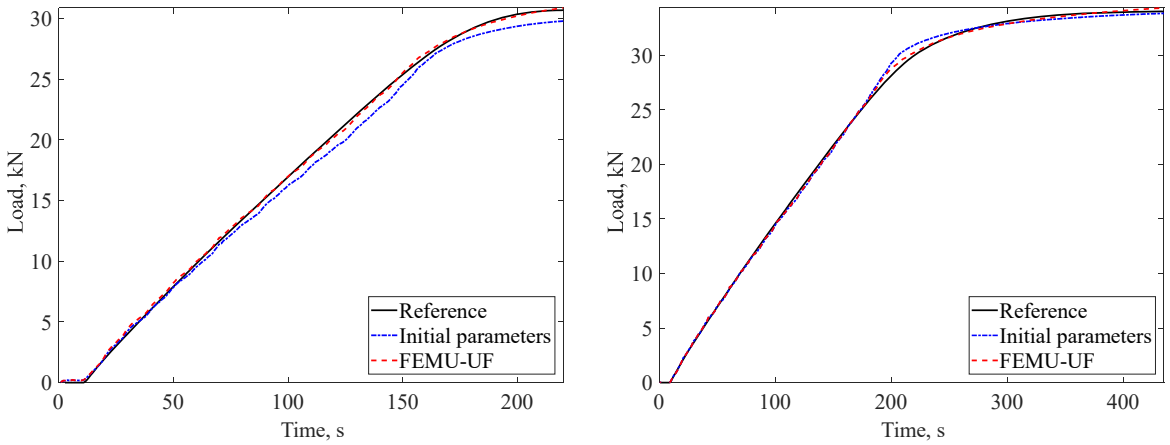

Figure 2. Comparison of measured load and reaction forces extracted from the FE model computed with the initial and calibrated elastoplastic parameters. (a) Dogbone sample, (b) DIN sample.

From the presented results it is concluded that the geometry of the tested sample plays a significant role in identifiability of the sought material parameters. The Dogbone sample has a more complex geometry than the DIN sample, which contributes to higher parameter sensitivities as observed from the Hessian matrices. Furthermore, the thinned gauge area of the Dogbone sample ensures strain localization in the thinnest part. Although the sensitivities for yield stress and hardening modulus were greater for the DIN sample, overall, the Dogbone sample provided better parameter sensitivities thus leading to parameters that describe more closely the real material response.

Acknowledgements

This work was performed within the FULLINSPECT project supported by the Croatian Science Foundation (UIP-2019-04-5460 Grant).

References

[1] G. Besnard, F. Hild, S. Roux. *"Finite-element" displacement fields analysis from digital images: Application to Portevin-Le Chatelier bands*, Exp.Mech, 46(6):789-803, 2006

[2] J.M.P. Martins, A. Andrade-Campos, S. Thuilier. *Comparison of inverse identification strategies for constitutive mechanical models using full-field measurements*, Int. J. Mech. Sci., 145 :330-45. 2018

[3] Z. Tomičević, J. Kodvanj, F. Hild. *Characterization of the nonlinear behavior of nodular graphite cast iron via inverse identification – Analysis of uniaxial tests*, Eur.J.Mech.A Solids, 59:140-154, 2016

[4] Z. Tomičević, J. Kodvanj, F. Hild. *Characterization of the nonlinear behavior of nodular graphite cast iron via inverse identification – Analysis of biaxial tests*, Eur.J.Mech.A Solids, 59:195-209, 2016

[5] H. Leclerc, J. Neggers, F. Mathieu, F., Hild, S. Roux, *Correli 3.0*, IDDN.FR. 001.520008.000.S.P.2015.0.0.0.31500

SHAKE TABLE TESTS OF RAISED FLOOR SYSTEMS

Angela POPOSKA[1], Filip MANOJLOVSKI[2], Antonio SHOKLAROVSKI[3], Lidija KRSTEVSKA[4], Aleksandra BOGDANOVIC[5]

[1] Institute of earthquake engineering and engineering seismology, University "Ss. Cyril and Methodius in Skopje, N. Macedonia angela@iziis.ukim.edu.mk
[2] Institute of earthquake engineering and engineering seismology, University "Ss. Cyril and Methodius in Skopje, N. Macedonia, filipmanojlovski@iziis.ukim.edu.mk
[3] Institute of earthquake engineering and engineering seismology, University "Ss. Cyril and Methodius in Skopje, N. Macedonia, antonio@iziis.ukim.edu.mk
[4] Institute of earthquake engineering and engineering seismology, University "Ss. Cyril and Methodius in Skopje, N. Macedonia, lidija@iziis.ukim.edu.mk
[5] Institute of earthquake engineering and engineering seismology, University "Ss. Cyril and Methodius in Skopje, N. Macedonia, saska@iziis.ukim.edu.mk

With the development of the new technologies and the modern residential and industrial buildings typology, the nonstructural components and systems become major part of the total value in building construction. Their damage may result in loss of functionality, economic loss due to damage and even life safety hazards. Since their design is seldomly covered by building codes, their seismic response is relatively unknown, and they are potentially more vulnerable to earthquake shaking-induced damage than the primary structural system.

In this paper presented are results of experimental testing of different raised floors systems performed at the Dynamic Testing Laboratory in the Institute of Earthquake Engineering and Engineering Seismology - IZIIS, Skopje, Republic of N. Macedonia. Seismic clarification of this systems has been conducted according to the AC-156 - Acceptance criteria for seismic qualification by shake table testing for nonstructural components.

In general, two different types of raised floors systems were tested. However, taking into the consideration few possible variables, regarding the bracings and the load, 24 different configurations of raised floors were tested. Thus, huge number of results have been obtained in terms of accelerations, displacements and strains in characteristic points. The systems showed good performance and it was confirmed that all acceptance criteria have been fulfilled during and after the seismic tests. All configurations resisted the applied excitations, without damage of the main and following elements and according to this, successfully passed the seismic tests and fulfilled the acceptance criteria for non-structural components and systems as set in the ICC AC-156.

Keywords: Non-structural elements; Raised floors; Shake table test; AC156

ECCOMAS MSF 2021 THEMATIC CONFERENCE
30 June – 2 JULY 2021, SPLIT, CROATIA

NUMERICAL IDENTIFICATION OF STRAIN-DEPENDENT COEFFICIENT OF PERMEABILITY BY COMBINING THE RESULTS OF NUMERICAL AND EXPERIMENTAL OEDOMETER TEST WITH FREE LATERAL MOVEMENT

Anis Balic[1], Emina Hadzalic[1], Samir Dolarevic[1]

[1] Faculty of Civil Engineering, University of Sarajevo,
anis.balic@gf.unsa.ba, emina.hadzalic@gf.unsa.ba, samir.dolarevic@gf.unsa.ba

INTRODUCTION

The main parameter that determines the shape of the embankment consolidation curve is the coefficient of permeability. In numerical computations, the coefficient of permeability is usually taken as porosity-dependent. However, because of the different strain and stress states across the soil under the embankment, various authors suggest that the strain-dependence of the coefficient of permeability should also be taken into account [1, 2]. To establish the relation between the strain state and the coefficient of permeability, the results of oedometer tests can be used.

In a standard oedometer test, the lateral movements of the soil sample are restrained. The load is applied, and the settlements of the soil sample in time are monitored. The conditions simulated in the standard oedometer test are valid only in narrow central areas in the soil under the embankment, where the lateral movements are indeed prevented. However, in other areas this assumption no longer holds. Because of this, the modified oedometer test, which allows lateral movements, is introduced [3]. To be able to define a mathematical expression and to identify the values of the coefficients in the proposed expression, results of experimental tests have to be combined with the results obtained with a numerical model of the modified oedometer test.

In this paper, we present a two-dimensional axisymmetric numerical model of the modified oedometer test, which implements Biot's theory of consolidation. First, we briefly present the main details of the finite element formulation of the numerical model. Second, we present the results of the numerical simulations, and we compare the computed results against those obtained experimentally. Next, we establish the strain-dependence of the coefficient of permeability and we identify the unknown coefficients in the expression. Finally, we give our concluding remarks.

FINITE ELEMENT FORMULATION

Biot's theory of consolidation combines the equilibrium equation and continuity equation. Here, we assume that the soil is isotropic, linear elastic, the strains are small, the pore fluid is incompressible and the pore fluid flow is governed by Darcy's law.

The strong form of equilibrium equation is written as:

$$\begin{aligned} \frac{\partial \sigma_r}{\partial r} + \frac{\sigma_r - \sigma_\theta}{r} + \frac{\partial \tau_{zr}}{\partial z} = 0 \\ \frac{\partial \tau_{rz}}{\partial r} + \frac{\tau_{rz}}{r} + \frac{\partial \sigma_z}{\partial z} = 0 \end{aligned} \tag{1}$$

where σ_r is the radial normal stress, σ_θ is the tangential normal stress, σ_z is the vertical normal stress, τ_{rz} is the shear stress, r is the distance from the axis of symmetry, and z is the vertical coordinate axis.

The constitutive relations are given as:

$$\begin{aligned}\sigma_r &= (2\mu+\lambda)\varepsilon_r + \lambda\varepsilon_z + \lambda\varepsilon_\theta \\ \sigma_z &= \lambda\varepsilon_r + (2\mu+\lambda)\varepsilon_z + \lambda\varepsilon_\theta \\ \tau_{rz} &= \mu\gamma_{rz} \\ \sigma_\theta &= \lambda\varepsilon_r + \lambda\varepsilon_\theta + (2\mu+\lambda)\varepsilon_\theta\end{aligned} \tag{2}$$

where ε_r is the radial strain, ε_θ is the tangential strain, ε_z is the vertical strain, γ_{rz} is the shear strain, and λ and μ are Lame's coefficients. The strains are given as:

$$\varepsilon_r = \frac{\partial u}{\partial r}; \quad \varepsilon_z = \frac{\partial v}{\partial z}; \quad \varepsilon_\theta = \frac{2\pi(r+u)-2\pi r}{2\pi r} = \frac{u}{r}; \quad \gamma_{rz} = \frac{\partial u}{\partial z} + \frac{\partial v}{\partial r} \tag{3}$$

The strong form of continuity equation is written as:

$$\frac{\partial}{\partial t}\left(\frac{\partial u}{\partial r} + \frac{\partial v}{\partial z}\right) - \frac{k_r}{\gamma_w}\frac{1}{r}\frac{\partial p}{\partial r} - \frac{k_r}{\gamma_w}\frac{\partial^2 p}{\partial r^2} - \frac{k_z}{\gamma_w}\frac{\partial^2 p}{\partial z^2} = 0 \tag{4}$$

where k_r and k_z are the coefficients of permeability in the radial and vertical direction, p is the pore pressure, and γ_w is the unit weight of the pore fluid.

For finite element approximation of displacement and pore pressure fields, we use **Q8-P4** finite element, which assumes quadratic interpolation of the displacement field and linear interpolation of the pore pressure field. By performing the standard finite element discretization procedure, we obtain the following set of equations:

$$\begin{aligned}\mathbf{K}_m\mathbf{u} + \mathbf{C}\mathbf{p}_n &= \mathbf{f} \\ \mathbf{C}^{\mathrm{T}}\dot{\mathbf{u}} - \mathbf{K}_c\mathbf{p}_n &= \mathbf{0}\end{aligned} \tag{5}$$

where $\mathbf{K}_m$ is the stiffness matrix, $\mathbf{K}_c$ is the permeability matrix, $\mathbf{C}$ is the coupling matrix, $\mathbf{f}$ is the external load vector, $\mathbf{u}$ is the vector of unknown nodal displacements, $\dot{\mathbf{u}}$ is the vector of time derivatives of nodal displacements, and $\mathbf{p}_n$ is the vector of unknown nodal pore pressures.

The members of these matrices differ for the case of the standard oedometer test and modified oedometer test, where lateral movements are not restrained and strain ε_θ is not equal to zero. Due to this, in some members of the matrices, r appears in the denominator, which prevents the value of these members to be computed accurately when r approaches zero. To solve this problem, both equations in (5) are multiplied with r, which results in modified **B** and **T** matrices that contains the derivatives of shape functions and modified external load vector. The stiffness matrix $\mathbf{K}_m$, the permeability matrix $\mathbf{K}_c$, and the coupling matrix **C** for the case of standard and modified oedometer test are given below:

	Standard oedometer test	Modified oedometer test
Stiffness matrix $\mathbf{K}_m$	$\mathbf{K}_m = \iint \mathbf{B}^{\mathrm{T}}\mathbf{D}\mathbf{B} r\,dr\,dz$	$\mathbf{K}_m^* = \iint \mathbf{B}^{*\mathrm{T}}\mathbf{D}\mathbf{B}^* dr\,dz$
Permeability matrix $\mathbf{K}_c$,	$\mathbf{K}_c = \iint \mathbf{T}^{\mathrm{T}}\mathbf{K}\mathbf{T} r\,dr\,dz$	$\mathbf{K}_c^* = \iint \mathbf{T}^{*\mathrm{T}}\mathbf{K}\mathbf{T}^* dr\,dz$
Coupling matrix **C**	$\mathbf{C} = \iint \left[\frac{\partial N}{\partial r(z)}\right]\mathbf{N} r\,dr\,dz$	$\mathbf{C}^* = \iint \left[\frac{\partial N}{\partial r(z)}\right]^* \mathbf{N} r\,dr\,dz$

(6)

where

$$\mathbf{D}=\begin{bmatrix} \lambda+2\mu & \lambda & 0 & \lambda \\ \lambda & \lambda+2\mu & 0 & \lambda \\ 0 & 0 & \mu & 0 \\ \lambda & \lambda & 0 & \lambda+2\mu \end{bmatrix};\quad \mathbf{K}=\begin{bmatrix} \frac{k_r}{\gamma_w} & 0 \\ 0 & \frac{k_z}{\gamma_w} \end{bmatrix};$$

$$\mathbf{B}=\begin{bmatrix} \frac{\partial N_1^u}{\partial r} & 0 & \dots & \frac{\partial N_i^u}{\partial r} & 0 & \dots & \frac{\partial N_8^u}{\partial r} & 0 \\ 0 & \frac{\partial N_1^u}{\partial z} & \dots & 0 & \frac{\partial N_i^u}{\partial z} & \dots & 0 & \frac{\partial N_8^u}{\partial z} \\ \frac{\partial N_1^u}{\partial z} & \frac{\partial N_1^u}{\partial r} & \dots & \frac{\partial N_i^u}{\partial z} & \frac{\partial N_i^u}{\partial r} & \dots & \frac{\partial N_8^u}{\partial z} & \frac{\partial N_8^u}{\partial r} \\ \frac{N_1^u}{r} & 0 & \dots & \frac{N_i^u}{r} & 0 & \dots & \frac{N_8^u}{r} & 0 \end{bmatrix};\quad \mathbf{T}=\begin{bmatrix} \frac{\partial N_1^p}{\partial r} & \frac{\partial N_1^p}{\partial z} \\ \frac{\partial N_2^p}{\partial r} & \frac{\partial N_2^p}{\partial z} \\ \frac{\partial N_3^p}{\partial r} & \frac{\partial N_3^p}{\partial z} \\ \frac{\partial N_4^p}{\partial r} & \frac{\partial N_4^p}{\partial z} \end{bmatrix}; \tag{7}$$

Here, λ and μ are Lame's coefficients, N^u denotes quadratic interpolation function for displacement field, and N^p denotes linear interpolation function for pore pressure field.

NUMERICAL RESULTS

All numerical implementation and numerical simulations are performed in Fortran. The global system of equations is solved by using **θ** time-stepping scheme.

Standard and modified oedometer test on clay sample is simulated. The geometry of the model, boundary conditions, and finite element mesh for standard oedometer test are shown in Figure 1a, and for modified oedometer test in Figure 1b.

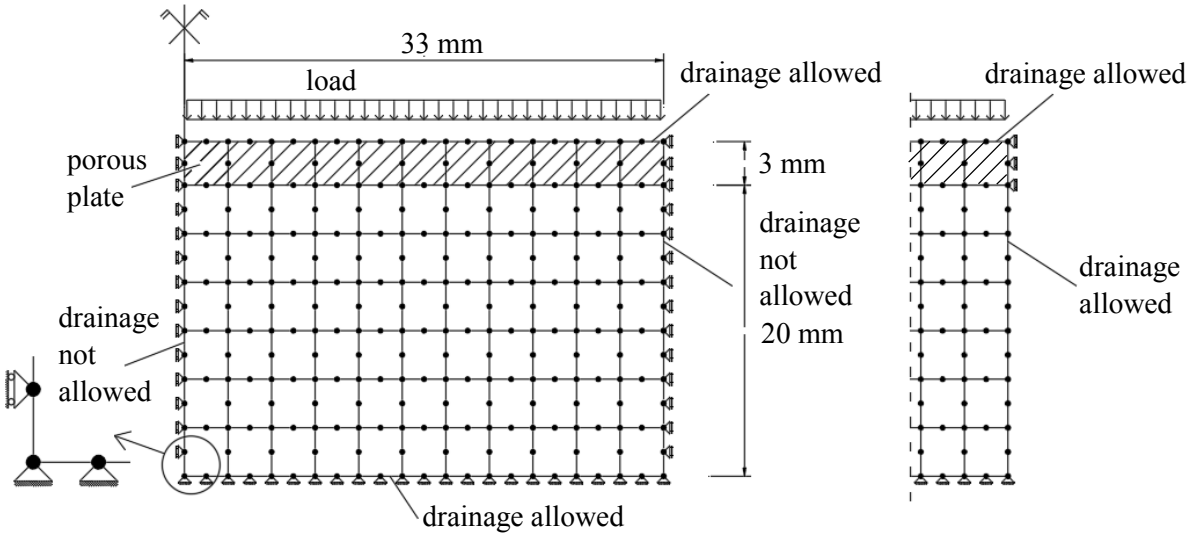

Figure 1: Geometry of the model, boundary conditions and finite element mesh (a) standard oedometer test (b) modified oedometer test

In all numerical simulations, we assume that the coefficient of consolidation remains constant c_v=4.16x10^{-4} cm^2/s, while the coefficient of the permeability and oedometer modulus M_s change in time. The initial value of the oedometer modulus is obtained from the experimental standard oedometer test, and the final value of the oedometer modulus is obtained by matching the computed value of total settlement with the measured value. The value of the oedometer modulus at each time step is computed

by assuming linear interpolation between the initial and final value. We assume that the coefficients of permeability in radial and vertical direction have the same value, and we denote the coefficient of permeability with k. The coefficient of permeability at each time step is then obtained from known values of coefficient of consolidation and oedometer modulus following the expression:

$$k = \frac{c_v \gamma_w}{M_s} \tag{8}$$

First, we simulate the standard oedometer test and we compare the computed consolidation curve against experimental results and results obtained with software Plaxis. The computed results are shown in Figure 2, where we observe a good match between the computed results and reference values.

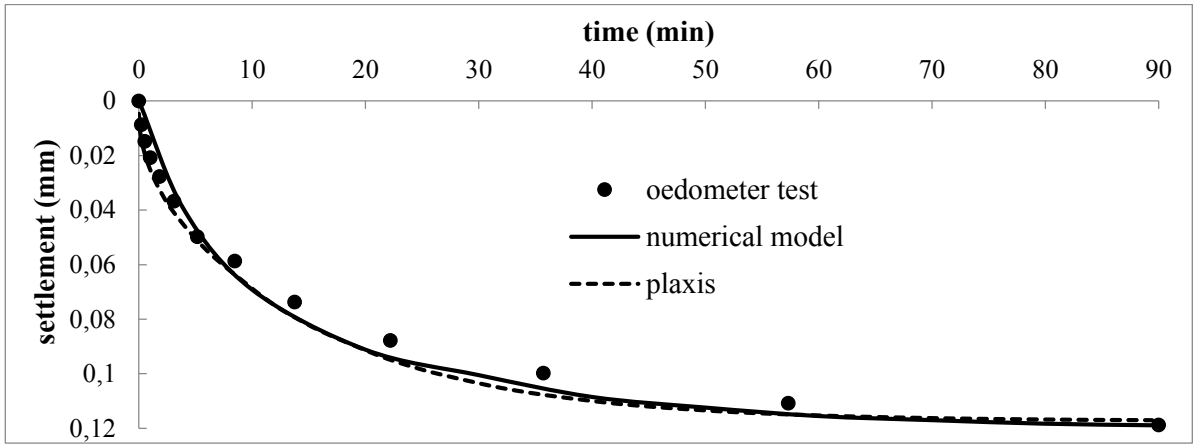

Figure 2: Computed consolidation curve for the standard oedometer test

Second, we simulate the modified oedometer test and we compare the computed consolidation curve against experimental results. The computed consolidation curve is shown in Figure 3. We can conclude that a good match between the computed and experimentally obtained curves is obtained.

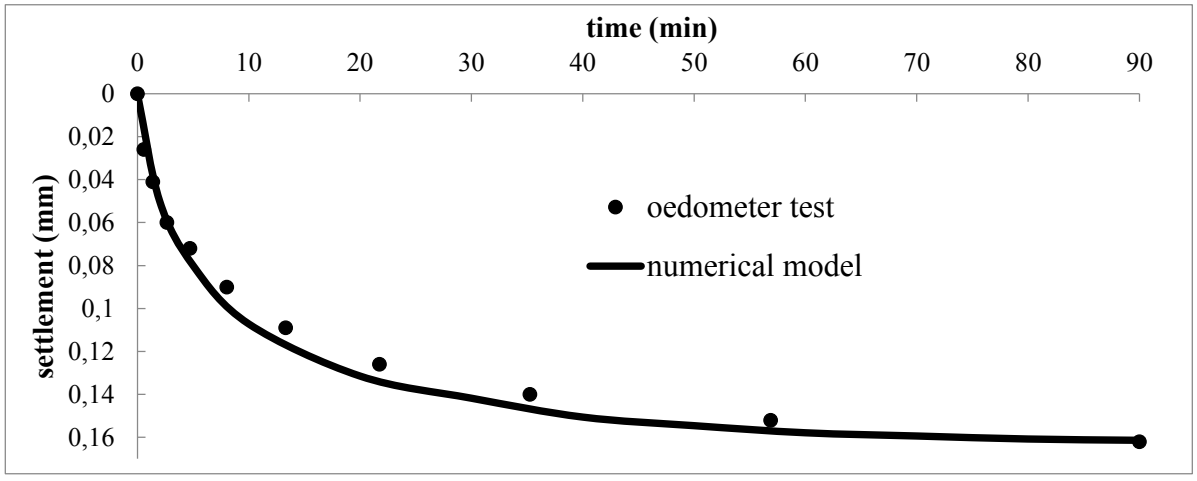

Figure 3: Computed consolidation curve for the modified oedometer test

Next, we aim to define the strain-dependence of the coefficient of permeability. We assume that the strain-dependence of the coefficient of permeability is defined by the following expression:

$$k = \alpha \cdot \frac{\varepsilon_s / \varepsilon_v}{0,66} \cdot k_0 \cdot 10^{\frac{e_0 - e}{c_k}} \tag{9}$$

where α is the coefficient of the change in the permeability, ε_s is the shear strain, ε_v is the volumetric strain, k_0 is the inital coefficient of permeability, e_0 is the inital void ratio, e is the void ratio in time t, and c_k is the constant $c_k = (0,4 - 0,5)\, e_0$.

At each time step, we compute the shear strain, volumetric strain, and void ratio. As said previously, the coefficient of the permeability at each time step is obtained from Equation 9. Hence, the only unknown coefficient left to identify in Equation 10 is the coefficient of the change in the permeability α. Following the results of the numerical simulations of the modified oedometer test, we can identify the coefficient of the change in the permeability α of the clay sample. The identified value of α is equal to $\alpha = 0.354$.

CONCLUDING REMARKS

In this paper, we presented the numerical model of the modified oedometer test, which is based on Biot's theory of consolidation. We proposed the procedure for solving the issue of computation of matrices members, which arises due to the appearance of r in the denominator. By combining the experimental results with the numerical simulations, we were able to establish the strain-dependence of the coefficient of permeability and to identify the corresponding coefficient of the change in the permeability α for the clay sample analyzed in this paper. This procedure can be used for computing the embankment consolidation, where based on the experimental results and results of numerical simulations of modified oedometer test on soil samples, we can identify the unknown parameter α and then use this value to compute the embankment consolidation with the strain-dependent coefficient of permeability.

References

[1] P.W. Rowe. *Measurement of the coefficient of consolidation of lacustrine clay*, Geotechnique, 9(3): 107-118, 1959.
[2] E. Nonveiller. *Mehanika tla i temeljenje građevina*, Zagreb: Školska knjiga, 1979.
[3] A. Balić. *Doctoral thesis: Consolidation analysis with deformation-dependent coefficient of soil permeability,* University of Sarajevo, 2018.

ECCOMAS MSF 2021 THEMATIC CONFERENCE
30 June – 2 JULY 2021, SPLIT, CROATIA

NUMERICAL ANALYSIS OF EMBANKMENT CONSOLIDATION WITH STRAIN-DEPENDENT COEFFICIENT OF PERMEABILITY

Anis Balic[1], Emina Hadzalic[1], Samir Dolarevic[1]

[1] Faculty of Civil Engineering, University of Sarajevo,
anis.balic@gf.unsa.ba, emina.hadzalic@gf.unsa.ba, samir.dolarevic@gf.unsa.ba

INTRODUCTION

The main challenge in the design of highway embankments is in predicting the consolidation time, which influences the construction time. Namely, the works on the pavement structure can commence after the design-determined embankment settlement has happened. This design-determined value of the embankment settlement is smaller than the predicted total value of the settlement and is obtained by subtracting the allowed value of the settlement that can occur during and after the construction of the pavement structure from the predicted total value of the embankment settlement. Thus, in order to determine the time at which the works on the pavement structure can begin, we ought to compute the consolidation curve.

For computing the consolidation curve, numerical models that implement Biot's theory of consolidation are commonly used. The input parameter in these models, that determines the consolidation time and the consolidation curve, is the coefficient of permeability. The porosity-dependence of the coefficient of permeability is commonly used in numerical analysis and is implemented in various geotechnical software, such as Plaxis. However, various authors suggest that the coefficient of permeability should be also taken as dependent on the deformation mechanism [1,2], since the deformation and stress states vary in different areas of the soil under the embankment. The strain-dependent coefficient of permeability is proposed in [3], which is validated with experimental and numerical results on modified oedometer test with free lateral movement.

In this paper, we perform a numerical analysis of embankment consolidation by assuming strain-dependent and porosity-dependent coefficient of permeability. First, we give a brief finite element formulation of the plane-strain numerical model of consolidation. Second, we perform a numerical analysis of the embankment consolidation, and we compare computed results against in-situ measurements and reference values from the literature. Finally, we give our concluding remarks.

FINITE ELEMENT FORMULATION

The numerical model of plane-strain consolidation is based on Biot's theory of consolidation. Biot's theory of consolidation assumes that the soil is isotropic, linear elastic, the deformations are small, the pore fluid is incompressible and the pore fluid low is governed by Darcy's law.

The governing equations in the model are the equilibrium equation and continuity equation. The strong form of equilibrium equations is written as:

$$\frac{\partial \sigma_x^{'}}{\partial x}+\frac{\partial \tau_{xy}}{\partial y}+\frac{\partial p_n}{\partial x}=0$$
$$\frac{\partial \tau_{xy}}{\partial x}+\frac{\partial \sigma_y^{'}}{\partial y}+\frac{\partial p_n}{\partial y}=0 \tag{1}$$

where σ'_x and σ'_y are the effective normal stresses, τ_{xy} is the shear stress, x and y are the horizontal and vertical coordinate axes, and p_n is the pore pressure.

The strong form of equilibrium equations with implemented kinematic and constitutive relations is written as:

$$\frac{E(1-\upsilon)}{(1+\upsilon)(1-2\upsilon)}\left[\frac{\partial^2 u}{\partial x^2}+\frac{(1-2\upsilon)}{2(1-\upsilon)}\frac{\partial^2 u}{\partial y^2}+\frac{1}{2(1-\upsilon)}\frac{\partial^2 v}{\partial x \partial y}\right]+\frac{\partial p_n}{\partial x}=0$$
$$\frac{E(1-\upsilon)}{(1+\upsilon)(1-2\upsilon)}\left[\frac{1}{2(1-\upsilon)}\frac{\partial^2 u}{\partial x \partial y}+\frac{\partial^2 v}{\partial y^2}+\frac{(1-2\upsilon)}{2(1-\upsilon)}\frac{\partial^2 v}{\partial x^2}+\right]+\frac{\partial p_n}{\partial y}=0 \tag{2}$$

where E is Young's modulus of elasticity, ν is the Poisson's ratio, u is the displacement along the x-axis and v is the displacement along the y-axis.

The strong form of continuity equation is written as:

$$\frac{\partial}{\partial t}\left(\frac{\partial u}{\partial x}+\frac{\partial v}{\partial y}\right)-\frac{k_x}{\gamma_w}\frac{\partial^2 p_n}{\partial x^2}-\frac{k_y}{\gamma_w}\frac{\partial^2 p_n}{\partial y^2}=0 \tag{3}$$

where k_x and k_y are the coefficients of permeability in the horizontal and vertical direction, and γ_w is the unit weight of the pore fluid.

For finite element discretization, we use **Q8-P4** finite element, with quadratic interpolation of the displacement field and linear interpolation of the pore pressure field. The end result of the standard finite element discretization procedure is the following set of equations:

$$\mathbf{K}_m\mathbf{u}+\mathbf{C}\mathbf{p}_n=\mathbf{f}$$
$$\mathbf{C}^{\mathrm{T}}\dot{\mathbf{u}}=\mathbf{0} \tag{4}$$

where $\mathbf{K}_m$ is the stiffness matrix, $\mathbf{K}_c$ is the permeability matrix, $\mathbf{C}$ is the coupling matrix, $\mathbf{f}$ is the external load vector, $\mathbf{u}$ is the vector of unknown nodal displacements, $\dot{\mathbf{u}}$ is the vector of time derivatives of displacements and $\mathbf{p}_n$ is the vector of unknown nodal pore pressures.

$$\mathbf{K}_m=\iint \mathbf{B}^{\mathrm{T}}\mathbf{D}\mathbf{B}dxdy;\ \mathbf{K}_c=\iint \mathbf{T}^{\mathrm{T}}\mathbf{K}\mathbf{T}dxdy;\ \mathbf{C}=\iint\left[\frac{\partial N}{\partial x}\right]\mathbf{N}dxdy \tag{5}$$

$$[D]=\begin{bmatrix}\lambda+2\mu & \lambda & 0\\ \lambda & \lambda+2\mu & 0\\ 0 & 0 & \mu\end{bmatrix};\ [K]=\begin{bmatrix}k_x & 0\\ 0 & k_y\end{bmatrix};$$

$$[B]=\begin{bmatrix}\frac{\partial N_1^u}{\partial x} & 0 & \dots & \frac{\partial N_i^u}{\partial x} & 0 & \dots & \frac{\partial N_8^u}{\partial x} & 0\\ 0 & \frac{\partial N_1^u}{\partial y} & \dots & 0 & \frac{\partial N_i^u}{\partial y} & \dots & 0 & \frac{\partial N_8^u}{\partial y}\\ \frac{\partial N_1^u}{\partial y} & \frac{\partial N_1^u}{\partial x} & \dots & \frac{\partial N_i^u}{\partial y} & \frac{\partial N_i^u}{\partial x} & \dots & \frac{\partial N_8^u}{\partial y} & \frac{\partial N_8^u}{\partial x}\end{bmatrix};\quad [T]=\begin{bmatrix}\frac{\partial N_1^p}{\partial x} & \frac{\partial N_3^p}{\partial x} & \frac{\partial N_5^p}{\partial x} & \frac{\partial N_7^p}{\partial x}\\ \frac{\partial N_1^p}{\partial y} & \frac{\partial N_3^p}{\partial y} & \frac{\partial N_5^p}{\partial y} & \frac{\partial N_7^p}{\partial y}\end{bmatrix} \tag{6}$$

Here, λ and μ are Lame's coefficients, N^u denotes quadratic interpolation function for displacement fields, and N^p denotes linear interpolation function for pore pressure field.

NUMERICAL ANALYSIS OF EMABNKMENT CONSOLIDATION

All numerical implementation and numerical simulations are performed in Fortran. The global system of equations is solved by using **θ** time-stepping scheme.

In all numerical simulations, we assume that the coefficient of permeability is porosity-dependent and strain-dependent [3]:

$$k = \alpha \cdot \frac{\varepsilon_s / \varepsilon_v}{0,66} \cdot k_0 \cdot 10^{\frac{e_0 - e}{c_k}} \tag{7}$$

where α is the coefficient of the change in the permeability, ε_s is the shear strain, ε_v is the volumetric strain, k_0 is the inital coefficient of permeability, e_0 is the initial void ratio, e is the void ratio in time t, and c_k is the constant $c_k=(0,4-0,5)e_0$.

5m HIGH EMBANKMENT

In this numerical example, we perform a numerical analysis of embankment consolidation where we aim to show the influence of the strain-dependent coefficient of permeability on the shape of the consolidation curve. The five meters high embankment lies on the ten meters thick clay layer. Young's modulus of elasticity of clay is E=5000 kPa, Poisson's ratio is ν=0.3. We perform a numerical analysis for three different values of α: 0.9 (k_1), 1.5 (k_2), and 2.5 (k_3).

The computed results are shown in Figure 1. We can conclude that the consolidation time at which the works on the pavement structure usually commence is smaller for the case of the variable value of coefficient of permeability, which is previously suggested in [2], and confirmed with in-situ measurements of object settlements.

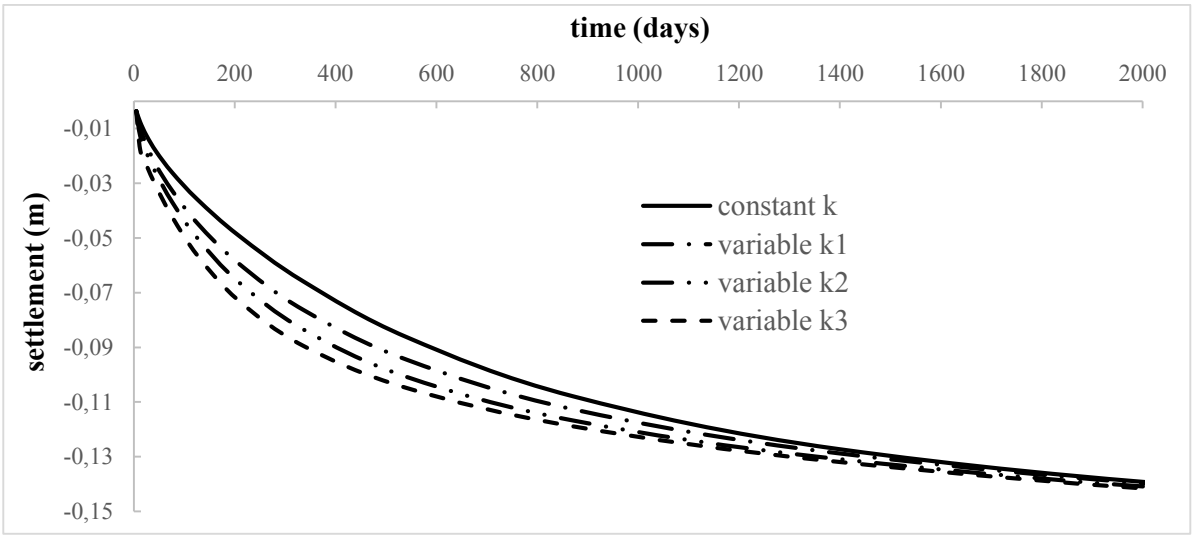

Figure 1: Computed consolidation curves for constant and variable value of coefficient of permeability

In Figure 2, the ratios of the coefficient of permeability in finite elements with respect to the coefficient of permeability in the finite element in the upper left corner are shown.

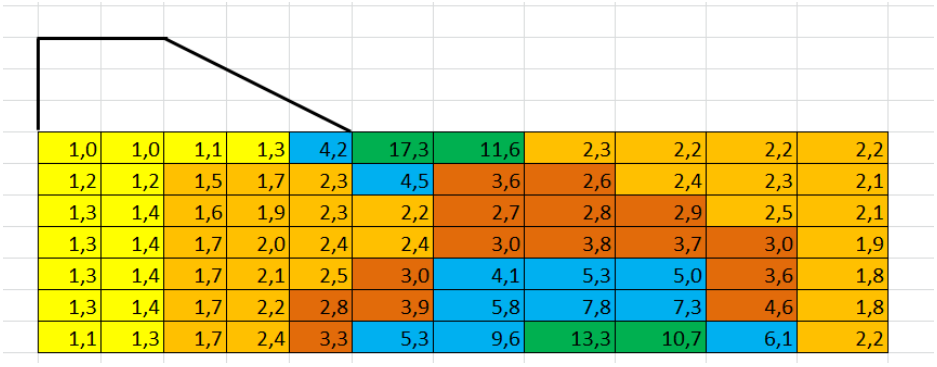

Figure 2: Computed ratios of coefficient of permeability

ROAD EMBANKMENT NEAR THE CITY SAGE

We perform a numerical analysis of the road embankment near the city Sage. The geometry of the model, boundary conditions, and finite element mesh are shown in Figure 3.

The earth profile consists of four layers. The material properties of each layer are shown in Table 1. The value of the coefficient of the change in the permeability is $\alpha=0.9$.

The computed results are shown in Figures 4 and 5. We compare the computed results against measurement data and reference values provided by Jinchun [4]. We can conclude that a good match between the results is obtained.

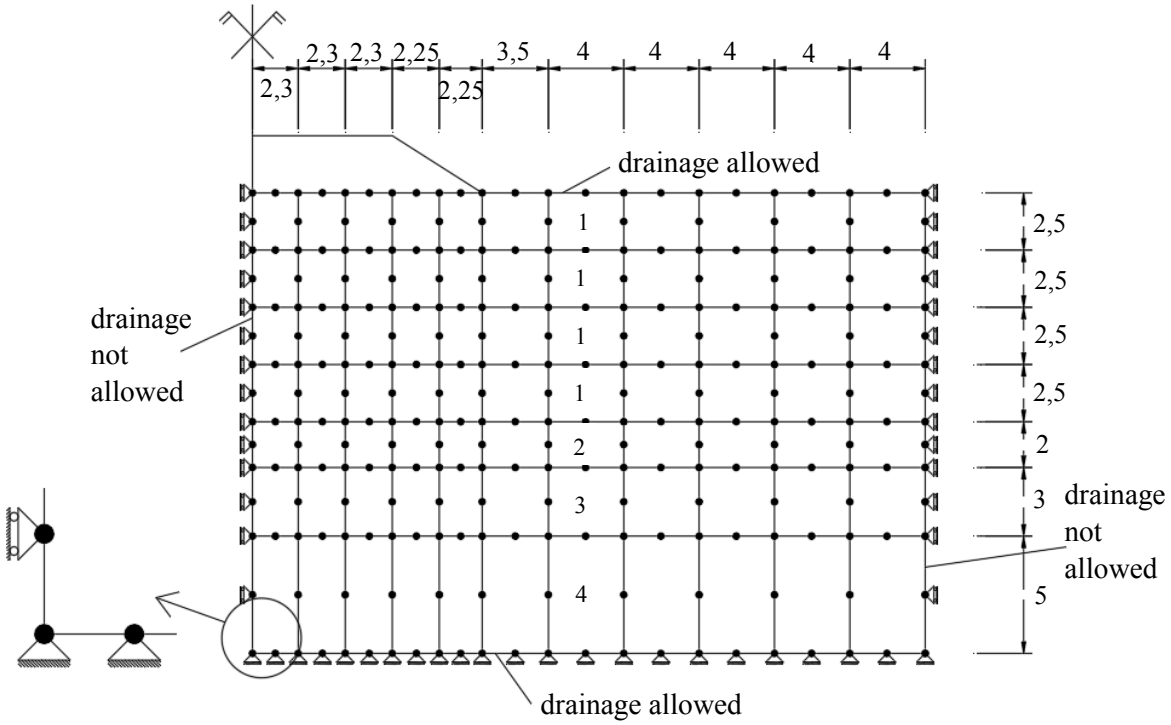

Figure 3: Geometry of the model, boundary conditions and finite element mesh

Layer	k_x [m/day]	k_y [m/day]	E [kN/m^2]	ν
1	0.000795	0.00053	235	0.3
2	0.002625	0.00175	235	0.3
3	0.25	0.25	20000	0.25
4	0.25	0.25	37500	0.25

Table 1: Material properties of soil layers

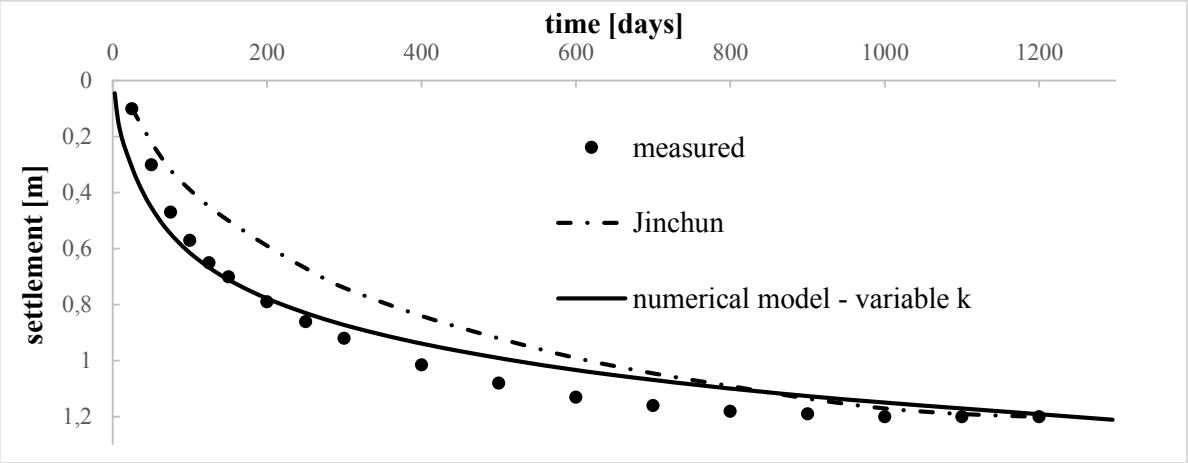

Figure 4: Computed consolidation curve

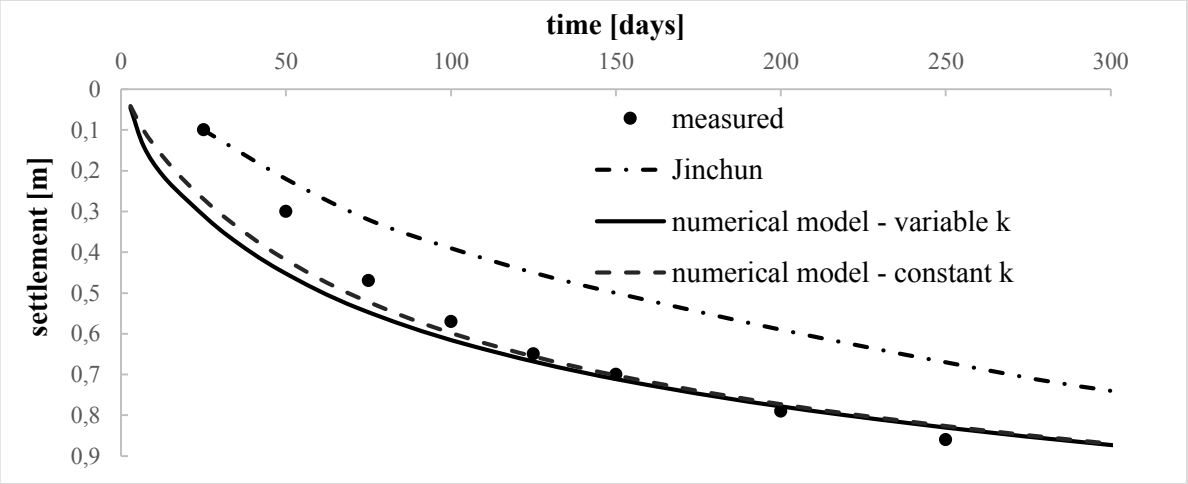

Figure 5: Initial part of the computed consolidation curve

CONCLUDING REMARKS

In this paper, we performed several numerical simulations of embankment consolidation with the aim to demonstrate the influence of the strain-dependent and porosity-dependent coefficient of permeability on the shape of the consolidation curve and consolidation time. Based on the results presented in this paper, we can conclude that in order to more precisely predict the embankment consolidation time at which the works on the pavement structure can commence, we ought to assume the strain-dependent coefficient of the permeability.

References

[1] P.W. Rowe. *Measurement of the coefficient of consolidation of lacustrine clay*, Geotechnique, 9(3): 107-118, 1959.
[2] E. Nonveiller. *Mehanika tla i temeljenje građevina*, Zagreb: Školska knjiga, 1979.
[3] A. Balić. *Doctoral thesis: Consolidation analysis with deformation-dependent coefficient of soil permeability,* University of Sarajevo, 2018.
[4] C. Jinchun, I. Yutaka, H. Takenori, C. John. *Finite element simulation of an embankment on soft clay - Case study,* Computers and Geotechnics, 48: 117-126, 2013.

TOWARDS A REDUCED ORDER MODEL OF BATTERY SYSTEMS: APPROXIMATION OF THE COOLING PLATE

M.Sc. Anna Szardenings [1], Nathalie Hoefer [2], Prof. Dr. Heike Fassbender [3],

[1a] Institute for Numerical Analysis, TU Braunschweig
[1b] Volkswagen Group Components, anna.szardenings@volkswagen.de
[2] Ostfalia University of Applied Science, n.hoefer@ostfalia.de
[3] Institute for Numerical Analysis, TU Braunschweig

Abstract

In order to analyze the thermal performance of battery systems in electric vehicles complex simulation models with high computational cost are necessary. Using reduced order methods, real-time applicable model can be developed and used for onboard monitoring. In this work a data driven model of the cooling plate as part of the battery system is built and derived from a computational fluid dynamics (CFD) model. The aim of this paper is to create an approximation model of the cooling plate that estimates the temperature at the boundary for different heat flow rates, mass flows and inlet temperatures of the cooling fluid. In order to do so, the cooling plate is simulated in a CFD software (ANSYS Fluent ®). A data driven model is built using the design of experiment and various approximation methods in Optimus ®. The model can later be combined with a reduced model of the thermal battery system. The assumption and simplification introduced in this paper enable an accurate representation of the cooling plate with a real-time applicable model.

1. Introduction

In the development of battery systems for electric vehicles, simulation techniques have gained importance in order to evaluate the design and performance of the system for different scenarios. Especially the thermal behavior of the battery needs to be examined, to ensure safety and reliability of the system [1, 2]. An important part of the thermal management is the cooling system, which is used to regulate the temperatures of the battery cells. Computational fluid dynamics (CFD) is commonly used to analyze such high dimensional systems, -> but unsteady CFD-system simulation are not always feasible due to computational cost.
It is therefore necessary to create real-time applicable model of the battery systems. One part of this reduced model is the cooling plate, which is the focus of this work. The cooling plate model is built to calculate the heat transfer from the thermal battery system into the cooling plate.
Previous works focus on estimating the fluid parameters such as pressure drop and velocity using data driven models [8]. For the estimation of heat transfer geometrical input parameters have been used for the approximation models, using up to 15 input parameters [12, 11, 15].
However here a fixed cooling plate geometry is considered and thus input and output parameters differ from previous works. The aim is to create a real-time applicable model of the cooling plate, in order to calculate an accurate boundary condition from the cooling plate. Later this model can be coupled with a thermal model of the battery system. Much more input parameters are needed for this application compared to other heat transfer models which will be described in Section 3. Further, this paper proposes several assumptions and simplifications to the cooling plate.

2. Data driven models

Data driven models approximate a correlation of inputs and outputs from for example a CFD model using various numerical methods regardless of the physical equation of the underlying problem. Those models tend to have much lower computation cost then the CFD model itself [7]. Various approaches have been already studied for the approximation of fluid and heat transfer models. For data driven models especially deep neural networks (DNN) for the approximation of the navier-stokes equation and fluid dynamics have been emphasized [8, 9]. For the approximation of heat transfer problems neural networks have been successfully applied using multiple input and output parameters from test data or simulation [10, 11, 12, 13, 14]. A further approximation model in fluid dynamics and simulation is the kriging method, which is mostly used for optimization problem [15, 7]. Based on the previous work we therefore focus on neural networks and kriging methods.
The data set for the meta-model is created using a design of experiments (DOE), where input parameter variations are set to depict the design space of the model. Different methods exist to define the input parameter values. Here, a large number on input parameters is necessary, thus Latin hypercube sampling (LHS) is proposed as method. LHS is a space filling sample design. From all input parameter permutations, the LHS choses randomly a number of permutations so that each sub interval of each parameter is only included once in the sampling size, reducing the number of input parameter variations [16].

3. Cooling plate model

The considered CFD model in our work is the cooling plate of a battery system which is placed beneath the battery cells. This bottom cooled system uses a water based coolant. The cooling plate is simulated in a CFD software (ANSYS Fluent ®). The model is used only to calculate the heat transfer from the battery system into the fluid. Hence, several assumptions and simplifications can be made to the model. For the fluid a fully developed flow is assumed at every time step at a certain flow rate and temperature.

Further, the fluid is assumed to be laminar. A steady and stable flow pattern and no vortexes are expected. Through this assumption it is possible to calculate the flow stationary, with velocity and

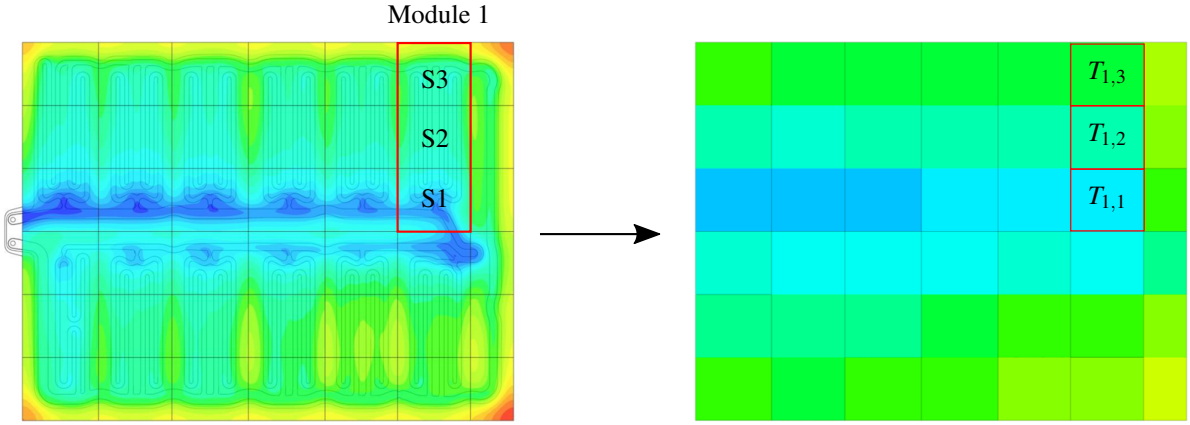

Figure 1: Approximation of the fluid cooling plate with averaged values of temperature T on the cooling plate surface at three surfaces (S1, S2 and S3) per module and junction box interface

pressure values independent from time.
In the coupled battery system model the cooling plate and thermal battery system are coupled through the heat flow rate of neighboring faces, satisfying the following equation [17, 18]:

$$\dot{Q} = A\alpha \cdot (T_{\text{plate}} - T_{\text{bat}}) \tag{1}$$

Where $\dot{Q}$ is the specific heat flow rate through a face of area A, α the heat transfer coefficient, T_{plate} is the temperature at the cooling plate top and T_{bat} is the temperature at the bottom of the battery system. When separating the cooling system from the thermal model, each of those values can be used as a conservative

boundary condition.
In the cooling plate model the values from equation 1 are calculated at the interface of the cooling plate to the battery modules. The values are averaged over three areas per module interface to represent the different flow sections of the cooling plate. The simplification is shown in Figure 1. The three surfaces per module were chosen to depict the different areas under each module, which is sufficient for the correct calculation of the temperature in the battery system. This results in a total 42 surfaces.
For validation the thermal battery system was simulated with averaged bounday conditions (BC) from the cooling plate and the resulting temperatures were compared with a coupled model of the system (cooling plate and thermal system). The averaged values at the cooling plate faces were obtained from simulations of the CFD model of the cooling plate. Three different types of boundary conditions were tested, fixed temperature, heat transfer coefficient (HTC), heat flow rate boundary. The results are shown

Table 1: Temperature deviation in thermal battery model for different BCs

	BC HTC		BC Heat flow rate		BC Temperature	
	ΔT Abs.	ΔT Rel.	ΔT Abs.	ΔT Rel.	ΔT Abs.	ΔT Rel.
Average	0.77 K	0.9 %	2.01 K	3.4 %	-0.23 K	0.8 %
Maximum	2.79 K	4.8 %	4.41 K	7.5 %	1.63 K	2.8 %

in Table 1. The temperature BC shows the best results in the thermal model. Based on the previous assumptions an averaged error of -0.23 K is estimated in the batteries temperatures when comparing the full battery system model and the decoupled model. The maximal temperature of the battery module are on average 1.63 K lower in the decoupled system.

4. Approximation model of the cooling plate

To create a real-time applicable model a data driven meta model is proposed. For this, snapshots are calculated from the fluid model at each input parameter set using a design of experiments (DOE). Here input parameters are the fluid temperature at the inlet T_{fluid}, the mass flow rate at the inlet $\dot{m}_{\text{fluid}}$ and the heat flow rate $\dot{Q}_{\text{cooling}}$ at the boundary condition from a thermal model of the battery system. Output parameters are the temperatures at the cooling plate T_{plate}. In total this results in 44 input and output parameters.
The DOE and approximation model is built in Optimus ®. The software is chosen as tool, since it can directly be coupled with Ansys Fluent ® simulation to generate the snapshots and is able to provide a solver independent FMU of the model, that can be imported into any software and model of choice [19]. The workflow is shown in Figure 2. The generated model will be exported as a FMU and simulated in

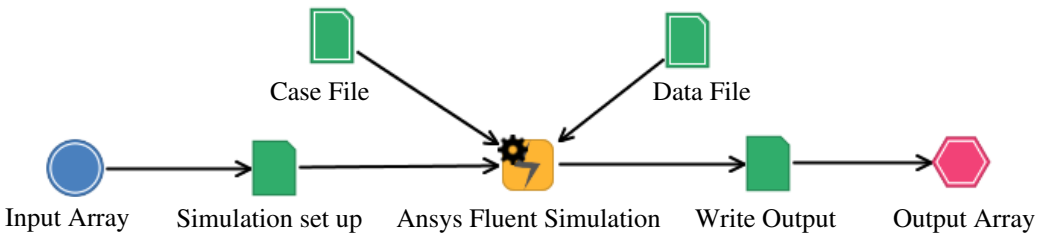

Figure 2: Optimus workflow for the calculation of snapshots from the Ansys Fluent model

Simulink using input parameter sets different from the training data. The model output is then compared to the averaged surface values of the CFD simulation. Further, the computation time for both, the CFD and approximation model will be evaluated.

References

[1] Christian Julien, Alain Mauger, Ashok Vijh, and Karim Zaghib. Lithium batteries. In *Lithium Batteries: Science and Technology*, pages 29–68. Springer International Publishing, Cham, 2016.

[2] Zhonghao Rao and Shuangfeng Wang. A review of power battery thermal energy management. *Renewable and Sustainable Energy Reviews*, 15:4554–4571, 2011.

[3] Ahmad A Pesaran, Andreas Vlahinos, Steven D Burch, et al. *Thermal performance of EV and HEV battery modules and packs*. National Renewable Energy Laboratory, 1997.

[4] Ahmad A Pesaran. Battery thermal management in ev and hevs: issues and solutions. *Battery Man*, 43(5):34–49, 2001.

[5] Matthias Fleckenstein, Oliver Bohlen, and Bernard Bäker. Aging effect of temperature gradients in li-ion cells: Experimental and simulative investigations and the consequences on thermal battery management. *World Electric Vehicle Journal*, 5:322–333, 2012.

[6] Joel H Ferziger, Milovan Perić, and Robert L Street. *Computational methods for fluid dynamics*, volume 3. Springer, 2002.

[7] Jack PC Kleijnen. Kriging metamodeling in simulation: A review. *European journal of operational research*, 192(3):707–716, 2009.

[8] Connor Schenck and Dieter Fox. Spnets: Differentiable fluid dynamics for deep neural networks. *arXiv preprint arXiv:1806.06094*, 2018.

[9] J Nathan Kutz. Deep learning in fluid dynamics. *Journal of Fluid Mechanics*, 814:1–4, 2017.

[10] Jiang-Zhou Peng, Xianglei Liu, Nadine Aubry, Zhihua Chen, and Wei-Tao Wu. Data-driven modeling of geometry-adaptive steady heat transfer based on convolutional neural networks: Heat conduction. *arXiv preprint arXiv:2010.03854*, 2020.

[11] Yasar Islamoglu. A new approach for the prediction of the heat transfer rate of the wire-on-tube type heat exchanger—-use of an artificial neural network model. *Applied Thermal Engineering*, 23(2):243–249, 2003.

[12] GN Xie, QW Wang, M Zeng, and LQ Luo. Heat transfer analysis for shell-and-tube heat exchangers with experimental data by artificial neural networks approach. *Applied Thermal Engineering*, 27(5-6):1096–1104, 2007.

[13] Jules Thibault and Bernard PA Grandjean. A neural network methodology for heat transfer data analysis. *International Journal of Heat and Mass Transfer*, 34(8):2063–2070, 1991.

[14] K Jambunathan, SL Hartle, S Ashforth-Frost, and VN Fontama. Evaluating convective heat transfer coefficients using neural networks. *International Journal of Heat and Mass Transfer*, 39(11):2329–2332, 1996.

[15] Kyoungwoo Park, Park-Kyoun Oh, and Hyo-Jae Lim. The application of the cfd and kriging method to an optimization of heat sink. *International Journal of Heat and Mass Transfer*, 49(19-20):3439–3447, 2006.

[16] Thomas J. Santner, Brian J. Williams, William I. Notz, and Brain J. Williams. *The design and analysis of computer experiments*, volume 1. Springer, 2003.

[17] Donatello Annaratone. *Engineering heat transfer*. Springer Science & Business Media, 2010.

[18] Bernhard Weigand, Juergen Koehler, and Jens von Wolfersdorf. *Thermodynamik kompakt*. Springer Berlin Heidelberg, 3. edition, 2013.

[19] Noesis Solutions, Gaston Geenslaan 11, 3001 Leuven, Belgium. *OPTIMUS REV 2019.2 - USERS MANUAL*, 2019.2 edition, March 2019.

ECCOMAS MSF 2021 THEMATIC CONFERENCE
30 June – 2 JULY 2021, SPLIT, CROATIA

A PROMETHEE MULTIPLE-CRITERIA METHODOLOGY FOR COMBINED SEISMIC AND HYDRAULIC RISK ASSESSMENT: THE CASE STUDY OF FERRARA (ITALY)

Arianna Soldati[1], Andrea Chiozzi[2], Zeljana Nikolic[3], Elena Benvenuti[4]

[1] University of Ferrara, arianna.soldati@edu.unife.it
[2] University of Ferrara, andrea.chiozzi@unife.it
[3] University of Split, zeljana.nikolic@gradst.hr
[4] University of Ferrara, elena.benvenuti@unife.it

Many regions worldwide are threatened by multiple natural and technological hazards, the number of this disasters significantly increase during the last decades. These disasters acted as indicators of a greater exposure to multi-risk situations and showed an increased vulnerability of our societies to more complex risks.
The awareness of this worrying trend has increased the need for appropriate supports, tools and methodologies in order to be able to address these problems and lead to sustainable risk management activities (prevention, mitigation, crisis management and recovery) [1]. Considering a joint analysis of multiple hazards numerous challenges and difficulties arise that's why the development of the modelling of multi risks analysis scheme is still in the early stages [2].
The first difficulty is linked to the comparability of hazardous events: the risk associated with different types of natural hazards are often estimated using different procedures leading to the results not to be comparable, when the events themselves could be highly correlated [3]. The second difficulty concerns the comparison of the vulnerabilities of the exposed elements.
Moreover, another issue is related to the weighting of the relevance of certain hazards of exposed elements for the territory: stakeholders may have different perceptions on the importance of each single risk. Lastly it is also necessary to take into account the difficulty to collect data and information.
The purpose of this work is to describe the methodology used for the evaluation of the combined seismic and hydraulic risk of the territory of Ferrara.
The Visual PROMETHEE software, based on outranking methods (PROMETHEE methods), was used as a tool for data implementation.
Visual PROMETHEE, known for its simplicity and an important number of applications in different fields, it is based on pair-wise comparisons and allows a decision-maker to full rank a finite set of *actions* that are evaluated over a set of *criteria*. The information related to each criterion is aggregated through the definition of preference functions, each criterion also have a weight expressed by a non-negative number that represents the importance of the different criteria: the higher the weight the more important the criterion. The weights reflect a major part of the "brain" of the decision maker. [4]
In this application the hydraulic and seismic risk have been broken down into their components: probability of occurrence of the flood, seismic hazard (PGA), exposure (land use, strategic buildings, population density) and vulnerability (age of buildings); they have been included in Visual PROMETHEE as "criteria", while the municipalities of the Ferrara territory as "alternatives". These data were collected from both the Consorzio di Bonifica Pianura di Ferrara and the Municipality of Ferrara websites.
The result of the analysis made it possible to highlight the areas most affected by the hydraulic-seismic risk (Fig. 1) but also the criteria that most positively and negatively influence the municipalities of Ferrara (Fig. 2).

These results depend on the personal choices of the individual stakeholders in the selection of parameters (weights and preference functions), however some small deviations in the determination of these values do not often induce important modifications.

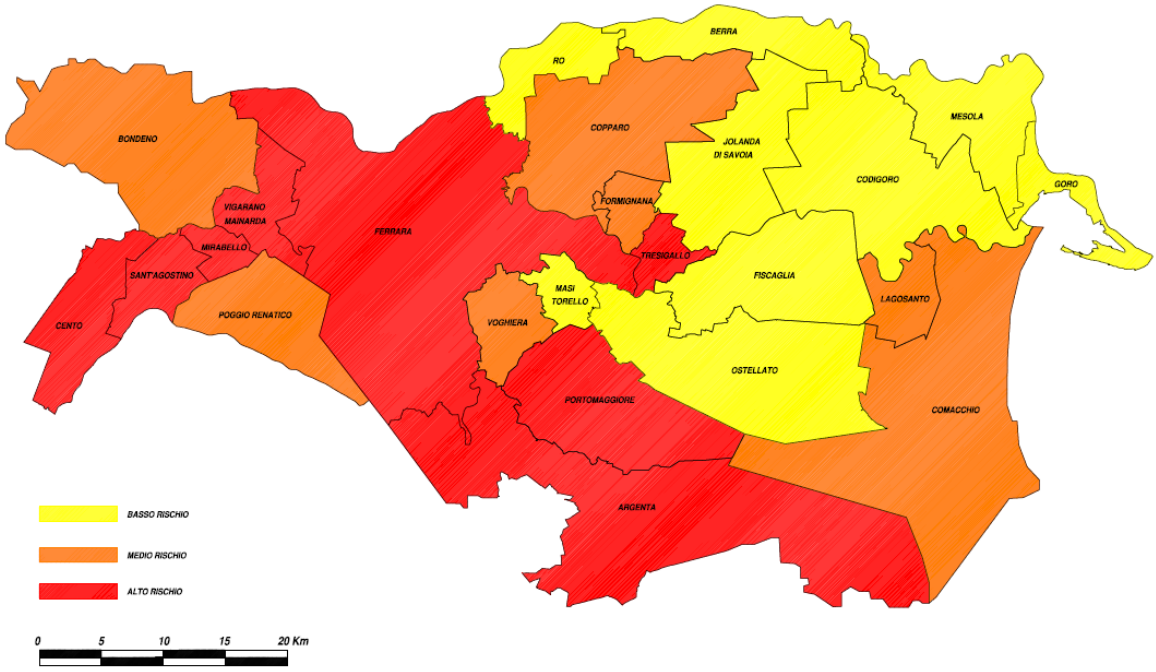

Figure 1. Hydraulic-seismic risk map of the territory of Ferrara

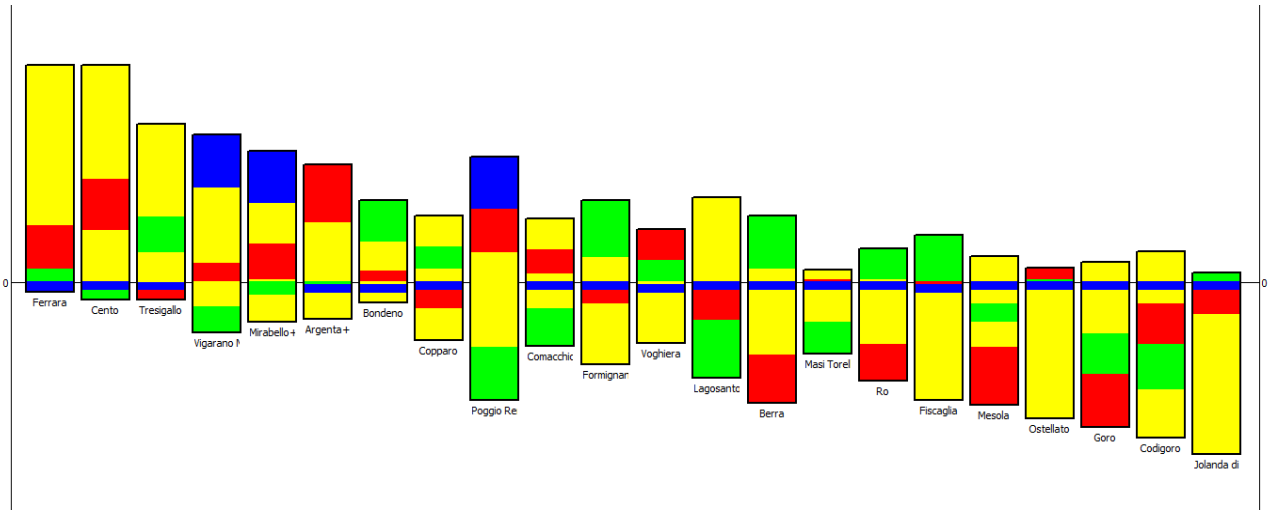

Figure 2. Promethee Rainbow.

Acknowledgements

This work has been supported by the project "Preventing, Managing and Overcoming natural-hazards risks to mitiGATE economic and social impact" (PMO-GATE), funded by the European Union in the context of the Interreg Italy-Croatia program.

References

[1] A. Carpignano, E. Golia, C. Di Mauro, S. Bouchon, J-P. Nordvik, *"A methodological approach for the defenition of multi-risk maps at regional level: first application"*, Journal of Risk Research, 12, 2009.

[2] M.S Kappes, K. Gruber, S. Frigerio, R. Bell, M. Keiler, T. Glade, *"The MultiRISK platform: The technical concept and application of a regional-scale multihazard exposure analysis tool"*, Geomorphology, 151-152, 139-155, 2012.
[3] F. Nadim, Z. Liu, *"New methodologies for multi-hazard and multi-risk assessment methods for Europe", MATRIX*, D5.2 Framework for multi-risk assessment, 2013.
[4] J-P. Brans, B. Mareschal, "Chapter 5 Promethee Methods", In: J. Figueira, S. Greco, M. Ehrgott, (Eds.), Multiple Criteria Decision Analysis: State of the Art Surveys. Springer Science + BusinessMedia, Inc., pp. 163–196, 2005.

ECCOMAS MSF 2021 THEMATIC CONFERENCE
30 June – 2 JULY 2021, SPLIT, CROATIA

ALGORITHM FOR SOLVING MAXIMUM ENTROPY PROBLEM BASED ON FINITE BASIS FUNCTIONS

Blaž Gotovac, Nives Brajčić Kurbaša, Vedrana Kozulić, Hrvoje Gotovac

University of Split, Faculty of Civil Engineering, Architecture and Geodesy,
blaz.gotovac@gradst.hr; nives.brajcic@gradst.hr; vedrana.kozulic@gradst.hr;
hrvoje.gotovac@gradst.hr

Abstract

The Maximum Entropy (MaxEnt) principle is a versatile tool for statistical finding of the probability density function (pdf) from its moments as a least-biased estimation among all other possible pdf's. The MaxEnt algorithm transforms the original constrained optimization problem to the unconstrained dual optimization problem using Lagrangian multipliers. The Classic Moment Problem (CMP) uses algebraic power moments, causing typical conventional numerical methods to fail for higher-order moments due to different sensitivities of Lagrangian multipliers and unbalanced nonlinearities. These difficulties can be overcome by using orthogonal polynomials which enable roughly the same sensitivity for all Lagrangian multipliers.

In this paper the Fup MaxEnt Algoritam (FMEA) that based on using finite basis functions $Fup_4(x)$ with compact support is presented. These basis functions can exactly describe algebraic polynomials up to the fourth order while polynomials of high orders describe approximately. FMEA solves the CMP finding an optimal pdf with better balanced Lagrangian multipliers. The algorithm is numerically very efficient due to localized properties of Fup_4 basis functions implying a weaker dependence between Lagrangian multipliers and faster convergence. Application of Fup MaxEnt algoritam is demonstrated on continuous beta distribution as pdf example.

1. Introduction

Many physical processes cannot be characterized deterministically due to the presence of intrinsic or parametric uncertainty due to their physical nature, interpretation or measurements. Therefore, results are usually given in the form of a certain number of the first few statistical power moments or rarely as a probability density function (pdf). The MaxEnt principle [8] presents a robust tool for pdf prediction in terms of statistical moments.

MaxEnt problem can be defined as the following optimization problem [1, 10]

$$\max H(f) \tag{1a}$$

$$\int_{x_{min}}^{x_{max}} h_i(x) f(x) dx = \mu_i \,; \quad i = 0, \dots, \mathrm{m} \tag{1b}$$

where $H(f)$ is Shannon information entropy [9] defined in a broader sense as

$$H(f) = -\int_{x_{min}}^{x_{max}} ln\big(f(x)\big) f(x) dx \tag{2}$$

and (1b) are known constraints that represent the statistical moments of the basis functions $h_i(x)$.

The MaxEnt algorithm transforms the original constrained optimization problem (1) to the unconstrained dual optimization problem by introducing the Lagrange function and the corresponding multipliers λ_i

$$\mathcal{L}(f,\lambda_i) = H(f) - \sum_{i=0}^{m}\lambda_i \cdot \left[\int_{x_{min}}^{x_{max}} h_i(x)f(x)\,dx - \mu_i\right] \tag{3}$$

where μ_i are the known moments of the basis functions $h_i(x)$ and $f(x)$ is the probability density function. The analytical form of MaxEnt pdf is

$$f(x) = e^{-1-\sum_{i=0}^{m}\lambda_i \cdot h_i(x)} \tag{4}$$

Finally, by introducing MaxEnt pdf (4) into constraints (1b) the MaxEnt problem is reduced to determining Lagrange multipliers from a nonlinear system of $(m\ +\ 1)$ equations

$$\int_{x_{min}}^{x_{max}} h_j(x) \cdot e^{-1-\sum_{i=0}^{m}\lambda_i \cdot h_i(x)}dx = \mu_j, \quad j = 0,\dots,m \tag{5}$$

The CMP takes algebraic monomials x^i for basis functions $h_i(x)$ which causes numerical difficulties in solving a nonlinear system (5) by conventional iterative methods: due to unbalanced nonlinearities of Lagrangian multipliers for moments $m >\ 5\text{—}10$ the number of iterative steps is large and convergence is slow. These difficulties can be significantly reduced by using orthogonal polynomials, such as Chebyshev polynomials [2].

2. Fup MaxEnt algorithm (FMEA)

Although the use of orthogonal polynomials significantly increases the efficiency of iterative procedures for the CMP (5), many numerical difficulties are still present. Moreover, the drawback remains of a strong connection between polynomials and their influence on the moment changes.

The original idea behind the proposed algorithm is to use finite and localized basis functions with a compact support, so that the correction of the multiplier λ^k in each iteration step changes only a few moment equations in system (5), namely, the ones that belong to the neighboring basis functions.

The FMEA algorithm [7] uses Atomic Basis Functions (ABF) of the algebraic type $Fup_n(x)$ whose properties and application are elaborated in [3-7]. The basis functions $Fup_n(x)$ describe accurately polynomials up to and including the order n, so the basis functions $Fup_4(x)$, used in this paper, will accurately describe polynomials up to and including the fourth order of polynomials and polynomials of order higher than four approximately, ie.

$$\begin{aligned} x^i &\equiv \sum_{j=0}^{4} d_{ij} \cdot Fup_{4j}(x) && for \quad i = 0,\dots,4 \\ x^i &= \sum_{j=0}^{m} d_{ij} \cdot Fup_{4j}(x) + \varepsilon_i(x), && for \quad i = 5,\dots,m \end{aligned} \tag{6}$$

where $\varepsilon_i(x)$ are residual functions that describe the difference between monomials of the mth order and their Fup_4 approximation.

Using Eq. (7), we can relate classic power moments and Fup_4 moments

$$\mu_i - \Delta\mu_i^{(l-1)} = \sum_{j=0}^{m} d_{ij} \cdot \mu_j^{Fup_4(l)}; i = 0,\dots,m \tag{7}$$

where μ_i, $\Delta\mu_i^{(l-1)}$ and $\mu_j^{Fup_4(l)}$ are moments of monomials, residual and Fup_4 basis functions, respectively.

Since moments of residual and Fup_4 basis functions are unknown, the algorithm must be defined in an iterative way, where l is a counter of iteration steps. An algorithm starts with an initial pdf guess $(l = 0)$. In each iteration step, the residual moments are first calculated from the previous iteration or initial conditions, then Fup_4 moments are obtained from the system (7).

Finally, the MaxEnt nonlinear system with respect to only Fup_4 moments is obtained

$$\int_0^1 Fup_{4i}(x) \cdot e^{-1-\sum_{j=0}^{m}\gamma_j \cdot Fup_{4j}(x)}dx = \mu_i^{Fup_4}, \quad i = 0,\dots,m \tag{8}$$

The procedure is repeated until convergence is achieved. The Fup MaxEnt algorithm is reduced to CMP over the moments of Fup_4 basis functions. Finally, the optimal pdf has the form

$$f^*(x) = exp\left(-1 - \sum_{j=0}^{m} \gamma_j \cdot Fup_{4j}(x)\right) \tag{9}$$

3. Pdf example

Application of the Fup MaxEnt Algorithm is presented on illustrative continuous pdf example. We consider the unimodal beta distribution

$$f(x) = \frac{\Gamma(\alpha+\beta)}{\Gamma(\alpha)\,\Gamma(\beta)} x^{\alpha-1}(1-x)^{\beta-1} \tag{9}$$

which is defined on interval $[0,1]$ and depends on two parameters α and β, while Γ is the gamma function. In this example, $\alpha = 3$ and $\beta = 5$, defining a slightly skewed pdf.

FMEA uses Fup_4 basis functions, which means that at least 6 basis functions are needed for algorithm ($m = 5$). It is well known that the Gaussian distribution is indeed also the MaxEnt pdf for $m = 2$. So, the Gaussian pdf is a very good starting vector, but in this example we use the constant function as the initial pdf with value equal 1. Then, we gradually increase the number of moments until the Fup optimal pdf converges to the exact pdf, so that the previous pdf solution is the initial pdf for the next simulation. The accuracy of the algorithm through the iterative procedure is controled by the absolute moment error between the given and calculated power moments over all moments with taken threshold $\eta = 10^{-1}$.

Fig.1 shows that six moments (six Fup_4 basis functions; $m = 5$) produce a larger error at the left boundary. Seven moments (7 Fup_4 basis functions; $m = 6$) reduce the differences between the exact and optimal pdf, especially for the right tail. Eight moments quite accurately describe all pdf features, while 11 moments ($m = 10$) completely reproduce the exact pdf.

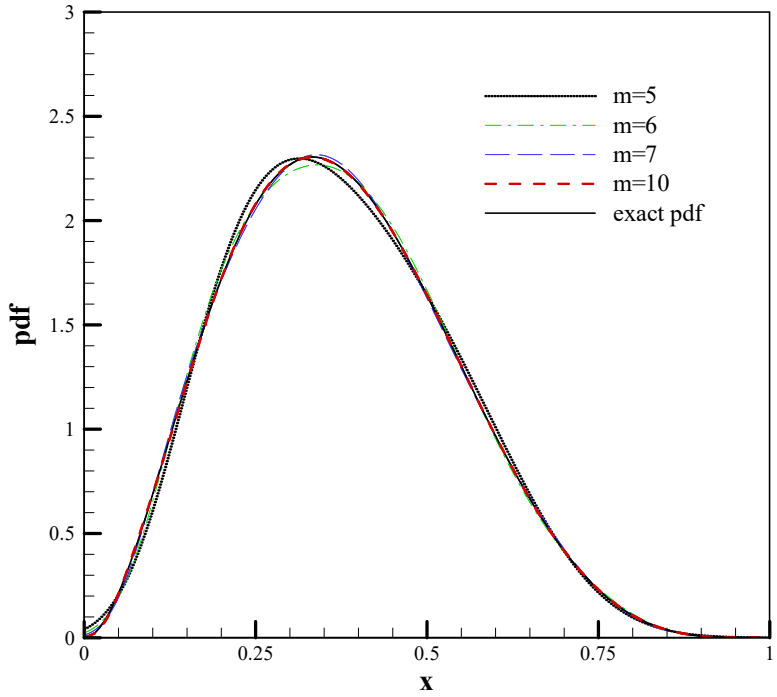

Fig. 1 Fup MaxEnt approximation of the beta pdf using moments up to $m = 10$

Fup MaxEnt Algorithm is characterized by a stable nonlinear solver due to localized properties of Fup_4 basis functions and converges regardless the initial vector which is the most important property for an ill-posed MaxEnt problem.

4. Conclusions

The proposed algorithm solves higher-order MaxEnt moment problem with only low order Fup_4 basis functions which is opposite to all existing MaxEnt algorithms. Only consequence is an iterative

algorithm defined by Eq. (7), while classic MaxEnt algorithms directly solve CMP due to exact relation between monomials and orthogonal polynomials. However, iterative scheme (7) converges very quickly due to small residual moments and their weak influence on changes of Fup_4 moments.

References

[1] A.L. Berger, S.A. Della Pietra, V.J. Della Pietra. *A maximum entropy approach to natural language processing*, Comp. Linguistics 22 (1) 39–71, 1996.

[2] K. Bandyopadhyay, A. Bhattacharya, P. Biswas, D. Drabold. *Maximum entropy and the problem of moments: A stable algorithm*, Phys. Rev. E 71 (5), 2005.

[3] B. Gotovac, V. Kozulic. *On a selection of basis functions in numerical analyses of engineering problems*, Int. J. Eng. Model., 12 (1–4) 25–41, 1999.

[4] B. Gotovac, V. Kozulic. *Numerical solving the initial value problems by Rbf basis functions*, Struct. Eng. Mech. 14 (3) 263–285, 2002.

[5] H. Gotovac, R. Andricevic, B. Gotovac. *Multi-resolution adaptive modeling of groundwater flow and transport problems*, Adv. Water Res. 30. 1105–1126, 2007.

[6] H. Gotovac, V. Cvetkovic, R. Andricevic. *Adaptive Fup multi-resolution approach to flow and advective transport in highly heterogeneous porous media: methodology accuracy and convergence*, Adv. Water Res. 32. 885–905, 2009.

[7] H. Gotovac, B. Gotovac. *Maximum entropy algorithm with inexact upper entropy bound based on Fup basis functions with compact support*, J. Comput. Phys. 228, 9079–9091, 2009.

[8] E.T. Jaynes. *Information theory and statistical mechanics*, Phy. Rev. 106 620–630, 1957.

[9] C.E. Shannon, Bell Syst.Tech.J.27 (1948) 379–623. reprinted in C.E. Shannon and W.Weaver,The Mathematical Theory of Communication (University of Illinois Press, Urbana, 1949.

[10] Y.-K. Tung, B.-K. Yen, C.S. Melching. *Hydrosystems Engineering Reliability Assessment and Risk Analysis*, McGraw-Hill, New York, p. 495, 2006.

ECCOMAS MSF 2021 THEMATIC CONFERENCE
30 JUNE – 2 JULY 2021, SPLIT, CROATIA

HYBRID-STRESS FORMULATION AND CONSERVING/DECAYING SCHEMES FOR VISCO-PLASTIC PROBLEM IN DYNAMICS

Cong Uy Nguyen[1], Hermann G. Matthies[2], Adnan Ibrahimbegovic[3]

[1] Sorbonne Université-Université de Technologie Compiègne, Laboratoire Roberval de Mécanique, France; Institute of Scientific Computing/Technical University of Braunschweig, 38106 Braunschweig, Germany, cong-uy.nguyen@utc.fr
[2] Institute of Scientific Computing/Technical University of Braunschweig, 38106 Braunschweig, Germany, h.matthies@tu-bs.de
[3] Sorbonne Université-Université de Technologie Compiègne, Laboratoire Roberval de Mécanique, Chaire de Mécanique, France, adnan.ibrahimbegovic@utc.fr

In this work, the visco-plastic behaviour of solids is formulated based on the Hellinger–Reissner variational principle. The latter provides a choice to obtain an better computation of stress by using discretization of both displacement and stress fields, see [3] and [4]. The formulation is further developed for dynamics problem. For this class of problem, we propose the algorithmic modifications leading to conserving and decaying energy schemes, see [3]. The former can preserve the total energy of system under elastic regime, and thus control the overall stability of numerical computations over long period of time. While the former can dissipate higher engery modes out of the system. Several numerical examples are presented to illustrate a very satisfying performance of the proposed approach and algorithm.

The formulation is adapted to 1D beam element to simulate the response of a long tube under internal pressure, see Fig. 1. Several numerical simulations are done in static analysis then the results are compared with the analytic solution [1] as well as the result from Q4/P1 element. The comparison clearly shows a good performance of the proposed formulation, see Figs. 2-4. Regarding the visco-plastic regime, the element is used to compare with Q4/P1 and Hughes & Taylor [2] elements. The result shows a high agreement between the current formulation and Hughes & Taylor [2] , see Figs. 5-8. To demonstrate the ability to perserve the total energy of system under elastic regime (see Fig. 9), the element is equipped with conserving energy scheme in the free vibration. Along with that, the decaying energy scheme is also employed to dissipate higher modes governing by dissipation parameters α and β (see Fig. 10, the external load is generated in the way that it can excite high frequency modes in the system.

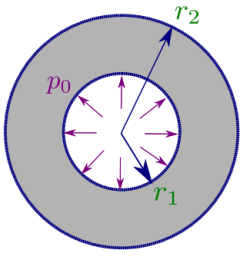

Fig 1 : Pipe geometry and internal load

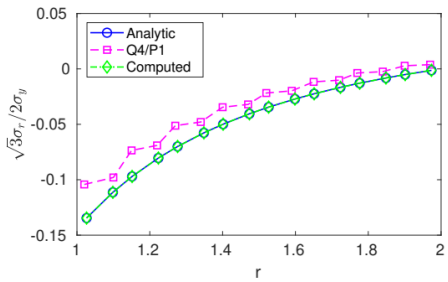

Fig 2 : Stress σ_r in elastic regime

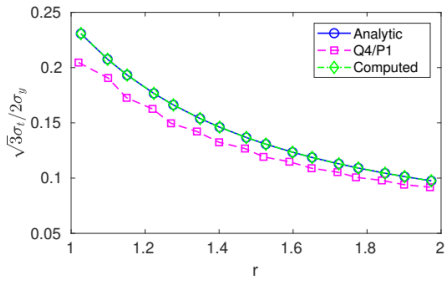

Fig 3 : Stress σ_t in elastic regime

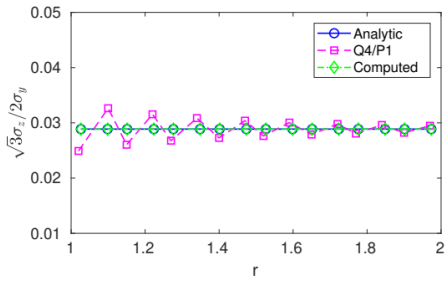

Fig 4 : Stress σ_z in elastic regime

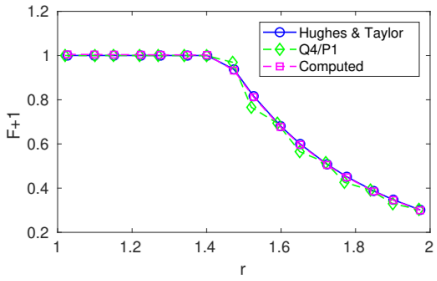

Fig 5 : F+1 function in visco-plastic regime

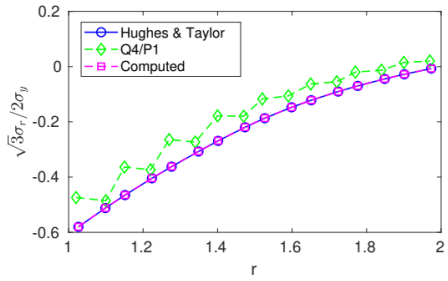

Fig 6 : Stress σ_r in visco-plastic regime

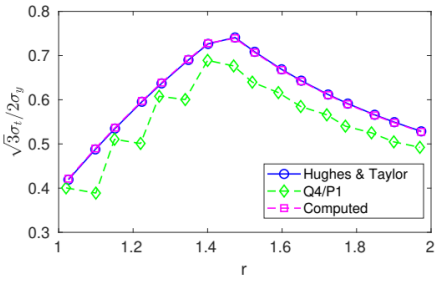

Fig 7 : Stress σ_t in visco-plastic regime

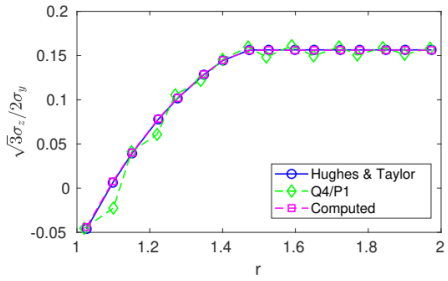

Fig 8 : Stress σ_z in visco-plastic regime

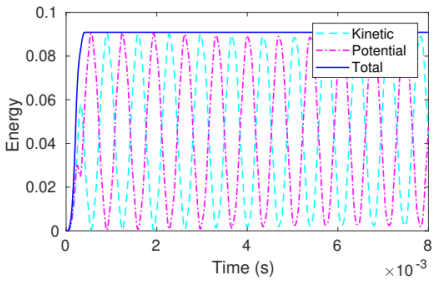

Fig 9 : Total energy under free vibration in elastic regime

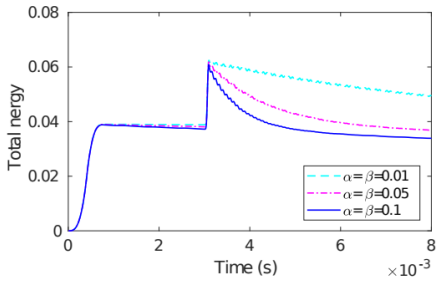

Fig 10 : Total energy under free vibration in visco-plastic regime

REFERENCES

[1] J. Lubliner, Plasticity theory. *Courier Corporation*., 2008.

[2] T.J.R Hughes and R.L. Taylor, Unconditionally stable algorithms for quasi-static elasto/visco-plastic finite element analysis. *Computers & Structures*., Vol. **8**, pp. 169-173, 1978.

[3] C.U. Nguyen and A. Ibrahimbegovic, Visco-plasticity stress-based solid dynamics formulation and time-stepping algorithms for stiff case. *International Journal of Solids and Structures.*, Vol. **196-197**, pp. 154-170, 2020.

[4] C.U. Nguyen and A. Ibrahimbegovic, Hybrid-stress triangular finite element with enhanced performance for statics and dynamics. *Computer Methods in Applied Mechanics and Engineering.*, Vol. **372**, 2020.

MESO-SCALE THERMAL AND SOLIDIFICATION MODELLING FOR METALLIC ADDITIVE MANUFACTURING PROCESSES

Daniel Dreelan [1], Gowthaman Parivendhan [1], Philip Cardiff [1], David Browne [1], Alojz Ivanković [1]

[1] SMME, University College Dublin, daniel.dreelan@ucdconnect.ie

1. Introduction

The emergence of additive manufacturing (AM) in recent decades signifies a paradigm shift in how we think about manufacturing. Throughout history, breakthroughs in manufacturing were focused on mass production, with a "one size fits all" mentality. Whilst for large batch size applications this has invariably decreased unit manufacturing costs, increased throughput and decreased prices for customers, it also imposes significant limitations for small batch production. Conventional manufacturing requires many highly specialised steps and equipment, requiring significant resources to establish and setting the barrier to entry unfeasibly high for fledgeling SMEs to enter the manufacturing space. Coupled with this, it inevitably forces manufacturers to be unresponsive to their customers' needs, as changes to a product or manufacturing process are costly, and require significant machine downtime. Additive manufacturing on the other hand offers virtually limitless freedom to the manufacturer to make changes to a product, even for a one-off bespoke application, without significant machine downtime or costly modification to the manufacturing process. Perhaps even more importantly, since parts are generated additively many of the restrictions that traditional machining imposes on part design no longer apply, allowing for near-net-shape, highly optimised structures to be realised. However, these advantages do not come without a cost. Widespread adoption of AM is still hampered by less than ideal mechanical performance.

2. Modelling

During metallic additive manufacturing processes such as powder bed fusion (PBF), a 3D part is generated progressively spreading and subsequently melting a fine layer of powder with a high energy heat source such as a laser or electron beam. The physics involved during the laser/electron beam processing is extremely dynamic and challenging to be captured using experimental procedures due to the spatial and temporal scales involved. Numerical modelling of the PBF process can predict thermal behaviour, melt pool hydrodynamics, microstructure evolution during solidification etc. which can be used to estimate the macroscopic properties of the finished component. Extreme thermal gradients and cooling rates resulting from these aggressive heating and cooling cycles, present many modelling challenges.

In order to feasibly model domain sizes up to an entire part, trade-offs need to be made between accuracy and computational efficiency. Our ambition is to use a multi-scale, multi-physics approach to model the entire PBF process: from the deposition of powder, to melting and trapping of bubbles in the solidifying melt pool, to the prediction of grain structure and solidification induced porosity.

2.1. Thermofluid modelling

To understand the mechanisms that lead to defects in Additively Manufactured components, it is necessary to model the melt pool formation, flow and subsequent solidification. A mesoscale approach is

considered where the powder bed is modelled as a granular media rather than a continuous medium. Discrete Element Method (DEM) is used to model the interaction between particles during Powder deposition. A "Rain-drop model" is used to generate particles in the domain and allowed to settle on the bedplate under the influence of gravity. Particles that exist above the desired layer thickness are removed to create a Powder Bed model similar to the Powder deposition process.

The melting and flow of the metal particles due to the laser beam is a highly dynamic and complex process. A custom foam-extend solver has been developed that includes several phenomena such as flow due to buoyancy, Marangoni convection, capillary forces and heat losses due to convection, radiation and evaporation are taken into account [1, 2]. A volume of fluid approach is used to solve the momentum equation with surface forces acting on the metal/gas interface. The interface is tracked using isoAdvector algorithm. The temperature is determined from the heat equation with heat losses and source acting at the interface. Source based method proposed by Voller et al[3] has been implemented to model phase change. The size and position of each particle are then transferred to a Finite Volume Mesh in OpenFOAM. A utility sets the material volume fraction for each cell, thus creating the initial state for the thermofluid modelling of laser processing during the PBF process. The developed model is used to numerically predict the melt pool formation and the influence of various process parameters have been studied. The melt pool profile of one such model is shown in Figure 1.

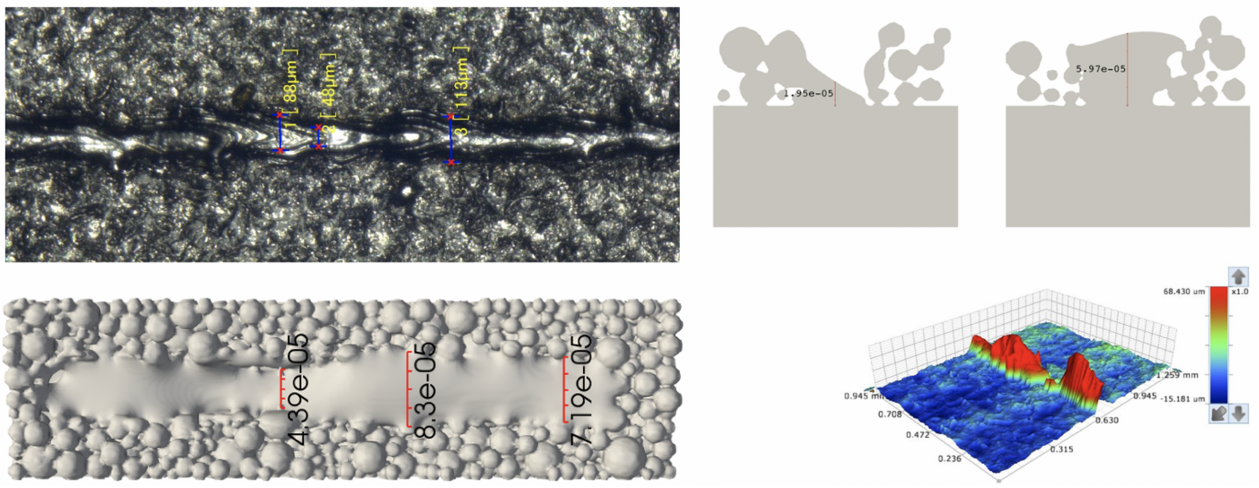

Figure 1: Validation of Melt pool dimensions with Experimental data

2.2. Importance of microstructure and porosity

The mechanical performance of a material is not simply determined by its nominal chemical composition, but perhaps more importantly by the distribution of phases and porosity throughout its crystallographic microstructure. The thermal conditions inside the solidifying melt pool are integral to the determining grain size, morphology, crystallographic texture, as well as the size, shape and distribution of porosity; all of which contribute to the mechanical fracture and fatigue properties of the final part.

Due to high thermal gradients and solidification rates, and the fact that previous layers are partially or fully remelted with every pass, a predominantly columnar microstructure is generally observed, with the crystallographic orientations being aligned with the thermal gradient during solidification. This can lead to high anisotropy in mechanical properties, as well as an elevated risk of hot cracking or tearing at the boundaries between columnar grains during solidification and subsequent cooling to room temperatures.

2.3. Grain structure prediction

Fast and efficient cellular automata-based models are used to make grain structure predictions for the as-solidified 3D microstructure, based on the thermal conditions in the melt pool during solidification.

Their defining feature is that they are semi-discrete, as each cell can exist in only one of a discrete number of states at any given moment. For solidification, these discrete states are naturally liquid and solid. To model solidification continuously, a single layer of interface cells are defined to separate regions of solid and liquid as depicted in Figure 2.

The advantage of using discrete states here is that growth is only calculated for each of the interface cells, which typically only make up a small fraction of the cells in the domain, allowing for the simulation of the nucleation and growth of a large number of individual crystals, in domain sizes up to the scale of an entire additively manufactured part.

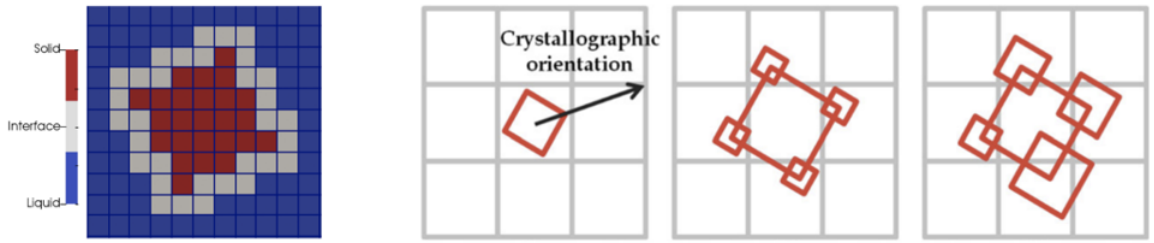

Figure 2: Cellular automata representation of the discrete states of the solidification model (left). Schematic representation of the interface propagation algorithm used [4] (right).

The driving force for solidification is considered to be thermal undercooling, i.e. the temperature difference below the liquidus. Growth velocity is proportional to the magnitude of local undercooling and is governed by the KGT dendrite tip kinetics law [4]. The propagation of the interface is managed by the decentred square algorithm [5], which takes advantage of the fact that FCC and BCC crystals grow approximately as squares in 2D and octahedra in 3D.

Grain size, morphology and orientation is intimately determined by the growth of many individual randomly orientated crystals as they compete for space in the solidifying melt pool. Grains with crystallographic orientation most closely aligned with the thermal gradient will grow preferentially, and over time will outgrow and mechanically block other grains, as well as potential nucleation sites for new grains. It is by this generative process that the columnar dominant microstructures observed in as-printed AM parts evolve. This is demonstrated in Figure 3, showing the growth of an initially completely random fine equiaxed microstructure in a thermal gradient.

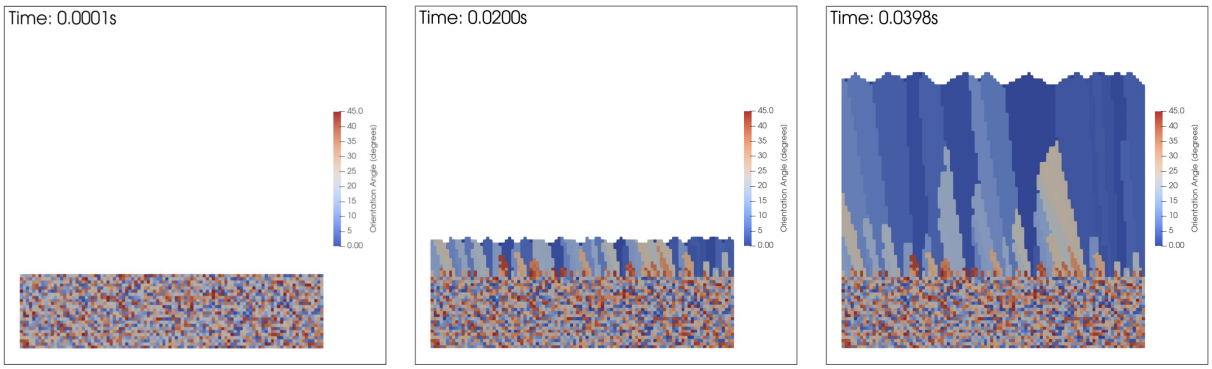

Figure 3: Evolution of a columnar microstructure during solidification in a uniform thermal gradient.The orientation of each grain in the fine equiaxed region at the base of the domain is completely random. As they grow and compete for space, grains that the most closely aligned with the direction of heat flow (*shown in blue*) will grow preferentially and prevail.

This crystallographic texture adversely affects mechanical performance, as it introduces significant anisotropy in the properties of the material. Inducing an equiaxed grain morphology is desirable for the vast majority of applications, and remains to be a considerable material engineering challenge. Models

such as these are proving to be a valuable tool for the metallurgist, as deep understanding of the relationship between processing parameters and the resulting microstructure of AM produced parts is still being developed.

2.4. Thermal stress prediction

Hot cracking and porosity are the main culprits responsible for the relatively poor fatigue performance of AM produced parts. Rapid and anisotropic thermal contraction during solidification and subsequent cooling results in regions of localised stress at grain boundaries. As the microstructure develops, pockets of liquid can become cut off from the melt pool and may no longer be sufficiently fed with liquid to account for the volumetric contraction during the liquid to solid phase transformation and further contraction as the surrounding solid cools. Modelling the pressure drop in these intergranular regions during these last stages of solidification is key to predicting the size and distribution of solidification induced porosity. This challenging problem is currently being addressed by the authors.

References

[1] J. L. Tan, C. Tang, C. H. Wong *Study and modeling of melt pool evolution in selective laser melting process of SS316L.*, MRS Communications 8, no. 3, 1178-1183, 2018.

[2] A. S. Khairallah, A. T. Anderson, A. Rubenchik, W. E. King. *Laser powder-bed fusion additive manufacturing: Physics of complex melt flow and formation mechanisms of pores, spatter, and denudation zones.*, Acta Materialia 108, 36-45, 2016.

[3] V. R. Voller, C. R. Swaminathan *ERAL Source-based method for solidification phase change.*, Numerical Heat Transfer, Part B Fundamentals 19.2, 175-189, 1991.

[4] W. I. Kurz, B. Giovanola, R. Trivedi. *Theory of microstructural development during rapid solidification.*, Acta Metallurgica 34.5, 823-830, 1986.

[5] C. A. Gandin, M. Rappaz. *A 3D cellular automaton algorithm for the prediction of dendritic grain growth.*, Acta Materialia 45.5, 2187-2195, 1997.

DATA DRIVEN MULTISCALE MODELING USING LATTICE MODEL ON THE LOWER SCALE

Eduard Marenić[1], Mijo Nikolić[2]

[1] Institut Clement Ader (ICA), Université de Toulouse, CNRS-INSA-UPS-ISAE-Mines Albi, Toulouse, France
[2] University of Split, Faculty of Civil Engineering, Architecture and Geodesy, 21000 Split, Croatia

Data driven computational mechanics (DDCM) [1] is a generalization of traditional, modeling approach, where material behavior is described with a model, $\hat{\sigma}(\varepsilon)$. The traditional approach in the computational mechanics considers the formulation of material models whose development relays on the data. Those data are usually collected either through experimental measurements (extensometry, force cells, fullfield kinematic/thermal measurements, etc.) or simulation (different methods, discretization techniques and scales can be considered). While in the 1960s the available data were sparse, at least across certain regimes, nowadays we live in the era of data generation and collection. Thus, before one needed a great deal of intuition and experience to develop a quality model from sometimes scarce input, with the goal to generalize experimental measurements made on simple test. The transition to the data rich era progressively happened in all scientific domains, and as a result we ought to deal with the big-data even in computational mechanics. On the other hand, traditional models were developed in a different context which sometimes makes them incompatible with the data rich environment, finally causing the model with it's assumed properties to downgrade the available data. In other words, traditional fitting of a model to the rich data is often ill-posed and can cause modeling errors which might severely impact the accuracy of the solution. Thus, the basic idea behind DDCM is to use the provided measurements as constitutive data (or big-data) directly in the computation, skipping entirely the modeling step and the usage of the constitutive model. DDCM, introduced in [1], is a reformulation of the boundary value problems aiming to search for the solution in the set of mechanically admissible states, A, by minimizing the distance to the material data set, D. In the classical sense, mechanically admissible state is a tuple (strain, stress) which satisfies equilibrium and kinematic relations, as well as boundary conditions. In this context, DD problem is defined with minimization:

$$\min_{\mathbf{y}\in A}\min_{\mathbf{z}\in D} d^2(\mathbf{y},\mathbf{z})$$

where d^2 is the squared distance in phase space $(\boldsymbol{\epsilon},\boldsymbol{\sigma})$, and the objective is to find admissible state $\mathbf{y}$ in A the closest to the state $\mathbf{z}$ in D. To solve DD problem a distance-based solver is introduced to iteratively minimize the distance between $\mathbf{y}$ and $\mathbf{z}$. In each iteration within a staggered solution scheme we are: a) projecting the data state to admissible set which boils down to solving two linear systems resulting from FE discretization, and b) searching the closest point in D to the previously calculated point in admissible set. From it's introduction the performance of the new 'model-free' computational paradigm was presented in statical [1, 2] and dynamical [3] context. The convergence analysis of the proposed solver is presented for the linear and non-linear [4, 5] elastic behavior. In last five years the model-free approach is emerging as an alternative to model-based computing and was extended to inelasticity [6] and fracture [7].

Current trend in engineering practice is to replace as much as possible expensive and sometimes hardly realizable experiments with virtual test. In line with this trend goes the development of the multiscale (MS) methods aiming to promote the coupling between different scales in virtual testing and increase predictiveness. One of the most developing MS strategies is based on computational homogenization [8] permitting to take into account the influence of the underlying material microstructure

explicitly in the macroscopic constitutive response through the analysis of Representative Volume Elements (RVEs). Thus, the constitutive relation at the macroscale is not a priori required, it is inferred from the RVE homogenization results. In this context one can model a complex microstructure geometry in the expense of often huge computational cost due to the need for homogenized RVE results on-the-fly in each material (integration) point and each iteration.
More importantly the absence of the constitute model on the macro scale opens the possibility to couple standard MS analysis with the previously described DD approach where the macro scale material behaviour is fed by database created from off-line RVE simulations. An example of the DD multiscale method, with nested boundary value problems treated with finite elements (FE) on both scales, is presented in [9]. However, it is possible to use distinct numerical methods for the solution of either the macro and micro-problems, see [10] for the application related to granular materials simulated with discrete element method.

In this work we explore the possibility of using lattice model [11, 12] on the RVE (micro) scale. In the first place is the problem of generating the data set that will be used for the subsequent data driven predictions with the material data being extracted from lower-scale, lattice simulations. The DD prediction depends entirely on the material data base and it's quality. We focus here firstly on the off-line sampling targeting to generate data base which is sufficient for the chosen examples. More precisely, we impose on the lattice RVE deformational component of the local state and by running an equilibrium RVE simulation we seek a work conjugate, that is, homogenized local stress. In this context, we discuss the optimal sampling of the input strain.

Acknowledgement This work has been supported through the project 'Parameter estimation framework for fracture propagation problems under extreme mechanical loads' (UIP-2020-02-6693), funded by the Croatian Science Foundation.

References

[1] T. Kirchdoerfer and M. Ortiz. Data-driven computational mechanics. *Computer Methods in Applied Mechanics and Engineering*, 304:81–101, June 2016.

[2] Trenton Kirchdoerfer and Michael Ortiz. Data Driven Computing with Noisy Material Data Sets. *Computer Methods in Applied Mechanics and Engineering*, 326:622–641, November 2017.

[3] T. Kirchdoerfer and M. Ortiz. Data-driven computing in dynamics: Data-driven computing in dynamics. *Int. J. Numer. Meth. Engng*, 113(11):1697–1710, March 2018.

[4] Lu Trong Khiem Nguyen and Marc-André Keip. A data-driven approach to nonlinear elasticity. *Computers & Structures*, 194:97–115, January 2018.

[5] S. Conti, S. Müller, and M. Ortiz. Data-Driven Problems in Elasticity. *Arch Rational Mech Anal*, 229(1):79–123, July 2018.

[6] R. Eggersmann, T. Kirchdoerfer, S. Reese, L. Stainier, and M. Ortiz. Model-Free Data-Driven inelasticity. *Computer Methods in Applied Mechanics and Engineering*, 350:81–99, June 2019.

[7] P. Carrara, L. De Lorenzis, L. Stainier, and M. Ortiz. Data-driven fracture mechanics. *Computer Methods in Applied Mechanics and Engineering*, 372:113390, December 2020.

[8] V. Kouznetsova, W. A. M. Brekelmans, and F. P. T. Baaijens. An approach to micro-macro modeling of heterogeneous materials. *Computational Mechanics*, 27(1):37–48, January 2001.

[9] Rui Xu, Jie Yang, Wei Yan, Qun Huang, Gaetano Giunta, Salim Belouettar, Hamid Zahrouni, Tarak Ben Zineb, and Heng Hu. Data-driven multiscale finite element method: From concurrence to separation. *Computer Methods in Applied Mechanics and Engineering*, 363:112893, May 2020.

[10] K. Karapiperis, L. Stainier, M. Ortiz, and J.E. Andrade. Data-Driven multiscale modeling in mechanics. *Journal of the Mechanics and Physics of Solids*, 147:104239, February 2021.

[11] M. Nikolic, A. Ibrahimbegovic, and P. Miscevic. Brittle and ductile failure of rocks: Embedded discontinuity approach for representing mode I and mode II failure mechanisms. *Int. J. Numer. Meth. Engng*, 102(8):1507–1526, May 2015.

[12] M. Nikolić, E. Karavelić, A. Ibrahimbegovic, and P. Miščević. Lattice Element Models and Their Peculiarities. *Archives of Computational Methods in Engineering*, 25(3):753–784, July 2018.

STOCHASTIC IDENTIFICATION OF DAM OVERLOAD BY BAYESIAN INFERENCE IN A NUMERICAL MODEL OF ACOUSTIC DAM-RESERVOIR INTERACTION

Emina Hadzalic [1], Emir Karavelic [1], Adnan Ibrahimbegovic [2,3] Samir Dolarevic [1]

[1] Faculty of Civil Engineering, University of Sarajevo, Bosnia and Herzegovina,
emina.hadzalic@gf.unsa.ba, emir.karavelic@gf.unsa.ba, samir.dolarevic@gf.unsa.ba
[2] Université de Technologie de Compiègne, Laboratoire Roberval de Mécanique, France,
adnan.ibrahimbegovic@utc.fr
[3] Institut Universitaire de France, France

INTRODUCTION

The current state of a dam structure and the potential risk of a failure are mainly investigated using numerical models and numerical simulations. To more precisely determine the overall safety of the dam structure the variability of the parameters has to be taken into account, whether it results from the construction process itself or is due to long-term degradation of the structure. This suggests that the probability based methods should be used in combination with numerical models.

In this paper, we use Bayesian inference in numerical model of acoustic dam-reservoir interaction in order to identify the dam overload and thus determine the overall safety of the dam structure against failure.

The numerical model of dam-reservoir interaction is presented in [1, 2]. The main feature of the model is the representation of the structure in terms of the saturated poro-plastic media. The structure response is modeled with coupled discrete beam lattice model, which implements Biot's porous media theory. The external fluid motion is modeled with acoustic wave theory and mixed displacement/pressure based finite element approximation. The selected approximations for the structure response and the external fluid motion feature both displacement and pressure degrees of freedom, which allows for the issue of the fluid-structure interface to be solved directly through finite element assembly procedure.

In this work we focus in particular upon uncertainty propagation that allows connecting the inelasticity at multiple scales, starting from the fine scale (here meso-scale model) where the heterogeneous composite failure mechanisms and the variability of model parameters can be captured much better by corresponding representation of different phases. The main goal is to provide the corresponding macro-scale reduced model, which can significantly increase the computational efficiency and render the analysis of complex structures feasible (such as dam structure). Two different methods for Bayesian inference have been tested and compared in the proposed approach, both based upon the Bayes theorem that allows incorporating new information generated in a particular loading program. Each unknown parameter of reduced model is modeled as a random variable (which can also be high-dimensional). Such description has two constituents, the measurable function and the measure. One method, Markov Chain Monte Carlo (MCMC), is identified as updating the measure, whereas the other method, Polynomial Chaos Expansion Kalman Filter (PceKF), changes the measurable function [3].

FINITE ELEMENT FORMULATION OF NUMERICAL MODEL

Structure built of saturated poro-plastic media

The proposed coupled discrete beam lattice model is based on Voronoi cell representation of the domain with inelastic Timoshenko beam finite elements enhanced with additional kinematics in terms of embedded strong discontinuities in axial and transverse directions as cohesive links, which allows to model crack formation and localized failure in the structures. The internal coupling, i.e., the copling

between the solid phase and the pore fluid is handled with Biot's porous media theory. The numerical implementation of the internal coupling results with an additional pore pressure degree of freedom placed at each node of the Timoshenko beam.

The strong form of equilibrium equation is written as

$$\frac{dN}{dx}+n(x)=0; \quad \frac{dV}{dx}+q(x)=0 \quad \frac{dM}{dx}+V+m(x)=0 \tag{1}$$

where n, q, and m are the distributed external loads, $N=N'-bpA^e$ is the axial force, $V=V'$ is the shear force, and $M=M'$ is the bending moments, A^e is the area of a cross section, p is the pore pressure and b is Biot's constant. Following Terzaghi's principle of effective stresses, the superscript $'$ denotes effective force.

The strong form of continuity equation is written as

$$\frac{1}{M}\dot{p}+b\nabla\cdot\dot{u}-\nabla\cdot\left(\frac{k}{\gamma_f}\nabla p\right)=0 \tag{2}$$

where M is Biot's modulus, u is the axial displacement of the solid phase, k is the coefficient of permeability of isotropic porous media, and γ_f is the specific weight of the pore fluid.

External fluid motion

The small and irrotational motion of external fluid is modeled with acoustic wave theory and mixed displacement/pressure finite element formulation. The strong form of governing equations is written as [4]

$$\nabla p+\nabla\times\mathbf{\Lambda}-\mathbf{f}^b=0; \quad \nabla\cdot\mathbf{u}+\frac{p}{\beta}=0; \quad \nabla\times\mathbf{u}-\frac{\mathbf{\Lambda}}{\vartheta}=0 \tag{3}$$

where p is the pressure, $\mathbf{u}$ is the displacement vector, $\mathbf{\Lambda}$ is the 'vorticity moment' and ϑ is the penalty parameter. The parameter β is the bulk modulus of the external fluid, and $\mathbf{f}^b$ is the external load vector.

Acknowledgements: This work was supported by project funded by FMON - Federal Ministry of Education and Science of Bosnia and Herzegovina. This support is gratefully acknowledged.

References

[1] E.Hadzalic, A.Ibrahimbegovic, S. Dolarevic. *Fluid-structure interaction system predicting both internal pore pressure and outside hydrodynamic pressure*, Coupled Systems Mechanics, 7(6):649-668, 2018.

[2] E.Hadzalic, A.Ibrahimbegovic, S. Dolarevic. *Theoretical formulation and seamless discrete approximation for localized failure of saturated poro-plastic structure interacting with reservoir*, Computers & Structure, 214:73-93, 2019.

[3] A. Ibrahimbegovic, H.G. Matthies, E. Karavelic *Reduced model of macro-scale stochastic plasticity identification by Bayesian inference in application to quasi-brittle failure of concrete*, Comp. Methods Appl. Mech. Eng., doi.org/10.1016/j.cma.2020.113428, 2020

[4] KJ.Bathe, C.Nitikitpaiboon, X.Wang. *A mixed displacement-based finite element formulation for acoustic fluid-structure interaction*, Computers & Structures, 56(2-3):225-237, 1995.

ECCOMAS MSF 2021 THEMATIC CONFERENCE
30 June – 2 JULY 2021, SPLIT, CROATIA

APPLICATION OF COMET SOFTWARE IN DEFINING YIELD OF GROUNDWATER

Emina Hadžić [1], Hata Milišić [2], Suvada Šuvalija[3]

[1] Faculty of Civil Engineering, University of Sarajevo, eminahd@gmail.com
[2] Faculty of Civil Engineering, University of Sarajevo, hata.milisic@gmail.com
[3] Faculty of Civil Engineering, University of Sarajevo, suvadasuvalija69@gmail.com

Abstract

A problem that often occurs due to long-term and unplanned use of groundwater is excessive exploitation, ie exploitation that is greater than naturally renewable quantities. The consequences of this can sometimes be catastrophic, not only due to the constant lowering of groundwater levels, depletion of static reserves, but can also significantly reflect on the degradation of groundwater quality. It should be taken into account that the quantities of water captured cannot be equated with the yield of water intake facilities (eg wells), nor can they be viewed as values that are constant over time. Other very important factors should be considered when defining the maximum exploitation quantities from groundwater sources. These factors depend on the filtration stability of the sub-well zone [1], natural characteristics of aquifers, the way of water source management, providing sufficient water retention time, preservation of quality characteristics of water sources and the like, ie the task should be approached holistically. According to its physical essence, the maximum yield of a spring can be viewed as the amount of water that is renewed, ie the flow rate of water, which depends on the recharge of the groundwater source, [2].

In this regard, defining the maximum amounts of water that can be taken from a source is a very complex task. There are several approaches to solving such tasks. With the development of computer technology, the application of numerical methods for solving basic equations is becoming more common. The advantage of their use is most simply manifested through the possibility of relatively easy implementation of many hydrodynamic calculations of groundwater flow, simulation of different exploitation schemes, forecasting their effects on the groundwater source, and helps define optimal amounts of water from a groundwater source, for given input data and criteria, in the analyzed period.

In this paper, an analysis and reinterpretation of previous research in the wider area of the Sokolovići groundwater source is made, which provided the initial, necessary data and information for the application of the mathematical model. The modeling process began with the formation of a conceptual model, which represents a schematization of the space in which the groundwater flow takes place, as well as the conditions prevailing inside or in the environment, and their characteristics, [3]. As is known, the mathematical model implies the basic differential equation of groundwater flow (Boussinesq's equation), initial and boundary conditions. Since this is a more complex conceptual model, which cannot be solved directly, it is necessary to use numerical methods, ie computer programs. Most computer programs for groundwater modeling are based on one of the numerical methods for solving complex mathematical equations. The paper presents the solution of the Boussinesq equation by the finite volume

(MKV) method. The computer program Comet was used, [4]. Comet[1] is a multi-purpose CCM software written in ANSI standard C and ANSI FORTRAN 77, the Linux operating system, and is used to solve problems of continuum mechanics (liquids and solids). The software package is written in a modular form, with the possibility of further development and improvement.
By applying the finite volume method for groundwater flow in quasi-stationary conditions, different exploitation quantities from the Sokolovići spring were simulated with the aim of determining the main feeding directions, as well as the quantities flowing from the model boundaries for the given conditions. In order to define the optimal amounts of water (optimal yield) that can be taken from a source, there are other limiting factors that result from: well catchment capacity, filtration stability of the well zone, aquifer characteristics, as well as control constraints caused by human factors. Combining the results obtained by applying mathematical modeling and hydraulic-hydrological analyzes, the paper performed a multi-criteria optimization that served to define the optimal amounts of water that can be captured from groundwater sources in Sokolovići, for the given initial and boundary conditions.

Key words: groundwater, modeling, COMET, optimization

References

[1] Pušić. M, *Dinamika podzemnih voda,* Book ISBN 86-80887-78-1, Univerzitet u Beogradu Građevinski fakultet, Beograd, 2000.
[2] Hadžić, E, *Osnovi zaštite podzemnih voda u granularnim sredinama*, Book ISBN 978-9958-638-39-8, Građevinski fakultet Univerziteta u Sarajevu, Sarajevo, 2013
[3] Hadžić, E, *Prilog optimizaciji eksploatacionih količina izvorišta Sokolovići*, Građevinski fakultet Sarajevo, Magistarski rad, 2001.
[4] Demirdžić, I:, Muzaferija, i.: *Introduction to Computational Fluid Dynamics*, University of Sarajevo, Sarajevo, 1997.

[1] Comet, CCM software, Produced and distributed first by ICCM Institute for Computational Continuum Mechanics, (since 1997) and by CD adapco Group (from 2001), www.cd-adapco.com

ECCOMAS MSF 2021 THEMATIC CONFERENCE
30 June – 2 JULY 2021, SPLIT, CROATIA

DEVELOPMENT OF FLOOD HAZARD AND RISK MAPS IN BOSNIA AND HERZEGOVINA, KEY STUDY RIVER ZUJEVINA

Emina Hadžić [1], Giuseppe TITO Aronica[2], Hata Milišić [3], Suvada Šuvalija[4] , Suada Džebo[5], Ammar Šarić[6]

[1] Faculty of Civil Engineering, University of Sarajevo, eminahd@mail.com
[2] University of Messina - Department of Engineering, Italy, giuseppetito.aronica@unime.it
3 Faculty of Civil Engineering, University of Sarajevo, hata.milisic@gmail.com
[4] Faculty of Civil Engineering, University of Sarajevo, suvadasuvalija69@gmail.com
[5] Faculty of Civil Engineering, University of Sarajevo, suada.dzebo.gf@gmail.com
[6] Faculty of Civil Engineering, University of Sarajevo, ammarsaric@yahoo.mail

Abstract

Floods represent extreme hydrological phenomena that affect populations, social and ecological systems. After the catastrophic floods that hit Europe and the World in recent decades, the flood problem has become more current, [1]. At EU level, a legal framework has been put in place with the entry into force of Directive 2007/60 / EC on Flood Risk Assessment and Management (Flood Directive). Two years after the entry into force of the Flood Directive, Bosnia and Herzegovina adopted a Regulation on the types and contents of plans for the protection against harmful effects of water, through which key steps and activities from the Flood Directive were taken.
Accordingly, activities for the preparation of the Flood Risk Assessment Preliminary for each river basin district were completed in 2015 for the territory of Bosnia and Herzegovina. Activities are underway to develop a Hazard Map and a Flood Risk Map. In the next phase of implementation of the Flood Directive - the phase of development of the Flood Risk Management Plans, the results of model predictions of possible climate change risk increase should be included, [2].
"Methodology for the development of flood risk and hazard maps" (Methodology) for the territory of Bosnia and Herzegovina has been developed, which is in line with the Methodologies used in most EU Member States, but with some adjustments in accordance with the specificities of Bosnia and Herzegovina, [3].
In accordance with the foregoing, the paper will give an example of the development of the hydrodynamic model of the Zujevina River, as well as the development of risk maps. Flood risk maps will be provided for medium probability floods (100-year return period) and high probability floods (20-year return period). Particular attention will be given to explaining the Methodology used in Bosnia and Herzegovina.

Accordingly, in this article, new flood hazard and risk maps were developed using the results of field research obtained by the LiDAR technique, for a part of the Zujevina river. It was observed that there are large differences in the obtained flood maps compared to the old ones obtained using georeferenced topographic maps.

Key words: flood risk, GIS, HecRAS

References

[1] Imamović. A, Uz*roci poplava u slivu rijeke bosne s osvrtom na poplave u maju 2014. ANUBiH, Konferencija, Sarajevo, 2015.*
[2] Hadžić, E, Bonacci, O. *Okolišno prihvatljivo upravljanje vodotocima*, Knjiga, Građevinski fakultet Univerziteta u Sarasjevu, 2019.
[3] Jabučar, D, Lukavac, N. *Implementacija EU Direktive o poplavama u BiH, . ANUBiH, Konferencija, Sarajevo, 2015.*

IDENTIFICATION BY BAYESIAN INFERENCE OF STOCHASTIC PLASTICITY MACRO-SCALE MODEL

Emir Karavelic [1], Emina Hadzalic [1], Adnan Ibrahimbegovic [2,3]

[1] Faculty of Civil Engineering, University of Sarajevo, Bosnia and Herzegovina,
emir.karavelic@gf.unsa.ba, emina.hadzalic@gf.unsa.ba
[2] Université de Technologie de Compiègne, Laboratoire Roberval de Mécanique, France,
adnan.ibrahimbegovic@utc.fr
[3] Institut Universitaire de France, France

INTRODUCTION

Of special interest for this work are stochastic models that can capture localized failure sensitivity to initial and induced defects for structures built of heterogeneous composite material, such as concrete. The potential scientific gain provided by such models is in better prediction of crack spacing and opening, which can be used to improve concrete durability. The latter is of direct benefit and interest for many industrial applications, given that concrete is probably the most used material in construction and that many such structures are rapidly aging. From standpoint of constructing predictive stochastic plasticity fracture models, this kind of composite material has rather favorable features with: two-phase meso-structure (aggregate vs. cement), non-local dimension brought by typical fracture modes of massive structures with significant contribution of fracture process zone (FPZ), and fabrication that is comparable to large-scale additive-manufacturing, where the complete structure is cast with the same material rather than an assembly of various components. The latter is the crucial hypothesis that can render the proposed macro-scale stochastic plasticity model feasible in terms of predicting probability-distribution-based estimates of structure properties. The main novelty is seen in the fact that all scales are to be treated probabilistically, and not only capturing the average response on the larger scale. This is particularly important for testing of heterogeneous cement-based composites, where the scales in test specimen are in general not well separated. Such is the case when testing reduced size specimen with respect to meso-structure heterogeneities, where significant variability occurs in the test results due to small-scale uncertainty. Yet more important for these quasi-brittle composite materials is fracture sensitivity to small-scale defects that trigger crack coalescence and accelerates structure failures. This is especially visible under non-proportional loading, where only fine-scale models representing material heterogeneities can provide sufficiently predictive results, whereas those based upon homogenization, employing average properties, typically fail predictions in the tests where several failure mechanisms are active. In this work we focus in particular upon uncertainty propagation that allows connecting the inelasticity at multiple scales, starting from the fine scale (here meso-scale for concrete) where the heterogeneous composite failure mechanisms and the variability of model parameters can be captured much better by corresponding representation of different phases (here aggregate versus cement paste)[1]. The main goal is to provide the corresponding macro-scale reduced model, which can significantly increase the computational efficiency and render the analysis of complex structures feasible. The proposed approach can be considered as a part of a scale-coarsening strategy, but much different from ad-hoc choices. Namely, once the crack pattern at meso-scale has stabilized, we will use an efficient Bayesian updating, replacing subsequently meso-scale by macro-scale generalized ED-FEM element with parameters/arrays as random variables (RV) or random fields (RF). The probability distribution of such random field will be computed separately between microstructure variability and loading program variability, which allows to capture the influence of both initial and induced defects. With such an approach we can recover a re-

duced model that defines probability distribution of fracture parameters describing localized failure with both volume and surface dissipation [2]. Two different methods for Bayesian inference have been tested and compared in the proposed approach, both based upon the Bayes theorem that allows incorporating new information generated in a particular loading program. Each unknown parameter of reduced model is modeled as a random variable (which can also be high-dimensional). Such description has two constituents, the measurable function and the measure. One method, Markov Chain Monte Carlo (MCMC), is identified as updating the measure, whereas the other method, Polynomial Chaos Expansion Kalman Filter (PceKF), changes the measurable function [**?**, 4]. We formulate both methods as functional approximation of stochastic problems, and introduce especially in combination with the second method a new procedure which does not need any sampling, hence works with subsequent update in deterministic manneer. It also seems to be the fastest and more reliable when compared with other methods. We show by example that it also works for highly nonlinear non-smooth problems with non-Gaussian measures.

Acknowledgements: This work was supported by project funded by FMON-Federal Ministry of Education and Science of Bosnia and Herzegovina. This support is gratefully acknowledged.

References

[1] Karavelic E, Nikolic M, Ibrahimbegovic A and Kurtovic A *Concrete meso-scale model with full set of 3D failure modes with random distribution of aggregate and cement phase. Part I: Formulation and numerical implementation* Comp. Methods Appl. Mech. Eng. 344, 1051-1072, 2019

[2] Karavelic E, Ibrahimbegovic A and Dolarevic S, *Multi-surface plasticity model for concrete with 3D hardening/softening failure modes for tension, compression and shear*, Computers and Structures, 221, 74-90, 2019

[3] A. Ibrahimbegovic, H.G. Matthies, E. Karavelic *Reduced model of macro-scale stochastic plasticity identification by Bayesian inference in application to quasi-brittle failure of concrete*, Comp. Methods Appl. Mech. Eng., doi.org/10.1016/j.cma.2020.113428, 2020

[4] Ibrahimbegovic A *Nonlinear Solid Mechanics: Theoretical Formulations and Finite Element Solution Methods*,London - Springer.

ECCOMAS MSF 2021 THEMATIC CONFERENCE
30 June – 2 JULY 2021, SPLIT, CROATIA

SHAKE TABLE TESTS OF PUFJ AND FRPU EARTHQUAKE PROTECTED STRUCTURES

Filip Manojlovski[1], Arkadiusz Kwiecień[2], Antonio Shoklarovski[3], Angela Poposka[4], Zoran Rakicevic[5], Aleksandra Bogdanovic[6], Theodoros Rousakis[7], Alper Ilki[8], Matja Gams[9], Alberto Viskovic[10]

[1] Institute of earthquake engineering and engineering seismology, Skopje, R.N. Macedonia filipmanojlovski@iziis.ukim.edu.mk
[2] Cracow University of Technology, Poland, akwiecie@pk.edu.pl
[3] Institute of earthquake engineering and engineering seismology, Skopje, R.N. Macedonia antonio@iziis.ukim.edu.mk
[4] Institute of earthquake engineering and engineering seismology, Skopje, R.N. Macedonia angela@iziis.ukim.edu.mk
[5] Institute of earthquake engineering and engineering seismology, Skopje, R.N. Macedonia zoran_r@iziis.ukim.edu.mk
[6] Institute of earthquake engineering and engineering seismology, Skopje, R.N. Macedonia saska@iziis.ukim.edu.mk
[7] Democritus University of Thrace, Greece trousak@civil.duth.gr
[8] Istanbul Technical University, Turkey, ailki@itu.edu.tr
[9] University of Ljubljana, Slovenia, matija.gams@fgg.uni-lj.si
[10] G. D'Annunzio University of Chieti – Pescara, Italy, a.viskovic@unich.it

The flexible and ductile structures can sustain severe earthquakes and large displacements by their ability to dissipate the input earthquake energy. On the other hand, the brittle components such as masonry infills may suffer from the excessive drifts and experience significant in or out of plane damage. To get better insight of the behavior and to validate a new flexible RC-infill joint protection strategy, shake table tests of three-dimensional model have been performed in the framework of INMASPOL SERA Horizon 2020 project.

This paper presents the testing procedure and results from the experimental shake table tests of three-dimensional reinforced concrete structure with brick walls as infills as well as the innovative protection using flexible polyurethane resin joints (PUFJ) at the concrete-infill interface. Also, when noticeable damage occurred, PUs were used to bond the glass fiber grids to the weaken masonry to form Fiber Reinforced PU (FRPU) as emergency repair. The results from seismic excitations are presented in form of time history plots for the accelerations and displacements whereas the results from ambient vibrations measurements are presented in frequency domain.

The innovative protection solution proved to be efficient and promising for further development and implementation in structures built in earthquake prone areas.

Keywords: shake table, experimental testing, polyurethane, RC, masonry

MODELLING OF FREE RADICAL POLYMERIZATION DURING VAT PHOTO-POLYMERIZATION MASK PROJECTION PROCESS

Filip Volarić [1], Philip Cardiff [2], Alojz Ivanković [2]

[1] I-Form & University College Dublin, School of Mechanical and Materials Engineering ,filip.volaric@i-form.ie
[2] University College Dublin, School of Mechanical and Materials Engineering

Despite the growth of Additive Manufacturing (AM) in recent years, correlation between process parameters and mechanical properties is still not fully understood. One of the widely used AM techniques is mask projection Vat Photopolymerization (VPP), commonly also known as Digital Light Projection (DLP). In the VPP process UV light reflects off a Digital Micromirror Device (DMD) triggering a complex chemical reaction called photopolymerization which rapidly converts liquid monomer to solid polymer [1,2]. During photopolymerization reaction active radicals, which are created by the decomposition of a photoinitiator, attach to monomers to start propagation of polymer chains. Growth of the polymer chain network causes the change of microstructural properties like molecular weight, polymer chain length and crosslink density. These changes of microstructure affect macroscopic properties such as Young's Modulus, relaxation time, glass transition temperature and volume shrinkage [2]. To predict the behaviour of additively manufactured parts it is necessary to model the kinetics of the chemical reactions. The current project is focussed on the development of an OpenFOAM based mechanistic model to simulate reaction kinetics.
The mechanistic model adopted in this work solves the first-order differential equations to evaluate the concentration of individual species, including photoinitiators, free radicals, oxygen and monomers. The rates are a function of reactant concentrations, reaction constants and reaction conditions. It is important to state that the implemented model includes a diffusion-controlled termination rate [2]. Figure 1 shows excellent agreement between the implemented model and data obtained from the literature.

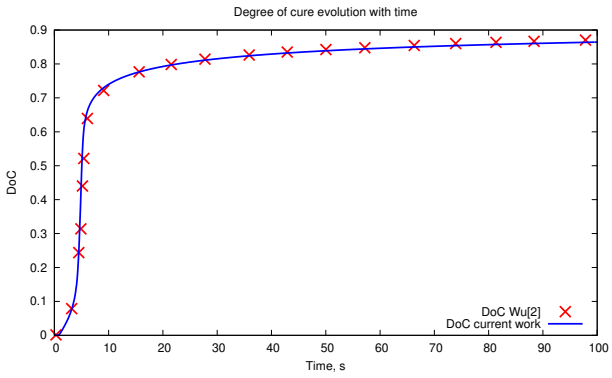

Figure 1: Validation of reaction kinetics model (DoC - Degree of cure)

The previously mentioned reaction kinetics model was implemented and used in the simulation of the VPP process. The VPP simulation mimics the recently observed columnar structure of the cured part. The columnar structure is created due to the geometry of the DMD device. To control which pixel is cured, micromirrors in the DMD device can reflect the light away from the resin but to do so they are

separated by thin gaps. These gaps create semi-cured areas in between cured columns as it can be seen in Figure 2a. It shows the simulation of the VPP process for a simple rectangular bar. Figure 2a was taken after the twentieth layer was cured. Each layer is 50 μm thick and irradiated for 5 seconds. Figure 2b shows the cross-sectional degree of cure distribution for the first layer after the twentieth layer was added. Figure 2b shows that a degree of cure drops by 10% in the semi-cured regions for the simulated resin formulation.

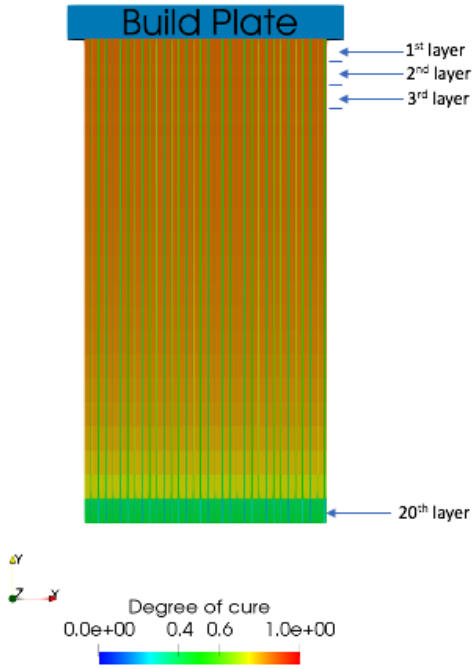

a) VPP simulation

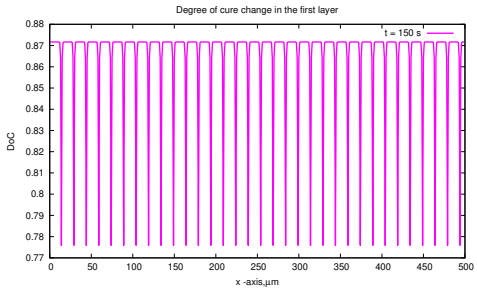

b) Cross-sectional distribution of degree of cure for the first layer

Figure 2: Initial result of the VPP process model

Acknowledgments

Financial support is gratefully acknowledged from I-Form Advanced Manufacturing Research Centre, funded by Science Foundation Ireland (SFI) Grant Number 16/RC/3872, co-funded under European Regional Development Fund and I-Form industry partners. Additionally, the authors wish to acknowledge the DJEI/DES/SFI/HEA Irish Centre for High-End Computing (ICHEC) for the provision of computational facilities and support (www.ichec.ie).

References

[1] I. Gibson, D. Rosen, B. Stucker *Additive manufacturing technologies: 3D printing, rapid prototyping, and direct digital manufacturing, second edition*, 2015.

[2] J. Wu, T. Author *Constitutive Modeling of Photopolymerization and Its Application To 3D Printing,*, PhD Thesis, 2018.

SOME ASPECTS OF THE ANALYSES OF GLASS STRUCTURES EXPOSED TO IMPACT LOAD

Gabrijela Grozdanić[1], Mirela Galić[1], Pavao Marović[1]

[1] University of Split, Faculty of Civil Engineering, Architecture and Geodesy,
gabrijela.grozdanic@gradst.hr; mirela.galic@gradst.hr; pavao.marovic@gradst.hr

As one of the most attractive materials of the modern age, glass has become an irreplaceable element of structures. To be able to respond to the structural challenges, it has become the subject of many researches, especially those in which the behavior of glass elements exposed to different types of loads is analyzed. This paper will present some of the aspects in structural analyses of glass upon impact loads. For a good analysis of glass response, it is important to be acquainted with the production process. The majority of today's flat glass is produced by the Float process. The most used type of glass is soda-lime glass composed of SiO_2 – Na_2O – CaO (with additional ingredients). It can be used without any additional treatment if there is no demand for increased strength and safety. Considering part of Float process in which heated glass is slowly cooled to release residual stresses, untreated glass is called annealed glass. Basic mechanical properties of glass are shown in Table 1.

Properties	Middle value	Interval
Density	ρ = 2.500 kg/m³	2.250 – 2.750 kg/m³
Young's modulus	E = 70.000 MPa	63.000 MPa – 77.000 MPa
Poisson number	μ = 0,22	0,20 - 0,25

Table 1. Basic mechanical properties of glass according to prEN 13474 [1]

It is very important to point out that glass is eco-friendly, recyclable material. It can be melted over numerous times and reused to produce new glass products. Compared with other building materials it does not lose its properties when reprocessed. By combining different additional elements it is possible to affect some glass properties, such as heat resistance, colour, etc. Apart from adding elements to chemical structure, there are treatments that improve glass mechanical properties. When focusing on the safety and strength of glass elements it is important to mention tempering. Tempered glass is a glass of increased strength with the ability of safe breakage, meaning the glass will not break into sharp and heavy pieces that can cause injury. Tempering can be produced by chemical treatment or by heating and fast cooling. The final effect of both processes is developing compression on the surface and tension inside, resulting in increased tensile strength of glass element. The most obvious difference between annealed and tempered glass is in their breakage pattern (Figure 1). Heat strengthened glass is tempered glass exposed to slower cooling, consequently producing lower stress on surface and inside the glass.

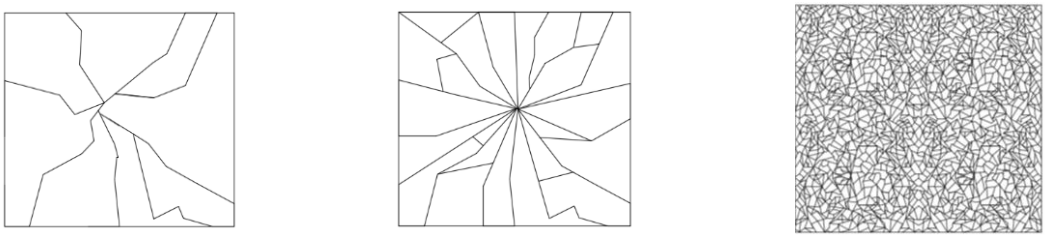

Annealed glass / float glass Heat strengthened glass Thermally toughened glass

Figure 1. Breakage pattern for different types of glass

Most types of glass can be involved in the process called lamination. Laminated glass is made of at least two glass sheets connected with an interlayer. Interlayer ensures integrity after breakage and in case of the unbroken sheet it provides post-breakage capacity. Glass as a structural material (primary or secondary) ought to sustain different types of actions. Due to its brittle nature, elements are usually designed to be robust. Lack of post-failure behavior is replaced by additional substructure elements or improvements within glass elements (as laminated glass). Glass behavior under static load is linear-elastic until failure, where it breaks without any plastic deformation. Griffith [2] developed a well-known theory of surface flaws, asserting that glass surface is not perfectly smooth but it contains small flaws invisible to the naked eye but of great importance to the material strength. In further observation, to avoid the problem of infinite stress at the peak of the sharp flaw from linear elastic theory, Griffith used a reversible thermodynamic system to model a static crack. Using the theorem of minimum energy and adding an increase in potential energy, caused by work from destroying cohesive forces in crack formation, Griffith describes energy balanced concept. Further, critical stress related to critical crack length is defined. Equation (1) defines the relation between crack length and critical stress describing at what stress the propagation will occur for defined crack length a_c:

$$\sigma_f = \sqrt{\frac{2 \cdot E \cdot \gamma}{\pi \cdot a_c}} \tag{1}$$

Griffith's equation accurately defines only the behavior of brittle materials. Following Griffith's work, Irwin defined a new fracture criterion. The criterion is based on a stress intensity factor K_1 and a comparison with the value of critical stress intensity factor K_{Ic} (fracture toughness) which is a property of the material [3]:

$$K_1 \geq K_{1c} \tag{2}$$

Known theories [2, 3 and 4] are only the basic starting points in the analyses of glass structures exposed to impact load, which demand definitions of certain coefficients and design guidelines for better simulations for these kinds of loads.

It could be said that regulations in Europe are late behind architecture and construction works with glass. European draft standard prEN 13474 [1] was released in 2009. In 2014 the Guidance for European Structural Design of Glass Components [5] was released as a second draft edition for future Eurocode. The guidance contains basic information about material properties, products made of glass, and the basis for the design. Impact load, as one of the most common dynamic loads, tends to cause great damage in brittle materials. Current regulations do not provide enough information to determine the resistance of glass elements on different types of impact loading. According to regulations [5] impact loading classification is divided into hard body and soft body impact. The division is characteristic for glass because of its unfavourable effects in contact with other hard substances with hardness greater than the glass [5].

EN 356:1999 (HRN EN 356:2006) [6] is a norm that defines experimental test as hard body impact with steel sphere. The test is developed for the classification of security glazing products. EN 12600:2002 (HRN EN 12600:2006) [7] is a norm that provides a classification for impact resistance of glass panels exposed to pendulum impact (soft body impact). Classification is defined by determination of glass damage at defined drop height. In Guidance [5] requirements for improving and developing regulations related to glass floors and horizontal glazing accessible for maintenance are described. Demand is to specify verification for static and dynamic load and post-failure resistance. Post failure resistance is an important demand in floor structures made of glass, and therefore it is forbidden to use only tempered glass in most national regulations. Also, glass barriers and glass parapets are described and the suggestion is to provide classification according to bearing type. From the aspect of dynamic impact load the Guidance [5] suggests the norm EN 12600:2002 (HRN EN 12600:2006) [7] as an experimental test remarking that larger panels, different substructure stiffness, and support characteristics are not taken into consideration. Besides experimental verification, Guidance [5] is describing two dynamic calculations. Method 1 uses transient numerical methods to define stress evolution in the glass panel, while Method 2 uses equivalent loads defined through a double mass

oscillator. Both methods are considering impact energy E=100 Nm which is developed from a body mass of 80 kg at impact speed v=2.04 m/s with 60% resonance mass [5].

Simulating fracture and fragmentation of brittle material is a great challenge for researchers. Today there are different computational methods developed to accurately simulate the breakage and fragmentation of brittle material. Depending on the stress condition inside the glass panel different types of breakage patterns are achieved, each of them appropriate for different use. Modelling those types of fragmentation can be provided with numerical programs that are based on continuum or discontinuum methods. Wang et al. [8] made a comparison study of four methods encompassing continuum methods FEM and XFEM, and discontinuum based methods DEM and FEM/DEM. Models are focused on the simulation of dynamic fracture for glass beam exposed to low-velocity hard body impact. FEM analysis uses smeared model for simulating discontinuous cracking failure with crack initiation according to Rankine theory. It considers only Mode 1 for crack initiation but adopts Mode 1 and Mode 2 for crack propagation. XFEM is using phantom nodes and linear elastic fracture mechanics with additional functions. Phantom nodes use overlapping elements to bridge discontinuity and to avoid introducing additional unknowns [8]. DEM discretizes the observed domain in a large number of elements connected with the boundaries. Those numerous particles act like individuals when force is applied, producing realistic simulations for progressive fracturing of brittle materials. FEM/DEM is using the same crack initiation criteria and critical energy release as FEM. To model Mode 1 behavior, stress - displacement curve is used. In the strain-softening interval, the softening function is used to describe a decrease in bond stress, zero occurs at the point where the crack is initiated. The softening function is defined with the constants determined from the experimental results of the observed material. Shear behavior is also calculated using a softening function and penalty function method [8]. By comparing four described methods Wang et al. [8] found that FEM/DEM is the most accurate method for predicting the real behavior of glass under different types of low-velocity impact. XFEM results differ most in the manner of fragmentation.

Defining behavior and energy release in pendulum test is a step to better understanding glass behavior under the soft impact. Lately, many researchers work on a numerical solution for this type of loading, so that expensive experimental tests and geometry limitations could be avoided. Pacios et al. [9] performed an experimental pendulum test, on specimens made of tempered glass and annealed laminated glass, with varying different types of support and different drop heights. The conclusion was that type of support is of great influence on the dynamic response of the glass panel. Referring to DIN 18008, EN 12600:2002 (HRN EN 12600:2006) [7], and Pacios [9] experiment, Parra et al. [10] analyze the real amount of load that is transferred from pendulum to panel. They observed a difference between the initial energy of pendulum (for drop height) and load applied to the glass plate. It is assumed that energy dissipation occurs during the contact of pendulum and glass panel. A simplified two-degree freedom (2DOF) model is used to analyze contact between components. The conclusion is that global energy is divided into energy that is affecting the glass panel (effective) and residual energy that applies to the remaining parts of the test configuration. Approximately 20% of pendulum energy is transformed in deformation and excitation of the remaining elements from the test configuration, transferring ~80% of total energy on the glass panel. Similar studies and models are developed for the automotive industry where tests are performed for head impact during a car accident. Brendler et al. [11] made a numerical model in LS DYNA of pendulum impact test on toughened and insulated glass while Pelfrene et al. [12] developed a numerical model in two different computer programs SJ MEPLA and ABAQUS. Both authors compared the model with the results of experimental tests. Schneider [13] describes how to model soft body impact by two proposed numerical methods from regulation [5]. Regarding the pendulum impact test, a transient numerical method is described. It is a method for determination of time-dependent structural behaviour of glass. The basis of the method is in incremental solving dynamic equilibrium. It is required to first develop a model with proper elements presenting pendulum and glass plate. Then, the model needs to calibrate. The second method presented is a simplified engineering model with equivalent static loads. The method uses 2DOF model simulating a coupled system of glass plate and pendulum. Besides the pendulum test other types of impact tests are performed to predict glass strength. Van Dam et al. [14] performed small scale drop weight tests on annealed glass with the addition of safety window film to study resistance and post-failure performances of glass reinforced with safety window film. Quasi-static punch tests and low velocity impact tests are presented by Osnes et al. [15] with the intention of verifying the Strength Prediction Model (SPM). SPM is combining FEM to

determine stress and strain with Monte Carlo simulation to locate artificial surface flaws to finally evaluate fracture strength of glass panel. Model is capable of predicting fracture force, displacement, and initiation position of fracture. It uses linear elastic fracture mechanics comparing stress intensity factors for Mode 1 with fracture toughness. For purpose of defining more accurate failure prediction for dynamic loading, Osnes et al. [15] presented a strain-rate dependent dynamic fracture toughness K_{ID}. Overall, SPM showed very good results for modelling rate dependent fracture strength.

There are different approaches to determine glass behaviour under impact loads, still mostly verified through experiments. We can corroborate to a significant progress in numerical modelling of glass behaviour. These numerical models are appropriate for different analyses of glass structures. In this paper, different numerical models will be presented with special reference to the advantages, disadvantages, and application's peculiarities of each of them. These models should be verified in comparison with experimental results, which can improve design guidelines.

Significant progress in modelling and experimental testing of glass behaviour is evident in the last ten years, so it could be said that the glass structures era is yet to come.

References

[1] prEN 13474-3:2009 *Glass in building - Determination of the Strength of Glass Panes - Part 3: General Method of Calculation and Determination of Strength of Glass by Testing*, European Committee for Standardization, Brussels, 2009.

[2] A.A. Griffith. *The Phenomena of Rupture and Flow in Solids*, Philosophical Transactions, Series A, 221, 163-198, 1920.

[3] M. Overend, S. Gaetano, M. Haldimann. *Diagnostic Interpretation of Glass Failure*, Structural Engineering International, 2, 151-158, 2007.

[4] E. Orowan. *Fracture and Strength of Solids*, Reports on Progress in Physics, XII, 185, 1948.

[5] *Guidance for European Structural Design of Glass Components.* European Commission, Joint Research Centre, Report EUR 26439 EN, Luxembourg, 2014.

[6] HR EN 356:2006 (EN 356:1999) *Glass in Building – Security Glazing – Testing and Classification of Resistance against Manual Attack*, Croatian Standards Institute, 2006.

[7] HR EN 12600:2006 (EN 12600:2002) *Glass in Building – Pendulum Test – Impact Test Method and Classification for Flat Glass*, Croatian Standards Institute, 2006.

[8] X. Wang, J. Yang, Q. Liu, Y. Zhang, C. Zhao. *A Comparative Study of Numerical Modelling Techniques for the Fracture of Brittle Materials with Specific Reference to Glass*, Engineering Structures, 493-505, 2017.

[9] A. Pacios, S. Postigo, C. Huerta. *Relationship Between Characteristic Parameters of Impact Test for Safety Glasses*, Stahlbau Spezial, 61-66, 2011.

[10] J.A. Parra, J. Alonso, A. Pacios, M.C. Huerta. *Effective Energy Applied to a Glass Plate During an Impact Test*, International Journal of Impact Engineering, 130, 11-18, 2019.

[11] S. Brendler, A. Haufe, T. Ummenhofer. *A Detailed Numerical Investigation of Insulated Glass subjected to the Standard Pendulum Test*, LS-DYNA Anwenderforum, Bamberg, 2004.

[12] J. Pelfrene, S. van Dam, J. Kuntsche, W. van Paepegem. *Numerical Simulation of the EN 12600 Pendulum Test for Structural Glass*, Challenging Glass, 5, Ghent, 2016.

[13] J. Schneider, S. Schula. *Simulating Soft Body Impact on Glass Structures*, Structures and Buildings, 169(SB), 416-431, 2013.

[14] S. van Dam, J. Pelfrene, S. De Pauw, W. van Paepegem. *Experimental Study on the Dynamic Behaviour of Glass Fitted with Safety Window Film with a Small-scale Drop Weight Set-up*, International Journal of Impact Engineering, 73, 101-111, 2014.

[15] K. Osnes, O.S. Hopperstad, T. Børvik. *Rate Dependent Fracture of Monolithic and Laminated Glass: Experiments and Simulations*; Engineering Structures, 212, 2020.

ADAPTIVE NUMERICAL MODELING USING HIERARCHICAL FUP BASIS FUNCTIONS AND CONTROL VOLUME ISOGEOMETRIC ANALYSIS

Grgo Kamber [1], Hrvoje Gotovac [2], Vedrana Kozulić [3]

[1] Faculty of Civil Engineering, Architecture and Geodesy, University of Split, Matice hrvatske 15, 21000 Split, Croatia, grgo.kamber@gradst.hr
[2] Faculty of Civil Engineering, Architecture and Geodesy, University of Split, Matice hrvatske 15, 21000 Split, Croatia, hrvoje.gotovac@gradst.hr
[3] Faculty of Civil Engineering, Architecture and Geodesy, University of Split, Matice hrvatske 15, 21000 Split, Croatia, vedrana.kozulic@gradst.hr

1. Introduction

In this paper, a novel adaptive algorithm that is based on Fup basis functions [1, 2] that belong to the class of atomic functions and can be regarded as infinitely differentiable splines [3], is presented. Hierarchical Fup (HF) basis functions are closely related to the hierarchical B-splines (HB) and truncated hierarchical B-splines (THB). HF have the option of local *hp*-refinement such that they can replace certain basis functions at one resolution level with new basis functions at the next resolution level that have higher order (*p*-refinement) but also a smaller length of the compact support (*h*-refinement). This feature provides spectral convergence [4] and presents a substantial improvement in comparison to THB that enable polynomial convergence. HF basis functions are implemented into control volume IGA (CV-IGA) formulation. Poisson's equation is used for verification test.

2. Methodology

Fup basis functions belong to the class of atomic functions (see [1,3]) and span vector space of algebraic polynomials, while their properties are closely related to the more known B-splines.

Basis function Fup_n^l defined on a knot vector Ξ^l can be represented as a linear combination of $n+2$ Fup_{n+1}^{l+1} basis functions defined on Ξ^{l+1},

$$Fup_n^l(\xi) = \sum_{k=0}^{n+1} C_{n+1}^k \cdot Fup_{n+1}^{l+1}\left(\xi - \frac{k}{2^{n+1}} + \frac{n+1}{2^{n+2}}\right), \tag{1}$$

where n represents basis functions order and C_{n+1}^k are the refinement coefficients

$$C_{n+1}^k = \frac{1}{2^{n+1}}\binom{n+1}{k} \tag{2}$$

The $n+2$ basis functions Fup_{n+1}^{l+1} are called the *children* of Fup_n^l, denoted as

$$chdFup_n^l(\xi) = \left\{ Fup_{n+1}^{l+1}\left(\xi - \frac{k}{2^{n+1}} + \frac{n+1}{2^{n+2}}\right) \middle| k = 0,1,...,n+1 \right\} \tag{3}$$

Figure 1a shows a basis function Fup_1^l defined on a knot vector $\Xi^l = \{0,1,2,3\}$, and Figure 1b shows its three children $\mathrm{Fup}_2^{l+1}\left(\xi - \frac{k}{2^2} + \frac{2}{2^3}\right)$ defined on a knot vector $\Xi^{l+1} = \left\{0, \frac{1}{2}, 1, \frac{3}{2}, 2, \frac{5}{2}, 3\right\}$, where $k =$

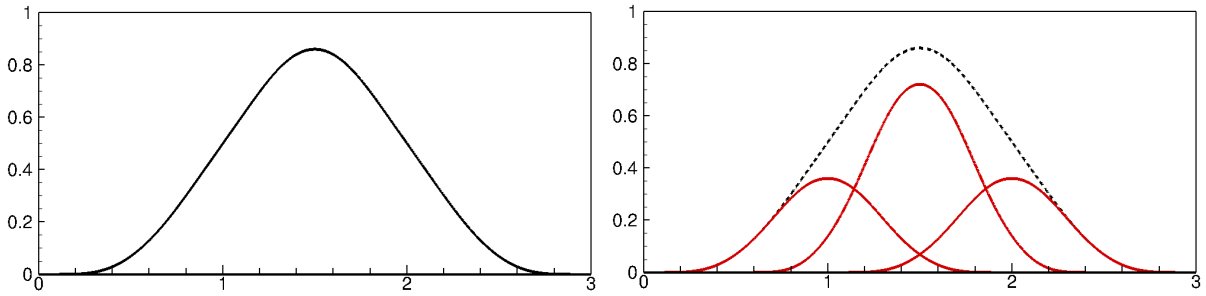

(a) $\mathrm{Fup}_1^l(\xi)$ (b) $C_2^k \mathrm{Fup}_2^{l+1}\left(\xi - \frac{k}{2^2} + \frac{2}{2^3}\right); (k = 0,1,2)$

Figure 1: Refinability of a $\mathrm{Fup}_1(\xi)$ basis function. (a) $\mathrm{Fup}_1^l(\xi)$ is defined on the knot vector $\Xi^l = \{0,1,2,3\}$; and (b) $\mathrm{Fup}_2^{l+1}\left(\xi - \frac{k}{2^2} + \frac{2}{2^3}\right)$ are defined on a knot vector $\Xi^{l+1} = \left\{0, \frac{1}{2}, 1, \frac{3}{2}, 2, \frac{5}{2}, 3\right\}$ with $C_2^k = \frac{1}{2^2}\binom{2}{k}$ for $k = 0,1,2$.

$0,1,2$. According to Eq. (1), Fup_1^l (Figure 1b - black dashed curve) can be represented by a weighted summation of its three children Fup_2^{l+1} (Figure 1b - red solid curve). In contrast to THB, hierarchical Fup basis functions (HF) enable *hp*-adaptive methods because each next resolution level not only decreases compact support but also increases the order of the basis functions (*hp*-refinement). Multidimensional Fup basis functions are obtained as tensor products of the one-dimensional basis functions defined for each coordinate direction.

To derive CV-IGA, the 2D parameter space defined by uniform (open) knot vector is shown on Figure 2. Domain is subdivided into a set of CVs such that each CV surrounds one corresponding vertex (Figure 2 - black circles) of basis functions and CVs boundary is defined at half distance between neighboring vertices.

In Figure 2, the focus is on the grid point $V_{i,j}$ (represents vertex), which has the grid points V_l, V_r, V_u and V_d as its neighbors and $CV_{i,j}$ boundaries (Figure 2 - red line) are marked as $\Gamma_{i,j,l}, \Gamma_{i,j,r}, \Gamma_{i,j,d}, \Gamma_{i,j,u}$.

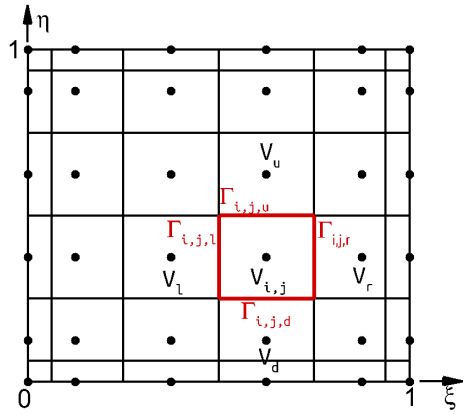

Figure 2: Control volume scheme for two-dimensional case.

Figure 3 shows a nested sequence of CVs domain, together with the corresponding vertices for each resolution level l, where each CV is linked with only one vertices i.e., the number of basis functions corresponds to the number of CVs.

CVs on the higher level $(l \geq 1)$ are build in a slightly different way then on starting level where all CVs are nonoverlapping. Each CVs boundary on the higher level (see Figure 3) are positioned exactly half the length of the characteristic intervals $\Delta\xi$, $\Delta\eta$ from the corresponding Fup basis function vertex, thus higher levels (CVs) are overlapping with lower levels (CVs). Overlapping process makes this algorithm even more robust, but at the cost of more expensive numerical integration.

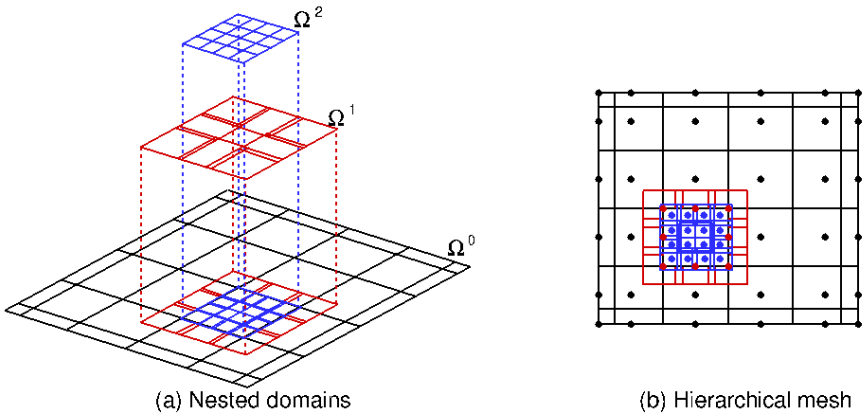

Figure 3: A nested sequence of CV domains for the construction of the Fup hierarchy according to relation $\Omega^l \supseteq \Omega^{l+1}$ for $l = 0, 1, 2$ for two-dimensional case.

3. Numerical example

Poissson equation, so called wavefront well problem is considered for verification test. It is commonly used example for testing adaptive refinement algorithms because of a steep wave front in the interior of the domain [5–7]. Parameters determine the steepness and location of the wave front.

Problem is defined in the form

$$\nabla \cdot (-\kappa \nabla u(x,y)) = f(x,y) \quad (x,y) \in \Omega \tag{4}$$

with boundary conditions

$$u(x,y) = u_D(x,y) \quad (x,y) \in \partial\Omega \tag{5}$$

The numerical simulation domain is defined by a square area $\Omega = [0,1]x[0,1]$ where the boundaries are $\Gamma_D = \partial\Omega$ and $\Gamma_N = \emptyset$ (see Figure 4a). The exact analytical solution for the pressure field is given by:

$$u(x,y) = \arctan(\alpha(r - r_0)) \quad \text{where} \quad r = \sqrt{(x-x_c)^2 + (y-y_c)^2} \tag{6}$$

where x_c and y_c represents center of the circular wave front, r_0 is the distance from the wave front to the center of the circle, and α gives the steepness of the wave front.

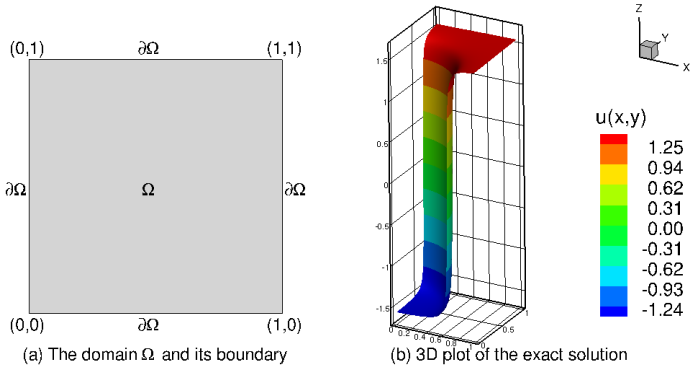

Figure 4: Numerical domain and exact solution plot of the wave well problem defined by Eq. (4)

Figure 5 presents the numerical solution of the wave front given by Eq. (4). Numerical solution becomes closer to the real solution (see Figure 5 1b-6b) with every new level. Adaptive criteria is used to check conservation error for each quarters of the particular i-th CV on the current resolution level. Quarters of the CVs are used because CV formulation exactly satisfies governing equation (i.e., the weak integral form of the conservation law), over each CV on the current resolution level. Adaptive procedure is repeated until conservation error is less then the prescribed threshold at each quarter of the CVs. The

adaptive grid captures the front (see Figure 5 1c-6c). For given parameters $x_c = y_c = -0.05$, $r_0 = 0.7$ and $\alpha = 100$ and using HF, six levels are needed in order to find numerical solution that has conservation error less then prescribed error threshold $(\varepsilon_s = 1 \cdot 10^{-4})$ on all quarters of the CVs.

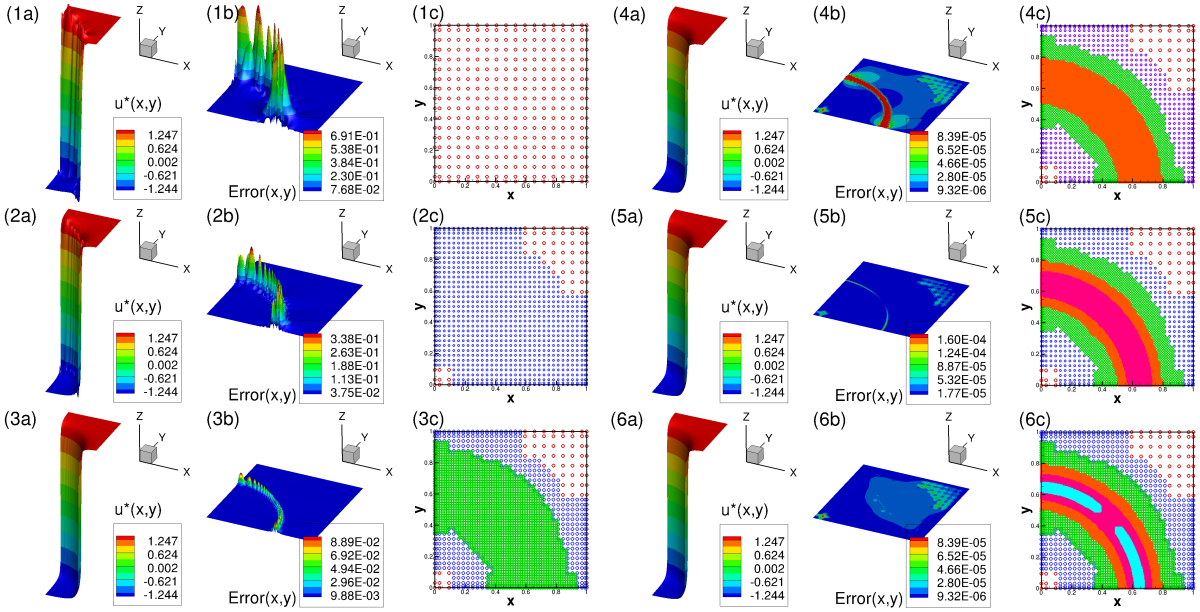

Figure 5: Numerical solution of the wave front well problem defined by Eq. (4). (a) HF approximation, (b) the absolute difference between the numerical and exact solution and (c) the adaptive grid on different resolution levels where each color represents Fup basis function vertices on different level.

4. Conclusions

A novel adaptive algorithm based on hierarchical Fup (HF) basis functions and the control volume IGA formulation is presented. Fup basis functions (infinitely differentiable splines) belong to the class of atomic functions and have the option of local *hp*-refinement. The application of hierarchical Fup basis functions enables higher continuity and smoothness of the solution, and at the same time, provides spectral convergence, while control volume formulation retains the conservation property of governing equations.

References

[1] V. L. Rvachev and V. A. Rvachev. On a finite function. *Dokl. Akad. Nauk Ukrainian SSR, ser. A*, (6):705–707., 1971.

[2] Blaz Gotovac. *Numerical modelling of engineering problems by smooth finite functions (In Croatian)*. PhD thesis, 1986.

[3] B. Gotovac and V. Kozulic. On a selection of basis functions in numerical analyses of engineering problems. *International Journal for Engineering Modelling*, 12(1-4):25–41, 1999.

[4] G. Kamber, H. Gotovac, V. Kozulic, L. Malenica, and B. Gotovac. Adaptive numerical modeling using the hierarchical fup basis functions and control volume isogeometric analysis. *International Journal for Numerical Methods in Fluids*, 92(10):1437–1461, 2020.

[5] W. Rachowicz, J.T. Oden, and L. Demkowicz. Toward a universal h-p adaptive finite element strategy part 3. design of h-p meshes. *Computer Methods in Applied Mechanics and Engineering*, 77(1-2):181–212, December 1989.

[6] J.T. Oden and Abani Patra. A parallel adaptive strategy for hp finite element computations. *Computer Methods in Applied Mechanics and Engineering*, 121(1):449 – 470, 1995.

[7] William F. Mitchell. A collection of 2d elliptic problems for testing adaptive grid refinement algorithms. *Applied Mathematics and Computation*, 220:350 – 364, 2013.

MODELLING SETTLING TIME USING 3D SMOOTHED PARTICLE HYDRODYNAMICS

Haris Kalajdžisalihović[1], Nerma Lazović[2], Ajla Mulaomerović-Šeta[3]

[1] Faculty of Civil Engineering in Sarajevo, haris.kalajdzi@gmail.com
[2] Faculty of Civil Engineering in Sarajevo, nermaligata@gmail.com
[3] Faculty of Civil Engineering in Sarajevo, ajlasam@yahoo.com

Sand particles settling is a common process in hydrotechnical practice, carried out in drinking and waste water treatment. Particles will settle at different rates, depending in their size and medium in which the settling process takes place. For this reason, different structures are used in technological filtering process, removing particles from water according to their size. Initial stage in sand removal is filtration process which involves the use of so-called "chamber". Chambers are structures constructed as reservoirs, whose purpose is to reduce velocity supporting settling process. All particles larger than 0.25 mm in diameter will be settled in this facility. In this research, settling of 3D models of ball shaped and rotated cube particles using DualSphysics open source code are analyzed. The results represent the time it takes particles of equal volume and different shapes to settle in the same medium.

Analytical and experimental solutions
For settling particle it is necessary to be satisfied:

- Particle density must be greater than medium density, otherwise the particles will float
- Particle size must be greater than 10^{-6} m, i.e. gravity dominant

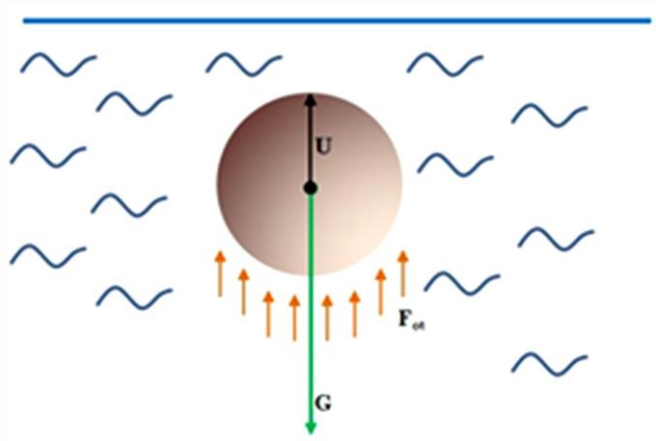

Fig. 1. Forces that act on particle

Forces acting on the particle are shown in the Figure 1. , and the equation describing the equilibrium state is:

$$G - U - F_{OT} = 0$$

Where are: G- weight of particle, U- uplift force, F_{ot} - resistance force

Resistance force depends on velocity of streaming and its own area, so it could be related to Re number as:

$$\mathrm{Re} = \frac{\mathrm{v} \cdot \mathrm{L}}{\nu}$$

Where are: v - velocity, L - linear dimension characteristics, ν - kinematic viscosity

Numerous experimental results gave velocity of settling (ball shaped) particles depending on its size. Using these results a resistance coefficient is determined (Fig 2.), after which it is possible to determine settling time as:

$$v_s = \sqrt{\frac{4 \cdot d_C \cdot \left(\rho_C - \rho_F\right) \cdot g}{3 \cdot \phi \cdot \rho_F}}$$

Where:
v_s - settling velocity, d_C - particle diameter, ρ_C - solid density, ρ_F - fluid density, g - gravitational acceleration, ϕ - shape coefficient Fig. 2. In case of this article analytical solution satisfy Newtonian law. For different sizes of settling particles there are numerous experimental velocity results.

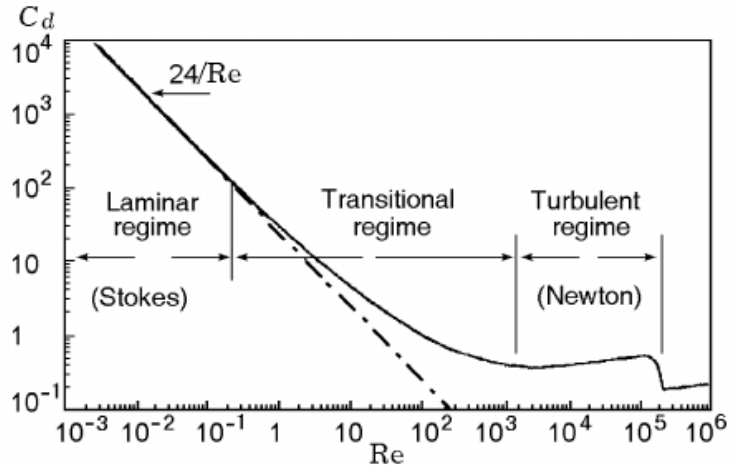

Fig. 2. Drag coefficients related to Reynolds number in logarithmic order [1]

Model results, ball settling particle is shown in set of time frames in 2D central cross section of 3D model.

Model setup

Model input file is done in FreeCAD 1.7. version.

- Entire domain is box 0.15x0.15x0.5m filled with water up to 0.4m of height, fig.3.
- Water media density is $\rho = 1000 \mathrm{kg/m^3}$
- Both, ball and rotated cube particles densities are $\rho = 2000 \mathrm{kg/m^3}$
- Viscosity coefficient of water media is $\nu = 10^{-6} \mathrm{m^2/s}$
- Sound coefficient (verified on experimental solution) is 200 times

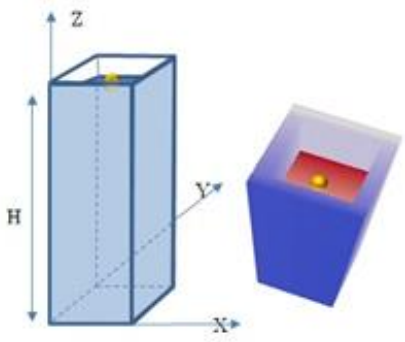

Fig. 3. Box domain with ball particle 2cm in diameter

Position of ball particle with diameter of 2 cm at five different times is presented in Fig 4.

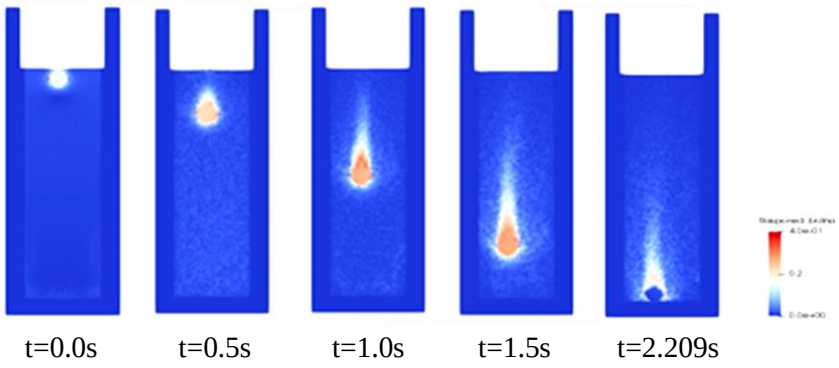

Fig. 4. Total time needed for settling ball particle 2 cm in diameter in box domain is 2.209s

After modelling settling boll shaped particles and fitting data to previous solution done by Ruud van Ommen [1], next step of this research is modelling settling process of rotated cube having same mass and volume.

Three settling velocity modeled values, using particles 2, 2.5 and 3 cm in diameter, are presented in Fig 5., side by side with analytic/experimental results. Three different particle size are involved in order to evaluate their fit to the experimental results.

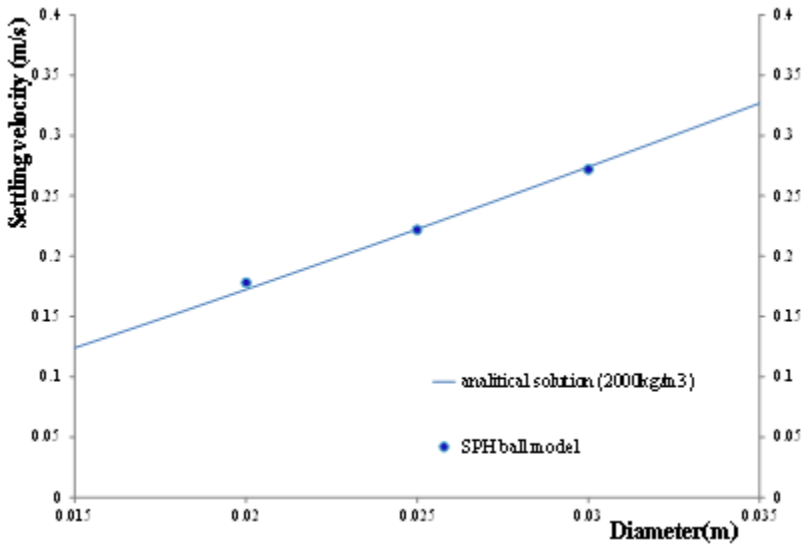

Fig. 5. Evaluation of ball particle settling model

After evaluation of a ball model, new shape model, rotated cube, can be introduced. This cube has dimensions that keep its mass equal to mass of ball particle with diameter 2 cm and other larger balls.

After evaluating ball settling model to analytical solution, rotated cube settling model is described. It is shown that rotated cube has higher values of velocities and shortened settling time than ball model.

References

[1] Ruud van Ommen, TU Delft, Sedimentation, JMBC+OSPT Course particle Technology, 2010.
[2] L. L. B. ., "A numerical approach to the testing of the fission hypothesis," Astron J., vol. 82, p. 1013–24, 1977.
[3] G. a. Monaghan, "Smoothed particle hydrodynamics - Theory and application to non-spherical stars," Monthly notice of the Royal Society, vol. 181, pp. 375-389, 1977.
[4] H. Wendland, Computational aspects of radial basis function approximation, Elsevier, 1995.
[5] S. a. L. W. Li, "Moving least square Kernel Galerkin method (II) Fourier analysis,"Comput. Methods Appl. Mech. Engineering, pp. 139-159, 1996.
[6] J. J. Monaghan, "On the Problem of Penetration in Particle Methods," Journal Computational Physics, vol. 82, p. 1–15, 1989.
[7] M. a. Colagrossi, "A simple procedure to improve the pressure evaluation in hydrodynamic context using the SPH," Elsevier science, 2009.
[8] Leimkuhler, "A symplectic integrator for riemannian manifolds," J. Nonlinear Sci, vol. 6, pp. 367-384, 1996.

DEVELOPING NEW WEIR TYPE USING SMOOTHED PARTICLE HYDRODYNAMIC MODEL

Haris Kalajdžisalihović[1], Zoran Milasinović[2], Alen Harapin[3]

[1] Faculty of Civil Engineering in Sarajevo, haris.kalajdzi@gmail.com
[2] Faculty of Civil Engineering in Sarajevo, zoran.milasinovic@gf.unsa.ba
[3] Faculty of Civil Engineering, Architecture and Geodesy in Split, alen.harapin@gradst.hr

Within this paper different types of weir models and comparison of their efficiency will be established. A broad crested weir is structure type that has a length L and a height large enough relate to the depth of the realized water that flows over it so that a current formed image has streams parallel to structure and implicate hydrostatic pressure distribution, V. T. Chow [1]. Theoretical solution of broad crested weir together with observed laboratory data at single stepped weir model are used as upper boundary condition for numerical Smoothed particle hydrodynamics model (SPH). An open source code SPHysycs, compiled in Cuda compiler, is used to simulate single step weir model and fit to observed data and partly to theoretical solution. Open source code use weakly compressible Smoothed particle hydrodynamics method (WCSPH) with dynamic boundary condition to simulate water flow.

Analytical solution (broad crested weir):

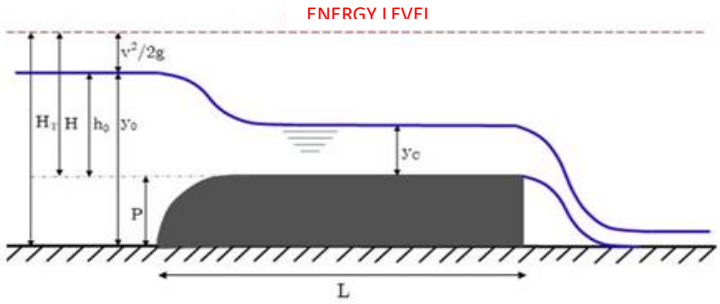

Fig. 1. Broad crested weir

Flowing over a broad crested weir and exploring the characteristics of that flow have captured the attention of many researchers. Already the first research on this topic was done by Bazin [2].

A differential equation for a stationary slightly variable flow in an open channel, described by V. T. Chow, will be used to describe a slightly variable flow [1].

$$\frac{dy}{dx} = \frac{S_0 - S_f}{1 - \alpha Q^2 T / gA^3}$$

Where are: y - depth, x -coordinate in flow direction, S_0 -bottom slope, S_f - energy slope, Q - discharge, T - width, g -gravitational acceleration, A - cross section area, α - coriolis coefficient

Observed data (single stepped weir):

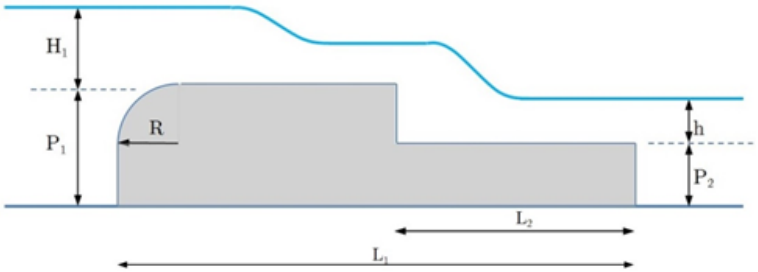

Fig 2. Single stepped weir

The results of experiments taken from the work of Hamid H. et al. [3], defined on a channel with a horizontal bottom, dimensions 0.5 m wide, 10 m long, 0.45 m high, in which the dimensions of the threshold, lengths L_1 and L_2 given in Figure 2.are varied, while the values of parameters P_1 are fixed P_1=12 cm, P_2 = 6 cm, R = 6 cm.

Fig. 3. Laboratory model [3]

SPH Model setup:

In order to achieve the desired discharge in the system, it is necessary to set higher energy values at the upstream end of the domain. It is defined trough higher upstream water level than the initially defined water level in the rest of the channel. Reservoir is directly connected downstream to the considered channel. Different initial water levels in the reservoir and different sizes of connection holes with the channel will result in different values of discharges that will be realized in the channel.
The water recycle from the end of the channel to the tank from where it flows through the channel again. After a few seconds of simulation, a steady state discharge in the channel is achieved, Fig. 4.

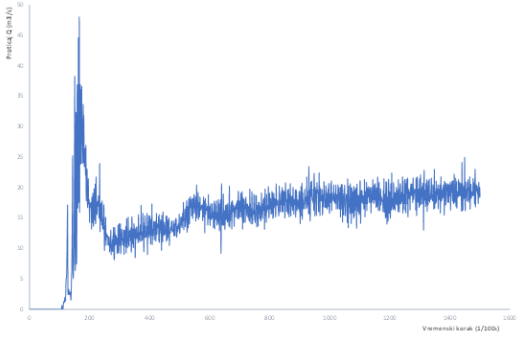

Fig 4. Time series of discharges. Reaching steady state in few seconds

After numerous (more than 40) simulations performed for flow over the single stepped weir the following parameters were reached. Simulation GPU time was 12h 50min in nVidia GeForce 1050Ti.

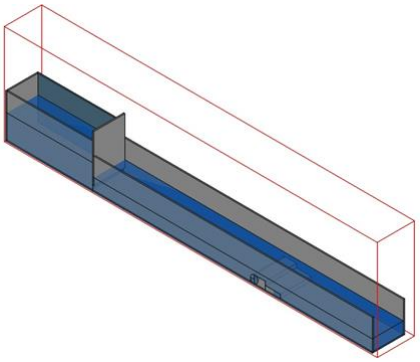

Fig 5. Image of model domain done in preprocessing FreeCAD software

Model weir dimensions: channel length 6m, channel width 0.5 m, channel depth 0.5 m, P_1=12 cm, P_2=6 cm, L_1=48 cm, L_2=24 cm, R=6 cm,

Other model parameters: fluid particle size in the description: 0.015 m, dynamic fluid viscosity: 10^{-6} m^2/s, integration scheme: Symplectic, accuracy: Single, Multiplication factor for the force of friction with a solid structure in relation to the viscosity of the fluid: 10000 (the coefficient of friction in contact with the type of structure is 10000x higher than in the fluid-fluid relationship), specific mass correction: each time step deltaSPH, flow control was performed by tabular constitution and level in the upstream reservoir, level in the upstream tank, upstream contour condition: 0.5 m
Clearance under the plate structure, as a contour condition: 0.09 m to achieve Q=19.85 l/s, downstream contour condition: no back water of the weir (downstream depth less than the weir height), achieved with a horizontal bottom, number of particles: 466000, simulation time: 15s, output frequency .vtk files: 100 Hz

Results of SPH model:

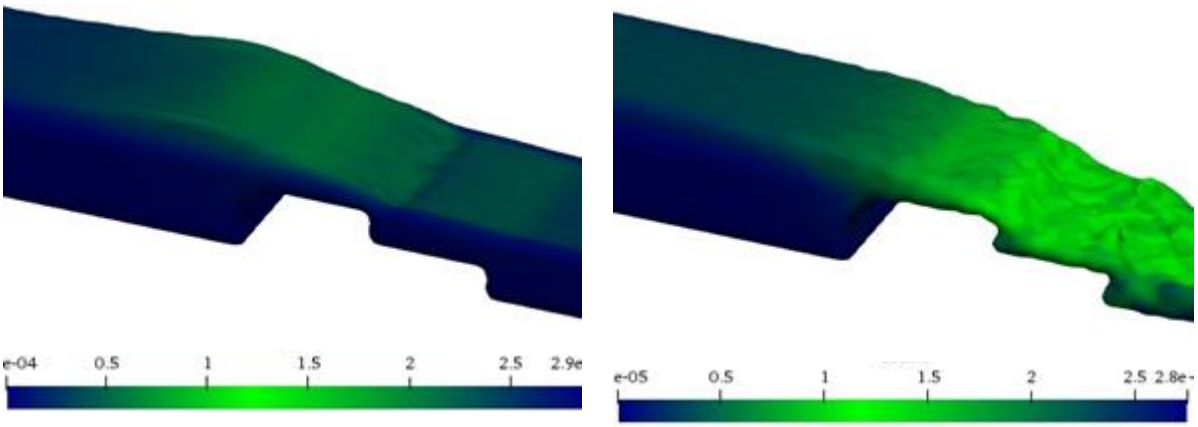

2s 15s

Fig 6. Modelled water flow velocities after 2s and 15s

Further, another two different types of suggested weirs will be modelled in SPHysics using the same parameters from previous work. Purpose of new developed structures should be higher dissipation energy ratio.

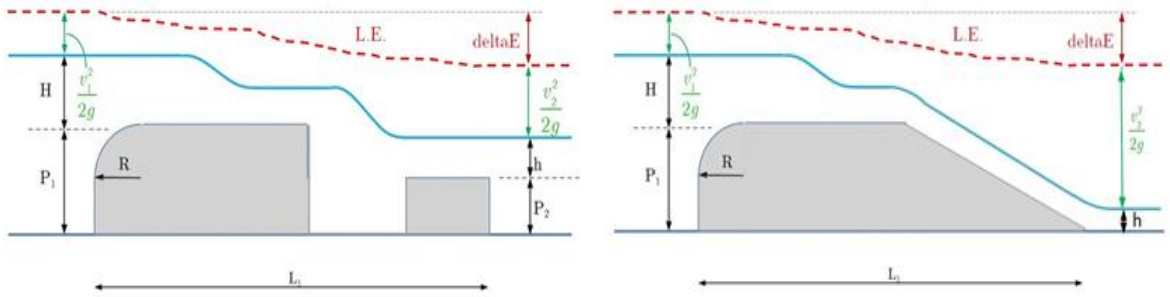

Fig. 7. Proposed separated and downstream sloped weir

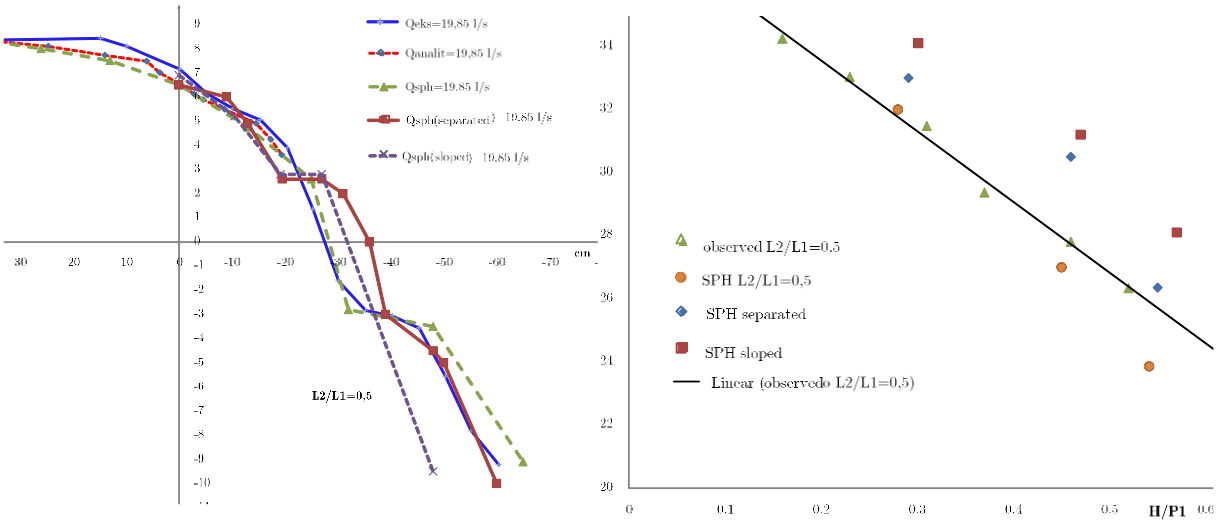

Fig. 8. Results of single stepped and other types of weirs. Left: eater levels, right: energy dissipation

Conclusion:

The most efficient in terms of energy dissipation is the proposed type of weir with downstream inclined step (called sloped) analyzed in this paper.
Based on the analyzed cases and the obtained results physical models are necessary in complex geometries to give reliable results, but SPH analyzes can significantly decrease range of the physical model and real structure type choice.

References:

[1] Chow, V. T., Open channel hydraulics, 1959, New York, McGraw-Hill.
[2] Bazin, Open channel hydraulics 1896, USA, McGraw-Hill.
[3] Hamid H., Inam A. K. and Saleh J. S., Improving the Hydraulic Performance of Single Step Broad-Crested Weirs, Journal of Civil Engineering, Pages 1-12, volume 7, issue 1, 2010.

ECCOMAS MSF 2021 THEMATIC CONFERENCE
30 June – 2 JULY 2021, SPLIT, CROATIA

HYDRAULIC MODELLING OF FLOODPLAIN MAPPING

Hata Milišić[1],Suvada Jusić[2],Emina Hadžić[3],Aldijana Šanjta[4]

[1] Faculty of Civil Engineering, University of Sarajevo, hata.milisic@gmail.com
[2] Faculty of Civil Engineering, University of Sarajevo, eminahd@gmail.com
[3] Faculty of Civil Engineering, University of Sarajevo, suvadasuvalija69@gmail.com
[4] IPSA Institute, Sarajevo, sanjtaaldijana@gmail.com

Abstract. Flood is a natural disaster and causes loss of life and property destruction. The objective of this study was to analyze flood inundation area mapping at Veseočica River in Vrbas River basin in B&H. The flooded areas along of catchment area have been mapped based on the depths and flow rates for different return periods using the HEC-RAS model, GIS for spatial data processing and HEC-GeoRAS for interfacing between HEC-RAS and GIS. Calibration and verification of the HEC-RAS model was performed based on the results of the numerical model MIKE11, because there is no water meter station at the Veseočica River. The results of calibration and verification showed very good agreement with the results from the numerical model MIKE11. The areas along the main reach in the study area were simulated to be inundated for 20, 100 and 500 years return periods. The flood inundation maps for 20, 100 and 500 years return periods were prepared using ArcGIS. The present study also focus on various hydraulic modeling software's and usefulness of Geographic Information System as a tool on the field of water resources engineering and management.
Keywords: Floods, Hydrodynamic Modeling, HEC-RAS, HEC-GeoRAS, ArcGIS

1 Introduction

Overbank floods resulting from high flows have had important socio-economic consequences all over the world. During the period from 2001 to 2014, more than a billion of the world's people were affected by flooding, and almost 80 thousand died [1]. The main hydrologic-hydraulic factors giving rise to flooding are relief, type and intensity of precipitation, vegetation cover, drainage capacity, geology, river morphology with extension of channel and floodplain, channel-floodplain interaction and roughness. To minimize the socio-economic impacts of flooding, solutions for preventing it have consisted of either structural or non-structural measures. Usually, non-structural measures are financially more viable, focusing on prevention and conservation to give better harmony between the environment and urban areas along the river [1]. One of the more widely known non-structural measures is the mapping of areas susceptible to flooding, a financially viable option which is useful in risk studies. Flood mapping commonly uses 1D and 2D hydraulic mathematical models (conceptual or empirical) to represent the hydraulic phenomena that determine water-levels (1D and 2D) and the area flooded [2]. For example, due to the 1D, 2D, and combined 1D-2D stream flow modeling capability [2], the HEC-RAS software is the most widely used tool within flood hazard and risk mapping studies, for real time flood forecasting, and even for remodeling past flood events. Hydraulic modeling requires information that adequately represents flooded areas, including (a) data or estimates of flows upstream of the reach of interest and (b) good quality data on regional topography and bathymetry. In this framework, the ability to generate flood hazard maps based on new computer algorithms and hydraulic modeling software and integrating the results within a Geographical Information Systems (GIS) database are important foundations for any flood mitigation efforts [2].

2 Methodology

2.1 Study Area

The Veseočica River is located in Bosnia and Herzegovina, in the Bugojno municipality, and is a left tributary of the Vrbas River (Figure 1). The length of the stream is about 7 km with a catchment area of 135 km^2. Veseočica is formed by two rivers, Duboka and Pršljanica. In the area of Bugojno municipality, many riverbeds are poorly developed and cannot accept larger flows, which is why water flows from riverbeds (Vrbas, Veseočica, Poričnica) to coastal areas and floods very valuable areas along watercourses. The risk of flooding on the banks of the Veseočica River is high. In periods of heavy rainfall and snowmelt in the municipality of Bugojno, new springs are characteristic, which turn into streams and torrents that cause material damage and cause danger to people, especially in the area flowing through the city, suburbs and rural settlements.
Characteristic floods occurred: December 1906, November 1925, November 1969, November 1975, November 1981, April 2001, March and April 2004, and January 2010 (Figure 1).

Fig.1 Veseočica River (left) and Settlement Vrbas (right) - Floods in January 2010 (Source: https://bug.ba/okom-nase-kamere-vesocnica-izmedju-naselja-vrbas-i-jaklica.html)

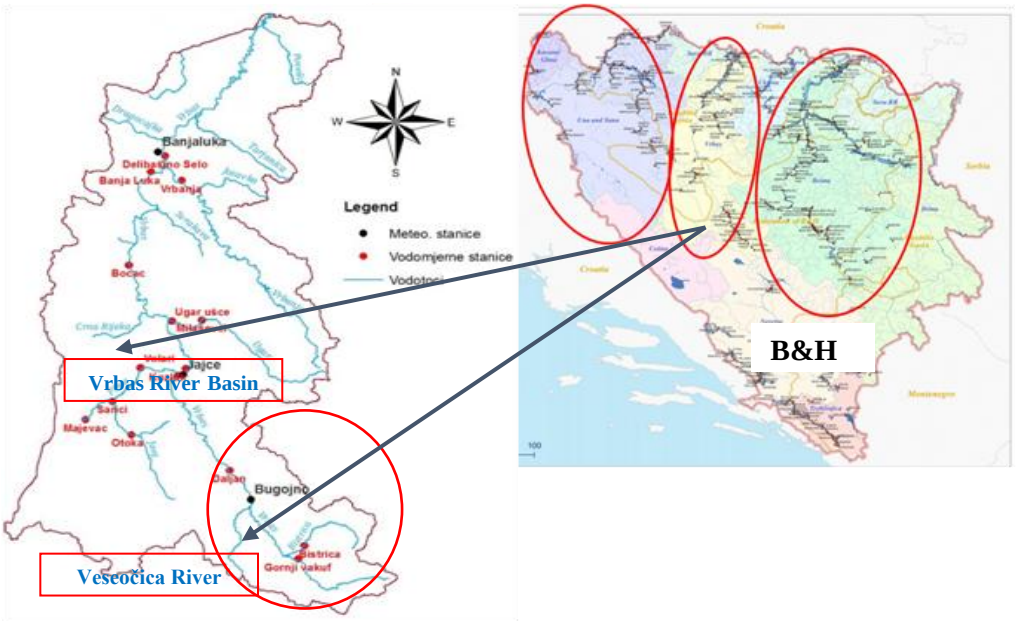

Fig.2 Vrbas River Basin with meteorological and hydrological stations

Taken as a whole, the flood protection works so far have been partial and focused primarily on the protection of only the central parts of some settlements. Relatively small results have been achieved, so that no settlement has a secure level of flood protection.

2.2 Hydraulic Modelling and Mapping of Flood-Prone Areas

2.2.1 Overview of HEC-RAS Software

Originally designed in 1995, the United States Army Corps of Engineers Hydrologic Engineering Center's River Analysis System (HEC-RAS) is "software that allows you to perform one-dimensional steady and unsteady flow river hydraulics calculations, sediment transport-mobile bed modeling, and water quality analysis" [2]. The software version available since 2016 called HEC-RAS 5.0 allows the analysis of two-dimensional turbulent fluid flow. Version 5 allows full 1D modeling (HEC-RAS 1D), full 2D modeling (HEC RAS 2D) or a combination of 1D / 2D modeling in which the main riverbed is modeled as a 1D model and the floodplain as a 2D model [2]. The possibility of combined modeling in the same non-stationary model allows the user to work with larger river systems. In this analysis work, version 5.0.7 of HEC-RAS was used [3].

2.2.2 Input data for modeling

The model requires data on flow, localized change in flow (non-permanent regime), boundary conditions, topographic-bathymetric information at each transverse section, a roughness coefficient for each transverse section, and a post-processing DEM to spread the flood into a pseudo 2D, since velocities in the two-dimensional plane are not simulated.
For create a geometrical model of the river bed of Veseočica (main channel and flood plains on the left and right bank) i.e. to define the geometry of the trough, the following data and backgrounds were used [4]:

- Recorded the main bed of the river Veseočica by the method of cross – section profiles,
- LIDAR image of the valley area (wider inundation zone on both banks) to the water mirror of the river and
- Aero-photo background of the LIDAR recording area (basic trough and inundation).

All pre-processing for HEC-RAS (definition of transverse sections, channel and margins, geometric data) used the ArcGIS software extension HEC-GeoRAS 5.0.

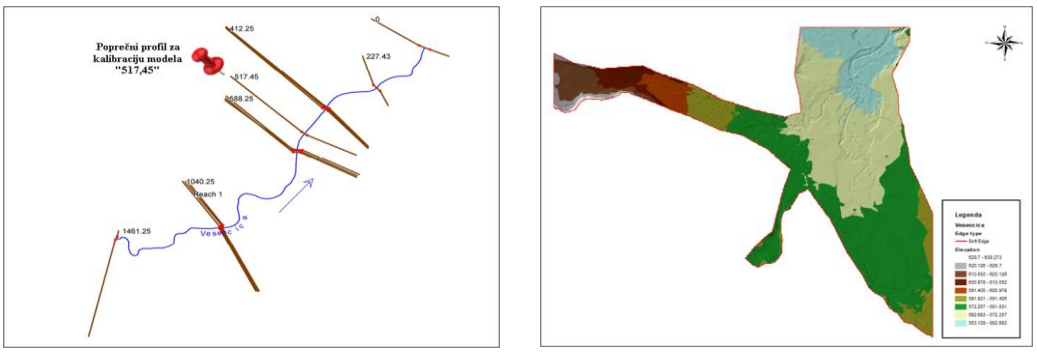

Fig.3.The cross - sections and DMT downstream of the Veseočica River [3]

Accordingly, based on the available data [4], the aim of the study was to carry out a hydraulic analysis of water flow through the natural riverbed of the Veseočica River. The study reach is about 1,5 km long and has 13 cross – sections. Numerical modeling of the Veseočica River flow (establishment, development, calibration and verification of the model) was done for one-dimensional unsteady flow [3]. The Flood hydrograph and rating curve [4] at estuary of the Veseočica into Vrbas River have been considered as upstream and downstream boundary conditions respectively. The Manning's roughness coefficient (n) was the only parameter calibrated in the model HEC-RAS, because of its sensitivity to hydraulic conditions. Floods for two years 2015 and 2014 have been selected for the model calibration and verification as peak discharges in flood conditions [3].

3 Results

The comparison of observed and simulated flow hydrograph (calibration and verification) at Veseočica gauging station is shown in Figure 4 [3].

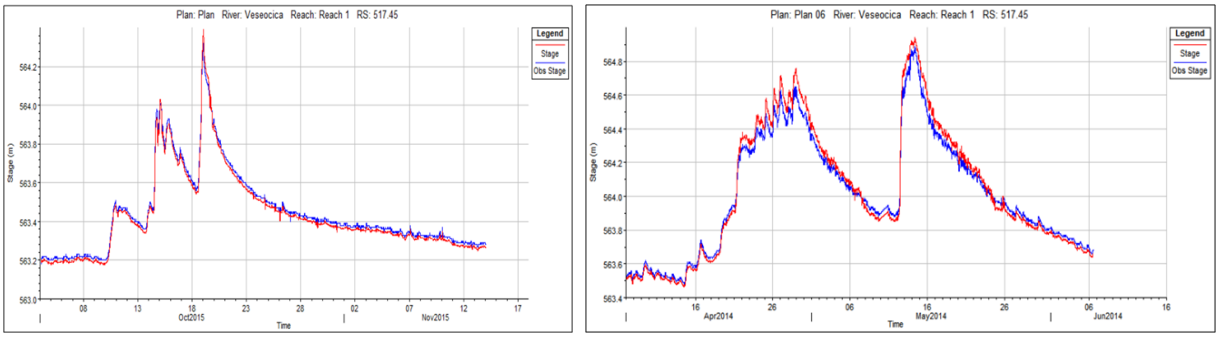

Fig.4.The comparison of observed (results of MIKE 11 model) and simulated flow hydrograph for 2015 (calibration) and 2014 year (verification) at Veseočica gauging station [3]

Flood inundation maps have been generated by exporting GIS data to the HEC-RAS for different return intervals (T = 1/20, 1/100 and 1/500). These maps show submergence area in plan maps which are shown in Figure 5 for floodplain and water depth [3].

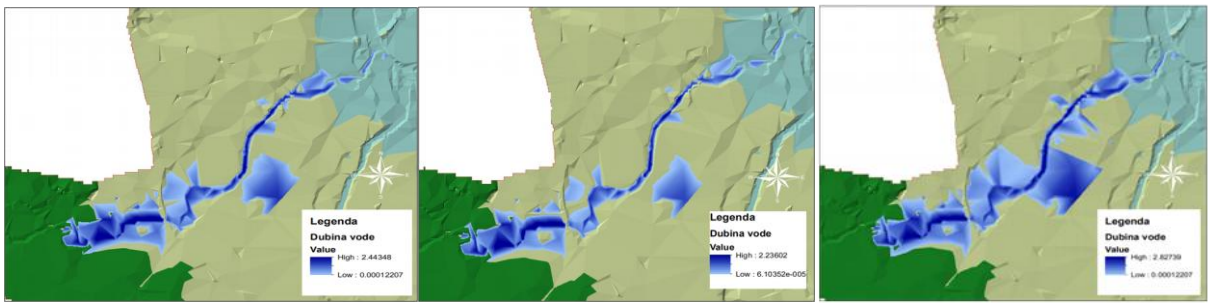

Fig.5. Hazard maps computed by HEC-RAS for water depth on the Veseočica River, considering T = 20, 100 and 500 years [3]

4 Conclusions

In this paper, we describe the development, calibration and validation of a flood model of the Veseočica River (B&H) by the HEC-RAS software. Two geometric models were constructed on the basis of a digital terrain model (DTM) using the Arc-GIS and HEC GeoRAS software after processing the collected topographic data. The flood model was applied to reconstruct recent flood events, as well as to simulate flood inundation due to rainfall events of varying return periods. Flood inundation maps will be an important tool for Engineers, Planners for emergency actions plans and for flood management in Bosnia and Herzegovina (B&H).

References

[1] B. Emanoel Omena Monte, D. Duda Costa, M. Bazilio Chaves, L. F. De Oliveira Magalhaes, Cintia B. Uvo: *Hydrological and hydraulic modelling applied to the mapping of flood-prone / areas*, Brazilian Journal of Water Resources.: Vol. 21 - Nº., 2016.

[2] Betsholtz A., Nordlöf B.: *Potentials and limitations of 1D,2D, and coupled 1D-2D flood modelling in HEC-RAS*, Master thesis, Lund University, 2017.

[3] Šanjta A.: *Numeričke simulacije tečenja u prirodnim vodotocima*, Master rad, Građevinski fakultet Univerziteta u Sarajevu, 2020.

[4] UNDPBIH-16-026-VRBAS-Zavod za vodoprivredu Bijeljina i Sarajevo __Hydraulic Report: *Izrada mapa opasnosti i mapa rizika od poplava na slivu rijeke Vrbas u BiH – Razvoj hidrauličkog modela rijeke Vrbas*, 2016.

ECCOMAS MSF 2021 THEMATIC CONFERENCE
30 June – 2 JULY 2021, SPLIT, CROATIA

ESTIMATION OF RIVER NERETVA DISPERSIVITIES USING A TRACER SALT TEST AND MIKE 11 NUMERICAL MODEL

Hata Milišić[1],Roko Andričević[2],Emina Hadžić[3],Zoran Milašinović[4]

[1] Faculty of Civil Engineering, University of Sarajevo, hata.milisic@gmail.com
[2]Faculty of Civil Engineering, Architecture and Geodesy, Univ. of Split, roko.andricevic@gradst.hr
[3] Faculty of Civil Engineering, University of Sarajevo, eminahd@gmail.com
[4] Faculty of Civil Engineering, University of Sarajevo, zoran_milasinovic@gf.unsa.ba

Abstract. Accurate estimation of longitudinal dispersion coefficient is required in several applied hydraulic problems such as: river engineering, environmental engineering, intake designs, estuaries problems and risk assessment of injection of hazardous pollutant and contaminants into river flows. Investigation of quality condition of natural rivers by 1-D mathematical models requires the best estimations for longitudinal dispersion coefficient. The main purpose of this paper is to evaluate the performance of river water systems dispersion modeling, based on tracer experiments data for calibration and validation. The present work describes the methodology used in the monitoring programs, basically consisting in the injection of a tracer salt (Sodium Chloride) in an upstream river section and follow-up of the salt cloud along the river to determine the water dispersion behavior in situ. In the paper it is compared the results of measurements of water quality indicators on the Neretva River (Bosnia and Herzegovina) with the numerical simulation obtained using a software package MIKE 11. The conclusions show that the mathematical modeling is an important tool of investigation under the conditions of existence experimental data obtained in situ.
Keywords: Water pollution, longitudinal dispersion, tracer salt test, MIKE 11 model

1 Introduction

River hydrodynamics and pollutant discharge dispersion characteristics are determinant factors in river basin planning and management. In addition to continuously high-levels pollution, accidental spills are the greatest ecological and economic danger for rivers. Generally, the knowledge of transport processes in both large and small rivers are of increasing importance concerning the prediction of the pollutant distribution in aquatic systems [1]. Thus, the quantification of parameters related to transport and dispersion of soluble pollutants into natural water streams is of great importance in the planning and management of water resources, especially in accidental or intentional cases, when it is necessary to warn the populations located downstream of the discharge site about the risks they are subjected when taking water from watercourses to meet their basic needs [1]. While pollutants are dispersed longitudinally, laterally and vertically through diffusive and advective transport processes, longitudinal dispersion is the governing process for the concentration gradient along rivers where the cross-sectional mixing is completed [2]. In this regard, one-dimensional (1D) mathematical models, which allow the fate of pollutants to be simulated, are widely used to address RWQ degradation [2]. Mass and pollutant transport in natural open channels is generally governed by the advection–dispersion equation (ADE). There are analytical and numerical approaches to predict pollutant transport by solving the ADE. To that end, hydraulic conditions should be correctly simulated. In addition, the Fickian-type assumptions under the ADE (e.g. there is a balance between diffusion and advection) should be valid [1].

2 Material and Methods

2.1 Scope of Study

This paper presents a study on estimation of longitudinal dispersion coefficient in natural streams. It also includes a comprehensive review of various models available in literature for prediction of longitudinal dispersion coefficient [3]. The modeling and field work were conducted on the Neretva River in Bosnia and Herzegovina [4]. The main purpose of this paper is to evaluate the performance of river water systems dispersion modelling, based on tracer experiment data for calibration and validation. The present work describes the methodology used in the monitoring programs, basically consisting in the injection of a tracer (salt - NaCl) in an upstream river section and follow-up of the salt cloud along the river to determine the water dispersion behaviour in situ. In the study MIKE 11 transport model based on one-dimensional dispersion equation are presented [4]. The model was developed to simulate different water quality management scenarios on reach of the Neretva River. The model was calibrated and validated in order to produce operational tools used to estimate the probabilistic leading edge/peak/tail times, the pollutant losses by volatilization, adsorption, precipitation, etc. and remaining concentrations. The good correlation between experimental and simulated data allows us to conclude that the applied model is accurate enough to describe and predict conservative pollutant transport under different hydrodynamic scenarios [4].

2.2 Study Area

The study area occupies the middle part of the Neretva river basin, located in the north region of Bosnia and Herzegovina. The Neretva River is the largest river in the catchment of the Adriatic Sea. The river length and basin is about 225 km and total area in FB&H of approximately 5745km^2 [4].

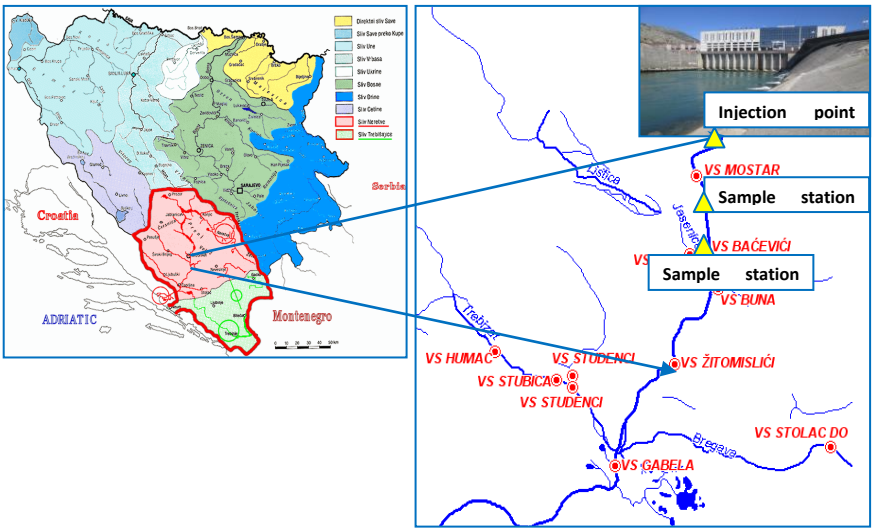

Fig. 1 Neretva river basin and sampling stations [4]

The river reach considered in this work begins downstream from the Hydropower station Mostar and Žitomislić hydrometric station (Fig.1), with a length of approximately 26 km. Three sampling sites were considered, with site P0 (Raštani – downstream of the HHPP Mostar) being the upstream tracer salt injection point. The three gauge station in the studded river reach is located in Mostar, Bačević and Žitomislić. The location of sampling stations was established according to their accessibility (bridges), mixing conditions, weirs location, logistics and human resources availability. The flow regime of this river reach is strongly influenced by the Mostar reservoir water level. Water levels at Mostar reservoir were recorded during the monitoring program. The flow discharge values considered for calculations were obtained from flow gauge stations records and ADCP measurements.

2.3 Field Tracer experiment

Tracer test was carried out in the Neretva River in October 2013. The experiment consisted in instantaneous (slug) injections of tracer. The tracer used in this study was salt (NaCl), recommended by its characteristics: not toxic, not reactive, good diffusivity, good detectability, low sorptive and acidity and inexpensive. Conductivity concentrations were measured at two downstream sections with a sampling period of 60 s using portable field conduct meters (HACH CO150 and HACH HQ14d). Background concentration conductivity is taken in all sampling sites. The location of the injection and the measurement sections was chosen so that the study reach could be considered as approximately uniform. The distance from injection allowed the tracer to be well mixed over the cross-section at the measurement stations. A monitoring program was carried out after injecting tracer in order to characterize in situ the transport and dispersion behaviour of the river under one hydrodynamic regime: frequent (150 m^3s^{-1}) flow. Table 1 presents the information concerning the tracer injection performed during the sampling program included in this study. Sampling sites location (Figure 1) were established according to the aims of this monitoring program, the sites accessibility (bridges), river physics characteristics, mixing conditions, weirs location, logistical means and human resources availability.

Table 1.Data of tracer injections / sampling information [4]

Injection/ Sampling site	Date	Hour	Site	Flow (m^3/s)	*Distance m*	Salt / NaCl mass (kg)
Injection site	2013-10-20	10:40 AM	P0	115	0	2000
Sampling site	2013-10-20	12:05 PM	P1	147	5570	
Sampling site	2013-10-20	13:10 PM	P2	152	10968	

The discharges and velocity values considered for calculations are obtained from conducted ADCP measurements of the velocity and discharge on October 20th, 2013 at three transects (see Figure 2). Mean water velocity in reach was calculated with mean travel time and distances between sampling sites (Table 1).

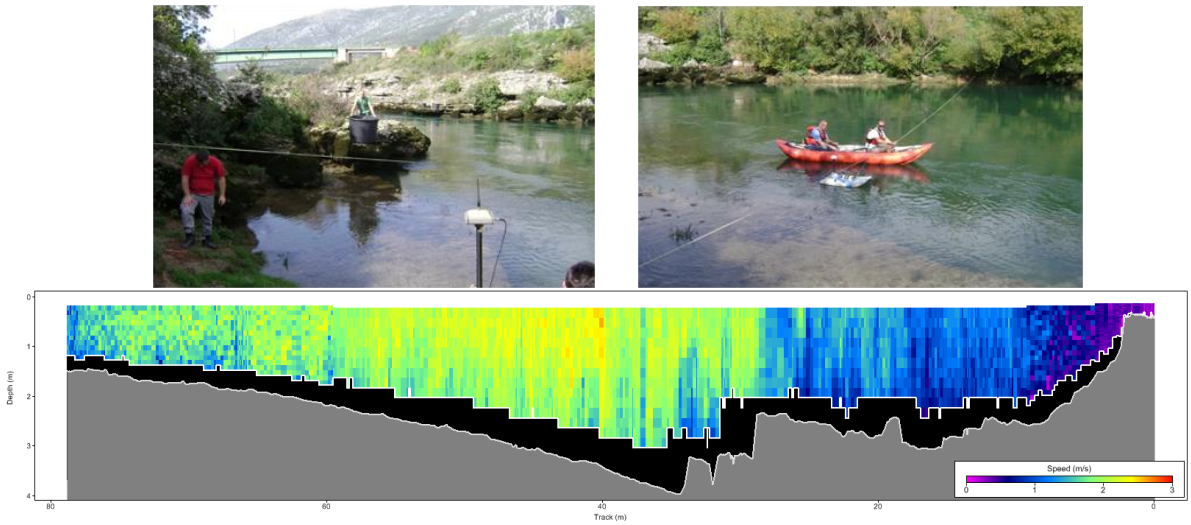

Fig.2 ADCP measurements of the velocity and discharge on October 20th, 2013 at three transects (Injection site P0, sampling site P1 and P2) [4]

3 Results and Discussion

3.1 Experimental and Numerical Results

The model calibration procedure (Fig. 3) included the adjustment of the friction bottom values and the longitudinal dispersion coefficients. Table 4 compares average velocity, travel time and dispersion

results obtained from Neretva river model simulations with experimental tracer data. The model results show a good correlation with experimental data, accurately reproducing the tracer peak concentrations and the travel time between consecutive sampling stations. Data on water quality (conductivity), collected in 2013 was used for the verification of the AD - MIKE 11 model (did not give results in this paper) [4].

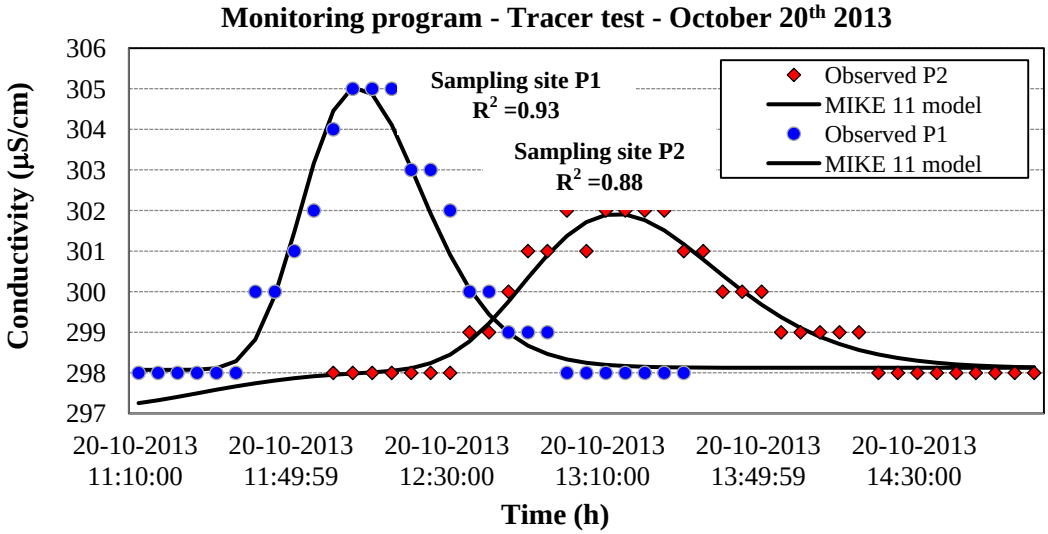

Fig. 3 The Neretva River model calibration with field data [4]

Table 2. The Neretva River model calibration results (Experimental and numerical model results) [4]

River - Reasch	Average velocity		Travel time		Dispersion coeff.	
	(m/s)		(h)		(m^2/s)	
Neretva	Exper.	Model	Exper.	Model	Exper.	Model
P1 - P2	**1,26**	**1,16**	**1,15**	**0.98**	**206.28**	**225**

4 Conclusions

The MIKE 11 software is a useful tool to develop accurate river models and to simulate pollutants transport in water bodies with different dispersive characteristics. In general, models results showed a satisfactory agreement with experimental data, allowing a reasonable support for impact assessment of different pollutant load scenarios in the river water quality. This procedure is of paramount interest in river basin management strategy for defining early warning or alarm systems, minimizing the effects from accidental pollutant spills, and to improve water sources protection practices. These capabilities of the MIKE 11 model therefore ensure its use for the present as well as future plans of the Neretva River.

References

[1] Ahsan, N.,: *Estimating the coefficient of dispersion for a natural stream*, World Acad Sci, Eng Technol. 44:131-135, 2008.

[2] Balicki M., Cornelius S.,Stuart G.,: *Mary River Dispersion Study - Model Development, Calibration and Analysis*, DHI Water And Environment Pty Ltd, Project No 43800339, 2011.

[3] Duarte, A. L. & Boaventura, R. A. *Pollutant dispersion modelling for Portuguese river water uses protection linked to tracer dye experimental data*. WSEAS Transactions on Environment and Development, 12, 1047–1056, 2008.

[4] Milišić, H.: *Terenska i numerička istraživanja koeficijenta uzdužne turbulentne disperzije u transportnim procesima otvorenih vodotoka*, Doktorski rad, Građevinski fakultet Univerziteta u Sarajevu, 2017.

NUMERICAL ANALYSIS OF MASONRY STRUCTURES BY COMBINED FINITE-DISCRETE ELEMENT METHOD

Hrvoje Smoljanović[1], Željana Nikolić[1], Lidija Krstevska[2], Nikolina Živaljić[1], Ivan Balić[1], Pavao Marović[1], Ante Munjiza[1]

[1] University of Split, Faculty of Civil Engineering, Architecture and Geodesy, hrvoje.smoljanovic@gradst.hr, zeljana.nikolic@gradst.hr, nikolina.zivaljic@gradst.hr, ivan.balic@gradst.hr, pavao.marovic@gradst.hr, ante.munjiza@gradst.hr
[2] Institute of Earthquake Engineering and Engineering Seismology in Skopje, lidija@pluto.iziis.ukim.edu.mk

Building construction using stone or clay bricks that are held together by mortar is one of the oldest building techniques that is still in use today. Among the oldest construction are masonry stone huts in a form of a circle found nearby lake Hullen in Israel that come from a period between 9.000 and 8.000 BC [1]. The first masonry structures were amazing piles of natural stone. As humans became more skilled and began using tools, masonry structures began to be more symmetrical. Later humans learned to make bricks moulding them from mud or clay leaving them to dry in the air and later baking them in ovens. Bricks were strong, uniform and easy to make. In addition to improving the techniques of making blocks various cultures began to use architectural features such as pillars to obtain the height or beams, arches and domes for bridging over the spans of distance. Masonry has a long worldwide tradition of use in construction due to its simplicity. The durability of masonry structures is evident in the number of structures that are still in use after hundreds or even several thousands of years. A few examples of structures that have become symbols of certain cultures are the Egyptian pyramids that have their origin from a period between 2800.-2000. BC, the Parthenon in Greece from the fifth century BC, The Great Wall of China whose construction began in fifth century before Christ and the Colosseum in Rome from first century.

In spite of the simplicity that is manifested during the construction of masonry structures, understanding and describing mechanical behaviour of those structures, especially in conditions of seismic loading, represents a true challenge due to the nature of masonry structure which due to the presence of joints among blocks that can but don't have to be filled in with mortar shows a complex and particular nonlinear behavior.

Various methods and numerical models are used for analysis of dry-stone masonry structures, based upon the degree of complexity, volume of input data and accuracy of required solution. There are two basic approaches in numerical modelling of masonry structures: idealization using continuum, and discontinuum.

The most commonly used numerical tool in continuum approach is finite element method [1], where different modelling strategies at micro, meso and macro scale have been developed to model masonry structure with desired accuracy. Although the great number of numerical models based on finite element method, the need for modelling the discontinuities and mutual mechanical interaction, finite displacement and rotation including complete detachment of the structure, which is especially expressed in the masonry structures under dynamic loading conditions, led to the development of numerous discontinuum models represented through the framework of discrete element method.

The main idea behind the application of the discrete element method to masonry refers to the idealisation of the structure as a discontinuum, where the blocks are represented by rigid discrete elements, while the joints are modelled as contact surfaces between different blocks.

In recent times, a number of numerical models combine the advantages of discrete and finite element methods. One of the methods which combine the advantages of continuum and discontinuum approach is a combined finite-discrete element method (FDEM) pioneered by Munjiza [3, 4]. FDEM was developed mainly for the simulation of fracturing problems considering deformable blocks that may split and separate during the analysis. Within the framework of this method, the blocks are discretised by triangular (2D) or tetrahedral (3D) finite elements. The material model in the finite elements is linear elastic, while the material nonlinearity, fracture and fragmentation of discrete elements are considered through displacement-based contact elements implemented within a finite element mesh. The interaction between discrete elements is considered through the contact interaction algorithm for normal forces, which is based on potential contact forces. The method uses an explicit numerical integration of the motion equation.

The purpose of this paper is to present the application of combined finite-discrete element method in analysis of dry stone masonry structures [5-7], masonry structures with mortar joints [9] and confined masonry structures [9]. For the purpose of validation of the method in analysis of dry stone masonry structures, experimental analysis [10] were conducted and compared with numerical results.

Acknowledgements
This paper is supported by the Croatian Government and the European Union through the European Regional Development Fund - the Competitiveness and Cohesion Operational Programme under the project KK.01.1.1.02.0027.

[1] P.B. Lourenço, T. *Computational strategies for masonry structures*, Ph.D. Dissertation, Delft University of Technology, Delft, The Netherlands, 1996.
[2] D.V. Oliveira. *Experimental and numerical analysis of blocky masonry structures under cyclic loading*, Ph.D. Dissertation, University of Minho, Minho, Portugal, 2003.
[3] A. Munjiza, *The Combined Finite-Discrete Element Method*, John Wiley & Sons, 2004.
[4] A. Munjiza, E.E. Knight, E. Rougier. *Computational Mechanics of Discontinua*. John Wiley & Sons; 2011.
[5] H. Smoljanović, N. Živaljić and Ž. Nikolić. *A combined finite-discrete element analysis of dry stone masonry structures*, Engineering Structures, 52, 89-100, 2013.
[6] H. Smoljanović, N. Živaljić, Ž. Nikolić, A. Munjiza. *Numerical analysis of 3D dry-stone masonry structures by combined finite-discrete element method*, International Journal for Solids and Structures , 136 (137), 150-167, 2018.
[7] H. Smoljanović, N. Živaljić, Ž. Nikolić; A. Munjiza. *Numerical Simulation of the Ancient Protiron Structure Model Exposed to Seismic Loading*, International Journal of Architectural Heritage, 13, 1-11, 2019.
[8] H. Smoljanović, Ž. Nikolić and N. Živaljić. *A combined finite–discrete numerical model for analysis of masonry structures*, Engineering Fracture Mechanics, 136, 1-14, 2015.
[9] H. Smoljanović, N. Živaljić, Ž. Nikolić, A. Munjiza. *Numerical model for confined masonry structures based on finite discrete element method*, International journal for engineering modelling, 30(1/4), 19-35, 2017.
[10] Ž. Nikolić, L. Krstevska, P. Marović, and H. Smoljanović. *Experimental investigation of seismic behaviour of the ancient Protiron monument model*, Earthquake Engineering and Structural Dynamics, 1–21, 2019.

ECCOMAS MSF 2021 THEMATIC CONFERENCE
30 June – 2 JULY 2021, SPLIT, CROATIA

CONTROL VOLUME ISOGEOMETRIC ANALYSIS IN GROUNDWATER HYDRAULICS

Hrvoje Gotovac[1]

[1] Faculty of Civil Engineering, Architecture and Geodesy, University of Split, Croatia,
hrvoje.gotovac@gradst.hr

Abstract

Many important flow and transport applications in groundwater hydraulics, especially in large, highly heterogeneous aquifers, require extensive computational resources, a multiresolution (multiscale) approach to resolve the different heterogeneity scales and an accurate calculation of the velocity field. Common methods, such as finite volumes and elements, assume a discontinuous conductivity field introducing velocity discontinuities along the cell or element interfaces due to using classic discrete operators or Lagrangian basis functions. Over the last decade, the development of isogeometric analysis (IGA) eliminates many of the aforementioned limitations bridging the gap between CAD and numerical analysis. Since classic IGA uses the Galerkin and collocation approach, in this paper, we present a third concept in the form of **C**ontrol **V**olume **I**so**G**eometric **A**nalysis (CV-IGA) enabling local and global mass conservation as well as multiresolution description of all heterogeneity scales. Due to the approximation properties of spline basis functions, the velocity field and its derivatives are continuous and are obtained by an optimal convergence rate. CV-IGA enables calculation of accurate and smooth velocity solution which is essential for realistic transport simulations with velocity dependent dispersion tensor.

Control Volume Isogeometric Analysis (CV-IGA)

Spline methods have been attracted scientific attention since its discovery in the 1950s. However, the research has developed in two separate directions, one for CAD and geometry description, and another for numerical analysis for solving of the boundary (initial) value problems. Hughes et al. 2005 ([1]) linked these two directions so that all variables, geometry and solutions (such as head and velocity), are described by a linear combination of spline basis functions. For example, Figure 1 presents the IGA scheme of how one 2-D subdomain or patch (defined as general four-sided object; we limit our considerations in this section to the one patch) is transformed from the parameter space (transformed domain) to the physical space (real domain) using the following spline representation:

$$x(\xi,\eta)=\sum_{j=1}^{N} x_j \phi_j(\xi,\eta) \;\; ; \quad y(\xi,\eta)=\sum_{j=1}^{N} y_j \phi_j(\xi,\eta) \qquad (1)$$

where x_j and y_j are coordinates of N control points $\mathbf{B}(x_j, y_j)$ in the physical space, while ξ and η are coordinates in the parameter space. The key elements of (1) are spline basis functions (ϕ_j) which are obtained by Cartesian product of 1-D basis functions from each direction. Number and position of basis functions in both directions inside the patch are defined by knot vectors (Figure 1). Here, we use open uniform knot vector as an ordered set of increasing parameter values $\Xi = \{\xi_1, \xi_2, \ldots, \xi_{k+n+1}\}$, $\xi_i \leq \xi_{i+1}$ where ξ_i is the *i-th* knot, k is the number of basis functions and n is the polynomial order (Figure 1, for

example in the ξ direction). The knot vector divides the parametric space into intervals usually referred to as knot spans. Knot has a multiplicity m if knot value is repeated m times in the knot vector. In this paper, uniform open knot vectors are used where the first and last knots have a multiplicity $m=n+1$, while all other knots are different and uniformly spaced between the first and last knot (see for example review of Nguyen et al., 2015 in [3]). Moreover, knots define distribution of parent elements in the parametric space (located between neighboring knots, Figure 1) which have the same role as finite elements in FEM. Therefore, patch is divided to the parent elements which can serve as a basic integration element. After integration over all parent elements, assembling process is the same as in FEM.

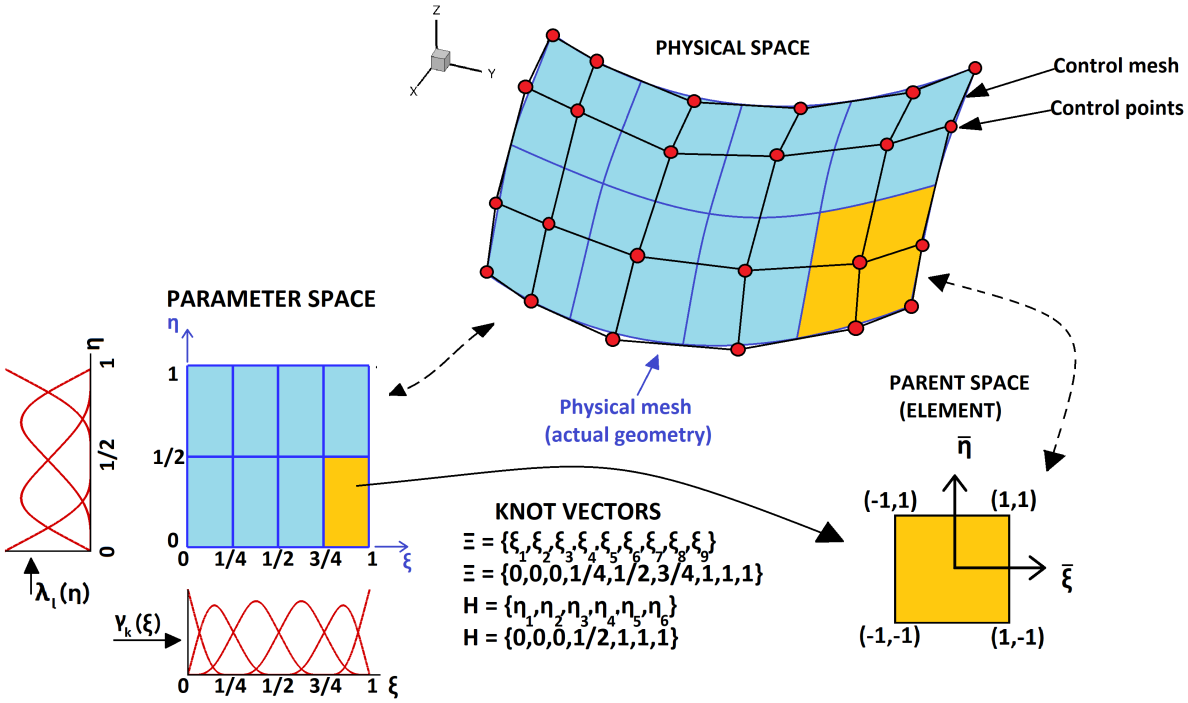

Figure 1. Schematic illustration of isogeometric analysis (IGA): physical space with control mesh and control points, parameter space with B_2 spline basis functions and related parent elements and knot vectors.

The control points define the control mesh in physical space, which enables the designer to create a wide range of desired objects, for instance in the car or aviation industry. Expression (1) presents that coordinates of control points directly define mappings from the parametric to the physical space. Figure 1 also illustrates that spline mapping for an arbitrary set of control points. Number of control points is equal to the number of basis functions which is on the other side defined by a knot vectors in both directions. The control grid-mesh (which defines the connectivity between control points) is also shown. The non-interpolatory nature of control points in the interior of the domain is evident and represents a notable difference over conventional Lagrangian meshes [3].

In classic IGA, B-splines and NURBS are widely recognized as suitable spline basis functions with the following main properties: a) compact support, implying localized approximation properties; b) strictly positive values, implying positive definiteness; c) partition of unity; d) enables continuity up to the desired order and e) enables multiresolution or multiscale representation and construction of efficient adaptive procedures. Supplementary material presents a short description of the B-splines and Fup basis functions that will be used in this paper. Multidimensional spline representation uses a tensor product of basis functions from each direction (Figure 1). Expression (1) shows that IGA operates only with basis functions in the regular parameter space, since transformations from the real to the transformed domain, and vice versa, are defined by Jacobian, and its inverse, as in classic FEM [2]. Now, the solution as the head, velocity or concentration in the groundwater hydraulics can also be described with independent set of basis functions in the parameter space:

$$u(\xi,\eta) = \sum_{j=1}^{N} \alpha_j \varphi_j\,(\xi,\eta) = \alpha_j \varphi_j\,(\xi,\eta) \qquad (2)$$

Isogeometric analysis (IGA) means that the geometry and solution description use the same type of basis functions (Figure 1). The number and order of basis functions may not be the same in (1) and (2).

In order to introduce the control volume framework, for example in case of flow problem in heterogenous porous media, the Gauss divergence theorem should be applied on each control volume cell:

$$\int_{\Omega} div(\mathbf{q}) d\Omega = \int_{\partial\Omega=\Gamma} \mathbf{q}\cdot\boldsymbol{n}\, d\Gamma \qquad (3)$$

where q is Darcy velocity (Gotovac et al., 2021; [4]). Introducing (3) to flow equation yielding:

$$-\int_{\partial\Omega=\Gamma} \mathbf{q}\cdot\boldsymbol{n}\, d\Gamma = \int_{\Omega} \mathrm{q}_0 d\Omega \qquad (4)$$

This formulation is reduced to the mass balance between discharges through the cell boundaries and pumping/recharge as an external loading over the cell, where **n** is external normal vector. Applying Darcy law to the mass balance flow equation (for each cell/control volume:

$$\int_{\Gamma} (\boldsymbol{K}\cdot\nabla h)\cdot\boldsymbol{n}\, d\Gamma = \int_{\Omega} q_0\, d\Omega \qquad (5)$$

Comparison of (5) to the weak formulation of flow problem in porous media leads to the conclusion that control volume formulation (5) can be regarded as weak flow formulation with constant piecewise test functions (unit on control volume, elsewhere zero, see [4]). First, control volumes are defined around the corresponding the Greville points (related to the position of particular basis functions; [4]). Non-overlapping control volumes based on Greville points cover the whole domain, implying exact satisfaction of the local and global mass balance. Introducing (1), (2) in (5), the mass balance flow equation is formulated via CV-IGA at each control volume in the parameter space:

$$\alpha_k^j \sum_{r_l=1}^{4} \int_{\Gamma_{r_l}} \left(\boldsymbol{K}\cdot\nabla\varphi_k^j\right)\cdot\boldsymbol{n}\, detJ_{r_l} dt_{r_l} = \int_{\Omega_l} q_0 detJ d\boldsymbol{\xi}_l + \int_{\Gamma_{N_l}} q_N detJ_{N_l} dt_{N_l} \qquad (6)$$

where *k* is the subscript for index of basis functions and *l* represents index of control volumes. Due to weak formulation, Neumann boundary conditions in (6) are satisfied in the same way as in Galerkin-IGA. Dirichlet boundary conditions imply that test Dirichlet boundary function is unit function on that boundary control volume (part of Dirichlet boundary with end points at half distance between neighboring boundary Greville points), elsewhere is zero. In that case, Dirichlet boundary conditions are satisfied by:

$$\alpha_k^j \int_{\Gamma_{D_l}} \varphi_k^j detJ_{D_l} dt_{D_l} = \frac{1}{L_{D_l}} \int_{\Gamma_{D_l}} h_D detJ_{D_l} dt_{D_l} \qquad (7)$$

Flow simulations

In order to show additional application of CV-IGA to the description of flow in heterogeneous porous media in the complex geometry, for the highly heterogeneity representation (*Var(lnK)=8*), flow domain is transformed to the L-shape. Now, left and lower boundaries have Dirichlet boundary conditions (h_{left}=10m and h_{lower}=0m), while other two boundaries are no-flow.

Figure 2a presents the classical L-shape benchmark test case. L-shape flow test case exhibits well known numerical problems in this classical fluid mechanics benchmark containing two mentioned corner

"singular" points where velocity in both directions has discontinuity. Two bilinear no-flow boundaries are also two streamlines. However, neighboring streamlines cannot satisfy no-flow boundary conditions close to the singular points. As discretization decreases, problematic zones around corners are smaller [4].

Figure 2b presents convergence analysis for L-shape problem. Contrary for smooth flow problem, in case of L-shape domain due to singular two corners and partially Jacobian discontinuity between two patches, the convergence rate is reduced (Figure 2b). Higher order basis functions slightly improve the convergence rate and accuracy, but it is still far from the optimal rate. However, it is well known that any singular effects in terms of heterogeneity or geometry can reduce accuracy and convergence rate. Thus, convergence rate – p is less than two for n = 1 and 2, as well as less than four for n = 3 and 4 if n is order of the Fup basis functions (Fig 2b). In that case, significance of higher order basis functions is significantly reduced.

However, many results from the IGA community proved that only adaptation property of B-splines and corresponding IGA adaptive scheme enables significant improving of solving problems with discontinuities and singularities. Recently, our numerical group developed hp adaptive CV-IGA procedure with hierarchical Fup basis functions (see Kamber et al., 2020 in [5]). We can conclude that higher order Fup/spline basis functions need to be involved through the adaptive IGA modelling in order to solve heterogeneity or geometry discontinuities and/or singularities as pumping/recharge points, sharp transition zones or narrow discharge areas.

CV-IGA [4] enables calculation of accurate and smooth velocity solution which is essential for realistic transport simulations with velocity dependent dispersion tensor [6].

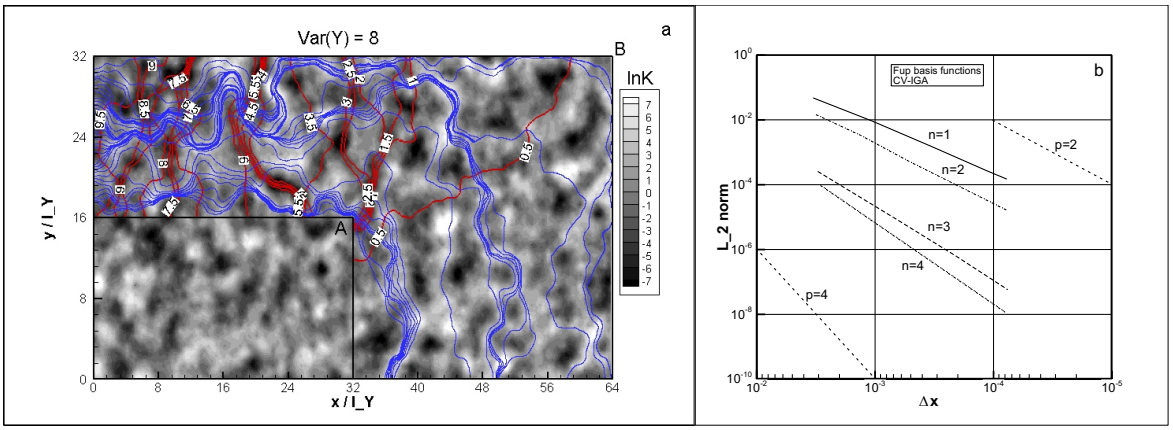

Figure 2. L-shape flow test case with heterogeneity description *Var(Y=lnK)=8*, a) flow solution, b) convergence analysis in terms of L_2 norm.

References

[1] Hughes, T.J., Cottrell, J.A. and Y. Bazilevs, Isogeometric analysis: CAD, finite elements, NURBS, exact geometry and mesh refinement, Computer Methods in Applied Mechanics and Engineering, 194, 39-41, 4135–4195, 2005.

[2] Cottrell, J. A., Hughes, T. J. R. and Y. Bazilevs, Isogeometric Analysis Toward Integration of CAD and FEA, pp. 335, Wiley and Sons, ISBN: 978-0-470-74873-2, 2009.

[3] Nguyen, V.P., Anitescu, C, Bordas, P.A. and T. Rabczuk, Isogeometric analysis: An overview and computer implementation aspects, Mathematics and Computers in Simulation, 117, 89-116, 2015.

[4] Gotovac, H., Malenica, L., Gotovac, B. Control Volume Isogeometric Analysis for groundwater flow modeling in heterogeneous porous media, Advances in Water Resources, 148, 103838, 2021.

[5] Kamber, G, Gotovac, H, Kozulić, V, Malenica, L, Gotovac, B. Adaptive numerical modeling using the hierarchical Fup basis functions and control volume isogeometric analysis. *Int J Numer Meth Fluids*. ; 92: 1437– 1461. 2020.

[6] Zheng, C., Bennett, G.D., „Applied Contaminant Transport Modeling", 2nd Edition, John Wiley and Sons, pp. 656, ISBN: 978-0-471-38477-9, 2002.

ECCOMAS MSF 2021 THEMATIC CONFERENCE
30 June – 2 JULY 2021, SPLIT, CROATIA

UNCERTAINTIES IN MODELLING HISTORICAL MASONRY AGGREGATES USING THE EQUIVALENT FRAME APPROACH

Igor Tomić[1*], Katrin Beyer[2]

[1] École Polytechnique Fédérale de Lausanne (EPFL), School of Architecture, Civil and Environmental Engineering (ENAC), Earthquake Engineering and Structural Dynamics Laboratory (EESD), Lausanne, Switzerland, igor.tomic@epfl.ch
2 École Polytechnique Fédérale de Lausanne (EPFL), School of Architecture, Civil and Environmental Engineering (ENAC), Earthquake Engineering and Structural Dynamics Laboratory (EESD), Lausanne, Switzerland, katrin.beyer@epfl.ch

In many historical centres of European cities, stone masonry buildings form building aggregates, which often developed over a long course of time as the layout of the city densified. It is common for units to have different material properties, floor levels, floor orientations or distribution of openings. At the same time, masonry walls of facades are often connected by dry joints. Opening of the joints leads to significant changes in the behaviour of a building aggregate and potential pounding between the units. This extends the list of epistemic and aleatoric uncertainties affecting the seismic assessment of historical masonry buildings. Principal sources of epistemic uncertainty are material and modelling properties and the displacement capacity of elements. Non-linear connections, such as joints between the units, are another source of uncertainty, with a potentially significant impact on the overall response.

The development of analysis methods or modelling guidelines for such typologies has been very challenging due to the lack of large-scale experimental campaigns. A large scale experimental campaign on a stone masonry aggregate was performed in EUCENTRE in Pavia, Italy, both in the unretrofitted and retrofitted configuration [1, 2]. Different authors performed analyses of masonry aggregates using the equivalent frame approach. Senaldi et al. [3, 4] evaluated the vulnerability of a structural unit within aggregate using a nonlinear macroelement [5] implemented in TREMURI software [6]. Formisano et al. [7-9] used advanced numerical analyses to calibrate a simplified assessment procedure for assessing large scale seismic vulnerability of aggregates. Maio et al. [10] assesed stone masonry aggregates using equivalent frame modelling, hybrid techniques and vulnerability index formulation. One thing in common to the studies was that the units were modelled either as perfectly connected or isolated.

In this work, the equivalent frame model (EFM) approach was extended to the modelling of aggregates by implementing a new non-linear interface model for simulating the interaction between the neighbouring units. The EFM was built-in OpenSees [11] using, in particular, a recently implemented macro-element [12], which can capture the in-plane and the out-of-plane response of masonry panels. To fully take into an account the ability to model both failure modes, detailed modelling of connections between walls, floors and walls, and units of an aggregate was necessary. The modelling approach was applied to a case study of a stone masonry aggregate with two units, located inside the Diocletian's Palace in Split, Croatia. The model was subjected to a non-linear time history analysis using different modelling approaches regarding the interface: fully connected units, isolated units, 1D non-linear interface, and a newly developed nD non-linear interface material model. To assess the influence of the

selected material and modelling parameters on the response, a probabilistic approach was applied to generate sets of the input parameters, and incremental dynamic analyses were carried out for each of the modelling approaches.

Based on the case study results, we conclude: (i) not only the PGA leading to failure is sensitive to the uncertain input material and modelling parameters, but so is the failure mode and the failure location in the aggregate and (ii) simplifying assumptions such as a perfect connection between the units or no interaction between the units can lead to demand estimates on the various structural components that are a multiple below or above for the same set of parameters. Therefore, the uncertainties related to the modelling approach and the modelling and material parameters are especially relevant when the analysis serves as an input for the design of retrofit interventions.

References

[1] Senaldi, I. E., Guerrini, G., Comini, P., Graziotti, F., Penna, A., Beyer, K., Magenes, G. *Experimental seismic performance of a half-scale stone masonry building aggregate.* Bulletin of Earthquake Engineering, 18(2), 609-643, 2020.

[2] Guerrini, G., Senaldi, I., Graziotti, F., Magenes, G., Beyer, K., Penna, A. *Shake-table test of a strengthened stone masonry building aggregate with flexible diaphragms.* International Journal of Architectural Heritage, 13(7), 1078-1097, 2019.

[3] Senaldi, I., Magenes, G., Penna, A. *Numerical investigations on the seismic response of masonry building aggregates.* In Advanced Materials Research (Vol. 133, pp. 715-720). Trans Tech Publications Ltd, 2010.

[4] Senaldi, I., Guerrini, G., Solenghi, M., Graziotti, F., Penna, A., Beyer, K. *Numerical modelling of the seismic response of a half-scale stone masonry aggregate prototype.* 127-135, XVIII convegno ANIDIS, 2019.

[5] Penna, A., Lagomarsino, S., Galasco, A. *A nonlinear macroelement model for the seismic analysis of masonry buildings.* Earthquake Engineering & Structural Dynamics, 43(2), 159 – 179, 2014.

[6] Lagomarsino, S., Penna, A., Galasco, A., Cattari, S. *TREMURI program: an equivalent frame model for the nonlinear seismic analysis of masonry buildings.* Engineering structures, 56, 1787-1799, 2013.

[7] Formisano, A., Castaldo, C., & Mazzolani, F. M. *Non-linear analysis of masonry building compounds: a comparison of numerical and theoretical results*. In Proceedings of the fourteenth international conference on civil, structural and environmental engineering computing, Civil-Comp Press, Stirlingshire, UK, Paper (Vol. 66), 2013.

[8] Formisano, A., Florio, G., Landolfo, R., Mazzolani, F. M. *Numerical calibration of an easy method for seismic behaviour assessment on large scale of masonry building aggregates*. Advances in Engineering Software, 80, 116-138, 2015.

[9] Formisano, A. *"Theoretical and Numerical Seismic Analysis of Masonry Building Aggregates: Case Studies in San Pio Delle Camere (L'Aquila, Italy)*," *J. Earthq. Eng.*, vol. 21, no. 2, pp. 227–245, 2017.

[10] Maio, R., Vicente, R., Formisano, A., Varum, H. *Seismic vulnerability of building aggregates through hybrid and indirect assessment techniques*," *Bull. Earthq. Eng.*, vol. 13, no. 10, pp. 2995–3014, 2015.

[11] McKenna, F., Fenves, G. L., Scott, M. H., Jeremic, B. *Open system for earthquake engineering simulation (OpenSees).* Univ. of California, Berkeley, CA, http://opensees.berkeley.edu, 2000.

[12] Vanin, F., Penna, A., Beyer, K. *A three-dimensional macroelement for modelling the in-plane and out-of-plane response of masonry walls*. Earthquake Engineering & Structural Dynamics, 49(14), 1365-1387, 2020.

ECCOMAS MSF 2021 THEMATIC CONFERENCE
30 June – 2 JULY 2021, SPLIT, CROATIA

OPTIMIZED CROSS-SECTIONAL ANALYSIS OF BIAXIALLY LOADED ELEMENTS

Igor Gjorgjiev[1], Borjan Petreski[2]

[1] Institute of Earthquake Engineering and Engineering Seismology, Skopje, igorg@iziis.ukim.edu.mk
[2] Institute of Earthquake Engineering and Engineering Seismology, Skopje, borjan@iziis.ukim.edu.mk

Many research studies have their focus on the different analytical and numerical methods for determining of the most accurate and efficient algorithms to compute the interaction surfaces for sections of arbitrary shape. Bonet et al. [1] have presented a comparison for different computational methods for integration of stresses within rectangular and circular sections. They demonstrated that the integration methods based on the Gauss-Legendre quadrature turn out to be very effective for computation of the axial force – bending moment interaction diagrams and optimization of the procedure results in massive decrease of the time required to design the reinforced concrete section. Furthermore, Sousa and Muniz [2] expand the analytical integration of the cross-section to more materials adding the steel and composite sections to the reinforced concrete section considered in this paper. They present a unified methodology for the sectional numerical analysis with an ability to analyse a wide range of section geometries as well as uniaxial constitutive laws.

In the design of earthquake resistant buildings in the seismic prone areas reinforced concrete walls comprised of two or more rectangular parts, such as L, T and U shapes are very common. These elements provide greater stiffness in the both directions in general but their performance under earthquake loading is more complex than that of the regular shaped rectangular shear wall components. Beyer et al. [3] show that the most critical direction in the response of shear walls possessing irregular sections is the diagonal one: For this direction of loading the maximum attained moment is less than what plastic hinge analysis would predict, while at the same time the displacement capacity is smallest.

Sfakianakis [4] proposed a new method based on the fiber model concept and pixel originated computer graphics in order to study reinforced concrete sections of various shapes and contours subjected to biaxial bending. He introduced a stable and accurate tool for cross-sectional analysis that can be used both for nonlinear analysis and design of the failure surfaces for any type of reinforced concrete cross-section including composite sections, sections with reinforced concrete jackets and sections with holes. Papanikolau [5] in his analysis of arbitrary sections in biaxial bending and axial load implements a moment-curvature response analysis of the reinforced concrete and composite sections, in conjunction with the capacity calculation through interaction curves and 3D failure surfaces. Using this improvement, not only the capacity at the ultimate limit state of the sections is assessed but information about the sections' inelastic response up to failure is provided manipulating the moment-curvature data.

In this paper particularly, a new approach regarding the analysis method of various regular and irregular reinforced concrete sections under biaxial bending and axial force is presented. Graphical interface, finite element meshing and two separate stress integration procedures along with the updatable material behavior relationships are applied in order to construct the 3D failure surface of the cross-sections. In the end, a procedure for construction and calculation of the capacity ratios and moment-curvature diagrams of the arbitrary section is presented and a comparative study is performed.

The current version of the software presented in this paper is adapted to comply with the latest Eurocode 2 draft making it operational in the countries practicing the European codes and for researchers making comparative studies with those regulations. However, using the modular programming technique that separates the functionality of the program into independent modules for the development of the software, this feature is easily adaptable for upgrade.

The construction of the failure surface for a chosen section depends on the cross section shape, the amount of the steel reinforcement, its particular distribution across the section and a certain strain state. Then, by integration of two essential boundary condition equations, the plane failure surface with the ultimate bending moment and axial force can be constructed. Repeating the integration for a chosen finite number of strain conditions, in order for the description of the entire section capacity, from pure axial compression to pure axial tension, the limit values of the corresponding bending moments and axial forces are obtained, whose graphical representation is the diagram of interaction M–N.

The cross-sectional analysis of reinforced concrete structures demands optimized plane stress/strain finite element discretization of the infinite continuum and accordingly adjusted integration methods for substantial computational efficiency. In the process of development of an effectual and proficient software for biaxial bending analysis of arbitrary cross-sections, there is a wide variety of factors such as different material properties and asymmetrical cross-sectional shapes and loads, necessitating thorough consideration. Therefore, a guaranteed-quality two-dimensional mesh generating program – Triangle, [6], is applied and the infinite continuum is discretized by the mean of Ruppert's Delaunay refinement algorithm. Triangle is a freely available C program featuring meshing by triangulation including user-specified constraints on angles and triangle areas, user-specified holes and concavities, and the economical use of exact arithmetic to improve robustness. The Delaunay refinement is a technique for generating triangular meshes suitable for the finite element method which performs excellently in practice incorporating both coarse and fine meshes.

References

[1] J. Bonet, M. Barros, M. Romero. *Comparative study of analytical and numerical algorithms for designing reinforced concrete sections under biaxial bending*, Computers & Structures, 84(31): 2184-2193, 2006.
[2] J. Sousa, C. Muniz. *Analytical integration of cross section properties for numerical analysis of reinforced concrete, steel and composite frames*. Engineering Structures, 29(4): 618-625, 2007.
[3] K. Beyer, A. Dazio, M. Priestley. *Quasi-static cyclic tests of two U-shaped reinforced concrete walls*. Journal of Earthquake Engineering, 12(7): 1023-1053, 2008.
[4] M. Sfakianakis. *Biaxial bending with axial force of reinforced, composite and repaired concrete sections of arbitrary shape by fiber model and computer graphics*. Advances in Engineering Software, 33(4): 227-242, 2002.
[5] V. Papanikolaou. *Analysis of arbitrary composite sections in biaxial bending and axial load*. Computers & Structures, 98-99: 33-54, 2012.
[6] J. Shewchuk. *Delaunay refinement algorithms for triangular mesh generation*. Computational geometry, 22(1): 21-74, 2002.

EFFECT OF NON-LINEAR BEHAVIOR OF STRUCTURAL CONNECTIONS TO GLOBAL RESPONSE OF STEEL FRAME STRUCTURE IN DYNAMICS

Ismar Imamovic[1], Esad Mesic[1] and Adnan Ibrahimbegovic[2,3]

[1]Faculty of Civil Engineering, University Sarajevo, Bosnia and Herzegovina
Patriotske lige 30, 7100 Sarajevo
[2]Université de Technologie Compiégne, Laboratoire Roberval de Mécanique, France
Rue du Dr Schweitzer, 60200 Compiègne
[3]Institut Universitaire de France

The moment-resistant steel frame is frequently used as a bearing structure, especially in seismic regions. They provide a very ductile response and a large potential to dissipate energy, which is crucial in the case of earthquakes. These characteristics provide the economical design of the structure and increase resistance with respect to the seismic security. Structural connections between beams and columns play a crucial role in the response of a steel frame structure. They can significantly change the response of the structure, sometimes up to 20%.

In this work, we study effects of non-linear connection behavior to global response of steel frame structures in dynamics. The dynamic response is crucial for quantification of structure damage during earthquakes, where the connection behavior plays important role. The study is performed by using improved numerical beam models [1, 2, 3], which are implemented in large displacement framework, including plasticity and very complex constitutive coupled plasticity-damage model for representation of connection behavior The improvement is concentrated to adding dynamic in existing models.

Throughout several numerical simulations, the effect of connections behavior is presented pointing to significant changes in global response.

References

[1] I. Imamovic, A. Ibrahimbegovic, E. Mesic. *Nonlinear kinematics Reissner's beam with combined hardening/softening elastoplasticity*, Computers and Structures, **189**, 17-20, 2017.
[2] I. Imamovic, A. Ibrahimbegovic, E. Mesic. *Coupled testing-modeling approach to ultimate state computation of steel structure with connections for statics and dynamic*, Coupled systems mechanics, **7**(5), 555-581, 2018.
[2] I. Imamovic, A. Ibrahimbegovic, E. Hajdo. *Geometrically exact initially curved Kirchhoff's planar elasto-plastic beam*, Coupled systems mechanics, 8(6)**,** 537-553, 2019.

ECCOMAS MSF 2021 THEMATIC CONFERENCE
30 June – 2 JULY 2021, SPLIT, CROATIA

COMBINED FINITE-DISCRETE ELEMENT METHOD FOR THE ANALYSIS OF THIN PLATE AND SHELL STRUCTURES

Ivana Uzelac Glavinić[1], Hrvoje Smoljanović[1], Ante Munjiza[1], Bernardin Peroš[1]

[1] Faculty of Civil Engineering, Architecture and Geodesy in Split, ivana.uzelac@gradst.hr

Thin plate and shell structures occupy a significant place in civil engineering, mainly due to aesthetic and structural advantages. Their small thickness indicates efficiency in load transfer. Curved structures, such as shells, support external loads by virtue of their geometrical form and, as a result, are stronger and stiffer compared to flat structures [1]. This efficiency is manifested by transmission of transverse loads with longitudinal stresses, thus reducing the amount of bending moment in favor of compressive and tensile stresses. Therefore, shell structures are usually subjected to transverse (flexural) and in-plane (membrane) stresses and can be classified as membrane-dominated, moment-dominated or mixed shells. On the other hand, plates are initially flat and resist transverse forces primarily by means of bending i.e. flexural stresses. It is only when maximum plate deflection increases in relation to its thickness that membrane stresses get activated.

As is well known, in certain areas small thickness becomes a weakness. In the area where we have tensile in-plane stresses full utilization of the material is possible. In the area where compressive stresses occur loss of stability must be taken into account. These losses are mostly dependent on the thickness of the structure, the thinner the structure the lower the amount of compressive stress that is allowed. This can significantly reduce the bearing capacity of the structure, which is why the loss of stability must be taken into account when designing/analyzing these kind of structures. It should be also noted that in the process of design effort should be made to place as much of the structure as possible under tensile stresses.

The analysis of thin plate and shell structures is most often performed by using available numerical methods, the reason being a number of practical engineering problems for which finding an analytical solution presents complex mathematical problem [1], [2]. Even in the cases where analytical solutions are available they refer to special, mostly axisymmetric geometries with specific load cases. Consequently, we resort to numerical methods that describe the exact solution only in discrete points (nodes), which allows the analysis to be performed while achieving satisfactory accuracy. The finite element method (FEM) has proven to be the most widespread tool [2], [3]. Within the framework of this method, it is necessary to understand the behavior of an individual finite element, which further describes the flat or curved geometry and implements the conditions of continuity between the elements together with the boundary conditions. Recent research on these structures also includes the boundary element method [4], [5], meshfree method [6], [7] and the combined finite-discrete element method [8], [9].

This paper will present the applications of the combined finite-discrete element method (FDEM) in the analysis of thin plate and shell structures. Detailed presentation of the finite element, discretization of the structure and the mechanisms for the calculation of in-plane and transverse stresses will be shown. Since FDEM uses an explicit time integration scheme (meaning there is no need for stiffness of mass matrices to be calculated) the numerical model is reduced to calculation of nodal forces based on the initial and current coordinates of finite element nodes [10]. It is also important to mention that dynamics, large deflections, geometrical non-linearity and stability are included in FDEM by default [9]. Numerical examples will be presented and discussed in order to illustrate the accuracy and application of the proposed numerical model.

References

[1] E. Ventsel, T. Krauthammer. *Thin Plates and Shells Theory, Analysis and Applications*, New York, Marcel Dekker, Inc., 2001.
[2] M. Radwańska, A. Stankiewicz, A. Wosatko, J. Pamin. *Plate and Shell Structures: Selected Analytical and Finite Element Solutions*, John Wiley & Sons Ltd, 2017.
[3] D. Chapelle, K.-J. Bathe. *The Finite Element Analysis of Shells – Fundamentals*, Springer, 2011.
[4] P.H. Wen, M.H. Aliabadi, A. Young. *A boundary element method for dynamic plate bending problems. International Journal of Solids and Structures*, 37(37), 5177-5188, 2000.
[5] J. Useche, E.L. Albuquerque. *Transient dynamic analysis of shear deformable shallow shells using the boundary element method*, Engineering Structures, 87, 1-7, 2015.
[6] H.-S. Oh, C. Davis, J.W. Jeong. *Meshfree particle methods for thin plates*, Computer Methods in Applied Mechanics and Engineering, 209-212, 156-171, 2012.
[7] L.M.J.S. Dinis, R.M. Natal Jorge, J. Belinha. *A natural neighbour meshless method with a 3D shell-like approach in the dynamic analysis of thin 3D structures*, Thin-Walled Structures, 49(1), 185-196, 2011.
[8] A. Munjiza, Z. Lei, V. Divić, P. Bernardin. Fracture and fragmentation of thin shells using the combined finite discrete element method, Internationa Journal for Numerical Methods in Engineering, 95 (6), 478–498, 2013.
[9] I. Uzelac, H. Smoljanovic, M. Batinic, B. Peroš, A. Munjiza. *A model for thin shells in the combined finite- discrete element method*, Engineering Computations, 35 (1), 377-394, 2018.
[10] A. Munjiza, *The Combined Finite-Discrete Element Method*, John Wiley & Sons Ltd, 2004.

DERIVATION MATRICES IN MECHANICS – DATA APPROACH

Ivica Kožar[1], Marina Plovanić[1], Tea Sulovsky[1]

[1] Faculty of Civil Engineering University of Rijeka, ivica.kozar@gradri.uniri.hr
[1] Faculty of Civil Engineering University of Rijeka, marina.plovanic@gradri.uniri.hr
[1] Faculty of Civil Engineering University of Rijeka, tea.sulovsky@gmail.com

Great part of mechanics is involved with derivation of some kind, e.g., differential equations. In the long history of mechanics, a lot of mathematical and numerical methods have been developed for their solution. However, today we have an additional component that strongly influences approach to the solution of problems in mechanics. Namely, existence of data allows us to use solution methods that would otherwise be inapplicable.

A significant tool towards formalization of the solution process is use of derivation matrices that reduce the derivation operation and solution of differential equations to linear algebra operations [1]. Prerequisite for application of derivation matrices is availability of data, recorded displacements or velocities or accelerations.

Derivation matrices are formulated by applying numerical methods in matrix notation, like finite difference schemes. However, it is rather difficult to control precision in those schemes, so another well-known approach is via Pade approximation, as in [1]. Here we are developing a novel formulation based on Lagrange polynomials. The main advantage of the approach is straightforward formulation, clear engineering insight into the process and (almost) arbitrary precision through choice of the interpolation order.

Let us assume quadratic function interpolation and interpolation of the function value in some point '*j*' is represented using the equation

$$p_j(x) = u_l L_l(x) + u_j L_j(x) + u_d L_d(x)$$

where '*u*'s are unknown function values in discretization points, '*L*'s are Lagrange interpolation polynomials, e.g., $L_l(x) = \prod_{i\neq l}^{i=j,d} \frac{x-x_i}{x_l-x_i}$; indices '*l*' and '*d*' represent the left and the right point in the adopted discretization scheme.

Value of the derivative in point '*j*' is $w_j(x) = p_j'(x)$ that gives the equation

$$p_j'(x) = u_l L_l'(x) + u_j L_j'(x) + u_d L_d'(x)$$

It is clear that we only have to differentiate the Lagrange polynomials, which is straightforward.

Special care should be taken at boundary points; otherwise, the precision is reduced there. In order to preserve a uniform precision, usually an extra point is added at the boundary.

The result of our procedure is the derivation matrix of the dimension [n×n], where '*n*' is the number of data points (just the data points that are relevant for our problem). The resulting matrix is singular (of rank '*n-1*') until boundary/initial conditions are introduced. However, that does not prevent us to successfully differentiate our unknown function represented with the recorded data points.

Application of derivation matrices will be presented on one-dimensional dynamic problem: determination of unknown damping of an oscillating mass where we have recorded mass displacements (positions) in time [2]. The system equation is

$$\ddot{x}(\mathrm{t}) + 2\xi\dot{x}(\mathrm{t}) + \omega^2 \mathrm{x}(\mathrm{t}) = 0$$

where $\omega = \sqrt{\frac{k}{m}}$ and ξ is damping. We have assumed homogenous equation since displacements are usually recorded after the excitation of a structure. Analytical solution is known $x(t) = x_0 A_1(\xi, t) + v_0 A_2(\xi, t)$ and x_0, v_0 are initial conditions. It is evident that the damping ξ is implicit parameter and its estimation from analytical solution is difficult. Moreover, one has to know initial conditions x_0, v_0. It will be demonstrated that with the data approach damping determination is straightforward and one does not need to know initial conditions.

Determination of unknown damping ξ could start from the force balance equation given above since even such a naive approach works well. The above equation is multiplied with derivation matrices and ξ is extracted

$$\xi + \omega^2 \mathrm{x}(\mathrm{t}) = -\frac{D_X x^T \cdot (\omega^2 x + {D_X}^2 x)}{2\omega(D_X x \cdot D_X x)}$$

Numerical example with 20 data points gives accuracy better then 2.8% and better then 0.4% for 50 data points.

Derivation matrix approach is easily applicable to a wide range of engineering problems, like those from [3] or [4]. This methodology could be extended to dynamic system with multiple degrees of freedom and adapted when velocities or accelerations are recorded instead of displacements. Additional adjustments are needed when one records a reduced set of parameters (less then one set of data for each degree of freedom). It is also possible to determine the initial conditions and damping at the same time.

Acknowledgment: This work has been supported through project HRZZ 7926 ”Separation of parameter influence in engineering modeling and parameter identification” and project KK.01.1.1.04.0056 ”Structure integrity in energy and transportation”, which is gratefully acknowledged.

References

[1] I. Kožar, N. Torić Malić. *Spectral method in realistic modelling of bridges under moving vehicles*, Engineering Structures (50), 149-157, 2013.
[2] I. Kožar. *Application of HP Prime for inverse model of linear dynamical system (in Croatian)*, Proceedings of 10th assembly of Croatian Society for Mechanics Slavonski Brod, 1-6, 2020.
[3] I. Kožar, D. Lozzi-Kožar. *Flux determination using finite elements: global vs. local calculation*, Technical Gazette (24), 247–252, 2017.
[4] I. Kožar, T. Rukavina. *The effect of material density on load rate sensitivity in nonlinear viscoelastic models*, Archive of applied mechanics (89), 873-883, 2019.

ECCOMAS MSF 2021 THEMATIC CONFERENCE
30 June – 2 JULY 2021, SPLIT, CROATIA

SIMPLE FACTOR ANALYSIS OF MEASURED DATA

Ivica Kožar[1], Danila Lozzi Kožar[2] , Neira Torić Malić[1]

[1] Faculty of Civil Engineering University of Rijeka, ivica.kozar@gradri.uniri.hr
[2] Croatian Waters - Unit Rijeka, danila.lozzikozar@voda.hr
[1] Faculty of Civil Engineering University of Rijeka, ntoric@gradri.uniri.hr

Quite often we have a lot of measurement data and would like to find some relation between them. One common task is to see whether some measured data fit into another measured data, see e.g., [1],[2] or [3]. The problem can be visualized since data could generally be presented as curves in Cartesian coordinate plane (or space in the case of 3D data). Each curve could be represented as a vector '$\boldsymbol{q}$' and a mathematical formulation of our problem is $\boldsymbol{Q} = \sum_{\boldsymbol{i=1}}^{\boldsymbol{m}} c_i \boldsymbol{q_i}$, where 'i' is one measurement, '$\boldsymbol{q}_i$' is the result of that measurement in a vector form, 'c_i' is an unknown coefficient and '$\boldsymbol{Q}$' is total result. In most cases we have measured '$\boldsymbol{Q}$', we know '$\boldsymbol{q}_i$' (from the theory of the problem we are analyzing) and would like to determine (unknown) coefficients 'c_i'. This problem could be presented in more complex variants, e.g., a constant could be added, some missing (unknown) data vector could be added to the measured summary vector, instead of constant factors 'c_i' we could have polynomials, like $\boldsymbol{Q} = \sum_{\boldsymbol{i=1}}^{\boldsymbol{m}} (c_{i0} i^2 + c_{i1} i + c_{i2}) \boldsymbol{q_i}$, etc. All of them could be solved with slightly extended version of the procedure presented in the sequel.

Solution procedure could be devised using the measurement matrix '$\boldsymbol{H}$' and reformulating the problem, so the solution is $\boldsymbol{c} = \boldsymbol{H}^{-1}\boldsymbol{Q}$, where '$\boldsymbol{H}^{-1}$' is the generalized inverse of the measurement matrix '$\boldsymbol{H}$' and '$\boldsymbol{c}$' is vector of unknown coefficients 'c_i'.

Our measurement problem often has some error involved in the measurement data, so the general formulation is $\boldsymbol{Q} = \sum_{\boldsymbol{i=1}}^{\boldsymbol{m}} (c_{i0} i^2 + c_{i1} i + c_{i2}) \boldsymbol{q_i} + \boldsymbol{q}_{error}$, where '$\boldsymbol{q}_{err}$' is the measurement error vector. We assume that terms in the error vector are *iid* (independent and identically distributed) with zero-mean distribution, i.e. $E(\boldsymbol{q}_{err}) = 0$, see [4]. In the case of rank deficiency of the measurement matrix '$\boldsymbol{H}$' we could apply some regularization technique like e.g., Tikhonov regularization (see [2]).

Error vector is not known in advance and cannot be included into the solution procedure. However, the assumption (property) that error is represented as a random filed with a stationary mean could be used to improve the procedure for recovery of unknown coefficients, based on the assumption that we could use the equality $E(\boldsymbol{q}_{err}) = 0 = \int f(x) p(x)\, dx$. In order to apply the equation we must assume the error distribution, e.g., uniform distribution [4]. Now, we could calculate the mean (for uniform distribution $E(\boldsymbol{q}_{err}) = 0 = {}^{1}/_{m} \int f(x)\, dx$ and the simplest form of our measurement equation becomes $\int \boldsymbol{Q} = \sum_{\boldsymbol{i=1}}^{\boldsymbol{m}} c_i \int \boldsymbol{q}_i + h(0)$. In practice we use numerical integration; trapezoidal scheme is as good as any other, it is only important to use the same scheme for all data vectors so that errors would cancel out.

Various numerical examples have been performed, with and without an error, and the effectiveness of the proposed method has been demonstrated. Also, we have some examples where missing data has been successfully identified.

Acknowledgment: This work has been supported through project HRZZ 7926 ”Separation of parameter influence in engineering modeling and parameter identification” and project KK.01.1.1.04.0056 ”Structure integrity in energy and transportation”, which is gratefully acknowledged.

References

[1] I. Kožar, D. Lozzi-Kožar. *Flux determination using finite elements: global vs. local calculation*, Technical Gazette (24), 247–252, 2017.
[2] D. Lozzi-Kožar, I.Kožar. *Estimation of the eddy thermal conductivity for Lake Botonega*, Engineering Review (37), 322–334, 2017.
[3] I. Kožar, D. Lozzi Kožar, Ž. Jeričević. *Limit kriging in finite element environmental modeling*, MIPRO 11, 342-345, 2011.
[4] JCGM 100:2008. *Evaluation of measurement data – Guide to the expression of uncertainty in measurement*, Joint Committee for Guides in Metrology, 2008.

ECCOMAS MSF 2021 THEMATIC CONFERENCE
30 June – 2 JULY 2021, SPLIT, CROATIA

DISCRETE LATTICE MODEL FOR NONLINEAR ANALYSIS OF REINFORCED CONCRETE STRUCTURES

Jadran Čarija[1], Mijo Nikolić[1], Željana Nikolić[1]

[1] Faculty of Civil Engineering, Architecture and Geodesy, University of Split, Split

The development of reinforced concrete structures began in the 19th century, and their expansion started in the 20th century, which continues into the 21st century. Many residential and infrastructural and energy facilities, such as bridges, power plants, dams, are built of reinforced concrete. Accurate description and representation of the fracture process in RC structures subjected to the static or dynamic loading are needed to design new and make existing buildings safer. A failure inside reinforced concrete structures occurs due to crack propagation in concrete, buckling of reinforcement and it's pulling out from concrete. For a better representation of the force transfer and fracture development within reinforced concrete structures, it is necessary to model the bond mechanisms between concrete and reinforcement obtained from the pull-out test [1,2]. Generally speaking, the bond mechanisms is an interactive mechanism that allows the force transfer between the reinforcing bars and the surrounding concrete, which ensures a composite action between the two materials. The bond mechanism has a significant impact on the formation, development and propagation of cracks in the structure, and on the ductility of the structure [3]. Therefore, modelling the bond characteristics between reinforcement and concrete is an important component in obtaining a reliable numerical model for simulating a reinforced concrete structure subjected to static and dynamic loading. Understanding and modelling the local failures in RC structures like crack propagation in concrete, plastic yielding of reinforcement and bond-slip is an important condition for maintaining or extending the service life of structures [4]. When RC structures are subjected to dynamic loading such as earthquake, the representation of the cycling opening and closing of cracks is one of the key factors for more accurate computation of energy dissipation [5]. Discrete models have the advantage in representing discontinuity over continuum models. The main advantage is in an appropriate meso-scale representation of material heterogeneities, that affects realistic simulations of crack formation, coalescence and propagation [6].

In this paper, concrete material is discretized with 2D Voronoi cells with Timoshenko beams as cohesive links between them [7,8]. Reinforcement (steel bar) is added in the discrete lattice model as Timoshenko beams, and it is positioned irrespective of the Voronoi cells. That provide us to analysis various reinforced concrete structures. Reinforcement nodes are generated at the position, where reinforcement crosses the Voronoi cells. Interaction between concrete and reinforcement is modelled with new bond elements represented in terms of Timoshenko beams. Bond elements connect Voronoi nodes (concrete nodes) and reinforcement nodes and represent bond-slip characteristic between reinforcement and concrete (Figure 1).

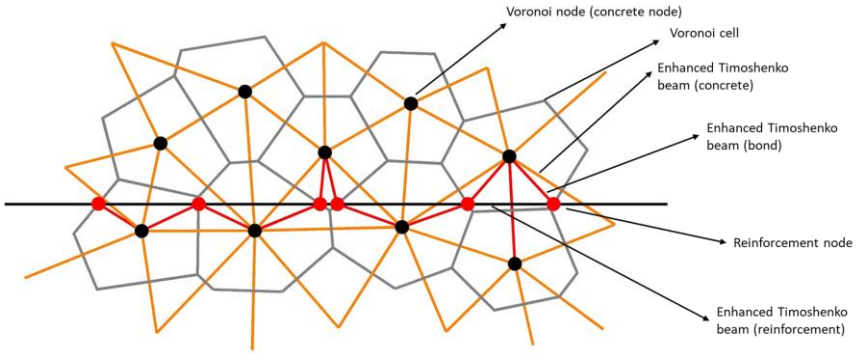

Figure 1: Discrete lattice model with Voronoi cells as particles of concrete and cohesive links between them with reinforcement elements connected to concrete elements with bond elements.

All the elements (concrete, reinforcement and bond) in this discrete model are Timoshenko beams with embedded strong discontinuity, enabling us to model crack propagation in concrete, a rupture of reinforcement, bond-slip and pulling out of reinforcement. The advantage of this model is in the realistic representation of the cracking process, and by using embedded discontinuity approach, we get mesh independent response.

Acknowledgments

This work has been supported through the project Development of numerical models for reinforced concrete and stone masonry structures under seismic loading based on discrete cracks (IP-2014-09-2319), funded by the Croatian Science Foundation, and the project KK.01.1.1.02.0027, co-financed by the Croatian Government and the European Union through the European Regional Development Fund - the Competitiveness and Cohesion Operational Programme.

References

[1] H. Ogura, M. Kunieda, H. Nakamura: *Tensile Fracture Analysis of Fiber Reinforced Cement Based Composites with Rebar Focusing on the Contribution of Bridging Forces*, Journal of Advanced Concrete Technology, 17(5), 216-231, 2019.

[2] U. Farooq, H. Nakamura, T. Miura, Y. Yamamoto: *Proposal of bond behavior simulation model by using discretized voronoi mesh for concrete and beam element for reinforcement*, Cement and Concrete Composites, 110, 103593, 2020.

[3] Lundgren K: *Bond between ribbed bars and concrete. Part 1: Modified model*, Magazine of Concrete reserch, 57(7), 371-382, 2005.

[4] Ibrahimbegovic A, Boulkertous A, Davenne L, Brancherie D: *Modelling of reinforced-concrete structures providing crack-spacing based on X-FEM, ED-FEM and novel operator split solution procedure*, International Journal for Numerical Methods in Engineering, 83(4), 452-481, 2010.

[5] Ž. Nikolić, N. Živaljić, H. Smoljanović, I. Balić: *Numerical modelling of reinforced-concrete structures under seismic loading based on the finite element method with discrete inter-element cracks*, Earthquake Engineering & Structural Dynamics, 46(1), 159-178, 2017.

[6] M. Nikolić, E. Karavelić, A. Ibrahimbegovic, P. Miscević.: *Lattice Element Models and Their Peculiarities, Archives of Computational Methods in Engineering*, Vol.25, No.3, 2018., pp. 753-784.

[7] M. Nikolić, A. Ibrahimbegovic: *Rock mechanics model capable of representing initial heterogeneities and full set of 3D failure mechanisms*, Computer Methods in Applied Mechanics and Engineering, 290, 209-227, 2015.

[8] E. Karavelić, M. Nikolić, A. Ibrahimbegovic, A. Kurtović: *Concrete mesoscale model with full set of 3D failure modes with random distribution of aggregate and cement phase. Part I: Formulation and numerical implementation*, Computer Methods in Applied Mechanics and Engineering, 344, 1051-1072, 2019.

WAVE PROPAGATION SIMULATION IN POROUS MEDIUM

Edip K.[1], Sheshov V.[2], Bojadjieva J.[3], Kitanovski T.[4] and Ivanovski D.[5]

[1] Institute of Earthquake Engineering and Engineering Seismology, Skopje, N.Macedonia, kemal@iziis.ukim.edu.mk
[2] Institute of Earthquake Engineering and Engineering Seismology, Skopje, N.Macedonia, vlatko@iziis.ukim.edu.mk
[3] Institute of Earthquake Engineering and Engineering Seismology, Skopje, N.Macedonia, jule@iziis.ukim.edu.mk
[4] Institute of Earthquake Engineering and Engineering Seismology, Skopje, N.Macedonia, tonik@iziis.ukim.edu.mk
[5] Institute of Earthquake Engineering and Engineering Seismology, Skopje, N.Macedonia, ivanovski@iziis.ukim.edu.mk

The wave propagation phenomenon in porous domains is of a great importance in the field of geotechnical earthquake engineering. In these kinds of problems, the elastic waves propagate from the interior to the exterior domain and require a special treatment at the computational level since apart from displacement in the solid state there is a p-wave which takes place in the pore water phase. In this paper, a study on implementation of multiphase finite elements is presented. The proposed algorithm is implemented in the ANSYS finite element software and tested on one-dimensional wave propagation considering both pore pressure wave propagation and displacement fields. The simulation of porous media such as soils, the behavior is governed largely by the interaction of the solid skeleton with water and/or air in the pores. Therefore, coupled problems of fluid flow and deformation of solid skeleton are considered in a detailed way.

In describing soil media, various approaches are presented in literature as given in De Boer [1]. One of the main advantages of using this particular numerical model is that the model is able to simulate distinct mechanical properties of the porous geo-materials. Simulation of different problems in porous media considering finite elements in time domain has been implemented in literature in the last years (Oettl [2], Schrefler [3], Edip [4] etc.)

In defining porous media, one of the great difficulties is to mathematically represent the phases involved. In describing these porous soil media, factors like water saturation and pore pressure have a strong impact on the load distribution. In the description of the material, the macroscopic approach has been followed in which the soil behavior is homogenized over a representative volume element. The concept of volume fraction has been used to evaluate the participation of each constituent in formulation of the equilibrium equations for each phase and to take into consideration the interaction among the phases. Following the concept of volume fractions, the entire volume consists of solid fraction Vs and pore volume Vp. Following the work of authors the finite element equations for the numerical model can be summarized as follows:

$$\begin{pmatrix} \mathbf{M} & \mathbf{0} & \mathbf{0} \\ \mathbf{M_w} & \mathbf{0} & \mathbf{0} \\ \mathbf{M_g} & \mathbf{0} & \mathbf{0} \end{pmatrix} \begin{pmatrix} \ddot{\mathbf{u}} \\ \mathbf{0} \\ \mathbf{0} \end{pmatrix} + \begin{pmatrix} \mathbf{C} & \mathbf{0} & \mathbf{0} \\ \mathbf{C_{sw}}^{\mathbf{T}} & \mathbf{P_{ww}} & \mathbf{C_{wa}} \\ \mathbf{C_{sa}}^{\mathbf{T}} & \mathbf{C_{aw}} & \mathbf{P_{aa}} \end{pmatrix} \begin{pmatrix} \dot{\mathbf{u}} \\ \dot{\bar{\mathbf{p}}}_{\mathbf{w}} \\ \dot{\bar{\mathbf{p}}}_{\mathbf{a}} \end{pmatrix} + \begin{pmatrix} \mathbf{K} & -\mathbf{C_{sw}} & -\mathbf{C_{sa}} \\ \mathbf{0} & \mathbf{H_{ww}} & \mathbf{0} \\ \mathbf{0} & \mathbf{0} & \mathbf{H_{aa}} \end{pmatrix} \begin{pmatrix} \bar{\mathbf{u}} \\ \bar{\mathbf{p}}_{\mathbf{w}} \\ \bar{\mathbf{p}}_{\mathbf{a}} \end{pmatrix} = \begin{pmatrix} \mathbf{f_u} \\ \mathbf{f_w} \\ \mathbf{f_a} \end{pmatrix} \quad (1)$$

The nodal degrees of freedom for displacement, water and air pressure are taken into consideration as **u**, $\mathbf{p_w}$ and $\mathbf{p_a}$. Their first and second time derivative of solid phase complete the system of equations. The different matrices of the system of equations describe different properties of the numerical model. The indices provide information about the nature and function of the matrix, which can be interpreted as follows. The coupling matrices **Csw**, **Csa** describe the interaction of the solid phase with water and air phases. The mutual influence of the fluids with each are represented by **Cwa**. The compressibility of the various phases and their effects on the entire media is considered by compressibility matrix **Pww**. The Permeability matrix **Hww** on the other hand, concerns the flow behaviour.

In simulation the propagation of waves in a water saturated soil column the degrees of freedom for air phase have been considered to be atmospheric enabling the simulation of soil medium as fully saturated domain. The soil column of 10m height and 0.5m width is simulated by applying a heavyside load type function of σ=1kPa. The corresponding physical properties of the soil column are given in Table 1 and correspond to the work of Shanz and Cheng [5].

Table 1. Physical properties of the soil column

E (kPa)	v	n	ρ_s (t/m^3)	ρ_w (t/m^3)	k (m^2)	η_w (kNs/m^2)	K_s (kPa)	K_w (kPa)
254424	0.3	0.48	2.7	1	$3.55\text{x}10^{-12}$	$1\text{x}10^{-6}$	$1\text{x}10^{7}$	$3.3\text{x}10^{6}$

Initially, gravity load is applied to the column while in the second load step (which has a duration of 0.3s) a sudden application of σ=1kPa at the top of the column is applied and results shown in Figure 1.

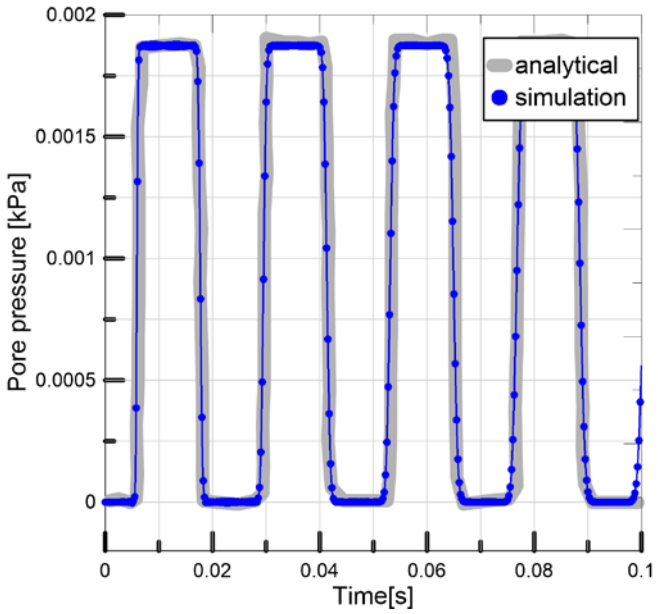

Figure 1. Evolution of pore water pressure for the bottom of the column compared to analytical solution

As can be seen from Figure 1 the results relating the evolution of pore water pressure at the bottom of the column show a satisfying agreement with the analytical solution given in the work of Shanz and Cheng [5].

On the other hand, when comparing the displacement at the top of the soil column it is seen that the numerical simulation follows the analytical solution of Shanz and Cheng [5] in a correct manner as given in Figure 2.

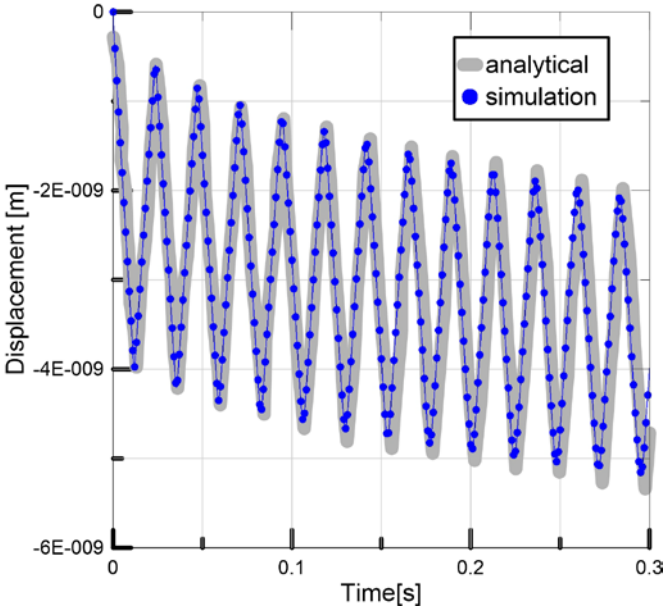

Figure 2. Evolution of displacement at the top of the column compared to analytical solution

As given in Figure 2, the displacement development in the solid phase follows a triangular scheme which reflects the wave propagation nature in the porous medium. The similarity of analytical and numerical simulation shows the correctness of the developed numerical model. In conclusion, it can be stated that the numerical simulation of porous model is essential since both deformations and pore pressures are considered simultaneously.

References

[1]. De Boer, R., *Development of porous media theories—a brief historical review.* transport in porous media, 1992. **9**(1-2): p. 155-164.
[2]. Oettl, G., R.F. Stark, and G. Hofstetter, *Numerical simulation of geotechnical problems based on a multi-phase finite element approach.* Computers and Geotechnics, 2004. **31**(8): p. 643-664.
[3]. Schrefler, B.A. and Z. Xiaoyong, *A fully coupled model for water flow and airflow in deformable porous media*. Water Resources Research, 1993. **29**(1): p. 155-167.
[4]. Edip, K., et al., *Development of coupled numerical model for simulation of multiphase soil.* Computers and Geotechnics, 2018. **96**: p. 118-131.
[5]. Schanz, M. and A.-D. Cheng, *Transient wave propagation in a one-dimensional poroelastic column.* Acta Mechanica, 2000. **145**(1-4): p. 1-18.

NUMERICAL AND EXPERIMENTAL INVESTIGATION OF RATE-DEPENDENT MODE-I DEBONDING OF ADHESIVE JOINTS

Leo Škec [1], Giulio Alfano [2]

[1] Faculty of Civil Engineering, University of Rijeka, Rijeka, Croatia, leo.skec@uniri.hr
[2] College of Engineering, Design and Physical Sciences, Brunel University, London, UK, giulio.alfano@brunel.ac.uk

Adhesive joints are nowadays widely employed to join structural parts in a variety of modern industries (aerospace, aeronautical, automotive, packaging, etc.). Their main advantages over traditional joining methods (welding and riveting) are the weight reduction, a simple way of joining different materials and an improved load transfer. Debonding or delamination is one of the most prevailing failure mechanisms in of such structural systems. Adhesives based on epoxies are also known for their visco-elastic behaviour. Therefore, rate dependence of crack propagation is important in many cases of engineering applications of adhesives.

A rate-dependent CZM, which well captures rate-dependent crack growth along rubber interfaces, has been developed in the framework of fractional-calculus based viscoelasticity [1]. Postulating the existence of a rate-independent rupture energy, associated with the rupture of bonds, a damage variable is introduced, which is assumed to evolve as a rate-independent function of part of the elastic energy. The overall rate-dependent response is retrieved by introducing additional internal variables associated with viscous dissipation.

Excellent correlation between experimental and numerical results was found for the case of a DCB made of two steel arms bonded along a rubber interface, for the entire range of the tested speeds, which spanned about 5 logatithmic decades. Further numerical simulations with the same interface parameters but over a much wider range of prescribed speeds showed that the work of separation for this case turns out to be a monotonically increasing function of the crack speed. A rheological model representing the fractional standard linear solid (FSLS) model is shown in Figure 1, where E_1 and E_2 denote the stiffness values of the springs in the elastic and inelastic arms, respectively; α and $\hat{\eta}$ denote the relative displacement and the material constant of the Scott Blair element.

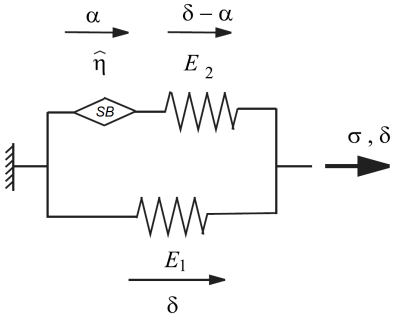

Figure 1: Rheological representation of the cohesive zone specialisation of the FSLS model.

In [2], thermodynamic and micro-mechanical arguments were used to extend the formulation to cases where the fracture energy does not increase monotonically with the crack speed, which is in better qualitative correlation with the behaviour of some glassy polymers. The presented material law is implemented in interface elements used for finite element DCB test simulations.

Due to symmetry, only one half of the specimen is modelled. The total number of degrees of freedom of the problem is further reduced with respect to the model proposed in [1] by substituting 2D solid elements with 2-noded Timoshenko beam elements. In [3] and [4] it was shown that using Timoshenko beam elements instead of 2D solid elements for DCB simulations does not result in any significant loss of accuracy and, on the other hand, makes the analysis faster and more robust. This is also a very important feature when in comes to parameter identification because the identification of the 6 parameters of the fractional CZMs proposed in [1, 2] is not a trivial task and requires the solution of a large number of 'forward' problems, which can be time consuming.

Furthermore, when the size of the cohesive zone is large relatively to the specimen dimensions, such as in the case studied in [1], the shape of the traction-separation law may have an influence on the structural response. It will be shown how such shape changes as the result of different damage evolution laws, and how the relevant parameters can be identified.

DCB tests are performed on specimens made of aluminium Al6082 T6 plates bonded with Araldite® 2015 whose dimensions are reported in Figure 2. Four logarithmic decades of cross-head speeds have been used, from 0.1 mm/min to 1000 mm/min. Rate-dependent behaviour of adhesive was clearly observed, resulting in an increase in the fracture resistance for higher speeds. Failure of the adhesive was not always cohesive; occasional interfacial failure or voids trapped inside the adhesive were noticed in all specimens, independently on the speed. This caused scatter of the results that in some cases made difficult to asses the rate-dependency of the adhesive. This was the motivation for developing a method for evaluating the actual fracture resistance of the adhesive, rather than the apparent one. This method, based on a post-mortem graphical analysis of fracture surfaces, identifies the effective area of the interface and gives an excellent estimation of the actual fracture resistance of the adhesive.

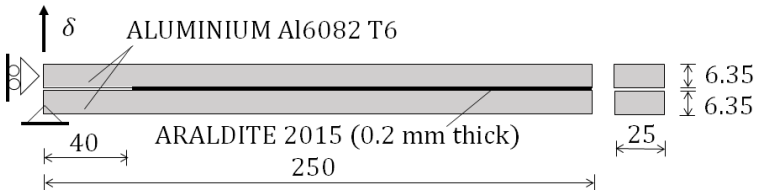

Figure 2: Geometrical and material properties of tested DCB specimens.

Experimental data is also processed using the recently proposed Enhanced Simple Beam Theory (ESBT) data reduction scheme [4] based on the concept of equivalent crack length [5]. This method does not require the measurement of the crack length, which makes it very practical and, as shown in [4], it is at least as accurate as the most accurate method from the current ASTM and ISO standards. This method also allows for a simple identification of the fracture resistance (expressed as the critical energy release rate) vs. crack speed plot. Because the model is very fast and robust, identification of parameters is made easier. Future work should include implementation or more advanced parameter-identification algorithms in order to optimise the process of finding the optimal values of the parameters.

References

[1] Musto, M. and Alfano, G., A Fractional Rate-Dependent Cohesive-Zone Model. *International Journal for Numerical Methods in Engineering*. **103**: 313-341, 2015.

[2] Alfano, G. and Musto, M., Thermodynamic Derivation and Damage Evolution for a Fractional Cohesive Zone Model. *Journal of Engineering Mechanics - ASCE*. **143**:D4017001, 2017.

[3] Škec, L., Jelenić and G., Lustig, N., Mixed-mode delamination in 2D layered beam finite elements. *International Journal for Numerical Methods in Engineering*. **104**: 767-788, 2015.

[4] Škec, L., Alfano, G. and Jelenić, Enhanced simple beam theory for characterising mode-I fracture resistance via a double cantilever beam test. *Composites Part B: Engineering*. **167**: 250-262, 2019.

[5] Škec, L., Alfano, G. and Jelenić, On G_c, J_c and the characterisation of the mode-I fracture resistance in delamination or adhesive debonding. *International Journal of Solids and Structures*. **144-145**: 100-122, 2018.

ECCOMAS MSF 2021 THEMATIC CONFERENCE
30 June – 2 JULY 2021, SPLIT, CROATIA

PULLOUT TESTS ON INJECTION ANCHORS IN RUBBLE STONE MASONRY

Maria Pia Ciocci[1,2], Serena Van Nimwegen[1], Arash Askari[1], Francesco Vanin[1], Paulo B. Lourenço[2] and Katrin Beyer[1]

[1] Earthquake Engineering and Structural Dynamics Laboratory (EESD), École Polytechnique Fédérale de Lausanne (EPFL), mariapiaciocci@gmail.com, katrin.beyer@epfl.ch (corresponding author)
[2] Institute for Sustainability and Innovation in Structural Engineering (ISISE), University of Minho, pbl@civil.uminho.pt

Unreinforced masonry (URM) buildings are one of the most seismically vulnerable building typologies, whose damage has caused significant human, cultural and economic losses during past earthquakes [1]. Efficient wall-to-diaphragm (WTD) connections are required to reduce the vulnerability of these buildings, since they represent a *sine qua non* condition to prevent the premature activation of out-of-plane overturning of facades or parts of facades [2–4].

As an intervention technique, injection anchors have been widely used for improving WTD connections. This system is typically composed of steel rods injected in masonry using a variety of materials (e.g. lime-based mortar, cement-based mortar and epoxy adhesive resin). Despite their use, little information is still available on injection anchors in masonry, especially in stonework.

Past experimental pullout tests [5–14] have shown that typical failure modes for injection anchors are: 1) cone breakout failure; 2) bond failure for slippage at the injection material-masonry interface; 3) bond failure for slippage at the injection material-rod interface; and 4) tensile failure of the steel rod. In addition, it has been shown that their performance can depend on several parameters including masonry typology and anchor's dimension and configuration.

This paper presents the quasi-static cyclic pullout tests that were performed to investigate the behavior of anchoring systems injected in stone masonry walls, when cone-breakout failure occurs. As shown in Figure 1, two different anchoring configurations were adopted, namely: anchors parallel to each other (specimen label: PA) and anchors inclined at an angle (β) of 23° in the horizontal plane (specimen label: IA). For each series, four wall specimens were tested.

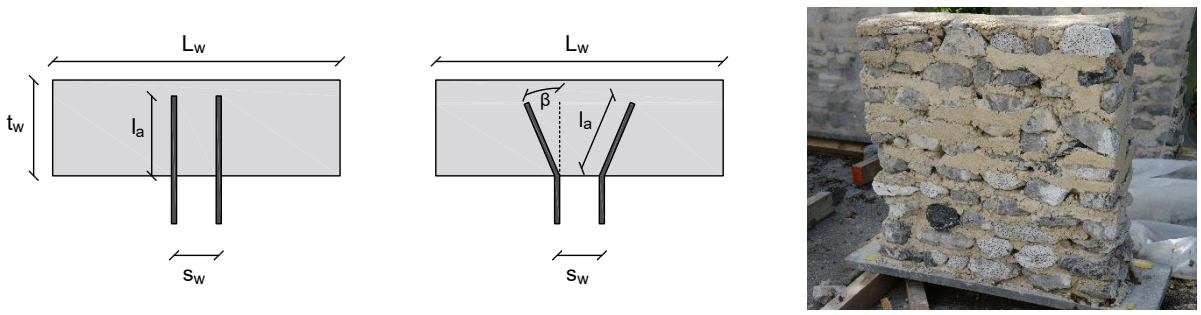

(a) (b)

Figure 1. Specimens' details: (a) anchoring configurations; (b) masonry wall.

Each specimen implemented an anchoring system that was injected in a double-leaf stone masonry wall with dimensions of 900 mm x 900 mm x 300 mm (H_w x L_w x t_w). The anchoring system consisted of a pair of steel threaded rods injected using a two-component epoxy (Hilti HIT-RE 500). For all specimens, the system was installed at mid-height of the wall, with an embedment length (l_a) of 250 mm. The rods had a diameter of 16 mm and were spaced apart by 140 mm.

The quasi-static pullout tests were performed in two phases for all specimens. Each specimen was initially subjected to a vertical stress (σ_v), and then the pullout load (F) was applied to the two steel rods simultaneously. Three levels of the vertical overburden stress were considered, namely: 0.1, 0.2 and 0.3 MPa. In addition to load cells and linear variable differential transformers (LVDTs), Digital Image Correlation (DIC) technique and optical fiber sensors were adopted in this experimental program.

For the tested specimens, the obtained force-displacement curves showed a near-linear branch before the maximum pullout force (F_{max}) was reached, with no visible damage on the wall surfaces at the peak pullout force. Afterwards, a rapid cracking propagation occurred in the masonry walls, and a significant decrease in force was observed in the post-peak behavior. Figure 2a shows the results obtained for specimen PA4. As intended, cone breakout was obtained for both specimens' series. Overlapping between the masonry cones that developed around the anchors was noted, resulting in a truncated cone-shaped block (Figure 2b).

This work investigated the influence of the adopted anchoring detail and vertical overburden stress. No significant influence in terms of maximum pullout force was observed for specimens which were tested under same value of overburden stress, independently on their anchoring detail. For an overburden stress of 0.20 MPa, the mean pullout force capacity was 54.1 kN (CoV = 5%). On the other hand, the vertical overburden stress had a stronger effect on the peak pullout force. As shown in Figure 2c, the maximum pullout force increased linearly with increasing overburden stress (R^2 = 0.88). In terms of damage, the specimens with inclined anchors showed a truncated cone-shaped block with smaller depth and larger dimensions on the wall surface when compared to PA specimens.

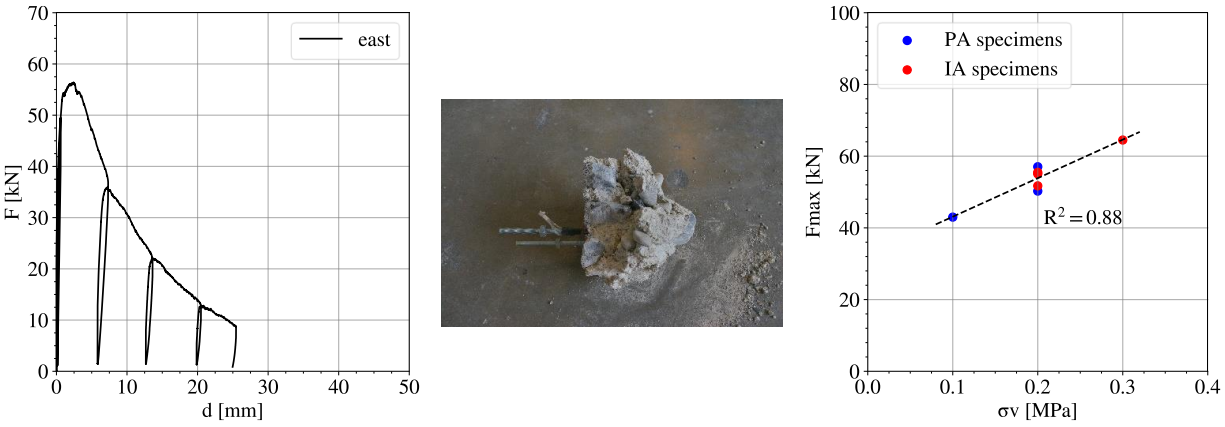

(a) (b) (c)

Figure 2. Experimental results: (a) force-displacement curve obtained for specimen PA4; (b) cone breakout failure; (c) influence of the vertical overburden stress on the peak pullout force.

References

[1] R. Spence, Saving lives in earthquakes: successes and failures in seismic protection since 1960, Bull. Earthq. Eng. 5, 139–251, 2007. https://doi.org/10.1007/s10518-006-9028-8.

[2] D.F. D'Ayala, S. Paganoni, Assessment and analysis of damage in L'Aquila historic city centre after 6th April 2009, Bull. Earthq. Eng. 9, 81–104, 2011. https://doi.org/10.1007/s10518-010-9224-4.

[3] A. Penna, P. Morandi, M. Rota, C.F. Manzini, F. da Porto, G. Magenes, Performance of masonry buildings during the Emilia 2012 earthquake, Bull. Earthq. Eng. 12, 2255–2273, 2014. https://doi.org/10.1007/s10518-013-9496-6.

[4] M. Tomaževič, Earthquake-resistant design of masonry buildings, 1st ed., Imperial College Press, London, United Kingdom, 1999.

[5] B. Gigla, Bond Strength of Injection Anchors as Supplementary Reinforcement Inside Historic Masonry, in: 13th Int. Brick Block Conf., Amsterdam, 119–128, 2004.

[6] S. Paganoni, D. D'Ayala, Testing and design procedure for corner connections of masonry heritage buildings strengthened by metallic grouted anchors, Eng. Struct. 70, 278–293, 2014. https://doi.org/10.1016/j.engstruct.2014.03.014.

[7] S. Moreira, L.F. Ramos, D. V. Oliveira, P.B. Lourenço, Experimental behavior of masonry wall-to-timber elements connections strengthened with injection anchors, Eng. Struct. 81, 98–109, 2014. https://doi.org/10.1016/j.engstruct.2014.09.034.

[8] F. Silveri, P. Riva, G. Profeta, E. Poverello, C. Algeri, Experimental Study on Injected Anchors for the Seismic Retrofit of Historical Masonry Buildings, in: F. Peña, M. Chávez (Eds.), Int. J. Archit. Herit., 2014. https://doi.org/10.1080/15583058.2015.1113333.

[9] L. Contrafatto, R. Cosenza, Behaviour of post-installed adhesive anchors in natural stone, Constr. Build. Mater. 68, 355–369, 2014. https://doi.org/10.1016/j.conbuildmat.2014.05.099.

[10] D. Dizhur, A. Schultz, J. Ingham, Pull-Out Behavior of Adhesive Connections in Unreinforced Masonry Walls, Earthq. Spectra. 32, 2357–2375, 2016. https://doi.org/10.1193/011115EQS006M.

[11] F. Silveri, P. Riva, G. Profeta, E. Poverello, C. Algeri, Experimental Study on Injected Anchors for the Seismic Retrofit of Historical Masonry Buildings, Int. J. Archit. Herit. 10, 182–203, 2016. https://doi.org/10.1080/15583058.2015.1113333.

[12] R. Muñoz, P.B. Lourenço, S. Moreira, Experimental results on mechanical behaviour of metal anchors in historic stone masonry, Constr. Build. Mater. 163, 643–655, 2018. https://doi.org/10.1016/j.conbuildmat.2017.12.090.

[13] R. Muñoz, P.B. Lourenço, Mechanical Behaviour of Metal Anchors in Historic Brick Masonry: An Experimental Approach, in: R. Aguilar (Ed.), Struct. Anal. Hist. Constr., 788–798, 2019. https://doi.org/10.1007/978-3-319-99441-3_85.

[14] L. Giresini, M.L. Puppio, F. Taddei, Experimental pull-out tests and design indications for strength anchors installed in masonry walls, Mater. Struct. 53:103, 2020. https://doi.org/10.1617/s11527-020-01536-2.

ECCOMAS MSF 2021 THEMATIC CONFERENCE
30 June – 2 JULY 2021, SPLIT, CROATIA

MULTI-HAZARD RESILIENCE ASSESSMENT OF PRESTRESSED HIGHWAY BRIDGE

Mariano Angelo Zanini[1], Lorenzo Hofer[2], Carlo Pellegrino[3], Carmelo Maiorana[4]

[1] Department of Civil, Environmental and Architectural Engineering – University of Padova (Italy)
marianoangelo.zanini@dicea.unipd.it
[2] Department of Civil, Environmental and Architectural Engineering – University of Padova (Italy)
lorenzo.hofer@dicea.unipd.it
[3] Department of Civil, Environmental and Architectural Engineering – University of Padova (Italy)
carlo.pellegrino@dicea.unipd.it
[4] Department of Civil, Environmental and Architectural Engineering – University of Padova (Italy)
carmelo.maiorana @dicea.unipd.it

Introduction

The exposure of structures to natural hazard has significant consequences on national economies and societies [1], [2], [3]. A significant example of the importance of multiple hazard effects is the 2011 Tohoku (Japan) earthquake and the resulting tsunami. During this catastrophic event, the country's rail network was strongly affected: 23 stations were washed away, tracks and bridge piers were either eroded or buried, passenger and freight trains derailed [4]. Therefore, resilience assessment of an infrastructure asset to extreme events and sequences of different hazards plays a key role on the development of suitable risk and resilience-based managing strategies. Hazard interactions and cascading effects can be classified differently, while modelling of multiple hazards is a relatively new research area [5], [6]. Scientific literature provides some examples of multi-hazard fragility curves [7], [8], [9], but very few integrated frameworks for assessing the resilience of a structure struck by multiple hazard have been treated so far [6], [10], [11]. Despite many applications of resilience analysis for residential buildings [12], industrial facilities [13] and bridges [14] subject to a single catastrophic event (mainly earthquakes) are present in scientific literature, very little theory has been developed for multiple extreme events. Therefore, this paper aims to help filling this gap by showing the impact on resilience of a flood-scoured bridge struct by a seismic event.

Case study

The case study is represented by a three span pre-stressed concrete bridge exposed to a sequence of flood and earthquake excitations. The main bridge geometrical characteristics are shown in Figure 1, further details in [10].

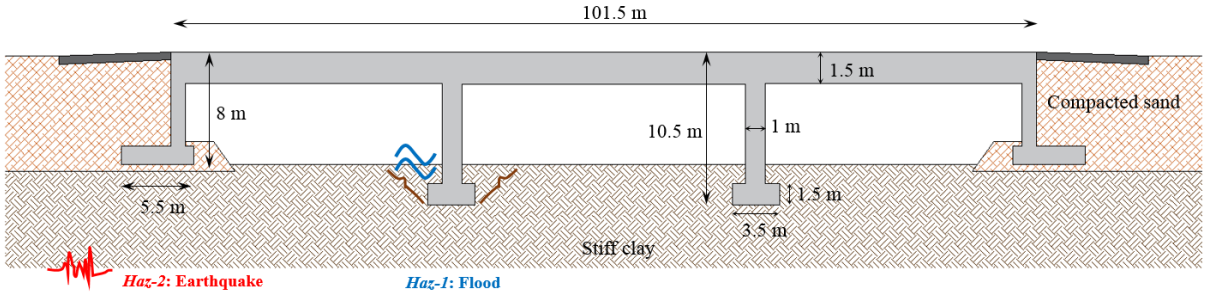

Figure 1: The bridge analyzed in the case study (adapted from [10])

Figure 2 represent the theoretical background that was implemented in this work. First the recovery curve of the bridge functionality *Q(t)* associated to the flood event (*Haz-1*) is computed according to [15]. During the recovery from *Haz-1*, a seismic event (*Haz-2*) is supposed to happen, and thus the recovery curve *Q(t)* is updated for considering the loss of functionality caused by the occurrence of the second hazard. Finally, the resilience index is computed according to [16]:

$$R = \frac{1}{t_h - t_0} \int_{t_0}^{t_h} Q(t)dt$$

where t_0 represent the occurrence of the first hazard and t_h is the time at which the complete bridge restoration is reached.

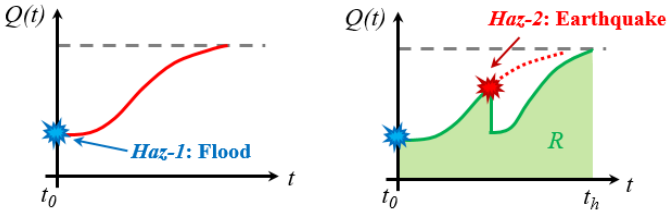

Figure 2: Theoretical background for the multi-hazard resilience assessment (adapted from [11])

Numerical models were adopted for studying the effect of the local scour on the foundation and on the entire bridge; the seismic action was added to model later, as described in [17] and [10]. Two progressive scour depths were analyzed, corresponding to $1D_f$, and $2D_f$, where D_f = 2.5m is the foundation depth. Seismic fragility analyses were performed for each scour depth, by scaling to different intensity level five real accelerometric records. The progressive structural damage was defined based on the exceedance of the cracking and yielding moments for critical sections of the deck, pier and abutment. Figure 3a represents the fragility curves for *Haz-1*, while Figure 3b and Figure 3c shows respectively the seismic fragility curves in case of scour depth equal to $1D_f$, and $2D_f$. Seismic fragility curves in case of no-scour are dotted in Figure 3b and Figure 3c. The fragility parameters for flood only are based on limited numerical analysis and contain engineering judgement for covering the particular needs of this work.

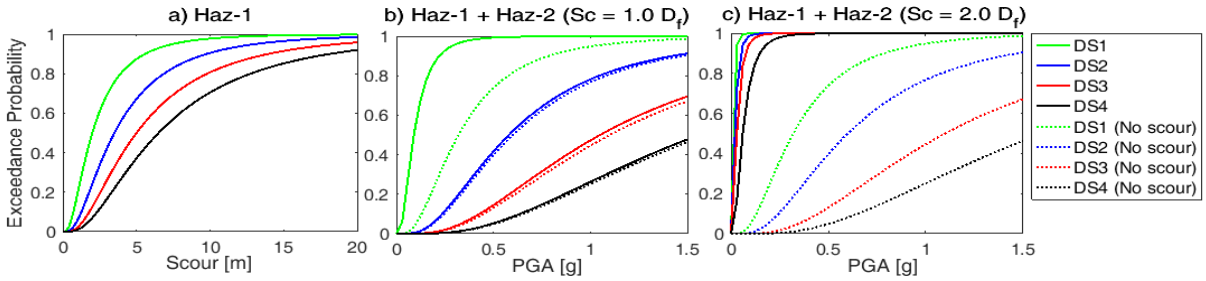

Figure 3: Fragility curves for Haz-1(a) and combined Haz-1 and Haz-2 (b-c)

Table 1 lists the parameters adopted for the restoration curves, both for the single hazard (*Haz-1*) and for the combined hazards (*Haz-1* and *Haz-2*). For the case study herein presented, *Haz-1* was assumed occurring before than *Haz-2*. The first and simplest case, is when the *Haz-2* occurs after the total recovery of the bridge from *Haz-1*; in this case the two events are totally independent and the resilience computable considering the time at which the bridge is recovered from the second hazard.
In the second case, the seismic event occurs during the recovery process from the previous flooding event. This second situation is more complex than the first, since the effect on the bridge recovery is influenced by the temporal occurrence of the seismic events. In this paper, three different specific times have been selected, corresponding on the instant in which the recovery process has reached the 5% of recovered functionality, the 50% and the 95%. The first condition represents the worst case in which there is the immediate succession of *Haz-1* and *Haz-2*, while the last situation represents the

case in which *Haz-2* occurs slightly before the total recovery from *Haz-1*. These three limit situations, are investigated by assuming two different scour levels ($1D_f$, and $2D_f$) and three peak ground acceleration (PGA) values, 0.10 g, 0.75 g, and 1.5 g.

Table 1: Parameters of the restoration function [10]

Hazard:	**Flood**			**Earthquake**		
Damage State	μ [days]	σ [days]	Idle time [days]	μ [days]	σ [days]	Idle time [days]
DS1 - Minor	7	1.4	3.5	2	0.4	1.0
DS2 - Moderate	15	3.0	6.8	7	1.4	3.2
DS3 - Extensive	30	6.0	12.0	14	2.8	5.6
DS4 - Complete	360	72.0	126.0	45	9.0	15.8

Hazard:	**Flood + Earthquake**			
Scour	*Damage State*	μ [days]	σ [days]	Idle time [days]
Sc = 1.0 D_f	*DS1 - Minor*	9	1.8	4.5
	DS2 - Moderate	14	2.8	6.7
	DS3 - Extensive	21	4.2	9.1
	DS4 - Complete	52	10.4	19.3
Sc = 2.0 D_f	*DS1 - Minor*	32	6.4	15.2
	DS2 - Moderate	37	7.4	17.6
	DS3 - Extensive	44	8.8	27.8
	DS4 - Complete	75	15	126

The bridge resilience curves have been computed according to [15] as a mean recovery weighted on each damage state probability. If *Haz-2* occurs when the recovery from the previous calamitous event is still ongoing, the bridge restoration process strictly depends on the time of occurrence. Parameters of both fragility and restoration functions, have been assumed recovering during the restoration process proportionally to the recovered functionality level. The effects on the recovery process of three ground shaking levels, occurring at three different times with scour equal to $1D_f$, are shown in Figure 5. Figure 5a shows that a minimum PGA of 0.25g g soon after the occurrence of *Haz-1*, is sufficient for dropping the bridge functionality to zero. This mainly depends on the low low post-flood initial functionality, and on the high bridge seismic vulnerability soon after *Haz-1*. In general, the effect of *Haz-2* on the recovery lowers when it occurs long time after the occurrence of the previous flood event. Figure 6 shows the second case in which earthquakes occurs after a flood event able to cause a scour equal to 2 D_f. With this second scour, a PGA = 0.25g, occurring soon after the flood event, causes a complete loss of the bridge functionality for almost 60 days. Higher levels of PGA significantly compromise the bridge functionality even when occurring for intermediate level of recovered functionality. Figure 6c shows that a PGA = 1.5 g is able to reset the bridge functionality even if occurring at the end of the recovery process from *Haz-1*.

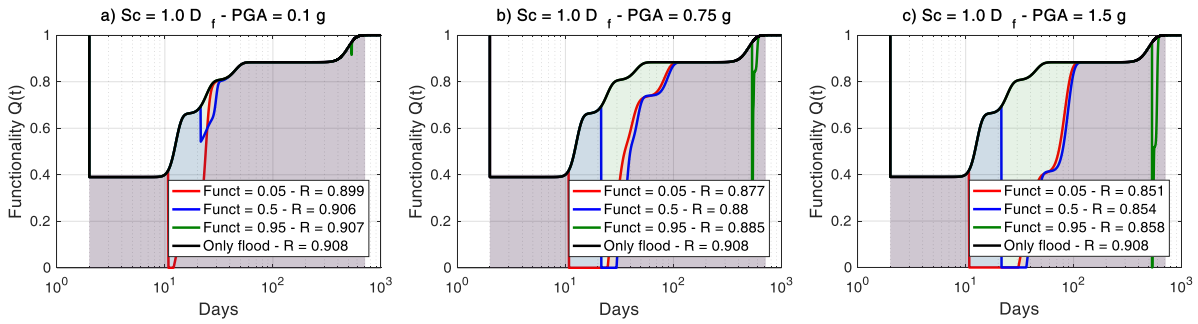

Figure 5: Restoration curves when Haz-2 occurs during the recovery after Haz-1 with Sc = 1 D_f: PGA = 0.10 g (a), PGA = 0.75 g (b) and PGA = 1.5 g (c).

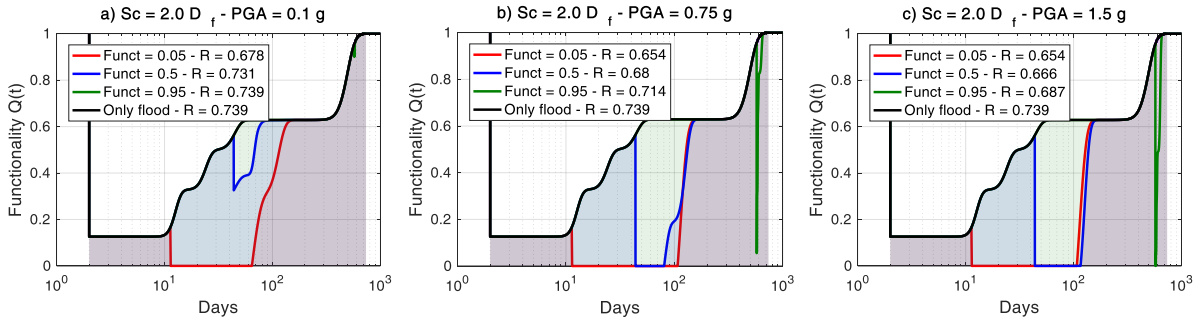

Figure 6: Restoration curves when Haz-2 occurs during the recovery after Haz-1 with Sc = 2 D_f: PGA = 0.10 g (a), PGA = 0.75 g (b) and PGA = 1.5 g (c).

Results discussion and conclusions

Figure 7 compares the values of the resilience indexes computed for all the presented cases. The cases in which *Haz-2* occurs after the complete recovery from *Haz-1*, are the less impacting situations in terms of resilience. The most critical condition is when *Haz-2* occurs soon after *Haz-1*, due to the low residual functionality and the high structural vulnerability caused by *Haz-1*. When comparing resilience of a structure subject to two possible hazards, each one influencing the other, is thus fundamental to consider all the relative occurrence times. When dealing with multiple hazards, their interaction has to be properly taken into account and the resulting effects have to be considered at each stage of the resilience assessment.

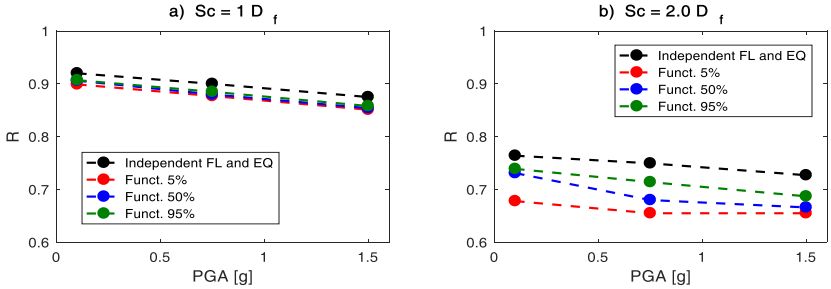

Figure 7: Resilience index comparison in case of scour equal to 1D_f (a) and 2D_f (b)

References

[1] L. Hofer, M.A. Zanini, P. Gardoni. *Risk-based catastrophe bond design for a spatially distributed portfolio*, Structural Safety, 83-101908, 2020

[2] M.A. Zanini, L. Hofer, C. Pellegrino. *A framework for assessing the seismic risk map of Italy and developing a sustainable risk reduction program*, International Journal of Disaster Risk Reduction, 3, 74-93, 2019.

[3] M.A. Zanini, C. Vianello, F. Faleschini, L. Hofer, G. Maschio, *A framework for probabilistic seismic risk assessment of NG distribution networks*, Chemical engineering transactions, 53, 163-168, 2016.

[4] E. Krausmann, A.M. Cruz, *Impact of the 11 March 2011, Great East Japan Earthquake and Tsunami on the Chemical Industry*, Natural Hazard, 67(2), 811-828, 2013.

[5] M. Bruneau, M. Barbato, J. Padgett, A.E. Zaghi, J. Mitrani-Reiser, Y. Li. (2017). *State of the art of Multihazard Design*, Journal of Structural Engineering, 143(10), pp. 03117002.

[6] I. Girdaris, J.P. Padgett, A.R. Barbosa, S. Chen. *Multiple-Hazard Fragility and Restoration Models of Highway Bridges for Regional Risk and Resilience Assessment in the United States: State-of-the-Art Review*, Journal of Structural Engineering, 143(3), 2017.

[7] P. Gehl, M. Wang, K. Taalab, D. D'Ayala, F. Medda, T. Cheng. *Use of multi-hazard fragility functions for the multi-risk assessment of road networks*, ICONHIC 2016, 28-30 June 2016, Greece.

[8] K.W. Liao, N.D. Hoang, J. Gitomarsono. *A probabilistic safety evaluation framework for Multi-hazard assessment in a bridge using SO-MARS learning model*, KSCE Journal of Civil Engineering, 22(3), 903-915.

[9] G.G. Prasad, S. Banarjee. *The Impact of Flood-Induced Scour on Seismic Fragility Characteristics of Bridges*, Journal of Earthquake Engineering, 17, 803-828, 2013.

[10] S. Argyroudis, L. Hofer, M.A. Zanini, S.A. Mitoulis, Resilience of critical infrastructure for multiple hazards: Case study on a highway bridge, ICONHIC 2019, 23-26 June 2019, Greece
[11] S. A. Argyroudis, S.A. Mitoulis, L. Hofer, M.A. Zanini, E. Tubaldi, D.M. Frangopol, *Resilience assessment framework for critical infrastructure in a multi-hazard environment: Case study on transport assets*, Science of the Total Environment, 714, 136854, 2020.
[12] A.A. Ghazanfar, Y. Dong. *Seismic resilience of retrofitted RC buildings.* Earthquake Engineering and Engineering Vibration, 19, 561–571, 2020.
[13] L. Hofer, M.A. Zanini, F. Faleschini, C. Pellegrino. *Profitability Analysis for Assessing the Optimal Seismic Retrofit Strategy of Industrial Productive Processes with Business-Interruption Consequences*. Journal of Structural Engineering, 144, 4017205, 2018.
[14] M.A. Zanini, F. Faleschini, C. Pellegrino. *Probabilistic seismic risk forecasting of aging bridge networks*, Engineering Structures, 136, 219-232, 2017.
[15] HAZUS-MH. (2011). Multi-hazard Loss Estimation Methodology: Earthquake model Hazus-MH MR5 technical manual. Federal Emergency Management Agency, Washington, DC.
[16] P. Bocchini, D.M. Frangopol. *Optimal Resilience-and Cost-Based Postdisaster Intervention Prioritization for Bridges Along a Highway Segment*, Journal of Bridge Engineering, 17(1), 117-129, 2010.
[17] S. Argyroudis, S. Mitoulis, A.M. Kaynia, M.G. Winter. *Fragility Assessment of Transportation Infrastructure Systems Subjected to Earthquakes*, Geotechnical Special Publication, 292, 174-183, 2018

ECCOMAS MSF 2021 THEMATIC CONFERENCE
30 June – 2 JULY 2021, SPLIT, CROATIA

IMPROVEMENT OF INFORMATION SYSTEM FOR BRIDGES AND RETAINING STRUCTURES WITH SEISMIC RISK ASSESSMENT

Marija Vitanova[1], Julijana Bojadjieva[2], Slobodan Micajkov[3], Vlatko Sheshov[4]

[1] Institute of Earthquake Engineering and Engineering Seismology, marijaj@iziis.ukim.edu.mk
[2] Institute of Earthquake Engineering and Engineering Seismology, jule@iziis.ukim.edu.mk
[3] Institute of Earthquake Engineering and Engineering Seismology, micajkov@iziis.ukim.edu.mk
[4] Institute of Earthquake Engineering and Engineering Seismology, vlatko@iziis.ukim.edu.mk

Abstract

Bridge and retaining structures as as a vital part of the transportation networks are usually exposed to multiple hazards, originated from different environmental and man-made sources. In the aftermath of that type of disasters, it is increasingly recognized that while their occurrence is often inevitable, proactive risk management through adequate prioritization and preventative measures ought to be of utmost importance. Regions with large infrastructure networks (e.g. roadway bridges and retaining walls) exposed to different types of hazards and structural ageing/deteriorating over time are particularly vulnerable. Such vulnerability can become even more relevant in developing countries, which can face higher challenges in coping with extreme events. This study tends to focus on the risk evaluation of the transport infrastructure. Obtaining quality information about the geometric and structural characteristics of the assets in a bridge and retaining structure inventory is fundamental to reliably estimate the physical vulnerability and potential economic losses due to natural hazards on these elements.
For that purpose, information system for seismic risk assessment had been developed in Institute of Earthquake Engineering and Engineering Seismology (IZIIS) Skopje, dealing with bridges and retaining structures as crucial parts of transport network. This system provides risk assessment and management of a static current insight into the risk at a certain time and place that is changed by the dynamics of the hazard and the dynamics of the parameters affecting the vulnerability of the structures.

Key words: information system, bridges, retaining structures, hazard, exposure, risk assessment

Introduction

In recent years, the use of large-scale assessment has become increasingly popular to evaluate the seismic risk of a specific region to an earthquake event through the compilation of hazard, exposure and vulnerability. This study tends to focus on the evaluation of the transport infrastructure, which is of great importance when determining a community's resilience to a disaster and its ability to resume normal activities.
It is important to note that generally, risk assessment system in transportation infrastructure is usually mandatory for bridges. As reported in the Guide to asset management of earth retaining structures prepared for National Cooperative Highway Research Program [4] there are thousands of Earth Retaining Structures (ERS) along U.S. highways and there is no exact number because only a few highway agencies have inventoried their ERS. Catastrophic failures of Earth Retaining Structures (ERS)

are relatively rare, but some serious incidents in recent years have called attention to the need for better management of ERS [4].
The experience of past earthquakes worldwide reveals that geotechnical structures are quite vulnerable to earthquake shaking. In addition to life and material losses, damage to roadway and railway elements (tunnels, embankments, trenches, levees, slopes, retaining walls and others) can seriously affect the transportation of people and products in both short-term (emergency actions) and long-term periods (Argyroudis et al., 2013) [5].

Obtaining quality information about the geometric and structural characteristics of the assets in a bridge and retaining structure inventory is fundamental to reliably estimate the physical vulnerability and potential economic losses due to natural hazards on these elements.
For that purpose information system for seismic risk assessment had been developed in IZIIS, dealing with bridges [1], [2], [3]. The framework is expanded by adding retaining structures in the system and is part of the investigation realized in the framework of the internal scientific project of the Institute of Earthquake Engineering and Engineering Seismology (IZIIS), Skopje, Republic of North Macedonia. The retaining structures of interest are those associated to the road infrastructure in the country, and their connection and closure to bridge structures is also taken into account.

With this goal, it is necessary to collect statistical information on the bridge and retaining wall inventory, which are collected and processed by the IZIIS team using multiple sources of data.
A thorough review of available information has been carried out, which includes inputs from open sources like OpenStreetMap (www.openstreetmap.org), as well as a more detailed account of the bridge inventory obtained from Google Street View (www.maps.google.com) photography, in addition to other local sources (e.g. national/regional databases in the three countries). Additionally, detailed information was collected by performing site inspections, thus allowing the geometry and structural configurations of representative bridges in each country to be fully characterized.
The processing of this information has led to the definition of a preliminary exposure model of existing bridges and retaining structures in Macedonian region, as well as valuable typology and geometrical information that can be used to assess the fragility of the inventory.
In order to collect the information about different bridge and retaining walls typologies, IZIIS, developed a digital collection form which generic, so that it can be used in other countries. The collection form for bidges includes information about the location, material type, deck and pier details, information on the supports and bearings in addition to general information on the current condition of the bridge with regards to damage and ageing. Retaining walls form includes data for location, structural type, height of wall, tickness, foundation height, width, soil type, slope etc. Using this data collection form, users may compile the relevant information in two ways: 1) a desktop study whereby users do not physically visit the structures but rather make use of information that may be gathered online from sources like Google Street View or OpenStreetMaps; or 2) via a full inspection by visiting the structures.
To categorize the differing levels of bridge information that may be collected for different sources, this has been divided in levels of knowledge as follows:

- Level 0: Information of the existence, location and overall length of the bridge. This information is used to determine the total amount of bridges in the inventory.
- Level 1: Basic information of the structural system and material of the bridge is known, as well as incomplete geometrical characteristics of the structural elements. This information can be used to classify the assets according to a taxonomy scheme and in some cases, derive simplified calculations on the structural behavior of the bridge.
- Level 2: Complete information of the bridge geometry is known as well as information regarding the current state of the bridge, visible damage of the structure is known and recorded. This information is usually gathered though a site inspection.

- Level 3: Information on the structural reinforcement configurations, material properties and foundation characteristics are known. This information is gathered by processing and examination of construction blueprints.

Bridges:

Initially, data was collected using OpenStreetMap to get a general idea of the overall bridge populations. Using this, the quantity and length of bridges could be identified and disaggregated at a provincial level for each case study using GIS software, and constituted the base of the bridge exposure model.

For all these types of structures, a certain number of data will be given and entered in the system. For most of these structures, detailed level 3 data are available. In addition to location and total length of the structure, these data include data on the structural system, complete geometry, foundation and reinforcement. Data on the type of soil will also be integrated in the system. This will enable considerable upgrading and improvement of the already existing information system that will represent a good basis for further activities of applicative, research, i.e., scientific character. In addition to the basic geometrical data and data on damages, the information system is anticipated to integrate data referring to the vulnerability of each structure that will be the basis for definition of the seismic risk for each individual structure. Most of the structures that will be part of the information system belong to one of the different structural typologies for which two levels of vulnerability have already been defined. For the remaining ones that are not within the elaborated typologies, assessment of vulnerability will be done for each individual structure by conducting nonlinear dynamic analyses. Finally, all relevant data in the already existing system will be harmonized. In the second phase, the hazard conditions will be implemented for each structure depending on the local soil conditions and the seismic hazard of the site.

The hazard will be defined through three parameters of expected seismic events: 1) location (where), 2. Genesis and evolution (to what extent) and 3) intensity (degree). Mapping of the hazard consists of consistent and uniform discretization of the territory of Macedonia into smaller territorial units of a size suitable for reasonable monitoring of changes of all parameters referring to the distribution and concentration of the hazard. These data are basic for the realization of the last phase.

The third phase involves activities related to risk assessment. It represents a factor that is not constant but changes in the course of time. The frame for risk assessment and management provides a static current insight into the risk at a certain time and place that is changed by the dynamics of the hazard and the dynamics of the parameters affecting the vulnerability of the structures. In this phase, assessment of the current risk for the structures included in the information system will be made.

Retaining structures:

Simplified methodology is proposed to assess the vulnerability and risk of existing retaining structures with special focus on those located on the road infrastructure. At first retaining structures with available design projects since 2013 will be assessed. The methodology can be extended further including other existing retaining structures which will be assessed by field inspections. Figure 1 represents flowchart of the suggested methodology for seismic risk assessment of retaining structures:

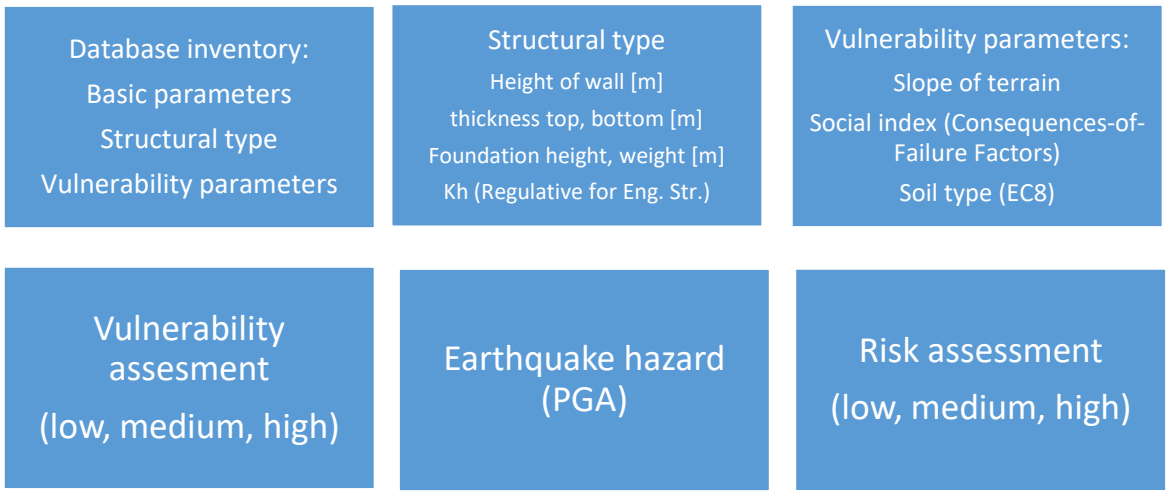

Figure 1. Proposed framework for seismic risk assessment system for retaining structures

The database inventory is consisted of 3 groups of parameters:

1) Basic parameters (name, number, coordinates, closure to bridge, road infrastructure etc.
2) Structural type and geometric characteristics of the retaining structure
3) Vulnerability parameters (slope of the terrain behind the wall, social index and soil type beneath the retaining structure according to Eurocode 8)

Based on the parameters simplified approach based on height, soil type and slope is proposed to assess the vulnerability level. The seismic hazard is defined through PGA and is divided in 3 categories. Based on the vulnerability and hazard values seismic risk assessment is defined. The simplified proposed framework is a good large scale starting point to recognize the most vulnerable retaining structures for which further detailed seismic analysis can be performed to obtain information regarding displacements, stresses and failure mechanisms and fragility curves if possible, such as given in [5].

References:

[1] Vitanova, M., Salic, R., Kemal, E., Micajkov, S., Sesov, V., Petreski, B., Zafirov, T., Dimitrovski, M., Tomic, D., Trajcevski, J., and Nanevska, A. *N. Macedonian Bridge Exposure Database and its Relation to the Seismic Hazard Estimates*, SECED2019 – Society for Earthquake and Civil Engineering Dynamics, London, UK, 2019

[2] Vitanova, M., Salic, R., Kemal, E., Micajkov, S., Sesov, V., and Petreski, B. *Safe Bridges toward an Earthquake Resilient Society, Safety Assessment of Regional Bridge Infrastructure Exposed to Seismic Hazard*, Presing - The Macedonian Chamber of certified architects and certified engineers, Vol. 46, December. 2019

[3] Sheshov, V., Vitanova, M., Salic, R., Edip, K., Micajkov, S., and Petreski, B. Safety Assessment of Bridge Structures Exposed to Earthquake Hazard, Scientific Journal of Civil Engineering, Vol. 8, No.2, 2019

[4] Brutus, O., & Tauber, G. (2009). *Guide to asset management of earth retaining structures* (pp. 1-120). US Department of Transportation, Federal Highway Administration, Office of Asset Management.

[5] Argyroudis, S., Kaynia, A. M., & Pitilakis, K. (2013). Development of fragility functions for geotechnical constructions: application to cantilever retaining walls. *Soil dynamics and earthquake engineering*, *50*, 106-116.

ECCOMAS MSF 2021 THEMATIC CONFERENCE
30 June – 2 JULY 2021, SPLIT, CROATIA

MULTYPHYSICS MODELING OF TRACER TRANSPORT IN KARST AQUIFERS

Marin Zelenika[1], Hrvoje Gotovac[2], Krste Živković[2]

[1] Hydro Power King d.o.o., Zagreb, Croatia, marin.zela@gmail.com
[2] Faculty of Civil Engineering, Architecture and Geodesy, University of Split, Croatia, hrvoje.gotovac@gradst.hr, kzivkovic@gradst.hr

Abstract

Multiphysics becomes one of the most important research multidisciplinary area because most of the unresolved problems cannot be solve using the common separate disciplines and methodologies [1]. Among others, Multiphysics problems in complex water systems including the interaction of surface and subsurface waters in karst aquifers have been already recognized as typical examples where separate analysis do not present realistic and acceptable solutions [2]. Critical points regarding the Multiphysics modelling in surface-subsurface systems are: physical formulations, coupling between surface and subsurface for flow as well as mass and energy transport, quality and properties of applied numerical techniques, resolving multiscale and multiresolution nature of these processes, solving of large problems including huge number of related equations requiring high parallel computing, related software to be able to solve such heterogenous problems and finally verification and validation of computational models.

Problem formulation and methodology

Karst flow and transport algorithms lie on the control volume methodology which enables local and global mass and/or flux conservation and fewer efforts for numerical integration in comparison to classical FEM. Karst algorithms use discrete-continuum (hybrid) approach, in which a three-dimensional subsurface matrix flow and transport is coupled with a one and two dimensional surface flow and transport. 1-D surface flow describes flow in channels, rivers or karst deep conduits. 2-D surface flow describes runoff flow over the upper surface of the domain or fracture flow in fractured (karstified) porous medium. Mathematical model for subsurface flow is described by 3-D Richards nonlinear equation which presents unsaturated flow conditions. Mathematical model for surface flow is described by shallow water equations or usually by its simpler version using the nonlinear diffusive wave equation which can describe laminar and turbulent flow as well as pressurized or free flow [2]. Mass and energy transport in both domains are described by well known advection-dispersion equation. Numerical flow karst flow model is based on Control Volume Isogeometric Analysis (CV-IGA; [2,3] which is verified under strongly controlled laboratory conditions. Tracer transport model is based on Eulerian-Lagrangian methodology [2] where advection is based on backward particle tracking, while dispersion term as well as sink-source exchange term between matrix and conduits is based on CV-IGA using the same algorithm as for flow model.

Numerical verification

All numerical algorithms is verified by extensive experimental laboratory measurements using the existing sandbox (4*2.5*2m) new Laboratory in Zrnovnica near Split. Salt and heat tracer tests are performed to verify simulations of surface-subsurface interactions in karst models. Simultaneously, we measure flow variables such as flow rates in porous matrix and channels/conduits or heads in peizometers as well as transfer of salt using multiple sensors for measuring electrical conductivity and temperatures. Additionally, rainfall station above 3-D sandbox can produce desired level of precipitation and can be useful for investigation of runoff or enhanced flow and transport in karst conduits. All measurements are obtained in real time and stored in the cluster [2].

In this paper we use conservative salt and heat tracer tests. In that case tracers are simple mixture of salt and fresh water. Since we have extensive experimental equipment for pressure and concentration – electrical conductivity, it is possible to conduct flow and salt tracer tests. However, additional proposed temperature measurements enable heat tracer tests which are complementary to the salt tracers and yield additional information about surface-subsurface interactions. Also, tracer is only heating water, relatively inexpensive experiment which enables much more data than only salt tracing. Except advection and dispersion, conduction between heat tracer water and solid phase is also important additional process which is not present for salt tracers. It means that proposed tracer tests are mutually complementary.

Conclusions

Proposed flow and tracer results yielding robust parallel 3-D adaptive and verified algorithms under the strongly controlled conditions that will give perspective to the future application of the karst flow and transport models to the more realistic catchment scale.

References

[1] Hammond, G.E., Lichtner, P.C. and R.T. Mills, Evaluating the performance of parallel subsurface simulators: An illustrative example with PFLOTRAN, Water Resources Research, 50, 208-228, doi: 10.1002/2012WR013483. (2014).
[2] Malenica, L., Gotovac, H., Kamber, G., Simunovic, S., Allu, S. and V. Divić, Groundwater flow modeling in karst aquifers: Coupling 3-D matrix and 1-D conduit flow via control volume isogeometric analysis-experimental verification with a 3-D physical model, Water, 10, 12, DOI: 10.3390/w10121787. (2018).
[3] Gotovac, H., Malenica, L., Gotovac, B. Control Volume Isogeometric Analysis for groundwater flow modeling in heterogeneous porous media, Advances in Water Resources, 148, 103838, (2021).
[4] Zheng, C., Bennett, G.D., „Applied Contaminant Transport Modeling“, 2nd Edition, John Wiley and Sons, pp. 656, ISBN: 978-0-471-38477-9, (2002).

ECCOMAS MSF 2021 THEMATIC CONFERENCE
30 June – 2 JULY 2021, SPLIT, CROATIA

THE RESILIENCE AND DURABILITY OF EXISTING MASONRY STRUCTURES

Naida Ademovic[1], Adnan Ibrahimbegovic[2]

[1] Faculty of Civil Engineering in Sarajevo, University of Sarajevo, naidadem@yahoo.com
[2] UT Compiegne – Sorbonne Univ. & Institut Universitaire de France, adnan.ibrahimbegovic@utc.fr

Abstract Unreinforced masonry (URM) is the most widespread buildings throughout the world. Deterioration of these structures due to different atmospheric and mechanical actions is inevitable. The need for prolonging the life of the existing buildings has highly increased the need for their repair, rehabilitation, and strengthening. This is especially true in the developed countries due to the existence of numerous structured built before more than 100 years. Most of the masonry structures that were built after the 1950s did not take durability issues into the consideration. The issue of durability and sustainability has been raised in the last centuries for buildings made of different materials as well as masonry structures. The elements that are more exposed to the environmental and mechanical actions are the ones having direct contact with the environmental impacts (external walls, veneer walls, façades, etc.). The paper gives examples of durability and integrity issues in masonry structures and possibilities of their repair with the goal to extend the service life of existing masonry structures.

Keywords: durability, integrity, masonry structures, deterioration, repair

Introduction

Unreinforced masonry structures represent the largest building stock in the entire world, up to 70 % [1]. One may argue that massive construction of the building started with masonry, from low-raised, mid-raised to high raised structures. Throughout their long life, these structures have been exposed to various atmospheric and mechanical actions. Throughout this time masonry structures were exposed to various environmental effects (wind, high temperatures, rain, and snow) and manmade hazards. Of course, deterioration of masonry as a construction material is inevitable, however, due to the existence of masonry structures for several centuries, it may be argued that clay masonry structures are the most durable structures of all.

Cooper [2] defined durability as the "*ability of a product to perform its required function over a lengthy period under normal conditions of use without excessive expenditure on maintenance or repair*". Taking this definition into account it is evident that the durability of masonry structures (herein referring to clay brick) depends on the properties of the final product which characteristics are dependent on the quality of the raw material and production procedure. Once the structure is constructed, the brick is exposed to various actions, and the durability will highly depend on the protection and maintenance of the structure, and finally on the rehabilitation measures.

Masonry as a material is prone to deterioration and this is a process that cannot be stopped, however with the application of adequate measures it can be slowed down and prolonged. The causes of material deterioration can be of various nature. Masonry structures could be damaged due to the effect of various extreme loads (earthquakes, fires, etc.) [3]. Most of the masonry structures as they have been build many centuries before were constructed under empirical rules, as there were no seismic codes at that time. This indicated that the seismic actions were not taken into account, which as a result showed their

deficiencies under earthquake actions. According to [4], the lack of maintenance has been identified as one of the major causes of deterioration.

Choice of building material and constructive element for retrofit procedures

Due to the large variation of masonry structures and different typologies strengthening measures for one type of masonry construction may not apply to another one. Most of the investigation of the strengthening/retrofitting procedures were done on individual elements (walls, wallets, columns), so it can not be stated with a high degree of certainty how would a retrofitted structure behave as a whole once exposed to different actions. Together with experimental simulations, numerical modeling has been conducted, which has been identified as a rather powerful tool. However, what is the current state of the structure's components, what is the current stress state, what is the level of material deterioration, etc.? The data regarding these issues is unknown so assumptions are made. How good are the assumptions remains an unanswered question?

To maintain its integrity, it is necessary to conduct some kind of strengthening/retrofitting measures. The integrity of the structure can be seen as "*the state of being whole and undivided*". This means that the structure exposed to different natural and manmade hazards will perform adequately without failure. One of the measures proposed in Eurocode 8 for obtaining the integrity of masonry structures is the construction of vertical and horizontal confining elements so that the structure has a "box" effect. However, this may not be easy to conduct on existing structures on one hand, and on the other hand, it has to be economically feasible. Changing the seismic behavior of the structure may be even counter-effective, as a hammering effect may be obtained. As a result of "hybrid behavior", the out-of-plane actions are noted [5]. In historic masonry structures tie bars are very often used to increase their integrity. The increase in strength and ductility can be obtained by the application of vertical ties [6].

One needs to keep in mind that most of the masonry structures are older than 70 years so, in that respect, most of them can be treated as historic structures. For adequate strengthening of existing masonry structures, comprehensive knowledge of the structure, mechanical properties of its material, as well as conditions of usage has to be known. Historic structures should be preserved as much as possible with the application of strengthening procedures that are to be least invasive and strengthening materials should respect the aspect of the origin of the material and authentic documents [7]. In the last years, there has been a massive production and usage of different Fibre Reinforced Polymers (FRPs) as strengthening measures of existing masonry structures. However, several cons have been identified regarding the usage of organic resin, poor behavior of epoxy resins at temperatures above the glass transition temperature, costly repair, and probable threats for the manual workers [8]. Additionally, water-vapor permeability is prevented by the application of the epoxy resin, which is a major issue in existing old masonry structures. In the last years, the FRP has been replaced by the application of different Textile-Reinforced Mortar technique (TRM) which has been identified as beneficial in respect to out-of-plane failure as well reduction of in-plane damage and prevention of brittle failure. In terms of strength increase, the application of TRM is 65-70% effective in comparison with the FRP, however, deformability characteristics are much more effective [9].

Adequate reparations and retrofits of the external walls and construction of secondary structures can extend the life expectancy of masonry structures. The environmental factors like rain, snow, thaw and freezing effects, temperature change, etc., have an important impact on the durability, affecting physical and mechanical properties of masonry, and consequently impacting the strength and carrying capacity of structures. The material deterioration is caused by degradation processes which are usually related to moisture effects, which will decrease the performance level and consequently impact the service life of the structure.

Effects of the wind-driven rain

March [10] stated "*All buildings, whatever shortcomings they may have, are required to possess two fundamental characteristics. They should be structurally sound and they should exclude moisture.*" Simultaneous occurrence of wind and rain results in wind-driven rain (WDR). The wind-driven rain (WDR) and rainwater runoff are important features that greatly influence the durability of the façades of masonry buildings. Usually, the wind gives the horizontal velocity component to the WDR, the rain falls under an angle and is driven against the windward façade of the building [11].

The durability of the masonry façades is mostly affected by wind-driven rain [11, 12]. The concentration of moisture can have different degradation effects on masonry structures, from rain penetration [13-15], degradation of material and its components due to biological and chemical effects, structural cracking caused by moisture and thermal gradients, etc. [15]. The problem of rain penetration can be found in loadbearing and non-load bearing walls. Matthews et al. [16] in their research concluded that 33% of all buildings deteriorated to an unacceptable level before the end of their design life. This problem is still vivid in the construction of modern masonry buildings mainly due to the inadequate architectural design which lacks required façade detailings with cornices, parapets, etc. all to obtain smooth building façades. To understand the effect of the WDR on the façade, it is necessary to investigate the impinging effect of the WDR on the wall before the raindrop impact and the response of the building once the raindrop hits the façade wall (Figure 1.).

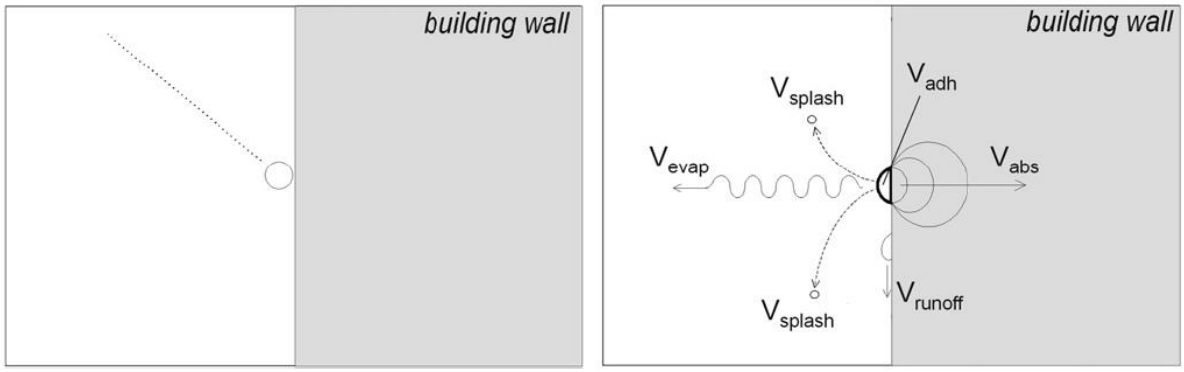

a) b)

Figure 1. Schematic representation of the WDR research [17] a) before raindrop impact; b) after raindrop impact

The volume of the impinging raindrop consists of several parts. Depending on the material characteristic some part of the raindrops can be absorbed if the material is porous as well as depending on the roughness of the façade a part can be trapped by adhesion. On the other hand, a part of the drops can be lost due to splashing and evaporation. If during splashing drops are merged they may form a film. As the thickness of the film increases, this will cause that the gravity forces become larger than the tension forces, enabling the film to run down the façade. So, the total volume of impinging raindrops can be represented by an equation (1):

$$V_{drop} = V_{adh} + V_{abs} + V_{splash} + V_{evap} + V_{runoff} \quad (1)$$

The interaction of the WDR and the building façades can be divided into two parts. The first part (Figure 1 a)) considers the assessment of the impinging WDR intensity, and once the drop hits the façade the response of the building is assessed. This is a very complex process which depends on numerous factors, from building geometry, type, details on the façade, location of the building in the environment, and on the other hand, characteristics of the rain parameters have to be accounted for (raindrop-size distribution, the intensity of rain, direction, and speed of wind). Briggen et al. [15] conducted a numerical simulation, full-scale validation, and sensitivity analysis of the WDR on the façade of a monumental tower. Blocken and Carmeliet [17] presented a simplified numerical model for rainwater runoff on building façades.
The data at the weather stations that is measured is the wind speed, wind direction, and horizontal rainfall. Measurement of the WDR is usually not done. Thought out the experimental investigations it was concluded that the WDR increases approximately proportionally with wind speed and amount of horizontal rainfall. Hoppestad (1955) developed the WDR index and the WDR relationship, which were the basis for the development of all semi-empirical models. Semi-empirical models provide only rough estimates of the probable quantity of WDR on the façade. To determine the spatial and temporal wind-driven-rain exposure different numerical methods have been developed, however, this is a time and computer-consuming process [18-23].

A simplified solution is presented by the Nusselt solution with its assumptions is applied for a thin film flow of an isothermal Newtonian liquid having constant density and kinematic viscosity due to gravity. The flow is regarded as laminar and there is no spatial change of the film thickness. The air friction on the liquid surface is not taken into account and air is pure without any contaminants. Neglection of the spanwise gradients reduced the problem to 2D, and the streamwise velocity can be presented by an equation (2), as defined in [17] and shown in Figure 2:

$$u(y) = \frac{g_r}{2\upsilon} sin\beta(2h_N y - y^2) \tag{2}$$

where: y – is the transverse coordinate; g_r – is the gravitational acceleration; υ – is the kinematic viscosity; h – is the film thickness-

The film flow rate is defined as per equation (3):

$$q_N = \frac{g_r h_N^3}{3\upsilon} sin\beta \tag{3}$$

and consequently, the average velocity is given by equation (4):

$$u_N = \frac{g_r h_N^2}{3\upsilon} sin\beta \tag{4}$$

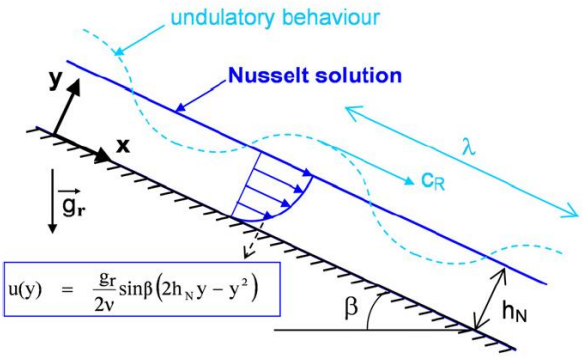

Figure 2. Runoff of a thin film down a wall at an angle [17]

Due to a very large number of parameters and their interaction various solutions are possible. Even though the Nusselt solution was adopted for both statically-steady and transient flow a good quantitative and qualitative agreement in terms of runoff flow rates was obtained once numerical and measured values were compared.

Inadequate attention to detail can cause material degradation and have a direct impact on the durability of masonry structures. The effect of the wind-driven rain can be identified in numerous examples, especially in the application of inadequate sill solution as shown in Figure 3 a) and installation of air-conditioning systems, as shown in Figure 3 b).


Figure 3. a) Inadequate sill solution on a masonry structure (https://pxhere.com/en/photo/779893); b) inadequate air-conditioning

Conclusion

Existing masonry structures make up 70% of the entire building stock in the world. The majority of the masonry buildings that were built before the II World War did not consider the component of durability. External masonry walls are exposed to various atmospheric and mechanical actions. One of the elements which has a major impact on the external masonry walls is the wind-driven rain which can be partly absorbed and trapped by the wall itself, partly evaporated and splashed, and some raindrops if amalgamated can form films that with the increase of thickness will run down the façade affecting the durability of the masonry wall. Attention to detailing in the construction of new masonry buildings is very important especially in the areas prone to high driving rain. Adoption of architectural and secondary structures is of essential importance to minimize the saturation of water and increase the durability of the masonry structure.

References

[1] Matthys, H. and Noland, L. *Strengthening and retrofitting masonry buildings, A*n international seminar on evaluation, TMS: Colorado, USA, 1989.

[2] Cooper, T. *Beyond Recycling: The Longer Life Option*, The New Economics Foundation, London, 1994.

[3] Ibrahimbegovic, A. and Ademović, N. *Dynamics of Structures Under Extreme Transient Loads*, 1st Edition, CRC Press, Taylor & Francis Group, LLC, 2019.

[4] Binda, L., Baronio, G., Anti, L. and Anzani, A. *Measurement of the rate of deterioration of masonry materials and of conservation treatments*, British Masonry Society 4, 1990.

[5] Ademović, N. *Earthquakes as Natural Disasters and their Effects on Cultural Heritage Buildings*, Cities and Cultural Landscapes, edited by Greg Bailey, Francesco Defilippis, Azra Korjenic and Amir Čaušević, 77–97, Cambridge Press, 2020.

[6] Binda, L., Saisi, A. and Tiraboschi, C. *Investigation procedures for the diagnosis of historic masonries*, Construction Building Materials, 14(4), 199–233, 2000.

[7] Charter of Venice, *International charter for the conservation and restoration of monuments and sites. Decision and resolutions*, ICOMOS, Paris, 1964.

[8] Corradi, M., Osofero, A.I., Borri, A. and Castori, G. *Strengthening of Historic Masonry Structures with Composite Materials*, Handbook of Research on Seismic Assessment and Rehabilitation of Historic Structures (2 Volumes), IGI Global, Editors: Panagiotis G. Asteris, Vagelis Plevris, 2015.

[9] Papanicolaou, C. G., Triantafillou, T. C., Kyriakos, K. and Papathanasiou, M. *Textile-reinforced mortar (TRM) versus FRP as strengthening material of URM walls: in-plane cyclic loading*, Materials and Structures, 40(10), 1081–1097, 2007.

[10] Marsh, P. *Air and rain penetration of buildings*. The Construction Press Ltd., Lancaster, England, 1977.

[11] Blocken, B. and Carmeliet, J. *A review of wind-driven rain research in building science*, Journal of Wind Engineering and Industrial Aerodynamics, 92(13), 1079–1130, 2004.
[12] Franke, L. and Schumann, I. *Damage atlas: classification and analyses of damage patterns found in brick masonry*, European Commission Research report nr. 8, vol. 2, Fraunhofer IRB Verlag, 1998.
[13] Newman, A.J., Whiteside, D., Kloss, P.B., and Willis, W. *Full-scale water penetration tests on twelve cavity fills - Part I. Nine retrofit fills*. Building and Environment, 17(3), 175–191, 1982.
[14] Newman, A.J., Whiteside, D. and Kloss, P.B. *Full-scale water penetration tests on twelve cavity fills - Part II. Three built-in fills*. Building and Environment, 17(3), 193–207, 1982.
[15] Briggen, P.M., Blocken, B. and Schellen, H.L. *Wind-driven rain on the facade of a monumental tower: numerical simulation, full-scale validation and sensitivity analysis*, Building and Environment, 44(8), 1675–1690, 2009.
[16] Matthews, R.S., Bury, M.R.C. and Redfearn, D. *Investigation of dynamic water penetration tests for curtain walling*, Journal of Wind Engineering and Industrial Aerodynamics, 60, 1–16, 1996.
[17] Blocken, B. and Carmeliet, J. *A simplified numerical model for rainwater runoff on building facades: Possibilities and limitations*, Building and Environment, 54 59–73, 2012.
[18] Blocken, B., Desadeleer, W. and Carmeliet, J. *Wind, rain and the building envelope: studies at the Laboratory of Building Physics*, 6th Symposium on Building Physics in the Nordic Countries, Trondheim, Norway, June 17–19, 579–586, 2002.
[19] Nespor, V. and Sevruk, B. *Estimation of wind-induced error of rainfall gauge measurements using a numerical simulation*, Journal of Atmospheric and Oceanic Technology, 16, 450–464, 1999.
[20] Choi, E.C.C. *Numerical modeling of gust effect on wind-driven rain*, Journal of Wind Engineering and Industrial Aerodynamics, 107–116, 1997.
[21] Sankaran, R. and Paterson, D.A. *Computation of rain falling on a tall rectangular building*, Journal of Wind Engineering and Industrial Aerodynamics, 72, 127–136, 1997.
[22] Blocken, B. and Carmeliet, J. *Driving rain on building envelopes—I: numerical estimation and full-scale experimental verification*, Journal of Thermal Envelope and Building Science, 24(1), 61–85, 2000.
[23] Segersson, D. *Numerical quantification of driving rain on buildings, Reports Meteorology and Climatology*, No. 103, Swedish Meteorological and Hydrological Institute (SMHI), 2003.

SEDIMENT TRANSPORT EQUATION ASSESSMENT FOR SELECTED RIVERS

Nerma Lazović[1], Emina Hadžić[2], Haris Kalajdžisalihović[3]

[1] Faculty of Civil Engineering, University of Sarajevo, nerma.lazovic@gf.unsa.ba
[2] Faculty of Civil Engineering, University of Sarajevo, emina_hadzic@gf.unsa.ba
[3] Faculty of Civil Engineering, University of Sarajevo, haris.kalajdzi@gmail.com

Abstract. The paper presents and analyzes experimental data including suspended load, bed load, bed material and flow discharge at three study sites at Bosna River and Željeznica River in Bosnia and Herzegovina. The sediment transport equation assessments have been carried out using Ackers-White, England-Hansen, Laursen-Copeland, Meyer, Peter - Muller and Yang.
To evaluate the accuracy of the computed and measured values, a discrepancy ratio (r) has been used, defined as: r = q (computed) / q (measured).

1. Introduction and Motivation

The flow of water and sediments in rivers are inseparable processes and together with the riverbed they form a dynamic morphological system of watercourses.
The issue of river sediment is very topical today, which confirms the inclusion of river sediment issues in European legislation such as the EU Water Framework Directive (WFD) and EU Floods Directive (FD).
According to the WFD, each river basin must have its own River Basin Management Plan (RBMP), which is updated every six years, and which, among other things, should regulate various issues related to river sediment.
In Bosnia and Herzegovina, systematic monitoring of sediments has never been carried out on any watercourse. Most often, for the needs of hydro-energy facilities and reservoirs, short-term sporadic measurements and calculations were performed. The decision and the Modernization Program of the basic network of hydrometeorological stations in B&H from 1986, provided for the establishment of sediment monitoring on nine profiles of the main tributaries of the Sava River, as well as several (together with Croatia) on its main course. However, the realization of this program never took place.

2. Background theory and Equations

There are a large number of theoretical and empirical equations for estimating the sediment transport, which is a reflection of the complexity of the phenomenon and the inability to accurately describe it analytically.
From a conceptual point of view, the equations for calculating sediment transport are based on: (i) the use of boundary condition parameters - critical velocity or stress; (ii) direct assessment of the

concentration of the sediment in the moving bed; (iii) consideration of river energy relations; (iv) considering the stochastic nature of the process.
In this paper, the sediment transport equation assessments have been carried out using Ackers-White, England-Hansen, Laursen-Copeland, Meyer, Peter - Muller and Yang.

Method	**Equatation for calculation**	**Input data**
ACKERS-WHITE (1973)	$D_* = \left[\frac{(s-1)g}{\nu^2}\right]^{1/3} d_{35}$ $F_{gr} = \frac{u_*^n}{\sqrt{gd_{35}(s-1)}}\left[\frac{V}{\sqrt{32}\log\left(\frac{10h}{d_{35}}\right)}\right]^{1-n}$ $G_{gr} = c(\frac{F_{gr}}{A} - 1)^m$, $q_s = G_{gr}\nu d_{35}\left(\frac{V}{u_*}\right)^n$	d_{35}- representative particle diameter (m) h – water depth (m) ν- kinematic viscosity coefficient (m^2/s), u_*- shear velocity (m/s) V- mean velocity (m/s) s - specific density (ρ_n/ρ)
ENGLAND-HANSEN (1967)	$\varphi = \frac{q_s}{\sqrt{(s-1)gd_{50}^3}}$, $\theta = \frac{u_*^2}{(s-1)gd_{50}}$ $q_s = \frac{0.05V^5}{(s-1)^2 g^{0.5} d_{50} C^3}$	V- mean velocity (m/s), C- Chezy's koeficient ($m^{1/2}/s$) u_*- shear velocity (m/s) d_{50}- mean partlice diameter (m) s - specific density (ρ_n/ρ)
LAURSEN-COPELAND (1958)	$C_m = 0.01\gamma\left(\frac{d_s}{D}\right)^{7/6}\left(\frac{\tau_o'}{\tau_c} - 1\right) f\left(\frac{u_*}{\omega}\right)$	d_s - mean partlice diameter (m) D - depth (m), u_* - shear velocity (m/s), ω – velocity of deposition (m/s)
MEYER, PETER - MULLER (1948)	$q_{vm} = c_{mp}(\tau_o - \tau_{oc})^{3/2}$, $c_{mp} = \frac{a^{-3/2}}{g\cdot\sqrt{\rho}}\left(\frac{\rho_s}{\rho_s - \rho}\right)$ $\tau_{oc} = \theta_c \cdot g(\rho_s - \rho)d$	d - mean partlice diameter (m), τ_o – shear stress (Pa), τ_{oc} - critical shear stress (Pa)
YANG (1973)	$\log c_t = I + J\log\left(\frac{VS - V_{cr}S}{w_s}\right)$ $I = 5{,}435 - 0{,}286\log\left(\frac{w_s d_{50}}{\vartheta}\right) - 0{,}457\log\left(\frac{u_*}{w_s}\right)$ $J = 1{,}799 - 0{,}409\log\left(\frac{w_s d_{50}}{\vartheta}\right) - 0{,}314\log\left(\frac{u_*}{w_s}\right)$	V – mean velocity (m/s), V_{cr} – critical velocity (m/s), h - water depth (m), S – fall of riverbed, w_s - velocity of deposition (m/s), u_* - shear velocity (m/s), d_{50} - mean partlice diameter (m),

3. Experimental data

Field measurements were obtained along the selected cross section at Željeznica river (cross section – Vojkovići bridge) and Bosna River (cross section 1 – Maglaj bridge; cross section 2 – B.Šamac bridge).

a) Maglaj (Bosna river) b) B.Šamac (Bosna river) c) Vojkovići (Željeznica river)

A range of flow discharge measurement covering low and high regime is carried out by using current meter (type 2030R). Suspended load samples have been collected at each study site using sampler in accordance with the ISO 5667-1:2009 and ISO 5667-12:2017 standards. Bed load sample had been measured by using sampler (Fig. 1).

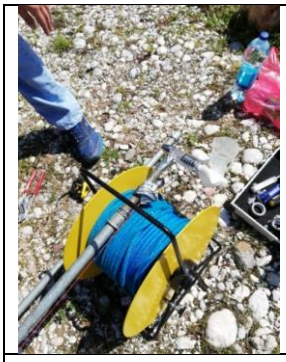

a) Current meter

b) Suspended load sampler

c) Bedload sampler

Fig. 1 – Field measurements equipment

Tab. 1 – Results field measurements

River	Date of measurement	Flow Q (m^3/s)	Cs (mg/l)	Depth (m)	Velocity (m/s)	Sediment transport Qs (kg/s)
Bosna (Maglaj)	03.01.2018.	123,42	60,19	1,12	0,94	7,43
	28.03.2018.	212,66	50,42	1,35	1,37	10,72
	29.06.2018.	231,38	531,89	1,64	1,25	123,07
	18.09.2018.	41,89	49,69	0,42	1,00	2,08
Bosna (Šamac)	27.12.2017.	1134,31	10,60	5,78	1,63	12,02
	27.03.2018.	378,17	20,90	8,09	0,39	7,90
	28.06.2018.	161,61	65,10	1,85	0,72	10,52
	17.09.2018.	75,69	67,95	1,10	0,57	5,14
Željeznica	17.05.2019.	17,42	29,98	0,71	1,10	0.52

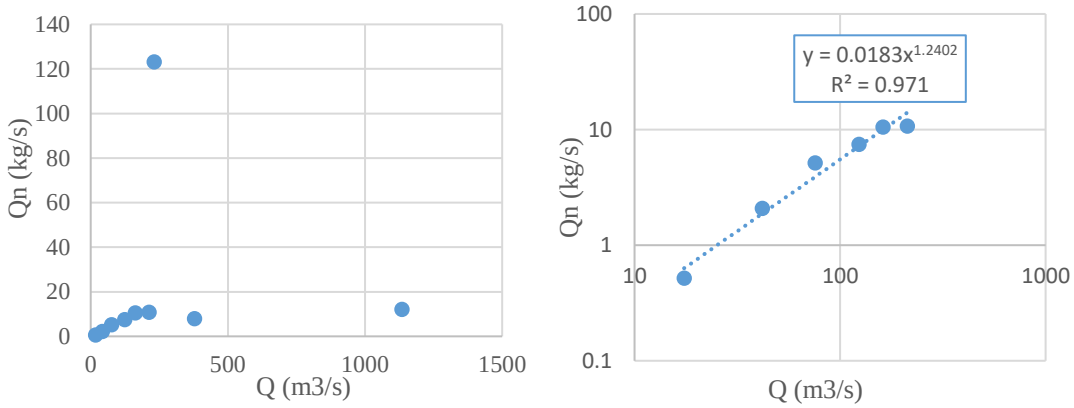

Fig. 2 – Sediment Transport Rating Curve

For all profiles and hydraulic conditions, sediment transport was calculated using the above analytical expressions.

To evaluate the accuracy of the computed and measured values, a discrepancy ratio (r) has been used, defined as: r = q (computed) / q (measured).

References

[1] Jovanović M. *Regulacija reka – rečna hidraulika I morfologija*, Građevinski fakultet Beograd, 2002.
[2] Zavod za vodoprivredu BiH. *Studija transporta riječnog sedimenta - Pilot projekat donji tok rijeke Bosne*, 2018.
[3] Chang C.T., et al. *Sediment Transport Equation Assessment for Selected Rivers in Malaysia*, Rivers'04 - 1st International Conference on Managing Rivers in the 21st Century: Issues & Challenges, 2004.
[4] Lazović N., Hadžić E. *Testing the sensitivity of the riverbed deformation model for changing the basic input parameters*, "ECCOMAS MSF 2019 – Multi-scale Computational Methods for Solids and Fluids", Univ.Sarajevo, 2019.
[5] U.S. Department of the Interior Bureau of Reclamation. *Erosion and Sedimentation Manual*, 2006.
[6] Gomez et al. *An Assessment of Bed Load Sediment Transport Formulae for Gravel Bed Rivers*, 1989.
[7] Van Rijn, L. *Sediment transport, part I: Bed load transport*, Journal of Hydraulic Engineering, ASCE, Vol.110, no.10, 1431-1456. 1984.

REDUCED INTEGRATION-BASED FINITE ELEMENT TECHNOLOGIES FOR GRADIENT-EXTENDED DAMAGE AND FRACTURE

Oliver Barfusz*, Tim van der Velden, Tim Brepols, Stefanie Reese

Institute of Applied Mechanics, RWTH Aachen University
*oliver.barfusz@rwth-aachen.de

Summary. The purpose of the present contribution is to extend a family of continuum finite elements which are based on reduced integration with hourglass stabilization towards the analysis of non-local damage and fracture. To this end, we present the incorporation of a gradient-extended two-surface damage plasticity model into solids and solid-shells with a reduced number of integration points (cf. [1]). Due to the analogy to fully-coupled thermo-mechanical problems, we adapt the derivation of a consistent hourglass stabilization from an earlier contribution for multi-field problems. Numerical examples of brittle and ductile fracture reveal the accuracy and efficiency of the proposed approach. Besides the ability to deliver mesh-independent results, the framework is especially suitable for highly constrained situations in which conventional low-order finite elements suffer from well known locking phenomena.

Introduction. The prediction of damage and fracture of solids and structures is a challenging task. Usually, damage is accompanied by softening until final failure occurs. Utilizing conventional 'local' continuum damage models typically leads to a pathological mesh dependence in finite element simulations. One possible solution is to use a gradient-extended damage model, which introduces an internal length into the material. Due to their simplicity and robustness, conventional low-order finite elements are frequently employed for the spatial discretization of the governing partial differential equations, even though it is well known that these elements exhibit poor performance in the limit of incompressibility (e.g. rubbers or metal plasticity) as well as bending dominated situations, respectively. These defects are known as volumetric and shear locking. One possible solution is to use the concept of reduced integration with hourglass stabilization (see e.g. [2],[3]). The purpose of this contribution is to utilize the gradient-extended two-surface damage plasticity model of [4] which is based on the micromorphic approach of [5] in conjunction with reduced quadrature point finite element formulations in order to obtain the following advantages: (i) a reliable and locking-free element response for the prediction of the damage onset and progress, (ii) an increase in computational efficiency coming from the usage of less elements together with a lower number of integration points and (iii) mesh distortion insensitivity which particularly improves the robustness in regions of highly localized damage.

Finite Element Technology. The starting point of our formulation is a two-field variational functional which is strongly related to the EAS method of [6]. This functional is extended by the weak form of the micromorphic balance equation. Overall this leads to three unknown global field quantities, namely the displacements $\boldsymbol{u}$, the enhanced strains $\boldsymbol{E}_e$ and the scalar micromorphic damage $\bar{D}$. Since the orthogonality condition has to be fulfilled elementwise, $\boldsymbol{E}_e$ can be eliminated via statical condensation. After the approximation of $\boldsymbol{u}$ and $\bar{D}$ with trilinear shape functions, the linearization of the weak forms leads to an extended global FE system which is solved iteratively using an arc-length method to capture potential snapback behavior. To achieve quadratic rates of convergence, four consistent tangent operators are computed analytically. In order to transfer the present multi-field problem into an equivalent reduced integration-based concept, a polynomial representation of all integrands is required. Therefore, further assumptions have to be made: First, the inverse Jacobian is approximated by a Taylor expansion with respect to the center of the element. Second, a truncated Taylor expansion of all constitutively dependent

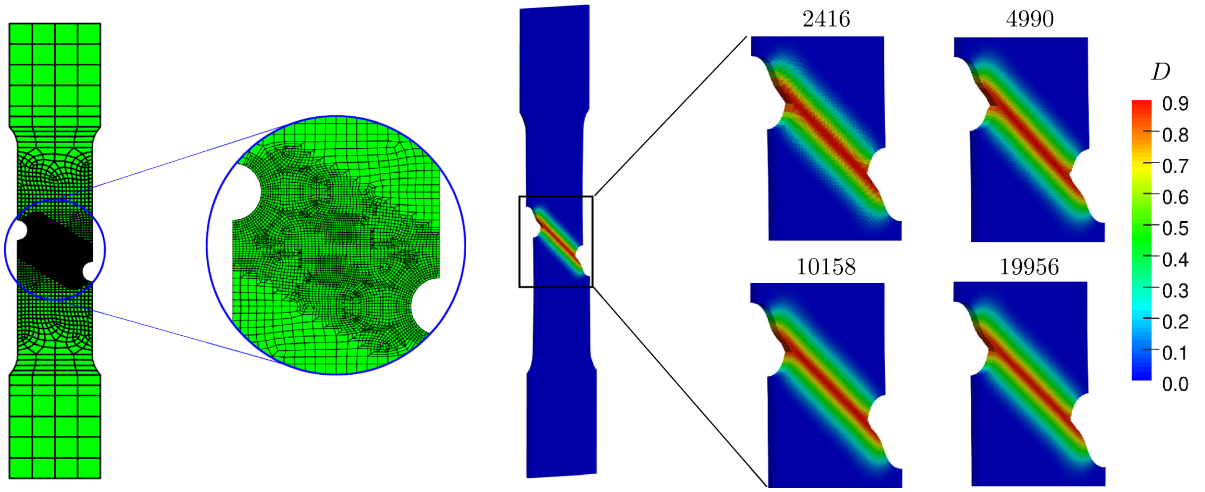

(a) Exemplary mesh with 4990 elements with detailed view of the refined region

(b) Comparison of the damage variable D at the end of the simulation for four different meshes with Q1STc

Figure 1: Asymmetrically notched specimen

quantities is carried out which leads to a consistent hourglass stabilization. The resulting stabilization is further modified to remain positive definite and constant within each load step to prevent an additional linearization. For the mechanical part it is important to employ an adaptive secant modulus, which takes into account softening.

Numerical Example. The main purpose of the numerical example is to demonstrate the benefits of the present reduced integration-based FE technology (Q1STc) in conjunction with gradient-extended damage plasticty models at finite strains. To this end, we consider an asymmetrically notched specimen which is clamped at the bottom and pulled at the top. The total lenght of the specimen is 110 mm. The assumed material parameters of the constitutive model are the same as in [4]. For the following study of convergence, different meshes are utilized. Figure 1(a) shows an exemplary discretization with 4990 elements. The detailed view suggests that the region between the notches must be refined in order to achieve mesh convergence. Furthermore, only one element is used in thickness direction whereby the displacement in this direction is fixed, leading to a plane strain state. Figure 1(b) shows the contour plots of the local damage variable D for four different meshes using Q1STc. A good agreement between the deformed geometries can be observed and the width of the damage zone is comparable for all cases. Furthermore, Figure 2 depicts the load-displacement curves obtained by the conventional low-order formulation Q1 as well as Q1STc, respectively. It can be easily recognized that Q1STc delivers more accurate results in terms of both, the prediction of the damage onset as well as progress. Finally, Q1STc is, in contrast to Q1, very insensitive against mesh distortions, which has particular impact on the robustness in regions of highly localized damage.

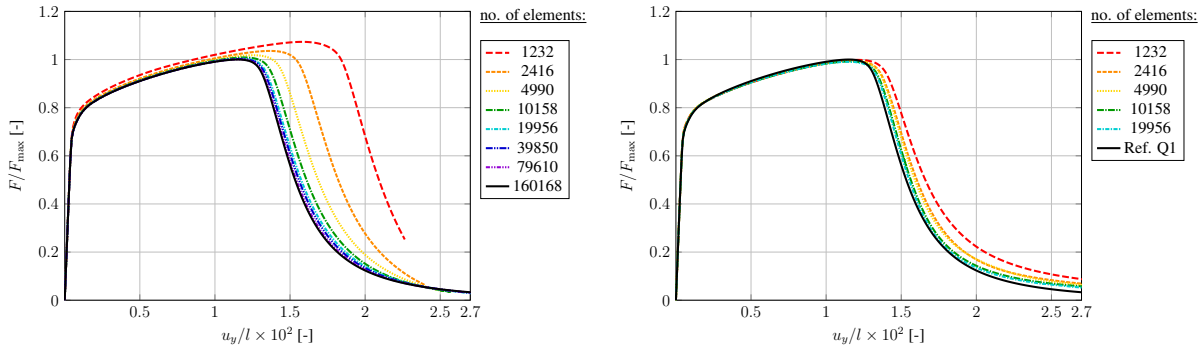

(a) Obtained by conventional formulation Q1

(b) Obtained by present formulation Q1STc

Figure 2: Comparison of load displacement curves

Conclusion. The extension of reduced integration-based FE formulations for the analysis of gradient-extended damage and fracture was presented. Due to the analogy to fully-coupled thermomechanical problems, we were able to adapt a similar derivation of a consistent hourglass stabilization which is based on the Taylor expansion of all constitutively dependent quantities. Utilizing a single Gauss point formulation within the numerical example, revealed the accuracy, efficiency, and robustness of the proposed methodology.

References

[1] O. Barfusz, T. Brepols, T. van der Velden, S. Reese, *A single Gauss point continuum finite element formulation for gradient-extended damage at large deformations*, Computer Methods in Applied Mechanics and Engineering, 113440, 2021

[2] S. Reese, *On a physically stabilized one point finite element formulation for three-dimensional finite elasto-plasticity*, Computer Methods in Applied Mechanics and Engineering, **194**: 4685–4715, 2005

[3] M. Schwarze, S. Reese, *A reduced integration solid-shell finite element based on the EAS and the ANS concept - Large deformation problems*, International Journal for Numerical Methods in Engineering, **85**: 289–329, 2011

[4] T. Brepols, S. Wulfinghoff, S. Reese, *A gradient-extended two-surface damage-plasticity model for large deformations*, International Journal of Plasticity, 102635, 2020

[5] S. Forest, *Nonlinear regularization operators as derived from the micromorphic approach to gradient elasticity, viscoplasticity and damage*, Proceedings of the Royal Society A: Mathematical, Physical and Engineering Sciences, **472**: 20150755, 2016

[6] JC. Simo, F. Armero, *Geometrically non-linear enhanced strain mixed methods and the method of incompatible modes*, International Journal for Numerical Methods in Engineering, **33**: 1413–1449, 1992

SIMULATIONS OF CHARACTERIZATION METHODS FOR THERMOELECTRIC NANO-DEPOSITED LAYERS

Pablo Moreno-Navarro[1], José L. Pérez-Aparicio[2], Luis Palomo[3]

[1] Mecánica Medios Continuos, Universitat Politècnica de València, pabmona@upv.es
[2] Mecánica Medios Continuos, Universitat Politècnica de València, jopeap@mes.upv.es
[3] Universitat Politècnica de València, luipara@etsid.upv.es

The main indicator of the efficiency of a thermoelectric (TE) material is the adimensional figure of merit zT that combines the contribution of the electrical conductivity γ, the Seebeck coefficient α, and the thermal conductivity κ as follows:

$$zT = \frac{\alpha^2 \gamma}{\kappa} T \tag{1}$$

In order to optimize zT, we seek a material with high values of α and γ, and low values of κ for a given temperature T. Thus, the characterization of material properties is an essential part of material science and numerical simulations to predict the best TE behavior. Also, a good characterization is crucial to obtain close results between experimental set-ups and the corresponding simulations.

In this work, two methods used to characterize TE properties for films with thicknesses of the order of nanometers are discussed: Van der Pauw and 3ω.

The former is a static method that is able to determine γ, α, κ. The first two material properties can be obtained with fairly good precision using Van der Pauw method because the substratum material where we deposit our TE film is chosen to be an electrical insulator. However, due to the thermal inertia and the impossibility to isolate completely the contribution of the substratum, κ has to be determined using other methods, such as 3ω. This method is dynamic as opposed to Van der Pauw's and is able to overcome the thermal inertia to get far more accurate values of κ.

Van der Pauw's method

This method consists of placing four electrical contacts on four different points of a TE sample [3]. An electric intensity I is introduced through contact 1 and extracted through contact 2. A measurement of the voltage difference on the other two contacts (contacts 3 and 4) is taken getting the electric resistance $R_{12,34}$. In Figure 1, we can see the described set-up for a rectangular TE film.

Another measurement is then taken, introducing I from contact 2 to 3 and measuring the voltage difference on contacts 4 and 1, getting $R_{23,41}$. These electric resistances can be defined using Ohm's law:

$$R_{12,34} = \frac{\Delta V_{34}}{I_{12}}\,; \qquad R_{23,41} = \frac{\Delta V_{41}}{I_{23}} \tag{2}$$

With both $R_{12,34}$ and $R_{23,41}$, the electric conductivity of the TE material can be obtained by solving the following equation:

$$\exp\left(-\pi\,\gamma\,d\,R_{12,34}\right) + \exp\left(-\pi\,\gamma\,d\,R_{23,41}\right) = 1 \tag{3}$$

where d is the thickness of the deposition. An analogous Van der Pauw to determine the thermal conductivity can be defined, featuring the thermal flux Q and the difference of temperatures ΔT instead of the I and ΔV respectively. We can obtain the thermal resistances as follows:

$$R^{\text{th}}_{12,34} = \frac{\Delta T_{34}}{Q_{12}}\,; \qquad R^{\text{th}}_{23,41} = \frac{\Delta T_{41}}{Q_{23}} \tag{4}$$

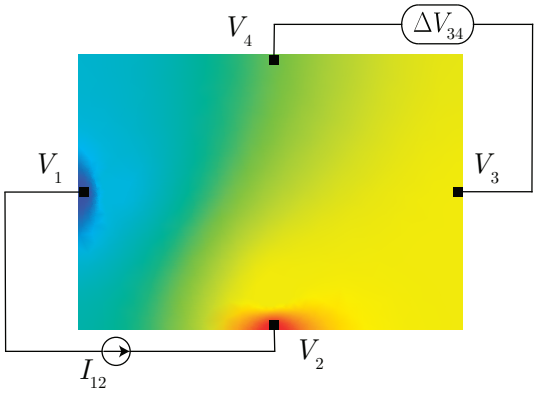

Figure 1: Van der Pauw set-up to determine the electric conductivity of the thermoelectric film

The corresponding thermal case is drawn in Figure 2.

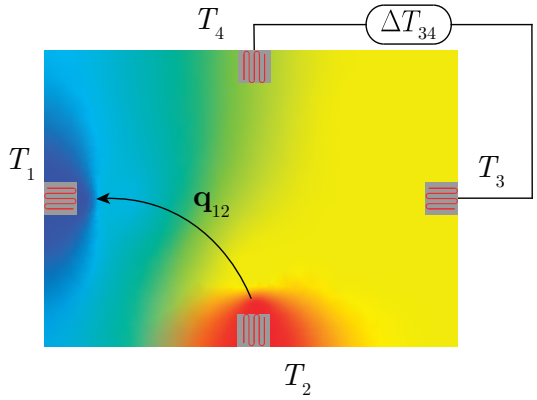

Figure 2: Van der Pauw set-up to determine the thermal conductivity of the thermoelectric film

The equation to solve to obtain κ is therefore:

$$\exp\left(-\pi\,\kappa\,d\,R^{\text{th}}_{12,34}\right)+\exp\left(-\pi\,\kappa\,d\,R^{\text{th}}_{23,41}\right)=1 \tag{5}$$

With this last set-up we can calculate the Seebeck coefficient as the following product by measuring now the voltage difference between contacts 3 and 4:

$$\alpha=-\frac{\Delta V_{34}}{\Delta T_{34}}=-\frac{\Delta V_{41}}{\Delta T_{41}} \tag{6}$$

These cases have been replicated using Finite Element method and computer code FEAP [2]. The TE element used is the 2D version of the one presented in [1] to simulate a thin deposition, with the possibility of introducing quadratic temperature-dependent properties. The substratum is represented with a 3D non-TE solid. All three equations (3), (5), and (6) are valid if the substratum is of the order of millimeters, obtaining very accurate results for γ and α. The error in κ is rather high for thicker substratums.

3ω method

This method is described in Figure 3 and consists of a heater (and thermal sensor) made of gold or silver and $35 \leq 2b \leq 90$ nm wide, a thermoelectric film with thickness d_F, and a substratum with thickness d_S [4]. An alternate electric intensity $I(\omega)$ with frequency ω is introduced through one of the heater ends. This $I(\omega)$ induces an alternate thermal flux $q(2\omega)$ due to Joule effect with frequency 2ω. Since material

properties are temperature-dependent, the electric resistance R depends on the temperature $T(2\omega)$. In turn, the voltage difference between both heater ends will have two main frequencies (ω and 3ω) and a constant term.

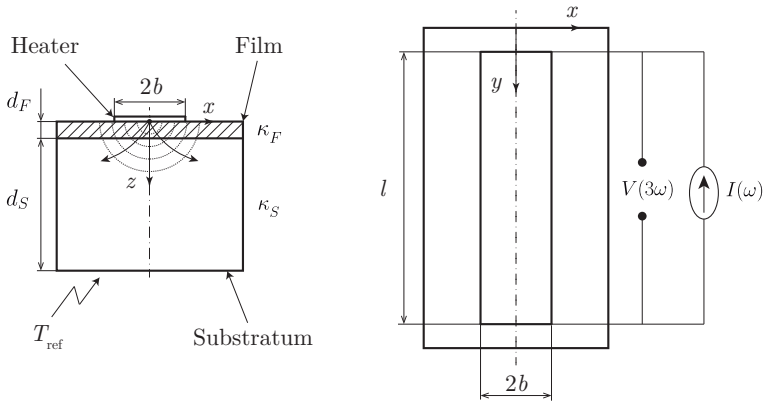

Figure 3: 3ω set-up to determine the thermal conductivity of the thermoelectric film

The 3ω term can be isolated using the Fourier transform. There are two different methods to solve the thermal conductivity of the film. The most accurate one needs the results of two different set-ups: one with the TE film and one without the film. Therefore, the thermal conductivity of the film κ_F is calculated as:

$$\kappa_F = \frac{d_F}{2}\left[\left(\frac{b\,T(2\omega)}{P_0}\right)_{SF} - \left(\frac{b\,T(2\omega)}{P_0}\right)_{S}\right]^{-1}_{\text{avg}} \tag{7}$$

where the average of the temperature is obtained and $P_0 = R_0 I_0^2$. The contours of T and V are displayed in Figure 4, at two different simulation times.

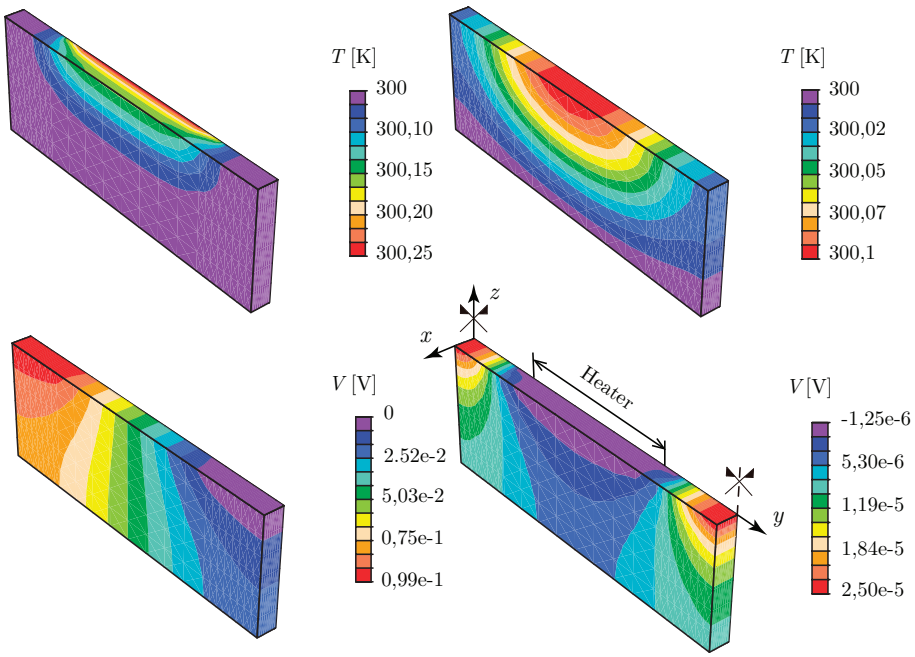

Figure 4: Temperature and voltage of 3ω simulations for two different time simulations: left 1.25×10^{-2} s, and right 2.50×10^{-2} s

The comparison between the thermal conductivity distribution and the obtained calculated values with 3ω method can be seen in Figure 5. The accuracy of this method is far superior than Van der Pauw's, getting errors below 5 % as opposed to 200 % with the latter.

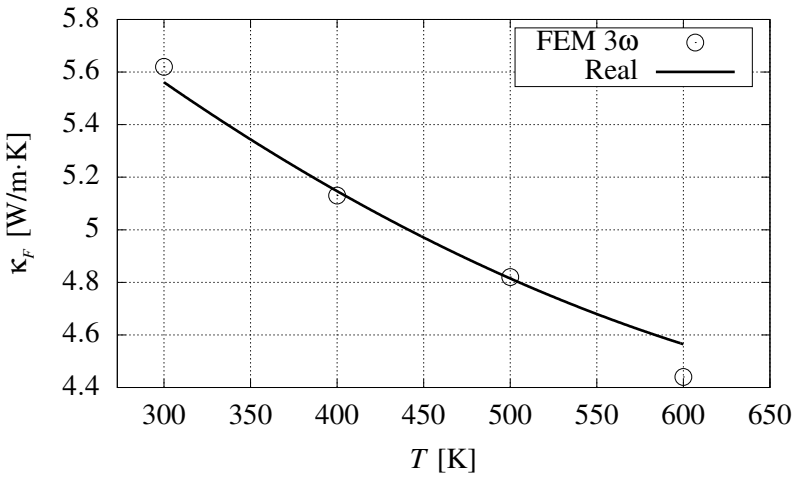

Figure 5: Thermal conductivity of the TE material for the studied temperature range obtained with 3ω method FEM simulation and the real distribution

Acknowledgments

This work was supported by Generalitat Valenciana PROMETEO/2020/016: Aplicaciones de aislantes Topológicos en spintrónica y Termoelectricidad (TOP-TERM). This support is gratefully acknowledged.

References

[1] R. Palma, J.L. Pérez-Aparicio, R. Bravo, *Study of hysteretic thermoelectric behavior in photovoltaic materials using the finite element method, extended thermodynamics and inverse problems*, Energy Conversion and Management, 65, 557-563, 2013.

[2] R.L. Taylor, *A Finite Element Analysis Program: User Manual*, University of California, Berkeley, 2010.

[3] L. J. V. der Pauw, *A method of measuring specific resistivity and Hall effects of discs of arbitrary shape*. Philips Research Reports, 13(1), 1-9, 1958.

[4] L. Acquaroli, *3-omega method for thermal properties of thin film multilayers*. Preprint submitted to Condensed Matter, 2018.

[5] T. M. Tritt, *Thermal Conductivity: theory, properties and applications*. Springer US, 2004.

ECCOMAS MSF 2021 THEMATIC CONFERENCE
30 June – 2 JULY 2021, SPLIT, CROATIA

PRESENTATION OF THE COMPUTER PROGRAM PRECON3D FOR ANALYZING RC AND PC CONCRETE STRUCTURES

Pavao Marović[1], Mirela Galić[2]

[1] University of Split, Faculty of Civil Engineering, Architecture and Geodesy, Matice hrvatske 15, HR-21000 Split, Croatia, marovic@gradst.hr
[2] University of Split, Faculty of Civil Engineering, Architecture and Geodesy, Matice hrvatske 15, HR-21000 Split, Croatia, mirela.galic@gradst.hr

It is a long tradition at the Faculty of Civil Engineering, Architecture and Geodesy of the University of Split to numerically model reinforced concrete structures and perform linear and non-linear analyzes. Development of our own computer programs started with late professor Frano B. Damjanić and his doctoral studies at the Swansea University [1, 2]. Furthermore, we jointly organize the International Conference on Computer Aided Analysis and design of Concrete Structures in 1984 in Split [3]. This Conference was the starting point of the series of conferences later known under the acronym EURO-C, Computational Modelling of Concrete Structures, organized every 3-5 years in winter times in Austria [4]. Due to some organizational, educational, scientific, and private interests, few groups started their own investigations and research in different fields of computational, phenomenological and professional areas for analyzing behavior of reinforced and prestressed concrete structures. The bases for continuations of our investigations were one book [5], two M.Sci. Theses [6, 7] and one Ph.D. Thesis [8], followed by dozens of conference papers and presentations as well as lot of journal papers of which only the most important are mentioned here [9-17].

In the developed computer program PRECON3D, nonlinear behavior of concrete is described by an elasto-plastic modified material model which is based on the Mohr-Coulomb law for dominant compression stresses and the modified Rankine law for dominant tensile stresses [8, 15]. A multisurface presentation of the model (Figure 1) is implemented in the model, enabling thus a rapid convergence of the mathematical procedure. The nonlinear, triaxial behavior is included into this model, with all dominant influences in concrete such as yielding in compression, cracking in tension, softening and hardening of concrete. For describing of all of these parameters, we have to define: (a) a fracture model for concrete with the tensile softening of cracked concrete and stress-strain relation of cracked concrete (Figure 2). Final reduction of normal stresses and plane of cracking an all combinations for compressive and tensile behavior in eight octahedral is presented in Figure 3. As nonlinear behavior of concrete for dominant stresses is described by an elasto-plastic material model based on the Mohr-Coulomb law, in the multisurface model presentation, the yielding surface is composed of six planes in the area of main stresses (Figure 4). The complete elastic, hardening and softening functions of concrete with respect to the total plastic strains are presented in Figure 5. Mathematical formulations and detailed descriptions for all previously mentioned procedures can be found in Refs. [8, 15, 17].

The nonlinear behavior of reinforcement bars and prestressed tendons are described by a one-dimensional elasto-viscoplastic model. Their geometry is described by a second order space function which is determined by its projections (Figure 6) [8, 14, 15, 17].

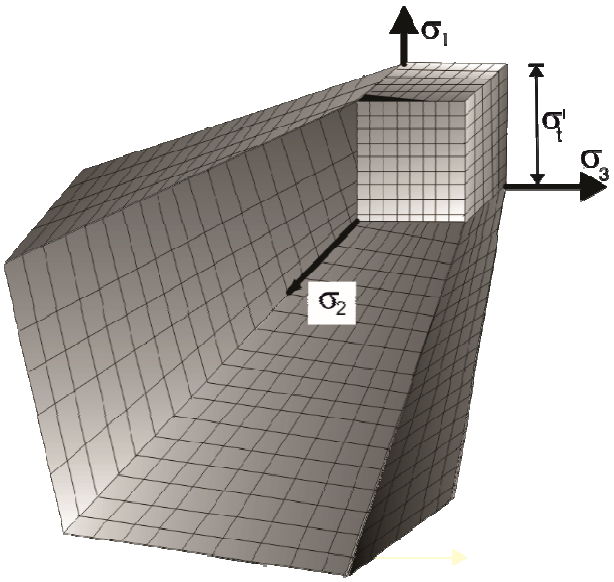

Figure 1: Multisurface presentation of material model for concrete

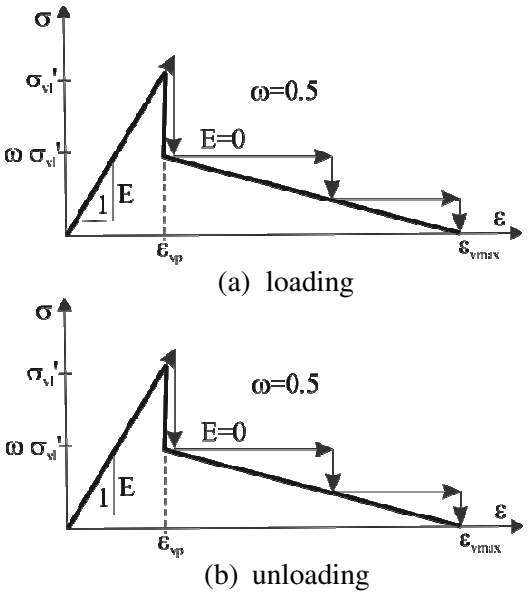

Figure 2: Tensile softening model for cracked concrete for loading (a) and unloading (b)

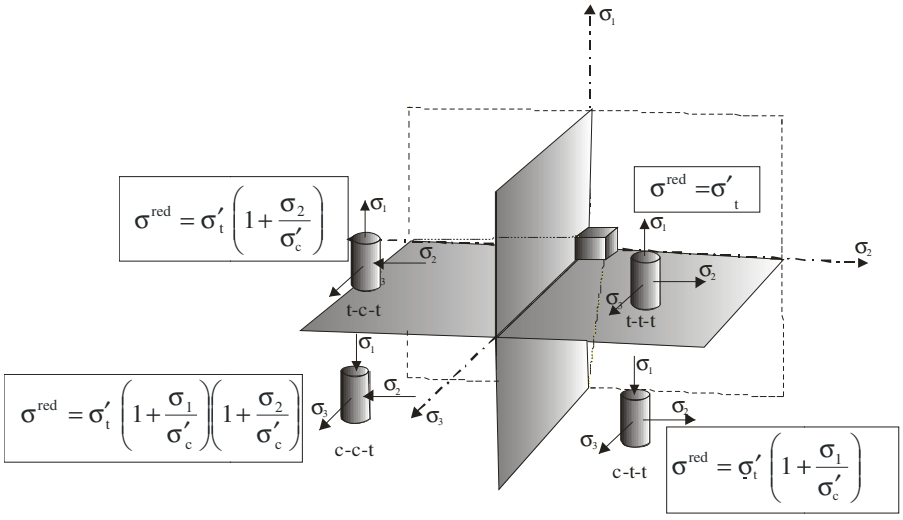

Figure 3: Final reduction of normal stresses and plane of cracking in all combinations for compressive (c) and tensile (t) behaviour in eight octahedrals

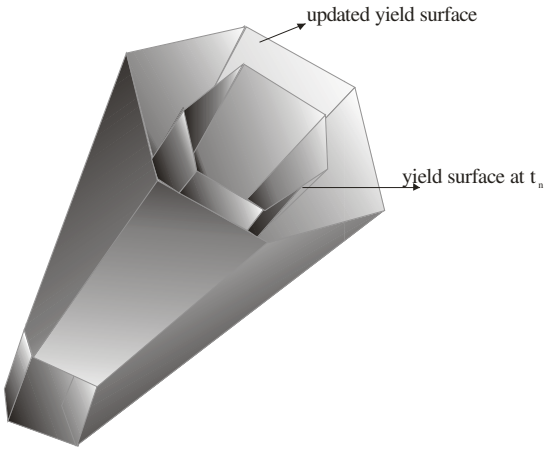

Figure 4: Triaxial presentation of the yielded surface development defined by hardening rule

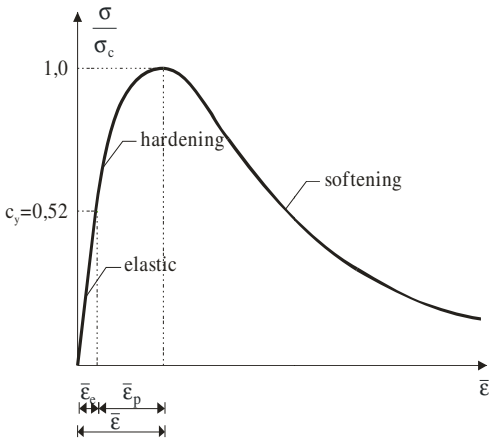

Figure 5: Hardening and softening functions with respect to the total plastic strains

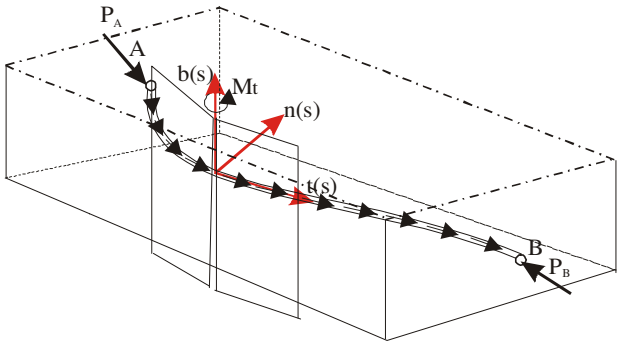

Figure 6: Space curvature of reinforcement bars and prestressed tendons

Numerical calculations and analyses as well as validations of developed computer program PRECON3D [8, 15] has been performed on many practical engineering structures like: (a) four point bending of rc beam in linear and nonlinear analysis [7, 8, 15] compared with MAFEM software and experiment results [18]; (b) prestressed non-prismatic girder clamped at one end and extended over the fixed support at the other end [7, 8, 11, 12] taken from [19]; (c) prestressed I-beam with one tendon [7, 8, 10-15] compared with other analytical and experimental results [20] and variation with two tendons [14]; (d) prestressed prismatic girder with different boundary conditions, i.e. clamped at one end and freely supported at the other end [12, 13] taken from [21] and compared with their analytical and experimental results; (e) simply supported rc beams in four point bending having different concrete strength (high and normal) according to [22] analyzed in 3D [16, 17] (Figure 7, left) and compared with their analyses in 2D and experimental results taken from [23]; (f) three point bending of rc beams with different degrees of reinforcement [17] taken from [24] compared with their computational and experimental results taken from [25]; (g) prestressed Π-beam [17] (Figure 7, right) analyzed and tested experimentally in [26].

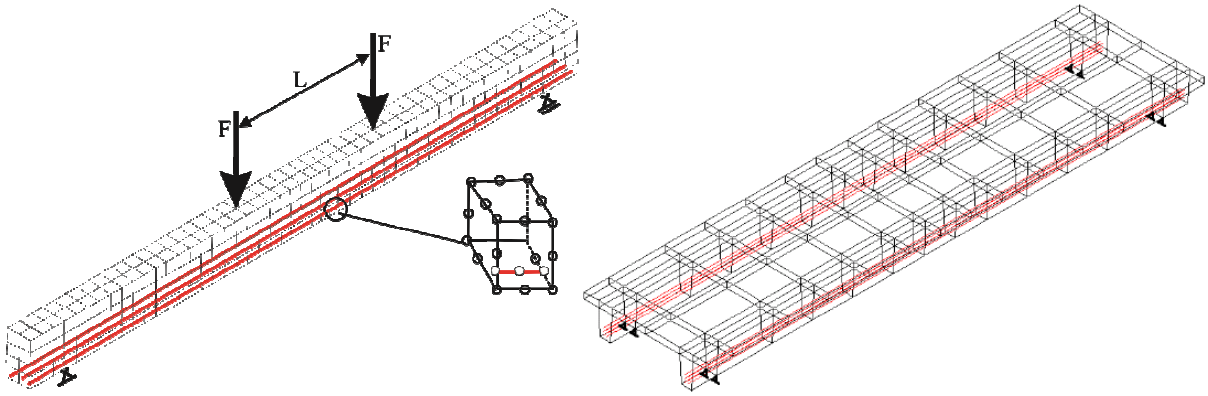

Figure 7: Some examples of discretization of rc (left) [16] and pc (right) concrete beams [17, 26]

Acknowledgement

This research is partially supported through project KK.01.1.1.02.0027, a project co-financed by the Croatian Government and the European Union through the European Regional Development Fund - the Competitiveness and Cohesion Operational Programme.

References

[1] F.B. Damjanić. *Reinforced Concrete Failure Prediction under both Static and Transient Conditions*, Ph.D. Thesis, C/Ph/71/83, University of Wales, Swansea, 1983.

[2] D.R.J. Owen, J.A. Figueras, F.B. Damjanić. *Finite Element Analysis of Reinforced and Prestressed Concrete Structures Including Thermal Loading*, Computational Methods in Applied Mechanical Engineering, 40, 323-366, 1983.

[3] *Proceedings of the International Conference on Computer Aided Analysis and Design of Concrete Structures*, Parts I and II, Eds.: F. Damjanić, E. Hinton, D.R.J. Owen, N. Bićanić, V. Simović, Split, September 17-21, 1984, Pineridge Press, Swansea, 1984.
[4] P. Marović, M. Galić. *Roger Owen – Eminent Scientist and Extraordinary Friend*, International Journal for Engineering Modelling, 33(1-2), 1-17, 2020.
[5] A. Mihanović, P. Marović, J. Dvornik. *Nonlinear Calculations of Reinforced Concrete Structures*, Society of Croatian Structural Engineers, Zagreb, 1993. (in Croatian)
[6] Ž. Nikolić. *Development of the Numerical Model for Post-tensioning of Plane Reinforced Concrete Structures*. M.Sci. Thesis, University of Split, Faculty of Civil Engineering, Split, 1993. (in Croatian)
[7] M. Galić. *Numerical 3D Model of Prestressed Concrete Structures*, M.Sci. Thesis, University of Split, Faculty of Civil Engineering, Split, 2002. (in Croatian)
[8] M. Galić. *Development of Nonlinear Numerical 3D Model of Reinforced and Prestressed Concrete Structures*, Ph.D. Thesis, University of Split, Faculty of Civil Engineering, Architecture and Geodesy, Split, 2006. (in Croatian)
[9] A. Mihanović, Ž. Nikolić. *Numerical Model for Posttensioning Concrete Structures*, International Journal for Engineering Modelling, 6(1-4), 35-43, 1993.
[10] Ž. Nikolić, A. Mihanović. *Non-linear Finite Element Analysis of Post-tensioned Concrete Structures*, Engineering Computations, 14(5), 509-528, 1997.
[11] P. Marović, Ž. Nikolić, M. Galić. *Comparison of Two-dimensional and Three-dimensional Analysis of Reinforced and Prestressed Concrete Structures*, International Journal for Engineering Modelling, 17(3-4), 49-59, 2004.
[12] P. Marović, Ž. Nikolić, M. Galić. *Some Aspects of 2D and/or 3D Numerical Modelling of Reinforced and Prestressed Concrete Structures*, Eng. Computations, 22(5/6), 684-710, 2005.
[13] M. Galić, Ž. Nikolić, P. Marović. *Three-dimensional Model of a Prestressed Tie*, Građevinar, 58(4), 271-280, 2006. (in Croatian)
[14] M. Galić, P. Marović, Ž. Nikolić. *Mathematical Formulation of the Space Curvature of the Tendon in the PC Structures*, Int. Journal for Engineering Modelling, 21(1-4), 15-22, 2008.
[15] M. Galić, P. Marović, Ž. Nikolić. *Modified Mohr-Coulomb – Rankine Material Model for Concrete*, Engineering Computations, 28(7), 853-887, 2011.
[16] M. Galić, P. Marović, A. Harapin. *Parametric Analysis of Constant-Moment Zone Length in Four Point Bending of Reinforced Concrete Beams*, Materialwissenschaft und Werkstofftechnik, 44(5), 449-457, 2013.
[17] M. Galić, P. Marović. *Validation of the Developed Triaxial Nonlinear Material Model for Concrete*, Engineering Review, 37(3), 298-313, 2017.
[18] S. Majewski, R. Krzowyon. *Numerical and Experimental verification of FEM for elastoplastic analysis of RC Structures and Soil Structure Interaction Problems*, 7th Int. Conf. on Numerical Methods in Continuum Mechanics, Eds. V. Kompiš, M. Žmindak, B. Hučko, 519-524, 1998.
[19] N. El-Mezaini, E. Citipitioglu. *Finite Element Analysis of Prestressed and Reinforced Concrete Structures*, Structural Engineering, 117, 2851-2864, 1991.
[20] K.T. Nguyen. *Nonlinear Analysis of Concrete Beams with Unbounded Tendons*, EURO-C 1998, Eds. R. de Borst, N. Bićanić, H.A. Mang, G. Meschke, 749-755, 1998.
[21] D. Antoniak, P. Konderla. *General FEM Model of Prestressing Tendons*, Computer Assisted Mechanics and Engineering Sciences, 7, 435-448, 2000.
[22] A.P. Fantilli, I. Iori, P. Vallini. *Size Effect of Compressed Concrete in Four Point Bending RC Beams*, Engineering Fracture Mechanics, 74(1), 97-108, 2007.
[23] W.J. Weiss, K. Guler, S.P. Shah. *Localization and Size-dependent Response of Reinforced Concrete Beams*, ACI Structural Journal, 98(5), 686-695, 2001.
[24] T. Rabczuk, T. Belytschko. *Application of Particle Methods to Static Fracture of Reinforced Concrete Structures*, International Journal of Fracture, 137(1-4), 19-49, 2006.
[25] C. Bosco, P.G. Debernardi. *Experimental Investigations on the Ultimate Rotational Capacity of EC Beams*, Politecnico di Torino, Dipartimento di Ingegneria Structurale, 1992.
[26] R. Markić. *Influence of Relation of Prestressed and Classical Reinforcement on the Behaviour of Concrete beam Structures*, Ph.D. Thesis, University of Split, Faculty of Civil Engineering, Architecture and Geodesy, Split, 2012. (in Croatian)

NOVEL METHOD FOR THERMAL CHARACTERIZATION OF MATERIALS BASED ON INFRARED THERMOGRAPHY.

Petra Bagavac[1], Lovre Krstulović-Opara[2], Željko Domazet[3]

[1] FESB, University of Split, R. Boškovića 32, 21 000 Split, Croatia, Petra.Bagavac@fesb.hr
[2] FESB, University of Split, R. Boškovića 32, 21 000 Split, Croatia, Opara@fesb.hr
[3] FESB, University of Split, R. Boškovića 32, 21 000 Split, Croatia, Domazet@fesb.hr

Abstract

By signal processing methods of active infrared thermography, it is possible to perform a non-destructive testing and evaluation of structures [1]. The method is most often used for non-destructive testing of metal sheets and composite materials [2]. It has also applicable on for the adhesive joint control of ribs and reinforcement in mechanical structures [3]. The test requires a high-resolution infrared camera with high-speed image acquisition, an external source of excitation, usually in the form of flashes [4], halogen lamps [5] or lasers [6, 7] and computer to collect and process measurement data. Since raw data are saturated with noise resulting from uneven surface emissivity, environmental reflection, and uneven surface heating of sample, data should always be subjected to post processing techniques. Some of the methods are based on mathematical operations such as thermographic signal reconstruction [8, 9 and principal component thermography [10]. Some measurement methods are based on comparison with the one-dimensional solution of Fourier cooling equation [11]. In order to achieve good results, mathematical models need to be supplemented with the thermal characteristics of a material. This contribution will propose an unconventional measurement of material thermal properties. The idea is to create a mathematical model of the experiment and to connect that model with the optimizer. Since output parameters (measurement results) are known from the infrared camera measurement, unknown thermal properties of material will be evaluated with the help of an optimizer, Fig. 1.

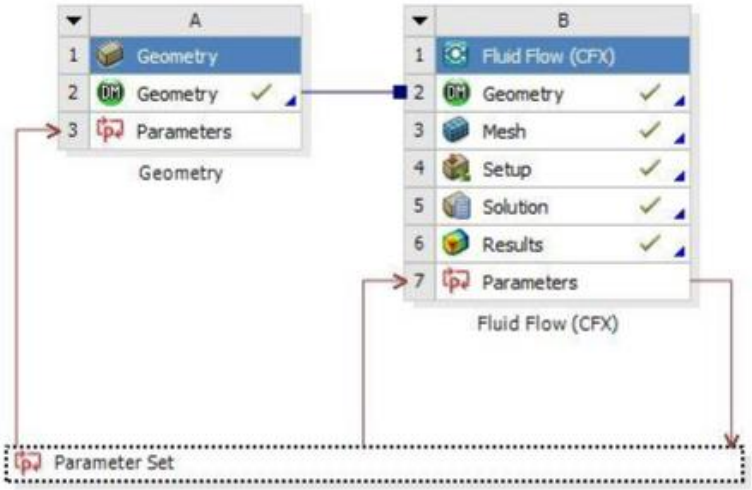

Figure. 1. Work space sheet

The proposed method will first be applied to metallic materials with known thermal properties, and then to composite materials of unknown thermal properties. The results will be compared with the measured values obtained by the commonly used Parker flash method [12].

References

[1] X. Maldague, Introduction to NDT by active infrared thermography, Mater. Eval. 60 (9) (2002) 1060–1073.

[2] Hernán D. Benítez; Clemente Ibarra-Castanedo; AbdelHakim Bendada; Xavier Maldague; Humberto Loaiza; Eduardo Caicedo (2008). Definition of a new thermal contrast and pulse correction for defect quantification in pulsed thermography. , 51(3), 160–167. doi:10.1016/j.infrared.2007.01.001.

[3] Tighe, R.C.; Dulieu-Barton, J.M.; Quinn, S. (2018). Infrared Techniques for Practical Defect Identification in Bonded Joints in Liquefied Natural Gas Carriers. Experimental Techniques, 42(2), 121–128. doi:10.1007/s40799-017-0200-7.

[4] M.A. Omar, Y. Zhou, A quantitative review of three flash thermography processing routines, Infrared Phys. Technol. 51 (4) (2008) 300–306, https://doi.org/10.1016/j.infrared.2007.09.006.

[5] Krstulović-Opara, L.; Domazet, Ž.; Garafulić, E. (2013). Detection of osmotic damages in GRP boat hulls. Infrared Physics & Technology, 60(), 359–364. doi:10.1016/j.infrared.2013.06.011.

[6] T. Li, D.P. Almond, D.S. Rees, Crack imaging by scanning pulsed laser spot thermography, NDT & E Int. 44 (2) (2011) 216–225, https://doi.org/10.1016/j.ndteint.2010.08.006.

[7] S. Burrows, S. Dixon, S. Pickering, T. Li, D. Almond, Thermographic detection of surface breaking defects using a scanning laser source, NDT & E Int. 44 (7) (2011) 589–596, https://doi.org/10.1016/j.ndteint.2011.06.001.

[8] S.M. Shepard, Reconstruction and enhancement of active thermographic image sequences, Opt. Eng. 42 (5) (2003) 1337, https://doi.org/10.1117/1.1566969., D.L. Balageas, J.M. Roche, F.H. Leroy, W.M.

[9] Liu, A.M. Gorbach, The thermographic signal reconstruction method: a powerful tool for the enhancement of transient thermographic images, Biosybern. Biomed. Eng. 35 (1) (2015) 1–9, https://doi.org/10.1016/j.bbe.2014.07.002.

[10] N. Rajic, Principal component thermography for flaw contrast enhancement and flaw depth characterisation in composite structures, Compos. Struct. 58 (4) (2002) 521–528, https://doi.org/10.1016/S0263-8223(02)00161-7.

[11] V. Vavilov, G. Xingwang, S. Wei and L. Yingtao. Peculiarities of detecting Teflon defect surrogates in CFRP by transient IR thermography. https://doi.org/10.21611/qirt.2004.019

[12] Parker, W. J.; Jenkins, R. J.; Butler, C. P.; Abbott, G. L. (1961). Flash Method of Determining Thermal Diffusivity, Heat Capacity, and Thermal Conductivity. 32(9), 1679–0. doi:10.1063/1.1728417

ECCOMAS MSF 2021 THEMATIC CONFERENCE
30 June – 2 JULY 2021, SPLIT, CROATIA

DETERMINISTIC APPROACH OF PARAMETER IDENTIFICATION FOR CONCRETE MODELING

Samir Suljevic [1,3], Adnan Ibrahimbegovic [1,2], Samir Dolarevic [3]

[1] Université de Technologie de Compiègne, Laboratoire Roberval de Mécanique, France,
samir.suljevic@utc.fr , adnan.ibrahimbegovic@utc.fr
[2] Institut Universitaire de France, France
[3] Faculty of Civil Engineering, University of Sarajevo, Bosnia and Herzegovina,
samir.suljevic@gf.unsa.ba , samir.dolarevic@gf.unsa.ba

Abstract. The main aim of this paper is the identification of the model parameters for the constitutive model of concrete and concrete-like materials capable of representing different failure mechanisms under various stress states.

Identification procedure is performed taking into account multi-scale character of concrete as a structural material. Mono-scale model is used as a model on the identification procedure is based, while multi-scale model based on idea that each element of macro-scale mesh act as a container of a refined mesh built with appropriate micro-scale discretization is used for numerical simulation of experimental results.

It is already known that concrete passes through several distinct phases in process of deformation until complete localized failure. In that sense, mono-scale model contains all ingredients to account for both types of dissipative mechanisms. These are bulk dissipation which leads to the appearance of microcracks, as well as a surface dissipation in localization zones in terms of the macro-cracks. Here plasticity model with Drucker-Prager yield criterion is considered. On the other side, 3D multi-scale analysis assuming strong coupling between scales is performed. From a practical point of view in terms of FEM implementation, instead of computation element tangent stiffness matrices and the residual vectors, assembly of micro-scale computations is performed whose contributions are statically condensed at the coarser level. The compatibility between both scales is accomplished by imposing a constraint on the displacement field over their interface (displacement based coupling). Dealing with localized failure mechanisms is enabled through the implementation of embedded strong discontinuity in macro-scale elements. The computation is performed by using the operator split iterative solution procedure on both micro and macro-scales.

Complexity of identification procedure is determined by the choice of experimental or numerical setup. Several numerical examples for various kinds of experiments are performed to illustrate performance of the proposed methodology for identifying the corresponding material parameters. Identification procedure is divided into three completely separate stages to utilize the fact that all material parameters of mono-scale model have clear physical interpretation. In this way, computational cost is significantly reduced as solving three simpler identification steps in a batch form is much more efficient than the full-scale problem. A variety of techniques is available to identify material parameters via optimization method. In this work, downhill simplex is adopted as an optimization algorithm used to find minimum of objective function.

Acknowledgements: This work was supported by the French Ministry of Foreign Affairs, and French Embassy in Bosnia and Herzegovina. Professor Adnan Ibrahimbegovic was supported by the funding for Chaire de Mécanique Picardie (120-2015 RDISTRUCT-000010 and RDISTRUCT-000010), EU funding (FEDER) and IUF-Institut Universitaire de France (Membre Senior). These grants and financial supports are gratefully acknowledged.

References

[1] Karavelic, E., Ibrahimbegovic, A., Dolarevic S. (2019), Multi-surface plasticity model for concrete with 3D hardening/softening failure modes for tension, compression and shear, *Computers and Structures*, **221**, 74-90. https://doi.org/10.1016/j.compstruc.2019.05.009

[2] Ibrahimbegovic, A. (2009), *Nonlinear Solid Mechanics: Theoretical Formulations and Finite Element Solution Methods*, Springer, Dordrecht, Germany.

[3] Kucerova, A., Brancherie, D., Ibrahimbegovic, A., Zeman, J., Bittnar, Z. (2009), Novel anisotropic continuum-discrete damage model capable of representing localized failure of massive structures- Part II: identification from tests under heterogeneous stress field, *Engineering Computations*, **26**, 128-144, https://doi.org/10.1108/02644400910924834

[4] Rukavina, I. (2021), Cyber-physics intrinsic modeling for smart systems, Ph.D. Thesis. France: University of Technology in Compiègne;

ECCOMAS MSF 2021 THEMATIC CONFERENCE
30 June – 2 JULY 2021, SPLIT, CROATIA

PUNCHING SHEAR RESISTANCE OF REINFORCED CONCRETE SLAB

Džemal Herenda[1], Senad Medić[2], Muhamed Zlatar[3]

[1] Faculty of Civil Engineering, University of Sarajevo, dzemal.herenda@gmail.com
[2] Faculty of Civil Engineering, University of Sarajevo, senad_medic@yahoo.com
[3] Faculty of Civil Engineering, University of Sarajevo, zlatar.muhamed@gmail.com

Abstract

Verification of punching shear resistance of reinforced concrete bridge deck exposed to monotonic loading is discussed in this paper. Experimentally obtained results are compared against finite element and analytical models. Brick elements with quadratic interpolation were used in combination with Total Strain Rotating Crack Model for concrete and von Mises constitutive law for embedded reinforcement. Design procedure was implemented according Eurocode 2 and Model Code 2010. Experimental results reveal significant reserve in structural resistance compared to calculated design capacity which can be important for reexamination of existing RC structures. Also, the resulting values of the resistance from numerical analyses appear to be higher than the estimates from analytical methods.

Keywords: punching shear, reinforced concrete slab, experimental research, numerical modeling, capacity reserves

1 Introduction

Shear capacity of girders is influenced by many factors which can be examined experimentally and numerically. Usually, different approaches for determination of ultimate shear capacity and crack pattern lead to large scatter of results. Both ModelCode 2010 [1] and Eurocode 2 [2] allow the use of nonlinear analysis to verify the design capacity of concrete objects. The nonlinear models are best validated and interpreted by simulating experiments. The gathered experience can be employed to minimize model and human errors when predicting the nonlinear behavior of concrete structures. Also, if a realistic nonlinear analysis of a concrete structure can be carried out, the safety of the structure is increased and the cost can frequently be reduced.
Concrete exhibits a complex structural response with various important nonlinearities: nonlinear stress-strain behavior, tensile cracking, compression crushing material failure and creep strains. All these nonlinearities depend strongly on the triaxial stress state, and in addition the nonlinearities introduced by reinforcing and prestressing steel should in general be taken into account [3].
Punching, which may be suffered by 2D reinforced concrete elements (such as flat slabs, plates, footings etc.) in regions under the action of concentrated load, is widely considered to be a type of shear failure. As a result, the methods applied by current codes of practice for designing against punching are essentially those applied to the shear design of RC beam-like elements with modifications that allow for characteristics of structural behavior particular to punching and to the geometry of the relevant structural elements. Furthermore, as for the case of shear capacity, the assessment of punching capacity is invariably based on the use of semi-empirical formulae calibrated by regression analyses of published experimental data [4].

2 Experimental setup

The experimental research of Rodrigues and Muttoni [5] was performed at the Structural Concrete Laboratory (IS-BETON) of the Ecole Polytechnique Fédéral de Lausanne (Figure 1) to study the actual behavior of a bridge cantilever without shear reinforcement. From the study, slab DR1-a was selected as a benchmark and denoted RS2. Analytical calculation of shear resistance was performed according to Model Code 2010 and EC2 using two levels of approximation. Bending capacity was determined employing the yield line method.

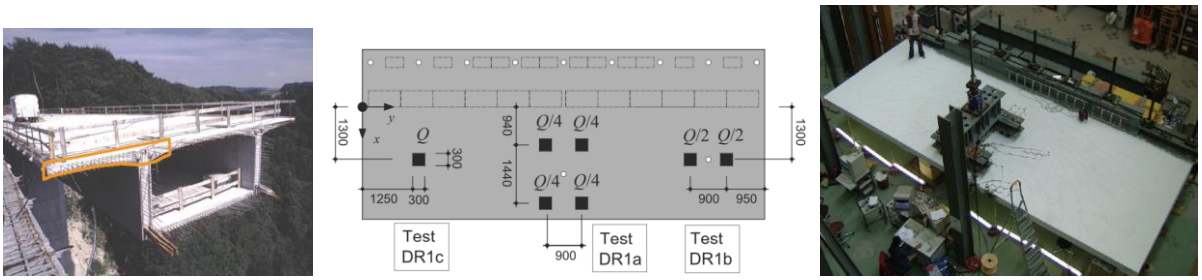

a) b) c)

Figure 1. a) Part of the real structure used for experiment, b) experimental model of structure exposed to loading, c) DR1-a test with 4 concentrated forces [5].

3 Numerical modeling

The establishment of an appropriate mathematical model for the analysis of an engineering problem is to a large degree based on sufficient understanding of the problem under consideration and a reasonable knowledge of the finite element procedures available for solutions. This observation is particularly applicable in nonlinear analysis because the appropriate nonlinear kinematic formulations, material models and solution strategies need to be selected [6].

The constitutive model of concrete used for modeling is based on total strain and it was developed along the lines of the Modified Compression Field Theory, originally proposed by Vecchio and Collins [7]. Like the multidirectional fixed crack model the total strain based crack models follow a smeared approach for the fracture energy. The three-dimensional extension to this theory is proposed by Selby and Vecchio [8]. The hypoelastic concept is used for description of the stress as a function of the strain, with a modification which includes secant unloading. Stress and strain are coaxial, which means that the stress-strain relations are evaluated in the principal directions of the strain vector. There are two approaches regarding the crack model which pertain to calculation of stress-strain law in a fixed (fixed upon cracking) or a rotating (cracks can continuously rotate with the principal directions of the strain vector) coordinate system. The parameters of concrete constitutive model are listed in Table 1.

The material model for reinforcement is von Mises with isotropic hardening. Interface between steel plate and the slab was assumed 10 mm thick made of concrete with normal stiffness and zero shear stiffness.

20-node solid elements (CHX60) with a full Gaussian integration scheme (3x3x3) were used to generate the finite element mesh in DIANA FEA [9] (Figure 2a). The average size of the finite element is 80x80x80 mm. In addition, due to the irregular geometry of the model, PY15L, TE12L and TP18L pyramidal finite elements were used to fill the spaces where the CHX60 finite element could not be used.

Secant stiffness matrix was employed in the analysis. It has proved to be robust and stable in reinforced concrete structures with extensive cracking [10]. Total deformations in vertical direction are shown in Figure 2b and the comparison of experimental and numerical solution in Figure 3.

Embedded reinforcement elements with 2 Gaussian points of integration along the bars were used to model the longitudinal and transverse reinforcement. A perfect bond between concrete and

reinforcement is assumed. For steel plates and AB supports, 20-node solid elements (CHX60) with a full Gaussian integration scheme (3x3x3) were also used. 20-node interface elements (CQ48I) with 4x4 Newton-Cotes integration scheme were used for the interface elements [11].

Table 1. Parameters of concrete.

Young's Modulus [N/mm^2]	36030
Poisson's ratio	0.3
Mass density [T/mm^3]	2.50E-09
"Total Strain based crack" model	
Crack orientation	Rotating
Tensile curve	Exponential
Tensile strength [N/mm^2]	2.94
Mode-I tensile fracture energy [N/mm]	0.141
Crack bandwidth specification	Rots
Poisson‘s ratio reduction model	Damage based
Compression curve	Parabolic
Compressive strength [N/mm^2]	39.11
Compressive fracture energy [N/mm^2]	35.308
Reduction due to lateral cracking	Without reduction
Confinement model	Selby and Vecchio

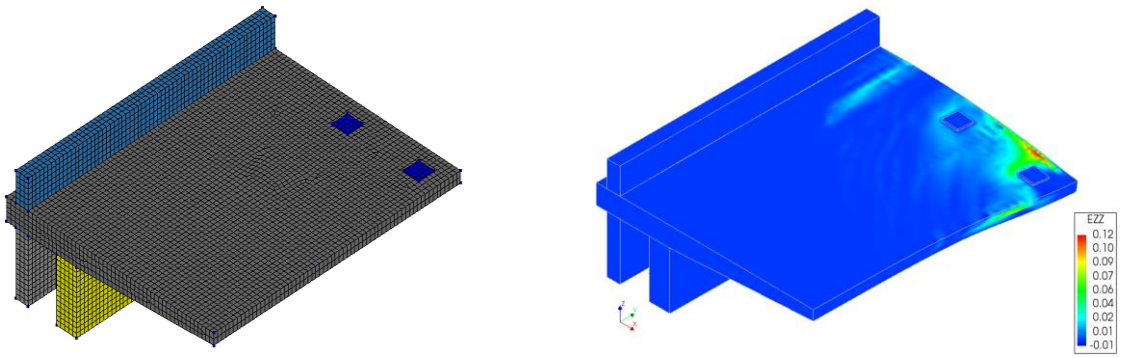

a) b)

Figure 2. a) Finite element mesh, b) total deformations in vertical direction.

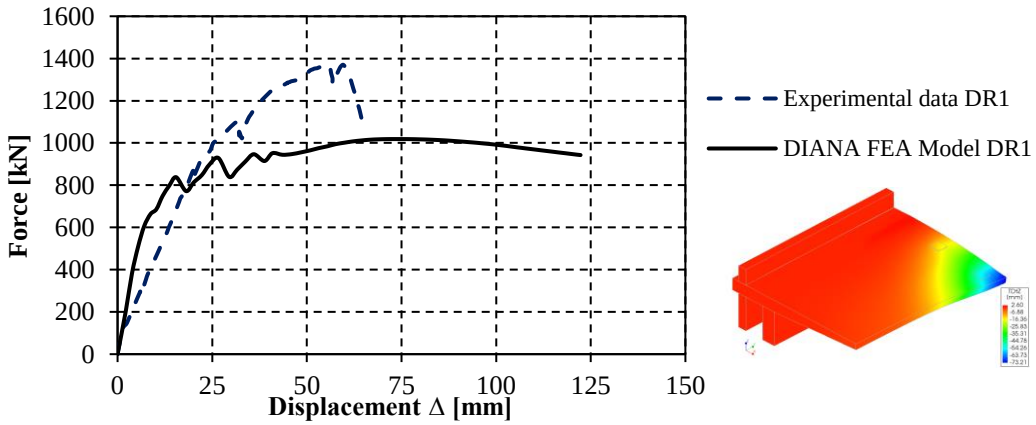

Figure 3. Force – displacement diagram: comparison of experimental and FE solution.

We notice that the initial stiffness of the numerical model and the experiment did not match, as well as that the maximum load capacity of the numerical model is less than the ultimate capacity obtained by the experiment. This can be explained by the fact that the slab tested experimentally was exposed to 200

loading and unloading cycles from Q = 0 to Q = 400 kN. This was not taken into account in the numerical modeling due to a very long calculation, so this factor very likely influenced the results.

5 Conclusion

Based on the obtained results, it can be concluded that the failure of the slab occurred due to the transverse force, i.e. due to critical cracks in vertical direction in the vicinity of the supports and on the axis of symmetry, which coincides with the experimental research. The longitudinal reinforcement started yielding, while the transverse reinforcement at the clamped end reached the tensile strength, indicating shear failure.
The results of various analyses with respect to the ultimate load bearing capacity are show in Figure 4.

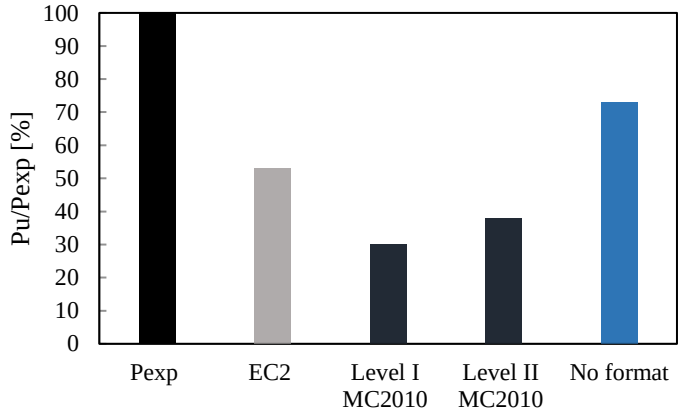

Figure 4. Ultimate load bearing capacities for analytical and numerical models versus experimental data.

Experimental results reveal significant reserve in structural resistance compared to calculated design capacity which can be important for reexamination of existing RC structures. Also, the resulting values of the resistance from numerical analyses appear to be higher than the estimates from analytical methods.

References

[1] fib. *fib Model Code for Concrete Structures*, Ernst&Sohn, 2010.
[2] CEN. *Eurocode 2 - Design of concrete structures - Part 1-1: General rules and rules for buildings*, EN 1992-1-1, Brussels, 2005.
[3] Bathe, K. J., Walczak, J., Welch, A., Mistry. *Nonlinear analysis of concrete structures*. Computers & Structures, 32(3-4), 563-590, 1989.
[4] Kotsovos, G. M., & Kotsovos, M. D. *Flat slabs without shear reinforcement: criteria for punching*. The Structural Engineer, 87(1), 2-8, 2009.
[5] Rodrigues, R. V. *Shear strength of reinforced concrete bridge deck slabs*. Ecole Polytechnique Fédérale de Lausanne, PhD thesis, 2007.
[6] Bathe, K. J. *Finite element procedures.* Prentice-Hall, Englewood Cliffs, NJ, 1996.
[7] Vecchio, F. J., and Collins, M. P. *The modified compression field theory for reinforced concrete elements subjected to shear*. ACI Journal 83, 22, 219–231, 1986.
[8] Selby, R. G., and Vecchio, F. J. *Three-dimensional Constitutive Relations for Reinforced Concrete*. Tech. Rep. 93-02, Univ. Toronto, dept. Civil Eng., Toronto, Canada, 1993.
[9] Rijkswaterstaat. *Guidelines for Nonlinear Finite Element Analysis of Concrete Structures*. Rijkswaterstaat Technical Document (RTD), 2017.
[10] TNO DIANA BV. *DIANA -User´s Manual*. Delft, The Netherlands, 2016.
[11] Herenda, Dž. *Numerical modeling of nonlinear behavior of RC slabs*, Master Thesis, Faculty of Civil Engineering, University of Sarajevo, 2020.

ECCOMAS MSF 2021 THEMATIC CONFERENCE
30 June – 2 JULY 2021, SPLIT, CROATIA

EXPERIMENTAL VS. NUMERICAL MODELING OF REINFORCED CONCRETE BEAM

Samir Vahida[1], Senad Medić[2], Muhamed Zlatar[3]

[1] Faculty of Civil Engineering, University of Sarajevo, samir.vaha@gmail.com
[2] Faculty of Civil Engineering, University of Sarajevo, senad_medic@yahoo.com
[3] Faculty of Civil Engineering, University of Sarajevo, zlatar.muhamed@gmail.com

Abstract

As a part of new Model Code 2020, nonlinear finite element analysis should be incorporated in design to keep up with the software development. In order to setup, perform and check NLFEA, experiments have to be analyzed to prove the safety concept and show the reliability of advanced nonlinear approaches. In this paper a response of a 3PB test on a simple beam performed by Vecchio and Shim is numerically predicted using DIANAFEA and certain modeling aspects are highlighted.

Keywords: DIANAFEA, reinforced concrete beam, nonlinear, 3PB experiment

1 Introduction

In the still-evolving field of nonlinear finite element analysis of reinforced concrete structures, the pioneering work started by Scordelis in the early 1960s was instrumental in defining the concepts and approaches generally followed by the research community since. Among Professor Scordelis' many contributions was a seminal paper describing the testing of a series of 12 reinforced concrete beams [1], aimed primarily at investigating shear-critical behavior, but also at providing data to support finite element development work. The beams tested covered a wide range of reinforcement and span conditions, and hence, a range of influencing factors and failure modes. These beams soon came to be regarded as a classic test series. They have since been used extensively as benchmark data for calibrating or verifying finite element models for reinforced concrete, particularly for modeling of beams critical in shear.

A test program was undertaken at the University of Toronto to recreate, as much as possible, the Bresler–Scordelis test series. First, it was sought to determine the extent of repeatability of the test results, particularly with respect to load capacity and failure mode, given that there would be some unavoidable differences in construction and testing procedures. Information on post-peak response was also sought; the load–deflection response reported for the Bresler–Scordelis beams abruptly terminated at the peak loads. Additional insight into the behavior of the beams, such as the nature of important influencing factors and critical behavior mechanisms, would also hopefully emerge from new first-hand test observations. Finally, insight into critical factors in the accurate finite element modeling of these beams was sought [2].

Nonlinear analysis poses far more challenges than solving a system of equations in linear elastic regime because there is not one unique solution procedure that is suitable for solving all nonlinear problems. For the execution of linear elastic analysis in DIANA [3] the user can usually rely on default solution procedures. However, for nonlinear analysis, an appropriate solution procedure must be selected. When the model definition is not ok or the solution procedures are not properly chosen, convergence issues

may arise in nonlinear analyses. Also, convergence issues can be raised because the iterative solution method is unable to find a solution for the nonlinear problem. Basically, three types of convergence issues can be raised: in nonlinear global equilibrium iterations, in local stress-return mapping iterations and in the iterative solution method. From experience in dealing with analysis models that include cracking and/or interface material models, usually such analyses require some experience or good-feeling of the user [4].
In classical design, usually a linear elastic analysis is conducted in the first step with the intention to obtain a realistic description of the distribution of internal forces. The second step consists of the design of all critical components of the structure using local non-linear models. The two steps are not consistent. The assumed linear elastic material behaviour of the structural analysis is a gross simplification, especially for concrete structures. This can lead to a modelled structural response and internal force distribution that deviates significantly from reality. To describe the structural response more realistically, non-linear analysis is becoming more widely used [5].

2 Experimental setup

Geometry of the analyzed beam is shown in Figure 1. Relationship between force and displacement at the midpoint is given in Figure 2.

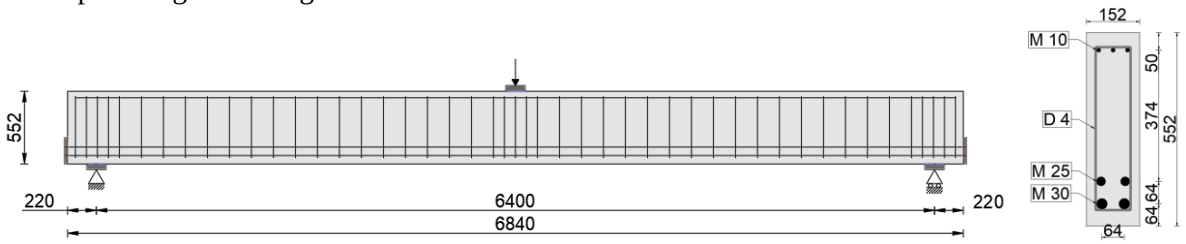

Figure 1. a) Longitudinal section with beam geometry and reinforcement layout, b) cross-section [6].

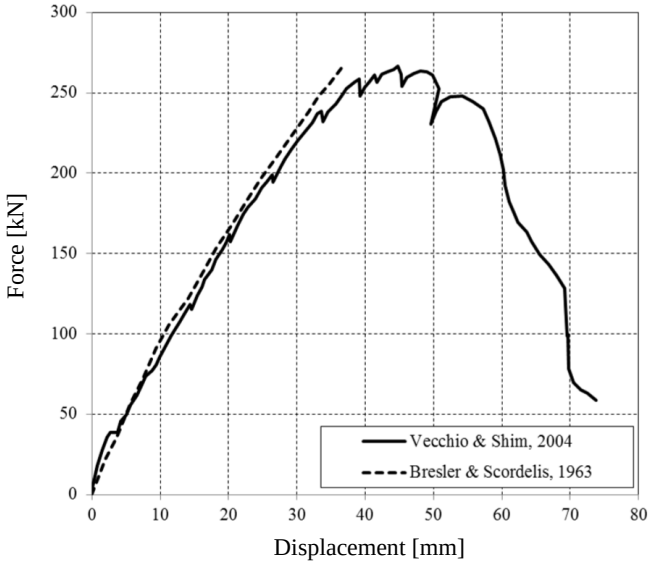

Figure 2. Force-displacement for the tested beam [2].

3 Numerical modeling

Details of numerical model are provided in [6, 7]. Concrete was modeled using Total strain rotating crack model, embedded reinforcement was assumed von Mises with isotropic hardening, linear interfaces were applied between steel plates and the beam, however with zero shear stiffness. The pushover curve and comparison with the experimental result are shown in Figure 3.

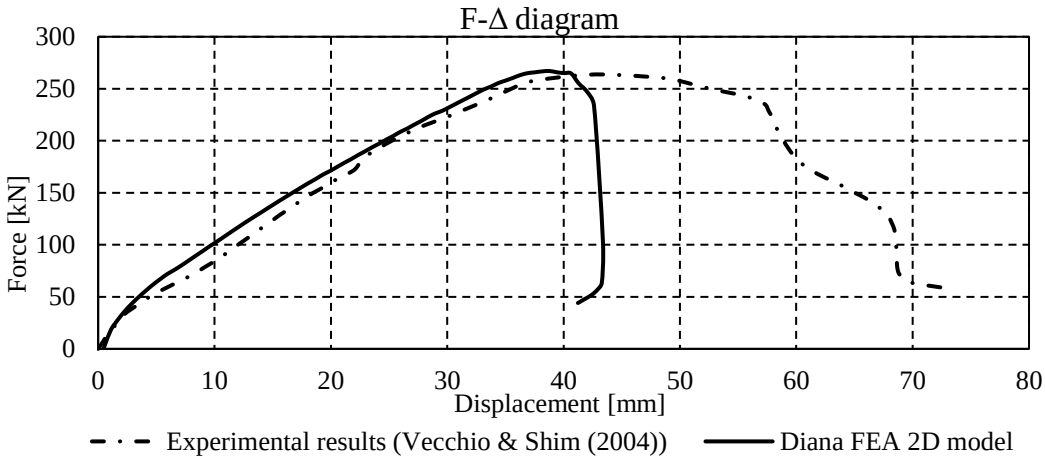

Figure 3. Force-displacement diagram of the tested beam [6] – experiment and numerical model.

Crack distribution is shown in Figure 4 (model south-side). Stresses in horizontal direction in concrete, vertical stresses in shear reinforcement and tension in the bottom M30 bar are displayed in Figure 5.

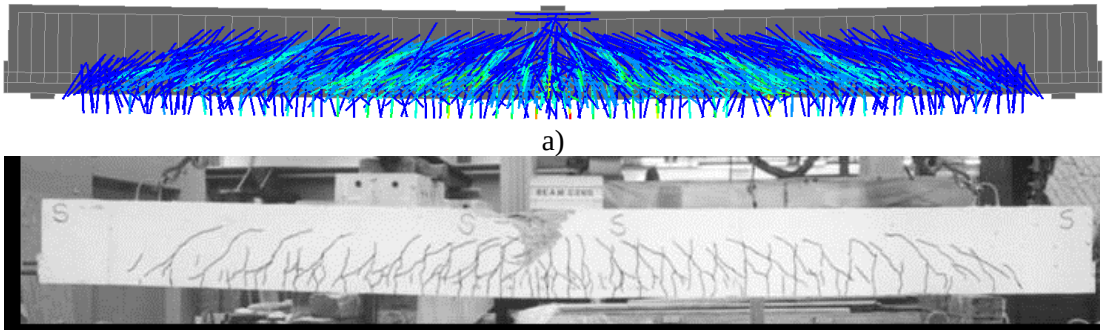

a)

b)

Figure 4. Comparison of crack distribution: a) numerical model, b) experiment (south-side)

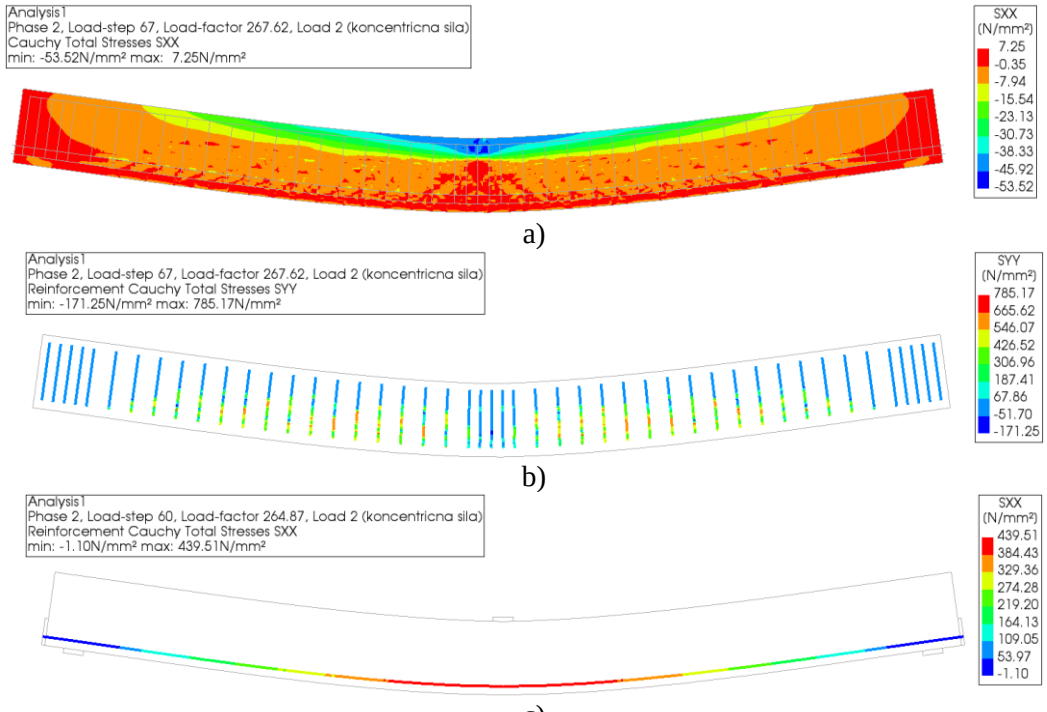

a)

b)

c)

Figure 5. a) Stress state prior to failure: a) concrete (Sxx), b) stirrups (Syy), c) lower bottom reinforcement M30 (Sxx)

4 Conclusion

In the tested beam which contains web reinforcement, flexural-compressive failure developed with the crushing, splitting and spalling of concrete in the flexural compression zone, especially close to the loading plate and yielding of reinforcement. The beam did not fail in a pure shear -critical manner. The numerical model nicely reproduced the observed phenomena in the experiment. The initial stiffness, the peak load and the global behavior were captured well. Further calibration is needed with respect to softening branch. The behavior of the beam is highly influenced by crushing of concrete beneath and adjacent to the loading plates. The disturbances around the loading plates introduce complex three-dimensional effects, making the modelling of interface elements placed between loading or supporting steel plates and the RC beam a fundamental aspect to be considered.

References

[1] Bresler, B., Scordelis, A. C. *Shear strength of reinforced concrete beams*. In Journal Proceedings (Vol. 60, No. 1, pp. 51-74), 1963.
[2] Vecchio, F. J., Shim, W. *Experimental and analytical reexamination of classic concrete beam tests.* Journal of Structural Engineering, 130(3), 460-469, 2004.
[3] TNO DIANA BV. *DIANA -User´s Manual*. Delft, The Netherlands, 2016.
[4] Palacio, K. *Practical recommendations for nonlinear structural analysis in DIANA*. TNO DIANA BV, Delft, 2013.
[5] Schlune, H., Plos, M., Gylltoft, K. *Safety formats for non-linear analysis of concrete structures.* Magazine of Concrete Research, 64(7), 563-574, 2012.
[6] Vahida, S. Numerical modeling of nonlinear behavior of RC beams, Master Thesis, Faculty of Civil Engineering, University of Sarajevo, 2020.
[7] Hendriks, M.A.N., de Boer, A., Belletti, B., *Guidelines for Nonlinear Finite Element Analysis of Concrete Structures*, Rijkswaterstaat Centre for Infrastructure, Report RTD:1016-1:2017, 2017.

ECCOMAS MSF 2021 THEMATIC CONFERENCE
30 June – 2 JULY 2021, SPLIT, CROATIA

NUMERICAL MODEL OF A MASONRY INFILLED RC FRAME

Amar Kadić[1], Senad Medić[2], Davorin Penava[3]

[1] INFRA Ltd., Sarajevo, amar.kadic@infra.ba
[2] University of Sarajevo, senad_medic@yahoo.com
[3] Josip Juraj Strossmayer University of Osijek, davorin.penava@gfos.hr

Abstract

The response of reinforced concrete frame structures with a masonry infill to seismic action can be represented by models of different levels of complexity such as: detailed and simplified micromodels or macromodels. Macromodels have the lowest requirement for the input of material properties and allow the shortest computational time without losing the accuracy of representing the response of the structure. In order to achieve the required accuracy of the macromodel, it is necessary to undergo a calibration procedure according to the test results. The calibration procedure indicates the high sensitivity of the model to the properties of the mortar joints at the contact of the wall and the frame. The calibrated macromodel, with slight deviations, corresponds to the response of the structure obtained by the tests.

Keywords: macromodel, RC frame, masonry infill, DIANAFEA, laboratory test, calibration

1 Introduction

Reinforced-concrete (R-C) frames infilled with masonry walls, with- or without openings, are a common architectural element in low- and medium-height buildings. The infill walls stiffen the frame and reduce the first-mode period, leading to a reduction of drift response to strong ground motion. At the same time, the addition of masonry wall within the frame tends to increase the base-shear response and reduce the drift capacity of the structure. The increase of shear force and reduction of drift capacity leads to serious vulnerabilities unless proper proportioning is exercised. The specific flaws in unintentional frame-wall systems were identified in the aftermath of the Skopje earthquake of 1963. These were: (1) weaknesses introduced by openings in the wall, (2) captive columns, (3) out-of-plane collapse of walls, and (4) column failures under reversals of combinations of shear and tensile or compressive forces. These flaws have continued to cause tragic consequences in subsequent urban earthquakes [1].
The influence of openings in infill on the behavior of reinforced-concrete frames infilled with masonry ("framed-wall") was experimentally investigated. Openings were of different types and positions and were executed with and without vertical confining elements around them. Ten specimens produced at a scale of 1:2.5, as practical true models, were tested under constant vertical and quasi-static cyclic lateral loading up to drifts when the infill failed. The frames were designed as medium ductility (DCM) bare frames. Masonry wall was produced with hollow-clay units and general purpose mortar. The frame and masonry were connected only by cohesion (Figure 1) [2].
Based on the experimental research, a macromodel was set up in the computer program DIANA FEA [3] and the analysis of a reinforced concrete frame with a masonry infill without openings was performed [4].

Figure 1. Specimens for laboratory investigation [2].

2 Macromodel

Due to the heterogeneity of the masonry infill, the construction of the computational model is more demanding. The requirement to know the properties of the material depends on the level of modeling and the type of calculation performed (e.g., linear or nonlinear). There are several possibilities or approaches to the modeling of masonry, such as those listed in [5], which are as follows: detailed micromodel; simplified micromodel or mesomodel and macromodel (Figure 2).
The approach selected and applied in this paper does not distinguish between individual wall elements and mortar joints and the infill wall is presented as a homogeneous anisotropic continuum. The chosen approach, in relation to the others, requires a significantly smaller number of material properties to feed the constitutive model, without consequences for accuracy in presenting the response of the structure. This simplification has made the modeling process more practical.

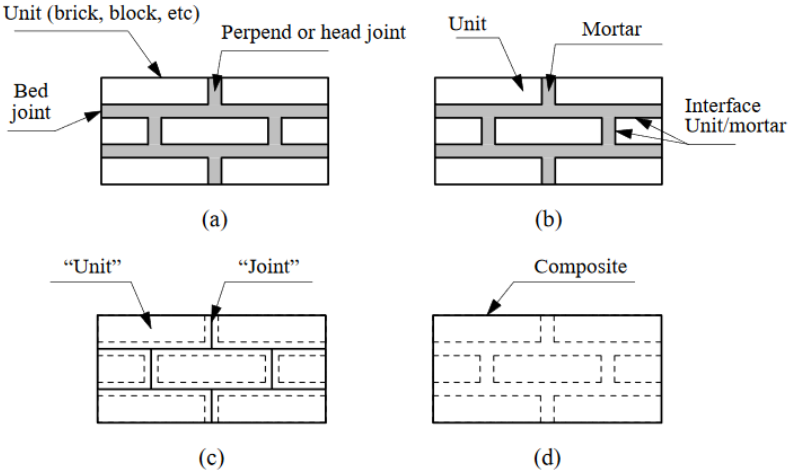

Figure 2. Modeling strategies for masonry: a) masonry wall, b) detailed micromodel, c) mesomodel (simplified micromodel), d) macromodel [5].

After earthquakes, field investigations and research results have shown that masonry infill placed within a structural RC frame (‘‘framed-masonry’’) has both positive and negative effects on the seismic performance of the system. The new composite ‘‘framed-masonry’’ system has smaller drifts and deformations in structural members, together with shear resistance of higher storey and global energy dissipation. On the other hand, the infill wall presence can have an extremely negative effect on the surrounding frame in terms of shear failure of captive columns, depending on the wall strength, as given in [6] and [7]. Previous experiments have shown that even at small drifts (approximately 0.05%) the infill wall behaves like a monolithic structure and the infill wall separates from the reinforced concrete frame. Increasing the floor displacement creates cracks along the formed compressive strut in the infill

wall. In order to correctly present the separation of the infill wall from the reinforced concrete frame in the macromodel, it is necessary to apply a contact element at the joint of the frame and the wall, which has the possibility of gapping in tension. A detailed overview of the properties of constitutive models is given in [4], and due to the scope and lack of space it is not covered by this text. The adopted macromodel is shown in Figure 3. A mesh 100x100 mm was chosen using CQ16MEM membrane elements with quadratic interpolation (compatible with geometric nonlinearity).

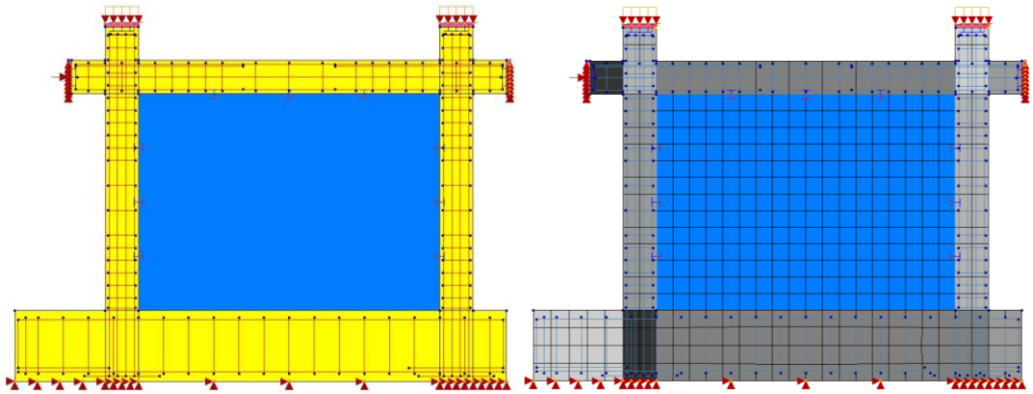

Figure 3. Macromodel and FE mesh (100x100mm) in DIANAFEA.

3 Results and conclusion

As in the experiment, the calculation was carried out entirely with force control. High sensitivity of the model to the properties of the contact elements placed between the frame and the infill wall was observed, which, in addition to physical ones such as initial shear strength, internal friction angle and tensile strength, also contain the so-called non-physical properties such as normal and tangential stiffness, the value of which needs to be assumed. For this reason, calibration was required. An additional problem arose when loading the structure model in the opposite direction (negative x-direction). It has been observed that during loading (when the beam is pulled) tensile stresses occur in the beam that exceed the value of tensile strength of the material, with large displacements. This problem was solved by introducing a rigid kinematic constraint, ie by equalizing the displacements in the longitudinal direction of the left and right ends of the beam.

Figure 4 shows a comparison of the responses obtained from the experimental tests [1] and the computational macromodel [4]. The highest achieved load capacity and initial stiffness in positive load cycles (positive x-direction) are in accordance with the results obtained by the test, while the corresponding values in negative cycles are 16% lower. The difference in values arises from the ability to maintain a constant value of the longitudinal compressive force, and thus from the effect of friction of the movable supports with the tops of the columns (rollers). In the representation of the model given in Figure 5, it is noticeable how the infill wall is crushed along the height of the column as well as in the corners of the frame (in red areas), which corresponds to the assumed behavior of the structure and test results.

The described macromodel of the reinforced concrete frame with masonry infill, calibrated according to the test results, is able to present the most important response characteristics of these types of structures, which are: load-bearing capacity, stiffness and type of masonry failure. The calibration procedure showed a high sensitivity of the computational macromodel to the properties of the contact elements that represent the joints of the mortar at the contact of the infill wall and the reinforced concrete frame. Additionally, it was necessary to take into account the occurrence of friction on the rollers on the tops of the columns as described in [8], which is enabled by a spring with a bilinear constitutive model.

The selected macromodel is the simplest approach that can describe the behavior of the infill wall using a computer program. It is capable of simulating test results with acceptable deviations. It does not require

large data set of input parameters as with computational micromodels, which makes it more practical and the calculation faster.

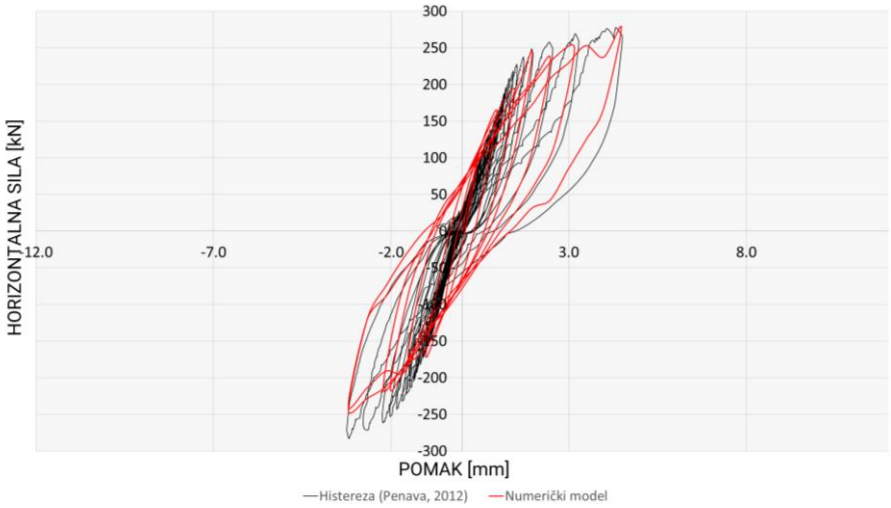

Figure 4. Hysteretic curves - comparison of experimental and numerical results.

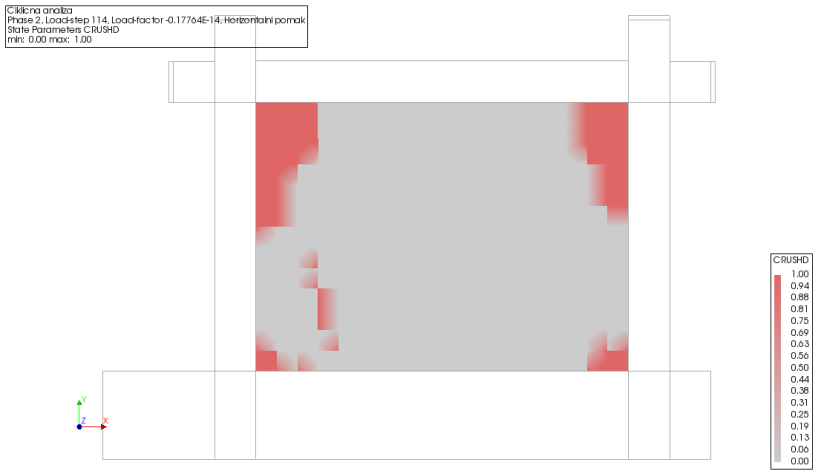

Figure 5. Crushing of masonry infill obtained by macromodel.

References

[1] Sigmund V, Penava D. *Influence of openings, with and without confinement, on cyclic response of infilled rc frames—an experimental study*. Journal of earthquake engineering. 18(1):113-46, 2014.

[2] Penava, D. *Influence of openings on seismic response of masonry infilled reinforced concrete frames*. Josip Juraj Strossmayer University of Osijek, Osijek, 2012.

[3] TNO DIANA BV. *DIANA -User´s Manual*. Delft, The Netherlands, 2016.

[4] Kadić, A. *Numerical modeling of RC frame with masonry infill*, Master Thesis, Faculty of Civil Engineering, University of Sarajevo, 2020.

[5] Lourenço P. *Computational strategies for masonry structures*, PhD, Technical University Delft, 1996.

[6] ATC. *Evaluation of earthquake damaged concrete and masonry wall buildings: basic procedures manual* (FEMA 306). ATC, Redwood City, 1998.

[7] Penava D, Sigmund V, Kožar I. *Validation of a simplified micromodel for analysis of infilled RC frames exposed to cyclic lateral loads*. Bulletin of earthquake engineering. 14(10):2779-804, 2016.

[8] Penava D, Sarhosis V, Kožar I, Guljaš I. Contribution of RC columns and masonry wall to the shear resistance of masonry infilled RC frames containing different in size window and door openings. Engineering Structures. 172:105-130, 2018.

ECCOMAS MSF 2021 THEMATIC CONFERENCE
30 June – 2 JULY 2021, SPLIT, CROATIA

FINITE ELEMENT MODEL OF CABLE NETS USING EQUIVALENT MEMBRANES

Aida Zaimović[1], Senad Medić[2], Samir Dolarević[3]

[1] Faculty of Civil Engineering, University of Sarajevo, idana.zaimovic89@gmail.com
[2] Faculty of Civil Engineering, University of Sarajevo, senad_medic@yahoo.com
[3] Faculty of Civil Engineering, University of Sarajevo, samir.dolarevic@gf.unsa.ba

Abstract

In this paper modeling of cable net as an equivalent membrane is presented. Nonlinear analysis is performed by finite element method where isoparametric three node cable element and four node membrane element with four sides are formulated. Validation of the model is done by the numerical example which is supported by experimental results. The finite elements are implemented in the programming language MATLAB.

Keywords: cable net, equivalent membrane, finite element method, MATLAB

1 Introduction

Structures consisting of these element types have a special aesthetics and place in architecture. Moreover, they can be utilized to span the largest distances (suspension and cable-stayed bridges, cable roof structure, etc.). However, regardless of the advantages, there are a few of them compared to the other structural types. One of the reasons is a poor understanding of the behavior of these structures. The main difference with respect to more traditional structural types pertains to their flexibility, i.e., lack of bending rigidity. Consequently, a change in the loading leads to a change in the form of structure. Therefore, the analysis cannot be performed without taking into account the geometric nonlinearity.
By exploiting the variational principle, the weak form of equilibrium equations was derived. In nonlinear analysis the Newton-Raphson method was employed to determine the unknown displacements. The finite elements based on the aforementioned formulation were implemented in the programming language MATLAB.

2 Variational formulation

Variational principles are now generally used as the foundation of the finite element method. The former principle is based on the concept of energy balance and it may be stated thus: Equilibrium state of the arbitrary elastic body constrained to prevent any kinematic movement is satisfied if the first variation of the total potential energy is in the stationary state:

$$\Pi = \Pi^{int} + \Pi^{ext}, \qquad \delta\Pi = 0 \tag{1}$$

where Π is the total potential energy, Π^{int} is the strain energy of the elastic body, and Π^{ext} is the energy of the external loads. Strain energy can be computed by integrating the strain energy density $\boldsymbol{W}$ across the volume of the body. For St. Venant-Kirchhoff material the strain energy density takes quadratic form in terms of the Green-Lagrange strain, $\mathbf{E}$, which can be seen in equation (2). Second Piola-Kirchhoff stress, $\mathbf{S}$, is computed as derivate of the strain energy density with respect to the Green-Lagrange strain.

$$W(\mathbf{E}) = 1/2\,\mathbf{E}\cdot\boldsymbol{C}\mathbf{E} \;\rightarrow\; \mathbf{S} = \partial W/\partial\mathbf{E} = \mathbf{C}\mathbf{E} \tag{2}$$

The virtual work equation for the cable structure is:

$$D_{\mathrm{w}}\Pi(\mathbf{u}) = \int_L \left(\delta E\; S\; A - \delta\mathbf{u}^{\mathrm{T}}\mathbf{p}\right)\mathrm{d}s = 0 \tag{3}$$

as well as for membrane structure:

$$D_{\mathrm{w}}\Pi(\mathbf{u}) = \int_A \boldsymbol{\Gamma}\cdot\mathbf{S}\; t\; \mathrm{d}A - \int_A \mathbf{w}^{\mathrm{T}}\mathbf{p}\; \mathrm{d}A = 0 \tag{4}$$

where δE and $\boldsymbol{\Gamma}$ are given in the subsequent equations:

$$\delta E = \left(\frac{\mathrm{d}\mathbf{x}^{\mathrm{T}}}{\mathrm{d}s} + \frac{\mathrm{d}\mathbf{u}^{\mathrm{T}}}{\mathrm{d}s}\right)\frac{\mathrm{d}\,\delta\mathbf{u}}{\mathrm{d}s}, \qquad \boldsymbol{\Gamma} = \frac{\mathrm{d}}{\mathrm{d}\alpha}\left[\mathbf{E}(\mathbf{u} + \alpha\;\mathbf{w})\right]\Big|_{\alpha=0} \tag{5}$$

3 Finite element formulation

Discretized form of the aforementioned equations is obtained by using shape functions in the form of Lagrangian interpolation polynomials.

Three noded cable element

Geometry of initial configuration is determined by nodal coordinates and discretized form is:

$$\mathbf{x}^h\Big|_{L^e} = \sum_{i=1}^{3}\mathbf{N}_i(\xi)\;\mathbf{x}_i = \mathbf{N}^{\mathbf{e}}(\xi)\mathbf{x}^{\mathbf{e}} \tag{6}$$

where $\mathbf{N}^{\mathbf{e}}$ is matrix that contains Lagrangian interpolation functions for the element ***e***. Considering the fact that presented finite element is isoparametric same approach for discretization of displacements is used. Following the procedure of discretizing the weak form of the equilibrium equations (equations (3) and (4)) subsequent equation is obtained:

$$\mathbf{f}^{int}(\mathbf{u}) - \mathbf{f}^{ext} = 0 \tag{7}$$

where $\mathbf{f}^{int}(\mathbf{u})$ is internal force vector and $\mathbf{f}^{ext}$ is an external force vector with the following forms:

$$\mathbf{f}^{int}(\mathbf{u}) = \sum_{e=1}^{nel}\mathbf{L}^{\mathbf{eT}}\left(\int_{L^e}\mathbf{B}^{\mathbf{eT}}(\xi)\left(\mathbf{B}^{\mathbf{e}}(\xi)\mathbf{x}^{\mathbf{e}} + \mathbf{B}^{\mathbf{e}}(\xi)\mathbf{u}^{\mathbf{e}}\right)\;S^e\;A^e\;\mathrm{d}s\right) \tag{8}$$

$$\mathbf{f}^{ext} = \sum_{e=1}^{nel}\mathbf{L}^{\mathbf{eT}}\left(\int_{L^e}\mathbf{N}^{\mathbf{eT}}(\xi)\mathbf{N}^{\mathbf{e}}(\xi)\mathbf{p}^{\mathbf{e}}\;\mathrm{d}s\right) \tag{9}$$

Derivation of the Lagrangian functions with respect to cable arc length is contained in matrix that is noted as **B** matrix.

Four node membrane element with four sides

Discretized geometry of initial configuration and displacements are formed analogously as for three node cable element, where shape functions, placed in matrix $\mathbf{N}^{\mathbf{e}}$, are obtained by multiplying Lagrangian first degree polynomials in terms of ξ and η:

$$\mathbf{x}^h\Big|_{\Omega^e} = \sum_{i=1}^{4}\mathbf{N}_i(\xi,\eta)\;\mathbf{x}_i = \mathbf{N}^{\mathbf{e}}(\xi,\eta)\mathbf{x}^{\mathbf{e}} \tag{10}$$

By discretizing the weak form of the equilibrium equations equation (7) is obtained, where $\mathbf{f}^{int}(\mathbf{u})$ and $\mathbf{f}^{ext}(\mathbf{u})$ have the following form for membranes:

$$\mathbf{f}^{int} = \sum_{e=1}^{nel} \mathbf{L}^{\mathbf{eT}} \left(\int_A \mathbf{B}^{\mathbf{eT}} (\xi,\eta) \mathbf{s}\ t\ \mathrm{d}A \right), \quad \mathbf{f}^{ext} = \sum_{e=1}^{nel} \mathbf{L}^{\mathbf{eT}} \left(\int_A \mathbf{N}^{\mathbf{eT}} (\xi,\eta) \mathbf{N}^{\mathbf{e}} (\xi,\eta)\ \mathrm{d}A \right) \mathbf{p}^{\mathbf{e}} \tag{11}$$

4 Linearization of a system of nonlinear equations

Aforementioned equilibrium equations for cable structure (equation (3)) and membrane structure (equation (4)) are nonlinear, therefore for its solving iterative methods are employed. In this work Newton-Raphson method is applied. Linearization of the equations (3) and (4) are performed:

$$L\left[\mathbf{R}\left(\mathbf{u}^{(i+1)}\right) = \mathbf{f}^{int} - \mathbf{f}^{ext} \right] = \mathbf{f}^{ext} - \mathbf{f}^{int}\left(\mathbf{u}\right) \Big|_{\mathbf{u}^{(i)}} - \mathbf{K} \Big|_{\mathbf{u}^{(i)}} \Delta\mathbf{u}^{(i)} = 0 \tag{12}$$

Tangent stiffness matrix for cable element is divided in two parts, geometric $\mathbf{K_g}$ and the remaining part of the tangent stiffness matrix $\mathbf{K_o}$ and their form read as follows:

$$\mathbf{K_g} \Big|_{\mathbf{u}^{(i)}} = \sum_{e=1}^{nel} \mathbf{L}^{\mathbf{eT}} \int_{L^e} S\Big|_{\mathbf{u}^{(i)}} \mathbf{B}^{\mathbf{eT}} \mathbf{B}^{\mathbf{e}} A^e\ \mathrm{d}s\ \mathbf{L}^{\mathbf{e}} \tag{13}$$

$$\mathbf{K_o} \Big|_{\mathbf{u}^{(i)}} = \sum_{e=1}^{nel} \mathbf{L}^{\mathbf{eT}} \int_{L^e} \mathbf{B}^{\mathbf{eT}} \left(\mathbf{B}^{\mathbf{e}} \mathbf{x}^{\mathbf{e}} + \mathbf{B}^{\mathbf{e}} \mathbf{u}^{\mathbf{e}(i)} \right) C^{\mathbf{e}} \left(\mathbf{x}^{\mathbf{eT}} \mathbf{B}^{\mathbf{eT}} + \mathbf{u}^{\mathbf{eT}(i)} \mathbf{B}^{\mathbf{eT}} \right) \mathbf{B}^{\mathbf{e}} A^e\ \mathrm{d}s\ \mathbf{L}^{\mathbf{e}} \tag{14}$$

As well as for cable element, tangent stiffness matrix for membrane element is also divided in two parts, except for this case in geometric $\mathbf{K_g}$ and the material tangent stiffness matrix $\mathbf{K_m}$:

$$\mathbf{K_g} \Big|_{\mathbf{u}^{(i)}} = \sum_{e=1}^{nel} \mathbf{L}^{\mathbf{eT}} \int_A \left(S_{11} \frac{\partial \mathbf{N}^{\mathbf{e}}}{\partial x}^T \frac{\partial \mathbf{N}^{\mathbf{e}}}{\partial x} + S_{22} \frac{\partial \mathbf{N}^{\mathbf{e}}}{\partial y}^T \frac{\partial \mathbf{N}^{\mathbf{e}}}{\partial y} + S_{12} \left(\frac{\partial \mathbf{N}^{\mathbf{e}}}{\partial x}^T \frac{\partial \mathbf{N}^{\mathbf{e}}}{\partial y} + \frac{\partial \mathbf{N}^{\mathbf{e}}}{\partial y}^T \frac{\partial \mathbf{N}^{\mathbf{e}}}{\partial x} \right) \right) t\ \mathrm{d}A\ \mathbf{L}^{\mathbf{e}} \tag{15}$$

$$\mathbf{K_m} \Big|_{\mathbf{u}^{(i)}} = \sum_{e=1}^{nel} \mathbf{L}^{\mathbf{eT}} \int_A \mathbf{B}^{\mathbf{eT}} \mathbf{D} \mathbf{B}^{\mathbf{e}}\ t\ \mathrm{d}A\ \mathbf{L}^{\mathbf{e}} \tag{16}$$

Now update of displacement matrix can be obtained, where displacement increment is calculated by the equation (12):

$$\mathbf{u}^{(i+1)} = \mathbf{u}^{(i)} + \Delta\mathbf{u}^{(i)} \tag{17}$$

This iterative process is repeated until convergence is obtained in two following norms, where ε is an error term and i is a number of iterations:

$$\left|\mathbf{R}(\mathbf{u})\right| = \left|\mathbf{f} - \mathbf{r}(\mathbf{u})\right| < \varepsilon; \quad i > i_{\max} \tag{18}$$

5 Implementation in MATLAB and numerical validation

MATLAB is a programming language specially designed for dealing with matrices. This makes it particularly suited for programming the finite element method [4]. Programming the finite element method involves the following steps: 1) data input, 2) computation of $\mathbf{f}^{int,\,e}$, $\mathbf{f}^{ext,\,e}$ and $\mathbf{K}^{\mathbf{e}}$ of an element ***e***, 3) assembly of $\mathbf{f}^{int,\,e}$, $\mathbf{f}^{ext,\,e}$ and $\mathbf{K}^{\mathbf{e}}$ in the global matrices and imposition of boundary conditions, 4) finding solution of nodal displacements, 5) computation of stresses and nodal forces from calculated displacements and 6) print of the results (Figure 1). For the validation purpose an example of a taut flat square cable net is presented. Verification of the FEM elements is obtained by the comparison between the experimental results [3] and results of the FEM. In addition, analytical results for equivalent membrane are given also. The results of the comparison are given in the table 1. Cable net is constructed from five orthogonal cables in each direction, spanning a distance of 152,4 cm (60 in). Diameter of used cable cord is 0,2381 cm (3/32 in) and modulus of elasticity is $10{,}342 \cdot 10^6$ N/cm^2. The pretension in each

cable is 533,78 N (120 lb). Every intersection point of a cable net is loaded by the concentrated load of 22,24 N (5 lb).

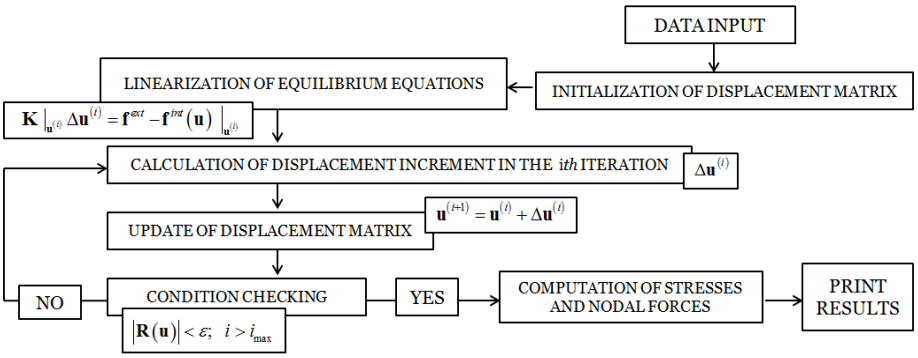

Figure 1. Solving system of nonlinear equations in MATLAB

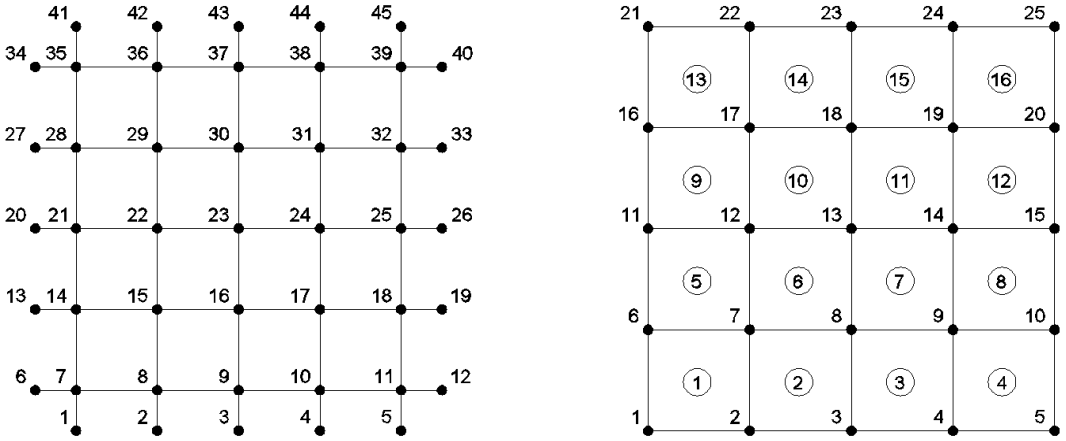

Figure 2. Discretization of cable net calculation models: a) cable net, b) equivalent membrane

FEM static analysis of cable net is executed in two different approaches. The cable net is first modeled as a discretized cable net consisting of three node cable elements, and second model is formed as an equivalent membrane discretized by the four node membrane element with four sides.

Table 1. Deflection of the node given by the different computation methods

Node of the cable net	7	8	9	15	16	23
Experimental [cm]	0,429	0,737	0,826	1,496	1,694	1,963
Analytical [cm]	0,342	0,671	0,760	1,435	1,658	1,927
FEM - Cable net	0,339	0,654	0,703	1,456	1,605	1,779
FEM - Membrane	0,187	0,489	0,575	1,281	1,521	1,854

Agreement between the experimental results and results obtained by the FEM is satisfying although the mesh is coarse. From previous results it is apparent that the use of an equivalent membrane as a model of cable net is adequate.

References

[1] A. Ibrahimbegović. *A Consistent Finite-Element Formulation of Nonlinear Elastic Cables*, Communications in Applied Numerical Methods, vol 8, 547-556, 1992.

[2] A. Ibrahimbegovic, *Nonlinear Solid Mechanics, Springer*, Heidelberg, 2009.

[3] M. Irvine, *Cable Structures*, MIT Press, Cambridge, 1981.

[4] A. Khennane, *Introduction to Finite Element Analysis Using MATLAB and Abaqus*, Taylor & Francis Group, Boca Raton, 2013.

ATOMIC STRING FUNCTIONS AND SPACETIME QUANTIZATION

S.Yu. Eremenko[1]

Keywords: Atomic string, atomic function, atomic soliton, spacetime, quantum

ABSTRACT

Based on a generalization of a well-known atomic function this paper introduces an *atomic string* (AString) as a kink-like function by joining of which on a periodic lattice it is possible to build one model for a flat and curved spacetime and explain gravitational warping effects. Physically AString may represent a spacetime warp/distortion/metriant composing *atomic quanta* that can grow, shrink and group into 'solitonic atoms' which can compose spacetime and other fields widespread in nature. AString and atomic function can be the new candidates for *atomic solitons* and elementary strings as fundamental blocks of spacetime fabric and matter fields. AString and closely related atomic function may find new areas of applications in lattice physics, string theory, quantum gravity, solitons and finite element methods.

Introduction.

An *atomic string* first introduced in this paper extends series of our publications [1-5] on nonlinear models of nature initiated by Academician V.L. Rvachev and his school with the involvement of new ideas from the theories of atomic functions [5-11], finite elements [12-14], solitons [15-17], strings [19-20], general relativity and spacetime physics [21-26], lattice physics [27-30], and astronomy [18,21-23,26]. More precisely, based on integration of an atomic function we introduce a soliton-like 'atomic string' (AString) from superposition of which - like from quantum wave-particles - it is possible to compose infinitely smooth flat and curved continua which may represent a fabric of spacetime, periodic atomic structures, matter and smooth bodies widespread in nature and universe. Being shaped like a wave swing but behaving like a particle in compositions, an atomic string along with closely related atomic function may be the good candidates for a new *atomic soliton* and *string* as a fundamental building block of nature.

[1] *Ph.D., Dr.Sc.(Eng.), Professor, Honorary Professor. Soliton Scientific, Australia; Email: eremenko@tpg.com.au.*

Atomic functions [5-11] (AF) described in multiple monographs, and dozens of papers have been published in 1971 by V.L. Rvachev and V.A. Rvachev and further developed by many followers, notably V.F. Kravchenko [5,10,11], for a wide range of applications in mathematical physics, boundary value problems, statistics, radio-electronics, telecommunications, signal processing and others. As per historical survey [9] available online, the analogs or subsets of AFs sometimes named differently (Fabius function, hat function, compactly supported function) have been rediscovered since 1970th by other scientists from different countries, but the most comprehensive development supported by multiple books and hundreds of papers has been performed by the school of V.L. Rvachev. An atomic function looking like a specifically shaped pulse belongs to the class of absolutely smooth functions defined, like splines, on a finite segment. A remarkable property of all derivatives being expressed through a superposition of shifted and stretched AFs makes it as significant as an exponent and leads to good approximation qualities like for splines widely used in finite element methods featured in our books and surveys [12-14] amongst many others. Another important property is the ability for AFs to exactly represent a unity (number 1) via the superposition of only a few nonlinear pulses, and this cannot be achieved so easily with other trigonometric, hyperbolic and pulse-like functions. This property will be important for an atomic string introduced hereafter to exactly represent a straight line to model the metric of spacetime.

Another component of the theory described here is the theory of solitons [15-17] which describes the solitons as the versatile phenomena relevant to many branches of physics, natural and life sciences studying nonlinear wave-particle behaviour of matter. Solitons in nature exist in the form of stand-alone waves, kinks, vortices, topological dislocations and their groups [15-17]. Most relevant are sine-Gordon and Frenkel-Kontorova soliton models [15-17] introducing kink-like functions shaped similar to AString introduced hereafter. The soliton kinks also appear in theory of skyrmions, domain wall, cosmic strings and instantons tied to elementary strings which postulated to be the foundation of matter in string theories [19,20]. The AString introduced hereafter may contribute to theories mentioned above due to the ability to construct 'solitonic atoms' and *atomic quantum* to model flat and curved spacetime and fields.

Introducing Atomic String idea.

There are many swing functions (Fig.1) often called *kinks* which play an important role in physics, mathematics, and statistics. For example, sigmoid function scaled and shifted by constants a, b, c, d

$$Sig(x) = \frac{1}{1+\exp(-x)},\ Sig(x,a,b,c,d) = d + c * Sig((x-b)/a) \quad (1)$$

is widely used in geometry, statistics, machine learning, artificial intelligence and other theories. Similar shape has the hyperbolic tangent function

$$tanh(x) = \frac{\exp(x) - \exp(-x)}{\exp(x) + \exp(-x)},\ Tanh(x, a, b, c, d) = d + c * tanh((x - b)/a) \quad (2)$$

used in geometry and physics including electromagnetic theory and special relativity. The following important soliton kink function

$$SGSoliton(x) = 4\arctan(\exp(x)),\ SGSoliton(x, a, b, c, d) = d + c * SGSoliton((x - b)/a) \quad (3)$$

describes sine-Gordon solitons, Frenkel-Kontorova soliton dislocations, a large pendulum swing, dynamics of vortices, skyrmions, and others [15, 16].

All these and similar functions have a common type of shape in the form of slow 'tale' followed by rising almost straight 'body' toward the slow 'head' like shown in Fig.1, b. Using visualisation in Fig.2, a, let's investigate what would be the shape of a combined curve if we join two kink functions one after another on a periodic grid structure represented by a coordinate system hoping that anti-symmetrically-similar 'tale- and head-connectors' may join like in Lego game and extend the body.

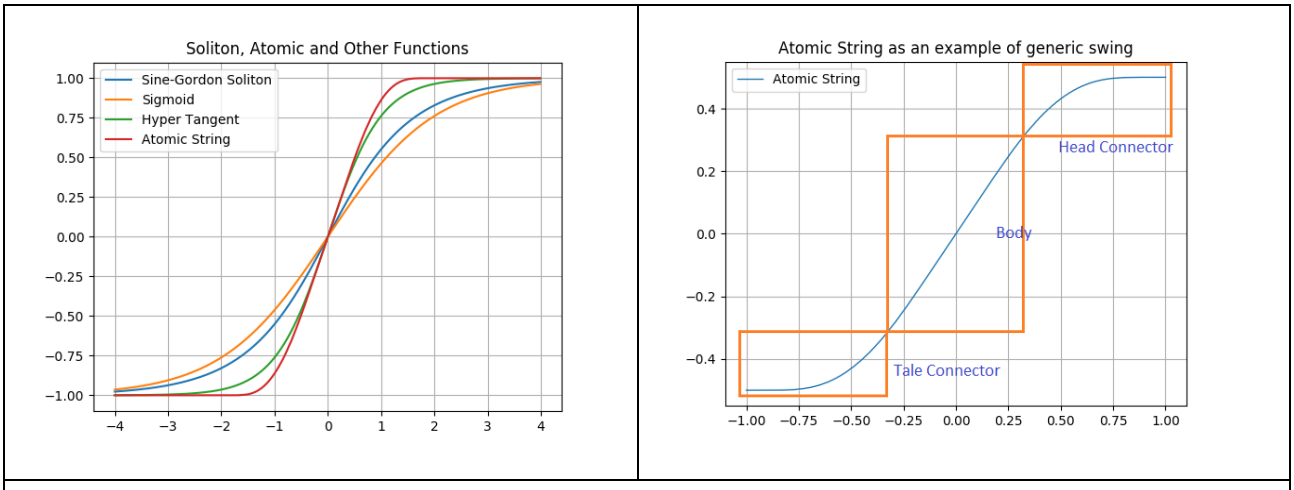

Fig. 1. a) Some important swing-like functions often called kinks b) Generic swing in the form of AString function

Simple mathematical analysis and fitting experiments in Fig.2, a show that joining of nonlinear functions (1) - (3) will create 'bumps' between joints which would deviate the combined shape from a straight-line segment. For example, function (3) represents the Frenkel-Kontorova soliton dislocations in periodic atomic structures [15,16], but a combination of them cannot describe a flat surface between atoms. The intriguing question arises whether it is possible to find an *infinitely smooth* kink function which would exactly represent the straight-line section $y = x$ as shown in

Fig.2, b with ‘tale- and head-connectors’ perfectly matching each other like in Lego game and extending the *straight* body.

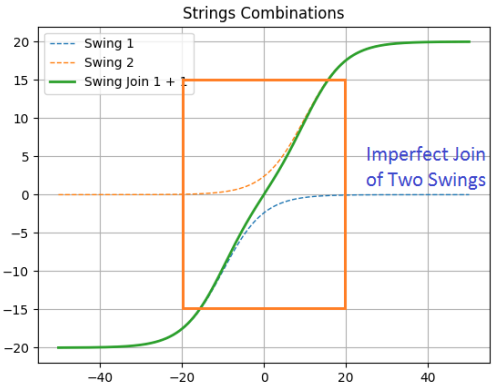

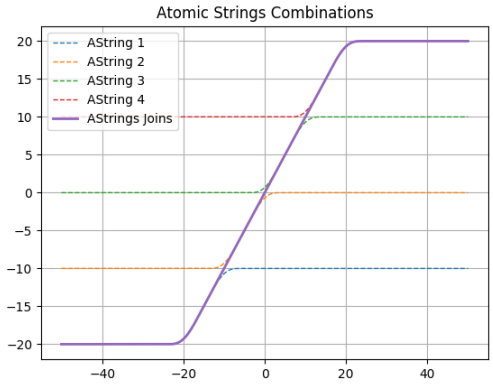

Fig. 2. a) Joining of ordinary swings does not produce straight body b) Joining of two atomic strings should produce perfectly straight line between joints.

Let’s note that widely used finite element methods [12-14] introduce many types of splines (B-splines, Hermit-splines) which can exactly represent a straight line and polynomial curves between adjacent points, but only with limited smoothness. Our goal is to discover *absolutely smooth* functions typical in major physical theories including general relativity, solitons and string theories. If such a function found, it may be a good candidate for an elementary quantum composing the *expanding* fabric of spacetime and generally other continua widespread in nature and the universe. Luckily, this function shown in Fig.1 which we would call an *atomic string* and denote as

$$AString(x),\ AString(x,a,b,c,d) = d + c * AString((x-b)/a) \tag{4}$$

can be constructed based on an extension of an *atomic function* $up(x)$ discovered in 1970th by V.L. Rvachev, V.A. Rvachev [5-11] and further developed by many followers, notably V.F. Kravchenko [5,10,11]. Mathematically, joining (summing) of $AStrings$ one after another on a grid with period s should extent the ‘body’ and produce a straight-line segment for a combined body between joints:

$$x \equiv \ldots AString(x-2s) + AString(x-s) + AString(x) + AString(x+s) + AString(x+2*s) + \cdots \tag{5}$$

or, being expressed via derivatives,

$$1 \equiv \ldots AString'(x-2s) + AString'(x-s) + AString'(x) + AString'(x+s) + AString'(x+2*s) + \cdots. \tag{6}$$

A derivative of a kink-like function should look like a pulse, and because of a remarkable property of an atomic function $up(x)$ described hereafter to exactly represent the number 1 via superposition of a few nonlinear pulses, we can construct $AString$ as an integral from $up(x)$:

$$AString(x) = \int_0^x up(x)dx. \quad (7)$$

It would represent the function in formulae (4) - (6) featured in Fig.2, b. Being derived from the atomic function, we would name this function 'an atomic string' highlighting its possible applications in string theory and be a building block of spacetime fabric, matter and cosmic strings discussed later. The properties of $AString$ would depend on its derivative – atomic function described hereafter.

Atomic Function.

Atomic functions (AF) have been discovered in 1970th by V.L. Rvachev and V.A. Rvachev [6-9] and intensively used by followers, notably V.F. Kravchenko [5,10,11]. Like well-known splines, the AFs belong to the class of 'finite functions' equal to zero elsewhere except a local segment of an *x*-axis (for example, $-1 \le x \le 1$) and satisfying a special type of *linear functional-differential equations with constant coefficients and 'shifted' arguments* [6-9]

$$y^{(n)}(x) + a_1 y^{(n-1)}(x) + \cdots + a_{n-1} y'(x) + a_n y(x) = \sum_{k=1}^{M} b_k\, y(ax - b_k), |a| > 1 \quad (8)$$

The simplest and the most important is the function $up(x)$ depicted in Fig.3, a and represented via Fourier series by the formula [6-11]

$$up(x) = \frac{1}{2\pi}\int_{-\infty}^{\infty} e^{itx} \prod_{k=1}^{\infty} \frac{\sin(t2^{-k})}{t2^{-k}} dt, \quad \int_{-1}^{1} up(x)dx = 1 \quad (9)$$

allowing along with other techniques [5-11] calculating the tabular and computer code representation provided in Appendix. This *finite* function has a remarkable property - its derivative can be expressed through the function itself shifted and stretched by the factor of 2

$$up'(x) = 2up(2x+1) - 2up(2x-1)\ for |x| \le 1, up'(x) = 0\ for\ |x| > 1, \quad (10)$$

and this equation can be used as a formal definition of AF. In fact, this function has originally been obtained to answer the following question [6-8]: what should be the form of a generic finite pulse function that a derivative of it (consisting of two similar pulses) would be representable via the stretching and shifting of an original function? For such a function, it would be easy to calculate the derivatives through the function itself, like for widely used function $exp(x)$ or sigmoid (1).

There are a few other properties of AF, for example, it is infinitely smooth, has finite support like a spline and non-analytical (cannot be exactly represented by Taylor's series). Another important property of AF is the ability to exactly represent the unity (number 1) by summing up of individual pulses set at regular points ... -3, -2, -1, 0, 1, 2, 3… as shown in Fig.3, b

$$\ldots up(x-2)+up(x-1)+up(x)+up(x+1)+up(x+2)+\cdots \equiv 1. \quad (11)$$

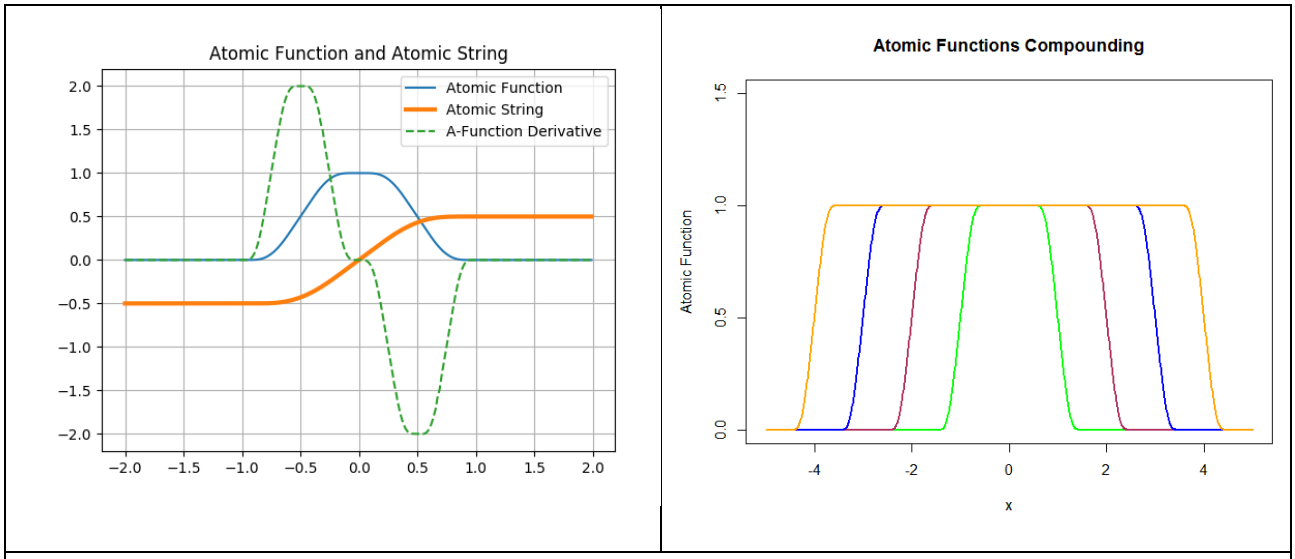

Fig. 3. a) Atomic function with derivative and integral. b) Representation of a constant by combining of atomic function pulses.

Like for continuous physical atomic structures consisting of individual atoms, it allows to *exactly* represent a constant (and linear and other functions) by combining only a few nonlinear wavy pulses, and due to this reason, it was named as an 'atomic' function [6-8]. For 50 years' history described in the survey [9], the AF and its variations have been intensively researched and applied in radio electronics, electrodynamics, superconductivity, the theory of optimisation, boundary value problems and others [6-11]. In this paper, we extend the theory to build an *atomic string* which, interestingly, can compose AF itself and have a wide range of applications overviewed hereafter.

Atomic String.

As been discussed, the atomic string (AString) is an integral (7) of an atomic function (9), (10) which due to special properties of AF can be conveniently expressed through AF itself [6,7]:

$$AString(x)=\int_0^x up(x)dx = up\left(\frac{x}{2}-\frac{1}{2}\right)-\frac{1}{2}\ for\ |x|\leq 1, AString(x)=\pm 0.5\ for\ |x|\geq \pm 1. \quad (12)$$

An integration constant can be chosen to have a swing height of 1 like shown in Fig.3, a depicting an AString along with the atomic function and its derivative. This expression also highlights that the symmetric pulse $up(x)$ can be represented by a combination of two opposite swings. The remarkable

property of shifted and stretched AFs to have the similar shape parts with both derivative and integral functions makes it unique and AString inherits some of these properties too. For example, atomic function itself with all its derivatives can be expressed via $Astring$:

$$up(x) = AString'(x),\ up'(x) = 2up(2x+1) - 2up(2x-1) = Astring''(x). \quad (13)$$

Importantly, a derivative operation can be replaced by simple stretching and shifting of two AStrings, and Fig.4, a shows that AF itself (along with all derivatives which are AF combinations) can be exactly represented by combining of two AStrings

$$up(x) = AString'(x) = AString(2x+1) - AString(2x-1), \quad (14)$$

This equation can be considered as a formal definition of AString. Recalling (5) that the AStrings combination can also present a straight segment (Fig.4, b) makes it distinct from other swing-like functions (1) - (3) which cannot possess such a unique set of properties.

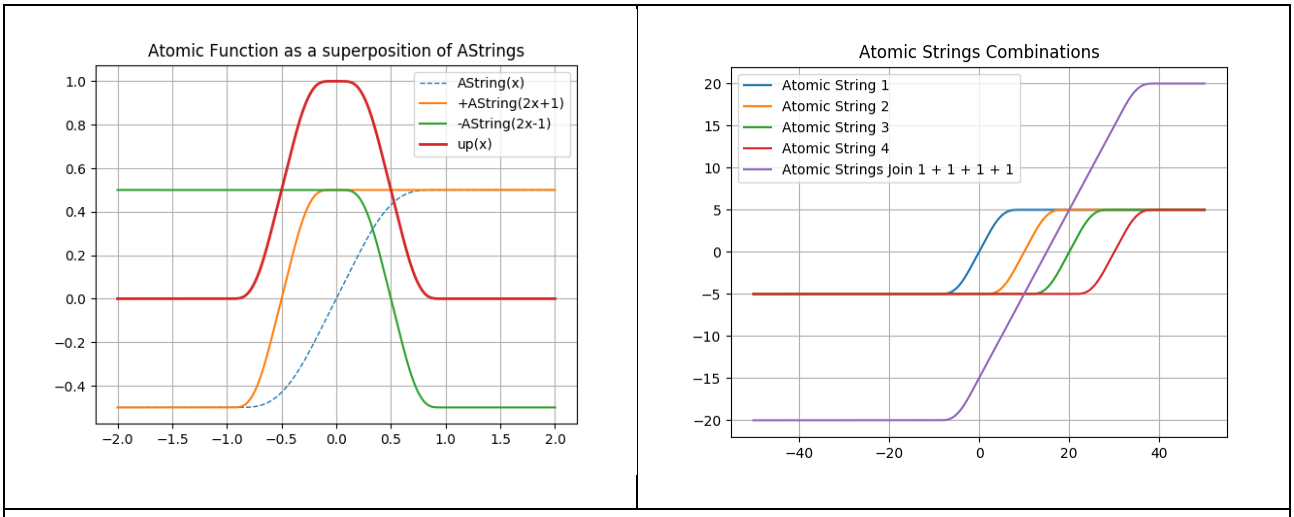

Fig. 4. a) Atomic function can be exactly represented by a combination of two atomic strings. b) Representation of a straight line segment by joining of atomic strings

Even wider variety of shapes (Fig.5), including almost rectangular ones which are hard to represent by limited Fourier series, can be obtained by combination of AStrings with different width $2a$, height c and centre positions b, d in space

$$AString(x, a, b, c, d) = d + c * AString((x-b)/a). \quad (15)$$

Unique properties of AStrings – ability to compose an atomic function, represent flat and curved surfaces and having all derivatives expressed via the combination of AStrings themselves - make them quite promising for a wide variety of applications and ideas briefly overviewed hereafter.

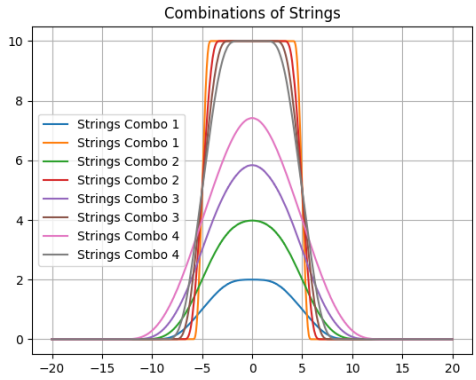

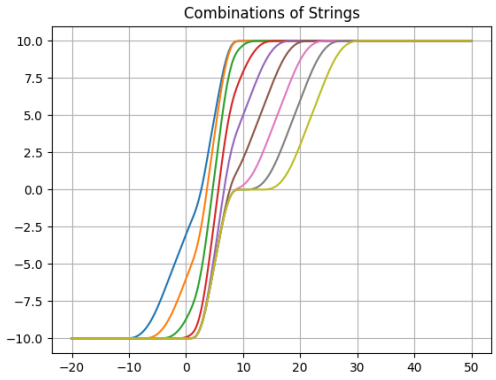

Fig. 5. a) Representation of wave-like pulses via AStrings. b) Representation of curved shapes via AStrings.

Atomic solitons.

A soliton refers to a group of nonlinear phenomena relevant to many branches of physics [15-17] studying nonlinear wave-particle behaviour of matter. For example, KdV soliton [15-17] describes a stand-alone wave-particle which can travel long distances in oceans and preserve the form during collisions with other solitons. Sine-Gordon kink function (3) depicted in Fig.1, a describes Frenkel-Kontorova (FK) soliton dislocation - missing atom in a periodic structure of atoms - which like a particle can grow, shrink, travel, group and be eliminated only by a collision with a negative-dislocation [15,16]. The combination of opposite soliton kinks can produce stable 'solitonic atoms' or breathers [15,16]. Solitons in the form of skyrmions and instantons have also been used in particle physics and string theory [15,19,20] as possible building blocks of matter.

AString introduced here also possesses wave-particle duality typical for solitons. Firstly, AString is a kink-like function (Fig.1,3) similar to SG-Soliton (3). Secondly, by joining of AStrings - like from 'Lego block particles' - it is possible to build extended straight and curved bodies (Fig.1,2,4). Thirdly, based on AString slope (up or down) it is possible to introduce 'positive' and 'negative' solitons which can annihilate each other exactly like Frenkel-Kontorova soliton dislocations [15]. Fourthly, as per (14) and Fig.4,1, joining of two AStrings produces an infinitely smooth and solitary atomic function pulse which simulates a 'solitonic atom' or 'breather' [15,16]. And lastly, using (14) it is possible to obtain two-dimensional equations for $AString(x-ct)$ travelling kink

$$AString'_t - cAString'_x = -2c * (AString(2(x-ct)+1) - AString(2(x-ct)-1)). \quad (16)$$

These properties make AString and closely related atomic function as the candidates for a new kind of *atomic solitons*. Typically, proving that a *nonlinear* function is a soliton requires the application

of *inverse scattering method* [17,16] which transforms the nonlinear differential equation into a linear one by a special substitution. However, the atomic string (12), (14) and function (9) are solutions of a special kind of *linear functional-differential equations with shifted arguments* (8), (10) [5-11] for which the inverse scattering method is not directly applicable. This fact significantly distinguishes the atomic string and function from other strongly nonlinear solitons in physics (such as Korteveg-de-Vries, sine-Gordon, Toda lattice) [15-17] while they may look quite similar in shapes (Fig.1,3,4). Therefore, we can assume that AString and AF may be the new kind of solitons for which the theory still needs to be developed. What makes AString and AF distinct from other solitons is the ability to compose both flat and curved structures by smooth joining of kink-like functions (Fig.2, b, Fig.3, b), and similarity of shapes for all derivatives. So, if we assume that AString is an 'atomic soliton', the derivatives would also be the combination of 'atomic solitons', and the similar true for an atomic function. Let's note that a sigmoid (1) also offers this property (of derivatives expressed via themselves), but from joining of a few sigmoids, it is not possible to compose neither a unity (number 1) nor straight-line segments shown in Fig.2.

Quantum and fabric of spacetime.

A unique property of AStrings to represent straight line segments via a simple combination of soliton-like wave-particles (Fig.2,4) makes tempting to apply them for a description of an elementary quantum and fabric of spacetime. Regarding the 'fabric' we assume 'modern' interpretation as a flexible texture created during Big Bang along with matter and stretching afterwards, or 'Higgs ocean' permeating the space [19,20,22,24]. Following Stephen Hawking terminology, a spacetime quantum could represent an elementary *spacetime warp*, or *spacetime distortion* [23]. There is another name for a quantum of space – *metriant* – introduced by A. Veinik in his general thermodynamics theory described in many monographs observed in [25]. Both definitions are conceptually similar to soliton dislocations [15] capable of growing, shrinking, grouping and evolving.

To construct an *atomic quantum*, we can use AString (15) with width *2a* and height c which by joining with other N quanta on a grid lattice with period s would produce a direction x_i in space

$$x_i \equiv \sum_{n=-N}^{n=N} AString(x_i, a, ns, c, 0) \; = MAstring(x_i, a, s, c, N). \qquad (17)$$

The shape of AString function (Fig.1,3) consists of the 'tale' and 'head' connectors which exactly compose a straight-line segment by joining on a periodic lattice, and only two AStrings are required to represent a straight segment between the joints. As we can see from Fig.1,2,4, the combined macro-

string denoted as $MAString$ in the last equation has perfectly straight 'body' while 'connectors' are shifted to the ends allowing two macro-strings to join further and extend the structure:

$$x_i \equiv (MAstring, x_i, a, s, c, N_1) + (MAstring, x_i, a, s, c, N_2) + \cdots. \quad (18)$$

It means that the space metric can be represented not only by joining of tiny strings but also macro-strings consisting of micro-strings allowing to apply the assembly method for all levels of spatial size hierarchy – from micro-, macro- to cosmic world. Lego game to build complex shapes by joining small and large pieces is a useful analogy to understand the idea, and in our case, a Lego piece is AString perfectly matching other curly pieces.

The similar representation can be performed for *time* component of inseparable, in Einstein-Minkowski theory [22-24], spacetime mathematically defined on a periodic grid with period s_t as a combination of AStrings with width $2a_t$ and height c_t:

$$t \equiv \sum_{n=0}^{n=N} AString(t, a_t, ns_t, c_t, 0) \; = MAstring(t, a_t, \; s_t, c_t, N). \quad (19)$$

In the same way, it is possible to build continuous flat and, as we will see later, curved structures in other dimensions, with up to 11 considered in different string theories [19,20].

Introducing the elementary soliton-like AStrings as the 'building blocks' of extended continua allows constructing different quanta in multiple dimensions, for example, 4-dimensional (4D) spacetime quantum consisting of 3 spatial coordinates and time combined into vector with basis ($\boldsymbol{e_1}, \boldsymbol{e_2}, \boldsymbol{e_{3,}} \boldsymbol{e_4}$):

$$\boldsymbol{AString}(x_1, x_2, x_3, t, a, b, c, a_t, b_t, c_t) = AString(x_1, a, b, c)\, \boldsymbol{e_1} + AString(x_2, a, b, c)\, \boldsymbol{e_2} + AString(x_3, a, b, c)\boldsymbol{e_3} + AString(t, a_t, b_t, c_t)\boldsymbol{e_t}. \quad (20)$$

Understanding the relationships between AString constants requires some assumptions regarding uniformity of spacetime, for example, setting up a certain size of 4D spacetime cube equal in spatial and time dimensions. This will link the widths $2a$ and $2a_t$, heights c and c_t and centres b and b_t of AStrings by a constant c_l measured as a velocity

$$a = a_t * c_l, c = c_t * c_l, b = b_t * c_l. \quad (21)$$

In Einstein-Minkowski [22-24] theory connecting spacetime via invariant ($x_1^2 + x_2^2 + x_3^2 - c_l^2 t^2 = 0$) it is a speed of light c_l - fundamental constant which can be introduced as a ratio between sizes of a quantum in space and time in the current universe, but potentially can be different in other (parallel) universes or differently constructed quanta (for example, in metric space theory of A. Veinik [25]).

The next constant to evaluate in 4D quantum (20) is c which denotes the height of AString. Chart 6, a shows different height AStrings, and the one closest to simplest line $y = x$ has a height $c = a$ (which is half-width of a pulse). More generic relationship can be expressed by the following simple formula with initial coefficient ρ close to 1 as will be discussed later:

$$c = \rho a, \rho \approx 1. \tag{22}$$

Parameter b in formula (20) for a 4D quantum is related to the position of the center of a swing. According to Fig.6, b, the combination of AStrings can only produce flat spacetime when the distance between lattice nodes $b = a$ meaning that the width of a quantum automatically defines the lattice size in the current universe, and the concept of a 'lattice' can be eliminated altogether. There is no lattice in the universe – just a size of an elementary quantum.

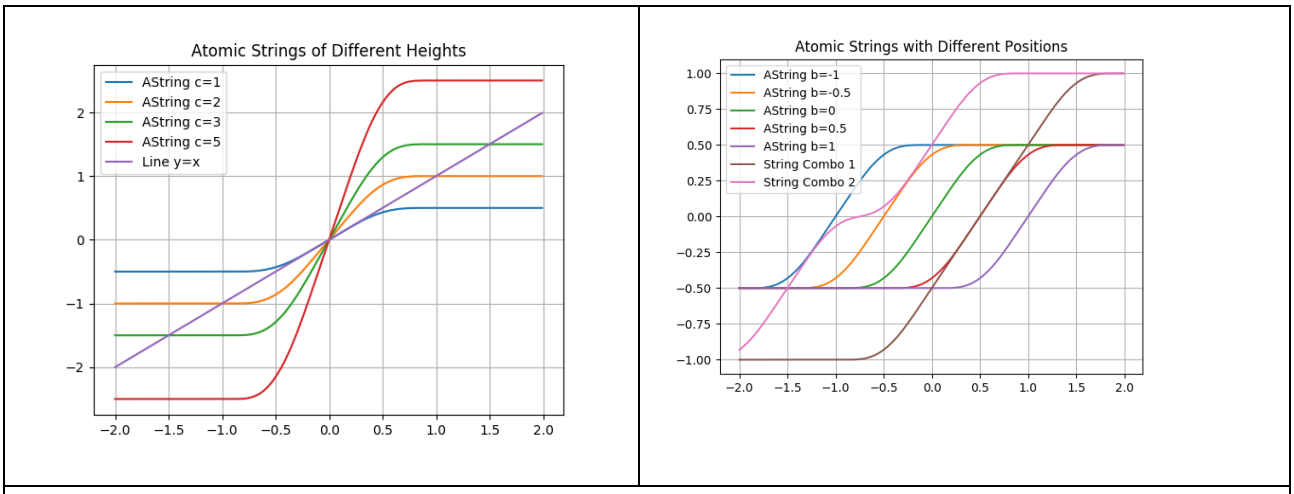

Fig. 6. a) Atomic strings of different heights. b)) Atomic strings combined at different locations

During the analysis above, we have identified the relations between elementary atomic quantum parameters allowing rewriting the formula (20) in the form

$$\boldsymbol{AString}(x_1, x_2, x_3, t, a, \rho, c_t) = AString(x_1, a, a, \rho a)\,\boldsymbol{e_1} + AString(x_2, a, a, \rho a)\,\boldsymbol{e_2} + AString(x_3, a, a, \rho a)\boldsymbol{e_3} + AString(t, a/c_l, a/c_l, \rho a/c_l)\boldsymbol{e_t} \tag{23}$$

which includes speed c_l as a ratio between quantum size in space and time, quantum width a and parameter ρ allowing to 'overload' a string with an additional property. Introducing quantum (23) completely replaces the notion of 'a point' in spacetime – exactly like in string theory [19,20]. To remind, the function $AString$ can be easily calculated, with tabular values and computer code provided in Appendix.

Let's note that the procedure of building a quantum in the form (17) - (23) can be applied for generic nature continua on lattice, from an elementary quantum string where grid period a can be the Plank length to solid bodies' atomic structures where a is the size of an atom to periodic galaxy structures in cosmic clusters. Like in Lego game, all depends on the size and the form of an elementary piece.

By joining the similar atomic quanta one after another, it is possible to build a flat spacetime continuum with perfectly smooth connections between quanta:

$$\boldsymbol{Spacetime} = \sum_{n1,n2,n3,n4}^{\infty} AString(x_1 + n_1 a, a, a, \rho a)\, \boldsymbol{e_1} + AString(x_2 + n_2 a, a, a, \rho a)\, \boldsymbol{e_2} + AString(x_3 + n_3 a, a, a, \rho a)\boldsymbol{e_3} + AString(t + n_4 a/c_l, a/c_l, a/c_l, \rho a/c_l)\boldsymbol{e_t}. \quad (24)$$

So, like a line segment constructed from translations of AStrings (5), the multi-dimensional spacetime continuum can be presented by joining of elementary quanta. Fig.7, a from an interesting paper [33] shows how a flat multidimensional surface can be *approximately* presented via the combinations of *many* 'Gaussian atoms'. AStrings allow doing it *exactly* with only *a few* kink-like pulses. The flatness and uniformity of the universe on micro- and grand- scales [19,21] confirm the tendency of nature to avoid imperfections.

Einstein-Minkowski spacetime with 4D quantum (23) is just one of many possible fabric and quanta definitions. For example, instead of using three spatial coordinates it is possible to introduce one radial coordinate and represent a distance in 3D space as a combination of quanta:

$$r \equiv \sqrt{x_1^2 + x_2^2 + x_3^2} = \sum_{n=-N}^{n=N} AString(r, a, na, \rho a, 0) = MAstring(r, a, a, \rho a, N). \quad (25)$$

AStrings may be used to build other quanta, for example, in atomic crystal lattices [16], biological cell structures or those permitting faster-than-light communications in quantum entanglement [19,20], warp drive and chronal fields [25] theories, or 'Higgs ocean' [19], dark matter [19,21], 'negative energy' [23] quanta – all interesting cases to research further together with quantum physics and string theory specialists. Spacetime quantisation and lattice theories [16, 27-30] are a quite well-researched area of physics where multiple soliton and quantum wave functions have been used, but the atomic quantum introduced here seems never been used before, most likely because of limited knowledge on relatively new atomic functions and their AString extensions.

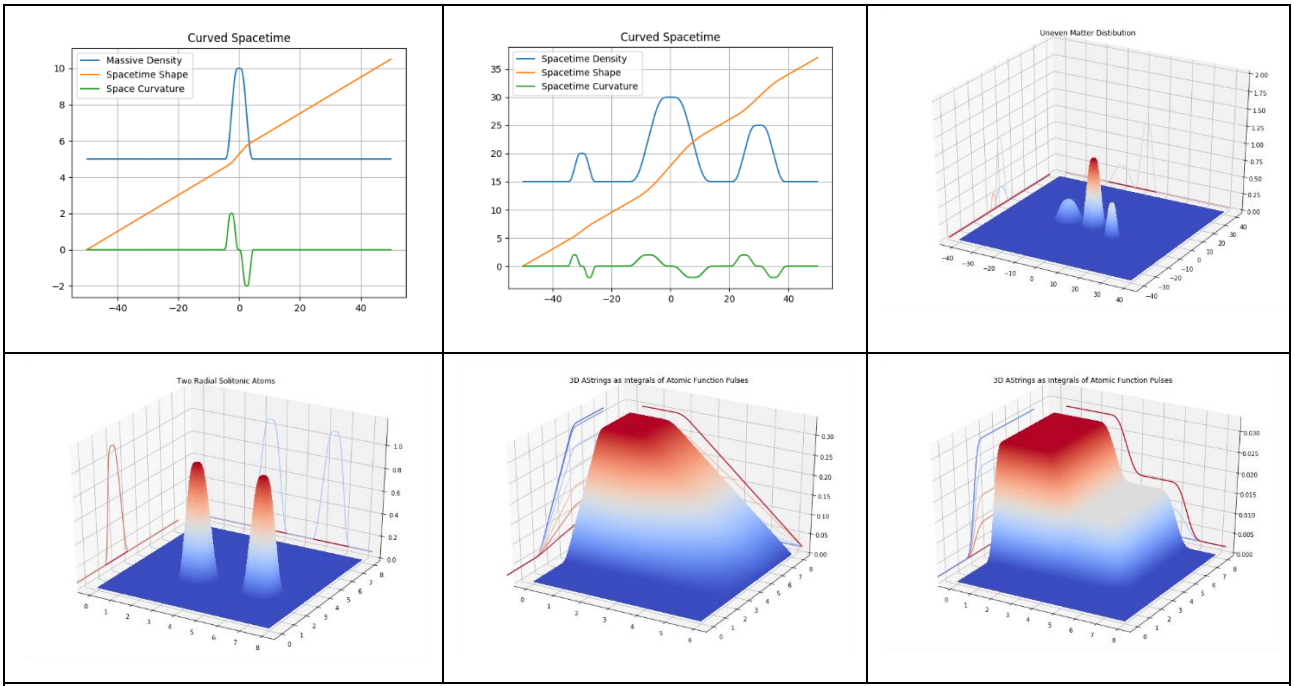

Fig. 7. a) A density fluctuation pulse curves spacetime geodesics. b) Curved spacetime shape, density, and curvature. c-f) Atomic Soliton pulses represent density of matter which changes the shape of geodesics of spacetime

Spacetime curvature and general relativity.

Representing a uniform spacetime by a combination of soliton-like AString wave-particles is only an initial step towards the goal of describing flat and curved continua within one model. An infinite variety of shapes including those depicted in Fig.4,5 can be obtained by introducing some imperfections like dislocations or topological defects [15,16] which can be simulated by different locations or sizes of neighbouring AStrings. For example, joining of four AStrings of the same width but different heights (ρ =1,2 in (23)) in Fig.8, a produces a curved 'spacetime shape' with bigger curvature around bigger AStrings. This combined curve may define geodesics 'radiating' from a body into infinity like shown in Fig.7, b. According to general relativity [22-24], a matter traveling along these geodesics changes trajectory – which is a manifestation of gravity.

As per the model (24), the uneven spacetime consists of AString combinations, and spatial derivatives, in a demonstration model without sheer spacetime deformations, would have a meaning of a spacetime density/deformation component (Fig.8, b):

$$Spacetime(x_i) = \sum_k AString(x_i, a_k, b_k, c_k)\,,\ Density(x_i) = \frac{d}{dx_i} Spacetime(x_i) = \sum_k up(x_i, a_k, b_k, c_k) = \sum_l AString(x_i, a_l, b_l, c_l) \quad (26)$$

Important to note that due to (13) the density can be expressed via atomic functions $up(x)$ which in turn can be represented by the combination (14) of AStrings. The second derivative from the spacetime function would have a meaning of a curvature

$$Curvature(x_i) = -\frac{d^2}{dx_i^2} Spacetime(x_i) = \sum_k \frac{d}{dx_i} up(x_i, a_k, b_k, c_k) = \sum_m AString(x_i, a_m, b_m, c_m), \quad (27)$$

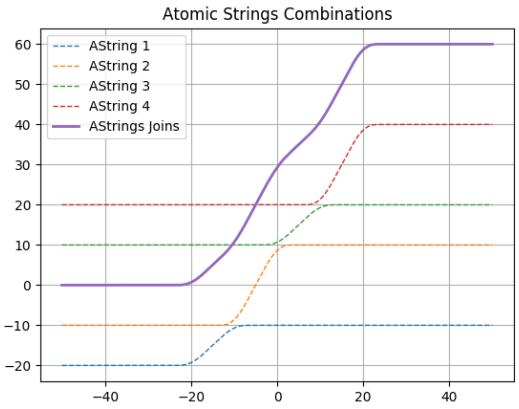

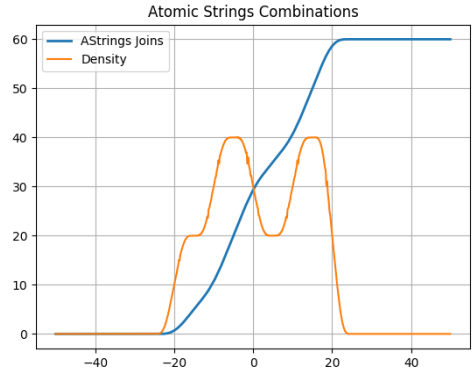

Fig.8. a) Joining AStrings of different heights simulates spacetime curving. b) Curved spacetime density

Fig.9 demonstrates the spacetime geodesics function, its density and curvature for an individual density pulse (Fig.9, a) and group of pulses (Fig.9, b). Importantly, all of them can be expressed through the combination of AStrings which also represent a spacetime quantum (23).

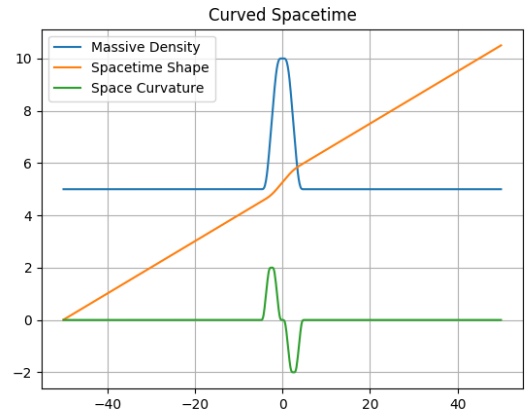

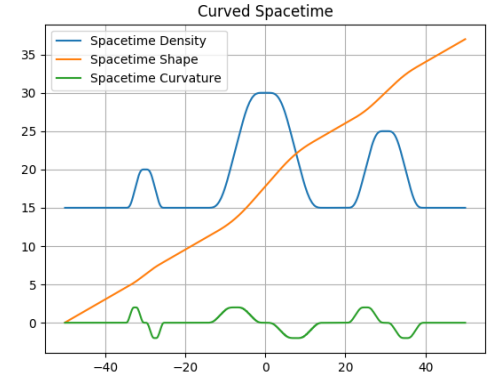

Fig. 9. a) A density fluctuation pulse curves spacetime geodesics. b) Curved spacetime shape, density, and curvature

The idea of A. Einstein that the metric of spacetime containing curvature tensors $G_{\mu\nu}$ exactly matches the distribution of energy-momentum $T_{\mu\nu}$ expressed via general relativity field equation [22-24] implies that spacetime shape, density and curvature (26), (27) and forces $T_{\mu\nu}$ should be expressed via the same set of basic AString functions also describing the spacetime quantum (23)

$$\sum_{im} AString(x_i, a_m, b_m, c_m) \sim G_{\mu\nu} = \frac{8\pi G}{c^4} T_{\mu\nu} \sim \sum_{im} AString(x_i, a_m, b_m, c_m). \quad (28)$$

It is quite challenging to show mathematically but intuitively easy to understand that if all functions in some complex equation are expressed via the combination of the same basic functions, it is possible to select shifting coefficients in such a way that pulses and swings would match exactly. So, AString function (15) describing an elementary quantum (23) can also describe both flat and curved spacetime and be incorporated into general relativity equations via curvature and force tensors $G_{\mu\nu}, T_{\mu\nu}$ which would include curvatures and densities (26), (27). Let's note that other similarly-shaped functions like (1) - (3) are not able to do that. Let's take sigmoid (1) for example – its derivatives are also expressed via themselves and being injected into (26) - (28) are able to produce sigmoid functions on both sides of (28). However, as has been discussed, a sigmoid cannot describe *finite* spacetime quantum and provide smooth connections between quanta (Fig.2). On the other hand, there are *finite* functions like B-splines capable to describe connections between quanta with some degree of smoothness, but their derivatives cannot be expressed via themselves and lead to (28). This makes AString and closely related atomic function quite interesting candidates to describe fundamental 'building blocks' of the fabric of spacetime and matter along with other functions used in string theory. It is only left to guess whether A. Einstein in his brilliant mind had envisaged a soliton-like pulse which would form the matter and bent the spacetime in a proportional way.

Following John Wheeler [22] famous saying "Matter tells Spacetime how to curve, and Spacetime tells Matter how to move" it is quite interesting to envisage a possible way how gravity operates. Two kink-like AStrings (spacetime warps/metriants) compose an atomic function (14) which represents a 'solitonic atom' (Fig.4, a, 3, b) from translations of which the complex matter is composed while related spacetime texture is made of AStrings too. Typical in nature irregularities/topological defects cause uneven distribution of matter which in turn changes the physical geometry of a local spacetime in quite a proportional way. Expressed by the same basic function, the matter and spacetime are deeply related to each other as general relativity prescribes, and, hopefully, quantum gravity specialists can validate this idea.

The idea of spacetime and matter quantisation based on AStrings offers interesting insight into a ratio m/r of body mass and a radial distance coordinate included in all gravitational theories including Newtonian gravitational potential and more complex Schwarzschild solution for a massive body radius [22-24]

$$P(m, r) = -Gm/r, r_s/M = 2G/c^2. \quad (29)$$

If following (25), we represent a radial function r via a combination of AStrings and find the density (26) of this distribution for one AString pulse

$$Density(r) = AString'(r, a, b, \rho a, d) = \rho a/a * AString'((r-b)/a) = \rho up((r-b)/a), \quad (30)$$

we can see that the parameter $\rho = height/width$ defines how tall an elementary density pulse in comparison with its width. In order for the spacetime fabric presumably consistent of similar quanta to uphold proportionality (29) we should conclude that in 'normal' conditions the ρ coefficient in formula (22) should be close to 1 meaning that adding more metriants/quanta to a volume should increase its size and 'radiational influence', and an elementary spacetime quantum (23) should have close to 'rounded' shape in Fig.9, b rather than 'squeezed' ones in Fig.9, a. However, to simulate Big Bang conditions of rapid expansion of the universe from infinitely dense matter localised in infinitesimally small volume [19,20], in atomic string model we have to hypothesize that AString spacetime quanta (metriants [25]) may have been 'packed in one slot' [25] before expanding. This implies the possibility of super dense strings schematically depicted in Fig.9, a and Fig.5, a in the primordial universe.

The findings described in this paragraph are quite known from the multi-decade history of general relativity, string theory, and cosmology. The focus of this publication is to show that spacetime quantisation hypothesis based on atomic functions and strings can explain well some quantum and gravitational effects. It may make atomic strings and functions the good candidates for further research by quantum gravity specialists and possible inclusion in many theories of physics and cosmology.

Atomic String Functions as mathematical building blocks of fields.

The combination of atomic strings can produce not only flat and curved surfaces, but also describe more complex formations abandon in the universe. One simple but probably the most important configuration is a 'solitonic atom' [15] sometimes called *breather* or *bion* [15,16] representing a pulse-like atomic function as a sum of two opposite AStrings (Fig.4, a). The significance of this formation is highlighted in Fig.3, a where the translations of 'atomic function atoms' can represent a uniform distribution of quantised matter (mass, atoms, cells) widespread in nature. The next typical shape is a 4-string wave in Fig.10, a visually looking like series of soliton waves appearing in fibre optic cables, nerve pulses and ocean standing waves [15]. These types of waves may model gravitational waves and the 'messenger particles' (gravitons, photons) carrying forces between particles [19,20,15]. Moreover, as per string theory main hypothesis [19,20], the elementary particles

may be considered as some vibration modes - waves - of elementary strings, and the intriguing question arises whether these waves can be represented as a combination of atomic strings and functions joined together like shown in Fig.4-10. What we try to show is how easy to compose different open and enclosed structures/manifolds from simple combinations of AStrings which may express elegant simplicity of the universe repeating itself from elementary formations like AStrings.

The concepts of stability and 'shape preservation' from small to big scales may play an important role in producing macro-strings and complex shapes composed of elementary AStrings. As per Fig.1,2, the AStrings consist of 'bodies' and 'connectors' which left 'free' at the ends of combined shapes. Like in Lego game, similar shapes with likewise connectors can easily join further producing larger structures, and the evolution of solid and biological matter by joining of similar molecules and cells is the direct confirmation of this pattern in nature.

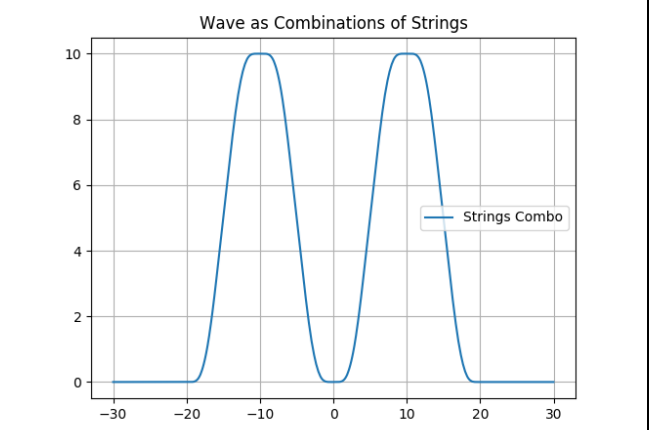

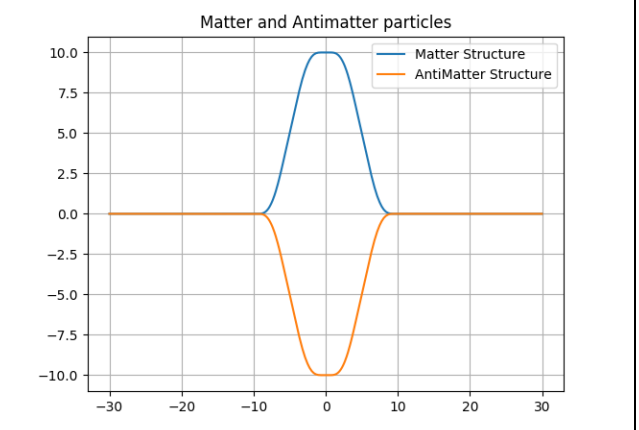

Fig.10 a) Joining of AStrings produce a wave. b) The shapes of matter and anti-matter quanta

Engaging AStrings and the notion of soliton dislocations – anti-dislocations [15] can also explain the concepts of antimatter and 'negative energy/mass' elaborated by Stephen Hawking [23] amongst others. They can be modelled by similarly shaped AStrings with opposite heights ('topological charges' [15]) which annihilate each other if meeting at one location as shown in Fig.10, b. Interestingly, the 'dark matter' [19-23] hardly interacting with ordinary matter can be modelled as AStrings (15) with different parameters a, b, c which can not smoothly join with ordinary AStrings and produce stable formations. As we can see, easy-to-use atomic strings and functions may describe not only the flexible spacetime fabric but also waves, solitonic atoms, matter, anti-matter and dark matter formations. More applications would be interesting to research further with specialists trying to apply AStrings to represent some strings in string theory [19,20].

Summary and future research directions.

This paper introduces a soliton-like atomic string as a generalisation/integral of an atomic function well-known since 1970th, with the main idea that an atomic string and closely related atomic function, with derivatives expressed via themselves, may be well suited to describe a spacetime quantum, flexible fabric of flat and curved spacetime, its curvature proportional to matter distribution, constancy of the speed of light as a parameter of the quantum, solitonic atoms as the mathematical building blocks of fields and expansion of spacetime by joining of similar AStrings. This theory may lead to novel model of spacetime, gravity and quantum gravity.

Appendix and Web Resources.

The Python script representing an atomic function, atomic string, and some paper pictures are presented in https://solitonscientific.github.io/AtomicString/AtomicString1.html.

Research Gate projects:

- https://www.researchgate.net/project/Atomic-Strings-Quantum-of-Spacetime-and-Gravitation
- https://www.researchgate.net/project/Atomic-String-and-Atomic-Function-New-Soliton-Candidates
- https://www.researchgate.net/project/Atomic-Machine-Learning-and-Artificial-Intelligence-with-Atomic-Soliton-and-R-functions
- https://www.researchgate.net/project/Atomic-Computer-new-generation-superfast-computing

References.

1. Rvachev, V.L. From the Special Theory of Relativity to Mathematics without the Archimedean Axiom and Back. Radiotekn. Elektron., 1995, Nos. 1–2, p. 58-68; No. 6, p.39-50.
2. Kravchenko, V.F.; Rvachev, V.L.; Shevchenko, A.N.; Sheiko, T.I. The interpretation of Certain Phenomena Observed in Deep Space by Using Non-Archimedean Calculi. Radiotekn. Elektron., 1995. No.7, p.1076-1094.
3. Eremenko, S.Yu. Combined Non-Archimedean Calculi. Foreign Radioelectronics: Achievements of modern radioelectronics. 1996, No. 8, pp. 57–65. https://www.researchgate.net/publication/320616255
4. Eremenko, S.Yu.; Kravchenko, V.F.; Rvachev, V.L. Combined Non-Archimedean Calculi and New Models of Relativistic Mechanics. Foreign Radioelectronics: Achievements of modern radioelectronics. 1997, No. 9, pp. 26–38. https://www.researchgate.net/publication/320616269
5. Kravchenko, V.F.; Rvachev, V.A. Application of atomic functions for solutions of boundary value problems in mathematical physics. Foreign Radioelectronics: Achievements of modern radioelectronics. 1996, No.8, p.6–22.
6. Rvachev, V. L., Rvachev, V. A. About one Finite Function, DAN URSR, A (6), 705-707, 1971.
7. Rvachev, V. L. Theory of R-functions and their applications. Kiev: Naukova Dumka, 1982.
8. Rvachev, V.L.; Rvachev, V.A. Non-classical methods in the theory of approximations in boundary value problems. Kiev: Naukova Dumka, 1982. 196p.
9. Kravchenko, V.F.; Kravchenko, O.V.; Pustovoit, V.I.; Pavlikov, V.V. Atomic Functions Theory: 45 Years Behind. DOI 10.1109/MSMW.2016.7538216. https://www.researchgate.net/publication/308749839.
10. Kravchenko, V. F. Lectures on the theory of atomic functions and their applications. Moscow: Radiotechnika, 2003.
11. Kravchenko, V.F.; Rvachev, V.L. Logic Algebra, atomic functions and wavelets in physical applications. Moscow: Fizmatlit, 2009.

12. Eremenko, S.Yu. Natural Vibrations and Dynamics of Composite Materials and Constructions. Kiev: Naukova Dumka, 1992. 182p.
13. Eremenko, S.Yu. Finite Element Methods in Mechanics of Deformable Bodies. Kharkov: Osnova, 1991. 272p. https://www.researchgate.net/publication/321171685
14. Eremenko, S.Yu.; Rvachev, V.L. A survey of variants of the structural finite-element method. Journal of Mathematical Sciences, 1998, V.90, No.2, pp.1917-1922.
15. Filippov, A.T. The Versatile Soliton. Modern Birkhauser Classics, 2000. 261p.
16. Braun, O.M.; Kivshar, Yu.S. The Frenkel-Kontorova Model: Concepts, Methods, and Applications. Springer, 2004.
17. Novikov, S. P.; Manakov S. V.; Pitaevskii, L. P.; Zakharov, V. E. Theory of Solitons: The Inverse Scattering Method, Springer-Verlag, 1984. 276p.
18. Rvachev, V.L.; Avinash, K. Quadratic redshift law and the non-Archimedean universe. Radio Physics and Radio Astronomy, 2001, v.6, No.2, pp.534-536.
19. Greene, B. The fabric of the cosmos: space, time and texture of reality. New York: Vintage Books, 2004. 570p.
20. Kaku, M. Introduction to Superstring and M-Theory (2nd ed.). New York: Springer-Verlag, 1999. 544p.
21. Pasachoff, J.M.; Filippenko, A. The Cosmos: Astronomy in the New Millennium. Cambridge: Cambridge University Press, 2014. 590p.
22. Taylor, E.F., Wheeler, J.A. Spacetime Physics: Introduction to Special Relativity. New York: W. H. Freeman, 1992. 340p.
23. Hawking, S., Mlodinov, L. The Grand Design. New York: Bantam Books, 2010. 190p.
24. The Collected Papers of Albert Einstein. Princeton, New Jersey: Princeton University Press, 1989.
25. Veinik, A.I. Thermodynamics of real processes. Minsk: Nauka i Technika, 1991. 576p.
26. Niedermann, F, Schneider, R. Radially stabilized inflating cosmic strings. Phys.Rev. D, 91 (6): 064010
27. Smit, J. Introduction to Quantum Fields on a Lattice. Cambridge: Cambridge University Press, 2002.
28. Rothe, H. Lattice Gauge Theories, An Introduction. World Scientific, 2005.
29. DeGrand, T.; DeTar, C. Lattice Methods for Quantum Chromodynamics, World Scientific, 2006.
30. Gattringer, C.; Lang, C. B. Quantum Chromodynamics on the Lattice. Springer, 2010.

RELIABILITY ESTIMATION FOR COMPLEX DEPENDENT DEGRADATION PROCESSES AT THE WHEEL-RAIL INTERFACE

Shan Jiang [1,2], Yan-Fu Li [2], Nikolaos Limnios [3]

[1] School of Information Engineering, Minzu University of China, jshan.susan@gmail.com
[2] Department of Industrial Engineering, Tsinghua University, liyanfu@tsinghua.edu.cn
[3] Laboratoire de Mathématiques Appliquées de Compègne (LMAC), Université de Technologie de Compiègne, Sorbonne University Alliance, nikolaos.limnios@utc.fr

This paper presents a dynamic reliability estimation model to deal with complicated dependent degradation processes. Wear and rolling contact fatigue (RCF) on rail steel at the wheel-rail interface are competitive phenomena, which are closely connected and directly affect the dynamic reliability. Wear will tend to block fatigue crack propagation due to cyclic contact stress by removing the material from the wheel-rail contact surface. Continuous-time Markov processes, which are non-ergodic with an absorbing state, are built to model the evolution of damage at the wheel-rail interface. In the proposed approach, the damage variable at the wheel-rail interface is considered as the sum of the crack length and the thickness loss due to wear. The states in the Markov processes are defined based on the relationship between the crack growth rate under the impact of wear and the damage variable. The generator matrix is estimated by using the maximum likelihood method [1]. In addition, this estimator of the generator matrix is used to obtain the explicit formulas for the reliability function, failure rate function and mean time to failure (MTTF) [2]-[4]. Asymptotic properties of the estimators, namely, consistency and asymptotic normality are given. Furthermore, the confidence intervals are derived and the confidence curves are obtained. Numerical results are obtained based on 69 samples data that are generated based on several sets of testing data observed on a time interval. It manifests that the proposed approach can effectively evaluate the dynamic reliability at the wheel-rail interface.

References

[1] A. Albert. *Estimating the Infinitesimal Generator of a Continuous Time Finite State Markov Process*, The Annals of Mathematical Statistics, page727-page753, 1962.

[2] A. Sadek, N. Limnios. *Nonparametric estimation of reliability and survival function for continuous-time finite Markov processes*, Journal of Statistical Planning and Inference, page1-page21, 2005.

[3] V. Girardin, N. Limnios. *Applied Probability - From Random Sequences to Stochastic*, Springer International Publishing, 2018.

[4] N. Limnios, G. Oprisan. *Semi-Markov Processes and Reliability*, Birkhauser, 2001.

BAYESIAN INFERENCE OF MECHANICAL PROPERTIES IN A REINFORCED CONCRETE MODEL AT DIFFERENT REFINEMENT LEVELS

Simona Dobrilla [1,2], Adnan Ibrahimbegovic [2], Hermann G. Matthies [1]

[1] Institute of Scientific Computing, Technische Universität Braunschweig,
38106 Braunschweig, Germany, e-mail: s.dobrilla@tu-bs.de, h.matthies@tu-bs.de
[2] Laboratoire Roberval de Mécanique, Université de Technologie de Compiègne /
Alliance Sorbonne Université, 60200 Compiègne, France, e-mail: adnan.ibrahimbegovic@utc.fr

1 Introduction

Resistance of civil engineering structures decreases over time due to material ageing, environmental effects and unfavorable external actions. These mechanisms gradually weaken the structures by introducing the microscopic damage. Initially unnoticeable and negligible cracks propagate over time leading to a more significant material degradation which represents a serious threat for structural durability and their service life-span. Mechanical models which are able to realistically describe and predict behaviour of the material are essential for reliable prediction of cracking and failure in RC structures. However, such deterministic models are not able to fully tackle the problem of deterioration of the structural properties over time, as the quantification of individual influences is not straightforward. Moreover, the structural response resulting from models describing the inelastic behaviour is greatly dependent on the material properties which are often not fully known.
More reliable predictions may be obtained by taking into account uncertainties in the material properties and loading conditions. Indirect observational data from structural monitoring or smaller scale experiments can be combined with model predictions to calibrate the uncertain parameters by solving the stochastic inverse problem [1]. To avoid regularisation, one can formulate the probabilistic problem in a Bayesian setting [2], which treats an inverse problem as a well-posed one by incorporating prior knowledge about the uncertain parameters.
The objective of this work is to estimate mechanical parameters of RC by using Bayesian approach, thereby reducing the uncertainty in the prior probability description given experimental data from the tension test, taking into account the inelastic behaviour of the composite. In addition, the parameter identification problem is herein observed at different levels of probabilistic refinement, i.e. with and without taking into account the spatial variability of the uncertain parameters.

2 Modelling of fracture in reinforced concrete

Computational modelling of damage propagation in RC comprises several distinctive phases. Initial linear elastic response is followed by the formation of the fracture process zone (FPZ) in the bulk material and progressive development of microscopic damage as the stress state exceeds the limit value. A further increase of loading leads to coalescence of the micro-cracks and propagation of a macro-crack upon reaching the ultimate stress of concrete. Moreover, localised failure in concrete leads to degradation of the bond and subsequently to a frictional slip of the steel bar with respect to surrounding concrete.

2.1 Strong embedded discontinuity model for simulation of localised failure in concrete

Progressive formation of microscopic cracks in the fracture process zone indicates the initiation of fracture in concrete, defined by a damage function $\bar{\phi}$ defined as

$$\bar{\phi} = \| \boldsymbol{\sigma} \|_{\mathbf{D}^e} - \frac{1}{\sqrt{E^c}}(\bar{\sigma}_f - \bar{q}) \overset{?}{\leq} 0, \tag{1}$$

where $\mathbf{D}^e$ is the elastic compliance tensor, E^c is the Young's modulus for concrete, $\bar{\sigma}_f$ is the elasticity limit and $\bar{q}$ is the stress-like hardening variable. This is a volume type of dissipation, described by an isotropic damage model with isotropic hardening [3].
The value of principal stress exceeding the ultimate stress $\bar{\bar{\sigma}}_f$ implies the progression of damage and appearance of a discontinuity surface. A discrete macro-crack opening in concrete at the discontinuity surface is a result of the surface dissipation due to development of a localisation zone. After the appearance of a macro-crack the material exhibits strain softening behaviour and is modelled in regards of an anisotropic multi-surface damage model [3]. As we assume herein, the fracture of concrete may be realised either as crack opening due to tensile stress (mode I) or as sliding along the discontinuity surface due to shear stress (mode II). In order to take into account both modes of fracture, we define damage functions $\bar{\bar{\phi}}_i$ for each direction at the discontinuity surface

$$\bar{\bar{\phi}}_1 = \mathbf{t} \cdot \mathbf{n} - (\bar{\bar{\sigma}}_f - \bar{\bar{q}}) \overset{?}{\leq} 0, \tag{2}$$

$$\bar{\bar{\phi}}_2 = |\mathbf{t} \cdot \mathbf{m}| - (\bar{\bar{\sigma}}_s - \frac{\bar{\bar{\sigma}}_s}{\bar{\bar{\sigma}}_f}\bar{\bar{q}}) \overset{?}{\leq} 0, \tag{3}$$

where the ratio $\frac{\bar{\bar{\sigma}}_s}{\bar{\bar{\sigma}}_f}$ relates the ultimate stress in shear $\bar{\bar{\sigma}}_s$ to the ultimate stress in tension $\bar{\bar{\sigma}}_f$ and the term $\bar{\bar{q}}$ refers to the traction-like softening variable.
A macroscopic damage is introduced into the finite elements as an embedded strong discontinuity (ED-FEM) [4]. The displacement jump is taken into account through an incompatible mode function, thus the total displacement field may be described as a sum of the standard and the incompatible part

$$\mathbf{u}^c(\mathbf{x}) = \mathbf{N}\mathbf{d}^c + \mathbf{M}\boldsymbol{\alpha}^c, \tag{4}$$

where $\mathbf{d}^c$ are the nodal displacements for standard degrees of freedom, whereas $\boldsymbol{\alpha}^c$ stand for the crack opening defined by the means of the incompatible displacements.

2.2 Degradation of the concrete-steel interface

Strength, durability and deformability of reinforced concrete is conditioned not only by the mechanical properties of concrete and steel, but by the properties of their interface as well. The principal role of the bond is to allow the redistribution of stresses between concrete and steel. At the locations of the macroscopic cracks in concrete, a relative displacement at the interface between concrete and steel occurs. Moreover, these are the locations where the dissipation of energy by the bond-slip induced by the fracture of concrete takes place

$$0 \leq \dot{\bar{\bar{D}}}_d = \frac{1}{2}\boldsymbol{\sigma}^{bs}\dot{\bar{\bar{\mathbf{D}}}}\boldsymbol{\sigma}^{bs} + \bar{\bar{q}}\dot{\bar{\bar{\xi}}}, \tag{5}$$

where $\bar{\bar{q}}$ is the stress-like hardening variable for bond-slip. The inelastic slip $\bar{\bar{\xi}}$ remains as the permanent difference between concrete and steel displacements and it is regarded as the inelastic deformation localised at the bond. The slip that occurs at the concrete-steel interface is modelled with the enhanced kinematics [5] within the extended finite element method (X-FEM) [6]

$$\mathbf{u}(\mathbf{x})|_{\Omega^e} = \sum_{a=1}^{n} N_a(\mathbf{x})\mathbf{d}_a^c + \sum_{b=1}^{n_{bs}} \psi_b(\mathbf{x})\alpha_b^{bs}, \tag{6}$$

where $\mathbf{d}_a^c$ are the standard nodal FE degrees of freedom, whereas α_b^{bs} denote the enhanced ones.

3 Probabilistic description and parameter identification via Bayesian inference

Parameterisation of the nonlinear model described in Section 2 has to take into account the influence of different sources of uncertainty. In Bayesian framework, unknown model parameters $q \in \mathbb{R}^n$ are described by prior probability densities (PDF) and their posterior probability description is inferred from indirect measurements by conditioning on the observed data. Mathematically, we can write it in terms of the Bayes rule [1]

$$\pi(\mathbf{q}|\mathbf{z}) = \frac{\pi(\mathbf{z}|\mathbf{q})\pi_0(\mathbf{q})}{P(\mathbf{z})} \propto L(\mathbf{q})\pi_0(\mathbf{q}), \tag{7}$$

where $\pi(\mathbf{q}|\mathbf{z})$ and $\pi(\mathbf{q})$ denote the posterior and prior PDF, respectively, $L(\mathbf{q})$ refers to the likelihood function which incorporates the information from the observations and $P(\mathbf{z})$ is a normalising factor assuring that the posterior conditional density integrates to unity.

In modelling of fracture in RC, the bond between concrete and reinforcement is an essential part of the composite which can in a large amount affect the modes of failure of a structure. With that in mind, we choose the bond modulus K_{bs} as the uncertain parameter modelled as a random variable (RV). K_{bs} can be understood as a measure of the force transfer between concrete and steel and therefore, as a measure of the quality of the bond. However, the phenomena which we are modelling, crack opening and bond degradation, rather have a local character. That implies that we shall also consider the spatial variability of the uncertain parameter K_{bs}, which is then mathematically modelled as a random field (RF). In this case the parameter space consists of an infinite number of RVs describing the uncertain quantity at each point of a continuous bounded domain and thus, it requires discretisation. For that purpose, we employ the Karhunen-Loève expansion (KLE) [7], which both reduces the dimension of the parameter space and removes the correlation between RVs constructing the RF, defined as

$$q_f(\mathbf{x},\omega) = \mu(\mathbf{x}) + \sum_{i=1}^{M_t} \sqrt{\lambda_i}\phi_i(\mathbf{x})\theta(\omega), \tag{8}$$

where $\mu(\mathbf{x})$ is the mean value of the forecasted RF $q_f(\mathbf{x},\omega)$, λ_i and $\phi_i(\mathbf{x})$ are eigenvalues and eigenfunctions of the generalised eigenvalue problem, respectively, and $\theta_i(\omega)$ are uncorrelated standard normal RVs of zero mean and unit variance. The expansion in eq. (8) is truncated after the M_t-th term, which is defined by the decay of the eigenvalues λ_i.

In this contribution, both random variable and random field representation of the uncertain parameter are considered and the difference in the accuracy of the posterior estimates is elaborated.

In order to accelerate the updating procedure, we employ a purely sampling-free update via Gauss-Markov-Kalman filter (GMKF) [8], where the unknown random variables are written as a functional approximation in a form of a polynomial chaos expansion (PCE) [9]. Their posterior PDF is assimilated in terms of PCE coefficients as

$$\forall \alpha \in \mathcal{J} : \mathbf{q}_a^{(\alpha)} = \mathbf{q}_f^{(\alpha)} + \mathbf{K}\left(\mathbf{z} - \mathbf{y}_f^{(\alpha)}\right), \tag{9}$$

where a stands for the assimilated and f for the forecasted quantities, resp., and $\mathbf{z}$ and $\mathbf{y}^{(\alpha)}$ are the PCE coefficients of the observations $\mathbf{z} = \hat{\mathbf{y}} + \hat{\varepsilon}$ and the forecasted response $\mathbf{y}_f = Y(\mathbf{q}) + \varepsilon$, respectively. The term $\mathbf{K}$ denotes the Kalman gain $\mathbf{K} = \mathbf{C}_{q_f,y_f}(\mathbf{C}_{y_f} + \mathbf{C}_\varepsilon)^{-1}$, consisting of the corresponding covariances.

4 Numerical example

Tension test results in a distinct crack pattern with detailed information about the crack spacing and opening and as such, it is suitable for parameter estimation of the bond properties. Fig. 1 shows the experimental setup of a RC specimen of dimensions 1.15 x 0.1 x 0.1 m subjected to a tension test [6] under displacement control, the results of which are used to learn about the bond modulus, K_{bs}, modelled as a lognormal random variable/field with mean $\mu_f = 40$ MPa and standard deviation 5%. In order to decrease the computational burden, just a quarter of the specimen is computed.

From the experiment we can recover the mean crack spacing, which is considered as a suitable observation or quantity of interest (QoI) for identification of K_{bs} modelled as a random variable. Fig. 2 illustrates the reduction of uncertainty after the update. A posteriori mean is slightly altered compared to the prior one and now takes the value of $\mu_a = 42.13$ MPa.

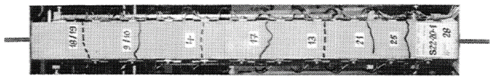

Figure 1: Crack pattern resulting from a tension test [10]

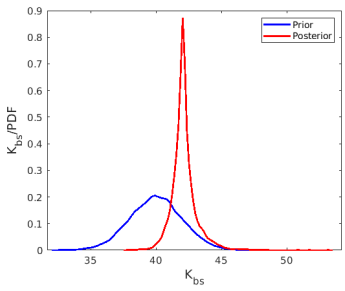

Figure 2: Prior and posterior PDF of the uncertain parameter K_{bs}

In the same manner we can identify the random parameter represented as a RF $K_{bs}(\mathbf{x}, \omega)$, with an appropriate choice of QoI, where the QoI needs to reflect the spatial variability, capturing the local effects.

5 Conclusion

Bayesian inference provides a powerful tool for an efficient estimation of the material parameters in mechanical systems in the presence of fracture, achieved by merging the information coming from two sources: our subjective knowledge contained in the prior model and the observations coming from the real experiments. The presented problem is further being investigated by taking into account additional sources of uncertainty, i.e. fracture energy of concrete and external loading.

Acknowledgements

Financial support has been provided by the German Research Foundation (DFG) in the framework of the Graduiertenkolleg 2075. This support is gratefully acknowledged.

References

[1] A. Tarantola. *Inverse problem theory and methods for model parameter estimation*, SIAM, 2005.

[2] A.M. Stuart. *Inverse problems: A Bayesian perspective*, Acta Numerica, vol. 19, 451-559, 1970.

[3] A. Ibrahimbegovic, S. Melnyk, *Embedded discontinuity finite element method for modelling of localised failure in heterogeneous materials with structured mesh: an alternative to extended finite element method*, Comp Mech, vol. 40, 149-155, 2007.

[4] A. Ibrahimbegovic, D. Brancherie. *Novel anisotropic continuum-discrete damage model capable of representing localized failure. Part I: theoretic formulation and numerical implementation*, Eng Comp, vol. 26, 100-127, 2009.

[5] T. Rukavina, A. Ibrahimbegovic, I. Kozar. *Multi-scale representation of plastic deformation in fiber-reinforced materials: application to reinforced concrete*, Lat. Am. j. solids struct., vol. 16, 2019.

[6] N. Moës, J. Dolbow,T. Belytschko, *A finite element for crack growth without remeshing*, Int J Numer Methods Eng, vol. 46, 131-150, 1999.

[7] Y. Marzouk, H. Najm. *Dimensionality reduction and polynomial chaos acceleration of Bayesian inference in inverse problems*, J Comp Phys, vol. 228, 1862-1902, 2009.

[8] H.G. Matthies et al. *Bayesian parameter estimation via filtering and functional approximations*, Arxiv, 2016.

[9] R. Ghanem, D. Higdon, H. Owhadi. *Handbook of Uncertainty Quantification*, Springer International Publishing, 521-551, 2017.

[10] B. Farra. *Influence de la résistance du béton et de son adhérence avec l'armature sur la fissuration*, PhD thesis, École polytechnique fédérale de Lausanne, 1993.

PARAMETER IDENTIFICATION FOR A MASONRY ARCH USING FEM/DEM

Soledad Mínguez [1], José L. Pérez-Aparicio [2], Rafael Bravo [3]

[1] Universitat Politècnica de València, somingo@etsid.upv.es
[2] Universitat Politècnica de València, jopeap@mes.upv.es
[3] Universidad de Granada, rbravo@ugr.es

The need of using historical structures for more and more demanding conditions and loads is arousing interest and funding on the study of the behaviour of this infrastructures, often difficult to replace or culturally valuable. This is the objective of an ongoing research project to study the complete behaviour of existing railroad masonry bridges in railways that today operate increasingly heavier trains of medium speed.

In the last two or three decades, Discontinuous Methods (DDA, DEM etc.) have been successfully applied for the simulation of masonry structures; the main reason is that, contrary from numerical methods based on pure Continuous Mechanics (e.g. FEM), they are able to take into account the discontinuities between blocks through algorithms of Contact Mechanics.

The problem of Contact Mechanics, besides its inherent theoretical difficulty, is that it requires additional parameters such as penalty stiffnesses, friction, cohesion etc: the number of parameters to properly study the structures increases significantly and, even worse, material coefficient uncertainty in constructions some times centenary, is very difficult to evaluate even at the block level and specially at the joints.

In order to fit some experimental data and validate the analyses, the material and contact properties are often obtained by trial and error such as in the reference [1], but it is much more accurate to try to adjust them with Optimization Algorithms. The current work describes preliminary results for these techniques: a simple pointed arch, for which experimental results are available [4] and has already been simulated in a previous publication [1], is studied by finding its optimal material and contact properties with a Genetic Algorithm. Instead of a rather simple Discrete Deformation Analysis (DDA) code that indirectly calculates stresses inside each block, the Discrete Element Method combined with the Finite Element Method (FEM/DEM) of the research code *Y*® from [3] has been used.

The arch drawn in Figure 1 is discretized into 16 blocks, each divided into four constant-strain FE

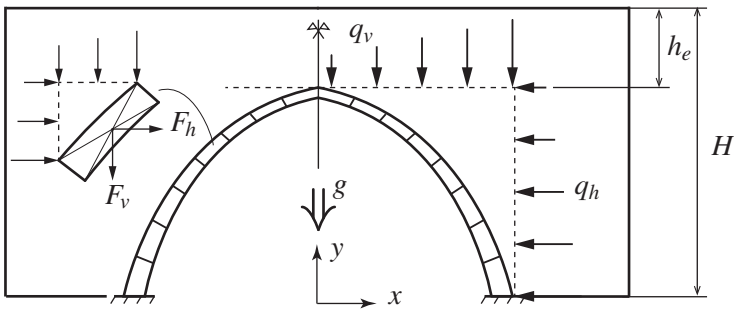

Figure 1: Pointed arch with variable embankment height h_e and equivalent vertical and horizontal forces of Eq. (1).

γ_f [kg/m^2]	γ_s [kg/m^2]	γ_e [kg/m^2]	ϕ_f	E [GPa]	ν [-]	σ_u [MPa]
1600	2300	1760	30°	32	0.15	10

Table 1: Material properties for stone, embankment and filling [1], [4].

triangles. Besides its own stone weight, the thrust of the terrain above (called embankment) and the lateral one (called filling) constitutes the external loads. The second is gravel with a friction angle ϕ_f, and the first is considered well-compacted, for which higher specific weight γ is applied. The traction and shear strength of all materials are assumed to be zero, and the ultimate strength is for compression of the stone. These properties are summarized in Table 1 and do not change through the optimization.

The remaining material coefficients are coulomb friction μ, cohesion c, and the contact coefficients are the normal p_n, tangential p_t and fracture p_f penalties along with the fracture energy G_f, see Table 3. The main objective is to determine the optimal values of these six variables that force the numerical and the experimental solutions to match. The difficulty lies in the fact that in the optimization process collapse modes of the arch intervene. The structure can be unstable or fail due to three reasons:

- For low h_e, lateral thrust of the filling prevails over the vertical loads of the embankment. Collapse occurs by peak elevation, Zone `I` in Figure 2.
- For intermediate h_e, the arch is stable but maximum stress can be exceeded in some blocks. Collapse occurs by breakage of the stone, Zone `II`.
- For high h_e, q_v forces prevail over those of q_h. Collapse occurs by peak descent, Zone `III`.

The arch is under non-uniform pressure, as a result of the gravity action of the filling, the embankment and the arch itself. At each block, the pressures q_v, q_h are converted into punctual loads inasmuch as only these loads are allowed in the solver Y®. The pressures are increased proportionally until the arch collapses under the final q_{v_f}, q_{h_f}; then the Safety Factor can be computed AS SF = q_{i_f}/q_{i_0}.

$$\begin{aligned} F_x &= \mathrm{SF}\cdot\int_{y_0}^{y_1} q_v(y)\,\mathrm{d}y = \mathrm{SF}\cdot\int_{y_0}^{y_1}\Big[(H-y)\;g\;\gamma_f + h_e\;g\;\gamma_e\Big]\,\mathrm{d}y \\ F_y &= \mathrm{SF}\cdot\int_{y_0}^{y_1} q_h(y)\,\mathrm{d}y = \mathrm{SF}\cdot\int_{y_0}^{y_1}(1-\sin\phi_f)\;q_v(y)\,\mathrm{d}y \end{aligned} \tag{1}$$

In general, a genetic algorithm (GA) solves unconstrained optimization problems; it starts with an initial population and one value for each variable of Table 3, and repeatedly modifies the population at each step. Over successive generations, the population evolves toward an optimal solution. GA are suitable in problems for which the objective function is discontinuous and highly nonlinear, and constantly evaluates the objective or cost function in pursuit of a local minimum. Therefore, the objective function should be well-chosen, or the calculation will never converge. The Matlab® function *ga* is used in this work.

To define the cost function, experimental results are needed; the experimental SF as a function of embankment height h_e from [4] is represented in Figure 2. Since there are six values to optimize, six conditions will be considered to define the function. Each i-condition is defined by four parameters:

- Safety factor SF in the abscissa of Figure 2.
- Embankment height h_e in the ordinate of the figure.
- Condition type: $type = 0$ means a stability condition (Zones `I`, `III` in the figure), and $type = 1$ a breakage condition Zone `II`.
- Condition "fulfilled": $fulfil = 1$ means that the condition established in $type$ must be fulfilled by the GA and $fulfil = 0$ means just the opposite.

i	SF	h_e	$type$	$fulfil$
1	1.0000	0.3260	0	0
2	3.7500	2.0000	1	0
3	3.8000	2.0000	1	1
4	1.8547	6.8087	0	1
5	1.8847	6.8087	0	0
6	1.0000	12.0599	0	0

Table 2: Safety Factor, embankment height, condition type, fulfilment requirement for each i-condition.

In other words, if $type = fulfil$ = 0 the arch should be unstable; if $type = 0$, $fulfil = 1$ the arch should be stable; if $type = 1$, $fulfil = 0$ the arch should not develop a crack and, finally, if $type = fulfil$ = 1 the arch should have a crack. These conditions are listed in Table 2; condition 1 represents the first estable point (asterisk) of the Figure 2; since it is inside Zone `I`, $type$ is set to 0. Conditions 2 and 3 are in Zone `II` one right above and the other right below the test curve, then $type$= 1; condition 2 should not be fulfilled inasmuch as the point under the curve ($fulfil = 0$), contrary to condition 3 ($fulfil = 1$). At every step, one simulation is executed for each condition, resulting in six simulations; once each simulation is completed, the output is post-processed.

The relevant variable for stability conditions ($type$ = 0) is the kinetic energy E_c of the whole arch: a unstable arch ($fulfil$ = 0) presents high kinetic energy but a stable one ($fulfil$ = 1) has a low energy. If the condition is fulfilled, the output variable is out = 0.0, whereas if it is not, out is set to E_c multiplied by a scaling factor. The main objective of the scaling factor is to force all entires of the out vector of comparable magnitude orders, and it is obtained from comparison of the simulations' values prior to the application of the GA.

The relevant variable for breakage conditions ($type$ = 1) is stress: for an arch with a crack ($fulfil$ = 1), the maximum stress σ_{mx} in the structure is greater than the maximum compression stress σ_u. As for stability conditions, if the condition is fulfilled, the output variable is out = 0, whereas if it is not, out is set to the difference between $\sigma_{mx} - \sigma_u$, both in MPa. Once the six simulations have been completed and the out vector defined, the cost function transformed into the " fitness value" fv defined as:

$$fv = \log_{10}\left[\left(\sum_{i=1}^{6} out_i\right) + 10^{-16}\right] \tag{2}$$

where the function log has been applied in order to avoid zeros and numerical instabilities.

	p_n [GPa]	p_t [GPa]	μ [-]	c [MPa]	p_f [MPa]	G_f [N/m]
Minimum	11.93	1.193	0	1	1	1
Maximum	596.27	59.627	2.5	10^4	10^4	20
Optimized variables GA	54.68	39.453	0.4288	11.57	9.75	1.355
Guessed variables [1]	10	10	0.577	–	–	–

Table 3: Calculation intervals with physical meaning from [1], [3]. Final optimized variables for penalties, friction and fracture energy; guessed variables from [1].

The possible intervals collected from the references along with the optimized final results from the GA are listed in Table 3; the guessed coefficients from [1] are the last line of the table. Notice that the GA results are inside the "physical" ranges and that all of them lie close to the lower values. The relevant penalty parameters p_n, p_t are five and three times higher than the ones from the reference, meaning that a stronger constraint in the contact algorithm was necessary. The friction is slightly lower and, in accordance with the guess of [1], finally the cohesion parameter is not very important.

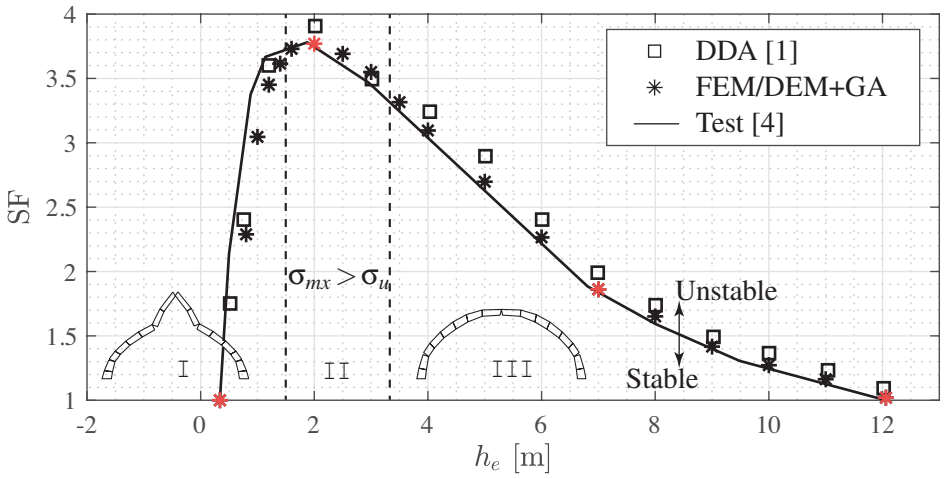

Figure 2: Safety factor SF vs. embankment thickness h_e for experimental and numerical results in a pointed arch. Failure by: `I` instability with peak raising; `II` compression breakage; `III` instability with peak descent. Red asterisks used as conditions in Table 2.

Figure 2 shows the evolution of SF as a function of the embankment height for: the experimental results of [4], the DDA analysis from [1] with guessed results and finally from the current FEM/DEM modeling [3] and the six optimized variables with GA. The red asterisks are the conditions of Table 2, which perfectly fit the experimental curve showing that the GA has converged properly. The other asterisks calculated with Y® do not perfectly fit but they are closer than the squares from [1], showing that even if a relatively low number of conditions have been applied, the optimized variables fit the model for all embankment heights.

Acknowledgments

This work has been supported by the project Railfabric RTI12018-093621-B-100 financed by the programme Retos of the Spanish Ministry of Science.

References

[1] J.L. Pérez-Aparicio, R. Bravo, P. Ortiz, *Refined Element Discontinuous Numerical Analysis of Dry-Contact Masonry Arches*, Engineering Structures, 48, 578-587, 2013.

[2] P.B. Lourenço, *Computational strategies for masonry structures*, FEUP, 1996.

[3] A. Munjinza, *The Combined Finite-Discrete Element Method*, Wiley, 2004.

[4] J. Delbecq, *Analyse de la stabilité des voûtes en maçonnerie par le calcul à la ropture*, J. de Méchanique Théorique et Appliqué, 11, 91-121, 1982.

ECCOMAS MSF 2021 THEMATIC CONFERENCE
30 June – 2 JULY 2021, SPLIT, CROATIA

GOOD MODELING PRACTICE OF WATER TREATMENT PROCESSES

Suvada Šuvalija[1], Hata Milišić[2], Emina Hadžić[3]

[1] Department of Sanitary and Environmental Engineering – GF Sarajevo, University of Sarajevo, suvadasuvalija69@gmail.com
[2] Department of Teoretical and Applied Hidromechanics and Hydraulic Structures and Facilities, GF Sarajevo, University of Sarajevo, hata.milisic@gmail.com
[3] Department of Water Resources and Environmental Engineering – GF Sarajevo, University of Sarajevo, eminahd@gmail.com

Abstract. Models for water treatment processes include simulation, i.e., modelling of water quality, flow hydraulics, process controls and design. Water treatment processes are inherently dynamic because of the large variations in the influent water flow rate, concentration and composition. Moreover, these variations are to a large extent not possible to control. Mathematical models and computer simulations are essential to describe, predict and control the complicated interactions of the processes. An accurate description of such systems can therefore result in highly complex models, which may not be very useful from a practical, operational point of view. The main objective is to combine knowledge of the process dynamics with mathematical methods for processes estimation and identification. Good modelling practice is way to obtain this objective and to improve water treatment processes (its understanding, design, control and performance- efficiency). By synthesise of existing knowledge and experience on good modelling practices and principles the aim is to help address the critical strategic gaps and weaknesses in water treatment models application.

Key-words — water treatment process, modelling practice, model application, water quality, process dynamics

1 Introduction

Every system can be accurately described by a mathematical model. Mathematical model (model in the following text) is model within a mathematical framework where equations of various types are defined to relate inputs, outputs and characteristics of a system [1]. A model is nothing more than a mathematical abstraction of a real process. In the real world it must be realized that a model is always a simplification of reality.

Models for water treatment processes can be used for different purposes like understanding of water treatment processes; optimization of water treatment plant design; optimization of process control (active control); predictions of the treatment plant performance under changing conditions (scenario studies) [2]. The behavior of real water treatment processes occurring in a water treatment reactor is complex and difficult to describe mathematically [3] [4]. The number of reactions and different mechanisms that are involved in the water treatment processes are very large. Some of the major problems when trying to model water treatment processes are lacking process knowledge (e.g., coagulation, flocculation, settling and filtration mechanism characteristics); several different unit processes interconnected by various internal feedbacks; highly non-linear processes; non-stationary

processes; time varying process parameters; practically non-controllable and highly variable process inputs; lack of adequate measuring techniques [5].

Also, one of the main problems with the existing work on dynamic modelling water treatment processes individually is a lack of understanding as to how these models fit together to develop a complete water treatment plant. The knowledge and understanding of the individual unit gained can direct the efforts in the production of complete water treatment plant models. There is a need for more mechanistic (dynamic and integrated) models [6]. It is a big challenge to define the best modeling practice for different purposes of water treatment processes modeling application.

2 Water Treatment Processes Modelling

The quality of drinking water is an important matter, because water of low quality may cause health-related and economic problems which have a considerable impact on people's daily lives [5]. The main task of water treatment plant (WTP) is to produce drinking water quality according to water quality standards. Also, within a perspective of sustainable development, treatment plants must be designed on the basis of technical, economic and environmental criteria. As a "treatment train", conventional drinking water treatment plant compounds of many processes /units (coagulation - flocculation, sedimentation, filtration and disinfection) [7]. Each of these units, its design and operation, could be optimized by modeling.

Fully automated treatment plants will require drinking water treatment plant simulator. Models are an essential part of the simulators since they represent the behavior of the treatment plant's processes. The purpose and objectives of water treatment modeling should include a clearly articulated set of user data requirements, processes to be represented, questions, functionalities, system boundaries and predictive quantities of interest [2] [8]. First of all, the model needs to have the ability to estimate the parameters/variables of interest for the process/unit at the right scale and resolution (i.e. temporal, spatial, and thematic) which matches the rate of change in the system of interest.

To achieve an accurate and adequate design of efficient WTPs operating at optimum conditions, commercial simulation software has been developed [9]. Unfortunately, there has been little application of water treatment modeling. Also, despite the long history of water treatment processes, their mathematical analysis is not a mature scientific discipline as possibly expected. In the water treatment simulation, the balance between empirical approach and formal mathematical modelling must be reconsidered. Good modeling practice is way for improvement of modelling development and application in water treatment sector.

3 Good Modeling Practice

From a development perspective, there are essentially four phases in the modelling and assessment process [1]. The phases tend to be iterative and can be described as

- Scoping (Model study plan including identifying model purpose and study objectives)
- Problem framing and formulation (including conceptualization)
- Analysis and assessment of options (Model Setup, and Calibration and Validation) and
- Communicating of findings (Simulation and Evaluation).

The quality and outcomes of a modelling process largely depend on the modelling practices that are undertaken at every step. Best practices should be proven-to-work practices for managing common problems encountered throughout the modelling process [10]. Identifying best practices helps to provide guidelines for improved modelling practice. Such improvements will ultimately lead to more accurate, credible and useful models, more insightful model-based recommendations, better-informed model adoption, and more importantly improved decision-making.
Best practice modelling means the best achievable procedures and outcomes taking into account intended purpose, and trade-offs in knowledge, data, resource and time constraints. The aim is to develop purposeful, credible models from data and prior knowledge, in consort with end-users, with

every stage open to critical review and revision. Various considerations influence the modeller's choice of the good modeling practice.

Information Technology tools for water treatment modeling will form the link between data, model, active control, research, education/training and design. The knowledge of operators, designers and researchers is based on different information. Operators get information from the full-scale plant, while designers obtain their data from pilot plants and researchers from experiments on the lab-scale [9]. Calibration or testing of models is performed experimentally by measuring the corresponding data on the pilot plant or the actual plant. Frequently pilot plants are available for calibration and validation of the models, while in full-scale plants the models can be tested and used for the improvement of the processes.

Development of good modelling practice means a review of existing water treatment simulators, to identify what would be needed for a new system. By this review has identified that there has been little usage of water treatment modelling, with the two main objections being the quantity of data required to calibrate the models, and the fragility of the models when applied outside the calibration region [7]. Web based, predictive and integrated computer models enabling control and optimization of existing water supply systems with respect to water quality, reliability, customer service level, environmental impact and costs.
Uncertainty assessment is increasingly being seen as a holistic process that should be a major consideration throughout the whole lifecycle of the modelling process
To be complete, uncertainty assessment and management in the water sector will almost always necessitate the use of qualitative assessments, with quantitative assessments wherever possible.

4 Conclusion

Models for water treatment processes are a reflection of the knowledge of the system and are fed by data and (new) hypotheses. This will lead to cost effective, high performance, stable and reliable treatments.
Although continuous progress has been made in recent years in improving the accuracy of mathematical models to predict water treatment processes, much research work still needs to be carried out. To ensure the successful implementations of mathematical models in the water industry, regulators, water companies and modelling experts need to come together to develop formal guidance on good modelling practices which describe how models must be used in water companies.

References

[1] U. Jeppsson. *Modelling Aspects of Wastewater Treatment Processes*, PhD Thesis, Department of Industrial Electrical Engineering and Automation (IEA) Lund Institute of Technology (LTH), Lund, Sweden, page 445, 2017.

[2] L.C. Rietveld. *Improving operation of drinking water treatment through modeling*, Ph.D. Dissertation, TU Delft, The Netherlands, 2005.

[3] F. Akinmolayan, *Mathematical Modelling of Clean Water Treatment Works*, PhD Thesis, Centre for Process Systems Engineering Department of Chemical Engineering, University College London, page 249, 2017.

[4] V.A. Ani. *Process modelling and simulation of a simple water treatment plant*", Int. J. Intell. Syst. Appl. Eng., 4(4), 84-94, 2016. https://doi.org/10.18201/ijisae.2016426378

[5] A.J. Jakeman, S. Elsawah, S. Cuddy, B.J. Robson, N. McIntyre and F.J. Cook, *Good Modelling Practice - a discussion paper*, Australian National University, Department of Science, Information Technology and Innovation (DSITI), Queensland, page 33, 2017.

[6] S.C. Ulinici, G. Vlad, D. Vâju, I. Balint, G. Băisan and M. Hetvary, *Numerical Modeling of Processes in Water Treatment Plants as a Basis for an Optimal Design*, ECOTERRA - Journal of Environmental Research and Protection, Volume 11 (3), page 41-57, 2014.

[7] S. Suvalija, Z. Milasinovic, Milišić, H. and E. Hadzic. *Models for drinking water treatment processes*, Coupled Systems Mechanics, Vol. 8, No. 6 (2019) 000-000 DOI: https://doi.org/10.12989/csm.2019.8.6.000
[8] M.M. Yoann, *Development of an integrated tool for Process Modelling and Life Cycle Assessment; Ecodesign of process plants and application to drinking water treatment*, PhD Thesis, Institut National des Sciences Appliquees de Toulouse (INSA Toulouse), Chemical and Process Engineering, Toulouse, page 357. 2013.
[9] J. Dudley and G. Dillon, *Water Treatment Simulators: State-of-the- Art Review*, Research and Technology—AQUA, Vol.57, No.1, page 13-21, 2014.
[10] R.W. Swan. *Optimization of Water Treatment Works using Monte-Carlo Methods and Genetic Algorithms*, PhD Thesis, School of Civil Engineering, University of Birmingham, Birmingham, page 298, 2015.

COASTAL FLOOD EXPOSURE ASSESSMENT DUE TO SEA LEVEL RISE AND EXTREME WAVE EVENTS

Toni Kekez[1], Francesco Piccioli[2], Elena Benvenuti[2], Željana Nikolić [1]

[1] University of Split, Faculty of Civil Engineering, Architecture and Geodesy, toni.kekez@gradst.hr, zeljana.nikolic@gradst.hr
[2] University of Ferrara, Engineering Department, francesco.piccioli@unife.it, elena.benvenuti@unife.it

Many coastal areas around the world are faced with an increase in flood risk due to sea level rise and other extreme events. Sea level rise, mostly induced by climate change, presents one of the biggest challenges that countries and regions with coastal lowlands will face in the medium term [1]. Sea level rise is a natural phenomenon that cannot be prevented and it will most likely continue to rise well beyond year 2100 [2].

In this research, a flood exposure analysis for the coastal area of Kaštel Kambelovac in Croatia (Fig. 1) is performed considering sea level rise impact of extreme waves on the coastline. The selected area could be faced with a significant flood risk in the future due to its low-lying topography and large number of cultural and household objects near the coastline. This research represents particular activities of the PMO-GATE Interreg CBC project, focused on preventing, managing and overcoming natural-hazard risks.

Fig. 1. Coastal area of Kaštel Kambelovac [3]

The EU Floods Directive 2007/60/EC on the assessment and management of flood risks [4] obliged each member state to carry out activities for identification of areas with a significant flood risk due to climate change. For such areas, flood risk maps as well as flood risk management plans must be developed, focusing on prevention, protection, and preparedness. Republic of Croatia developed a National Strategy for climate change adaptation [5], which recognized sea level rise as one of the most

significant climate-related factors. Furthermore, different sea level rise scenarios are presented in this Strategy for the period up to year 2100.

An analysis of different coastal flooding scenarios for the Kaštel Kambelovac area is performed following the EU Flood Directive requirements. Flooding scenarios are determined based on the combination of three different natural factors; tidal effect, atmospheric pressure and extreme coastal waves. Furthermore, coastal flooding scenarios are adapted to climate change impact and sea level rise projections for the Adriatic Sea.

Tidal effect is evaluated through harmonic analysis of the measured sea level data from a near gauging station, resulting with a frequency and period of tide events. By extracting the tidal effect from the measured sea level data, the impact of atmospheric pressure and other related effects is determined and separately evaluated. Climate change effect is implemented through sea level rise projections, reflecting through change of the mean sea level in comparison with the measured data.

Different wind and wave scenarios are independently evaluated for the analyzed area, and based on the measured data about wind direction and velocity critical wind directions are recognized. For the selected critical wind direction, different scenarios considering wind velocity are evaluated (low, moderate and high probability events) and transferred to the corresponding wave heights.

Finally, each coastal flooding scenario represents a combination of three stated factors (tide, pressure, wind). Extreme tide in combination with low atmospheric pressure and extreme waves on the coastline resulted with different flooding scenarios. Flood exposure analysis is performed based on the digital terrain model (DTM), resulting with a classification of the inundated area considering flooding probability as well as classification of the inundation depth with respect to each flooding scenario.

Acknowledgements

This work has been supported through the project preventing, managing and overcoming natural-hazards risks to mitigate economic and social impact (PMO-GATE), funded by the European Union through the programme Interreg Italy-Croatia, and the project KK.01.1.1.02.0027, co-financed by the Croatian Government and the European Union through the European Regional Development Fund - the Competitiveness and Cohesion Operational Programme.

References

[1] Antunes, C.; Rocha, C.; Catita, C. (2019): Coastal Flood Assessment due to Sea Level Rise and Extreme Storm Events: A Case Study of the Atlantic Coast of Portugal's Mainland. Geosciences, 9, 239

[2] IPCC, 2018: Summary for Policymakers. In Global Warming of 1.5 ˚C. An IPCC Special Report on the Impacts of Global Warming of 1.5 ˚C above Pre-Industrial Levels and Related Global Greenhouse Gas Emission Pathways, in the Context of Strengthening the Global Response to the Threat of Climate Change, Sustainable Development, and Efforts to Eradicate Poverty; Masson-Delmotte, V., Zhai, P., Pörtner, H.-O., Roberts, D., Skea, J., Shukla, P.R., Pirani, A., Moufouma-Okia, W., Péan, C., Pidcock, R., et al., Eds.; World Meteorological Organization: Geneva, Switzerland, 2018; p. 32.

[3] https://marinas.com/

[4] European Commission Directive 2007/60/EC of the European Parliament and of the Council of 23 October 2007 on the Assessment and Management of Flood Risks.

[5] Climate Change Adaptation Strategy in the Republic of Croatia for the period to 2040 with a view to 2070

QUANTIFICATION OF HYDRODYNAMIC EFFECTS IN COMPLEX DAM-FLUID DOMAIN USING THE HYDRODYNAMIC INFLUENCE MATRIX

Violeta Mircevska[1], Miroslav Nastev[2], Ana Nanevska[3], Trajce Zafirov[4]

[1] Professor, Institute of Earthquake Engineering and Engineering Seismology, Univ. Ss. Cyril and Methodius, Skopje, R.N. Macedonia (corresponding author), e-mail: violeta@iziis.ukim.edu.mk; mircevska.violeta@gmail.com
[2] Research Scientist, Natural Resources Canada, Geological Survey of Canada, Quebec City, Canada G1K 9A9. e-mail: miroslav.nastev@canada.ca
[3] PhD student, Institute of Earthquake Engineering and Engineering Seismology, Univ. Ss. Cyril and Methodius, Skopje, R.N. Macedonia., e-mail: nanevska@iziis.ukim.edu.mk
[4] PhD student, Institute of Earthquake Engineering and Engineering Seismology, Univ. Ss. Cyril and Methodius, Skopje, R.N. Macedonia, e-mail: trajce@iziis.ukim.edu.mk

Topic: Fluid-structure interaction

Various algorithms for simulation of fluid-structure interaction (FSI) problems have been developed in the past decades based on the coupled boundary elements – finite elements models (BEM-FEM). Their efficiency was addressed by numerous authors [1][2][3][4]. FEM is commonly applied to model the dam structure, whereas BEM revealed efficient in simulating the fluid domain. This discretization step is critical in managing the computation time for large dam-reservoir systems and/or dams with curved shape in complex terrains. A potential source of computational instability which requires particular attention comes from the constitutional disagreement between the FEM matrix (symmetric, sparse and positively defined) and BEM matrix (non-symmetric and fully populated). There are two major BEM-FEM techniques for fluid-structure coupling: direct coupling and iterative coupling.

The most common direct coupling BEM-FEM technique applies a single analytical scheme, i.e., the governing equations of one of the sub-domains are transformed into a form suitable for the other sub-domain, and both sets of equations are assembled into a single system. Two options are proposed for construction of the global set of coupled equations: (i) equivalent FEM technique based on the transformation of the BEM equations into displacement-based stiffness matrix, and (ii) equivalent BEM technique based on the transformation of the FEM stiffness matrix in a form suitable for application by the BEM technique, [5][6][7][8][9].

The iterative coupling BEM-FEM techniques are based on the decomposition of the dam structure-fluid domains into two physically distinct systems. The BEM and FEM equations are solved separately applying an iterative procedure to attain equilibrium of dependent variables of both domains at their interface until a desired convergence is achieved. The advantage of these methods lies in the application of advanced solvers designed to fit the matrix features for each domain. The application of the iterative methods is particularly suitable in elastoplastic analyses of the dam domain [10][11][12] [13], and in BEM formulations of infinite domains [14]. However, the iterative techniques also exhibit certain instability problems. These instabilities can result from the inadequate accuracy of the applied

BEM and FEM algorithms, and from the sensitivity of the assigned integration steps and the prescribed convergence criteria [15][16][11].

Notwithstanding the reported limitations, quantification of the fluid-structure interaction applying direct or iterative coupling BEM-FEM methods is widely used.

The objective of this paper is to document the theoretical development and validation of a novel and practical coupling method for analysis of complex dam-reservoir interaction problems [17].

The proposed approach benefits from the combination of BEM and FEM methods applied for an independent analysis of the two physically distinct domains, the dam structure and the reservoir-foundation domains. It involves the matrix of hydrodynamic influence (HDI) composed of predefined vectors of nodal influence based on the application of the virtual work principle to the BEM domain. Each of the vectors of nodal influence simulates the hydrodynamic effect in the BEM domain generated by the action of a unit acceleration imposed along the normal of the respective node. The nodes are located at the dam-fluid interface and at the canyon walls-fluid interface along the truncated reservoir. A direct computation of the vector of hydrodynamic forces is applied involving the hydrodynamic influence matrix (HDI) in the equation of the dynamic response of the FEM domain only. Equilibrium between the hydrodynamic forces and absolute accelerations is obtained by repetitive solution of the dynamic equation for the FEM domain until the Euclidean norm of the vector of residual errors at the interface nodes becomes smaller than the prescribed error tolerance. The efficiency of the proposed method is reflected in the preserved symmetry, sparsity and bandedness of the FEM stiffness matrix. The HDI matrix is calculated only once, stored in the memory and recalled in each time step, which results in considerably smaller CPU time. Opposite to direct or iterative coupling methods, the problems with solution instability caused mainly by the failure to achieve equilibrium at the interface are inexistent. It can be applied readily regardless the type of material behavior within of the FEM sub-domains. When solving the differential equation of motion, a constant or variable time step has to be defined within a given response intervals to achieve stability of the step-by-step direct integration process only. The corrective iterations are almost unnecessary, but there is a need for double repetition of each time step. In this way, first is calculated the vector of hydrodynamic forces according to the manifested field of total accelerations at the dam-fluid and fluid-rock interfaces, the step is then repeated to solve the dam response under the influence of the calculated hydrodynamic forces. The method allows effective consideration of compound wave-field of compressive and dilatational waves and wave scattering effects for a more realistic evaluation of the interaction phenomenon. In general, the magnitude of the hydrodynamic effects is proportional to the amount of energy transferred to the fluid domain. This energy is suppressed by the damping force caused by the dam motion in the fluid environment, energy dissipation of the acoustic waves by the deposits at the reservoir bottom and radiational damping of the outgoing waves. On the other side, the application of the HDI matrix method is limited to stationary wave motion of incompressible inviscid fluids. It is not applicable in the case of a nonlinear type of fluid-structure interaction (effect of non-linear convective acceleration), whenever there is a change of the specified essential type of boundary conditions, and in the case of treating infinite fluid-domains.

The algorithm developed for the HDI matrix method was embedded in the ADAD-IZIIS [18] software package for static and dynamic analyses of dam-reservoir-foundation systems. A comprehensive validation procedure was applied consisting of comparison against results of the classic Westergaard solution [19] for simple 2D and 3D rigid dam models, with results obtained with the commercial ADINA software [20]. To demonstrate the full capacity of the proposed method, a hypothetical 3D example of a concrete gravity dam is considered subjected to seismic excitation. The dam-reservoir system was subjected to the horizontal component of the 1989 M6.9 Loma Prieta earthquake, with peak ground acceleration of 0.62 g. The considered duration of the record was 10 s, assumed adequate for comparison of the response time histories.

Visually, excellent agreement between the amplitudes and phase variations predicted with both ADAD-IZIIS and ADINA software are observed. The discrepancies at the peak response are 7%, 8.8%, and 8.8% for the horizontal displacement at the dam crest, the hydrodynamic pressure at the

dam height of 50 m, and at the bottom of the dam, respectively. The respective maximum discrepancies are 20%, 28%, and 20%. Although they appear significant, the maximal discrepancies are all observed in the decaying part of the response (after the peak is attained) at lower response magnitudes and, what is more important, do not cumulate with time. To further improve the accuracy, equilibrium of the total vectors of displacement, velocity, and acceleration was imposed immediately after the peak of the excitation in order to minimize the error in the solution of the dynamic equation. This leads to improved equilibrium between the hydrodynamic forces and absolute accelerations especially if Euclidean norm of 0.01was assigned, which was achieved with five iterations following the input peak ground acceleration, whereas two to three iterations were generally sufficient after the subsequent important peaks. For Euclidean norm of 0.5, no iterations were required.

The local topographic settings can exert important impacts on the amount of generated energy in the fluid domain. These impacts have been unfairly ignored in BEM and FEM modeling of the reservoir. Herein, the importance of treating the terrain irregularities is demonstrated by including the required portion of the reservoir in the model. Namely, the truncation surface should be located sufficiently far from the dam so that further displacement away has a negligible impact on the amount of generated energy and respectively on the hydrodynamic effects. In order to get an insight into the amount of the generated hydrodynamic forces at the dam-fluid interface for regular and complex canyon topography, the components of calculated forces in streamwise, cross-stream, and vertical direction, are integrated separately over the interface at each time step. For easier comparison, shaking intensities, are also computed as an integral over time of the square of the componential hydrodynamic forces. These intensities represent a useful measure of the hydrodynamic shaking effect in the considered directions. Computed integrals are then normalized to the maximal value [21].

The presented analyses contribute to the quantification of the influence of the terrain irregularities on the amount of energy transferred to the fluid domain and further to the dam-fluid interface. The vibration of the dam along with the surrounding irregular terrain generates quite different time history of compressive and dilatation waves, which results in modification of the hydrodynamic distribution pattern mostly followed by remarkable higher magnitudes of hydrodynamic effects. In the case of a complex reservoir shape and dynamic excitation acting in the streamwise direction, the intensity of the hydrodynamic shaking is approximately 70% higher than that in the case of the regular reservoir shape. As well, it has been shown that, despite the fact that the magnitudes of hydrodynamic effects are lower when the seismic force acts in the cross-stream direction, the impact of the terrain irregularities is significant and gives rise to a remarkable modification of hydrodynamic distribution pattern and manifold magnification of the maxima of the hydrodynamic effects.

References:

[1] O. C. Zienkiewicz, D. W. Kelly, P. Bettes, *The coupling of the finite element method and boundary solution procedures*, International Journal for Numerical Methods in Engineering, 11, pp. 355–375, 1977.

[2] C. A. Brebbia, P. Georgiou, *Combination of boundaryand finite elements in elastostatics*, Applied Mathematical Modeling, **3**(3), pp. 212-220, 1979

[3] F. Medina and J. Domínguez, *Boundary elements for the analysis of the seismic response of dam including dam-water-foundation interaction effects*, Engineering Analysis with Boundary Elements, **6**(3), pp. 152-157, 1989.

[4] O. von Estorff, *Coupling of BEM and FEM in the time domain: Some remarks on its applicability and efficiency*, Computers & Structures, **44**(1-2), pp. 325-337, 1992.

[5] O. von Estorff, M. J. Prabucki, *Dynamic response in the time domain by coupled boundary and finite elements*, Computational Mechanics, **6**(1), pp. 35-46, 1190.

[6] O. von Estorff, H. Antes, *On FEM-BEM coupling for fluid-structure interaction analysis in the time domain*, International Journal for Numerical Methods in Engineering, **31**(6), pp. 1151-1168, 1991.

[7] G. Yu, W. J. Mansur, J. A. M. Carrer, S. T. Lie, *A more stable scheme for BEM/FEM coupling applied to two-dimensional elastodynamics*, Computers & Structures, **79**(8), pp. 811-823, 2001.
[8] M. Yazdchi, N. Khalili, S. Valliappan, *Nonlinear seismic behavior of concrete gravity dams using coupled finite element-boundary element technique*, International Journal for Numerical Methods in Engineering, **44**(1), pp. 101-130, 1999.
[9] O. Czygan, O. von Estorff, *Fluid-structure interaction by coupling BEM and nonlinear FEM*, Engineering Analysis with Boundary Elements, **26**(9), pp. 773-779, 2002.
[10] J. A. M. Carrer, J. C. F. Telles, *A boundary element formulation to solve transient dynamic elastoplastic problems*, Computers & Structures, **45**(4), 707-713, 1992.
[11] D. Jr. Soares, O. von Estorff, W. J. Mansur, *Iterative coupling of BEM and FEM for nonlinear dynamic analyses*, Computational Mechanics, **34**(1), pp. 67-73, 2004.
[12] D. Jr. Soares, J. A. M. Carrer, W. J. Mansur, *Nonlinear elasto dynamic analysis by the BEM: An approach based on the iterative coupling of the D-BEM and TD-BEM formulations*, Engineering Analysis with Boundary Elements, **29**(8), 761-774, 2005.
[13] D. Jr. Soares, O. von Estorff, W. J. Mansur, *Efficient nonlinear solid-fluid interaction analysis by an iterative BEM/FEMcoupling*, International Journal for Numerical Methods in Engineering, **64**(11), pp. 1416–1431, 2005.
[14] W. J. Mansur, *A time-stepping technique to solve wave propagationproblems using the boundary element method*, Ph.D. thesis, University of Southampton, Southampton, U.K., 1983.
[15] C. C. Lin, E. C. Lawton, J. A. Caliendo, L. R. Anderson, *An iterative finite element-boundary element algorithm*, Computers & Structures, **59**(5), pp. 899–909, 1996.
[16] Y. T. Feng, D. R. J. Owen, *Iterative solution of coupled FE/BE discretization for plate-foundation interaction problems*, International Journal for Numerical Methods in Engineering, **39**(11), 1996.
[17] V. Mircevska, M. Nastev, V. Hristovski, M. Sujan, M. Garevski, *Development and Validation of HDI Matrix Method for Fluid Dam Interaction*, American Society of Civil Engineering-ASCE, Journal of Computing in Civil Engineering, DOI:10.1061/(ASCE)CP.1943-5487.0000684, ASCE ISSN 0887-3801.
[18] ADAD-IZIIS, *Analysis and design of arch dams – User's manual*, Institute of Earthquake Engineering and Engineering Seismology – IZIIS, University of Ss. Cyril and Methodius, Skopje, R. N. Macedonia, 2018.
[19] H. M. Westergaard, *Water pressure on dams during earthquakes*, Transactions of the American Society of Civil Engineers, **98**(2), pp. 418–433, 1933.
[20] ADINA, *ADINA theory and modeling guide. Volume I: ADINA Solids and Structures*, Online Rep. ARD 13–8, ADINA R & R, Inc.,Watertown, MA, 2013.
[21] V. Mircevska, M. Nastev, V. Hristovski, I. Bulajic, *Arch dam-fluid interaction considering reservoir topology*, Journal of Earthquake Engineering, **18**(7), pp. 1083-1101, 2014.

ECCOMAS MSF 2021 THEMATIC CONFERENCE
30 June – 2 JULY 2021, SPLIT, CROATIA

WAVE PROPAGATION EFFECTS IN SSI PROBLEMS

Sheshov V.[1], Stojmanovska M.[2], Salic R.[3], Bogdanovic A.[4] and Edip K.[5]

[1] Institute of Earthquake Engineering and Engineering Seismology, Skopje, N.Macedonia, vlatko@iziis.ukim.edu.mk
[2] Institute of Earthquake Engineering and Engineering Seismology, Skopje, N.Macedonia, marta@iziis.ukim.edu.mk
[3] Institute of Earthquake Engineering and Engineering Seismology, Skopje, N.Macedonia, r_salic@iziis.ukim.edu.mk
[4] Institute of Earthquake Engineering and Engineering Seismology, Skopje, N.Macedonia, saska@iziis.ukim.edu.mk
[5] Institute of Earthquake Engineering and Engineering Seismology, Skopje, N.Macedonia, kemal@iziis.ukim.edu.mk

The wave propagation phenomenon in semi-infinite domains is of a great importance in the field of soil structure interaction (SSI). In these kinds of problems, the elastic waves propagate to the exterior domain and require a special treatment at the computational boundaries in order not to reflect back to the interior domain. In this work, a study on implementation of new type boundary conditions considering SSI phenomenon is presented. The proposed algorithm is implemented in the ANSYS [1] finite element software and tested on two-dimensional problems. In simulation of SSI problems, it is of importance that domains extending to infinity to be divided into two parts; an interior and an exterior domain with the separating boundary in-between. The exterior domain is the region where the propagating waves should be absorbed and not reflected back to the interior domain. In dynamic analysis using the linear elastic material models, the calculations are usually performed in frequency domain. However, in more realistic cases, in order to account for nonlinearities in structural response considering different effects, the time domain simulations have to be considered. In the last decades the unbounded soil media are presented by the infinite elements which take an important role in boundary simulations [2-5]. This type of approximation is local in time and space and the infinite elements function as absorbers. In this work, a new type of infinite element is developed by adding absorbing properties to all nodes of the infinite elements. The formulation of mapped infinite elements is the same as for the finite elements in addition to the mapping of the domain. The main advantage of the mapped infinite elements is the usage of the conventional Gauss-Legendre abscissa and weights. For impact of plane waves on element sides, normal and tangential stresses are derived as follows:

$$\begin{bmatrix} \sigma^n \\ \tau \end{bmatrix} = \begin{bmatrix} a\rho c^p & 0 \\ 0 & b\rho c^s \end{bmatrix} \begin{bmatrix} \dot{u}^n \\ \dot{u}^t \end{bmatrix} \tag{1}$$

where c^P and c^S indicate compression and shear waves, ρ is the density of soil medium. Transformation from local to global coordinates is done by ANSYS [1] software such that there is no need of defining transformation matrices. By adding together the parts from each element, the governing incremental equations for equilibrium in dynamic analysis are obtained. The programming of the infinite element has been done using the Programmable Features of ANSYS. For the sake of verification of the presented infinite elements, an unbounded two-dimensional soil region is considered in Figure 1. In order to verify

the absorbing properties of the newly programmed infinite elements, two-dimensional wave propagation is performed.

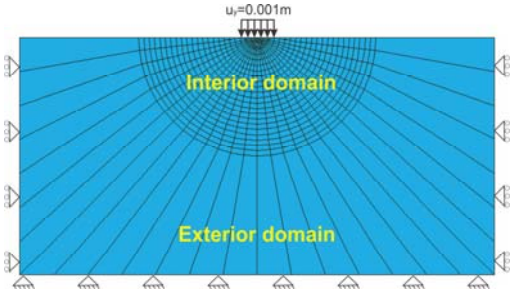

Figure 1. Soil domain of finite and infinite elements

The properties of the soil medium are taken as Young's modulus E=50000kPa, Poisson's ratio υ=0.35 and density ρ=2.7 ton/m3. The applied displacement is considered to be of the impulse type. In this case, displacement of uy=0.001m is applied as an impulse function at the very beginning of the time.

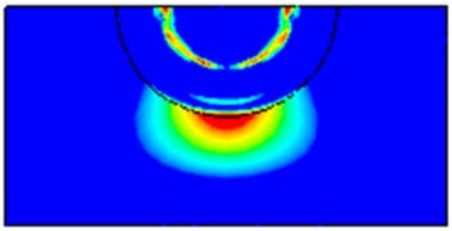
Figure 2. Soil domain of finite and infinite elements

As can be seen from figure 2, both P and S waves exist in the interior domain. At the time instant of t=0.07s when the P-wave reaches the boundary between interior and exterior domains the waves are absorbed in the exterior part not reflecting back to the interior. In this particular spot the P-wave is absorbed succesfully in the exterior field. Thus, the infinite elements with added absorbing characteristics which were implemented in this study provide a promising tool which is easy to implement in finite element analysis. On the other hand, when simulating soil structure interaction problems the waves propagating in the interior domain should be absorbed in the boundaries so that the structural response should not be influenced by reflecting waves. As given in Figure 3 the structure of interest rests on finite elements where the expected wave propagation is of importance.

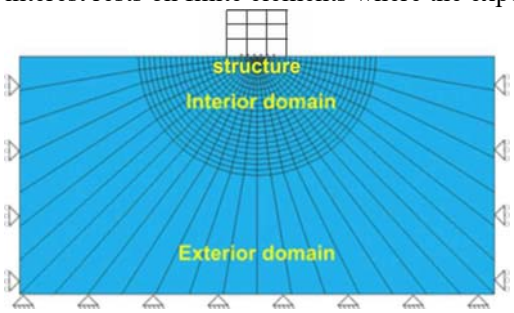

Figure 3. Coupled soil-structure system of a three storey frame

The usage of infinite elements absorbs the waves, not letting them propagate back to the soil domain. Thus, the effect of earthquake forces upon structural elements is real without wave reflections from the boundaries. In order to show the effects of wave propagation in SSI problems an earthquake time history of of Bitola earthquake with magnitude of M=5.2 and the time domain presentation is given below in Figure 4.

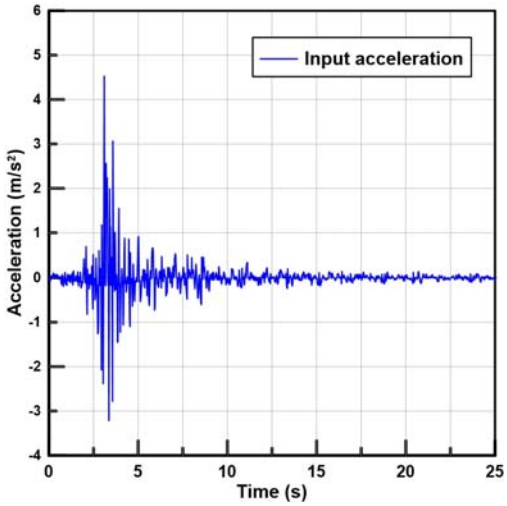

Figure 4. Bitola earthquake time history

The results obtained from coupled SSI analsys show interesting outcomes in which it is shown that the effect of infinite elements on exterior domain gives promising results when considering the structural response. It can be stated that the results obtained from the analysis show that effects of soil exterior modelling is important and has to be considered correctly in simulation of SSI problems.

References

[1]. ANSYS. *Fem Software*. 2006.
[2]. Zienkiewicz, O., et al., *Mapped infinite elements for exterior wave problems.* International Journal For Numerical Methods In Engineering, 1985. **21**(7): p. 1229-1251.
[3]. Medina, F., *An axisymmetric infinite element.* International Journal For Numerical Methods In Engineering, 1981. **17**(8): p. 1177-1185.
[4]. Bettess, P., *More on infinite elements.* International Journal For Numerical Methods In Engineering, 1980. **15**(11): p. 1613-1626.
[5]. Sesov, V., et al., *Development of New Infinite Element for Numerical Simulation of Wave Propagation in Soil Media*, in *Experimental Research in Earthquake Engineering*. 2015, Springer. p. 423-436.

ECCOMAS MSF 2021 THEMATIC CONFERENCE
30 June – 2 JULY 2021, SPLIT, CROATIA

OPTIMIZATION OF IRREGULAR STRUCTURES UNDER SEISMIC LOADING

Zlatko Džanić[1], Mustafa Hrasnica[2], Senad Medić[3]

[1] Keller Grundbau GmbH, Vienna, Austria;
dzanic_z@yahoo.com
[2] Faculty of Civil Engineering, University of Sarajevo, Sarajevo, Bosnia and Herzegovina;
hrasnica@bih.net.ba
[3] Faculty of Civil Engineering, University of Sarajevo, Sarajevo, Bosnia and Herzegovina;
senad_medic@yahoo.com

In this paper is implemented a fully automated optimization procedure of reinforced concrete structures exposed to earthquakes by using GA (genetic algorithm) [1] optimization method. Given the extremely stochastic nature of the earthquake, its ultimate consequences, and possibly catastrophic consequences, special attention must be paid to solving this problem [2]. The behavior of structural systems under earthquake load was analyzed using nonlinear dynamic analysis. Nonlinearities are taken into account by using finite elements that can realistically describe the hysteresis behavior of reinforced concrete structures under cyclic loading. The problem of optimization of the structure comes down to achieving the optimal response of the structure under earthquake load with minimal material consumption. It should be emphasized that the main goal of optimization is to achieve a favorable, desired, response of the structure where minimum consumption of materials is a priority of lesser importance. The seismic load is modeled in the form of an artificially generated accelerogram whose response spectrum closely approximates the design acceleration spectrum that is defined by the corresponding seismic code [3]. The optimization procedure defines the target performance levels, with the imposed limits of the largest interstory drifts, for two levels of seismic load. The first target performance level refers to earthquakes of lower intensity and shorter return period and must prevent the occurrence of excessive damages. The second target performance level, represents earthquakes with the highest expected intensity in the observed area, with longer return periods. For this behavior level, the collapse of the building must be prevented. The first target performance level is also the main goal of the optimization procedure, and after the successful completion of this part of the calculation, the second part of the analysis (for the highest expected level of seismic load) is performed. A numerical example is defined as an irregular structure with sudden changes of geometry and stiffness. For analyzed example, optimization by using the GA method (which is directly connected to nonlinear dynamic analysis in an automated interactive process) has resulted in structures that fully meet the previously imposed constraints. The optimized structure has easily achieved an ideal (favorable) response to earthquakes.

References

[1] D.Kalyanmoy:Optimization for Engineering Desing, Algorithms and Examples,2012.
[2] FEMA P-58: FEMA P-58-1, Seismic Performance Assessment of Buildings, Volume 1 - Methodology , 2012. FEMA P-58-2, Seismic Performance Assessment of Buildings, Volume 2 - Implementation Guide ,2012.
[3] Eurocode 8: Design of structures for earthquake resistance – Part 1: General rules, seismic actions and rules for buildings, 2004.

ECCOMAS MSF 2021 THEMATIC CONFERENCE
30 June – 2 JULY 2021, SPLIT, CROATIA

ESTIMATION OF DIGITAL VOLUME CORRELATION MEASUREMENT UNCERTAINTY ON POLYMER COMPOSITES WITH DIFFERENT FIBER ARCHITECTURES

Zvonimir Tomičević[1], Ante Bartulović[2], Ante Bubalo[3], François Hild[4]

[1] University of Zagreb, Faculty of mechanical engineering and naval architecture, Ivana Lučića 5, 10002 Zagreb, Croatia, zvonimir.tomicevic@fsb.hr
[2] INETEC – Institute for Nuclear Technology, Dolenica 28, 10250 Lučko, Croatia, ante.bartulovic@inetec.hr
[3] Yazaki Europe Limited, Slavonska Avenija 26/6, 10000 Zagreb, Croatia, ante.bubalo@yazaki-europe.com
[4] Université Paris-Saclay, ENS Paris-Saclay, CNRS, LMT - Laboratoire de mécanique et technologie, 91190 Gif-sur-Yvette, France, francois.hild@ens-paris-saclay.fr

X-ray computed tomography (XCT) is nowadays a comprehensive non-destructive technique for inspection of composite materials [1, 2]. Further, high resolution 3D images of the underlying microstructure can be used for ex-situ or in-situ monitoring of damage inception and growth as a function of loading. The kinematics in the bulk of the composite material, due to the applied load, can be measured via Digital Volume Correlation (DVC) [3]. The first challenge when dealing with 3D images is that the actual microstructure of the material can hardly be modified in the bulk in order to enhance contrast. Second, the characterization of materials can be limited by artifacts that arise in the reconstruction procedure. These image imperfections are introduced by numerous sources [4] and they can be recognized as gray level variations or specific features. Because of acquisition noise, reconstruction artifacts, and the registration procedure, perfect match between the reference and deformed volumes is never achieved. Hence, it is necessary to the conduct *a priori* analyses of the measurement protocol in order to evaluate the measurement uncertainties.

Measurement uncertainties are evaluated by performing DVC analyses between acquired reference and artificially deformed scans [5] (*e.g.* adding noise and/or prescribing known motions) or on real test cases [6]. The method applied in this work consists in analyzing two consecutive scans of the sample in an unloaded state without additional rigid body motions. The main advantage of this protocol is that both sources of error are investigated at the same time for the material of interest.

Since image registration techniques face a considerable challenge, namely, their ill-posedness, there is an unavoidable compromise to be made between measurement uncertainty and spatial resolution [7]. In order to estimate commonly encountered strains, the uncertainty on displacements should be at most equal to 10^{-1} voxel [3].

In this work, measurement uncertainties are evaluated on a vinylester resin reinforced with four different glass fiber architectures, namely, mat (MAT), cross-directional (CD), unidirectional (UD) and woven fabric (WF) layers. The quantitative information about the composite architecture, fiber misalignments, manufacturing defects of the investigated GFRP composites are shown in Figure 1. Two consecutive scans of each GFRP were acquired with the same acquisition parameters with the *Werth Tomoscope S* scanner. The series of 800 radiographs per scan were used to reconstruct 3D images of the sample. The (cropped) initial scan size was 1133 × 1133 × 1461 voxels. The extracted volumes with an 8.8 µm/voxel resolution covered approx. 5.1 × 6 × 9 mm^3. In terms of image contrast for DVC analyses, it is observed that CD, UD and WF GFRP composites lead to low image gradients, and thus are more challenging for DVC analyses.

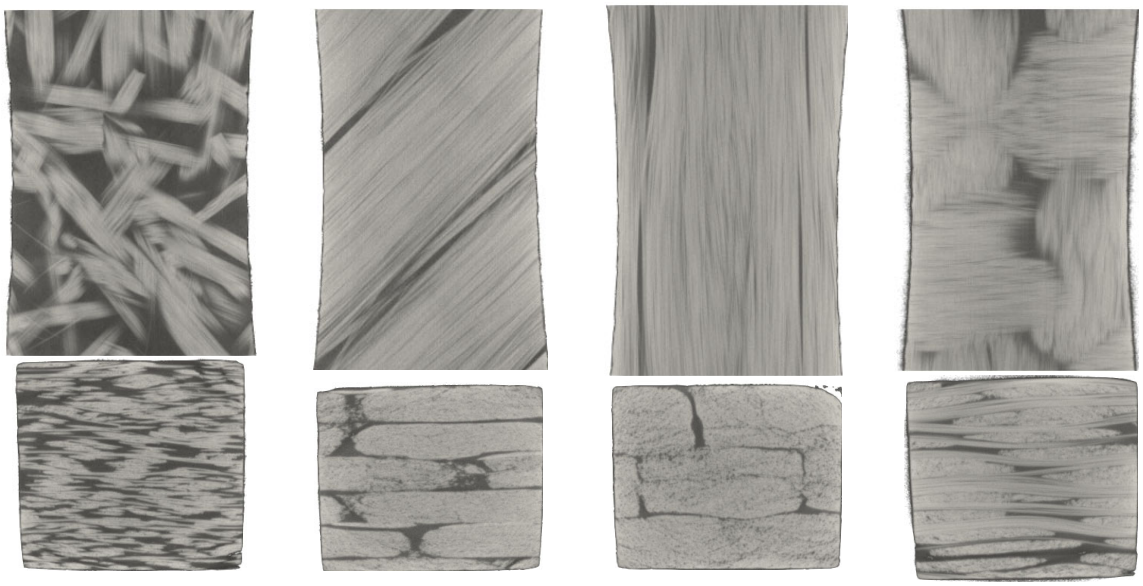

a) b) c) d)

Figure 1: Front and top mid slices of a) MAT, b) CD, c) UD and WF GFRP samples

The FE-DVC Correli 3.0 framework [8] was employed to measure 3D displacement fields to evaluate the uncertainty levels as functions of the element size. Thus, nine FE meshes were constructed over the same Region of Interest (ROI) with different element sizes ($90 < \ell < 8$ voxels). From the measured displacement fields, the measurement uncertainty was calculated as the standard deviation of the displacement field (Figure 2). The lowest uncertainty levels were achieved for the MAT fiber architecture, which was the most contrasted (Figure 1). In order to satisfy the criterion that 10^{-1} voxel standard displacement uncertainty be achieved, elements less than 12 voxels should not be used. For the CD GFRP composites, higher measurement uncertainties are reported. The acceptable element size should be at least 30 voxels. Finally, for the UD and WF laminates, approximately the same uncertainty levels are observed, where the smallest element size that could be used with satisfactory uncertainty is equal to 80 voxels.

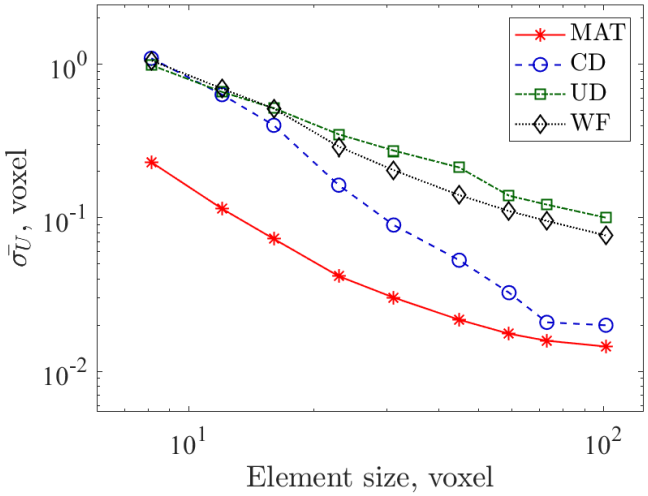

Figure 2: Mean standard displacement uncertainties as functions of the element size for the four analyzed composites (Figure 1)

From the presented results, it is concluded that the measurement uncertainty strongly depends on the fiber architecture of the observed samples. Further, the material microstructure defines the gray level histograms (Figure 3) and the distribution of the gray level (GL) over the entire ROI. The MAT GFRP microstructure provides a bimodal GL histogram while the other samples follow left skewed distributions. The lowest measurement uncertainty reported for the MAT architecture is correlated to the widest GL distribution. Conversely, the UD sample uses just partially the full dynamic range, thereby resulting in the highest uncertainty levels. The proposed study confirms the importance of performing such *a priori* DVC uncertainty analyses before dealing with mechanically deformed images since contrast and acquisition quality strongly impact the reliability of the measured displacements.

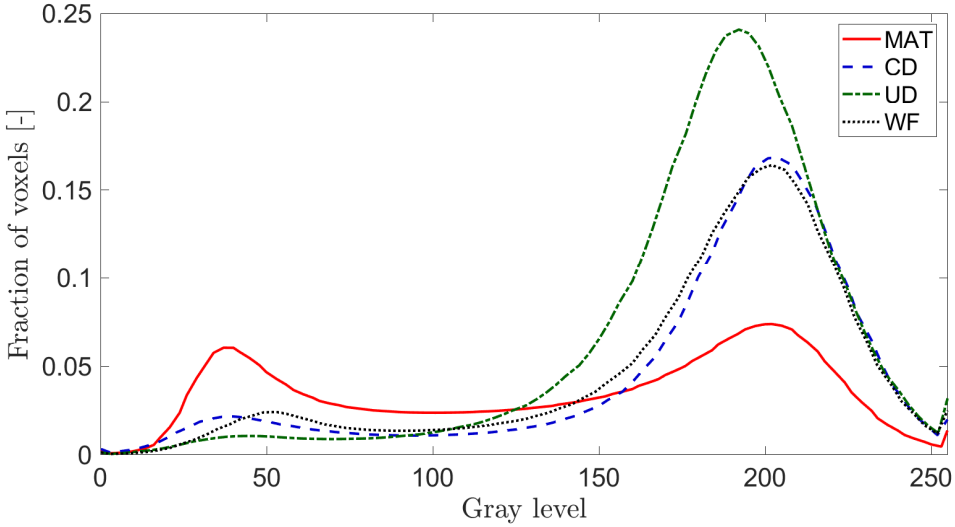

Figure 3: Gray level histograms of the four investigated GFRP composites

Acknowledgements

This work was performed within the FULLINSPECT project supported by the Croatian Science Foundation (UIP-2019-04-5460 Grant). We acknowledge the company Yazaki Europe Limited for provision of Werth Tomoscope S XCT scanner. The authors would also like to express their sincere gratitude to D. Zorica and J. Ribarić for numerous discussions and help in scanning the GFRP samples

References

[1] S.C. Garcea, Y. Wang, P.J. Withers. *X-ray computed tomography of polymer composites*, Compos. Sci. Technol., 156: 305-319, 2018

[2] E. Maire and P. J. Withers. *Quantitative X-ray tomography*, Int. Mater. Rev., 59(1): 1-43, 2014

[3] A. Buljac, C. Jailin, A. Mendoza, J. Neggers, T. Taillandier-Thomas, A. Bouterf, B. Smaniotto, F. Hild, S. Roux. *Digital Volume Correlation: Review of Progress and Challenges*, Exp. Mech., 58: 661–708, 2018

[4] G.R. Davis, J.C. Elliot. *Artefacts in x-ray microtomography of materials.* Mater. Sci. Eng., 22(9): 1011–1018, 2006

[5] S. Roux, F. Hild, P. Viot, D. Bernard, *Three-dimensional image correlation from X-ray computed tomography of solid foam*, Compos. Part A-Appl. S., 39: 1253-1265, 2008

[6] A. Buljac, T. Taillandier-Thomas, L. Helfen, T.F. Morgeneyer, F. Hild. *Evaluation of measurement uncertainties of digital volume correlation applied to laminography data*, J. Strain Anal. Eng., 53(2): 49-65, 2018

[7] H. Leclerc, J.-N. Périé, F. Hild, S. Roux, *Digital volume correlation: what are the limits to the spatial resolution?*, Mech. Ind., 13: 361-371, 2012

[8] H. Leclerc, J. Neggers, F. Mathieu, F., Hild, S. Roux, *Correli 3.0*, DOI: IDDN.FR. 001.520008.000.S.P.2015.0.0.0.31500

Index of authors

Proceedings:
P. Moreno-Navarro, E. Hadžalić

Local organizing committee:
A. Ibrahimbegovic, M. Nikolić, G. Grozdanić, E. Hajdo, E. Hadžalić,
I. Imamović, E. Karavelić